

Transactions of the ASME®

HEAT TRANSFER DIVISION
Chairman, J. R. LLOYD
Secretary, A. S. ADORJAN
Technical Editor, G. M. FAETH
Associate Technical Editor,
J. V. BECK
Associate Technical Editor,
I. CATTON
Associate Technical Editor,
R. GREIF
Associate Technical Editor,
H. R. JACOBS
Associate Technical Editor,
P. J. MARTO
Associate Technical Editor,
D. M. McELIGOT
Associate Technical Editor,
R. H. PLETCHER
Associate Technical Editor,
W. A. SIRIGNANO
Associate Technical Editor,
R. VISKANTA

BOARD ON COMMUNICATIONS
Chairman and Vice President
K. N. REID, JR.

Members-at-Large
J. T. COKONIS
M. FRANKE
M. KUTZ
F. LANDIS
J. R. LLOYD
T. C. MIN
R. E. NICKELL
R. E. REDER
R. ROCKE
F. W. SCHMIDT
W. O. WINER

President, R. ROSENBERG
Executive Director,
D. L. BELDEN
Treasurer,
ROBERT A. BENNETT

PUBLISHING STAFF
Mng. Dir., Publ., JOS. SANSONE
Managing Editor,
CORNELIA MONAHAN
Sr. Production Editor,
VALERIE WINTERS
Editorial Prod. Asst.,
MARISOL ANDINO

Transactions of the ASME, Journal of Heat Transfer (ISSN 0022-1481) is published quarterly (Feb., May, Aug., Nov.) for \$150 per year by The American Society of Mechanical Engineers, 345 East 47th Street, New York, NY 10017. Second class postage paid at New York, NY and additional mailing offices. POSTMASTER: Send address changes to The Journal of Heat Transfer, c/o THE AMERICAN SOCIETY OF MECHANICAL ENGINEERS, 22 Law Drive, Box 2300, Fairfield, NJ 07007-2300.

CHANGES OF ADDRESS must be received at Society headquarters seven weeks before they are to be effective. Please send old label and new address.

PRICES: To members, \$27.00, annually; to nonmembers, \$150.00.

Add \$12.00 for postage to countries outside the United States and Canada.

STATEMENT from By-Laws. The Society shall not be responsible for statements or opinions advanced in papers or . . . printed in its publications (B7.1, para. 3).

COPYRIGHT © 1988 by the American Society of Mechanical Engineers. Reprints from this publication may be made on condition that full credit be given the

TRANSACTIONS OF THE ASME,
JOURNAL OF HEAT TRANSFER,
and the author, and date of
publication be stated.

INDEXED by Applied Mechanics Reviews
and Engineering Information, Inc.

Journal of Heat Transfer

Published Quarterly by The American Society of Mechanical Engineers

VOLUME 110 • NUMBER 1 • FEBRUARY 1988

ANNOUNCEMENTS

- 2 1987 Heat Transfer Referees
- 213 Change of address form for subscribers

TECHNICAL PAPERS

- 5 *Max Jakob Memorial Award Lecture: Heat Transfer Research for Ocean Thermal Energy Conversion*
F. Kreith and D. Bharathan
- 23 Stochastic Analysis of Temperature Distribution in a Solid With Random Heat Conductivity
Da Yu Tzou
- 30 Methodology for Comparison of Inverse Heat Conduction Methods
M. Raynaud and J. V. Beck
- 38 Thermal Contact Conductance of Packed Beds in Contact With a Flat Surface
G. P. Peterson and L. S. Fletcher
- 42 Rectangular Heat Source on a Semi-infinite Solid—an Analysis for a Thin Film Heat Flux Gage Calibration (84-HT-46)
N. R. Keltner, B. L. Bainbridge, and J. V. Beck
- 49 Transient Temperature Fields in Crossflow Heat Exchangers With Finite Wall Capacitance
M. Spiga and G. Spiga
- 54 Thermal Effectiveness of Multiple Shell and Tube Pass TEMA E Heat Exchangers
A. Pignotti and P. I. Tamborenea
- 60 Shellside Waterflow Pressure Drop Distribution Measurements in an Industrial-Sized Test Heat Exchanger
H. Halle, J. M. Chenoweth, and M. W. Wambsgans
- 68 Heat Exchanger Shellside Pressure Drop: Comparison of Predictions With Experimental Data
R. S. Kistler and J. M. Chenoweth
- 77 The Effect of Condensible Impurities in the Working Fluid on the Performance of Cryogenic Regenerators
R. K. Sahoo and S. Sarangi
- 84 Heat Transfer From a Flat Surface to an Oblique Impinging Jet
R. J. Goldstein and M. E. Franchett
- 91 Local Heat/Mass Transfer Distributions Around Sharp 180 deg Turns in Two-Pass Smooth and Rib-Roughened Channels (86-GT-114)
J. C. Han, P. R. Chandra, and S. C. Lau
- 99 Natural Convection From a Vertical Heat-Generating Fin—a Conjugate Problem
P. K. Sarma, T. Subrahmanyam, and V. Dharmarao
- 103 Natural Convection Along Slender Vertical Cylinders With Variable Surface Temperature
H. R. Lee, T. S. Chen, and B. F. Armaly
- 109 Heat Transfer by Natural Convection of Helium Between Horizontal Isothermal Concentric Cylinders at Cryogenic Temperature
E. H. Bishop
- 116 Transient Natural Convection Between Two Zones in an Insulated Enclosure
P. A. Litsek and A. Bejan
- 126 Turbulent Thermal Convection in an Enclosure With Internal Heat Generation
B. Farouk
- 133 Non-Darcy Natural Convection in a Saturated Horizontal Porous Annulus
K. Muralidhar and F. A. Kulacki
- 140 Asymptotic Solution for Thermocapillary Flow at High and Low Prandtl Numbers Due to Concentrated Surface Heating
C. L. Chan, M. M. Chen, and J. Mazumder
- 147 Mixed Convection in a Liquid-Saturated Porous Medium
D. C. Reda
- 155 Effect of Maximum Density of Water on Freezing of a Water-Saturated Horizontal Porous Layer
M. Sugawara, H. Inaba, and N. Seki
- 160 Theoretical Analysis of Weld Pool Behavior in the Pulsed Current GTAW Process
C. L. Tsai and C. A. Hou

(Contents continued)

- 166 **Measurement of Total Hemispherical Emissivities of Metal Wires by Using Transient Calorimetric Technique**
H. Masuda and M. Higano
- 173 **Structure and Radiation Properties of Luminous Turbulent Acetylene/Air Diffusion Flames**
J. P. Gore and G. M. Faeth
- 182 **Structure of the Stabilizing Region of a Laminar Jet Diffusion Flame**
F. Takahashi, M. Mizomoto, and S. Ikai
- 190 **Group Combustion of a Cylindrical Cloud of Char/Carbon Particles**
K. Annamalai, S. Ramalingam, T. Dahdah, and D. Chi
- 201 **A Physical Model of the Evaporating Meniscus**
A. Mirzamoghadam and I. Catton
- 208 **Holographic Interferometry Investigation of Enhanced Tube Meniscus Behavior**
A. V. Mirzamoghadam and I. Catton
- 214 **Dynamics of Droplets Impacting on Thin Heated Strips**
S. C. Yao, L. E. Hochreiter, and K. Y. Cai
- 221 **Nucleate Boiling in Thermally Developing and Fully Developed Laminar Falling Water Films**
M. Cerza and V. Sernas
- 229 **An Experimental Study of Convective Boiling in a Partially Heated Horizontal Channel With Offset Strip Fins**
G. D. Mandrusiak, V. P. Carey, and X. Xu
- 237 **Experimental Measurement of Water Evaporation Rates Into Air and Superheated Steam**
M. Haji and L. C. Chow
- 243 **Heat Transfer-Based Reconstruction of the Concepts and Laws of Classical Thermodynamics**
A. Bejan

TECHNICAL NOTES

- 250 **Transient Temperature Resulting From Periodic On-Off Heat Flux for a Semi-Infinite Medium**
D. E. Glass and M. N. Özışık
- 252 **Heat Transfer in Laminar Flow Along Circular Rods in Infinite Square Arrays**
J. H. Kim and W.-H. Li
- 257 **Free Convection Flow of Non-Newtonian Fluids Along a Vertical Plate Embedded in a Porous Medium**
Han-Taw Chen and Cha'o-Kuang Chen
- 260 **The Mushy Zone in a Phase Change Model of a Semitransparent Material With Internal Radiative Transfer**
S. H. Chan and K. Y. Hsu
- 264 **Radiation Shape Factors for Channels With Varying Cross Sections**
T. L. Eddy and G. E. Nielsson
- 266 **Pool Boiling Enhancement of a Modified GEWA-T Surface in Water**
Z. H. Ayub and A. E. Bergles
- 268 **Effect of Surface Curvature on Laminar Film Condensation**
K. Taghavi
- 270 **Transient Experimental Technique for the Determination of the Thermal Diffusivity of Fibrous Insulation**
S. P. Rooke and R. E. Taylor

Heat Transfer Research for Ocean Thermal Energy Conversion

F. Kreith

University of Colorado,
Boulder, CO 80309

D. Bharathan

Solar Energy Research Institute,
Golden, CO 80401

In this lecture an overview of the heat and mass-transfer phenomena of importance in ocean thermal energy conversion (OTEC) is presented with particular emphasis on open-cycle OTEC systems. Also included is a short historical review of OTEC developments in the past century and a comparison of open and closed-cycle thermodynamics. Finally, results of system analyses, showing the effect of plant size on cost and the near-term potential of using OTEC for combined power production and desalination systems, are briefly discussed.

1 Introduction

The temperature difference between surface and deep water in the oceans represents a vast resource of thermal energy. A promising method for harnessing this resource is an ocean thermal energy conversion (OTEC) system that uses this temperature difference to operate a Rankine cycle system. Such OTEC power generation systems can be either open cycle or closed cycle. In a closed-cycle OTEC system, a working substance with low boiling point, such as ammonia or freon, is evaporated by warm surface water. The resulting vapor drives a turbine. The vapor is then condensed at the turbine outlet by cold seawater from the lower depth of the ocean. An example of such a system is the 100-kW pilot plant installed at Nauru shown in Fig. 1 [1].

In an open-cycle OTEC system, warm seawater from the surface at about 25°C is introduced into the evaporator section of a vacuum chamber in which the pressure is maintained below the vapor pressure of the incoming water. Thus, flash evaporation occurs, producing steam. The steam expands through a turbine placed between the evaporator and the condenser section where cold water at about 5°C pumped from a depth of about 1000 m is used to condense the steam. The turbine is mechanically linked to a generator that yields net power after providing the power required to pump the warm and cold water and to remove noncondensable gases released in the vacuum chamber. The condenser can be either direct contact, surface, or a combination of the two. A surface condenser can provide fresh water as a byproduct. An example of an open-cycle OTEC system is the proposed US Department of Energy (DOE) 165-kW pilot plant planned for construction in Hawaii and shown in Fig. 2 [2].

A closed Rankine cycle OTEC system was originally proposed by D'Arsonval [3] in 1881, and in 1930, Claude [4] demonstrated the operation of an open-cycle process off the coast of Cuba. In Claude's demonstration, surface water was flash-vaporized at 3 kPa to drive a turbine and was then condensed by direct contact with water at 11°C drawn from 700-m depth through a 1.6-m-dia, 1.75-km-long cold-water pipe (CWP). The first closed-cycle OTEC system was placed in operation on Aug. 2, 1979, on a barge moored 2 km off Keahole Point on the island of Hawaii. This system, called Mini-OTEC, is shown in Fig. 3; it provided the first demonstration of net power generation (10–15 kW electric) [5]. A somewhat larger power plant was installed in the

Republic of Nauru in Oct. 1981 by the Tokyo Electric Power Company and the Toshiba Corporation under the Japanese Sunshine Project [1].

In addition to the Japanese and American projects, French and Dutch engineers have recently conducted feasibility studies for OTEC plants on various islands in the South Pacific [6, 7]. DOE's current plans in the United States include constructing experiments at the Natural Energy Laboratory of Hawaii, and Japan plans to build an OTEC power plant on Okinawa.

2 Comparison of Open and Closed-Cycle Systems

For a given temperature potential, the open-cycle OTEC system is thermodynamically superior to the closed-cycle system because a larger portion of the temperature difference between the hot and the cold water is available to produce net power. This is because of the direct-contact heat transfer mode of the evaporator and condenser, as used in the open-cycle system. The steam in the vacuum chamber can attain the temperature of the warm water discharged from the evaporator. At the same time, the exhaust steam from the turbine can be condensed at a temperature approaching the condenser cold water exit temperature.

In a closed-cycle system, the working fluid passing through the turbine is separated from the warm and cold waters by a solid wall. Hence, in both the evaporator and the condenser, a temperature drop is necessary first to transfer the heat from the water through the wall to produce the vapor in the boiler, and then another temperature drop is required to condense the vapor of the working fluid at the outlet from the turbine by cold seawater. Consequently, the heat exchangers for closed-cycle OTEC plants require very large surface areas to minimize the thermodynamically required temperature losses. These exchange surfaces are continuously exposed to corrosion and biofouling in the harsh ocean environment. On the other hand, the turbine in a closed-cycle OTEC system is relatively small and is available as an "off-the-shelf" item. But, because of the low pressure in which the turbine must operate in the open-cycle system, the turbine is very large, and so far, no full-scale turbines for plants 1 MW and greater have been designed and operated.

Any ocean thermal energy conversion system faces the enormous challenge of producing net power with a temperature difference on the order of 20°C. Since the Carnot efficiency of such a plant is only on the order of 6 or 7 percent, any successful ocean energy conversion system must use as much of

Contributed by the Heat Transfer Division and presented at the ASME/JSME Thermal Engineering Joint Conference, Honolulu, Hawaii, March 22–27, 1987. Manuscript received by the Heat Transfer Division October 13, 1987.

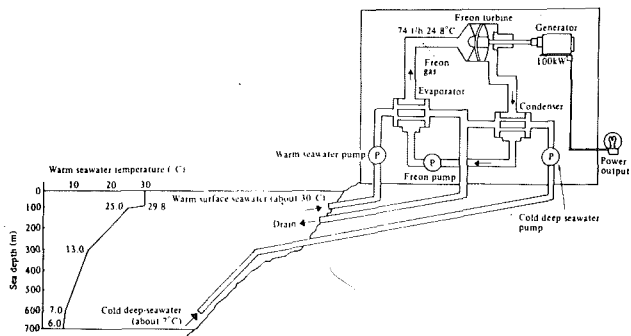


Fig. 1 Block diagram of 100-kW OTEC power plant at Nauru

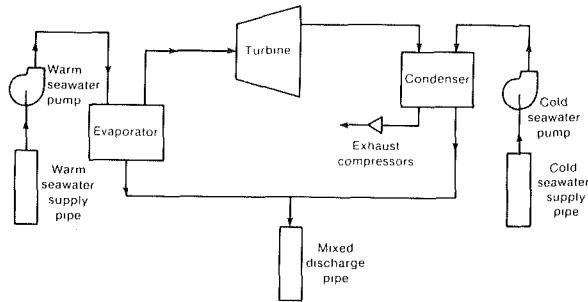


Fig. 2 Flow diagram and conceptual layout of the 165-kW OC-OTEC experiment

the temperature potential as possible and, at the same time, reduce parasitic losses to a minimum. The major parasitic losses in ocean thermal systems are the pumping power required to bring the cold water from a depth of about 1000 m to the surface, the power required to remove noncondensable gases in the open-cycle system, and the degradation of the available thermal energy by temperature drops across the heat transfer surfaces of a closed-cycle system.

In the final analysis, the decision whether or not to build an OTEC system will be based on economic, not thermodynamic criteria. As discussed in the System Analysis Section later, system tradeoff studies have shown that for pure electric power production in the range of 5 to 10 MW, land-based open-cycle plants are superior to closed-cycle configurations [8]. However, in applications where power production can be economically combined with desalination of seawater, systems with a direct-contact evaporator and two condensers, one a surface type for desalination and the other a direct-contact type, are economically optimum system configurations.

3 Review of Direct-Contact Evaporation and Condensation

There are four general classifications for direct-contact gas (or vapor) to liquid heat transfer: simple gas cooling, gas cool-



Fig. 3 Mini-OTEC moored off Keahole Point in Hawaii

ing with vaporization, gas cooling with partial condensation, and gas cooling with total condensation. These processes are very complex, and each of them is described by a separate set of relations. Direct-contact heat-exchange has traditionally been accomplished in one of the following devices: baffle tray columns, spray chambers, packed columns, cross-flow tray columns, or pipeline contactors. Schematics of some gas-liquid contact devices are shown in Fig. 4. Design methods for these were summarized in 1961 and 1972 by Fair [9]. The most common techniques used in industrial applications are the liquid spray column and the baffle plate column. Fair has compared these devices and shown that they typically have a performance in which the number of transfer units (NTU) is only about 1. This value is so low because back-mixing usually occurs, and in baffle columns there is also a large gas-side pressure drop. This is a particular disadvantage for OTEC applications where minimizing parasitic power consumption is of prime importance.

In addition to liquid spray and baffle plate columns, packed columns have been used in applications where a large rate of heat and mass transfer per unit volume was required. Until recently, the packings or inserts used in the columns were randomly distributed and thus created a very complex flow pattern with a large pressure loss (Fig. 5). In the past decade or so, however, new types of packing have been introduced in the United States, which in contrast to the classical, randomly placed packing elements are fitted in an ordered and structured manner in the column to carefully match its size and operation. These structured packings have shown excellent performance characteristics. In particular, they yield a relatively low ratio of pressure drop to heat- or mass-transfer coefficient per unit volume [10, 11].

Although the cost per unit volume of structured packings is higher than that of classical packings, their favorable efficiency and pressure drop characteristics make these packings preferable for many applications, especially when operating in a vacuum such as an OTEC condenser. These new packings also provide a means of continually redistributing the liquid flow, while supplying a relatively straight flow path for the vapor, which reduces the pressure drop to a minimum. Such packings made of plastic sheets have been used for some time in cooling towers (Fig. 6), but recent improvements in manufacturing have made those packings available in the form of gauze or wire-mesh sheets. These surfaces allow vapor-to-liquid contact on both sides and also provide for uniform liquid distribution due to capillary action. Structured gauze sheet packings increase the residence time of the liquid, and available data show that the entire area of the packing can be effective in mass transfer. These high-performance packings have been developed in Europe, and, unfortunately, per-

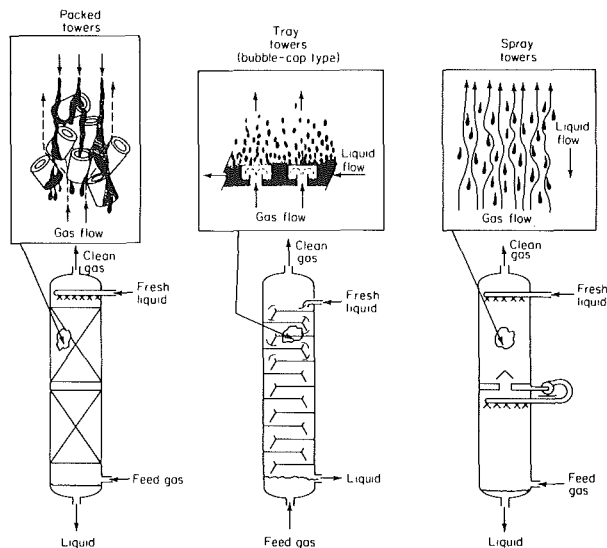


Fig. 4 Schematics of gas-liquid direct-contact transfer devices

formance data have been largely proprietary, although some design equations for gauze structured packings have been published recently by Bravo et al. [10, 11] over a limited range of operating parameters.

SERI began a research program in 1983 to develop a better understanding of the mode of operation of various packings for direct-contact heat and mass transfer and to provide experimental data with which a predictive model could be developed. SERI experiments have shown that with sheet-type packing a large percentage of the area is active [12] for condenser applications at high liquid loadings. This result is consistent with the correlation and analysis of Bravo et al. [10], which suggest that by using gauze the entire area can become effective even at low liquid loadings and that because of liquid mixing induced by the gauze the transfer process is gas-side controlled. Structured packing is expected to improve the performance characteristics of OC-OTEC direct-contact condensation over that obtainable with other types of contact devices.

Direct-contact condensers have potential in many process applications as well as in power plants. Probably one of the main reasons why direct-contact condensers are currently not more widely used is that engineers do not have reliable design and performance prediction methods. Direct-contact condensers are difficult to analyze because:

- 1 Vapor loading and heat and mass flux decrease continuously as condensation occurs.

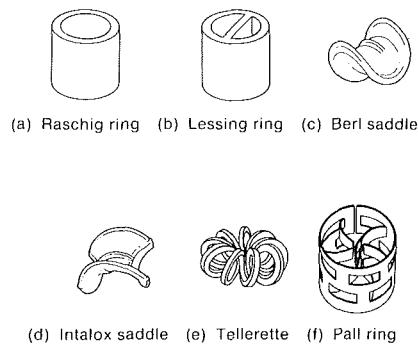
- 2 The latent heat of condensation is high and therefore a large ratio of liquid-to-vapor mass flux occurs (this is not typical of the mass transfer experience, and very little experimental data are available for that range of load ratios).

- 3 The velocity of the vapor in a direct-contact device varies appreciably with the distance traveled because continuous condensation is taking place; hence, use of average values of heat or mass-transfer coefficients for design are not sufficiently accurate.

- 4 Under most conditions, especially with seawater, non-condensable gases are present and their effects on the gas mass-transfer rates are difficult to predict quantitatively under constantly varying flows.

- 5 Finally, in many practical situations, transition from turbulent to laminar flow occurs; laminarization is not well understood in general and difficult to quantify under condensation conditions.

For all of these reasons the widely used NTU design



Source: Chemical Engineers Handbook

Fig. 5 Typical random packings for heat and mass-transfer processes

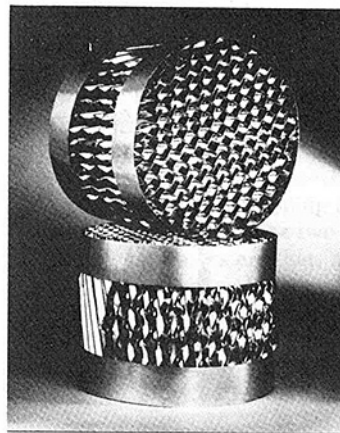


Fig. 6 Sheet-type structured packing (courtesy of Munters Corp.)

methodology will generally not suffice [13, 14] because the transfer coefficients are not uniform as assumed by this approach. Hence, it is necessary to integrate the rate of transfer numerically along the path of the vapor.

In his 1961 pioneer article presenting design methods for gas-liquid direct-contact heat transfer, Fair [9] noted that design information was more in the realm of proprietary art than based on solid engineering know-how. This situation was reconfirmed in the NSF-sponsored workshop on "Direct-Contact Heat Transfer" recently held at SERI [15]. Consequently, despite the attractiveness of direct-contact heat and mass-transfer devices, stemming from their simplicity, potential economy, and ability to handle a wide variety of fluids under unfavorable conditions that would cause excessive fouling, corrosion, or thermal stresses in conventional equipment, direct-contact heat transfer equipment has not been widely used. It is our hope and expectation that the research carried on as part of the DOE OTEC program will assist in providing information that not only can be applied to improving OTEC design methodology but can also be transferred to industrial applications that can use direct-contact transport to decrease equipment cost and reduce operational problems.

4 SERI Direct-Contact Transport Research Facility

In a typical OC-OTEC plant, approximately 15 kg/s of steam per 1 MW electric gross output must first be evaporated at about 25°C, then passed through a turbine and finally be condensed at a temperature of about 10°C. The mass fraction of noncondensable gases may vary from less than 1 percent up to 40 percent in the condenser as the exhaust steam from the turbine is progressively condensed. To provide the required heat sink, on the order of 3 m³/s of cold seawater per 1-MW_e of power output is required. The head loss in the cold water

Table 1 SERI direct-contact laboratory capabilities

Test condition	Warm-water loop	Cold-water loop
Heat input	0-300 kW	-
Heat rejection	-	0-300 kW
Temperature	3-30°C	3-30°C
Water flow rate	50 kg/s	50 kg/s
Vacuum threshold pressure	800 Pa	800 Pa
Leak rate (less than)	0.005 g/s	0.005 g/s
Vent capacity	0.57 m ³ /s	0.57 m ³ /s

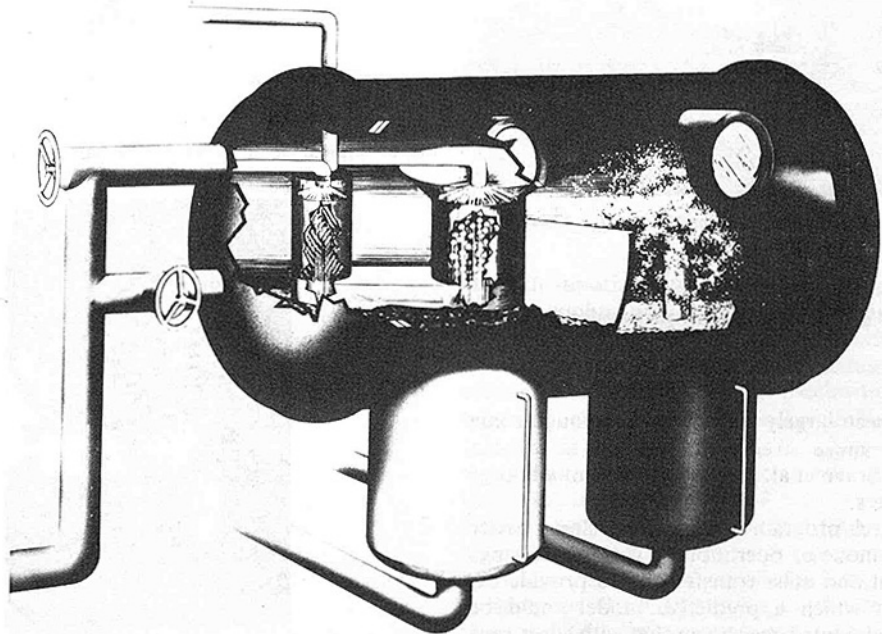


Fig. 7(a)

pipe, which typically extends 1 km below sea level, is about 5 m. Normally, a free fall of 2 m is available for the condenser, but each additional meter of head loss can reduce the OTEC power output up to 3 percent.

In addition to condensing the steam, the condenser must also efficiently concentrate noncondensable gases that come out of solution from the water and leak in from the atmosphere. Thus, the performance of the noncondensable gas removal system affects the overall OTEC plant efficiency. In a typical condenser, the steam from the turbine first enters a cocurrent condenser section where about 70 percent of the steam is condensed. The remainder then passes through a countercurrent section where condensation continues. This process enriches the inert gas to a mass fraction of about 30 percent in the mixture which must then be exhausted to atmosphere by the NCGR (noncondensable-gas-removal) system. The parasitic power consumed by the gas removal is between 10 and 15 percent of the gross output, and the performance of the NCGR system is therefore closely linked to that of the condenser.

The direct-contact heat and mass-transfer research facility at SERI was designed to study and improve methods of transferring heat and mass under small driving forces in a vacuum. Current investigations deal with innovative, direct-contact evaporation and condensation devices for OTEC systems, but the laboratory facilities are quite flexible and can be used for other problems, such as thermo-electric power conversion, concentration of liquid solutions by flash evaporation, vacuum drying, material degradation in vacuum environments, gas sorption and desorption from liquids, and other continuous and staged separation operations. An ability to introduce impurities allows less than ideal plant or process conditions to be examined.

The laboratory can supply 300 kW to a warm-water loop

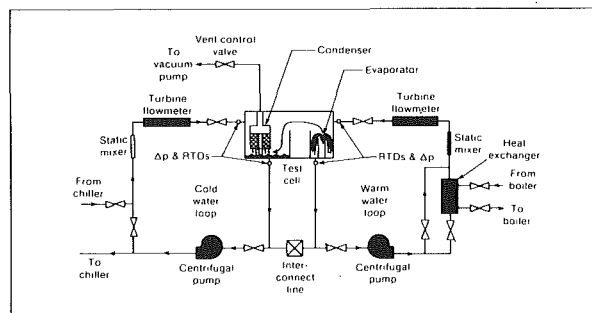


Fig. 7(b)

Fig. 7 Artist's sketch of test cell (a) and schematic (b) of SERI direct-contact evaporation and condensation test facility

with a gas-fired boiler and remove 300 kW from a cold-water loop with a vapor compression chiller (see Table 1). The warm and cold-water loops can exchange heat and mass through a variety of exchangers. The present setup uses an evacuated test cell with the warm water flowing through an evaporator at one end and cold water flowing through a condenser at the other (Fig. 7a). Heat and mass are exchanged by the warm water evaporating and the vapor condensing in a direct-contact condenser on the cold water side. Figure 7(b) is a schematic of the laboratory. Two pumps located 4 m below the waterline maintain a static head to prevent cavitation. After leaving the pumps, part of the cold water may be directed through a chiller and part of the warm water through a shell-and-tube heat exchanger fed with hot water from a boiler. The chilled or heated water recombines with the direct stream in static mixers.

The currently used test cell is a horizontal cylindrical steel vacuum chamber, 1.2 m in diameter and 1.8 m long. Reservoirs underneath the evaporator and the condenser sections

provide for separate water collections. Windows are provided for lighting, viewing, and photographing flow patterns in direct contact processes. The cell is evacuated with a three-stage vacuum pump and a threshold pressure of 800 Pa can be attained in the cell.

5 Direct-Contact Evaporation

The mechanism by which steam is generated in an open-cycle OTEC system is called direct-contact or “flash” evaporation. This process occurs when warm seawater is introduced into the evaporator at a pressure below the vapor pressure corresponding to the liquid inlet temperature, and steam is produced by the combined action of boiling and surface evaporation. Flash evaporation is usually quite violent as a result of the explosive growth of vapor bubbles from nucleation sites in the liquid. The growth of these bubbles shatters the liquid continuum and yields a wide range of droplet sizes. Because of the irregular geometry of the interface, it is practically impossible to define or measure the surface area from which evaporation takes place. Heat transfer in flash evaporation, therefore, cannot be described in terms of a conventional heat transfer coefficient. To quantify the process and present experimental data, we will introduce another parameter: the effectiveness ϵ . The effectiveness of flash evaporation is defined as the ratio of the temperature difference between the inlet and outlet liquid streams to the temperature difference between the inlet liquid stream and the vapor temperature corresponding to the chamber saturation pressure. This definition is similar to the effectiveness of a conventional heat exchanger since it is the ratio of the temperature difference actually achieved to the maximum temperature difference thermodynamically available.

Maa [16] performed experiments of evaporation from laminar jets of various liquids and described the mechanism of heat transfer as occurring in two steps: the transfer from the bulk of the liquid to the interface at an intermediate temperature, followed by molecular mass transfer from the interface to the vapor. The overall transfer rate is governed by the molecular transport within the liquid and the differential rate of molecular crossings at the interface. For seawater at 25°C, the interfacial heat transfer resistance is extremely small compared with the resistance in the liquid. A freshly exposed interface cools from the bulk temperature to the vapor temperature in less than a millisecond, which is a hundredfold smaller than the typical liquid residence time in the flash chamber. The accompanying growth of a thermal boundary layer on the liquid side, where the major temperature gradient resides, penetrates a distance of only 5–12 μm . Since this thickness is small compared with the typical thickness of the liquid layer, flash evaporation can be treated as a surface phenomenon with the first surface losing its potential for evaporation extremely fast. For effective flash evaporation it is therefore imperative that a large interfacial area be available and that fresh surfaces be continually created.

For laminar jets heat transport on the liquid side is governed by molecular diffusion, whereas for turbulent jets, enhanced heat transport may be expected due to increased mixing caused by eddies in addition to the molecular diffusion. Reported works on experimental investigation of flash evaporation from turbulent jets are few, and in most cases the jets are “shattered” into discontinuous fragments and droplets. Brown and York [17] proposed flash evaporation as a means of producing a fine spray of liquid droplets for aerosol applications. Balitskiy and Shurchkova [18] observed in experimental studies of flash evaporation from 15-cm-long water jets of 1, 3, and 5 mm diameters that for a liquid superheat of over 7°C, the emerging jets shattered into a spray of droplets. Miyatake et al. [19] studied flash evaporation from cylindrical water jets of 3.5, 5.0, and 8.2 mm in diameter

and of 12, 25, and 25 cm in length, respectively, and with exit Reynolds numbers ranging from 66,000 to 155,000. Photographs of increased jet shattering with increasing superheat were presented. Mills et al. [20] presented data for evaporation from 4-mm-dia circular turbulent water jets of 95, 133, and 171 mm in length. In their experiments, they took precautions to maintain a coherent jet and prevent jet shattering due to cavitation. For a jet Reynolds number in the range of 3000 to 25,000, the average Stanton number for these jets was found to be 3 to 11 times larger than predictions based on laminar flow, suggesting that turbulent transport played a major role. Analytical modeling of heat transport in coherent unshattered turbulent jets is complicated by the effect of turbulent mixing, the distribution of the effective eddy mixing across the jet, and the decay of turbulence downstream. Theofanous et al. [21] attempted to model turbulent transport in jets to include all these effects, but further work is necessary to resolve this problem.

As described in a previous review paper [22], three different geometries initially contended for the choice of evaporator in OC-OTEC plants: open-channel flow, falling films, and falling jets. These options are shown schematically in Fig. 8, and their relative merits are discussed in [22]. The open-channel flow design cannot achieve high effectiveness because the exposed interfacial area is limited, and boiling is suppressed by the hydrostatic pressure of the liquid. The two main shortcomings of the falling-film evaporators are that, as a result of the explosive growth of vapor bubbles, coherent films cannot be maintained and the liquid distribution manifold obstructs the escape of vapor. Falling jets were investigated under OTEC conditions by Green et al. [23], Kreith et al. [24], and Bharathan and Penney [25] for countercurrent vapor flow and by Sam and Patel [26] for crosscurrent vapor flow. Collective

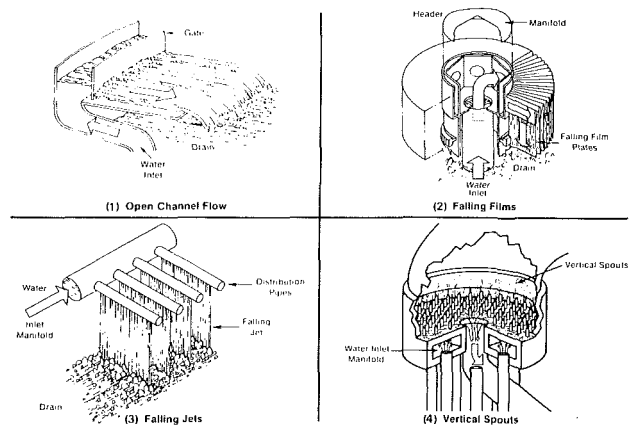


Fig. 8 Schematics of OTEC evaporator options initially considered

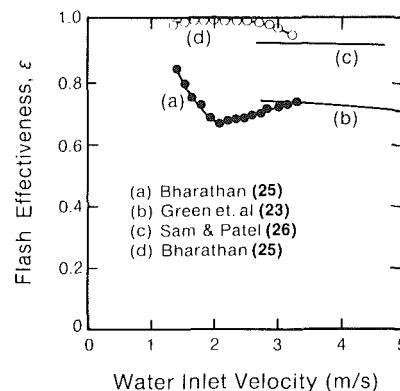


Fig. 9 Flash evaporator effectiveness as a function of water inlet velocity for falling jets

results for evaporation from flat jets are shown in Fig. 9 where the effectiveness is plotted versus jet inlet velocities. It was observed that the jets shatter into a spray of droplets when entering the evaporator. Green et al. [23] measured an evaporator effectiveness of 0.7 to 0.8 with deaerated water in countercurrent flow, while for crosscurrent flow an effectiveness of nearly 0.95 was achieved [25]. In both cases, the influences of initial water superheat and water flow rate were minimal. The differences between these results are ascribed to vapor flow losses incurred while passing through the water distribution manifold in the countercurrent experiments and the high initial air content of water in the experiments of Sam and Patel [26].

In early 1983, experiments were performed at SERI [25] on evaporation from a turbulent planar water jet in a configuration as shown in Fig. 10. Bharathan and Penney [25] found that the evaporation effectiveness of the jet was independent of initial jet thickness, indicating that once the jet shatters into droplets its initial thickness becomes irrelevant. These results confirmed the contention that evaporation is primarily controlled by the available interfacial surface area and the rate at which these surfaces are renewed. Following up on this hypothesis, screens were inserted in the jet to enhance its breakup. The variation in effectiveness with water inlet velocity is shown for several screen configurations in the planar jet in Fig. 11. With four screens to help the shattering process of the jet and renew the vapor liquid interfaces, an effectiveness approaching 1.0 was observed. Although extremely high effectiveness could be achieved by using screens in falling jets, the falling jet geometry requires a complex manifold liquid distribution system that results in additional vapor pressure losses and increases the required evaporator size.

Based upon these attempts to configure an effective OTEC

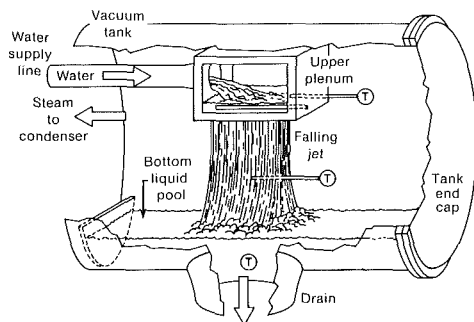


Fig. 10 Schematic of planar jet tested with different screen geometries

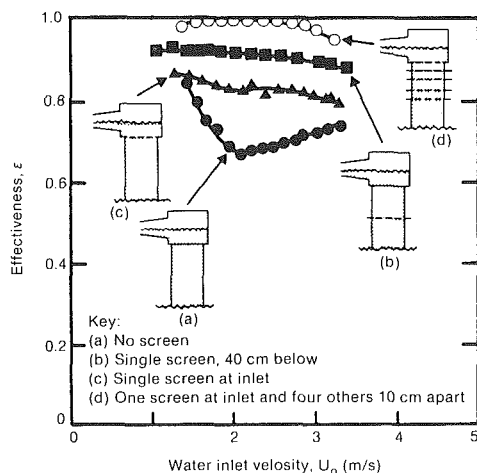


Fig. 11 Effects of single and multiple screens on effectiveness of planar jet

flash evaporation geometry, it was concluded that high evaporation effectiveness can be achieved irrespective of the inlet geometry, provided the liquid jet is broken up, large interfacial areas are exposed, and the vapor-liquid interfaces are continuously renewed. Thus, the design of an effective evaporator focused on the liquid distribution manifold to achieve low liquid and vapor pressure losses. This led to the development of an innovative evaporator design in which water is introduced into the evaporator through multiple vertical tubes that minimize pressure losses. This design, called the vertical spout evaporator, offers a simple liquid distribution, easy vapor separation with minimal obstructions in the vapor path, a low liquid pressure loss (0.5–0.7 m), and the potential of a modular evaporator design independent of plant size. The potential of this new concept was recognized by the Manufacturer's Association, who selected it to receive one of the IR100 awards in 1984 [27].

Extensive experiments were performed with vertical spout evaporators at the SERI Test Facility in 1983 and 1984. The arrangement in the test cell for these experiments with a single spout evaporator is shown in Fig. 12, and the effectiveness with and without screens is plotted as a function of water inlet velocity in Fig. 13. In all of these tests, the heat flux from the jet was maintained at 210 kW. The spout effectiveness measured in these tests varied between 0.90 and 0.97 with a liquid-side pressure drop of 0.7 m (spout height plus kinetic energy loss), somewhat less than for planar jets.

Photographs of the spout evaporator are shown in Fig. 14 with and without flashing. Case (a) shows that without evaporation the water jet exists smoothly and distributes itself as an axisymmetric sheet. Upon initiating evaporation by lowering the condenser inlet water temperature, bubbles begin to emerge from the spout and grow on the falling liquid sheet. Bubbles on the order of 10 cm in diameter can be seen at a heat flux of 100 kW [case (b)]. As the evaporation rate is further in-

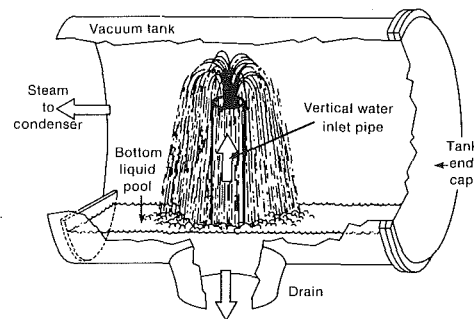


Fig. 12 Sketch of single-spout evaporator in SERI test chamber

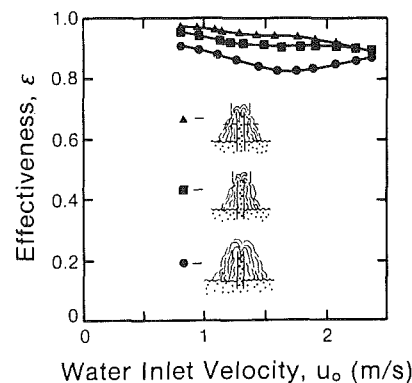


Fig. 13 Effectiveness of spout evaporator with and without screens versus water velocity

creased, the jet becomes more violent, vapor escapes from bursting bubbles, and explosive growth of the vapor shatters the jet into fragments and droplets. Most of the liquid escaping upward falls back on the incoming liquid and the coherent liquid sheet is totally destroyed, becoming a spray of droplets [case (c)]. The only disadvantage observed so far is that, because of its inherently low liquid-side pressure loss, the spout configuration is prone to water surges that could result from sea level fluctuations in an OTEC plant. For shore-based installations, hydraulic studies indicate that this is not a problem. Table 2 shows estimates of the improvements in the required water flow rates and the volumetric heat transfer coefficients achieved over the past five years with various design improvements for a 1-MW OC-OTEC system [28].

6 Direct-Contact Condensation

Direct-contact condensers were used widely in the 1920s when steam turbines were still relatively inefficient. These condensers used conventional spray nozzles that required a high

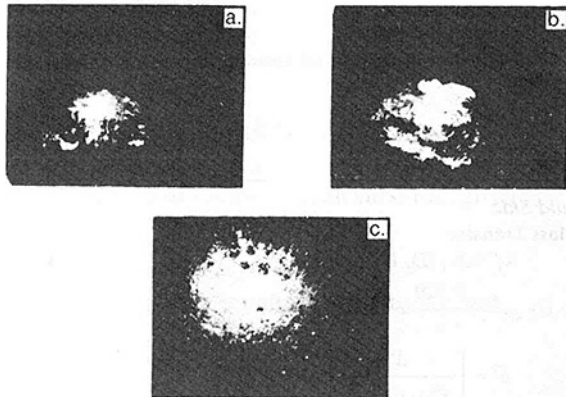


Fig. 14 Water steam from spout with and without evaporation

pressure for proper operation and a large volume condenser. As turbines became more efficient, direct-contact condensers were replaced by indirect shell-and-tube condensers. Recently, however, a renaissance of direct-contact condensers occurred in the power industry in regions where cold water is in short supply and an indirect Heller-type air cooling system is used. In such a system shown in Fig. 15 exhaust steam is condensed in a direct-contact condenser by cold water from a cooling tower. The warm water from the condenser is then returned to the cooling tower where it is cooled by heat transfer to atmospheric air and recycled to the condenser. Since the cooling water circuit is completely closed, the water quality in it is the same as that of the steam or feedwater, allowing the use of direct-contact condensers in the system. Research for suitable direct-contact condenser geometries has been carried on during the past decade at the Institute of Electric Power Research in Hungary and in the Soviet Union. The results of this work are summarized in [29–31] and suggest that falling water jets from flat nozzles with steam in crossflow are the convenient geometries for direct condensation in conventional power plants.

Research for OTEC condensers initially used the results of these and similar investigations. However, OTEC condensation is more complicated because ocean water contains a large amount of noncondensable gases that may come out of solution; in addition, the need to reduce parasitic power to a minimum is much more stringent than in a conventional power plant. With these additional restrictions in mind, the search for an efficient OTEC condenser moved from using falling jets to packed columns with structured packings of the type developed largely in Western Europe for the chemical industry.

The arrangement and flow pattern in direct-contact condensers for OC-OTEC plants must combine high efficiency and small volume and minimize parasitic power loss. The condenser, therefore, is placed at a barometric level below the exhaust from the turbine, and the steam flow is initially directed

Table 2 Comparison of performance characteristics of various evaporator designs for a 1-MW thermal OTEC system

Heat exchanger type	Required water flow, kg/s	Volumetric heat transfer coefficient, kW/m ³ K	Figure of merit, ⁶ 1/m ³
Union Carbide sprayed bundle shell-and-tube ¹ (closed cycle)	131	85	91
Trane plate-fin ² (closed cycle)	264	159	302
SERI falling jet ³ (open cycle)	68	268	1042
SERI falling film ⁴ (open cycle)	53	555	1647
SERI falling jet with screens ⁵ (open cycle)	53	427	1670
SERI vertical spout ⁵ (open cycle)	49	1883	7086

¹ "OTEC-1 Power System Test Program: Performance of One-Megawatt Heat Exchanger," ANL/OTEC-PS-10, Nov. 1981.

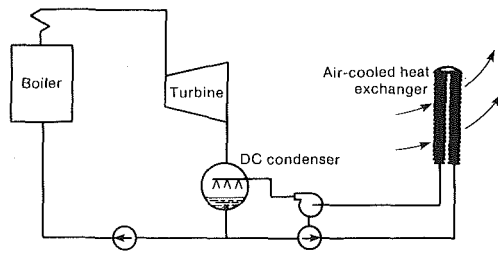
² "OTEC Performance Tests of the Trane Plate-Fin Heat Exchanger," ANL/OTEC-PS-7, Apr. 1981.

³ Green, et al., "Measured Performance of Falling-Jet Evaporators," SERI/TP-631-1270, Solar Energy Research Institute, Golden, CO, June 1981.

⁴ "Design Methodology for Direct-Contact Falling-Film Evaporators and Condensers for Open-Cycle Ocean Thermal Energy Conversion," SERI/SAI-083-83R, Feb. 1982.

⁵ Bharathan, D., and Penney, T., "Flash Evaporation From Turbulent Water Jets," ASME JOURNAL OF HEAT TRANSFER, Vol. 106, 1984, pp. 407–416.

⁶ The figure of merit is defined as heat transferred per unit volume divided by the parasitic power extended to pump the water.



Source: Heller (29)

Fig. 15 Schematic of Heller system condenser

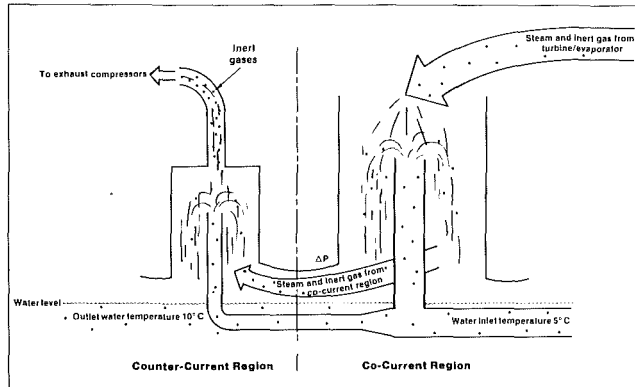


Fig. 16 Schematic of two-stage direct-contact condenser with typical OTEC parameters

vertically downward in cocurrent flow to allow the coolant to fall under gravity. Most of the condensation process occurs in downward, cocurrent flow, but to exhaust the noncondensable gases coming out of the water and steam effectively, it is necessary to maximize the concentration of these gases before they reach the exhaust pumps. To achieve this, a countercurrent flow section following the initial cocurrent condenser leg is necessary. This two-stage process is shown schematically in Fig. 16.

System studies [32] have shown that an optimum balance in an OTEC plant is achieved by condensing about 70 percent of the steam in a cocurrent mode and the rest in a countercurrent region. Despite the small percentage of steam condensed in the countercurrent region, this part of the condenser is important because it increases the ratio of noncondensable gases to steam from about 2 percent at the outlet of the cocurrent region to 40 percent or more at the outlet from the countercurrent region. This high concentration of noncondensable gases reduces the power requirements for exhausting the noncondensables and the remaining steam by nearly 80 percent. To minimize the exhaust pumping power required, an OC-OTEC exhaust system will require a series of staged compressors with interstaged coolers and condensers.

7 Analysis and Correlation of Test Results for Direct-Contact Condensation With Structured Sheet Packings

For the reasons given previously, it was decided to test experimentally and, if possible, improve structured packings for direct-contact OC-OTEC condensation. Sheet-type structured packings have been used in cooling towers and in mass transfer operations, but no experimental data for the operating conditions of an OTEC condenser have heretofore been available. The initial experiments performed at SERI used solid plastic sheets in a configuration shown in Fig. 17. In this geometry the cross section of the channel through which the vapor flows alternates between a triangle and a diamond. To obtain a periodic redistribution of the vapor and the liquid flowing between adjacent sheets, the axis of the vapor flow channel was inclined 30 deg from the vertical.

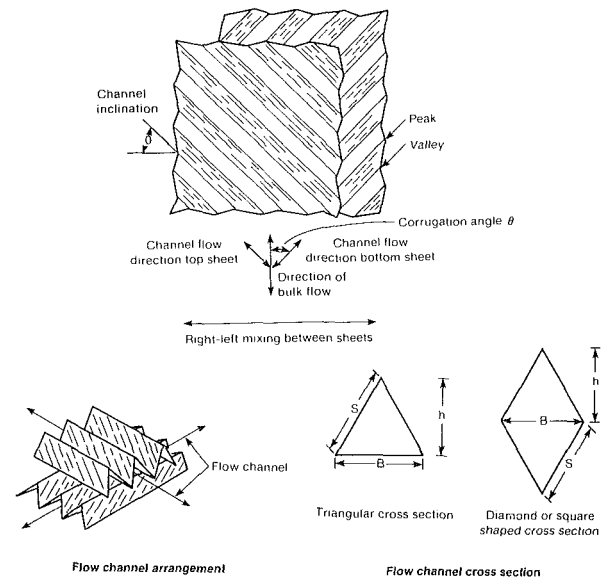


Fig. 17 Definition of structured packing dimensions and geometric orientation

Table 3 Correlations for SERI direct-contact condenser model

Liquid Side

Mass Transfer

$$k_L = 2\rho_L [D_L U_{L\text{eff}} / (\pi S')]^{1/2} \quad (\text{kg/m}^2 \text{ s})$$

$$U_{L\text{eff}}^\dagger = \frac{0.820}{n} \delta^{2/3} (\sin \alpha)^{1/2} \quad (\text{m/s})$$

$$\delta^\ddagger = \left[\frac{\Gamma}{82\rho_L \sqrt{\sin \alpha}} \right]^{3/5} \quad (\text{m})$$

$$S' = [(B/2 \cos \theta)^2 + h^2]^{1/2} \quad (\text{m})$$

$$\alpha = B / (2S' \cos \theta) \quad (\text{m})$$

$$\Gamma = L/a_f a_p \quad (\text{kg/s m})$$

Heat transfer

$$\left(\frac{h_L}{k_L C_{pL}} \right) = \left(\frac{Sc_L}{Pr_L} \right)^{2/3}$$

Gas Side

Mass Transfer

$$N_{Sh} = 0.0338 N_{Re}^{0.8} N_{Sc}^{0.333}$$

Heat transfer

$$\left(\frac{h_G}{k_G C_{pG}} \right) = \left(\frac{Sc_G}{Pr_G} \right)^{2/3}$$

Friction

$$f^\ddagger = 0.171 + 92.7/Re_G$$

$$Re_G = \rho_G \frac{U_{G\text{eff}} S}{\mu_G}$$

$$\text{and } N_{Re} = \rho_G (U_{G\text{eff}} \pm U_{L\text{eff}}) d_{eq} / \mu_G$$

* Use relative velocity, + for countercurrent flow, - for cocurrent.

† Dimensional equations using Mannings formula for open-channel water flow, given here in SI units. See for example equation (10.9) in *Introduction to Fluid Mechanics*, 2nd ed., by J. E. A. John and W. L. Haberman, Prentice Hall, Englewood Cliffs, NJ, 1980.

‡ Used as $\Delta p = f(L/d)\rho u^2/2$.

7.1 Analysis. Only a few publications have appeared to date in the open literature on the performance of structured packings. In our analysis we will follow the approach of Bravo et al. [10, 11] and, referring to Fig. 17, define an average equivalent diameter between the triangle and the diamond cross section for the vapor flow, d_{eq}

$$d_{eq} = Bh[1/(B+2s) + 1/2s] \quad (1)$$

where B = the base of the triangle, m; h = the height of the triangle or crimp height, m; s = the slanted side of the triangle (or corrugation spacing), m.

The results reported by Bravo et al. [10] were for packings made of gauze where the available area per unit volume, a_p , equals $4/d_{eq}$. For solid sheets, however, there is a loss in available area that can be approximated by

$$a_p = \left(1 - \frac{C_{\text{loss}}}{100}\right) 4\epsilon/d_{eq} \quad (2)$$

where $\epsilon = 1 - 4t/d_{eq}$ (the void fraction); t = sheet thickness, m; C_{loss} = contact area loss coefficient, percent.

The data correlations method proposed by Bravo et al. had to be further modified to consider the high liquid loading ($L \sim 30 \text{ kg/s m}^2$ in OTEC versus $\sim 3 \text{ kg/s m}^2$ for mass transfer). Also, for gauze packing, capillary forces spread the liquid into a thin film to cover almost the entire available area, a_p , while for sheet-type packing only a fraction a_f may be available. The reason is that the liquid film may wet only those surfaces that allow the liquid to flow over them. If we approximate those conditions by "open channel" flow, we can use the following expressions for the effective water film velocity over a surface inclined, α , from the horizontal (see Table 3):

$$U_{L,\text{eff}} = \frac{0.820}{n} \delta^{3/2} (\sin \alpha)^{1/2} \quad (3)$$

where n is the Manning roughness coefficient (= 0.010 for smooth surfaces) and δ is the film thickness (m), given by

$$\delta = \left[\frac{\Gamma}{82\rho_L \sqrt{\sin \alpha}} \right]^{3/5} \quad (4)$$

and Γ is the water flow per unit surface area (kg/sm)

$$\Gamma = \frac{L}{a_f a_p} \quad (5)$$

The typical distance over which liquid renewal occurs is the modified slanted side S' given by

$$S' = [(B/2 \cos \theta)^2 + h^2]^{1/2} \quad (6)$$

where θ is the channel inclination from horizontal and

$$\alpha = B/(2S' \cos \theta) \quad (7)$$

The liquid-side mass-transfer coefficient k_L for dissolved air liberation, based on the penetration theory of Higbie [33], can then be expressed as

$$k_L = 2\rho_L [D_L U_{L,\text{eff}} / (\pi S')]^{1/2} \quad (8)$$

where D_L is the air diffusivity in water (m^2/s).

Equation (8) differs from that of Bravo et al. [10], in that $U_{L,\text{eff}}$ is based on a turbulent flow on an inclined plane as opposed to a laminar flow on a vertical surface, and the renewal distance S' is dependent on θ . It should also be noted that in the range of parameters reported by Bravo et al. [10], the liquid-side resistance did not play a significant role in the overall mass transfer resistance.

The gas-side Sherwood number, $N_{\text{Sh}} (k_G d_{eq} / \rho_G D_G)$, based on extensive earlier investigation of wet-wall columns [34], is expressed as

$$N_{\text{Sh}} = 0.0338(N_{\text{Re}})^{0.8} (N_{\text{Sc}})^{0.333} \quad (9)$$

where the gas Reynolds number, based on a relative velocity, is

$$N_{\text{Re}} = d_{eq} \rho_G (U_{G,\text{eff}} \pm U_{L,\text{eff}}) / \mu_G \quad (10)$$

and the gas Schmidt number is

$$N_{\text{Sc}} = \mu_G \rho_G / D_G \quad (11)$$

Here, k_G represents the gas-side mass transfer coefficient ($\text{kg/m}^2 \text{ s}$), D_G is the gas-side diffusivity (m^2/s), and μ_G is the gas dynamic viscosity (kg/s m).

The effective gas velocity in $U_{G,\text{eff}}$ is dependent on the

superficial gas loading G (kg/s m^2), the void fraction of the packing ϵ , and the flow channel inclination θ , according to

$$U_{G,\text{eff}} = G / (\rho_G \epsilon \sin \theta) \quad (12)$$

Equation (9) was verified in the ranges $220 < N_{\text{Re}} < 2000$ and $0.37 < N_{\text{Sc}} < 0.78$ by Bravo et al., while, based on previous studies, Sherwood et al. [35] claim a validity range of $3000 < N_{\text{Re}} < 40,000$ and $0.5 < N_{\text{Sc}} < 3$. Thus, equation (9) is expected to be valid for an OTEC direct-contact condenser typical inlet parameter range of $200 < N_{\text{Re}} < 4000$ and $N_{\text{Sc}} \sim 0.44$. The gas-side and liquid-side heat transfer coefficients were obtained from the mass transfer correlations using the Chilton-Colburn analogy [36].

The validity of using such an analogy for direct-contact heat transfer using random packings was examined by Huang and Fair [37] with affirmative results.

There have been few data published on gas flow pressure loss in sheet-type packing, but Bravo et al. [11] correlated gas friction data for flow through gauze-type structured packing with the relation

$$f = 0.171 + 92.7/\text{Re}_G \quad (13)$$

where $\text{Re}_G = \rho_G U_{G,\text{eff}} s / \mu_G$.

Table 3 summarizes the correlations used for the analytical model developed in this study.

A comparison of the experimental results with model predictions requires a numerical, stepwise integration of the predicted condensation rate along the path of the vapor. We will demonstrate the numerical process here for the cocurrent mode of operation using a simplified model shown schematically in Fig. 18. Assume that the flow is one-dimensional and steady, that the coolant and the condensate are well mixed, and that the flux of inert gas desorbed from the coolant, w_i , is small compared with the condensate flux w_s . To determine the interface temperature between the coolant water and the condensing stream, we will postulate a stagnant film for which the rate of diffusion of condensing steam at any point through a layer of inert gas and steam mixture, w_s , is given by

$$w_s = k_G \ln \left[\frac{1 - y_{s,i}}{1 - y_s} \right] \quad (14)$$

where k_G = vapor-side mass-transfer coefficient, $\text{kg/m}^2 \text{ s}$; y_s = mole fraction of steam in the bulk mixture; $y_{s,i}$ = mole fraction of steam at the interface.

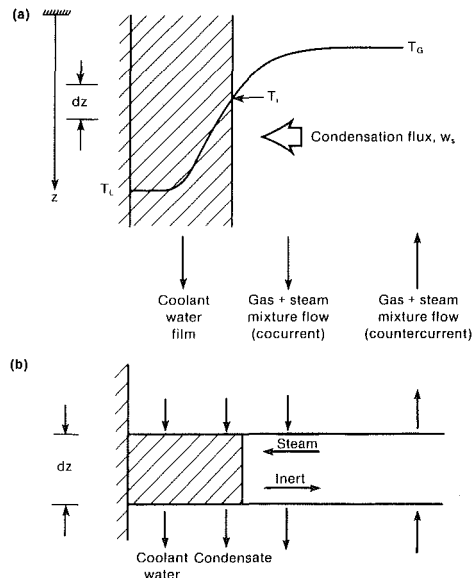


Fig. 18 (a) Temperature distribution at a section z across liquid and vapor streams and condensation flux direction; (b) schematic showing flow direction of coolant, condensate, steam, and inert gases

The heat flux to the coolant is equal to the sum of the sensible heat transferred from the gas and the latent heat due to condensation. Using the classical Colburn-Hougen approach [38], the steam flux and heat flux at any location can be related to the interface temperature by

$$h_L(T_i - T_L) = h_G \text{Ack}_h(T_G - T_i) + h_{fg} w_s \quad (15)$$

where

$$\begin{aligned} h_L &= \text{liquid-side heat transfer coefficient, kW/m}^2 \text{ K} \\ h_G &= \text{gas-side heat transfer coefficient, kW/m}^2 \text{ K} \\ h_{fg} &= \text{latent heat of condensation at } T_i, \text{ kJ/kg} \\ T_L, T_i, T_G &= \text{liquid, interface, and gas temperatures, respectively, K} \end{aligned}$$

$$\text{Ack}_h = \left[\frac{C_o}{1 - e^{-C_o}} \right]$$

= the Ackermann correction factor, which accounts for the high interfacial flux

$$\begin{aligned} C_o &= w_s C_{ps} / h_G \\ C_{ps} &= \text{specific heat of the steam, kJ/kg K} \end{aligned}$$

Equations (14) and (15) with the definition of Ack_h can be used to calculate T_i once the transfer coefficients h_L , h_G , and k_G are known.

The rate of transport of inert gas from the coolant into the steam is given by

$$w_i = k_L(x^* - x) \quad (16)$$

where k_L = liquid-side mass-transfer coefficient, $\text{kg/m}^2 \text{ s}$; x = inert gas mass fraction in the bulk of the coolant; x^* = inert gas mass fraction at equilibrium corresponding to the partial pressure of the inert gas, pp_i .

If the equilibrium condition is governed by Henry's law, the inert gas mole fraction y^* is

$$y^* = \text{He } pp_i \quad (17)$$

where He is the Henry's law constant and pp_i is the inert gas partial pressure.

Following an early work of Wassel et al. [39], the variation of temperature and pressure of the steam-inert gas mixture in the condensate can be obtained from the one-dimensional mass, momentum, and energy conservation equations:

Steam and condensate flow:

$$\frac{d\dot{m}_s}{dz} = -w_s a_f a_p A = \frac{d\dot{m}_L}{dz} \quad (18)$$

Inert gas flow and coolant in mixture:

$$\frac{d\dot{m}_{i,s}}{dz} = -w_i a_f a_p A = \frac{d\dot{m}_{i,L}}{dz} \quad (19)$$

Heat balance for liquid in condenser:

$$\frac{dQ}{dz} = h_L(T_i - T_L) a_f a_p A = \dot{m}_L C_{p,L} \frac{dT_L}{dz} \quad (20)$$

The interrelation between temperature and pressure of the steam-inert mixture is expressed by the following matrix:

$$\begin{aligned} \left[\begin{array}{cc} 1 - \frac{u^2}{RT} & \frac{\rho u^2}{T} \\ -\frac{u^2}{\rho C_{pG}} & 1 + \frac{u^2}{C_{pG} T} \end{array} \right] \left\{ \begin{array}{c} \frac{dp}{dz} \\ \frac{dT_G}{dz} \end{array} \right\} \\ = \left\{ \begin{array}{c} -u(\rho u)' - \tau_i(P/A) \\ \frac{Q}{C_{pG}} - \frac{u}{\rho C_{pG}} (\rho u)' \end{array} \right\} \quad (21, 22) \end{aligned}$$

where

$$\begin{aligned} (\rho u)' &= \text{rate of change of gas loading} = dG/dz, \text{ kg/s m}^3 \\ Q/C_{pG} &= \text{interfacial heat transfer rate per unit enthalpy flow rate} \\ &= \frac{h_G [\text{Ack}_h] [T_G - T_i] \exp(-C_o) a_f a_p A}{\dot{m}_G C_{pG}}, \text{ K/m} \end{aligned} \quad (23)$$

and

$$\begin{aligned} \tau_i(P/A) &= \text{the frictional pressure loss} \\ &= \frac{1}{2} \rho_G (U_{G,\text{eff}} \pm U_{L,\text{eff}})^2 f \{ [\text{Ack}_f] a_f a_p \\ &\quad + (1 - a_f) a_p \} \quad (\text{N/m}^2) \end{aligned} \quad (24)$$

where

$$\begin{aligned} u &= \text{the superficial gas velocity } (G/\rho A), \text{ m/s,} \\ U_{G,\text{eff}} \pm U_{L,\text{eff}} &= \text{the relative gas velocity, m/s} \\ f &= \text{the friction factor} \\ [\text{Ack}_f] &= \text{Ackermann correction factor for high mass fluxes} \\ &= (2w_s/\rho_G u f) / [1 - \exp(-2w_s/\rho_G u f)] \end{aligned} \quad (25)$$

Note that in the frictional term, the ineffective fraction of the available surface area/volume, $(1 - a_f)$, also contributes to the pressure loss. The Ackermann correction is applied only where mass transfer occurs, i.e., over the fractional area, $a_f a_p$, assuming that all contributions to the pressure loss occur by interfacial shear. Other contributions to friction, such as form drag, are neglected.

The previous set of equations can be integrated along the condenser to obtain the steam, inert gas, and coolant properties, as well as the steam-gas mixture partial pressure and temperature. A detailed description of the computer code is presented by Bharathan et al. [12]. But, as mentioned previously, the numerical work is predicated on knowing the values of h_L , h_G , and k_G as well as on having an accurate estimate of vapor pressure losses. All of these parameters must be obtained from correlations in the literature since they cannot be measured directly in the OTEC experimental setup. The empirical constants in these correlations, however, were modified to fit the OTEC application. For cocurrent operation the initial conditions of the water and steam entering the condenser are known and integration along the path is straightforward using a fourth-order Runge-Kutta scheme. A similar procedure was also developed for countercurrent operation in [12]. For this operating mode, a trial-and-error calculation is required since the physical locations of the inlets are at opposite ends of the condenser.

7.2 Experimental Procedure and Results. Figure 19 shows a schematic of the cocurrent condenser test setup. Steam and an inert gas mixture enter the top of the condenser and flow downward. Cooling water is introduced through a vertical central pipe from which it flows freely onto a metallic screen that distributes the water evenly over the contact medium. The warmed water from the condenser is collected in a drain pool and noncondensable gases and uncondensed steam from the bottom of the condenser are evacuated by the exhaust pumps. The contact medium chosen for the cocurrent condenser experiments was a plastic structured packing 0.61 m long, called PLASdek 19060, whose dimensions are summarized in Table 4 (see also [40]). Table 5 shows a summary of the experimental uncertainties in the derived quantities from tests for packing 19060 according to the Kline and McClintock [41] method.

A complete description of the test procedure and the experimental results is beyond the scope of this presentation, but one may be found in [12]. We will only illustrate typical results

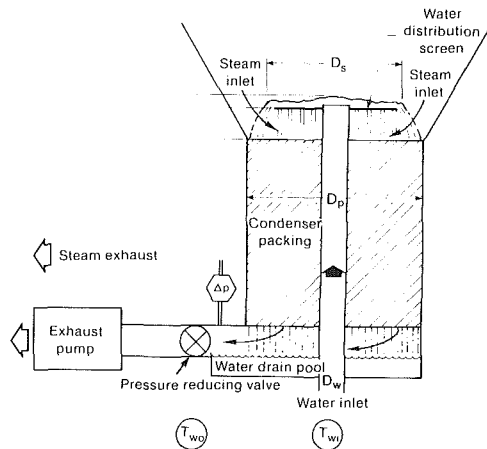


Fig. 19 Schematic of cocurrent condenser test arrangement

Table 4 Characteristic dimensions of structured packing tested at SERI

Characteristic	Units	19060	27060
Base	(mm)	48.26	73.00
Height	(mm)	19.05	27.18
Side	(mm)	30.74	45.51
Corrugation angle	(deg)	60.00	60.00
Packing diameter	(mm)	23.33	33.90
Vertical liquid fall distance	(mm)	51.88	77.90
Sheet thickness	(mm)	0.381	0.381
Void fraction	(-)	0.935	0.955
Contact blockage ¹	(percent)	13.55	5.92
Actual geometric area/volume	(m ² /m ³)	138.54	106.02

¹Based on quoted manufacturers' values for active surface areas of 138 m²/m³ and 98 m²/m³ respectively.

Table 5 Experimental uncertainty in derived quantities for condenser tests

Derived parameter	Cocurrent condenser error range, percent	Countercurrent condenser error range, percent
Gas loading	2.4-2.7	2.4-2.6
Jakob number	1.8-2.0	1.8-2.0
Inlet inert mass fraction	2.3-5.5	2.3-2.5
Outlet inert mass fraction	3.4-5.0	2.0-4.5
Effectiveness	0.17-0.75	0.19-0.70
Percentage condensed	1.7-5.0	1.7-2.0
Inlet pressure	0.12-0.14	0.12-0.20
Outlet pressure	0.38-0.93	0.40-0.94

here that show the capability of the analytic procedure to model the performance characteristics of direct-contact condensers.

For the presentation of the experimental data, we used the dimensionless parameters defined here:

Effectiveness (ϵ)

$$= \frac{\text{actual temperature rise}}{\text{maximum available temperature potential}}$$

$$= \frac{T_{\text{water,out}} - T_{\text{water,in}}}{T_{\text{steam,in}} - T_{\text{water,in}}} \quad (26)$$

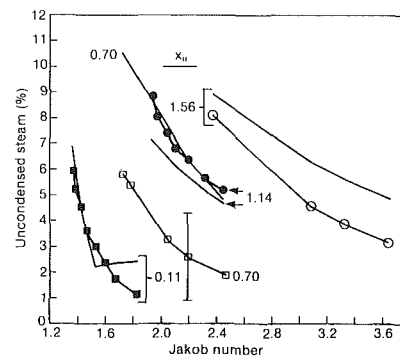


Fig. 20 Comparison between experimental and numerical performance of cocurrent condenser: percent uncondensed steam versus Jakob number for various mass fractions of inert gas

Steam loading (G)

$$= \frac{\text{inlet steam flow rate}}{\text{total flow cross-sectional area}}$$

$$= \frac{\dot{m}_{si}}{A_c} \quad (27)$$

Jakob number (Ja)

$$= \frac{\text{maximum possible rate of heat transfer}}{\text{steam mass flow rate} \times \text{latent heat}}$$

$$= \frac{\dot{m}_{wi} C_{pw} (T_{si} - T_{wi})}{\dot{m}_{si} h_{fg}} \quad (28)$$

Figure 20 illustrates a comparison between the experiment and the numerical predictions for a typical set of data in cocurrent flow at an average gas loading of 0.33 kg/s m². The percentage of measured uncondensed steam is plotted as a function of the operating Jakob number. For the model we assumed an effective area fraction of 1.0 and a condenser overall length of 0.8 m. The figure includes four sets of data for inert inlet mass fraction percent, X_{ii} , of 0.11, 0.70, 1.14, and 1.56 percent. The experimental data points are connected by straight lines to indicate their trends. The data for $X_{ii} = 0.11$ percent lie in the lower left-hand corner at a Jakob number range of 1.3 to 1.8. The model prediction for this set lies above the experimental data. At $Ja > 1.55$, the model prediction flattens out at a nominal uncondensed percent of 2.0. At this point the calculation was stopped because the gas relative velocity reached zero. The experiment, however, indicates that further condensation is possible. At $X_{ii} = 0.7$ percent and a liquid loading of 46 kg/s m², the model predicts approximately 3 percent more uncondensed steam than the experimental results. At $X_{ii} = 1.14$ percent and a liquid loading of 28 kg/s m², comparison between experiment and model is excellent, while at $X_{ii} = 1.56$ percent and a liquid loading of 39 kg/s m², the predicted uncondensed steam percent is about 2 percent greater than the measured value. Figure 21 shows a comparison of the measured and predicted water effectiveness for cocurrent flow. For a majority of the experimental points, the analytical model predicts the effectiveness over the entire test range within the limits of experimental accuracy shown in Table 5.

Figure 22 shows a comparison of the measured pressure loss with the loss predicted using equation (13). The measured pressure loss is seen to be considerably lower than the loss predicted by the Bravo correlation. We believe this difference is the result of having a finite water distribution area devoid of packing in the experiments, which according to the model is filled with the packing. Also, Bravo's results were obtained from

data for multiple stacks of packings, with successive stack rotated by 90 deg in a horizontal plane. The current condenser data is for a single stack of packing of 0.61 m length. The pressure-loss predictions of the analyses are thus conservative for the structured packing used in the tests.

A similar test arrangement was used in countercurrent flow with the steam and the inert gas mixture entering the condenser from the bottom of a cylindrical enclosure, while water was introduced into the condenser as in cocurrent flow. A water distribution plate on top of the condenser provided for uncondensed steam and inert gases to escape from above to the exhaust system. In addition to the PLASdek 19060, a larger sized packing (PLASdek 27060) was also tested in countercurrent flow. The comparisons between model predictions and experimental results were of similar quality for the countercurrent tests. Hence, the experimental results lend credence to the validity of the model, and we believe that a high-performance two-stage direct-contact OTEC condenser can be designed with confidence using the information gained by analysis and experiment conducted at SERI over the past few years.

8 Surface Condensers

The surface condenser was invented in 1765 by James Watt. The purpose of the condenser in a vapor power cycle is to reject heat from the turbine at the lowest possible vapor temperature and pressure to achieve high thermodynamic efficiency and recover the feedwater for return to the boiler. Since the lowest pressure in the vapor power cycle occurs in the condenser, all the noncondensable gases collect there and must be removed. These conditions are similar to all power plants.

No large surface condensers have so far been tested with steam under OTEC conditions. Consequently, the design and performance predictions of surface condensers to be used for desalination in open-cycle, hybrid OTEC plants must rely on experiments and experience obtained from condensers in power plant and marine applications. The condensers considered for OTEC service are quite similar to those used in power plant and marine applications. The main difference between those two applications is the lower pressure under which OTEC condensers operate [approximately 0.25 psia (1.5 kPa) in OTEC as compared with about 1 psia (7 kPa) in conventional power plants] and the larger amount of noncondensable gases that are expected to come out of solution in OTEC service. Despite these differences, however, engineering extrapolation of available information can be expected to yield a satisfactory design of an OTEC condenser for desalination service, keeping in mind that the accuracies of all correlations for condensation are subject to limitations in our general understanding of two-phase flow and condensation.

Most conventional power-plant condensers are rated thermally by standards proposed by the Heat Exchange Institute (HEI) in the United States or the British Electrical and Allied Manufacturers Association (BEAMA) in Europe. These standards assume that the overall heat transfer coefficient U_o is proportional to the square root of the cooling water velocity u_{water} , according to

$$U_o = CF_1 F_2 F_3 \sqrt{u_{\text{water}}} \quad (29)$$

where C is a coefficient that depends on the tube diameter; and the coefficients F_1 , F_2 , and F_3 correct for fouling, tube material and wall thickness, and cooling water inlet temperature. Since this rating method neglects conditions on the steam side, its predictions are subject to considerable error. In conventional steam condensers with a cooling water velocity of 1 to 3 m/s, the tube-side resistance may be control-

ling; but there are many other situations (e.g., in heat exchangers using titanium tubes for seawater service or in designs with tubing using enhancement methods) when the vapor-side resistance must be considered in a performance evaluation.

Estimates of heat transfer coefficients in condensation are traditionally based on Nusselt's [42] pioneering analysis of laminar film condensation on a single horizontal tube of diameter D that yielded the equation

$$N_{\bar{h}_{uD}} = \frac{\bar{h}_c D}{k} = 1.5 \left[\frac{\rho_L (\rho_L - \rho_G) g}{\mu_L^2 D^3 N_{Re_c}} \right]^{1/3} \quad (30)$$

Although this equation is based on idealized assumptions, such as a pure saturated vapor and uniform tube wall temperatures, the equation has been found useful with empirical modifications in real condensers where conditions are quite different from those postulated by Nusselt.

Complexities arise because of the presence of neighboring tubes in a large bundle, as shown in Fig. 23. In the idealized situation, shown in Fig. 23(a) and analyzed by Jakob [43],

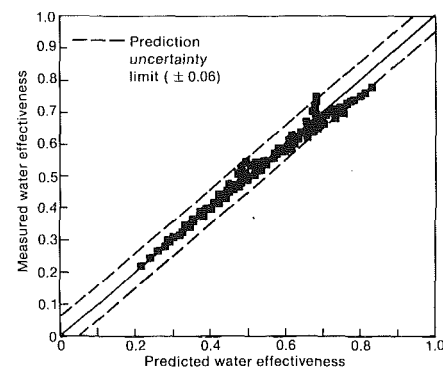


Fig. 21 Measured versus predicted effectiveness for cocurrent direct-contact condenser

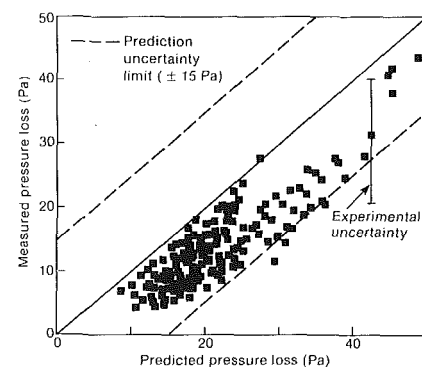


Fig. 22 Measured versus predicted pressure loss for cocurrent condenser

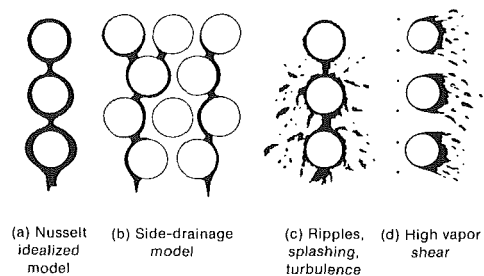


Fig. 23 Schematic of condensate flow according to Marto [47]

condensate from one tube drains by gravity to the tube below in a continuous laminar sheet. In reality, however, depending on the spacing-to-diameter ratio of the tubes and depending on whether the tubes are arranged in-line or staggered, the condensate may flow sideways as shown in Fig. 23(b). It has also been observed experimentally that the condensate does not drain in a continuous sheet but in droplets that produce splashing and turbulence in the condensate film as shown in Fig. 23(c). Perhaps most importantly, large vapor velocities perpendicular to the tube axis can create significant shear forces that strip the condensate from the tube surface. Kern [44] developed an empirical relationship to account for the disturbances shown in Fig. 23(c). The so-called inundation effect is given by the relationship

$$(\bar{h}_n/\bar{h}_1) = n^{-1/6} \quad (31)$$

where \bar{h}_n is the average coefficient for a tube in a bundle with n rows and \bar{h}_1 is the coefficient for tubes in the first row. Kern's empirical relationship has recently been verified in carefully conducted experiments of Marto and Wanniarachchi [45]. Berman [46], who conducted a comprehensive study of available film condensation data on horizontal tube bundles, concluded that existing variations in the experimental performance of operating condensers may be caused by factors such as bundle geometry (in-line versus staggered), tube spacing, type of condensing fluid, operating pressure, heat flux, local vapor velocity, and experimental difficulties in achieving good accuracies. In general, however, the Nusselt correlation with the Kern correction is conservative for pure vapors. For more complete information on condensation processes and condenser design, the excellent summaries in recent books and monographs edited by Marto and Nunn in 1981 [47], Diaz-Touz and Bell in 1983 [48], and Rohsenow et al. in 1986 [49] are recommended.

8.1 Effects of Noncondensables. The presence of noncondensable gases can reduce condensation heat transfer rates significantly because they interpose a gas layer through which vapor molecules must diffuse to reach the cold surface. Summaries of this phenomenon have been prepared by Chisholm [50] and Webb and Wanniarachchi [51]. To mitigate the detrimental effects of these gases, it is necessary to maintain a high vapor velocity throughout the condensing region. A recommended design approach for OTEC horizontal shell-and-tube condensers [22] uses radial inflow of vapor with a cylindrical tube bundle. This geometry provides adequate vapor flow over all the tubes and concentrates the noncondensable gases in the center of the bundle where they can be vented to the atmosphere.

Several investigators have measured the effect of air on the condensation rate of steam in surface condensers. An empirical relation that corrects the pure steam condensing heat transfer coefficient for the presence of air is [22]

$$F = \exp(-0.0536Y) \quad (32)$$

where Y is the local volumetric percentage of air and F is the correction factor by which the pure vapor heat transfer coefficient should be multiplied. Standiford [52], using data obtained by Meisenburg et al. [53], proposed a very simple conservative rule of thumb to estimate the noncondensable gas resistance R_{nc} , as a linear function of the air weight fraction w :

$$R_{nc} \approx 0.004w \quad (\text{m}^2 \text{ K/W}) \quad (33)$$

Since in steam power condensers the air-to-steam ratio at the turbine outlet is only about 0.001, the effects of noncondensable gases are generally small except when gas pockets are allowed to accumulate. The percent by volume of air in flashing seawater is on the order of 0.3 percent, which results only in a 2 percent reduction in the pure steam heat transfer

coefficient. While in itself this is not serious, this reduction occurs at the condenser entrance where the steam-to-air mass ratio is about 200. As the steam air mixture flows through the tube bundle, the concentration of air increases because more and more steam is condensed. This results in a progressive reduction in the condensation heat transfer coefficient. Since it is impractical to condense all of the steam because of the residual vapor pressure imposed by the coldest water, a suitable tradeoff must be made between the needed condenser surface area and the steam-air pumping power required for venting. In any case, proper condenser design should always allow for a well-defined vapor gas flow path to avoid stagnation regions where gas concentration can build up and retard heat transfer.

Panchal and Bell [54] have developed a theoretical model to analyze condensation in the presence of noncondensable gases on a vertical surface resembling OTEC conditions. They have also calculated the effects of fins on the performance of a vertical plate condenser and suggested a means of optimizing such a design.

8.2 Potential of Heat Transfer Enhancement. There have been many proposals for enhancing the heat transfer characteristics of condensers. Bergles [55], Mussalli and Gordon [56], and Webb [57] have provided extensive reviews of enhancement methods for use in condensers, including information from the technical and US patent literature. These methods may be divided into inside tube enhancement on the cooling water side, and shell-side enhancement on the steam condensation side. To enhance the single-phase turbulent forced convection inside the tube rough surfaces, they suggested internal fins, wire coil and twisted tape inserts, and helical flutes. In OTEC service attention must be paid that any enhancement methods do not result in increased corrosion and biofouling, unless the surface can be readily cleaned. Proposals for shell-side enhancement encompass techniques such as surface coatings, low integral fins, condensate drainage devices, and fluted or grooved tubes such as those shown in Fig. 24.

The main thermal resistance on the shell side is caused by the presence of the condensate film through which heat must be transferred by conduction. Whatever can be done to thin the film or introduce turbulence into it will benefit the heat transfer. In horizontal condenser tubes, thinning may be promoted by using fins or fluted surfaces and by improving condensate drainage. In vertical tubes, using a fluted shape that has surface tension effects has also proven effective to thin the film. Marto [58, 59], in two excellent summaries of the effects of heat transfer enhancement, points out that low fin tubing may have difficulties with condensate bridging across the fins. According to Marto, although some experimental data have shown external enhancement of 200 and 300 percent, so far no criteria exist for selecting an optimum low-fin tube for steam use. Mildly indented or "roped" tubes give modest enhancement of 20 to 50 percent. The use of microgrooves on these indented surfaces can increase the enhancement to nearly 100 percent. A wire wrapped around these tubes may provide additional improvement. Also, vertical-fluted tubes with properly designed drain-off skirts or vertical tubes coated with metal particles have been shown to give significant enhancement with thermal performance over three times that of smooth horizontal tubes. However, most of the shell-side enhancement results were obtained in the laboratory with single tubes, and very few data are available to verify those predictions in tube bundles where both condensing vapor shear and fouling are important.

In 1980, the Tennessee Valley Authority (TVA) completely retubed the condenser of the 300-MW Gallatin 1 power unit with a corrugated, enhanced surface, 90–10 Cu–Ni tubing in

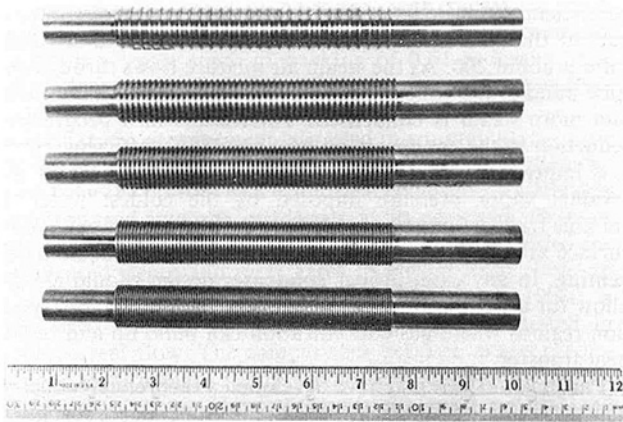


Fig. 24 Integrally finned tubes for shell-side enhancement; fluted and grooved tubes for condensate film thinning and shell-side enhancement

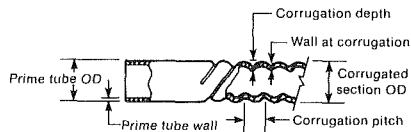


Fig. 25 Corrugated enhanced surface tube used by TVA

the first large-scale test comparing enhanced and standard tubes in service [60]. The corrugated enhanced surface tube used is shown schematically in Fig. 25. In a laboratory test this type of tube had previously shown an improvement of 50 percent or more in the overall heat transfer coefficients. During these inservice tests, the overall heat transfer coefficients for the clean corrugated tubes in the condenser were initially found to be 34 to 43 percent higher than for clean standard tubes. However, the overall heat transfer coefficient of the enhanced tube condenser in this application decayed to the approximate level of a condenser with plain tubes in two or four months as a result of accelerated fouling as shown in Fig. 26. Careful brush cleaning could restore the original thermal performance, but the friction factor of the corrugated tubes was twice that of plain tubes. Since brush cleaning is not a feasible option in OTEC service, the TVA-tested enhancement method may not be useful for OTEC, even if the increased pressure drop was acceptable.

8.3 Fouling of Condenser Tubes. The long-term performance of OC-OTEC surface condensers depends to a large extent on the effects of biofouling and corrosion of the heat transfer surface. Most experimental work reported in the literature is based on clean tubes because it is difficult to specify the rate at which fouling and corrosion occurs. Recently, however, a great deal of effort has been focused on the performance penalties associated with fouling and corrosion. Several specialized conferences dealing with fouling have been held in the past ten years, including the 1977 OTEC Biofouling and Corrosion Symposium in Seattle, WA, the 1979 International Conference on Fouling of Heat Transfer Equipment in Troy, NY, and the Condenser Biofouling Control Symposium in Atlanta, GA, sponsored by the Electric Power Research Institute (EPRI) in the same year.¹ The reason for this interest in fouling is the high energy costs, the deterioration of thermal performance, the increasing costs of materials that can resist fouling, and the high cost of plant downtime due to fouling. For desalination systems, large heat transfer surfaces are required, and fouling could determine the eventual viability of using OTEC systems for distilling seawater.

¹In the summer of 1987, NATO sponsored a symposium on "Advances in Fouling Science and Technology" at the University of Minho in Portugal.

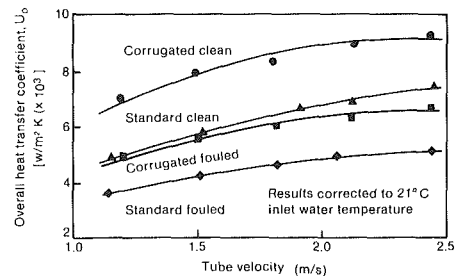


Fig. 26 Overall heat transfer coefficient versus tube velocity for clean and fouled tubes

An excellent summary of the state of the art of fouling of heat transfer surfaces has been presented by Knudsen [61]. In that overview he identified the following key issues of fouling processes: transport processes involving ions and molecules, solid particles, liquid droplets, nuclei and living organisms; deposition processes at interfaces; and deposition buildup and its effects on physical properties. He also emphasized the need for a standard measure of fouling to relate the results of laboratory studies with those of operating heat exchangers.

For OTEC design, it is believed that maintaining an adequate water velocity through the tubes (corresponding to Reynolds numbers of about 15,000) can inhibit growth of micro-organisms in the tubes. However, increasing the water velocity must be traded off with increased pressure drop on the coolant side. Recent data on cold-water fouling from Hawaii suggest that conditions encountered with cold seawater from deep in the ocean may not cause significant fouling of heat exchange surfaces. When fouling does occur, periodic chlorination may be effective in removing the deposits on the surface [62]. The question of fouling may become particularly important if consideration is given to enhancing the heat transfer coefficient on the interior of a conduit because most surfaces with enhancement methods are much more difficult to clean than plain surfaces.

A review of the rate of corrosion and fouling in steam condensers using seawater for nuclear power plants was performed by Michels et al. in 1978 [63]. Michels et al. point out that open ocean seawater, which is not contaminated with pollution, normally does not foul heat exchanger surfaces, except for biofouling. They also note that the marine industry has found that biofouling may not be a problem in copper-nickel piping systems, and copper-nickel exchangers may not have to use chlorine treatment to control biofouling.

Fouling on the outside of condenser tubes and conduits caused by condensing vapor may be a less serious problem than inside tubes, but additional data on fouling by condensing seawater vapor would be desirable to make a realistic assessment of the overall heat transfer coefficient in surface condensers for OTEC service as a function of time [64].

8.4 Surface Condenser Design. Engineering design and prediction of surface condenser performance is feasible with information available in the literature on heat transfer coefficients, vent rates, pressure drop, and effects of noncondensables. However, condenser design codes established by MEI and BEAMA are not adequate for OTEC application because of the limiting assumptions incorporated in them. For an adequate design, it is necessary to use computational procedures that consider the variations in heat transfer coefficient, vapor velocity, and pressure in the condenser. Davidson and Rowe [65] have summarized the computational procedures available for simulating power-plant condensers in the United States and in Europe. In this review, different approaches for computing the flow field and the problems associated with expressing the key empirical unidirectional relations for pressure drop and heat transfer in a form suitable for a multidimensional

system are discussed, and areas of uncertainty with current predictive schemes are delineated.

In the United States, a stepwise calculation procedure for local heat transfer parameters, developed by Standiford [52], has been used to predict the performance of shell-and-tube condensers, and Johnson et al. [66] have developed a numerical optimization technique for designing marine condensers. In England, computational methods for condenser design were developed by Davidson at the Glasgow National Engineering Laboratory [67, 68], and a model for three-dimensional flow in tube bundles was proposed by Butterworth [69]. In the USSR, an essentially empirical approach, based on equations proposed by Berman [70, 71], has been widely used, according to [65], and updated by Shklover and Grigorev [72]. In Japan, Shida et al. [73] developed a numerical analysis for flow and heat transfer in condensers.

Extensive summaries of current design technology for condensers operating with ocean water can be found in the collection of papers from the Condenser Workshop held in 1980 at the Naval Post Graduate School and edited by Marto and Nunn [47], the 1983 Symposium on Condenser Technology [48], and the 1985 edition of the *Handbook of Heat Transfer Applications* [49]. Publication of the test results from the DOE experiments in Hawaii will be a welcome addition to the literature all over the world, because power plants of the future will have to rely more and more on the oceans and the atmosphere for a heat sink.

9 OTEC System Analysis

The heat and mass-transfer research described in this lecture has emphasized the thermal requirements for an open-cycle system. These requirements are largely driven by the small total temperature difference available for energy conversion. Of the 20°C temperature potential available for an OTEC site, roughly half of the temperature drop is used to transfer heat in the evaporator and the condenser with the remaining half used as an enthalpy drop across the turboconversion system. The importance of the heat transfer performance becomes very clear when one considers that with a nominal value of 5°C available for evaporation or condensation, even a 0.5°C loss in approach between incoming steam and condenser water reduces the effectiveness to 90 percent and increases the water flow rate by 11 percent over the theoretical minimum. System analysis and subsequent design optimization is therefore necessary to resolve the dichotomy between increased turbine performance as the temperature drop across it is increased versus the increase in water flow and auxiliary power required to achieve the higher turbine output.

System analysis has been used to maximize the thermodynamic performance of an open-cycle plant by selecting optimum operating parameters such as seawater flow rate. A different optimization occurs if system cost parameters driven by things such as size and geometry are considered. Yet, a third optimization occurs when the cost of the service is the selection criterion and life and maintenance factors must be considered. All five of the major processes shown in Table 6 interact in a complex manner in response to variation in geometry and operating parameters.

We cannot select any one of the process operating parameters or a specific hardware geometry without considering the overall system performance and cost. It is not unusual for a designer to trade off heat transfer performance with hydraulic or pneumatic power to determine the optimum heat exchanger form and operating flow rates. But this is not possible for OTEC plants where the water flow rates per kilowatt of power are significantly higher than in a conventional plant. Moreover, in addition to this interaction or process coupling,

Table 6 Open-cycle processes and geometric parameters that influence them

Open-cycle processes	Influence parameters
Conversion	Turbine geometry and steam flow rate
Heat and mass transfer	Heat exchanger geometry, seawater and steam flow, and noncondensable gas fraction
Steam fluid dynamics	Duct and heat exchanger geometry and steam flow rate
Seawater hydraulics	Heat exchanger and seawater pipe geometry and seawater flow rates
Noncondensable gas purge dynamics	Seawater/gas sorption kinetics, seawater process path, and compressor system design

an open-cycle plant has the following additional complicating interactions:

- 1 Steam-side pressure losses, which are affected by duct sizes, mist eliminator efficiency, and flow distribution geometry in the heat exchangers.

- 2 Air purge effectiveness, which affects heat transfer performance, hydraulic pumping requirements, and compressor power.

- 3 Turbine performance and life, which depend on liquid and chloride content in the steam, steam fluid dynamic losses, air content, and fluctuations in seawater temperatures and flow rate.

Because the geometry and operating parameters affect the key processes in a highly interactive fashion, these five, first-order coupling effects and several additional second-order effects need to be understood and quantified before a successful commercial-scale plant can be designed and built.

CREARE performed extensive system analysis in 1984 and SERI in 1987 to ascertain the effects of plant size and the performance of various components on the economics and operations characteristics of an OTEC plant. Figure 27 shows the results of an analysis to ascertain the capital investment costs as a function of net power output. The capital cost curve flattens when the size of an OC-OTEC plant approaches 10 MW or more electric output. A reason for this reduction in plant size where OTEC can achieve most of the economies of scale lies in the reduction of cold seawater flow per megawatt of power produced.

Figure 28 shows the estimated breakout of major open-cycle OTEC subsystem costs. These estimates indicate that the total plant cost is dominated by the combined cost of the seawater supply subsystem and the turbine. Figure 29 shows that when performance and cost are considered on a system basis, the minimum cost occurs with a diffuser exhaust temperature of 10.5°C, which corresponds to a cold seawater flow rate of 35,600 kg/s and a warm water flow rate and temperature of 62,100 kg/s at 22.4°C. Similar studies have been made to determine the sensitivity of system cost to the following design and operational parameters: warm water flow rate, cold water flow rate, condenser area, condenser stage area rates, cold water pipe diameter, auxiliary mechanical efficiency, predeaeration effects, and diffuser performance.

As a result, the performance and cost of a 11.7-MW_e power plant specified in Table 7 is projected. All components for such a plant can be designed with confidence with the exception of the low-pressure turbine, which would have a diameter of approximately 12 m for a single rotor, and the large (approximately 5-m diameter) cold water pipe required. To circumvent the need for a large diameter turbine, it is possible to use several smaller turbine modules in parallel with commercially available turbine rotors from the low-pressure stages of a conventional power-plant turbine. An example of a dual flow configuration is illustrated in Fig. 30.

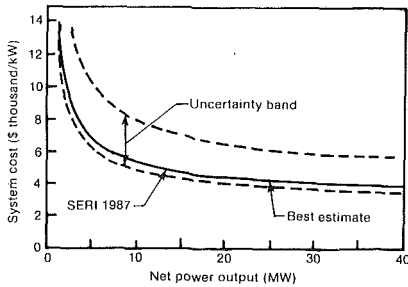


Fig. 27 Open-cycle OTEC system cost estimates

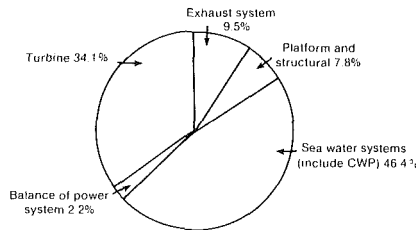


Fig. 28 Distribution of cost for 10-MW OC-OTEC plant

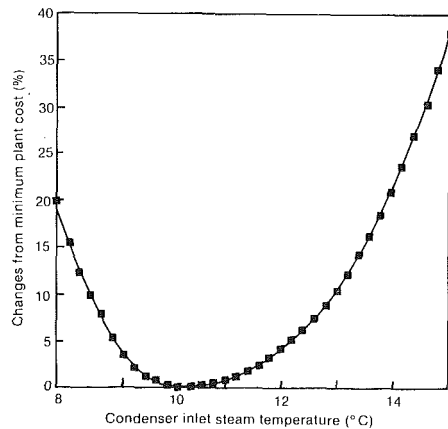
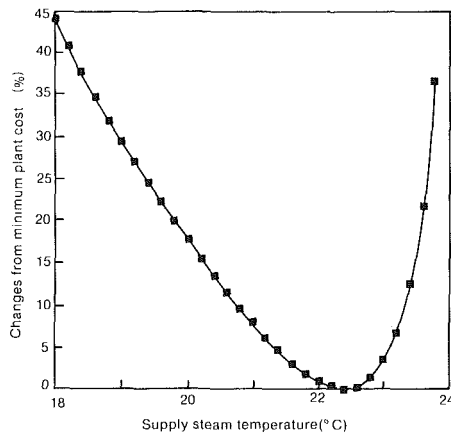


Fig. 29 Plant cost sensitivity

Given the information currently available, it is possible to describe, with reasonable accuracy, the performance of all components for a 10-MW electric open-cycle OTEC plant. Some factors that are still uncertain and have influence on the system design are the subject of an ongoing experimental research program at the Natural Energy Laboratory - Hawaii, e.g., effects of seawater and heat exchanger scaleup. The evaporator and condenser performance projected by analysis

Table 7 Design and performance specifications for a 10-MW_e open-cycle OTEC plant

Description	Specification
Warm water temperature	25°C
Warm water flow rate	62,100 kg/s
Warm water pipe diameter	9.27 m
Warm water pump power	1.03 MW
Evaporator size (planform area)	113 m ²
Turbine (number and rotor diameter)	(3) 5.3 m
Gross power	15.77 MW
Cold water temperature	5°C
Cold water flow rate	35,590 kg/s
Cold water pipe diameter	4.7 m
Cold water pump power	2.27 MW
Condenser size (planform area)	158 m ²
Purge system flow	1.30 kg/s @ 1.14 kPa
Compressor power	0.76 MW
Net power produced	11.7 MW

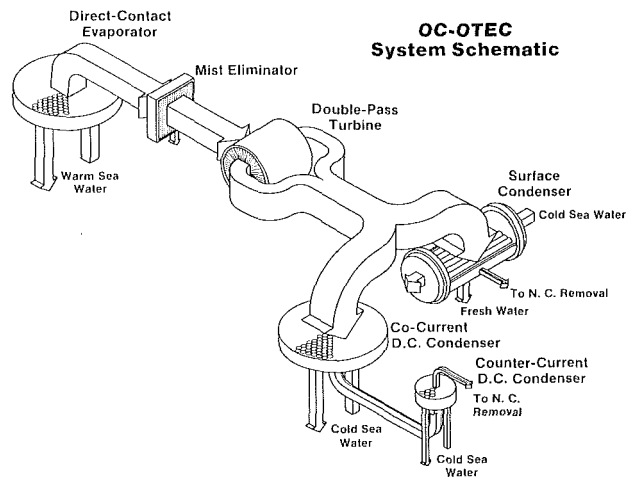


Fig. 30 OC-OTEC system schematic

and laboratory experiments go a long way toward establishing the economic feasibility of OC-OTEC technology.

While the optimization carried on at SERI was for a plant generating electricity, CREARE R&D, Inc. and the Florida Solar Energy Center (FSEC) [74] have also considered the possibility of combining electric power with seawater distillation through the use of surface condensers, as shown in Fig. 30. Based upon idealizations similar to those made at SERI, the system analysis indicated what the economic costs of such a plant might be. This analysis also considered certain appropriate applications for such a dual product plant in places such as the Virgin Islands or Puerto Rico. Where distilled water is at a premium, it may be possible to actually pay for part of the electric power from the sale of distilled water, as shown in Fig. 31. Since there are many islands in the Pacific that have large needs for distilled water for hotels and local industries, one of the first economic potentials for the open-cycle OTEC plant will be in an application where electric power and freshwater distillation can be combined.

10 Summary and Conclusions

A systems study conducted jointly by the Florida Solar Energy Center and CREARE under a SERI subcontract indicates that small-scale (approximately 5- to 10-MW) OTEC plants have near-term economic potential for island communities where distilled water as a byproduct of electric power has a high commercial value.

SERI experiments have provided sufficient information to design a spout direct-contact evaporator of high effectiveness, but additional experiments are recommended to ascertain possible interaction phenomena in multiple spout configurations and gas evolution under OTEC conditions.

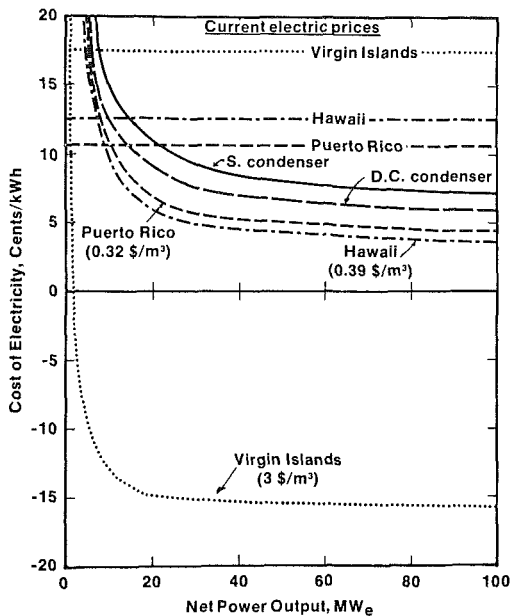


Fig. 31 Potential reduction in OC-OTEC electricity cost by selling fresh water at 1983 market prices (numbers in parentheses); real rate of return on investment is 10 percent

A direct-contact condenser with structured packing has shown high effectiveness in laboratory tests. These results are in good agreement with an analytic model that can be used for engineering design of an OTEC condenser with confidence, but so far no full-scale experiments under OTEC conditions have been performed.

Preliminary analysis and design have shown that it is possible to achieve high effectiveness and remove noncondensable gases in a two-stage, direct-contact condenser in which most of the steam is condensed in a cocurrent step, followed by a subsequent countercurrent flow configuration.

For seawater desalination in an open-cycle OTEC system it is necessary to use a large surface condenser. A suitable condenser could be designed with available information, but thermal performance characteristics and economic viability of a condenser with enhanced surface characteristics need to be tested and verified under seawater operation.

An experimental OC-OTEC apparatus capable of producing 165 kW gross power is being designed under the DOE program in Ocean Thermal Energy Conversion for testing at the Seacoast Test Facility in Hawaii. Experiments with this equipment are being planned in cooperation with the Pacific International Center for High Technology Research, which is also funded by the Japanese government to investigate the market potential of open-cycle OTEC in the Pacific basin.

The results of the direct-contact evaporation and condensation research offer potential for application in various commercial processes and systems such as bottoming cycles, liquid desiccant cooling systems using solar or waste heat for regeneration, Heller-type power cycles using dry air cooling for heat rejection, and gas-liquid heat and mass-transfer devices that use structured packing.

11 Acknowledgments

Many people and organizations have contributed to this lecture and we can only mention the most important contributors. A. Kogan of Technion, Israel, played a major role in the initial design and construction of the SERI test facility. J. Althof, J. Parsons, and Sung Ho Jo installed the instrumentation and carried out key experiments under T. Penney's supervision. B. Shelpuk and A. Trenka reviewed the manuscript and offered constructive comments. D. Johnson

provided valuable information on the DOE OTEC program perspective. P. J. Marto of the Naval Postgraduate School, Monterey, CA, provided important material on surface condensers, and A. Bergles of the Rensselaer Polytechnic Institute, NY, gave us valuable information on enhancement methods. We also express our appreciation to Munter's Corporation for providing the structured packing material for the direct-contact condensation experiments. Financial support was provided by the National Science Foundation under grant No. CBT-860-6595, E. Sparrow, Program Manager, and by the Department of Energy, Ocean Energy Technology Program, L. Rogers, Director.

References

- Ito, F., and Yutaka, S., *Present Situation and Future Outlook of OTEC Power Generation*, Tokyo Electric Power Co., Tokyo, Japan, Nov. 1982.
- Shelpuk, B., "A 165-kW Open Cycle OTEC Experiment," presented at the 12th Annual Intersoc. En. Conv. Eng. Conf., Miami Beach, FL, Aug. 1985; also SERI/TP-251-2725, Golden, CO.
- d'Arsonval, A., "Utilisation des forces naturelles. Avenir de l'électricité," *Revue Scientifique*, Vol. 17, 1891, pp. 370-372.
- Claude, G., "Power From Tropical Seas," *Mechanical Engineering*, Vol. 52, 1930, pp. 1039-1044.
- Owens, W. L., and Trimble, L. C., "Mini-OTEC Operational Results," *ASME Journal of Solar Energy Engineering*, Vol. 103, 1981, pp. 233-240.
- Dugger, G. L., et al., "Ocean Thermal Energy Conversion: Historical Highlights, Status, and Forecast," *Journal of Energy*, Vol. 7, 1983, pp. 293-303.
- Gauthier, M., "The French OTEC Project in Tahiti: Preliminary Results of the Site Environmental Study," *Oceans '85 Conference Proceedings*, Washington, DC, Sept. 10-12, 1985, pp. 359-363.
- Valenzuela, J., et al., "Thermo-Economic Analysis of Open Cycle OTEC Plants," presented at the ASME Winter Annual Meeting, Dec. 1984, Paper No. 84-WA/Sol-24.
- Fair, J. R., "Designing Direct Contact Coolers/Condensers," *Chem. Eng.*, Vol. 2, 1972, pp. 91-100; also "Design of Direct Contact Gas Coolers," *Petro/Chem. Engineer*, Vol. 2, 1961, pp. 203-209.
- Bravo, J. L., Rocha, J. A., and Fair, J. R., "Mass Transfer in Gauze Packings," *Hydrocarbon Processing*, Jan. 1985, pp. 91-95.
- Bravo, J. L., Rocha, J. A., and Fair, J. R., "Pressure Drop in Structures Packings," *Hydrocarbon Processing*, Mar. 1985, pp. 45-59.
- Bharathan, D., Parsons, B. K., and Althof, J. A., *Direct-Contact Condensers for Open-Cycle OTEC Applications: Model Validation for Structured Packings Using Fresh-water*, SERI/TR-252-3108, Solar Energy Research Institute, Golden, CO, in press.
- Kreith, F., and Bohn, M., *Principles of Heat Transfer*, 4th ed., Harper and Row, New York, 1986.
- Sherwood, T. K., Pigford, R. L., and Wilke, C. R., *Mass Transfer*, McGraw-Hill, New York, 1975.
- Kreith, F., and Boehm, R. F., eds., *Direct Contact Heat Transfer*, Hemisphere Publishing Company, New York, 1988.
- Maa, J. R., "Evaporation Coefficient of Liquids," *Industrial and Engineering Chemistry Fundamentals*, Vol. 6, No. 4, 1967, pp. 504-518.
- Brown, R., and York, J. L., "Sprays Formed by Splashing Liquid Jets," *AIChE Journal*, Vol. 8, No. 2, 1962, pp. 149-153.
- Balitsky, S. A., and Shurchkova, Y. A., "Flashing of a Superheated Liquid Under Vacuum," *Heat Transfer—Soviet Research*, Vol. 1, No. 3, 1969, pp. 106-109.
- Miyatake, O., et al., "An Experimental Study of Spray Flash Evaporation," *Desalination*, Vol. 36, 1981, pp. 113-128.
- Mills, A. F., et al., "Heat and Mass Transport in Turbulent Liquid Jets," *International Journal of Heat and Mass Transfer*, Vol. 25, No. 6, 1982, pp. 889-897.
- Theofanous, T. G., House, R. N., and Brumfield, L. K., "Turbulent Mass Transfer at Free, Gas-Liquid Interfaces, With Applications to Open Channel, Bubble, and Jet Flows," *International Journal of Heat and Mass Transfer*, Vol. 19, No. 6, 1976, pp. 613-624.
- Bharathan, D., et al., "Heat and Mass Transfer in Open-Cycle OTEC Systems," *Heat Transf. Eng.*, Vol. 5, 1984, pp. 17-30.
- Green, H. J., et al., "Measured Performance of Falling Jet Flash Evaporators," SERI/TP-631-1270, June 1981, Solar Energy Research Institute, Golden, CO.
- Kreith, F., et al., "A Study of Falling Film Flash Evaporators," SERI/TP-252-1415, Nov. 1982, Solar Energy Research Institute, Golden, CO.
- Bharathan, D., and Penney, T., "Flash Evaporation From Turbulent Water Jets," *ASME JOURNAL OF HEAT TRANSFER*, Vol. 106, 1984, pp. 407-416.
- Sam, R. G., and Patel, B. R., *Open Cycle Ocean Thermal Energy Conversion Evaporator/Condenser Test Program Data Report*, TN340, Oct. 1982, CREARE R&D, Inc., Hanover, NH.
- "IR100 Competition Winners," *Research and Development*, Mar. 1984.
- "Open Cycle Evaporator Breakthrough at SERI," *Solar Ocean Energy Liaison*, Chicago, IL, Mar. 1983, p. 34.

- 29 Bakay, A., and Jaszay, T., "High Performance Jet Condensers for Steam Turbines," Paper EC10, *VI International Heat Transfer Conference*, Toronto, Canada, 1978, pp. 61-65; see also Heller, L., *MTA Müszaki Tudományok Osztály Közleményei*, Jan. 1950, pp. 118-132.
- 30 Berredek, S., "Heat Transfer at the Condensation of Steam on a Turbulent Waterjet," *International Journal of Heat and Mass Transfer*, Vol. 19, 1976, pp. 448-50.
- 31 Isachenko, V. P., and Solodov, A. P., "The Heat Transfer of Steam Condensing on Continuous and Dispersed Fluid Jets," *Teplotenergetika*, Vol. 9, 1972, pp. 24-27.
- 32 Bharathan, D., *Open-Cycle OTEC Thermal-Hydraulic Systems Analysis and Parametric Studies*, SERI/TP-252-2330, 1984, Solar Energy Research Institute, Golden, CO.
- 33 Higbie, R., *Trans. Am. Inst. Chem. Engrs.*, Vol. 31, 1935, p. 365.
- 34 Gilliland, E. R., and Sherwood, T. K., *Industrial Engineering Chemistry*, Vol. 26, 1934, p. 516.
- 35 Sherwood, T. K., Pigford, R. L., and Wilke, C. R., *Mass Transfer*, McGraw-Hill, New York, 1975.
- 36 Chilton, T. H., and Colburn, A. P., "Mass Transfer (Absorption) Coefficients; Prediction From Data on Heat Transfer and Fluid Friction," *Industrial and Engineering Chemistry*, Vol. 26, Nov. 1934, pp. 1183-1187.
- 37 Huang, C. C., and Fair, J. R., "Direct-Contact Gas-Liquid Heat Transfer in Packed Columns," submitted for publication in *Heat Transfer Engineering*.
- 38 Colburn, A. P., and Hougen, O. A., "Design of Cooler Condensers for Mixtures of Vapors With Noncondensing Gases," *Industrial and Engineering Chemistry*, Vol. 26, Nov. 1934, pp. 1178-1182.
- 39 Wassel, A. T., et al., Science Applications International Corporation, "Design Methodology for Direct-Contact Falling Film Evaporators and Condensers for Open-cycle OTEC," SERI/STR-251-2256, Solar Energy Research Institute, Golden, CO, in press.
- 40 Munters Corporation Bulletin MF-3RR, On Surface Media for Cross-Flow Heat and Mass Transfer Applications, Sept. 1980.
- 41 Kline, S. J., and McClintock, F. A., "Describing Uncertainties in Single Sample Experiments," *Mechanical Engineering*, Jan. 1953, pp. 3-8.
- 42 Nusselt, W., "Die Oberflächen-Kondensation des Wasserdampfes," *VDI Zeitung*, Vol. 60, 1916, pp. 541-546; 569-575.
- 43 Jakob, M., *Heat Transfer*, Vol. 1, Wiley, New York, 1949, pp. 667-673.
- 44 Kern, D. Q., "Mathematical Development of Loading in Horizontal Condensers," *AIChE Journal*, Vol. 4, 1958, pp. 157-160.
- 45 Marto, P. J., and Wanniarachchi, A. S., "The Use of Wire-Wrapped Tubing to Enhance Steam Condensation in Tube Bundles," *Heat Transfer in Heat Rejection Systems*, S. Sengupta and Y. Mussalli, eds., ASME, New York, 1984.
- 46 Berman, L. D., "Heat Transfer With Steam Condensation on a Bundle of Horizontal Tubes," *Thermal Engineering*, Vol. 28, 1981, pp. 218-224.
- 47 Marto, P. J., and Nunn, R. H., eds., *Power Condenser Heat Transfer Technology*, Hemisphere Publishing Corp., New York, 1981.
- 48 Diaz-Tous, I. A., and Bell, R. J., eds., *Symposium on State of the Art Condenser Technology*, Meeting Planning Assoc., Menlo Park, CA, 1983.
- 49 Rohsenow, W. M., Hartnett, J. P., and Ganic, E. N., eds., *Handbook of Heat Transfer Applications*, McGraw-Hill, New York, 1985.
- 50 Chisholm, D., "Modern Developments in Marine Condensers: Non-condensable Gases: An Overview," *Power Condenser Heat Transfer Technology*, P. J. Marto and R. H. Nunn, eds., Hemisphere Publishing Co., New York, 1981, pp. 95-142.
- 51 Webb, R. L., and Wanniarachchi, A. S., "The Effects of Noncondensable Gases in Water Chiller Condenser—Literature Survey and Theoretical Predictions," *ASHRAE Transactions*, Vol. 86, Part 1, 1980, pp. 142-159.
- 52 Standiford, F. C., "Effect of Non-condensables on Condenser Design and Heat Transfer," *Chemical Engineering Progress*, Vol. 75, Part 2, 1979, pp. 59-62.
- 53 Meisenburg, S. J., Boarts, R. M., and Badger, W. L., *Transactions AIChE*, Vol. 31, 1935, pp. 622-638; Vol. 32, 1936, pp. 100-104, 449-450.
- 54 Panchal, C. B., and Bell, K. J., "Theoretical Condensation in the Presence of Noncondensable Gases as Applied to Open Cycle OTEC Condensers," presented at the ASME Winter Annual Meeting, New Orleans, LA, Dec. 1984.
- 55 Bergles, A. E., "Techniques to Augment Heat Transfer," *Handbook of Heat Transfer Applications*, W. M. Rohsenow, J. P. Hartnett, and E. N. Ganic, eds., McGraw-Hill, New York, 1986.
- 56 Mussalli, Y. G., and Gordon, L. S., "Use of Enhanced Heat Transfer Tubes in Power Plant Condensers," *Heat Transfer in Heat Rejection Systems*, S. Sengupta and Y. S. Mussalli, eds., ASME HTD-Vol. 37, 1984, New York, pp. 27-32.
- 57 Webb, R. L., "The Use of Enhancement Surface Geometries in Condensers: an Overview," *Power Condenser Heat Transfer Technology*, P. J. Marto and R. H. Nunn, eds., Hemisphere Press, 1981.
- 58 Marto, P. J., "Improving the Thermal Performance of Large Condenser Tube Bundles," *Symposium on the State-of-the-Art Condenser Technology*, I. A. Diaz-Tous and R. J. Bell, eds., pp. 1-25.
- 59 Marto, P. J., "Recent Program in Enhancing Film Condensation Heat Transfer in Horizontal Tubes," *Heat Transfer*, Vol. 1, C. L. Tien, V. P. Carey, and J. K. Ferrell, eds., Hemisphere, New York, 1986, pp. 161-170.
- 60 Boyd, L. W., et al., "Efficiency Improvement at Gallatin Unit 1 With Corrugated Condenser Tubing," ASME Paper No. 83-JPGC-PWR-4, 1983.
- 61 Knudsen, E. G., "Fouling of Heat Transfer Surfaces: An Overview," *Power Condenser Heat Transfer Technology*, P. J. Marto and R. H. Nunn, eds., Hemisphere, New York, 1981, pp. 375-424.
- 62 Larsen-Basse, J., "Effect of Biofouling and Countermeasures on Heat Transfer in Surface and Deep Ocean Hawaiian Waters—Early Results From the Seacoast Test Facility," *ASME/JSME Thermal Engineering Joint Conference Proceedings*, Vol. 2, Y. Mori and W. J. Yang, eds., ASME, New York, 1983, pp. 285-289; also *Proceedings: Advanced Ocean Thermal Energy Conversion Project Workshop*, Pacific International Center for High Technology Research, Aug. 1985, Kailua-Kona, HI.
- 63 Michels, H. T., Kirk, W. W., and Tuthill, A. H., "The Role of Corrosion and Fouling in Steam Conductive Performance," *Nuclear Energy*, Vol. 17, No. 4, 1978, pp. 335-342.
- 64 MacNair, "Fouling: Typical Experimental Results and Observations," *Power Condenser Heat Transfer Technology*, P. J. Marto and R. H. Nunn, eds., Hemisphere, New York, 1981, pp. 431-438.
- 65 Davidson, B. J., and Rowe, M., "Simulation of Power Plant Condenser Performance by Computational Methods: An Overview," *Power Condenser Heat Transfer Technology*, P. J. Marto and R. H. Nunn, eds., Hemisphere, New York, 1981, pp. 17-49.
- 66 Johnson, C. M., Vanderplaats, G. N., and Marto, P. J., "Marine Condenser Design Using Numerical Optimization," *ASME Journal of Mechanical Design*, Vol. 102, 1980, pp. 469-475.
- 67 Davidson, B. J., "Computational Methods for Evaluating the Performance of Condensers," *Proceedings of a Meeting on Steam Turbine Condensers*, Report 619, National Engineering Lab., Glasgow, Sept. 1974.
- 68 Davidson, B. J., "Flow of Steam in a Tube Nest—Numerical Analysis," *UK/USSR Symposium 1976*, Report No. 5, Section 5.2, Central Electricity Research Laboratories, Leatherhead, United Kingdom.
- 69 Butterworth, D., "The Development of a Model for Three Dimensional Flow in Tube Bundles," *International Journal of Heat and Mass Transfer*, Vol. 21, 1978, pp. 253-256.
- 70 Berman, L. D., "Engineering Design of Steam Turbine Condensers," *Teplotenergetika*, Vol. 22, No. 10, 1975, pp. 34-39.
- 71 Berman, L. D., "Influence of Vapour Velocity on Heat Transfer With Filmwise Condensation on a Horizontal Tube," *Thermal Engineering*, Vol. 26, No. 5, 1979, pp. 274-278.
- 72 Shklover, G. G., and Grigorev, V. G., "Calculating the Heat Transfer Coefficient in Steam Turbine Condensers," *Teplotenergetika*, Vol. 22, No. 1, 1975, pp. 67-71.
- 73 Shida, H., Kuragasaki, M., and Adachi, T., "On the Numerical Analysis Method of Flow and Heat Transfer in Condensers," *Heat Transfer 1982*, Vol. 6, Munich, 1982, pp. 347-352.
- 74 Block, D. L., and Valenzuela, J. A., *Thermoeconomic Optimization of OC-OTEC Electricity and Water Production Plants*, SERI/STR-251-2603, Solar Energy Research Institute, Golden, CO, May 1985.

Stochastic Analysis of Temperature Distribution in a Solid With Random Heat Conductivity

Da Yu Tzou

Research Scientist,
Institute of Fracture and Solid Mechanics,
Department of Mechanical Engineering
and Mechanics,
Lehigh University,
Bethlehem, PA 18015

Stochastic temperature distribution in a solid medium with random heat conductivity is investigated by the method of perturbation. The intrinsic randomness of the thermal conductivity $k(x)$ is considered to be a distribution function with random amplitude in the solid, and several typical stochastic processes are considered in the numerical examples. The formulation used in the present analysis describes a situation that the statistical orders of the random response of the system are the same as those of the intrinsic random excitations, which is characteristic for the problem with extrinsic randomness. The maximum standard deviation of the temperature distribution from the mean value in the solid medium reveals the amount of unexpected energy experienced by the solid continuum, which should be carefully inspected in the thermal-failure design of structures with intrinsic randomness.

1 Introduction

Stochastic response of a mechanical system to random excitations is always a focus in structural mechanics since the nature of the loading condition imposed on the system or the characteristics of the system itself are sometimes meaningful only in a statistical sense. The random response of a system subjected to random heat sources or random initial/boundary conditions can be studied by formulating the problem properly such that the responses of the system are represented by a unit response integral [1], for example. As a consequence of such a formulation, the statistical orders of the random responses of the system are the same as those of the random excitations (expected value of the random excitation renders the expected value of the random response, etc.). This is a general characteristic for problems with extrinsic randomness, and it can be found in open literature elsewhere. In the case when the system possesses intrinsic randomness, i.e., the randomness results from the characteristics of the system itself, the unit response integral, as in the case of extrinsic randomness, is difficult to obtain and as a consequence, the stochastic responses of the system will not be in the same orders as the random excitations. The expected value, for example, of the random response in this case will depend not only on the expected value of the random excitation but also on the other variances between the random response and the random excitation. In addition to the difficulties of dealing with partial differential equations with random coefficients, in this kind of problem one encounters the situation that the number of unknowns may be more than the number of equations and extra assumptions must be made to overcome this difficulty. The present paper will consider a special type of random heat conductivity in the solid medium for which the randomness is simulated by a distribution function with random amplitude varied either from specimen to specimen or for different locations in the same specimen. In a well-controlled manufacturing process, this kind of randomness is most likely the case and a typical example could be raised in the field of micromechanics. Due to some uncontrollable factors in the manufacturing processes, slight misimplantation of the substructures in the main structure may occur, which yields fluctuations of the physical quantities around the designed values. Stochastic analysis will be used in this work to investigate deviations of the temperature distribution and heat

flux from the mean values by considering several typical stochastic processes for this random fluctuation. The amplitude of the random fluctuation is weighted with respect to the designed value, and the use of a perturbation method by using this weighted quantity as the small parameter in the expansion provides a situation that the statistical order of the random response is the same as that of the intrinsic random excitation: a situation for the problems with extrinsic randomness.

A similar approach has been used in investigating the characteristics of wave propagation in a viscoelastic solid with intrinsic randomness [2, 3]. The approach used in this work is believed to be valuable in the thermal-failure analysis of the raisin-strengthened composites for which the slight misimplantation of raisin particles in the matrix material plays an important role as far as the initiation of local defects is concerned. Another situation under which the randomness of heat conductivity may be yielded is in the case of rapid heating to the solid continuum. It should be noticed that the dependence of thermal conductivity on the temperature $k(T)$ for temperature-sensitive materials is a mathematical concept resulting from the experiments under steady-state conditions. In the case that the rate change of temperature in the solid is so rapid and dramatic that the conductivity k of the solid at a certain temperature T_1 does not have sufficient time to respond to the corresponding value of $k(T_1)$ before the temperature changes from T_1 to T_2 , the deviation of the thermal conductivity at T_1 from the value $k(T_1)$ measured experimentally is expected. This deviation depends on the microstructures of the solid continuum such as irregular grain boundaries and sizes, and stochastic analysis in this case should be made to estimate the random responses of the system via the stochastic models established between the phase lag of the thermal conductivity at different temperature levels and the microstructural factors.

2 Formulation of the Problem

Consider a semi-infinite solid that occupies a region $x \geq 0$. Fourier's law of heat conduction in the solid can be written as

$$\frac{\partial}{\partial x} \left[k(x) \frac{\partial T}{\partial x} \right] = \rho c \frac{\partial T}{\partial t} \quad (1)$$

in which ρ and c are density and heat capacity of the solid, $T(x, t)$ is the temperature distribution, and k is the thermal conductivity. The density and heat capacity of the solid medium shall be treated as deterministic and constant in the

Contributed by the Heat Transfer Division for publication in the JOURNAL OF HEAT TRANSFER. Manuscript received by the Heat Transfer Division April 10, 1985.

following analysis. The thermal conductivity k is considered to be nonhomogeneous and a function of both space variable x and sample space α . The variable α ranges over a probability space Ω composed of all the specimen, and the probability density function $D(\alpha)$ in Ω is assumed to be measurable, which makes all of the statistical quantities (such as expected value, standard deviation, etc.) in the present analysis well defined. The initial and boundary conditions considered are

$$T(x, 0) = 0 \quad (2)$$

and

$$T(0, t) = f_1(t)$$

$$T(x, t) \text{ is bounded as } x \rightarrow \infty \quad (3)$$

The main complexity of dealing with the diffusion equation with random coefficients can be observed from equation (1) by taking statistical operators, say, expected value, on the entire equation

$$E[k]E\left[\frac{\partial^2 T}{\partial x^2}\right] + E\left[\frac{dk}{dx}\right]E\left[\frac{\partial T}{\partial x}\right] = \rho c E\left[\frac{\partial T}{\partial t}\right] - \text{Cov}\left[k, \frac{\partial^2 T}{\partial x^2}\right] - \text{Cov}\left[\frac{dk}{dx}, \frac{\partial T}{\partial x}\right] \quad (4)$$

where $E[Y]$ is the expected value for the random variable Y , and $\text{Cov}[X, Y]$ is the covariance between random variables X and Y . Through the knowledge about the expected values of k and its derivative from the ensemble space generated from the experiments, we may obtain the expected value for the temperature distribution by solving the resulting equation (4). Unexpectedly for a diffusion equation with random heat source, for which the expected value of the random response is only dependent upon the expected value of the random excitation, the expected value of the temperature in this case depends not only on the expected value of the thermal conductivity but also on the covariance between k and $\partial^2 T/\partial x^2$ and dk/dx and $\partial T/\partial x$. This is the situation for the general randomness of $k(x)$ in the solid. In the realistic engineering systems, however, the randomness resulted from the material nonhomogeneity is not completely unknown and some trend about the random variables can still be observed. We consider a raisin-strengthened composite as shown in Fig. 1(a). The raisin particles are implanted in the matrix material according to a well-controlled implantation rate such that the distribution of the raisin particles in the matrix is $g_1(x)$ depending on the strength requirement in the composite design. Then, according to the volume fraction rule, the resulting heat conductivity of the composite can be globally estimated as

$$k(x) \sim \frac{V_r(x)}{V} k_r \quad (5)$$

where V and V_r are the volume of the composite and the raisin particles, respectively, and k_r is the thermal conductivity of the raisin particles. Suppose the implantation rate is so well controlled that the global distribution for the volume of the

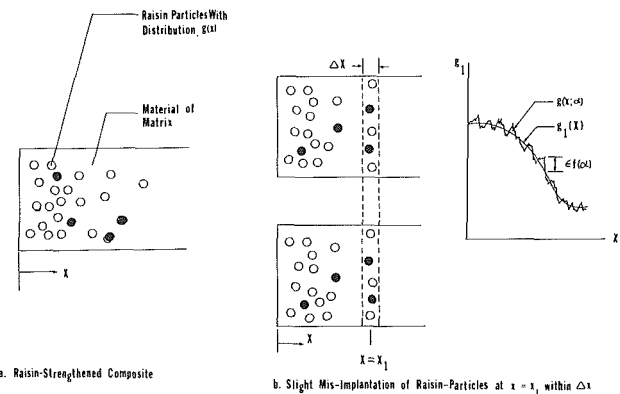


Fig. 1 Raisin-strengthened composite with slight variation of random heat conductivity

raisin particles is identical to the distribution function $g_1(x)$, but due to uncontrollable factors in the manufacturing processes, slight variation of the volume distribution $V_r(x)$ at $x = x_1$, say, may exist within a threshold Δx (Fig. 1b). As a consequence from equation (5), the distribution of thermal conductivity $k(x)$ may thus have the same global distribution $g_1(x)$ as that of the volume fraction of the raisin particles, while a random amplitude $\epsilon f(\alpha)$ should be placed in front of $g_1(x)$ to account for the random fluctuation on $g_1(x)$ due to the local misimplantation resulting from uncontrollable factors such as the bounding rate of raisin particles to the matrix material. $f(\alpha)$ is introduced into the amplitude of random fluctuation to account for the variation of randomness from measurements on different specimens in the ensemble space Ω . Therefore, the distribution of heat conductivity k can be expressed as

$$k(x; \alpha) = k_0 + \epsilon f(\alpha) g_1(x) = k_0 \left[1 + \frac{\epsilon}{k_0} g(x; \alpha) \right] \quad (6)$$

where $g(x; \alpha) = f(\alpha) g_1(x)$, and k_0 is introduced to weight the magnitude of the random fluctuation. In a well-controlled manufacturing process, the ratio ϵ/k_0 should be a small quantity which implies the applicability of the method of perturbation with ϵ/k_0 as the small parameter in the expansion of temperature. The governing system for the present problem is therefore specially organized in such a form that the method is conveniently applicable.

3 Solutions of Equations (1)–(3)

Equations (1)–(3) show a system of initial-boundary value problems to be solved. In order to exclude the statistical quantities with higher order appearing in the equation for the mean value of the temperature, as shown in equation (4), we shall use the method of perturbation in the following section to obtain the stochastic response of the system. By substituting

Nomenclature

a_0 = amplitude of time-dependent boundary condition	$g(\)$ = stochastic disturbance on the mean value of heat conductivity	V = deterministic distribution of temperature
b, p, β = parameters in distributions	k_0 = mean value of heat conductivity	α = state variable in sample space
c = heat capacity	q = heat flux vector	Γ = gamma function
$D(\)$ = probabilistic density distribution	s = variable in Laplace transform domain	κ = thermal diffusivity
$f(\)$ = random nature of the fluctuated amplitude	T = temperature field in the solid	ρ = density of the solid
		Ω = sample space
		$(\)$ = quantities in the Laplace transform domain

equation (6) into equation (1) and taking the Laplace transform of the resulting equation, we have

$$\frac{\epsilon}{k_0} \frac{dg}{dx} \frac{d\bar{T}}{dx} + \left(1 + \frac{\epsilon}{k_0} g\right) \frac{d^2 \bar{T}}{dx^2} = \frac{s}{\kappa} \bar{T} \quad (7)$$

where $\kappa = k_0/\rho c$ is the deterministic diffusivity of the solid defined according to the deterministic quantities. If the manufacturing processes in making the raisin-strengthened composite are well-controlled, which is the case in reality, the ratio ϵ/k_0 in equation (6) should be a small number since it weights the amplitude of the random fluctuation with respect to the design value. This implies the applicability of perturbation method in solving equation (7). By expressing $\bar{T}(x; s, \alpha)$ in terms of a series of ϵ/k_0

$$\begin{aligned} \bar{T}(x; s, \alpha) &= \bar{T}_0(x; s) + (\epsilon/k_0) \bar{T}_1(x; s, \alpha) \\ &\quad + (\epsilon/k_0)^2 \bar{T}_2(x; s, \alpha) + \dots \\ &= \sum_{n=0}^{\infty} (\epsilon/k_0)^n \bar{T}_n(x; s, \alpha) \end{aligned} \quad (8)$$

and substituting equation (8) into (7), a system of equations can be obtained by equating the same power of (ϵ/k_0) :

0th order system:

$$\frac{d^2 \bar{T}_0}{dx^2} = (s/\kappa) \bar{T}_0 \quad (9)$$

with $\bar{T}_0(0, s) = \bar{f}_1(s)$ and

nth order system:

$$\frac{d^2 \bar{T}_n}{dx^2} - (s/\kappa) \bar{T}_n = -g \frac{d^2 \bar{T}_{n-1}}{dx^2} - (dg/dx) \frac{d\bar{T}_{n-1}}{dx} \quad (10)$$

with $\bar{T}_n(0, s) = 0$ for $n = 1, 2, 3, \dots$

In a well-controlled process, the amplitude of the random fluctuation shall not exceed a design threshold, say, 10 percent of the designed value. This means, according to equation (8), the accuracy of the analysis could be on the order of 0.1 percent if the perturbation system is solved up to the second order. In a more serious situation, say, $\epsilon/k_0 = 0.5$, the same accuracy could be achieved by solving the perturbation system up to tenth order. In the present analysis, we shall consider the former case with $\epsilon/k_0 = 0.1$ and the perturbation system shall be solved to second order. Solutions in the system with higher orders can be incorporated into the system in the same manner as the ratio ϵ/k_0 is increased. As a numerical example, the time-dependent boundary condition at $x = 0$ is considered as

$$T(0, t) = f_1(t) = a_0(1 - \cos t) \quad (11)$$

with a_0 being a constant in the present analysis. The solutions for various orders in the perturbation system can be found as

0th order:

$$\bar{T}_0(x; s) = \bar{f}_1(s) \exp[-(s/\kappa)^{1/2} x] = \bar{V}_0(x; s) \quad (12)$$

1st order:

$$\begin{aligned} \bar{T}_1(x; s, \alpha) &= f(\alpha) \left\{ \frac{\bar{f}_1(s) \sqrt{\frac{s}{\kappa}} \left(\beta + \sqrt{\frac{s}{\kappa}} \right)}{\beta^2 + 2\beta \sqrt{\frac{s}{\kappa}}} \right. \\ &\quad \left[\text{Exp} \left(-\sqrt{\frac{s}{\kappa}} x \right) \right. \\ &\quad \left. \left. - \text{Exp} \left(-\sqrt{\frac{s}{\kappa}} - \beta \right) x \right] \right\} = f(\alpha) \bar{V}_1(x; s) \end{aligned} \quad (13)$$

2nd order:

$$\begin{aligned} \bar{T}_2(x; s, \alpha) &= f^2(\alpha) \left\{ \frac{\bar{f}_1(s) \sqrt{\frac{s}{\kappa}} \left(\beta + \sqrt{\frac{s}{\kappa}} \right)^2 \left(\sqrt{\frac{s}{\kappa}} - 2\beta \right)}{4\beta^2 \left(\beta + 2\sqrt{\frac{s}{\kappa}} \right)^2} \right. \\ &\quad \left. \cdot \text{Exp} \left[-\sqrt{\frac{s}{\kappa}} x \right] \right. \\ &\quad - \frac{\bar{f}_1(s) \left(\frac{s}{\kappa} \right) \left(\beta + \sqrt{\frac{s}{\kappa}} \right)^2}{\left[\beta^2 + 2\beta \sqrt{\frac{s}{\kappa}} \right]^2} \cdot \text{Exp} \left[-\left(\sqrt{\frac{s}{\kappa}} + \beta \right) x \right] \\ &\quad \left. + \frac{\bar{f}_1(s) \sqrt{\frac{s}{\kappa}} \left(\sqrt{\frac{s}{\kappa}} + \beta \right) \left(\sqrt{\frac{s}{\kappa}} + 2\beta \right)}{4\beta^2 \left(2\sqrt{\frac{s}{\kappa}} + \beta \right)} \right. \\ &\quad \left. \cdot \text{Exp} \left[-\left(\sqrt{\frac{s}{\kappa}} + 2\beta \right) x \right] \right\} = f^2(\alpha) \bar{V}_2(x; s) \end{aligned} \quad (14)$$

where $\bar{V}_j(x; s)$ with $j = 0, 1, 2$ are the complicated functions in the corresponding braces.

From these expressions for $\bar{T}_0(x; s)$, $\bar{T}_1(x; s, \alpha)$, and $\bar{T}_2(x; s, \alpha)$ in equations (12)–(14), and by noticing that the solution for the temperature distribution in the $(n-1)$ th order is always the nonhomogeneous term in the governing equation of the n th order, an useful relationship between the random function $f(\alpha)$ and the n th order solution may be rendered

$$\bar{T}_n(x; s, \alpha) = f^n(\alpha) \bar{V}_n(x; s), \text{ for } n=0, 1, \dots \quad (15)$$

Therefore, the temperature distribution in the solid can be written as

$$\bar{T}(x; s, \alpha) = \sum_{n=0}^{\infty} (\epsilon/k_0)^n f^n(\alpha) \bar{V}_n(x; s) \quad (16)$$

or, in the physical domain $(x, t; \alpha)$ with the third order and thereafter truncated,

$$\begin{aligned} T(x, t, \alpha) &= V_0(x, t) + (\epsilon/k_0) f(\alpha) V_1(x, t) \\ &\quad + (\epsilon/k_0)^2 f^2(\alpha) V_2(x, t) \\ &= \sum_{n=0}^2 (\epsilon/k_0)^n f^n(\alpha) V_n(x, t) \end{aligned} \quad (17)$$

with

$$V_j(x, t) = \frac{1}{2\pi i} \int_{\text{Br}} \bar{V}_j(x, s) \exp(st) ds, \quad j=0,1,2 \quad (18)$$

being the Laplace inversion of $\bar{V}_j(x; s)$ and Br the Bromwich contour of integration in the complex plane. The advantage of the present formulation to the diffusion phenomenon with intrinsic randomness is then clear from equation (17). By taking statistical operators, expected value and variance for example, on equation (17), we obtain

$$E[T(x, t)] = \sum_{n=0}^2 (\epsilon/k_0)^n E[f^n(\alpha)] V_n(x, t) \quad (18)$$

$$\text{Var}[T(x, t)] = (\epsilon/k_0)^2 \text{Var}[f(\alpha)] \sum_{m=0}^2 V_m(x, t) V_{2-m}(x, t) \quad (19)$$

and the standard deviation of the random temperature from the mean value can be obtained as

$$S[T(x, t)] = \sqrt{\text{Var}[T(x, t)]} \quad (20)$$

In other words, the statistical order of the random response of the system is the same as that of the random excitation under the present formulation; i.e., the mean value of the random response depends only on the mean value of the random excitation and the same situation holds for the variance. This is a characteristic similar to the problems with extrinsic randomness.

The heat flux vector can be obtained from the constitutive equation (Fourier's law) as:

$$q(x, t; \alpha) = -k(x; \alpha) \frac{\partial T}{\partial x} \quad (21)$$

and from equation (17) for the second-order expansion of the temperature, we have

$$E[q(x, t)] = -k_0 \sum_{n=0}^2 (\epsilon/k_0)^n \frac{\partial V_n}{\partial x} \left\{ E[f^n(\alpha)] + (\epsilon/k_0) g_1(x) E[f^{n+1}(\alpha)] \right\} \quad (22)$$

for the mean value

$$\text{Var}[q(x, t)] = -k_0(\epsilon/k_0)^2 \left\{ E[f^2(\alpha)] - E^2[f(\alpha)] + (\epsilon/k_0) \cdot \right.$$

$$\left. g_1^2(x) (E[f^3(\alpha)] - E^3[f(\alpha)]) \right\} \sum_{m=0}^2 \frac{\partial V_m}{\partial x}(x, t) \frac{\partial V_{2-m}}{\partial x}(x, t) \quad (23)$$

for the variance and

$$S[q(x, t)] = \sqrt{\text{Var}[q(x, t)]} \quad (24)$$

for the standard deviation of heat flux $q(x, t)$.

4 Random Function $f(\alpha)$ and Probability Density Distribution $D(\alpha)$

Several special cases of random fluctuations in thermal conductivity will be considered in this section in order to illustrate the application of the proposed approach in the present paper. The nature of the disturbance on the thermal conductivity is described by the function $f(\alpha)$, referring to equation (6). But since its randomness varied from specimen to specimen in the ensemble space, this function and the resulted temperature distribution do not have deterministic meaning, and their characteristics can only be defined in a statistical sense by taking averages over the entire ensemble space through the probability density function $D(\alpha)$ such as

$$E[f(\alpha)] = \int_{\Omega} f(\alpha) D(\alpha) d(\alpha) \quad (25)$$

as the mean value of α and

$$\text{Var}[f(\alpha)] = E\left\{f(\alpha) - E[f(\alpha)]\right\}^2 \quad (26)$$

as the variance of α , etc.

Through understanding of the statistical behavior of $f(\alpha)$ in a specific stochastic process with $D(\alpha)$ being the corresponding probability density function of the process, the statistical behavior of the temperature distribution in the solid medium with intrinsic randomness can be understood by solving equations (18)–(20) and (22)–(24) for the heat flux. $D(\alpha)$ and $f(\alpha)$ are measured in a pointwise manner in the realistic situation, and the expected value and variance for $f(\alpha)$ defined in equations (25) and (26) should be calculated via piecewise numerical integrations. In order to illustrate a worked example in this analysis, we will assume some simple

functions for $f(\alpha)$ and consider certain typical probability density function for $D(\alpha)$ in the stochastic processes. The first case we consider is an exponentially decayed function for $f(\alpha)$

$$f(\alpha) = \exp(-p\alpha) \quad (27)$$

in the ensemble space Ω , and assume the random variable α is specified by the density function of a gamma variate [5]

$$D(\alpha) = \begin{cases} \frac{\alpha^{b-1} \exp(-\alpha)}{\Gamma(b)}; & \alpha \geq 0 \\ 0; & \alpha < 0 \end{cases} \quad (28)$$

with b a constant specifying the characteristic of the distribution. The expected value for different orders of $f(\alpha)$ needed in the calculation and the variance can be calculated as

$$E[f(\alpha)] = (1+p)^{-b}, \quad E[f^2(\alpha)] = (1+2p)^{-b} \\ E[f^3(\alpha)] = (1+3p)^{-b} \quad (29)$$

$$\text{Var}[f(\alpha)] = [(p+1)^{2b} - (2p+1)^b] / [(2p+1)^b (p+1)^b]$$

The same random function $f(\alpha)$ can be considered under Gaussian (or normal) distribution; as another example

$$D(\alpha) = \frac{1}{b\sqrt{2\pi}} \exp\left(-\frac{\alpha^2}{2b^2}\right) \quad (30)$$

and the corresponding $E[f^n(\alpha)]$ for $n = 1, 2, 3$ and $\text{Var}[f(\alpha)]$ in this case are

$$E[f(\alpha)] = \exp\left(\frac{b^2 p^2}{2}\right)$$

$$E[f^2(\alpha)] = \exp(2b^2 p^2)$$

$$E[f^3(\alpha)] = \exp\left(\frac{9b^2 p^2}{2}\right)$$

$$\text{Var}[f(\alpha)] = \exp(2b^2 p^2) - 2 \exp(5b^2 p^2/2) + \exp(4b^2 p^2) \quad (31)$$

Another important case for $f(\alpha)$ results from the completeness of eigenfunctions $\{1, x, x^2, \dots\}$ or $\{\sin(n\alpha), \cos(n\alpha) \mid n = 0, 1, 2, \dots\}$ in the functional spaces. It indicates that any measured function $f(\alpha)$ can be expanded in terms of a power series

$$f(\alpha) = \sum_{p=0}^{\infty} A_p \alpha^p \quad (32)$$

or a Fourier series

$$f(\alpha) = \sum_{p=0}^{\infty} B_p \sin(p\alpha) + C_p \cos(p\alpha) \quad (33)$$

where $A_p, B_p,$ and C_p are the constant coefficients in the expansions. Therefore, if we consider a special type of function for $f(\alpha)$

$$f(\alpha) = \alpha^p \quad (34)$$

with p being a positive integer, the statistical temperature and heat flux distributions derived from this case will be the modal response of the general function shown by equation (32). A similar situation can be derived from equation (33) by considering $\sin(p\alpha)$ and $\cos(p\alpha)$ as the functions for $f(\alpha)$. In the present paper, we shall only consider the case of a power series expansion as an example, and the expected value and variance in this case can be obtained under Gaussian process as

$$E[f(\alpha)] = \frac{[1 + \cos(p\pi)] \Gamma\left(\frac{p+1}{2}\right)}{b^{-p} \sqrt{\pi} 2^{(2-p)}}$$

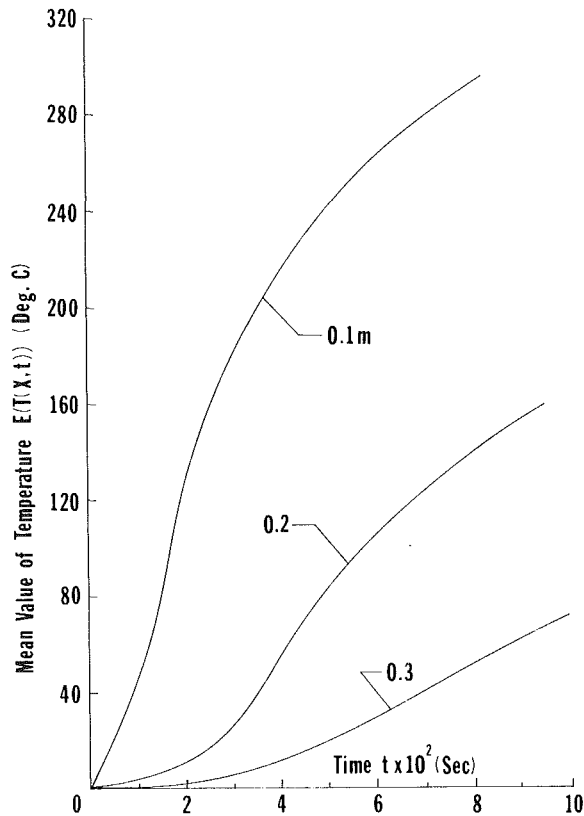


Fig. 2 Mean value of temperature distribution in the solid under the gamma process: $f(y) = \exp(-py)$

$$E[f^2(\alpha)] = \frac{\Gamma\left(\frac{p+1}{2}\right)}{b^{-2p}2^{-p}\sqrt{\pi}}$$

$$E[f^3(\alpha)] = \frac{[1 + \cos(3p\pi)]\Gamma\left(\frac{1+3p}{2}\right)}{b^{-3p}\sqrt{\pi}2^{(2-3p)}}$$

$$\text{Var}[f(\alpha)] = E[f^2(\alpha)] - E^2[f(\alpha)] \quad (35)$$

After the statistical behavior of $f(\alpha)$ is well understood, we may substitute equations (29), (31), and (35) into equations (18)–(20) for the statistical temperature distribution, and equations (22)–(24) for the statistical heat flux. The stochastic response for the present problem with intrinsic randomness is thus obtained.

5 Numerical Results

As shown in the previous section, the expected value and variance of the temperature distribution and heat flux in the solid medium are expressed in terms of the mean value and variance of the random fluctuation, respectively. The expressions depend on the probability density function $D(\alpha)$ in stochastic processes. The solutions in the physical domain (x, t) can then be obtained by taking the inverse transform on the statistical quantities in the Laplace transform domain by either analytical or numerical methods. In the present analysis, we will use an inversion scheme developed in [4] using Fourier series approximation to yield the solutions numerically. Such a method has been widely used in the investigation of viscoelastic response of solid media under loading conditions and the rate of numerical convergence is

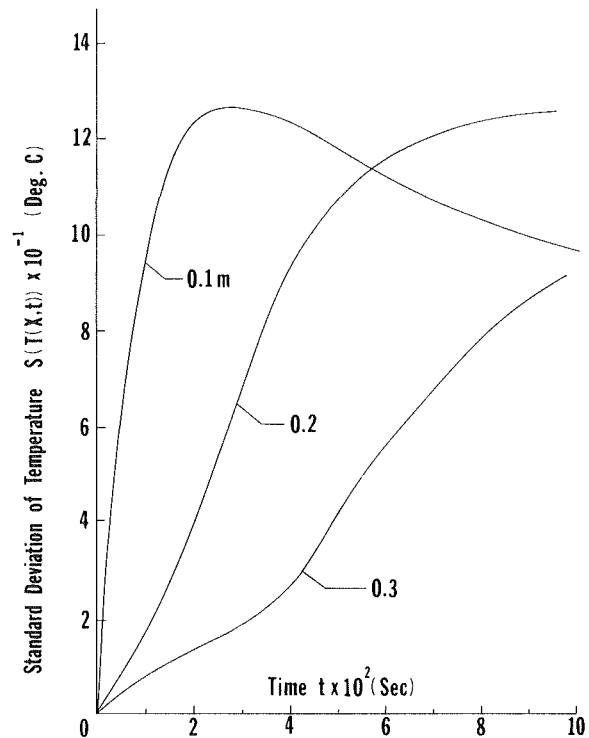


Fig. 3 Standard deviation of temperature distribution in the solid under the gamma process: $f(y) = \exp(-py)$

extremely fast and accurate if (i) the analytical forms of the solutions in the Laplace transform domain are known and (ii) the real part of the solutions in the Laplace transform domain can be roughly estimated. This method has been used in the IMSL packages in the CYBER computer system. In the case that the two conditions (i) and (ii) are not satisfied, say, the solutions in the Laplace transform domain are obtained numerically such that the analytical forms of the solutions are absent, a discrete method of numerical inversion used in [9, 10] can be employed instead. The deterministic quantities involved in the numerical calculations are

$$a_0 = 500 \text{ (}^\circ\text{C)}, \quad \kappa = 2 \times 10^{-5} \text{ (m}^2\text{/s)}$$

$$\beta = 1 \quad (36)$$

and (1) $b = 2$ and $p = 0.1$ in the case of gamma distribution defined as equations (28) and (29); (2) $b = 0.5$ and $p = 0.1$ in the case of Gaussian process with $f(\alpha) = \exp(-p\alpha)$ defined as equations (30) and (31); and (3) $b = 0.5$ and integers p from 0 to 5 in the case of Gaussian process with modal excitation $f(\alpha) = \alpha^p$ defined as equations (34) and (35).

Figure 2 shows the variation of expected value of temperature distribution with respect to time in the solid medium at different locations $x = 0.1$ (m), 0.2 (m), and 0.3 (m), and Fig. 3 shows the standard deviation of the temperature distribution under the same condition. A relative maximum of $S[T(x, t)]$ at $x = 0.1$ (m) can be observed at $t \cong 263$ (s) which indicates the occurrence of a maximum deviation of the temperature fluctuation from the mean value as a consequence of the intrinsic randomness. This phenomenon should be taken account of in the strength consideration of the composite design in thermal environments since the thermal stresses are proportional to the gradient of the temperature distribution in the solid medium and the magnitude of the deviation, as shown in equations (12)–(14), may have a change in order of magnitude if the boundary condition at $x = 0$ (m) renders the situation. A similar observation can be made in Figs. 4 and 5 for the case of the Gaussian process. The time in-

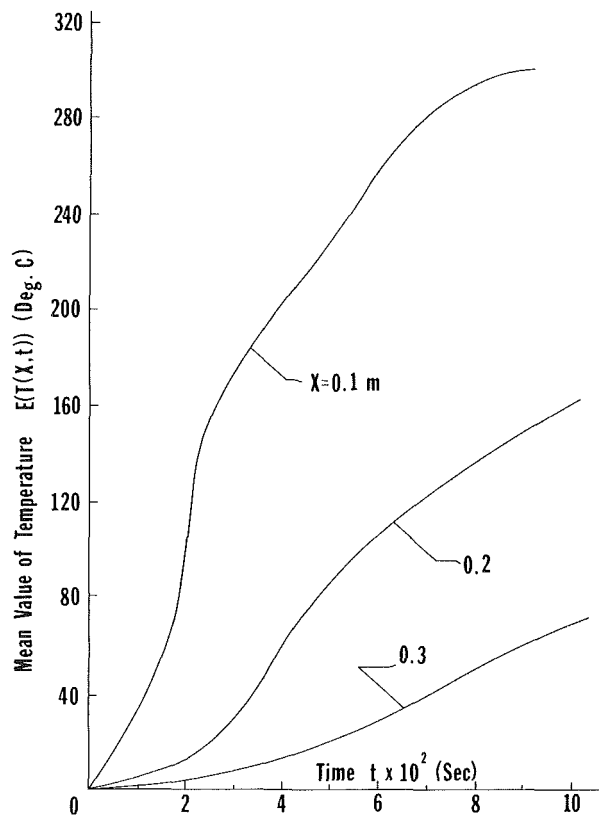


Fig. 4 Mean value of temperature distribution in the solid under the Gaussian process: $f(Y) = \exp(-pY)$

stant at which the standard deviation reaches its maximum is approximately 288 (s) while the magnitude of the maximum deviation is greater than that in the previous case under the same boundary condition. Figures 6 and 7 show the modal response of the expected value and variance of temperature distribution in the solid for the first six modes under the same Gaussian process as the second example. Typical responses at $(x, t) = (0.1 \text{ m}), 100 \text{ (s)}, 0.2 \text{ (m)}, 500 \text{ (s)},$ and $(0.3 \text{ m}), 700 \text{ (s)}$ are presented in the figures and continuous curves are made in these figures for the cases that the random fluctuations of $f(\alpha)$ are described by noninteger values of p in equation (34). The magnitude of the standard deviation in this case is greater than the previous cases which reveal the contribution of $f(\alpha)$, associated with the boundary condition at $x = 0 \text{ (m)}$ and the probability density function of the stochastic process, to the magnitude of the standard deviation from the mean value. The coefficients A_p shown in equation (32) in the power series expansion of $f(\alpha)$ should be incorporated in summing the modal response at various integers p to yield the general response described by the $f(\alpha)$. The expected value and variance of the heat flux can be obtained in the same manner by dealing with operations involving only different deterministic functions which are omitted in the present analysis.

6 Conclusions

The expected value and variance of the temperature distribution and heat flux in the solid medium with intrinsic randomness are obtained in terms of the expected value and variance of the random variables respectively. The intrinsic randomness of $k(x)$ is addressed in the problem through a random fluctuation on $k(x)$ with the amplitude varied from specimen in the ensemble space Ω . The formulation of the problem with such a randomness requires that the statistical order of the random response of the system is the same as that of the random excitation which is the case for the problem

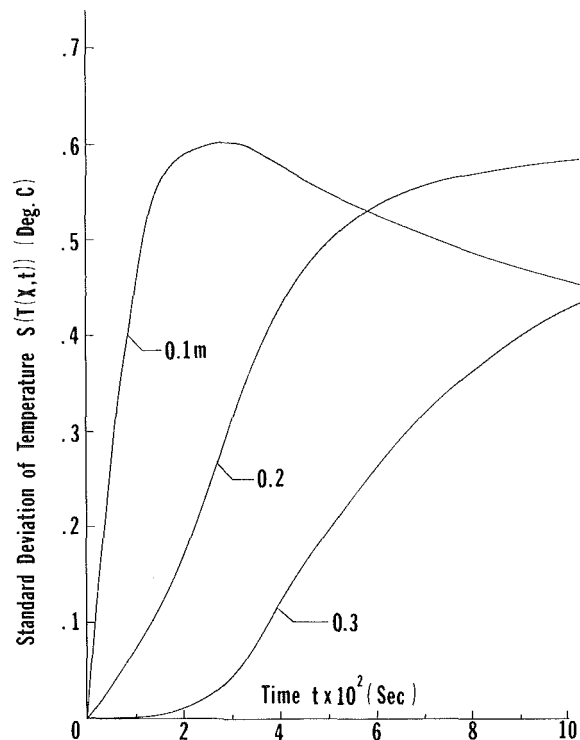


Fig. 5 Standard deviation of temperature distribution in the solid under the Gaussian process: $f(Y) = \exp(-pY)$

with extrinsic randomness. Numerical examples for the same random fluctuation $f(\alpha)$ under different stochastic processes (gamma and Gaussian) and the same stochastic process (Gaussian) with different random fluctuations (exponential and polynomial) are presented to illustrate the application of the present method. There are other situations in the engineering problems which the method presented in this paper can be applied as well. A typical example would be the diffusion process (heat or moisture) in porous media, such as ceramic material or water-saturated soil. The distribution of the porosity in such media are generally random and stochastic analysis is useful in revealing the maximum deviations of the system response from its mean value. Another useful application of the method is in the estimation of thermal resistance through two bodies with rough contact surfaces. Realistically, as shown in Fig. 8, the heat transfer process in the contact area between the two bodies A and B is governed by the heat conductivity of the body A , k_A ; the body B , k_B ; and the air gaps between the two bodies due to the irregular contact surfaces. The heat conductivity distribution for this case could be the one shown in Fig. 8. Due to the irregular distribution of the air gaps within the contact area, say, Δx , the transition characteristics of the thermal conductivity from k_A to k_B may fluctuate randomly, which may be simulated by a distribution function $g_1(x)$ with random amplitude $\epsilon f(\alpha)$, where $f(\alpha)$ is a random function change from case to case. The thermal conductivity in this case can be expressed as

$$k(x) = k_A \left\{ h(-x - \Delta x) + \frac{k_B}{k_A} h(x - \Delta x) + \frac{\epsilon f(\alpha)}{k_A} G(x) \right\} \quad (37)$$

with

$$G(x) = g_1(x) [h(x + \Delta x) - h(x - \Delta x)] \quad (38)$$

and

$$h(x - \Delta x) = \begin{cases} 1; & x \geq \Delta x \\ 0; & x < \Delta x \end{cases} \quad (\text{unit step function}) \quad (39)$$

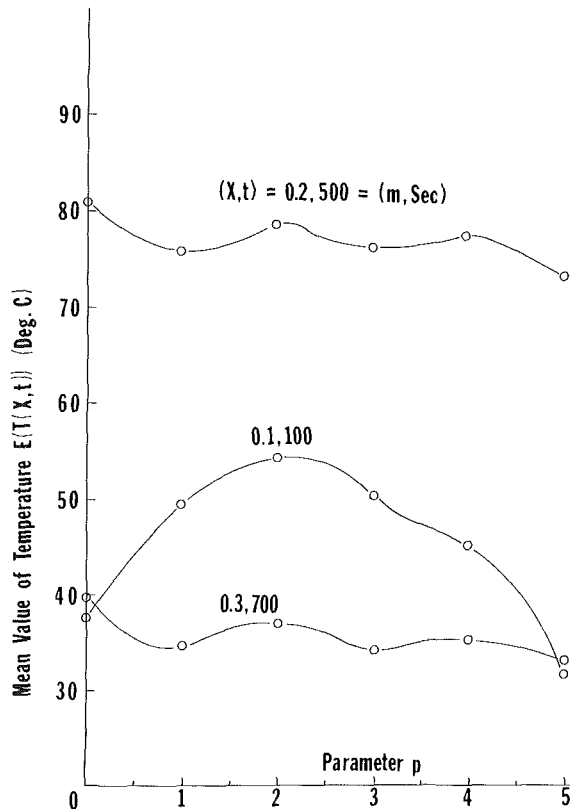


Fig. 6 Variation of mean value of temperature with respect to p for the Gaussian distribution: $f(Y) = Y^p$

This expression for the thermal conductivity can then be substituted into equation (1) and by selecting the ratio ϵ/k_A as the small parameter in the perturbation method, the statistical behavior of the temperature distribution as well as heat flux can be understood by solving the differential equations with variable, but deterministic coefficients in the various orders in the perturbation system. The other procedures can be repeated in the same fashion as we have gone through in the present analysis. The intrinsic randomness of the system will become more important as the global size of the solid medium becomes small, such as microchips. The maximum values of the standard deviation occurred in the neighborhood of the physical boundary at $x = 0$ (m), referring to Figs. 3 and 5. More detailed study about the size effects of the solid media on the amplification of the random fluctuations in physical systems should be done to understand this phenomenon quantitatively.

Development of local defects in structures has been studied in the open literature widely [6-10]. Application of the present method to the investigation of crack advancement in a material with intrinsic randomness is doubtless a challenging topic for the future research.

References

- 1 Tzou, D. Y., "Stress Intensity Factor of a Cracked Plate Under Stochastic Loading Spectrum," *J. Theoretical and Applied Fracture Mechanics*, 1985 (to be published).
- 2 Singh, G., and Singh, A., "Wave Propagation in Linear Random Nonhomogeneous Visco-elastic Semi-infinite Bar," *Indian J. of Pure and Applied Math.*, Vol. 11/8, 1980, pp. 1095-1104.
- 3 Roy Choudhuri, S. K., "Wave Propagation in Semi-infinite Elastic Bars With Randomly Varying Elastic Modulus," *ASME J. of Applied Mechanics*, Vol. 52, 1985, pp. 222-225.
- 4 Crump, K. S., "Numerical Inversion of Laplace Transforms Using a Fourier Series Approximation," *JACM*, Vol. 23, 1976, pp. 89-96.

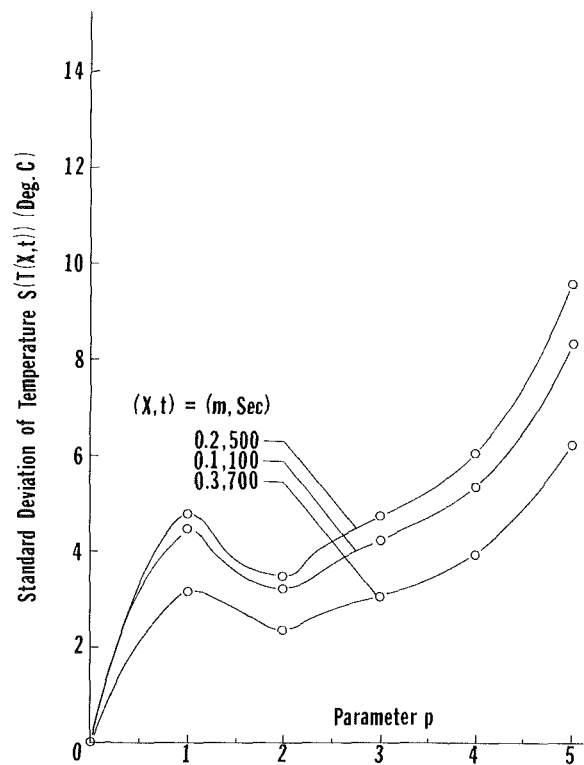


Fig. 7 Variation of standard deviation with respect to p for the Gaussian distribution: $f(Y) = Y^p$

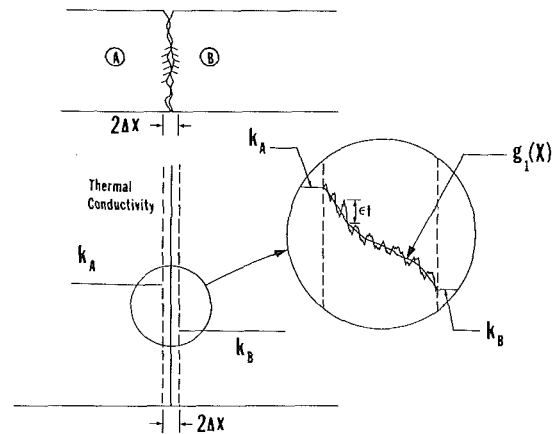


Fig. 8 Intrinsic randomness of thermal conductivity in the contact region between two bodies

5 Elishakoff, I., *Probabilistic Methods in the Theory of Structures*, Wiley Interscience, New York, 1983.

6 Sih, G. C., and Tzou, D. Y., "Crack Initiations in a Solid With Hyperbolic Nature of Heat Conduction," *J. of Theoretical and Applied Fracture Mechanics*, 1986 (to be published).

7 Sih, G. C., and Tzou, D. Y., "Mechanics of Nonlinear Crack Growth: Effect of Specimen Size and Loading Steps," *Proceedings on Modeling Problems in Crack Tip Mechanics*, J. T. Pindera, ed., Martinus Nijhoff, The Hague, 1984.

8 Tzou, D. Y., and Sih, G. C., "Crack Growth Prediction of Subsurface Crack in Yielded Material," *ASME Journal of Applied Mechanics*, Vol. 52, 1985, pp. 237-240.

9 Tzou, D. Y., "Intensification of Externally Applied Magnetic Field Around a Crack in Layered Composite," *J. of Theoretical and Applied Fracture Mechanics*, Vol. 4, 1985, pp. 191-199.

10 Tzou, D. Y., "Influence of Stacking Sequence on the Instability of Layered Composite," *Advanced Composite Materials and Structures*, G. C. Sih, ed., VNS Press, The Netherlands, 1985.

Methodology for Comparison of Inverse Heat Conduction Methods

M. Raynaud

J. V. Beck

Heat Transfer Group,
Mechanical Engineering Department,
Michigan State University,
East Lansing, MI 48824

The inverse heat conduction problem involves the calculation of the surface heat flux from transient measured temperatures inside solids. The deviation of the estimated heat flux from the true heat flux due to stabilization procedures is called the deterministic bias. This paper defines two test problems that show the tradeoff between deterministic bias and sensitivity to measurement errors of inverse methods. For a linear problem, with the statistical assumptions of additive and uncorrelated errors having constant variance and zero mean, the second test case gives the standard deviation of the estimated heat flux. A methodology for the quantitative comparison of deterministic bias and standard deviation of inverse methods is proposed. Four numerical inverse methods are compared.

1 Introduction

The inverse heat conduction problem (IHCP) involves the estimation of surface heat flux and/or temperature histories from transient measured temperatures inside solids. Due to the diffusive nature of heat flow, the surface temperature changes are damped in the solids. Thus in the IHCP, slight inaccuracies in the measured interior temperatures due to normal experimental errors are magnified at the surface and can lead to oscillations in the calculated surface conditions.

Various procedures have been presented to reduce the sensitivity to measurement errors. Miller [1], Miller and Viano [2], and Tikhonov and Arsenin [3] have introduced regularizer methods. Mollification methods have been used by Murio [4, 5] to smooth the prediction at the surface while Hensel and Hills [6] used smoothing functions on the input data. Beck [7, 8] has stabilized the IHCP using several future time temperatures with a least-squares method. This procedure has been combined with a regularization method by Beck and Murio [9]. Future time temperatures and built-in smoothing have been introduced by Raynaud and Bransier [10] in a space-marching finite difference method. Weber [11] has developed a space-marching method that uses the hyperbolic form of the heat conduction equation. Unfortunately, in all of the procedures, greater stability is only achieved with a loss of accuracy, i.e., the estimated input heat flux is in error.

It is often necessary to be able to estimate the deviation from the true heat flux due to the stabilization, herein called the deterministic bias, as well as the sensitivity to measurement errors of the method. Such an estimation was made by Hensel and Hills [6], but their concepts of analysis require that an explicit relation between the surface conditions and the known interior conditions be derived given the inverse algorithm. This may be easy for one method but difficult for another one. Moreover if the deterministic bias is desired, this relationship must be derived not only for the stabilized version of the surface estimates but also for the nonstabilized surface estimates. In the method proposed by Raynaud and Bransier [10], stabilization is incorporated within the algorithm; although the magnitude of the stabilization can easily be varied, it cannot be eliminated; thus the deterministic bias cannot be determined by this procedure. Consequently, another means of predicting deterministic bias and sensitivity to measurement error is needed.

The first purpose of this paper is to define two test prob-

lems. These two problems are readily applicable to all inverse methods. The first is a measure of the deterministic bias of the method while the second one indicates its sensitivity to measurement errors. With these two test cases, the tradeoff that exists between deterministic bias and sensitivity to measurement errors is clearly shown.

Numerous inverse methods have been proposed. Although some criteria for comparison have been given by Beck [12], the quantitative comparison of methods is difficult. The second purpose of this work is to demonstrate how these two test problems can be used to compare the results given by different inverse algorithms quantitatively. The ideal inverse method would be insensitive to measurement errors and would be able to reproduce the surface heat flux accurately; practically this means that both minimum deterministic bias and minimum sensitivity to measurement errors are desired. Unfortunately only a tradeoff is possible. For the same deterministic bias, it is possible to determine the method that is least sensitive to measurement errors; for the same sensitivity to measurement errors the most accurate method is the one that has the smallest deterministic bias.

The surface heat fluxes estimated by four inverse methods are compared to illustrate this evaluation of inverse procedures. The four compared methods [10, 11, 13, 14] were selected for their ease of implementation on computer and to give some insights on the IHCP. D'Souza's method [13] does not use future temperatures and cannot be stabilized for very small time steps. The three others, Raynaud and Bransier's method [10], Weber's method [11], and Beck's method [14] are stabilized using different principles and all of them use future temperatures.

In Section 2, the two test cases are defined. Section 3 briefly describes the selected methods. Section 4 presents results of numerical computations and an analysis of the effects of the stabilizing procedures on the deterministic bias and the sensitivity to measurement errors. The influence of the time step is also investigated. Section 5 gives a summary and some conclusions.

2 Test Cases

The one-dimensional linear heat conduction problem illustrated in Fig. 1 is selected as a basis for the application of the test cases. The temperature is known as a discrete function of time at the location $x=E$. The boundary at $x=L$ is insulated. It is desired to predict the transient flux history at $x=0$.

The problem in dimensional form is:

Contributed by the Heat Transfer Division and presented at the ASME Winter Annual Meeting, Miami Beach, Florida, November 17-22, 1985. Manuscript received by the Heat Transfer Division December 17, 1985.

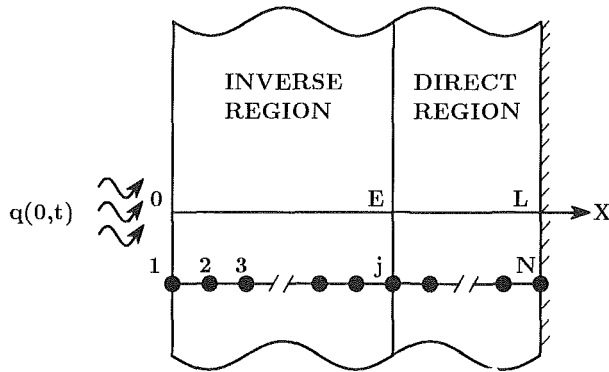


Fig. 1 Inverse heat conduction problem considered

$$\frac{\partial T}{\partial t} = \alpha \frac{\partial^2 T}{\partial x^2} \quad 0 \leq x \leq L \quad t > 0 \quad (1a)$$

$$T(E, T) = Y(t) \quad x = E \quad t > 0 \quad (1b)$$

$$\frac{\partial T}{\partial x} = 0 \quad x = L \quad t > 0 \quad (1c)$$

$$T(x, 0) = T_0 \quad 0 \leq x \leq L \quad (1d)$$

$$q(0, t) = -k \frac{\partial T}{\partial x} \Big|_{x=0} \text{ is to be estimated } t > 0 \quad (1e)$$

where T_0 is the uniform initial temperature. The above problem can be made dimensionless by defining

$$T^+(x^+, t^+) = \frac{T - T_0}{q_0 L / k}, \quad Y^+(t^+) = \frac{Y - T_0}{(q_0 L / k)} \quad (2a)$$

$$x^+ = \frac{x}{L}, \quad t^+ = \frac{\alpha t}{L^2}, \quad q^+ = \frac{q}{q_0}, \quad E^+ = \frac{E}{L} \quad (2b)$$

where q_0 is a nominal value of the surface heat flux. Hence equation (1) can be written as

$$\frac{\partial T^+}{\partial t^+} = \frac{\partial^2 T^+}{\partial x^{+2}} \quad 0 \leq x^+ \leq 1 \quad t^+ > 0 \quad (3a)$$

$$T(E^+, t^+) = Y^+(t^+) \quad x^+ = E^+ \quad t^+ > 0 \quad (3b)$$

$$\frac{\partial T^+}{\partial x^+} = 0 \quad x^+ = 1 \quad t^+ > 0 \quad (3c)$$

$$T^+(x^+, 0) = 0 \quad 0 \leq x^+ \leq 1 \quad (3d)$$

$$q^+(0, t^+) = - \frac{\partial T^+}{\partial x^+} \Big|_{x^+=0} \quad (3e)$$

For convenience in the remainder of the paper, the dimensionless terms in equation (3) are used with the + superscripts omitted.

The purpose of the first test case is to estimate the deterministic bias of inverse methods. In most inverse algorithms, the arbitrary $q(0, t)$ curve is approximated by a series of fluxes q^1, q^2, \dots, q^m that are constant during equally spaced time intervals Δt . The inverse algorithm predicts these heat flux components given the temperature history at one or more points remote from the surface. Many inverse methods are called sequential methods because the components are estimated one at a time. Consider a heat flux impulse that is constant and equal to unity over just one time step and zero at other times

$$q(0, t) = \begin{cases} 1 & t_0 - \Delta t/2 \leq t \leq t_0 + \Delta t/2 \\ 0 & t < t_0 - \Delta t/2 \text{ or } t > t_0 + \Delta t/2 \end{cases} \quad (4a)$$

or

$$q^n = \begin{cases} 1 & n = s \\ 0 & n \neq s \end{cases} \quad (4b)$$

How well a method can estimate this heat flux is fundamental for two reasons. First, this impulse flux is the smallest temporal fluctuation that can be estimated. Second, for a linear problem, due to the principle of superposition any time variation of surface flux can be represented by superposition of such basic elements. Most inverse methods estimate impulses of variable magnitude to approximate the $q(0, t)$ curve. Thus the ability of the method to estimate the impulse faithfully is of great importance. An algorithm capable of reproducing this impulse will be capable of closely determining any $q(0, t)$ curve. Such an algorithm is said to have a high resolving power [6] and has a low deterministic bias. On the other hand, an algorithm that smooths this impulse will not be able to estimate quick transients of the flux accurately. In this situation the resolution is low, that is, the deterministic bias is large.

One measure of the deterministic bias is the magnitude of the deviation from the exact heat flux at the time of the impulse

$$B_1 = 1 - \hat{q}^s \quad (5)$$

where \hat{q}^s is the estimated component of the flux at time $t_0 = s\Delta t$.

Another measure of the deterministic bias is obtained from

Nomenclature

B_1 = first measure of the bias (equation (5))

B_2 = second measure of the bias (equation (6))

E = sensor distance from heated surface

k = thermal conductivity

L = slab thickness

N = total number of spatial nodes

P = Fourier modulus = $\alpha \Delta t / \Delta x^2$

q = heat flux

q_0 = nominal heat flux

r = number of future temperatures

s = standard deviation of the estimates (equation (10))

T = temperature

T_0 = initial temperature

t = time

t_0 = instant of the impulse

x = distance from heated surface

Y = measured temperature

α = thermal diffusivity

γ = parameter (equation (17))

γ_m = maximum value of γ (equation (23))

Δt = time step size

Δt_E = time step made dimensionless with E : $\Delta t_E = \alpha \Delta t / E^2$

Δx = space step size

ϕ = sensitivity coefficient

Subscripts

E = relative to the sensor location

i = grid space number

j = grid space number at the sensor location

Superscripts

m = total number of time steps

n = time index

s = relative to the instant of the impulse $t_0 / \Delta t$

$+$ = dimensionless value

the square root of the sum of the squares of the deviations of the estimated components from the true components.

$$B_2 = \left[\sum_{n=1}^m (q^n - \hat{q}^n)^2 \right]^{1/2} \quad (6)$$

Note that B_2 does not depend on m since the \hat{q}^n tend to zero when $n \gg s$. One need only be careful to make m sufficiently large. These two measures emphasize different aspects of the deterministic bias. The first one, equation (5), does not take into account the possible lag of the signal but only expresses its amplitude, while the second one, equation (6), obtains its contribution from the whole time domain.

Exact temperature data are needed to effect this test case. The dimensionless temperature solution for a unit step increase in the surface flux is [15]

$$T(x, t) = t + \frac{1}{3} - x + \frac{x^2}{2} - \frac{2}{\pi^2} \sum_{k=1}^{\infty} \frac{1}{k^2} e^{-k^2 \pi^2 t} \cos(k\pi x) \quad (7)$$

The exact data for the impulse heat flux test case at time t are given by

$$t < t_0 - \frac{\Delta t}{2} \quad Y(t) = 0 \quad (8a)$$

$$t_0 - \frac{\Delta t}{2} \leq t \leq t_0 + \frac{\Delta t}{2} \quad Y(t) = T(E, t - t_0 + \frac{\Delta t}{2}) \quad (8b)$$

$$t > t_0 + \frac{\Delta t}{2} \quad Y(t) = T(E, t - t_0 + \frac{\Delta t}{2}) - T(E, t - t_0 - \frac{\Delta t}{2}) \quad (8c)$$

The number of terms in the summation of equation (7) is chosen such that the temperatures are known within six significant figures.

The purpose of the second test case is to study the sensitivity to measurement errors of inverse algorithms. In practical applications the temperature history at the measurement location is known as a discrete function of time Y^1, Y^2, \dots, Y^m . Each discrete temperature may or may not contain a random error. Consider the case where all input temperatures equal zero, except the temperature at time t_0 is equal to unity:

$$Y(t) = \begin{cases} 1 & t = t_0 \\ 0 & t \neq t_0 \end{cases} \quad (9a)$$

or

$$Y^n = \begin{cases} 1 & n = s \\ 0 & n \neq s \end{cases} \quad (9b)$$

These input data can be considered as an error of magnitude 1 at time t_0 . If this error were not present, all input temperatures would be zero and the estimated heat flux components would also be equal to zero. The estimated heat flux based on the input data of equation (9) shows the propagation of a single error. The magnitude of the disturbance in the surface heat flux depends on the sensitivity of the inverse algorithm to measurement errors. The higher the sensitivity to measurement errors, the larger the disturbance. It might seem inappropriate to study the effect of a single error because all temperatures are likely to have errors but we can make some assumptions on the statistical properties of measurement errors to show the adequacy of this test case. If the random errors are additive, uncorrelated, and have zero mean and constant variance σ^2 then the standard deviation of the heat flux components for linear problems is given by [17]

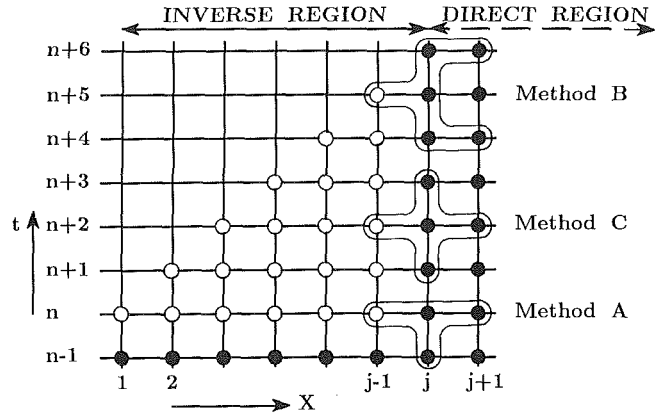


Fig. 2 Computation molecules; solid circles for known temperatures, open circles for temperatures to be calculated

$$\sigma_q = \left[\sigma^2 \sum_{n=1}^m \hat{q}^{n^2} \right]^{1/2} \quad (10)$$

where the \hat{q}^n values are calculated from the input temperatures of equation (9). For stable algorithms, the \hat{q}^n approach zero for $n \gg s$ since the effect of a single error decays with time. Thus σ_q , like B_2 , is not a function of m provided m is large enough. Equation (10) relates the standard deviation of the surface estimate to the standard deviation of the measurements. In the remainder of the paper σ is set equal to 1 in equation (10) so that σ_q expresses the ratio of the standard deviation of the estimated surface heat flux to the standard deviation of the measurement errors. It is important to note that the standard deviation of the heat flux components is constant for times far from the starting and ending times (for linear problems with the statistical assumptions of additive, uncorrelated errors with zero mean and constant variance). Hence this test case need be run only once with $t_0 > 10\Delta t$ to get the standard deviation of most of the surface flux estimates. Hills et al. [18] have shown that the standard deviation of the surface flux estimates given by an adjoint formulation, a direct estimation, and the impulse temperature test case are in excellent agreement when the above assumptions on the measurement errors are satisfied.

3 Description of the Methods

The geometry of the IHCP can be divided into a direct and an inverse region as shown in Fig. 1. The problem of the direct region $E \leq x \leq 1$ is a classical boundary value problem. Some inverse procedures first calculate the temperature field in the direct region and then calculate the temperature field in the inverse region. These methods can be termed space-marching techniques, and three of those described here incorporate that feature.

For each method the direct problem is solved using the Crank-Nicolson finite difference scheme. It has been found that the solution procedure in this region has a negligible influence on the final result [16].

The first method (Method A) was proposed by D'Souza [13]. The backward difference approximation for the time derivative and central difference approximation for the space derivative are used in equation (3)

$$\frac{T_{i-1}^n - 2T_i^n + T_{i+1}^n}{\Delta x^2} = \frac{T_i^n - T_i^{n-1}}{\Delta t} \quad (11)$$

Solving for T_{i-1}^n yields

$$T_{i-1}^n = \left(2 + \frac{1}{P}\right) T_i^n - T_{i+1}^n - \frac{1}{P} T_i^{n-1} \quad (12)$$

for $i=j, j-1, \dots, 3, 2$ and $n=1, 2, \dots, m$.

$$P = \Delta t / \Delta x^2 \quad (13)$$

where m is the total number of times for the measured temperatures. The computation molecule is shown in Fig. 2 and one can see that only past and present temperatures are used to obtain the present temperature estimate at node $i-1$. After calculating the temperature at node $j-1$, the temperature at node $j-2$ can be calculated in an explicit manner using equation (12). This is continued to the surface temperature.

The second method (Method B), proposed by Raynaud and Bransier [10], uses a double approximation for equation (3), both of which are given by energy balance equations. The first energy balance in dimensionless form is

$$\frac{\tilde{T}_{i-1}^n - \tilde{T}_i^n}{\Delta x} - \frac{\tilde{T}_{i+1}^{n+1} - \tilde{T}_{i+1}^n}{\Delta x} = \Delta x \frac{\tilde{T}_i^{n+1} - \tilde{T}_i^n}{\Delta t} \quad (14)$$

The second is

$$\frac{\tilde{T}_{i-1}^n - \tilde{T}_i^n}{\Delta x} - \frac{\tilde{T}_i^{n-1} - \tilde{T}_{i+1}^{n-1}}{\Delta x} = \Delta x \frac{\tilde{T}_i^n - \tilde{T}_i^{n-1}}{\Delta t} \quad (15)$$

Solving equation (14) to approximate \tilde{T}_{i-1}^n and equation (15) to approximate \tilde{T}_{i-1}^n , and taking the arithmetic mean leads to

$$T_{i-1}^n = \frac{\tilde{T}_{i-1}^n + \tilde{T}_{i-1}^n}{2} = \left[\left(1 + \frac{1}{P} \right) T_{i+1}^{n+1} + 2T_i^n + \left(1 - \frac{1}{P} \right) T_{i+1}^{n-1} - T_{i+1}^{n+1} - T_{i+1}^{n-1} \right] / 2 \quad (16)$$

for $n=1, 2, 3, \dots, m+i-j-1$ and $i=j, j-1, j-2, \dots, 2$. Notice that the calculations in the time direction are performed for a given spatial node, i , before proceeding to the next node. The computation molecule is shown in Fig. 2. Equation (16) is valid for $n=1$ since the initial temperature is known. On the other hand, equation (16) is not applicable at the end of the time period. Instead of modifying the equation, a preferred approach is to generate the solution up to a diagonal line as shown in Fig. 2. It can be seen in Fig. 2 that the estimation of the surface temperature at time n involves the measured temperature at time $n+j-1$ where j is the grid space number at $x=E$. Refining the grid has the effect of increasing the number of future temperatures and the number of steps done to reach the surface. At each step, T_{i-1}^n is approximated by the arithmetic average of \tilde{T}_{i-1}^n and \tilde{T}_{i-1}^n ; consequently the more space steps the cruder the approximation for the surface temperature. An efficient algorithm for this method is described in [10].

Weber [11] (Method C) used the hyperbolic form of the heat conduction equation

$$\gamma \frac{\partial^2 T}{\partial t^2} + \frac{\partial T}{\partial t} = \frac{\partial^2 T}{\partial x^2} \quad (17)$$

where γ is a nonnegative constant. Central differences in both time and space are used to approximate equation (17)

$$\gamma \frac{T_{i-1}^{n-1} - 2T_i^n + T_{i+1}^{n+1}}{\Delta t^2} + \frac{T_{i+1}^{n+1} - T_{i-1}^{n-1}}{2\Delta t} = \frac{T_{i+1}^n - 2T_i^n + T_{i-1}^n}{\Delta x^2} \quad (18)$$

Solving for T_{i-1}^n gives

$$T_{i-1}^n = \frac{\Delta x^2}{\Delta t} \left[\left(\frac{\gamma}{\Delta t} + \frac{1}{2} \right) T_{i+1}^{n+1} + \left(\frac{\gamma}{\Delta t} - \frac{1}{2} \right) T_{i-1}^{n-1} + \frac{2}{\Delta t} \left(\frac{\Delta t^2}{\Delta x^2} - \gamma \right) T_i^n \right] - T_{i+1}^n \quad (19)$$

for $n=1, 2, 3, \dots, m+i-j-1$ and $i=j, j-1, j-2, \dots, 3, 2$. The computation molecule is shown in Fig. 2 for T_{i-1}^{n+1} . The calculation of the temperatures proceeds toward the surface as for method B. The future temperature at time $n+j-1$ is involved in the estimation of the surface temperature at time n as in method B.

For these three methods, the surface heat flux is calculated from the temperature distribution using the following energy balance at the surface node:

$$\hat{q}^n = \frac{T_1^n - T_2^n}{\Delta x} + \frac{\Delta x}{2} \frac{T_1^{n+1} - T_1^{n-1}}{2\Delta t} \quad (20)$$

This equation is valid for $n=1, 2, \dots, m$ for method A. Using methods B or C, the surface heat flux components are only calculated for $n=1, 2, \dots, m-j$.

The fourth method (Method D) proposed by Beck [14] is a time-marching technique. At each time step the surface flux is calculated using a least-squares minimization procedure for the measurement-simulation temperature difference. The function

$$F(q^n) = \sum_{k=1}^r (Y^{n+k} - T_j^{n+k})^2 \quad (21)$$

is to be minimized, where r is the number of future temperatures. If $r=1$, the calculated temperature T_j^{n+1} equals the measured temperature Y^{n+1} , and no bias is introduced. For this method the heat flux component, q^n , best represents the surface heat flux at time $(n-0.5)\Delta t$. For further discussion of this method see [17].

4 Numerical Comparison

The case of a known temperature at $x=0.5$ with $t_0=10\Delta t$ ($s=10$); is selected as a basis for the application of the methods. For method D and for the impulse heat flux test case, $t_0=10\Delta t+0.5\Delta t$. This shift is done so that equations (5), (6), and (10) gives the most accurate values of the deterministic bias and standard deviation for the four methods. The heat flux is estimated over 25 time steps. It is well known that the parameter of prime importance for the IHCP is the time step. Three values are chosen: $\Delta t=0.005, 0.01$, and 0.05 . Thus the dimensionless time steps Δt_E based on the distance from the sensor location to the heated surface are, respectively, $\Delta t_E=0.02, 0.04$, and 0.2 , which are typical of practical IHCPs [17, 20].

The number of grid points is the only parameter to fix in methods A and B. Method B is stabilized by refining the spatial grid. For these two methods the results are presented with $N=5, 11$, and 21 for the sensor being at $x=0.5$. The number of future temperatures for Method B is 2, 5, and 10, respectively.

In order to facilitate the comparison, the numbers of future temperatures, r , in method D were chosen so that the deterministic biases were comparable with the ones of method B. The adopted values for r are 4, 5, and 7. The procedure is stabilized by increasing the number of future temperatures. The results of this method have been obtained using the code CONTA [19].

Method C can be stabilized with two parameters: N the number of grid points and the constant γ . Weber [11] indicated that γ should be chosen small and used $\gamma=0.01$. Unfortunately, the influence of γ depends on the values of the time and space steps. If Δx is fixed, equation (19) shows that the weight of a particular value of γ in the coefficients of T_{i+1}^{n+1} , T_i^n , and T_{i-1}^{n-1} depends on the size of Δt . Similarly, if Δt is fixed, the influence of γ varies with the value of Δx . This correlation between Δt , Δx , and γ does not facilitate the choice of γ . However, Weber's algorithm is stable provided

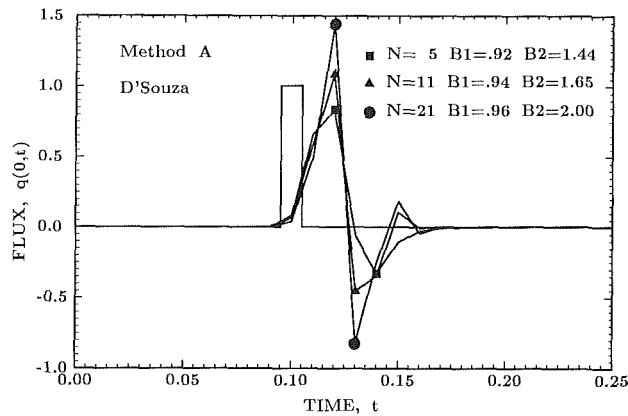


Fig. 3(a)

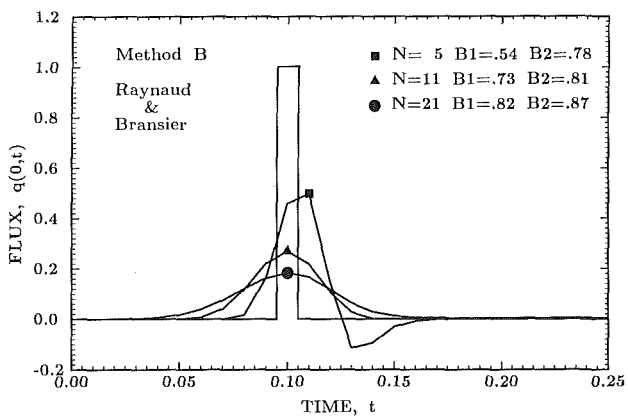


Fig. 3(b)

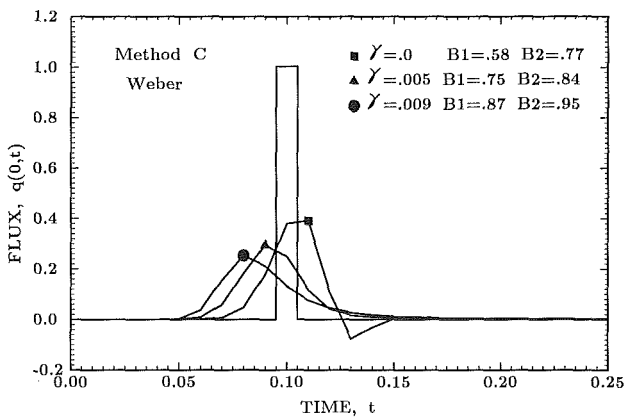


Fig. 3(c)

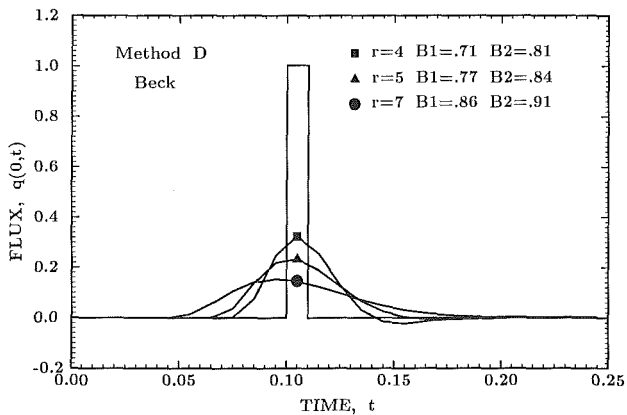


Fig. 3(d)

Fig. 3 Comparison between exact and estimated heat flux ($\Delta t = 0.01$): (a) Method A, (b) Method B, (c) Method C, (d) Method D

Table 1(a) First measure of the bias = B_1

Δt	.005	.01	.05
Method A	1.00	.94	.77
Method B	.70	.73	.73
Method C	.76	.75	.92
Method D	.71	.77	.85

Method A: $N = 11$ Method B: $N = 11$
 Method C: $\gamma = .5\gamma_m = 50\Delta t$ Method D: $r = 5$

Table 1(b) Second measure of the bias = B_2

Δt	.005	.01	.05
Method A	1.85	1.65	1.43
Method B	.79	.81	.80
Method C	.76	.84	1.03
Method D	.82	.84	.91

Method A: $N = 11$ Method B: $N = 11$
 Method C: $\gamma = .5\gamma_m = 50\Delta t$ Method D: $r = 5$

$$\gamma \leq \frac{\Delta t^2}{\Delta x^2} \quad (22)$$

All of the results presented here were computed with $N=11$ in order to introduce some future temperatures and γ was successively set equal to 0., $0.5\gamma_m$, and $0.9\gamma_m$ where γ_m was the maximum value given by the stability limit

$$\gamma_m = \frac{\Delta t^2}{\Delta x^2} \quad (23)$$

When $\gamma=0$, Weber's algorithm and the algorithm of Hensel and Hills [6] are very similar provided no smoothing function is used in the latter.

Evaluation of the Deterministic Bias. The deterministic bias is determined by using the impulse heat flux test case defined by equation (4). Figures 3(a, b, c, d) show the heat flux respectively estimated by methods A, B, C, and D when $\Delta t = 0.01$. The shape of the impulse is quite well reproduced in Fig. 3(a) when $N=5$ but is shifted in time, which gives a large value of the deterministic bias. As outlined by Beck [8, 14] an inverse method needs to incorporate future temperatures to anticipate abrupt changes of the surface heat flux because of the lag between surface and interior temperature changes. Since D'Souza's method does not use future temperatures the signal is not estimated at the correct time. Note that the smaller N , the better the results. For methods B, C, and D the effects of increasing the stabilizing parameters (N , γ , and r , respectively) is to spread the estimate of the impulse over more time steps and to decrease its amplitude. As the values of N , γ , and r are increased, the resolving power is significantly reduced and the deterministic bias is increased. For all methods, the sum of the heat flux components over the 25 time steps is equal to 1 or very near 1. Thus, conservation of energy is satisfied. Figure 3(b) shows that the estimates of method B are symmetric for $N=11$ and 21. They are not symmetric for $N=5$ because only two future temperatures are introduced, which is not enough for this sensor location and time step to predict the abrupt variation of heat flux at the surface. On the other hand Fig. 3(c) shows that method C anticipates too strongly the heat flux change when γ is increased. A comparison of Fig. 3(b) with $N=11$ (triangle symbol) and Fig. 3(c)

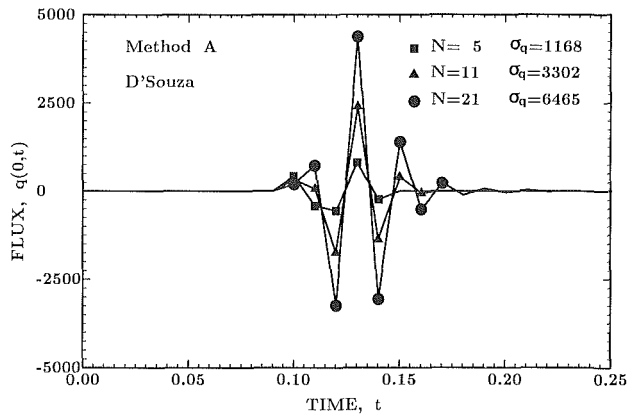


Fig. 4(a)

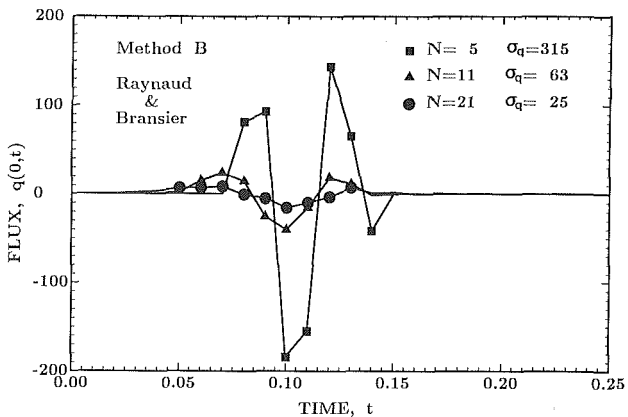


Fig. 4(b)

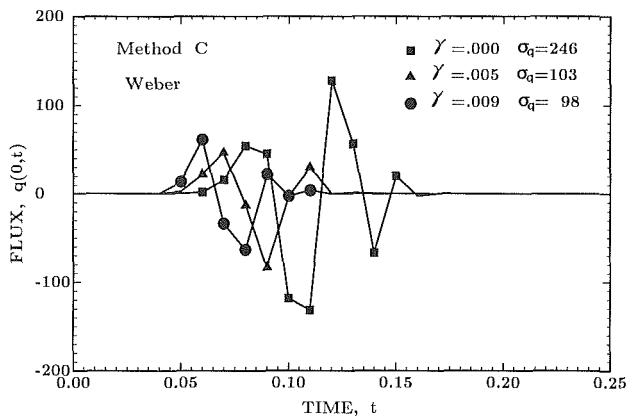


Fig. 4(c)

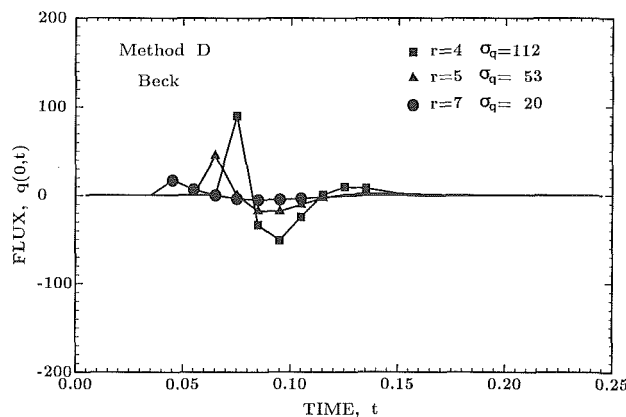


Fig. 4(d)

Fig. 4 Influence of a single error at time $t_0 = 0.1(\Delta t = 0.01)$: (a) Method A, (b) Method B, (c) Method C, (d) Method D

Table 2 Standard deviation of the estimates

Δt	.005	.01	.05
Method A	35832	3302	78.2
Method B	573	63	5.4
Method C	883	103	10.8
Method D	442	53	3.1

Method A: $N = 11$ Method B: $N = 11$
 Method C: $\gamma = .5\gamma_m = 50\Delta t$ Method D: $r = 5$

with $\gamma = 0$ (square symbol) indicates that the bias is greater in method B than method C, even though the same number of future temperatures is used.

The two measures of the bias B_1 and B_2 (equations (5) and (6)) are given in Tables 1(a, b) for the three studied time steps and for the parameter values of $N = 11$, $\gamma = 0.5\gamma_m$, and $r = 5$. The values of B_1 and B_2 given in Figs. 3(a, b, c, d) and Tables 1(a, b) show that, method A excepted, the two measures of the deterministic bias vary similarly with the second measure always being larger. For method A, B_2 is larger and differs from B_1 , because of the time lag. The deterministic bias is nearly constant for method B and increases slightly for methods C and D as the time step is increased.

The impulse heat flux test case clearly shows the loss of resolution due to the stabilization procedures; it indicates that the deviation from the true heat flux is nearly independent of the time step for constant values of the stabilizing parameters. Consider, for example the estimation of a given heat flux using an algorithm permitting a sufficiently small time step to represent the changes of the heat flux. Recall that the $q(0, t)$ curve is approximated by a series of constant heat flux components q^1, q^2, \dots, q^m . If an even smaller time step is used to describe the abrupt variations of the flux better and the same value of the stabilizing parameter is kept, then the deviation from the true heat flux is only slightly less than the one for the original time step. To improve the resolving power significantly (or equivalently to introduce less deterministic bias), it is necessary to change the value of the stabilizing parameter.

Evaluation of the Variance of the Estimates. The effects of the stabilizing processes on the sensitivity to measurement errors are now studied by using the impulse temperature test case defined by equation (9). The estimated heat fluxes are shown in Figs. 4(a, b, c, d) for methods A, B, C, and D, respectively. The values of the stabilizing parameters are identical to the ones taken to obtain Figs. 3(a, b, c, d). One can first notice that the disturbances caused by a single error are about 20 times larger for method A than for other methods. For this method the standard deviation of the estimates increases with N . Since the smallest deterministic bias was also obtained with small values of N , the best result for this method are obtained with a small number of grid points. For method C, Fig. 4(c) shows that the effects of error measurements are somewhat reduced when γ is increased. On the other hand, the sensitivity to measurement errors is greatly reduced when N and r are increased in methods B and D, respectively. Both methods give similar results. One can note that the error in the input data at time $t_0 = 10\Delta t$ gives rise to fluctuations at the surface at times smaller than at time t_0 . This is due to the use of future temperatures in methods B, C, and D. Comparison of Figs. 4(b) and 4(c) shows that, whatever the value of γ , method B is less sensitive to measurement errors than method C, even if the number of future temperatures is the same ($N = 11$ in Fig. 4(b) in both methods).

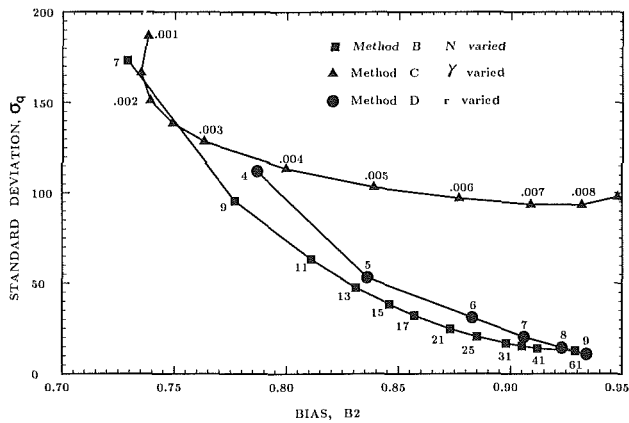


Fig. 5 Comparison of standard deviation versus bias for Methods B, C, and D, $\Delta t = 0.01$

Figures 3(a, b, c, d) and Figs. 4(a, b, c, d) indicate the tradeoff between resolving power and sensitivity to measurement errors. For a given inverse method, the only way of reducing the standard deviation of the surface estimates is to reduce the resolving power (i.e., increase the deterministic bias). This has been observed for method B for the estimation of a surface heat flux from experimental data [20].

Influence of the time step on the sensitivity to measurement errors is presented in Table 2. The parameters for each method are identical to those of Tables 1(a, b). For all the methods, the standard deviation of the estimated surface heat flux increases sharply as the time step decreases. Note that there is no reason to change the magnitude of the error when the time step is changed since when dealing with a given set of experimental data the standard deviation of the measurement is fixed and not influenced by the time step chosen in the inverse algorithm. Table 2 indicates the sensitivity of the inverse problem to random errors, particularly when small time steps are used. For example, if one uses method D with $r = 5$, the ratio of standard deviations of the estimates to standard deviation of measurement errors is only 3.1 when $\Delta t = 0.05$, but is 442 when the time step is ten times smaller. This test case shows an important characteristic of the IHCP. One may decide to decrease the time step to describe more accurately abrupt variations of the flux, but in doing so the sensitivity to measurement errors is increased. Furthermore it may be necessary to change the value of the stabilizing parameter to reduce the standard deviation of the estimates, resulting in the deterministic bias being increased. Consequently the global accuracy of the estimates is not necessarily improved by decreasing the time step.

For a given method and a given set of measurement data at a specific location, there is an optimal balance between deterministic bias and standard deviation of the estimated flux.

Comparison of Methods. The second objective of this work is to provide a methodology for the comparison of inverse methods. The methods should be compared for a given time step and sensor location. One approach is to determine which of the methods is the least sensitive to random errors for the same deterministic bias. This can easily be done by plotting, on the same graph and for each method, the standard deviation of the estimates versus the deterministic bias for different values of the stabilizing parameters. The second measure of the bias, B_2 , is used for this comparison. The curves obtained when $\Delta t = 0.01$ are shown in Fig. 5 for methods B, C, and D. Method A is not represented because the best point (for $N = 5$) has the coordinates (1.44, 1168) and is out of scale. Method B gives the most satisfying result, for this example, since it has the lowest sensitivity to measurement

errors for most of the range of the deterministic bias. For this time step, similar accuracy is obtained with methods B and D, particularly as N (method B) and r (method D) are large.

Not only does Fig. 5 allow the comparison of the methods, but it also indicates the sensitivity to the stabilizing parameters. For example, for method D the increase of r from 4 to 5 results in a 50 percent decrease of the standard deviation. It should be noted that changing the value of the stability parameters has much more effect on the standard deviation than on the deterministic bias. When r is increased from 4 to 9 in method D, the standard deviation is reduced by 90 percent while increasing deterministic bias by only 19 percent. This does not mean that one should always take a large value of the stability parameter. A particular application may require a small deterministic bias but could tolerate a large dimensionless standard deviation; if the actual measurement errors are small, a large dimensionless standard deviation may not result in a large actual standard deviation. Figure 5 helps to choose the appropriate value of the stabilizing parameter for $\Delta t = 0.01$.

All these results have been presented for a given sensor location. For another sensor location the relation developed by Raynaud [21] can be used instead of rerunning the two test cases.

5 Summary and Conclusions

The impulse heat flux test case provides a measure of the deviation of the estimated heat flux from the true heat flux. For linear problems, any time variation of surface heat flux can be represented by superposition of such impulses. How accurately a method can estimate this impulse flux is thus an indication of the ability of the method to predict a surface heat flux of any shape.

The impulse temperature test case shows the sensitivity of inverse methods to measurement errors. For linear problems, if the measurement errors are additive and uncorrelated and have zero mean and constant variance, then the standard deviation of the estimated heat flux can be predicted by running this test case.

The tradeoff between deterministic bias and sensitivity to measurement errors of inverse methods has been presented using the two test cases. For a given method reducing the sensitivity to measurement errors results in a greater bias.

For fixed value of a stabilizing parameter, the deterministic bias of a method increases slightly if the time step is decreased, while the sensitivity to measurement errors increases sharply. Thus decreasing the time step may not always be a good approach to gain accuracy since it may be necessary to lose resolution (by changing the stabilizing parameter) to control the standard deviation of the estimates. One can not simply choose a large time step, since in doing so the quick transient of the surface heat flux cannot be well represented. Another approach, such as the use of smoothing filters [22], can be tried in order to maintain a low sensitivity to measurement errors and yet not reduce the resolving power too much.

Besides insights into the inverse heat conduction problem, an important result of this paper is the development of a methodology for the quantitative comparison of deterministic bias and sensitivity to measurement errors of different inverse methods. Raynaud [22] has obtained very good agreement between the results of this methodology and the use of more usual test cases in comparing several inverse procedures. It is proposed that these two test cases be used to facilitate the comparison of existing and new inverse methods.

A relative ranking, for the test cases used, of the four methods can be done using Fig. 5. Method A is not shown in this figure because it is much too sensitive to random errors. Method C gives better results than method D only when γ is

small (low stabilization). Methods B and D give very similar results. Such a figure along with the criteria given by Beck et al. [12] should help the user in choosing the appropriate inverse method.

This paper gives quantitative measures for comparing various IHCP algorithms, unlike Beck et al. [12]. There are other considerations, however, such as the amount of computer time required and the ability of an algorithm to be extended to multidimensional problems. Method B is twice as fast as method D. But method D is the only one of those presented that extends in a direct manner to multidimensional problems [17] and can utilize multiple interior temperature measurement locations (see also [19]).

References

- 1 Miller, K., "Least Squares Methods for Ill-Posed Problems With a Prescribed Bound," *SIAM J. Math. Anal.*, Vol. 1, 1970, pp. 52-74.
- 2 Miller, K., and Viano, G., "On the Necessity of Nearly-Best Possible Methods for Analytic Continuation of Scattering Data," *J. Math. Physics*, Vol. 14, No. 8, 1973, pp. 1037-1048.
- 3 Tikhonov, A. N., and Arsenin, V. Y., *Solutions of Ill-Posed Problems*, V. H. Winston & Sons, Washington, DC, 1977.
- 4 Murio, D. A., "The Mollification Method and the Numerical Solution of an Inverse Heat Conduction Problem," *SIAM J. Stat. Comput.*, Vol. 2, 1981, No. 1.
- 5 Murio, D. A., "On the Estimation of the Boundary Temperature on a Sphere From Measurements at Its Center," *J. of Comp. and Applied Math.*, Vol. 8, No. 2, 1982, pp. 111-115.
- 6 Hensel, E. C., and Hills, R. G., "A Space Marching Finite Difference Algorithm for the One Dimensional Inverse Heat Conduction Problem," ASME Paper No. 84-HT-48, 1984.
- 7 Beck, J. V., "Surface Heat Flux Determination Using an Integral Method," *Nucl. Eng. Des.*, Vol. 7, 1968, pp. 170-178.
- 8 Beck, J. V., "Nonlinear Estimation Applied to the Nonlinear Inverse Heat Conduction Problem," *Int. J. Heat Mass Transfer*, Vol. 13, 1970, pp. 703-716.
- 9 Beck, J. V., and Murio, D.A., "Combined Function Specification Regularization Procedure for Solution of Inverse Heat Conduction Problem," *AIAA J.*, Vol. 24, 1986, pp. 180-185.
- 10 Raynaud, M., and Bransier, J., "A New Finite Difference Method for Nonlinear Inverse Heat Conduction Problem," *Num. Heat Transfer*, Vol. 9, No. 1, 1986, pp. 27-42.
- 11 Weber, C. F., "Analysis and Solution of the Ill-Posed Inverse Heat Conduction Problem," *Int. J. Heat Mass Transfer*, Vol. 24, No. 11, 1981, pp. 1783-1792.
- 12 Beck, J. V., "Criteria for Comparison of Methods of Solution of the Inverse Heat Conduction Problem," *Nucl. Eng. Des.*, Vol. 53, 1979, pp. 11-22.
- 13 D'Souza, N., "Numerical Solution of One-Dimensional Inverse Transient Heat Conduction by Finite Difference Method," ASME Paper No. 75-WA/HT-81, 1975.
- 14 Beck, J. V., Litkouhi, B., and St. Clair, C. R., "Efficient Sequential Solution of the Nonlinear Inverse Heat Conduction Problem," *Numer. Heat Transfer*, Vol. 5, 1982, pp. 275-286.
- 15 Carslaw, H. S., and Jaeger, J. C., *Conduction of Heat in Solids*, 2nd ed., Oxford, 1959.
- 16 Raynaud, M., "Détermination du Flux Surfaccique Traversant une Paroi à Partir de Mesures de Temperature Internes," Thèse, Paris VI, 1984.
- 17 Beck, J. V., Blackwell, B., and St. Clair, C. R., Jr., *Inverse Heat Conduction: Ill-Posed Problems*, Wiley, 1985.
- 18 Hills, R. C., Raynaud, M., and Hensel, E., "Surface Variance Estimates Using an Adjoint Formulation for a One-Dimensional Nonlinear Inverse Heat Conduction Technique," *Num. Heat Transfer*, accepted July 1986.
- 19 Beck, J. V., "User's Manual for CONTA—Program for Calculating Surface Heat Fluxes From Transient Temperatures Inside Solids," Sandia Nat. Lab. SAND 84-7134, 1983.
- 20 Raynaud, M., and Bransier, J., "Experimental Validation of a New Space Marching Finite Difference Algorithm for the Inverse Heat Conduction Problem," Eighth Int. Heat Transfer Conf., San Francisco, CA, Aug. 17-22, 1986.
- 21 Raynaud, M., "Some Comments on the Sensitivity to Sensor Location of Inverse Heat Conduction Problems Using Beck's Method," *Int. J. Heat Mass Transfer*, Vol. 29, No. 5, 1986, pp. 815-817.
- 22 Raynaud, M., "Combination of Methods for the Inverse Heat Conduction Problem With Smoothing Filters," AIAA Paper No. 86-1243, Boston, MA, 1986.

Thermal Contact Conductance of Packed Beds in Contact With a Flat Surface

G. P. Peterson

Assistant Professor.
Mem. ASME

L. S. Fletcher

Associate Dean of Engineering,
Professor.
Fellow ASME

Mechanical Engineering Department,
Texas A&M University,
College Station, TX 77843

An experimental investigation was conducted to determine the thermal contact conductance of packed beds of spherical particles in contact with flat surfaces. Beds comprised of four materials, Aluminum 2017-T4, Yellow Brass, Stainless Steel 304, and Chromium Alloy AISI 52100, all in contact with flat Stainless Steel 304, surfaces were evaluated in a vacuum environment, at a mean interface temperature of 66°C. In addition to the experimental program, an analytical expression was developed by combining previous work performed by other investigators. The results of the experimental investigation are compared with the analytical expression and indicate that an accurate method of predicting the thermal contact conductance at the interface between beds of spherical particles and nominally flat surfaces has been identified.

Introduction

Knowledge of the temperature drop that occurs at the interface formed when beds of spherical particles are in contact with a flat surface is necessary in order to determine the overall thermal characteristics of a wide variety of systems. Many of these systems, which include chemical catalytic reactors, cryogenic insulation, building insulation, heat exchangers, petroleum reservoirs, geothermal operations, and sphere-pac reactor fuels (Vafai and Alkire, 1984) require an accurate estimate of the thermal contact conductance for proper design and operation. Determination of this thermal contact conductance and the associated temperature drop, both analytically and experimentally, presents several rather unique problems not normally encountered with other types of geometry. Therefore, in order better to understand the parameters that govern the contact conductance in this physical arrangement, an experimental investigation of the thermal contact conductance occurring at the interface between packed beds of spherical metal particles and flat metallic surfaces was undertaken. Packed beds of four different materials were evaluated. These materials had a wide range of thermal and mechanical properties, as shown in Table 1, and included Aluminum 2017-T4, Yellow Brass, Stainless Steel 304, and Chromium Alloy AISI 52100, all in contact with nominally flat Stainless Steel 304 surfaces.

Review of Analytical Solutions

Heat transfer across an interface occurs by a combination of four different modes: conduction through the metal-to-metal contacts, conduction through the interstitial gases, convection in the interstitial gas region, and thermal radiation. The total contact conductance can be found by assuming that these four resistances occur in parallel. However, for metal surfaces in a vacuum with moderate interface temperature gradients, all but one of these, the metal-to-metal conduction, are either nonexistent or negligible.

Yovanovich (1971) developed a generalized analytical expression to predict the thermal constriction resistance between two metal paraboloids in contact, with the following assumptions:

(i) The radiation heat transfer effects were negligible.

(ii) There was no convection or conduction heat transfer in the surrounding fluids.

(iii) The effects of the surface roughness of the two surfaces were negligible.

$$k_m R_c = \frac{\psi [1/\rho]^{1/3}}{\left[12P \left(\frac{1-\nu_f^2}{E_f} + \frac{1-\nu_s^2}{E_s} \right) \right]^{1/3}} \quad (1)$$

Application of this technique to determine the thermal contact conductance between a single spherical surface in contact with a smooth flat surface has been presented by Yovanovich and Kitscha (1974). For the special case where the spherical surface and the flat surface are both located at the ends of two right circular cylinders, it was demonstrated that equation (1) may be simplified to

$$k_m R_c = \left[6Pr_s \left(\frac{1-\nu_f^2}{E_f} + \frac{1-\nu_s^2}{E_s} \right) \right]^{-1/3} \quad (2)$$

for metal-to-metal contact, where k_m is the mean harmonic conductivity expressed as

$$k_m = \frac{2k_s k_f}{k_s + k_f} \quad (3)$$

In an earlier work, Clausing and Chao (1965) presented an analytical technique for evaluating the effect of the constriction resistance of many microscopic asperities on the thermal contact conductance occurring between two semi-infinite solids. In developing this technique, which was in good agreement with the experimental results, the following assumptions were made:

Table 1 Material properties

Material*	Thermal conductivity, W/m ² ·°C	Modulus of elasticity, GPa
Aluminum 2017-T4	121.3	72
Yellow Brass	117.8	105
Chromium Alloy AISI 5200	44.8	197
Stainless Steel 304	17.3	190

*Manufactured by Specialty Ball Corporation.

Contributed by the Heat Transfer Division for publication in the JOURNAL OF HEAT TRANSFER. Manuscript received by the Heat Transfer Division October 27, 1986.

- (i) The areas of actual contact were uniformly distributed over the surface.
(ii) The actual contact areas of the asperities were circular and of identical radii.
(iii) The asperities deformed plastically under a load P such that the average pressure exerted between them was equal to the microhardness H .
(iv) The film resistance was negligible.

With these assumptions, it was found that if radiation was neglected, the thermal contact conductance between two rough surfaces in a vacuum could be expressed as

$$h_c = \frac{2a_s k_m n_s}{f(x_s) A_a} \quad (4)$$

where n_s is the number of contact points, A_a is the apparent contact area, $f(x_s)$ is the Roess microscopic constriction alleviation factor used by Clausing and Chao (1965)

$$f(x_s) = 1 - 1.40925x_s + 0.29591x_s^3 + 0.05254x_s^5 + 0.02105x_s^7 \quad (5)$$

and a_s is the contact radius for a spherical particle in contact with a flat surface, which can be found from the relationship developed by Hertz (Timoshenko and Goodier, 1951):

$$a_s = \sqrt[3]{\frac{3\pi}{4} \frac{P(k_1 + k_2)r_1 r_2}{r_1 + r_2}} \quad (6)$$

where

$$k_1 = \left(\frac{1 - \nu_1^2}{\pi E_1} \right) \text{ and } k_2 = \left(\frac{1 - \nu_2^2}{\pi E_2} \right) \quad (7)$$

Substituting for k_1 and k_2 and simplifying yields

$$a_s = \left[\frac{3P}{4} \left(\frac{1 - \nu_1^2}{E_1} + \frac{1 - \nu_2^2}{E_2} \right) \left(\frac{1}{r_1} + \frac{1}{r_2} \right)^{-1} \right]^{1/3} \quad (8)$$

Modifying the subscripts 1 and 2 to those for the flat and spherical surfaces, respectively, and recognizing that $r_f = \infty$ yields

$$a_s = \left[\left(\frac{3P_s r_s}{4} \right) \left(\frac{1 - \nu_s^2}{E_s} + \frac{1 - \nu_f^2}{E_f} \right) \right]^{1/3} \quad (9)$$

To maintain mechanical equilibrium, the total load must be equal to the load per sphere times the number of spheres, which can be found theoretically from

$$n_s \leq \left(\frac{\pi}{\sqrt{12}} \right) \left(\frac{A_a}{\pi r_s^2} \right) \quad (10)$$

where the first term on the right-hand side represents the area fraction of close-packed planes.

In comparing equations (2) and (4), it can be seen that if the Roess constriction alleviation factor is considered along with

the number of contacts n_s , the expression developed by Yovanovich and Kitscha (1974) and the one developed by Clausing and Chao (1965) are identical. Although the first expression was developed for single large metallic paraboloids and the second was developed for a large number of uniformly distributed microscopic asperities, the similarity of the two expressions is to be expected since Clausing's was derived from an extension of the Roess single point contact relationship. Because of this similarity, it is apparent that a single expression for the metal-to-metal contact resistance for a large number of uniformly distributed spherical metal particles in contact with a flat surface can be developed by modifying the results presented by Yovanovich and Kitscha (1974) to include the number of contacts and the constriction alleviation factor used by Clausing and Chao (1965).

The resulting expression, which describes the contact resistance between a packed bed of spherical metallic particles in contact with a flat metallic surface, may be written as:

$$R_c = \frac{f(x_s)}{k_m n_s} \left[6P_s r_s \left(\frac{1 - \nu_s^2}{E_s} + \frac{1 - \nu_f^2}{E_f} \right) \right]^{-1/3} \quad (11)$$

Equation (11) can then be combined with previously developed interstitial gas conduction and radiation terms (Yovanovich, 1971) to yield an expression for the total resistance at the interface existing between beds of spherical particles and flat surfaces.

In order to determine the accuracy of the contact resistance portion of this expression, an experimental investigation was conducted. In this investigation, the thermal contact conductance between flat metallic surfaces and four different types of spherical metallic particles, with different thermal and mechanical properties, was measured over a wide range of temperatures and pressures.

Experimental Apparatus

The experimental facilities used in this investigation, along with the details of the facility construction, operation, and accuracy, have been reported previously by Miller and Fletcher (1974). The apparatus shown in Fig. 1 consisted of a vertical column composed of a guard heater, a heat source, two similar metal test fixtures, the test bed specimen, a heat sink, a load cell, and a gas bellows. The test fixtures and test bed were arranged so that a cylinder of the test bed was "sandwiched" between the two metal test fixtures. The test bed particles were contained in a cylindrical tube constructed of a high-strength, temperature-resistant Teflon. The axial heat flux was provided by a 300 W band heater attached to the lower test fixture at the base of the column. In addition to the main heater, a guard heater was mounted at the base of the column to reduce the axial heat losses.

To determine the temperature distribution of the test beds, three chromel-alumel thermocouples with beads approximately the same size as the test bed particles were used. These ther-

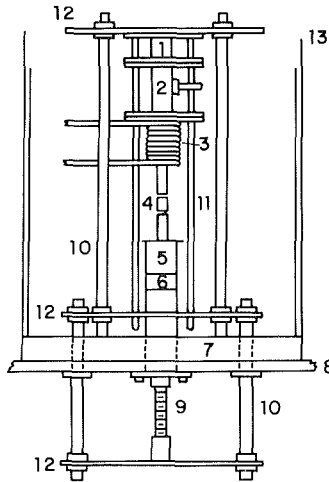
Nomenclature

A_a = apparent contact area
 a_s = actual contact radius
 E = modulus of elasticity
 $f(x)$ = microscopic constriction alleviation factor
 h_c = contact conductance
 k = material parameter
 k = thermal conductivity
 n = number of contact points
 P = contact load

P_s = contact load per sphere
 R = thermal resistance
 r_s = radius of the sphere
 T_m = mean temperature of the gap
 ϵ = emissivity
 ν = Poisson's ratio
 ξ = lower limit of integration
 ρ = radius of curvature of contact
 ψ = thermal construction resistance parameter

Subscripts

c = contact
 f = flat surface
 m = mean harmonic value
 r = radiation
 s = sphere
 1 = surface one
 2 = surface two



- | | |
|------------------|--------------------|
| 1 LOAD BELLOWS | 7 FEEDTHROUGH RING |
| 2 LOAD CELL | 8 BASE PLATE |
| 3 HEAT SINK | 9 SCREW JACK |
| 4 TEST SPECIMENS | 10 SUPPORT RODS |
| 5 HEAT SOURCE | 11 GUIDE RODS |
| 6 GUARD HEATER | 12 SUPPORT PLATES |
| | 13 BELL JAR |

Fig. 1 Experimental apparatus

thermocouples were located along the centerline of each of the test beds 2 cm from each end and at approximately 1.27 cm spacings. The exact positions of the thermocouples within the packed beds were measured directly from neutron radiographs taken of each of the samples. To enhance the thermocouple resolution, the thermocouple wires were stripped of insulation and lightly dusted with gadolinium powder. A thin layer of shrink wrap insulation was then applied around the lead wires to prevent contact of the bare wires with the metallic spheres.

Three thermocouples were located along the centerline of each test fixture at 1.27 cm intervals. These thermocouples were tightly packed into holes (number 56 drill) using powdered metal. The lead wires were wrapped around the test fixtures one time and epoxied onto the surface to improve the measurement accuracy. The temperatures at the interface surfaces of the two test fixtures were determined by extrapolating the measured temperatures along the fixture centerline.

Since losses to the support plates and surrounding chamber prevented the direct measurement of the electrical power, the heat flux was calculated indirectly using the measured centerline temperatures and the thermal conductivity of the test fixtures, which were constructed of materials whose thermal conductivity had been certified by the National Bureau of Standards.

Radial heat losses from the test column were minimized by placing radiation shields (made of sheet aluminum and asbestos) around the test column. Three 100 W electrical resistance band heaters, each with a surface-mounted thermocouple and individual power supply, were placed outside of the radiation shield. These heaters were attached so that the middle heater was located around the center of the test bed and the other two were located around the test fixtures. The radial temperature gradient within the test fixtures was monitored by a thermocouple embedded on the surface of each of the test fixtures. Using the temperatures as measured by these surface thermocouples and the measured centerline temperature, the radial heat losses could be computed.

The thermal contact conductance facility was operated in a vacuum environment to eliminate the effects of any interstitial fluids on the thermal conductivity. A vacuum of at least

5×10^{-5} Torr was maintained using a General Scientific model D500 roughing pump in series with an NRC VHJ-6 oil diffusion pump. A 46×76 cm Pyrex bell jar was used to encase the thermal contact conductance facility. Four NRC model 531 thermocouple gages, in conjunction with two Bayard-Alpert ionization gage tubes and a controller, were used to monitor the vacuum quality.

Experimental Procedure

Tests were conducted to determine the thermal contact resistance occurring at the interface between test beds comprised of spherical particles, 2.38 mm in diameter, and nominally flat Stainless Steel 304 surfaces. Particles made from four different materials were used: Aluminum 2017-T4, Yellow Brass, Chromium Alloy AISI 52100, and Stainless Steel 304. The mechanical and thermal properties for these materials as specified by the manufacturer are shown in Table 1.

The experimental procedure followed for all the tests was as follows: The spherical particles and fixture surfaces were wiped clean with acetone. The spherical particles were then loaded into a Teflon sleeve between the test fixtures and installed in the test facility. During the filling process, the bed was vibrated to insure that uniform settling occurred and that no large voids existed. The vertical column was then aligned visually and a slight load was applied to the test column to prevent the fixtures and test bed from shifting during the evacuation of the test chamber. The radiation shields and heaters were put in place and the specimens were allowed to out-gas for 4-5 h.

The temperature and axial load test conditions were set by adjusting the heater voltages and pressurizing the load bellows, respectively. During the initial test setup, care was taken to insure that the elastic limit of the spherical particles, as determined from the Hertzian equations (Timoshenko and Goodier, 1951), was not exceeded. Once a load had been applied, no measurements were made at lighter loads, in order to avoid any undesired effects caused by plastic deformation. Tests were conducted at a mean interface temperature of 66°C , and data were taken when the test specimen temperature did not vary more than 0.5°C over a 45 minute period.

Results and Discussion

Throughout the tests, the length of the bed thickness was monitored using an LVDT, to determine any changes resulting from axial load or temperature variations. Although the axial variation was somewhat larger for the aluminum than the stainless steel bed due to differences in the modulus of elasticity, the total variation was less than 1 percent of the overall length. These variations were considered in the determination of the thermal contact resistance, and were assumed to occur linearly.

In order to evaluate the overall experimental uncertainty, it was necessary to determine the magnitude of several factors. Most significant among these was the relative magnitude of the interface resistance and the resistance of the packed beds tested. Test results indicated that for the materials used, these two resistances were of the same order of magnitude and would therefore yield results with acceptable measurement errors. A second important factor in the determination of the experimental uncertainty was the radial heat losses occurring in the test fixtures and the packed bed. As mentioned previously, the radial heat losses were monitored using the measured centerline and surface temperatures. The three individual radiation shield heaters provided a mechanism by which these losses could be controlled and held to less than 1

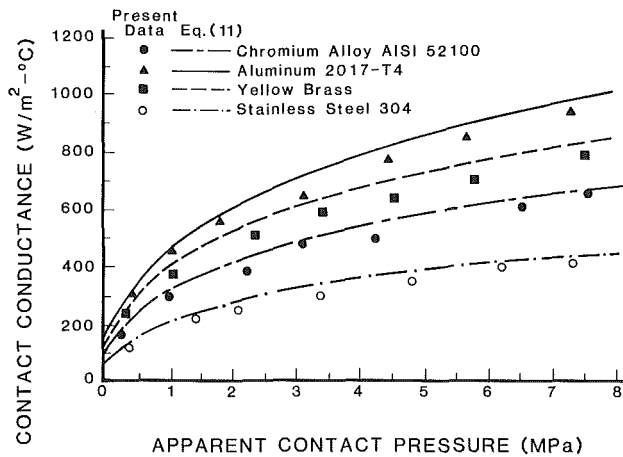


Fig. 2 Influence of the apparent contact pressure on the thermal contact conductance

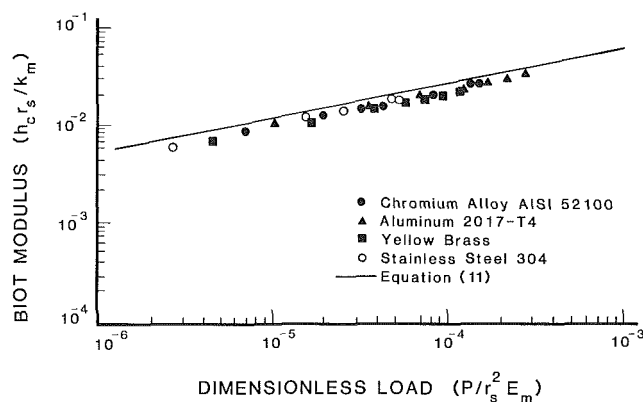


Fig. 3 Comparison of theoretical and experimental results

percent. The final factor in the determination of the experimental error was the heat transmitted axially through the Teflon sleeve. In order to determine this value accurately, it was necessary to know the cross-sectional area of the sleeve, the thermal conductivity of the material, and the contact resistance occurring between the Teflon sleeve and the stainless steel test fixtures. Because the cross-sectional area of the sleeve was small, 2.0771 cm², the thermal conductivity relatively low, and the contact between the fixture and the sleeve very loose, the axial component of the heat flux through the sleeve was assumed to be negligible. Using the uncertainty resulting from the axial conduction of the sleeve and the radial heat losses, along with the other more conventional uncertainties (thermocouple accuracy, etc.) the overall experimental error was estimated to be ± 8.2 percent for the aluminum, ± 7.1 percent for the yellow brass, ± 6.2 percent for the chromium alloy, and ± 5.6 percent for the stainless steel.

Figure 2 presents the experimental results compared with the predicted values as a function of the apparent contact pressure. As shown, the experimental values are consistently less than the values predicted by equation (11), but follow a similar trend. The largest variation occurs in the Aluminum 2017-T4 bed with the percentage of deviation decreasing slightly with respect to the hardness of the material.

In this comparison, the effects of conduction through the interstitial gases were neglected due to the quality of the vacuum in which the tests were performed. The contribution due to radiation heat transfer was calculated for several cases and was also found to be negligible due to the extremely small temperature drop occurring at the interface. Inclusion of the

radiation contribution, although very small, would shift the curve slightly upward, further increasing the disparity between the experimental and theoretical values.

If the contact conductance is nondimensionalized by multiplying by the radius of the spheres and dividing by the harmonic mean thermal conductivity, the result will appear in the form of the Biot modulus. The axial load can be nondimensionalized by dividing the load by the product of the square of the sphere radius and the harmonic mean modulus of elasticity. Combining these two nondimensionalized parameters with equation (11) results in a single line that describes the relationship that exists between the Biot modulus and the dimensionless load for all four materials. Figure 3 illustrates this comparison. As shown, the experimentally measured results are slightly lower than the theoretical predictions obtained. The overall trend, however, approximates the predicted values quite well.

Conclusions

In summary, an experimental investigation to determine the thermal contact conductance of packed beds of spherical particles in contact with flat surfaces has been conducted. Beds comprised of four materials—Aluminum 2017-T4, Yellow Brass, Stainless Steel 304, and Chromium Alloy AISI 52100—all in contact with flat Stainless Steel 304 surfaces, were evaluated in a vacuum environment, over an apparent contact pressure ranging from 0.2 to 8.0 MPa and a mean interface temperature of 66°C.

In addition to the experimental investigation, two separate expressions, one developed by Yovanovich and Kitscha (1974) for single large sphere-flat contacts, and one developed by Clausing and Chao (1965) for large numbers of microscopic asperities, have been compared and combined into a single expression. Comparison of the predictions based upon this expression with the experimental results obtained indicates that this expression is applicable to both large single-point contacts and small multiple contacts such as those encountered in beds of spherical particles in contact with flat surfaces. In addition, it was demonstrated that the thermal contact conductance existing at the interface between beds of spherical particles and flat surfaces can be predicted with a high degree of accuracy.

Acknowledgments

This work was sponsored in part by the Mechanical Engineering Division of the Texas Engineering Experiment Station.

References

- Clausing, A. M., and Chao, B. T., 1965, "Thermal Contact Resistance in a Vacuum Environment," *ASME JOURNAL OF HEAT TRANSFER*, Vol. 87, pp. 243-251.
- Kitscha, W. W., and Yovanovich, M. M., 1975, "Experimental Investigation on the Overall Thermal Resistance of Sphere-Flat Contacts," *AIAA Progress in Astronautics and Aeronautics: Heat Transfer With Thermal Control Applications*, Vol. 39, M. M. Yovanovich, ed., MIT Press, Cambridge, MA, pp. 93-110.
- Miller, R. G., and Fletcher, L. S., 1974, "A Facility for the Measurement of Thermal Contact Conductance," *Proc. of the Tenth Southeastern Seminar on Thermal Sciences*, New Orleans, LA, pp. 263-285.
- Timoshenko, S., and Goodier, J. N., 1951, *Theory of Elasticity*, McGraw-Hill, New York, pp. 409-413.
- Vafai, K., and Alkire, R. L., 1984, "Heat Transfer in Variable Porosity Packed Beds," *ASME Paper No. 84-WA/HT-100*.
- Yovanovich, M. M., 1971, "Thermal Constriction Resistance Between Contacting Metallic Paraboloids: Application to Instrument Bearings," *AIAA Progress in Astronautics and Aeronautics: Heat Transfer and Spacecraft Thermal Control*, Vol. 24, J. W. Lucas, ed., MIT Press, Cambridge, MA, pp. 337-358.
- Yovanovich, M. M., and Kitscha, W. W., 1974, "Modeling the Effect of Air and Oil Upon the Thermal Resistance of Sphere-Flat Contact," *AIAA Progress in Astronautics and Aeronautics: Thermophysics and Spacecraft Thermal Control*, Vol. 35, R. G. Hering, ed., MIT Press, Cambridge, MA, pp. 293-319.

Rectangular Heat Source on a Semi-infinite Solid—an Analysis for a Thin Film Heat Flux Gage Calibration

N. R. Keltner

B. L. Bainbridge

Thermal Test and Analysis Division,
Sandia National Laboratories,
Albuquerque, NM 87185

J. V. Beck

Department of Mechanical Engineering,
Michigan State University,
East Lansing, MI 48824
Mem. ASME

For a thin film heat flux gage designed to provide both rapid response and long use time, initial calibrations using standard techniques indicated differences between the literature and the estimated properties. In order to estimate thermophysical properties and subsequently the gage sensitivity, an analytical model of the response to a step change in heating current was developed. Starting from a Green's function description, the model is reduced to three algebraic expressions, which correspond to the early, middle, and late time regimes. These expressions provide a framework for least-squares estimates of gage parameters. This provides an in-situ, nondestructive measurement of the thermal impedance of the substrate. There is very good agreement between the model and the experimental data. The estimated parameter values demonstrated good to excellent repeatability and good agreement with both new literature data and results from destructive property measurements.

Introduction

Thin film resistance thermometers are used in a variety of situations to measure surface temperatures, which can be utilized to obtain heat fluxes and thermophysical properties [1, 2]. Typically, these gages are used for short-duration measurements requiring very rapid response.

For measuring heat fluxes, thin film gages are usually calibrated by using either a known external heat flux or by using the gage itself as a heating element. The external source may be a well-characterized radiant device or a wave front produced in a shock tube. The other technique, developed by Skinner [3], uses the gage as a resistive element, which responds to a change in the current flowing through the device. A change in the output of the gage, when exposed first to air and then to water using the same step heating current, is used to determine the calibration constant of the gage.

In a program to study hydrogen flame propagation in large tanks, a fast-response gage with a long use time was required. The fast response was necessary to obtain data during combustion, while the long duration enabled measurements over the cool-down period, following combustion, that could last for several hundred seconds [4].

An analysis of initial calibration experiments involving exposure to a constant radiant flux or the air/water sequence indicated a large discrepancy between the tabulated and estimated thermophysical properties. Also, the analysis of the air/water sequence using one-dimensional, semi-infinite body relations from [3] was inadequate for long heating periods.

In order to resolve these problems, an analysis using methods successful on other thermal sensors was initiated [5]. The sensor was modeled as a rectangular heat source on a semi-infinite body. Given the size of the body and its expected thermophysical properties, this should be a valid approximation over the period of use.

The effect of a rectangular heat source on a semi-infinite solid is a basic problem in heat conduction. It has been used in the analysis of cutting tool temperatures [6] and more recently for solid state electronic devices [7]. Steady-state results for

the maximum and average temperatures in the heated region have been given in terms of simple expressions [6, 8]. However, transient solutions are generally presented in the form of a very complicated integral.

A Green's function approach is used to develop an expression for the transient average temperature resulting from a step change in heat flux. The initial form is in terms of an integral. However, by making use of steady-state results and appropriate mathematical expansions, the final form is three algebraic expressions that cover the entire time range. Extensions of the step response solution cover linear ramp as well as periodic heating.

The analytical results are compared with experimental data. A thin film heat flux gage, with a rectangular resistance element, is driven by several electrical waveforms. The resistance of the element is assumed to be related to the average temperature of the element and is used for generating the experimental temperature histories.

Analysis for Step Heat Flux

The general transient solution is developed in the Cartesian coordinate system by using Green's functions. An isotropic,

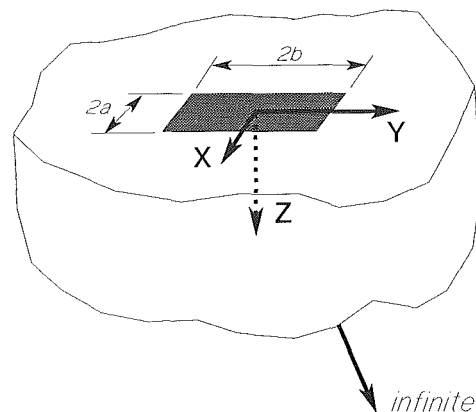


Fig. 1 Problem geometry

Contributed by the Heat Transfer Division for publication in the JOURNAL OF HEAT TRANSFER. Manuscript received by the Heat Transfer Division December 7, 1984. Paper No. 84-HT-46.

homogeneous, semi-infinite body is subjected to a step change in heat flux at time zero over a rectangular area on the surface of length $2b$ and width $2a$ (see Fig. 1). The remainder of the surface is adiabatic. There is no heat generation inside the body and the thermal properties are independent of temperature. The initial temperature T_∞ is uniform.

The surface temperature for this problem can be shown to be

$$T(x, y, 0, t) = T_\infty + \frac{\alpha}{k} \int_{\tau=0}^t d\tau \int_{x'_2=-a}^a \int_{y'=-b}^b G_{X00Y00Z20}(x, y, 0, t | x', y', 0, \tau) dy' dx' \quad (1)$$

where the three-dimensional Green's function can be found by using the product of the appropriate one-dimensional Green's functions [9]. The relation is

$$G_{X00Y00Z20}(x, y, 0, t | x', y', 0, \tau) = G_{X00}(x, t | x', \tau) G_{Y00}(y, t | y', \tau) G_{Z20}(0, t | 0, \tau) \quad (2)$$

The Green's function, $G_{X00Y00Z20}(\bullet)$, is for a point source in a semi-infinite body with an adiabatic surface at $z=0$. For this problem the source is located at the surface of the body. The one-dimensional Green's functions, $G_{X00}(\bullet)$ and $G_{Y00}(\bullet)$ are for a plane source in an infinite body. The one-dimensional Green's function, $G_{Z20}(\bullet)$, is for a plane source in a semi-infinite body with an adiabatic surface.

An objective of this paper is to provide an expression for the average temperature over the heated area

$$T(0, t) = \frac{1}{4ab} \int_{x=-a}^a \int_{y=-b}^b T(x, y, 0, t) dy dx \quad (3)$$

where $T(x, y, 0, t)$ is given by equation (1). To find the average temperature multiple integrations are needed: over x, x', y, y' , and τ . Fortunately, the integrations over x and x' involve only $G_{X00}(\bullet)$ and those over y and y' involve only $G_{Y00}(\bullet)$. Furthermore, the integrations involving $G_{X00}(\bullet)$ and $G_{Y00}(\bullet)$ are similar. The integration over τ is left to the last because it involves all three of the Green's functions.

The $G_{X00}(\bullet)$ function is

$$G_{X00}(x, t | x', \tau) = \exp[-(x-x')^2/4\alpha(t-\tau)]/(4\pi\alpha(t-\tau))^{1/2} \quad (4)$$

Because the source extends from $x'=-a$ to $x'=a$, this function is integrated to give

$$\int_{x'=-a}^a G_{X00}(x, t | x', \tau) dx' = \frac{1}{2} [2 - \operatorname{erfc}(x+a)/(4\alpha(t-\tau))^{1/2} - \operatorname{erfc}(-x+a)/(4\alpha(t-\tau))^{1/2}] \quad (5)$$

Integrating equation (5) over $x=-a$ to a gives

$$\int_{x=-a}^a \int_{x'=-a}^a G_{X00}(x, t | x', \tau) dx' dx = 2[a - (\alpha(t-\tau))^{1/2} ((1/\pi)^{1/2} - \operatorname{ierfc}(a/(\alpha(t-\tau))^{1/2})] \quad (6)$$

A similar expression is obtained for the y function.

The expression for $G_{Z20}(\bullet)$ is

$$G_{Z20}(z, t | z', \tau) = [\exp(-(z-z')^2/4\alpha(t-\tau)) + \exp(-(z+z')^2/4\alpha(t-\tau))]/(4\pi\alpha(t-\tau))^{1/2} \quad (7)$$

Equations (5) and (7) can be used with equation (1) to evaluate the temperature anywhere on the surface of the body. The temperature at any point in the body can be evaluated from equation (1) if z is used in the Green's function instead of being set to zero.

When these relations are used in equation (3), the expression for the average temperature of the source is

$$\bar{T} = T_\infty + (q_0\alpha/abk) \int_0^t [a - (\alpha(t-\tau))^{1/2} [(1/\pi)^{1/2} - \operatorname{ierfc}(a/(\alpha(t-\tau))^{1/2})] \cdot [b - (\alpha(t-\tau))^{1/2} [(1/\pi)^{1/2} - \operatorname{ierfc}(b/(\alpha(t-\tau))^{1/2})] \cdot (1/(\pi\alpha(t-\tau)))^{1/2} d\tau \quad (8)$$

which involves the final integration over the dummy time variable τ .

To simplify this expression, a dimensionless temperature \bar{T}^+ is introduced and $\lambda = t - \tau$ is used to give

$$\bar{T}^+(0, t) = \frac{\bar{T} - T_\infty}{(q_0 a/k)} = (\alpha/a\pi^{1/2}) \int_0^t [1 - (\alpha\lambda/a^2)^{1/2} (1/\pi^{1/2} - \operatorname{ierfc}((a^2/\alpha\lambda)^{1/2}))] \cdot [1 - (\alpha\lambda/b^2)^{1/2} (1/\pi^{1/2} - \operatorname{ierfc}((b^2/\alpha\lambda)^{1/2}))] \cdot [1/(\alpha\lambda)^{1/2}] d\lambda \quad (9)$$

Closed-form integration of equation (9) is not possible; however, in certain time regimes simplifications are possible that permit closed-form integration.

For part of the evaluation, it is helpful to rewrite this equation in terms of the steady-state value, which is known but which is difficult to obtain by direct evaluation of equation (9). This is done by rewriting the integral from 0 to t in equation (9) as an integral from 0 to ∞ and an integral from t to ∞ . This results in an equation of the form

$$\bar{T}^+(0, t) = \bar{T}^+(0, \infty) - (\alpha/a\pi^{1/2}) \int_t^\infty (\bullet) d\lambda \quad (10)$$

where (\bullet) is the integrand as in equation (9) and $\bar{T}^+(0, \infty)$ is given by

$$\bar{T}^+(0, \infty) = (2/\pi) \{ \ln[b^+ + (b^+ + 1)^{1/2}] + b^+ \ln[1/b^+ + (1/b^+ + 1)^{1/2}] + (1/3b^+) [1 + b^+ - (b^+ + 1)^{3/2}] \} \quad (11)$$

where $b^+ = b/a$ [6].

To obtain values at early times, equation (9) is solved using the observation that $\operatorname{ierfc}(x) < 10^{-4}$ if $x > 2.5$. If the arguments of both of the functions $\operatorname{ierfc}(\)$ are greater than 2.5 then setting these terms equal to zero gives

$$\bar{T}^+(0, t^+) = 2(t^+/\pi)^{1/2} - (t^+/\pi) [1 + (1 - 2(t^+/\pi)^{1/2}/3)/b^+] \quad (12)$$

where $t^+ = \alpha t/a^2$. The first term on the right is that for a semi-

Nomenclature

a = 1/2 rectangular source width	k = thermal conductivity	α = thermal diffusivity
$A(\)$ = see equation (20b)	q_0 = heat flux, W/m ²	β = early time solution parameters
b = 1/2 rectangular source length	s = Laplace transform variable	γ = late time solution parameters
$B(\)$ = see equation (20c)	t = time	λ = $t - \tau$
b^+ = geometric ratio = b/a	t^+ = dimensionless time = $\alpha t/a^2$	τ = time
$C(\)$ = see equation (20d)	T = surface temperature	ψ = see equation (20)
G = Green's function	T^+ = dimensionless temperature = $\Delta T/(q_0 a/k)$	ω = frequency, rad/s
j = $\sqrt{-1}$	x, y, z = axes of coordinate system, see Fig. 1	

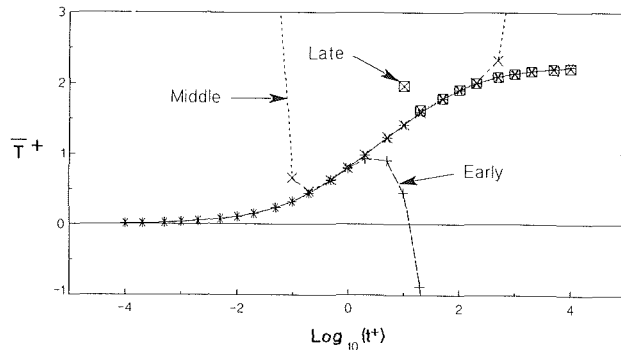


Fig. 2(a) Step heating response for $b^+ = 10$

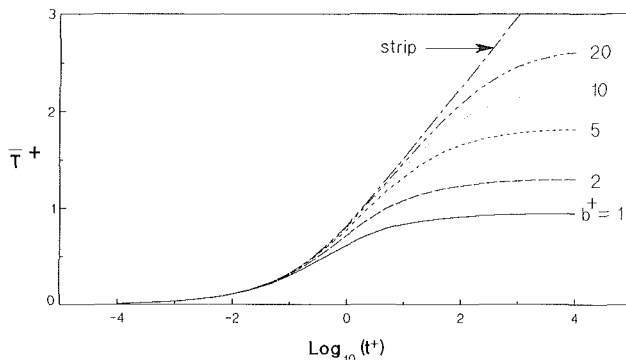


Fig. 2(b) Step heating response

infinite body with a uniformly heated surface. The term involving the 1 in the brackets is a correction for the finite source width in the x direction, while the second term in the bracket involves the correction for a finite source width in the y direction.

If the argument of the ierfc function is greater than 2.5 only for the y direction term (i.e., $(b^+ / t^{+1/2}) > 2.5$) then setting only that term to zero gives

$$\begin{aligned} \bar{T}^+(0, t^+) &= 2(t^+ / \pi)^{1/2} \\ &- (t^+ / \pi)[1 - (2\pi^{1/2})\text{ierfc}(1/t^{+1/2}) + E_2(1/t^+)] \\ &- (2t^+ / 3\pi b^+)[1 - (t^+ / \pi)^{1/2} \\ &+ ((1 + t^+) / t^{+1/2})(\text{ierfc}(1/t^{+1/2})) \\ &- (1/2)\text{erfc}(1/t^{+1/2})] \end{aligned} \quad (13)$$

where the second and third terms are again the corrections for a finite width source.

A simplified expression for equation (13) that differs from the exact solution only in the fourth significant figure is

$$\begin{aligned} \bar{T}^+(0, t^+) &= 2(t^+ / \pi)^{1/2} - (t^+ / \pi - 0.01t^{+7/2}) \\ &- (2t^+ / 3\pi b^+)[1.5 - (t^+ / \pi)^{1/2} + 0.022t^{+3}] \end{aligned} \quad (14)$$

which is the early time, algebraic expression.

For large times, which are defined as $t^+ > b^{+2}$, an expansion of the ierfc terms using

$$\text{ierfc}(x) = -x + \pi^{-1/2}(1 + x^2 - x^4/6 + x^6/30 - x^8/168) \quad (15)$$

can be used with equations (10) and (11) to obtain

$$\begin{aligned} \bar{T}^+(0, t^+) &= \bar{T}^+(0, \infty) - 2b^+ / (t^+ \pi^3)^{1/2} \{1 - (1 + b^+)^2 / 18t^+ \\ &+ [(1 + b^+)^4 / 5 + b^+ / 6] / 30t^+ \\ &- [(1 + b^+)^6 / 14 + b^+ / 2(1 + b^+)^2 / 15] / 84t^+ \} \end{aligned} \quad (16)$$

which is the late time, algebraic expression.

The accuracy of the late time approximation is related to the accuracy of the $\text{ierfc}(x)$ approximation. The worst case is when the argument is close to 1, where the approximation for $\text{ierfc}(x)$ is slightly better than 1 percent. The accuracy improves quickly and when the argument reaches 0.5 the accuracy has improved to better than 0.005 percent. The late time approximation is always much more accurate than the ierfc approximation, due to the small contribution of the ierfc terms.

For the intermediate times, $1 < t^+ < b^{+2}$, equation (10) can be written as

$$\begin{aligned} \bar{T}^+(0, t^+) &= \bar{T}^+(0, \infty) - \pi^{-1/2} \int_{t^+}^{t_m^+} (\bullet) d\lambda^+ \\ &- \pi^{-1/2} \int_{t_m^+}^{\infty} (\bullet) d\lambda^+ \end{aligned} \quad (17)$$

The first and third terms on the right-hand side are the same as those in equation (16) with $t_m^+ = b^{+2}$. In this intermediate time range, the function $\text{ierfc}(b^+ / \lambda^{+1/2})$ is not approximated very well by the expansion given in equation (15). As noted in the development of the early time solution the value of the function becomes small as $\lambda^+ \rightarrow 1$. By inspection, an approximation for the function of

$$\text{ierfc}(x) = 1/20x^4 \quad (18)$$

was obtained that gives reasonable accuracy as $x \rightarrow 1$ and while it gives increasingly larger relative errors as x increases, the overall effect on the integral in the second term in equation (17) is small. Using this approximation, the second term of equation (17) can be obtained in the form

$$\pi^{-1/2} \int_{t^+}^{t_m^+} (\bullet) d\lambda^+ = \psi(t_m^+, b^+) - \psi(t^+, b^+) \quad (19)$$

where $\psi(z, b^+)$ is given by

$$\psi(z, b^+) = \{A(z) - B(z)/b^+ \pi^{1/2} + C(z)/20b^{+5}\} / \pi \quad (20a)$$

$$A(z) = \ln z + 1/6z - 1/60z^2 + 1/504z^3 \quad (20b)$$

$$B(z) = z^{1/2}(2 + 1/3z - 1/45z^2 + 1/420z^3) \quad (20c)$$

$$C(z) = z^{1/2}(2z^2/5 - z/9 + 1/15 + 1/84z) \quad (20d)$$

Thus equation (17) can be written as

$$\bar{T}^+(0, t^+) = \bar{T}^+(0, b^{+2}) - \psi(b^{+2}, b^+) + \psi(t^+, b^+) \quad (21)$$

where $\bar{T}^+(0, b^{+2})$ is obtained from equation (16). Equation (21) is the middle time, algebraic expression.

This approximate solution performs the poorest for small values of b^+ and $t^+ \sim 1$. For $b^+ = 1$ and $t^+ = 1$ the error is approximately 0.5 percent. For $b^+ = 10$ and $t^+ = 1$, the error is ~ 0.1 percent.

Comparison of Approximate Solutions

The approximate solutions are compared to the exact solution, evaluated numerically, in Fig. 2(a). Note that each of the approximations has a definite region of applicability, outside of which it quickly departs from the exact solution.

The values obtained from the three algebraic approximations (14), (21), (16) are given in Table 1 for several values of b^+ . These values are also plotted in Fig. 2(b) along with those for a strip source ($b^+ = \infty$).

Time-Variable Heat Flux

The step heating case is useful for calibrating the thin film heat flux gage. However, switching transients introduced by the step change in power can affect the early time results. Two other useful heating functions are the ramp and the sinusoid.

The general form of Duhamel's equation for an arbitrary heat flux is

Table 1 Summary of dimensionless temperatures for a unit step heat flux for a rectangular heated region on a semi-infinite body

Rectangular Source Average Temperature						
Time	$b^+ = 1$	$b^+ = 2$	$b^+ = 5$	$b^+ = 10$	$b^+ = 20$	Strip $b^+ = \infty$
0.0001	0.0112	0.0112	0.0112	0.0112	0.0113	0.0113
0.0002	0.0158	0.0159	0.0159	0.0159	0.0159	0.0159
0.0005	0.0249	0.0250	0.0250	0.0251	0.0251	0.0251
0.001	0.0350	0.0352	0.0353	0.0353	0.0353	0.0354
0.002	0.0492	0.0495	0.0497	0.0498	0.0498	0.0498
0.005	0.0766	0.0774	0.0779	0.0780	0.0781	0.0782
0.01	0.1066	0.1081	0.1090	0.1093	0.1095	0.1097
0.02	0.1472	0.1502	0.1520	0.1526	0.1529	0.1532
0.05	0.2218	0.2291	0.2335	0.2349	0.2357	0.2364
0.10	0.2970	0.3110	0.3194	0.3222	0.3236	0.3250
0.20	0.3880	0.4145	0.4304	0.4357	0.4384	0.4410
0.50	0.5225	0.5811	0.6162	0.6279	0.6338	0.6395
1.00	0.6168	0.7184	0.7794	0.7997	0.8099	0.8195
2.00	0.7054	0.8497	0.9497	0.9833	1.0002	1.0171
5.00	0.7892	0.9954	1.1704	1.2321	1.2629	1.2939
10.0	0.8341	1.0793	1.3214	1.4151	1.4621	1.5093
20.0	0.8665	1.1420	1.4494	1.5867	1.6569	1.7274
50.0	0.8957	1.1994	1.5785	1.7849	1.9006	2.0176
100.	0.9105	1.2288	1.6485	1.9053	2.0684	2.2378
200.	0.9210	1.2497	1.6995	1.9992	2.2154	2.4583
500.	0.9303	1.2683	1.7455	2.0875	2.3691	2.7499
1000.	0.9350	1.2777	1.7689	2.1335	2.4549	2.9706
2000.	0.9384	1.2843	1.7854	2.1663	2.5184	3.1913
5000.	0.9413	1.2902	1.8002	2.1957	2.5761	3.4830
10000.	0.9428	1.2932	1.8076	2.2105	2.6056	3.7036
∞	0.9464	1.3004	1.8256	2.2464	2.6773	

Table 2 Summary of dimensionless temperatures for a ramp heat flux for a rectangular heated region on a semi-infinite body

Rectangular Source Temperatures for Ramp Heat Flux					
Time	$b^+ = 1$	$b^+ = 2$	$b^+ = 5$	$b^+ = 10$	$b^+ = 20$
0.0010	0.0000	0.0000	0.0000	0.0000	0.0000
0.0020	0.0001	0.0001	0.0001	0.0001	0.0001
0.0050	0.0003	0.0003	0.0003	0.0003	0.0003
0.0100	0.0007	0.0007	0.0007	0.0007	0.0007
0.0200	0.0020	0.0020	0.0021	0.0021	0.0021
0.0500	0.0076	0.0078	0.0079	0.0080	0.0080
0.1000	0.0208	0.0215	0.0219	0.0221	0.0221
0.2000	0.0554	0.0582	0.0598	0.0604	0.0606
0.5000	0.1949	0.2106	0.2200	0.2231	0.2247
1.0000	0.4831	0.5392	0.5729	0.5841	0.5897
2.0000	1.1528	1.3308	1.4461	1.4846	1.5039
5.0000	3.4212	4.1394	4.6780	4.8625	4.9547
10.000	7.4981	9.3595	10.955	11.533	11.822
20.000	16.028	20.517	24.898	26.646	27.529
50.000	42.560	55.827	70.716	77.746	81.474
100.00	87.779	116.65	151.67	170.42	181.22
200.00	179.44	240.75	319.50	366.40	396.27
500.00	457.46	619.07	837.78	982.29	1088.5
1000.0	924.01	1255.9	1717.3	2039.4	2298.0
2000.0	1861.0	2537.5	3495.9	4192.1	4790.0
5000.0	4681.5	6401.4	8879.3	10745.	12451.
10000.	9392.4	12861.	17901.	21766.	25417.
20000.	18826.	25805.	36008.	43933.	51596.

$$T(t) = \frac{\partial}{\partial t} \int_0^t q(\lambda) \phi(t-\lambda) d\lambda \quad (22)$$

$$T_R^+ = 1/t_0^+ \int_0^{t^+} T_s^+ d\lambda^+ \quad (24)$$

where the influence function $\phi(\bullet)$ is the temperature rise resulting from a step change in heat flux.

In this case, $\phi(\bullet)$ is actually composed of three separate functions. Each is applicable over its defined time regime. For the rectangular source, $\phi(\bullet)$ is the average temperature which can be obtained from equations (14), (16), or (21) for the different time regimes with q_0 equal to unity.

For a ramp heating

$$q(t) = q_0(t/t_0) \quad (23)$$

where t_0 is the nominal time at which $q(t) = q_0$. It can be shown that the average dimensionless temperature for a ramp flux input T_R^+ is

and can be obtained for the three time regimes as follows:

- (I) For $t^+ < 1$, the integration is carried out using the early time solution (14).
- (II) For $1 < t^+ < b^{+2}$, the integration is split into two parts with that from 0 to 1 using the early time result from (I) with $t^+ = 1$ and from 1 to t^+ using the midtime solution (21).
- (III) For $t^+ > b^{+2}$, the integration is given by the result from (II) evaluated at b^{+2} plus the integration from b^{+2} to t^+ of equation (16).

Table 2 gives the numerical results of this procedure for $b^+ = 1, 2, 5, 10, \text{ and } 20$.

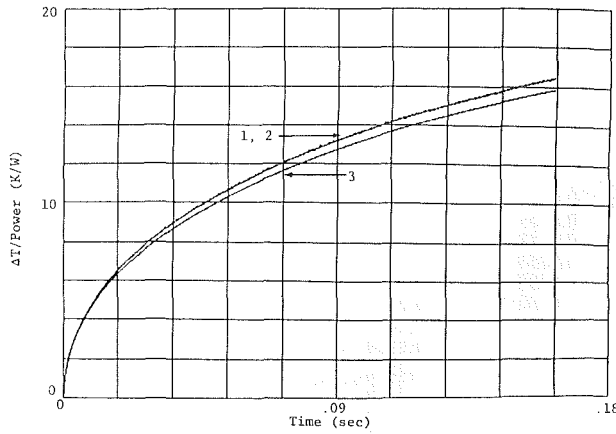


Fig. 3 Early time step response. Curves 1 and 2 show an experimental data set and the least-squares fit from the parameter estimation process, respectively. Curve 3 is the step response of the model using parameters produced from manufacturer's data. Power: 0.50 W, experimental data: $\beta_1 = 221.6$, $\beta_2 = 414.3$, manufacturer's: $\beta_1 = 215.3$, $\beta_2 = 414.4$.

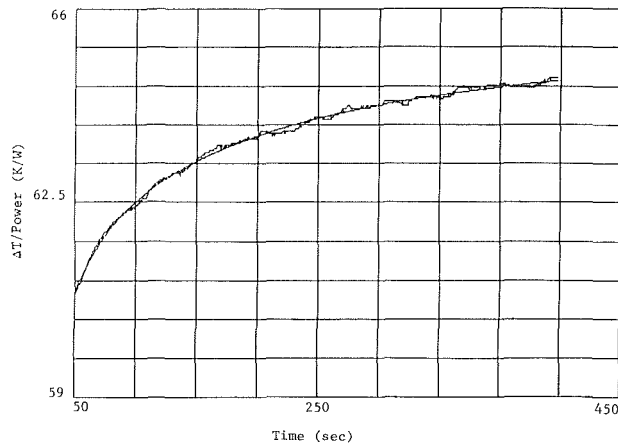


Fig. 4 Late time step response: experimental data and the least-squares fit of the corresponding model; power = 0.125 W, $\gamma_1 = 68.08$, $\gamma_2 = 62.24$, $\gamma_3 = 191.98$

For a sinusoidal excitation, the response is again derived from the Duhamel's integral (22) by taking the Laplace transform to get

$$\bar{T}^+(s) = s\bar{\phi}^+(s)q^+(s) \quad (25)$$

and noting that $s\bar{\phi}^+(s)$ has the form of a transfer function $G(s)$.

By restricting the excitation to "high" frequencies (to be defined later), the first two terms (i.e., the $t^{1/2}$ and t terms) of the early time equation (12) can be used to obtain

$$G(s) = (sa/k)[(\alpha/a^2s^3)^{1/2} - (\alpha/\pi a^2s^2)(1 + 1/b^+)] \quad (26)$$

The transfer function for a periodic excitation is obtained by substituting $j\omega$ for s ; this gives

$$G(j\omega) = (a/k)[(1/\sqrt{2})(\alpha/a^2\omega)^{1/2} - j((1/\sqrt{2})(\alpha/a^2\omega)^{1/2} - (1/\pi)(1 + 1/b^+)(\alpha/a^2\omega))] \quad (27)$$

This relation can be separated into the amplitude

$$A(j\omega) = (a/k)(\alpha/a^2\omega)^{1/2}[1 - (\sqrt{2}/\pi)(1 + 1/b^+)(\alpha/a^2\omega)^{1/2} + ((1 + 1/b^+)/\pi)^2(\alpha/a^2\omega)]^{1/2} \quad (28)$$

and the phase relation

$$\theta(j\omega) = \tan^{-1}[-1 + \sqrt{2}(\alpha/a^2\omega)^{1/2}(1 + 1/b^+)/\pi] \quad (29)$$

Parameter Estimation

Data from electrical heating tests were used with parameter estimation routines to provide thermophysical property values. Several property groupings are available depending upon whether the early time, late time, or steady-state solution is used.

If an early time solution is used (for either the step, ramp, or periodic excitation), two parameter groups can be estimated that correspond to the first two terms of the solution. Using data for $\Delta T/P$ (where P is the power) versus time, the two groups are

$$\beta_1 = 1/(ab(k\rho c)^{1/2}) \quad (\text{K/W}\cdot\text{s}^{1/2}) \quad (30a)$$

$$\beta_2 = (a + b)/(a^2b^2\rho c) \quad (\text{K/W}\cdot\text{s}) \quad (30b)$$

The only differences between the step, ramp, and periodic solutions are the coefficients multiplying β_1 and β_2 .

Theoretically, the steady-state solution could be used to estimate a grouping of k , a , b , and b^+ . However, the experiment requires almost an hour to reach equilibrium, so the late time solution (16) is used instead. There are three parameter groups from this solution

$$\gamma_1 = (\Delta T/P)_{ss} = \frac{T_{ss}^+}{4bk} = \frac{f(b^+)}{4bk} \quad (\text{K/W}) \quad (31a)$$

$$\gamma_2 = 1/(2\pi^{3/2}k\alpha^{1/2}) \quad (\text{K}\cdot\text{s}^{1/2}/\text{W}) \quad (31b)$$

$$\gamma_3 = (a^2 + b^2)/(36\pi^{3/2}k\alpha^{3/2}) \quad (\text{K}\cdot\text{s}^{3/2}/\text{W}) \quad (31c)$$

Original MACORTM product data, which are widely reproduced in the literature, give the value of the square root of the thermal impedance as $(k\rho c)^{1/2} = 0.138 \text{ W s}^{1/2}/\text{cm}^2\text{K}$. Initial estimates of this parameter, from both the radiant exposure tests and the electrical heating tests, differed from the above value by up to a factor of 2. As a result, a series of property measurements was made on samples machined from a gage body. These produced the values:

$$\begin{aligned} \text{Thermal conductivity} &= 0.0155 \text{ W/cmK} \\ \text{Density} &= 2.54 \text{ g/cm}^3 \\ \text{Specific heat} &= 0.8 \text{ J/gK} \end{aligned}$$

The gages used a cylinder of MACORTM, 80 mm in diameter by 50 mm long, for the substrate. A platinum resistance element, approximately 1 mm wide by 10 mm long by 300 Å thick, was sputtered onto the flat face. The gage surface was protected from moisture by a thin (vapor deposited) coating of aluminum oxide. Inspection of the gages indicated that the active element was not quite rectangular. However, measured dimensions were very close to the design dimensions.

To obtain an experimental calibration of the gages, the Loop Current Response technique was used [10]. A step change in heating current (from ~2 ma to ~100 ma) was imposed on the gage and the change in resistance and thus temperature was obtained from the output of a bridge circuit. The resistance versus temperature correlation had been obtained from an oven calibration of the gage. Typical early and late time responses are shown in Figs. 3 and 4.

Estimates of the early and late time model parameters were obtained from the experimental response data by using an ordinary least-squares curve fitting routine. The early time model used the terms involving $t^{1/2}$ and t of equation (12) or the corresponding early time ramp heating equation. The first three terms of the late time model (16) were used to estimate γ_1 , γ_2 , and γ_3 . The results of this procedure are also shown in Figs. 3 and 4. As can be seen, the functional form of the models fits the experimental data very closely.

Some of the parameter estimates are shown in Table 3. In each case, the agreement between the theoretical and experimental values becomes worse and the standard deviation increases for the higher order terms (eg., β_2 , γ_3). This is main-

Table 3 Parameter estimates

Model and data	Parameter	Theoretical value*	Average estimate value	Standard deviations, percentage	Number of tests
Early time step input	β_1	227.2	224.1	1.2	5
	β_2	434.6	422.3	4.4	
Late time step input	γ_1	69.2	68.1	0.7	5
	γ_2	63.1	62.7	11.2	
	γ_3	112.1	†	†	
Early time power ramp	β_1	227.2	226.9		1
	β_2	434.6	337		

*Theoretical values are based on properties obtained from a sample of the substrate. Estimated values are based on an ordinary least-squares fit of the appropriate model to experimental data. The standard deviations and the number of tests are for the estimated values.

†Estimated value was negative with a percentage standard deviation of over 400 percent.

Table 4 Thermophysical property estimates

	k , W/cmK	Standard deviations, percentage	$(k\rho c)^{1/2}$, $Ws^{1/2}/cm^2K$	Standard deviations, percentage
New product data	0.0168		0.18	
Property measurements (3 samples)	minimum 0.0141		0.17	
	average 0.0155		0.177	
	maximum 0.0163		0.18	
Thermal penetrator [11] (5 tests, 1 sample)	minimum		0.155	
	average		0.169	
	maximum		0.179	
Current work	minimum 0.015	3.6	0.166	7.7
	average 0.015		0.181	
	maximum 0.017	4.5	0.208	9.0

ly a result of rapidly decreasing sensitivity for the higher order terms.

The sensitivity of the estimates is time dependent. For the time ranges shown in Figs. 3 and 4, the sensitivity for the first parameter is approximately an order of magnitude more than the sensitivity of the second parameter. However, the increased level of noise, which is apparent in Fig. 4, contributes to the estimation problem for the late time model parameters. Convective heat loss from the gage surface was expected to be a problem at late times; however, for the response tests the loss is estimated to be less than 1 percent of the electrical power input.

The gage parameters, b , k , $(k\rho c)^{1/2}$, were calculated from the estimated parameters for β_1 , β_2 , and γ_1 . For the results shown below, the value of a was set to 0.5 mm. The average value of b , calculated from five early time data sets and five late time data sets used in all possible combinations, was 4.96 mm where the design value was 5.0 mm. The range of estimates was from 4.36 mm to 5.31 mm, with percentage standard deviations for groups of five test pairs (i.e., an early and a late time response) of 6.2 percent to 7.3 percent. The estimates of k and $(k\rho c)^{1/2}$ by the various methods are given in Table 4.

To test the model (28) for the periodic excitation case, a function generator was used to provide a voltage sine wave input to the resistance bridge in which one leg is the thin film gage. Because the model was developed from the early time solution, it should be applicable for frequencies above 5 Hz. Experimental data were generated for frequencies from 0.5 to 100 Hz. Figure 5 shows the results of the testing. The experimental data are shown as filled triangles while the model response for two different sets of parameters is shown as unfilled symbols. The upper curve was generated using

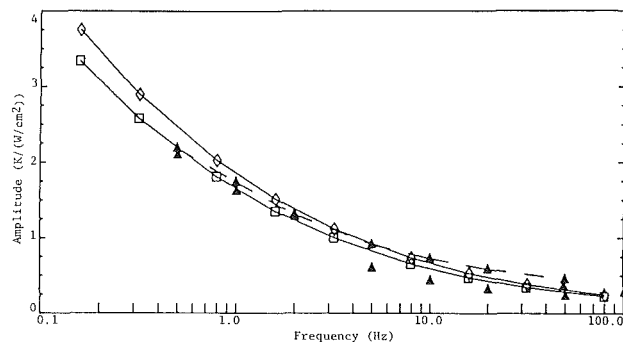


Fig. 5 Frequency response plot. Solid triangles represent experimental data while open symbols were produced by the model. The two modeled cases result from using either manufacturer's data (upper curve) or parameters obtained from the step response tests.

parameters derived from thermophysical property testing while the lower one resulted from parameters estimated using the step response tests (Figs. 3 and 4). The experimental data bracket the model results, but the overall behavior differs somewhat. The asymptotic value seems to be higher for the experimental data and the amplitude decay rate (decibels per decade) is lower.

An examination of work done in the areas of bridge-wire and resistor testing has provided information that explains some or all of the discrepancies that exist between the model and experimental results [12, 13]. The experimental results are complicated by the fact that the thin film acts as a nonlinear electrical resistance element. The output of the device becomes the sum of the fundamental as well as an infinite series of harmonics. The equations describing the performance of a

passive resistive element [12] show that the voltage-current behavior is similar to

$$I = \alpha V + \beta V^3 + \gamma V^5 \quad (32)$$

When the device is exposed to a periodic signal of the form

$$V = V_0 \sin(\omega t) \quad (33)$$

harmonic frequencies are produced. The first harmonic is described by

$$I = -[(\beta/4)V_0^3 + (5\gamma/16)V_0^5] \sin(3\omega t) \quad (34)$$

Note that the frequency is three times the fundamental. The amplitude of the harmonic is determined by the thermal characteristics of the device. For typical resistors used in electrical circuits, the amplitude is fairly small. The thermal response of the thin film gage is the desired signal, however, and the amplitude of the harmonic is significant (approximately 10 percent) when compared to the signal due to the fundamental frequency.

The best way to remove the discrepancy between the model and the experimental system is to couple the thermal equations describing the rectangular source with those for the electrical behavior of the bridge circuit. The harmonics would then become part of the model. The difficulty would lie in solving the set of nonlinear partial differential equations. To date, the solution has not been attempted.

Summary

A model for the average temperature of a rectangular heat source on a semi-infinite body has been developed. Starting from a Green's function definition of the problem, the model is simplified into the three algebraic expressions that cover the early, middle, and late time regimes.

The model developed for the step heating response is extended to the cases of ramp and periodic heating. All of the models are compared with experimental data with generally good results. The step and ramp heating models are used with the experimental data to estimate calibration parameters for a thin film heat flux gage. The improved accuracy of the calibration parameters produces a corresponding improvement in the accuracy of the heat flux measurements provided by the thin film gage.

Acknowledgments

The authors wish to acknowledge Dr. J. E. Shepherd for providing the gages and a detailed review of this paper, R. L. Weatherbee for conducting the calibration experiments, L. A. Kent for providing the thermal penetration measurements, and E. P. Roth for the thermophysical property measurements. The work was performed at Sandia National Laboratories and supported by the US Department of Energy under Contract No. DE-AC04-76DP00789.

References

- 1 Thompson, W. P., "Heat Transfer Gauges," in: *Methods of Experimental Physics*, Vol. 18B, R. J. Emrich, ed., Academic Press, New York, 1981.
- 2 Gustafson, S. E., et al., "Transient Heat-Strip Method for Measuring Thermal Conductivity and Specific Heat of Solids and Fluids: Second Order Theory and Approximations for Short Times," *J. Appl. Physics*, Vol. 53, 1982, p. 6064.
- 3 Skinner, G. T., "Calibrating of Thin-Film Backing Materials," *ARS Journal*, Vol. 31, 1962, pp. 671-672.
- 4 Shephard, J. E., et al., "Heat Transfer in Constant Volume Hydrogen Air Combustion," Sandia National Laboratories, Albuquerque, NM, Report No. SAND83-2658.
- 5 Keltner, N. R., and Beck, J. V., "Surface Temperature Measurement Errors," *ASME JOURNAL OF HEAT TRANSFER*, Vol. 105, 1983, pp. 312-318.
- 6 Carslaw, H. S., and Jaeger, J. C., *Conduction of Heat in Solids*, 2nd ed., Oxford University Press, 1959, p. 265.
- 7 Kadamvi, V., and Abuaf, N., "Axisymmetric and Three-Dimensional Chip-Spreader Calculations," 21st National Heat Transfer Conference, AIChE Symposium Series, Vol. 79, No. 225, Seattle, WA, July 1983.
- 8 Yovanovich, M. M., et al., "Transient Temperature Rise of Arbitrary Contacts With Uniform Flux by Surface Element Methods," AIAA 22nd Aerospace Sciences Conference, Reno, NV, Jan. 1984.
- 9 Beck, J. V., "Green's Function Solution for Transient Heat Conduction Problems," *Int. Journal Heat and Mass Transfer*, Vol. 27, 1984, pp. 1235-1244.
- 10 Kerlin, T. W., "In-Situ Response Time Testing of Platinum Resistance Thermometers," *ISA Transactions*, Vol. 17, No. 4, 1978, pp. 71-88.
- 11 Abdel-Wahed, R. M., et al., "An Instrument for Measuring the Thermal Penetration Property $\rho c K$," *Int. Journal of Heat and Mass Transfer*, Vol. 21, 1978, pp. 967-973.
- 12 English, A. T., et al., "Pulse Nonlinearity Measurements on Thin Conducting Films," *Journal of Applied Physics*, Vol. 49, No. 2, 1978, pp. 717-722.
- 13 Tarmy, B. L., and Bonilla, C. F., "The Application of Frequency Response Analysis to Thermal Conductivity Measurements," in: *Progress in International Research on Thermodynamic and Transport Properties*, ASME, 2nd Symposium on Thermophysical Properties, Jan. 1962, pp. 402-411.

Transient Temperature Fields in Crossflow Heat Exchangers With Finite Wall Capacitance

M. Spiga

Istituto di Fisica Tecnica,
Facoltà di Ingegneria,
Università di Bologna, 40136
Bologna, Italy

G. Spiga

Dipartimento di Matematica,
Università di Bari, 70125
Bari, Italy

Solutions are provided in nondimensional form for the transient analysis of direct-transfer crossflow heat exchangers, with both fluids unmixed and finite wall heat capacity. The two-dimensional transient temperature distributions of core wall and both fluids are determined by analytical methods for any externally applied variation of the primary fluid inlet temperature. The general solutions are derived by the local energy balance equations, and are presented as simple integrals of the Green's functions, which represent the pulse response following a deltalike perturbation in the inlet temperature of the primary fluid, and are deduced using the Laplace transform method. The Green's functions are expressed as integrals of modified Bessel functions, in terms of the heat capacity ratios, number of transfer units, heat transfer resistance and flow capacitance ratios.

Introduction

The transient response of crossflow heat exchangers is of increasing interest in many industrial fields. Any change, intentional or accidental, in the operation of the heat exchanger will produce a perturbation downstream that can have important consequences. For example, the lag introduced by the exchanger influences the shaft output transient behavior. The large-size units involve large capital and operating costs and, especially in nuclear engineering, must meet rigorous safety requirements. Hence a high integrity is required, and a thorough knowledge of the two-dimensional transient temperature distribution is necessary for both design and licensing purposes. In the past, approximate methods with the application of correction factors were used for crossflow heat exchangers; nowadays with the progress of mathematical tools and the availability of computers, there is no reason to evade the real two dimensionality of the problem.

In recent years a considerable effort has been made and a huge amount of work is found in literature concerning crossflow heat exchangers. While the steady-state solution is well established (Bačlic and Heggs, 1985), the transient solution is still the object of intense activity. Some authors proposed numerical solutions restricted to: mixed mean exit temperatures, step response, fluid-to-wall capacity ratios equated to zero (large wall capacitance). Romie (1983) shows a detailed review of this previous work and introduces the application of an analytical method to the problem (with the restrictions mentioned above). Yamashita et al. apply a finite difference method to investigate the effects of initial conditions on the outlet temperature responses. Gvozdenac (1986) and Spiga and Spiga (1987) present a more general analytical solution, determining the two-dimensional transient temperature distribution, with arbitrary initial and inlet conditions, but still for large wall capacitance. Unfortunately the hypothesis of zero fluid-to-wall heat capacity ratio is rather restrictive and limits the applicability of the solutions to gas-to-gas exchangers. Crossflow heat exchangers most often involve liquids (such as water, sodium, and phosphoric acid) and wall materials having small heat capacity; hence the heat capacity ratios can be significantly different from zero.

This work describes an improved solution (in space and

time) of the core and fluid temperatures, taking account of the finite wall capacitance. To the best knowledge of the authors this is the first paper dealing with such a matter. The general solutions, provided as integrals of the Green's functions, can be very useful to perform reliable thermal and stress analysis and, moreover, can be used to evaluate the average transient number of transfer units (Mullisen and Loehrke, 1986). The general solutions depend on a large number of parameters such as heat capacity ratios, number of transfer units, heat resistance and flow capacitance ratios, defined below, and inlet and initial conditions. These solutions can be simply used by industrial practitioners by choosing a suitable set of parameters. However the aim of this paper is the presentation of the general solutions, and the investigation of the Green's functions, which represent the two-dimensional transient temperatures following a deltalike perturbation at the inlet of the primary fluid.

Physical Model

Let us consider a direct-transfer, single-pass crossflow heat exchanger, with walls separating the two fluid streams (flowing at right angles). The problem will be tackled assuming the following hypotheses:

- neither fluid is mixed (the assumption of one fluid mixed should allow simplification of the problem);
- the physical properties and fluid capacity rates are uniform and constant;
- the thermal conductances on both sides are constant and inclusive of wall thermal resistance and fouling;
- the exchanger shell or shroud is adiabatic;
- change of flow distribution inside the exchanger and axial heat conduction are neglected;
- heat transfer area per unit base area and surface configurations are constant.

Introducing the dimensionless variables

$$t = \frac{(hA)_a \tau}{Mc_w} \quad x = \frac{(hA)_a}{(mc)_a} \frac{\xi}{L_a} \quad y = \frac{(hA)_b}{(mc)_b} \frac{\eta}{L_b} \quad (1)$$

the two-dimensional time-dependent temperature fields in both streams and in the wall separating the fluids are governed by the well-established partial differential equations expressing conservation of energy for wall and fluids

Contributed by the Heat Transfer Division for publication in the JOURNAL OF HEAT TRANSFER. Manuscript received by the the Heat Transfer Division December 1, 1986.

$$\begin{aligned} \frac{\partial T_w}{\partial t} + (1+R)T_w &= T_a + RT_b \\ \frac{\partial T_a}{\partial x} + V_a \frac{\partial T_a}{\partial t} + T_a &= T_w \\ \frac{\partial T_b}{\partial y} + \frac{V_b}{R} \frac{\partial T_b}{\partial t} + T_b &= T_w \end{aligned} \quad (2)$$

for $t \geq 0$, $0 \leq x \leq N_a$, $0 \leq y \leq N_b$. To obtain a well-posed partial differential problem, initial and boundary conditions must be prescribed

$$\begin{aligned} T_w(x, y, 0) &= 0 \\ T_a(0, y, t) &= \varphi(t) & T_a(x, y, 0) &= 0 \\ T_b(x, 0, t) &= 0 & T_b(x, y, 0) &= 0 \end{aligned} \quad (3)$$

assuming for simplicity that only the inlet condition of one fluid (labeled primary fluid henceforth) is perturbed, and that such a perturbation is uniform in the plane of the inlet section. This kind of perturbation is certainly the most important from a physical point of view. On the other hand, the transient can be induced by a variation of any of the five quantities on the left-hand side of equations (3), but, because of the linearity of equations (2), the general solution can be given by superimposition. The five responses relevant to one of the above quantities being prescribed and the other four being set equal to zero may be obtained in fact by a procedure similar to that described below.

Here and in the sequel the usual dimensionless physical parameters

$$\begin{aligned} N_a &= \frac{(hA)_a}{(mc)_a} & N_b &= \frac{(hA)_b}{(mc)_b} & R &= \frac{(hA)_b}{(hA)_a} \\ V_a &= \frac{(mc)_a}{Mc_w} \frac{L_a}{u_a} & V_b &= \frac{(mc)_b}{Mc_w} \frac{L_b}{u_b} & E &= \frac{(mc)_b}{(mc)_a} \\ \text{NTU} &= \left\{ (mc)_{\min} \left[\frac{1}{(hA)_a} + \frac{1}{(hA)_b} \right] \right\}^{-1} \end{aligned} \quad (4)$$

are used; of course E and NTU can be cast in terms of R , N_a , and N_b , with different expressions according to whether $(mc)_a \geq (mc)_b$. Hence the solutions depend on five nondimensional parameters. The quantities V_a and V_b , usually negligible in gas-to-gas exchangers, are consistently taken into account here. As is suggested by equations (2), and will be apparent later on, the effect of nonvanishing values of V_a and V_b is the

occurrence of propagation phenomena. The propagation speeds $1/V_a$ (or R/V_b) in the x (or y) direction, for a constant y (or x), correspond, in the physical coordinates, to the actual speeds u_a (or u_b).

General Solution

Taking a threefold Laplace transform with respect to t , x , y with complex parameters s, p, q , respectively, and defining

$$\begin{aligned} \tilde{T}_\alpha(p, q, s) &= \int_0^\infty e^{-st} dt \int_0^\infty e^{-px} dx \int_0^\infty e^{-qy} \\ & T_\alpha(x, y, t) dy \\ &= \mathcal{L}_q \mathcal{L}_p \mathcal{L}_s [T_\alpha(x, y, t)] \end{aligned} \quad (5)$$

with $\alpha = w, a, b$, leads to the set of algebraic equations

$$\begin{aligned} (s+R+1)\tilde{T}_w(p, q, s) - \tilde{T}_a(p, q, s) - R\tilde{T}_b(p, q, s) &= 0 \\ (p+V_a s+1)\tilde{T}_a(p, q, s) - \tilde{T}_w(p, q, s) &= \frac{1}{q}\tilde{\varphi}(s) \\ \left(q + \frac{V_b}{R}s + 1\right)\tilde{T}_b(p, q, s) - \tilde{T}_w(p, q, s) &= 0 \end{aligned} \quad (6)$$

where $\tilde{\varphi}(s) = \mathcal{L}_s[\varphi(t)]$. Introducing further

$$\begin{aligned} \tilde{G}_w(p, q, s) &= \left(q + \frac{V_b}{R}s + 1\right)P^{-1}(p, q, s) \\ \tilde{G}_a(p, q, s) &= \left[(s+R+1)\left(q + \frac{V_b}{R}s + 1\right) - R\right]P^{-1}(p, q, s) \\ \tilde{G}_b(p, q, s) &= P^{-1}(p, q, s) \end{aligned} \quad (7)$$

with

$$\begin{aligned} P(p, q, s) &= (s+R+1)(p+V_a s+1)\left(q + \frac{V_b}{R}s + 1\right) \\ & - \left(q + \frac{V_b}{R}s + 1\right) - R(p+V_a s+1) \end{aligned} \quad (8)$$

the solution of the algebraic system (6) reads as

$$\tilde{T}_\alpha(p, q, s) = \frac{1}{q}\tilde{\varphi}(s)\tilde{G}_\alpha(p, q, s) \quad (9)$$

with $\alpha = w, a, b$, and then, by the convolution theorem, the response to the general inlet datum $\varphi(t)$ is given by

$$T_\alpha(x, y, t) = \int_0^t T_\alpha^G(x, y, t')\varphi(t-t')dt' \quad (10)$$

in terms of the Green's functions

Nomenclature

A = heat transfer surface, m^2	NTU = number of transfer units	γ = incomplete gamma function
c = specific heat at constant pressure, $J/kg \cdot K$	P = function defined by equation (8)	$\delta(\cdot)$ = Dirac delta function
E = flow capacitance ratio	R = heat transfer resistance ratio	ξ, η = space variables, m
$G(\cdot)$ = Green's function	s, p, q = Laplace transform variables	φ = primary fluid inlet temperature, K
h = heat transfer coefficient, $W/m^2 \cdot K$	t = dimensionless time variable	τ = time variable, s
$I(\cdot)$ = modified Bessel function of the first kind	T = dimensionless temperature	
L = exchanger length, m	u = fluid velocity, m/s	Subscripts
\mathcal{L} = Laplace operator	$U(\cdot)$ = Heaviside step function	a = primary fluid
m = mass flow rate, kg/s	V = heat capacity ratio	b = secondary fluid
M = mass of the exchanger, kg	x, y = dimensionless space variables	w = solid wall
N = dimensionless exchanger length		α = general label

$$T_{\alpha}^G(x, y, t) = \int_0^y G_{\alpha}(x, y', t) dy' \quad (11)$$

which represent the temperature fields for a deltalike perturbation, $\varphi(t) = \delta(t)$, and allow the computation of all T_{α} for any assigned $\varphi(t)$.

The main task is the inverse threefold Laplace transform of the function G_{α} , which can be performed analytically. A first inversion with respect to p is just a matter of residue calculation and yields simply

$$\begin{aligned} \tilde{G}_b(x, q, s) = & (s+R+1)^{-1} \left(q + \frac{V_b}{R}s + 1 - \frac{R}{s+R+1} \right)^{-1} \\ & \exp \left[-x \left(V_a s + 1 - \frac{1}{s+R+1} \right) + xR(s+R+1)^{-2} \right. \\ & \left. \left(q + \frac{V_b}{R}s + 1 - \frac{R}{s+R+1} \right)^{-1} \right] \quad (12) \end{aligned}$$

Furthermore, since

$$\mathcal{L}_y^{-1} \left[\frac{1}{q} \exp(k/q) \right] = I_0(2\sqrt{ky}) \quad (13)$$

where I_n denotes the n th modified Bessel function of the first kind, it is not difficult to derive

$$\begin{aligned} \tilde{G}_b(x, y, s) = & (s+R+1)^{-1} \exp \left[-x \left(V_a s + 1 - \frac{1}{s+R+1} \right) \right. \\ & \left. - y \left(\frac{V_b}{R}s + 1 - \frac{R}{s+R+1} \right) \right] I_0 \left(2 \frac{\sqrt{Rxy}}{s+R+1} \right) \quad (14) \end{aligned}$$

and finally, bearing in mind that

$$\mathcal{L}_t^{-1} \left[s^{-1} \exp \left(\frac{k+h}{s} \right) I_n \left(2 \frac{\sqrt{kh}}{s} \right) \right] = I_n(2\sqrt{kt}) I_n(2\sqrt{ht}) \quad (15)$$

one can conclude, on using simple properties of the \mathcal{L} operator,

$$\begin{aligned} G_b(x, y, t) = & U \left(t - V_a x - \frac{V_b}{R} y \right) \\ & \exp \left[-x - y - (1+R) \left(t - V_a x - \frac{V_b}{R} y \right) \right. \\ & \left. I_0 \left[2\sqrt{x \left(t - V_a x - \frac{V_b}{R} y \right)} \right] I_0 \left[2\sqrt{Ry \left(t - V_a x - \frac{V_b}{R} y \right)} \right] \right] \quad (16) \end{aligned}$$

where U is the unit step function, accounting for the finite propagation speed of disturbances in the exchanger.

Analogous evaluations hold for the functions G_a and G_w , but for brevity the results are not reported here. Rather it is worth writing down explicitly the Green's functions T_{α}^G . They are in fact the most important quantities, from both practical and theoretical points of view, and characterize completely the response of the heat exchanger. They are expressed analytically in terms of integrals of modified Bessel functions as

$$\begin{aligned} T_w^G(x, y, t) = & U(t - V_a x) e^{-x - (1+R)(t - V_a x)} \left\{ I_0 \left[2\sqrt{x(t - V_a x)} \right] \right. \\ & + \int_0^{y^*} \left[\frac{R(t - V_a x) - V_b y'}{y'} \right]^{1/2} e^{-\left(1 - \frac{1+R}{R} V_b\right) y'} \\ & I_0 \left[2\sqrt{x \left(t - V_a x - \frac{V_b}{R} y' \right)} \right] \\ & \left. I_1 \left[2\sqrt{Ry' \left(t - V_a x - \frac{V_b}{R} y' \right)} \right] dy' \right\} \quad (17a) \end{aligned}$$

$$T_a^G(x, y, t) = e^{-x} \delta(t - V_a x) + U(t - V_a x) e^{-x - (1+R)(t - V_a x)}$$

$$\begin{aligned} & \left\{ \left(\frac{x}{t - V_a x} \right)^{1/2} I_1 \left[2\sqrt{x(t - V_a x)} \right] + (Rx)^{1/2} \right. \\ & \left. \int_0^{y^*} e^{-\left(1 - \frac{1+R}{R} V_b\right) y'} y'^{-1/2} I_1 \left[2\sqrt{x \left(t - V_a x - \frac{V_b}{R} y' \right)} \right] \right. \\ & \left. I_1 \left[2\sqrt{Ry' \left(t - V_a x - \frac{V_b}{R} y' \right)} \right] dy' \right\} \quad (17b) \end{aligned}$$

$$\begin{aligned} T_b^G(x, y, t) = & U(t - V_a x) e^{-x - (1+R)(t - V_a x)} \int_0^{y^*} e^{-\left(1 - \frac{1+R}{R} V_b\right) y'} \\ & I_0 \left[2\sqrt{x \left(t - V_a x - \frac{V_b}{R} y' \right)} \right] \\ & I_0 \left[2\sqrt{Ry' \left(t - V_a x - \frac{V_b}{R} y' \right)} \right] dy' \quad (17c) \end{aligned}$$

where

$$y^* = \min \left[y, \frac{R}{V_b} (t - V_a x) \right] \quad (18)$$

The existence of a wave front propagating in the x direction at a speed $1/V_a$ is thus clear. At any point (x, y) all temperatures are zero as long as $t < V_a x$. The integrals represent contributions brought to the temperatures by the other wave fronts propagating in the y direction at a speed R/V_b . The integration variable y' runs backward in the y direction starting from the point (x, y) . Integrations go back along the y axis up to the secondary fluid inlet section ($y' = y$) for $t > V_a x + yV_b/R$, but only up to a partial depth $y' = (t - V_a x)R/V_b$ for $V_a x < t < V_a x + yV_b/R$, due to the finite propagation speed.

In the intermediate case, $V_a x < t < V_a x + yV_b/R$, the y' integration does not go back up to the inlet section, since the wave front along the line at abscissa x has been able to travel only up to the ordinate $R(t - V_a x)/V_b < y$; in such a case all T_{α}^G are independent of y . Of course, the results of Spiga and Spiga (1987), relevant to gas-to-gas crossflow exchangers, are reproduced in the limit V_a and $V_b \rightarrow 0$. Once the T_{α}^G are known via equations (17), the response to any inlet datum $\varphi(t)$ is provided by equation (10).

As regards the integrals in equations (17), they can be easily computed numerically, since they are one-dimensional integrals of smooth continuous functions over a finite interval. The numerical integration has been performed resorting to an algorithm based on a two-point Gaussian tensor product formula, available in most computer routine libraries. On the other hand it is not difficult to obtain for these integrals an analytical expression in terms of an infinite series of incomplete gamma functions, by expanding all Bessel functions in power series with respect to their arguments and then using binomial expansions to single out integer powers of y' . For instance, T_a^G would read as

$$T_a^G(x, y, t) = e^{-x} \delta(t - V_a x) + U(t - V_a x) e^{-x - (1+R)(t - V_a x)}$$

$$\begin{aligned} & \left\{ \left(\frac{x}{t - V_a x} \right)^{1/2} I_1 \left[2\sqrt{x(t - V_a x)} \right] + \sum_{n=0}^{\infty} \sum_{k=0}^n \sum_{j=0}^{n+1} \right. \\ & \frac{(-1)^j (n+1)!}{(n-k)! (n-k+1)! k! (k+1)! j! (n+1-j)!} \\ & \frac{R^{2k+2} V_b^j}{[R - (1+R)V_b]^{k+j+1}} x^{n-k+1} (t - V_a x)^{n-j+1} \\ & \left. \gamma \left[k+j+1, \frac{R - (1+R)V_b y^*}{R} \right] \right\} \quad (19) \end{aligned}$$

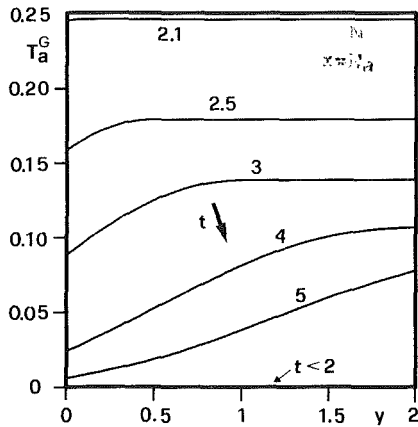


Fig. 1 Primary fluid temperature distribution in the exit section for various times

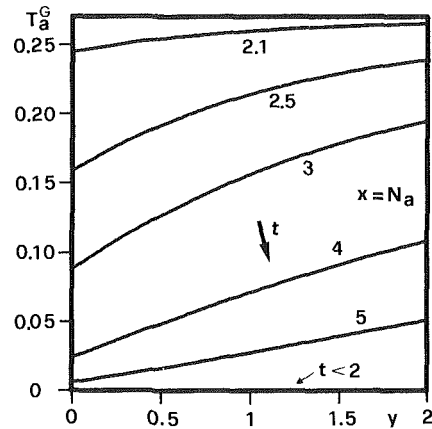


Fig. 3 Primary fluid temperature distribution in the exit section, for various times and $V_b = 0.01$

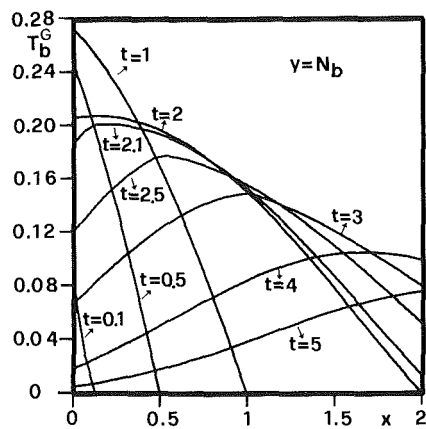


Fig. 2 Secondary fluid temperature distribution in the exit section for various times

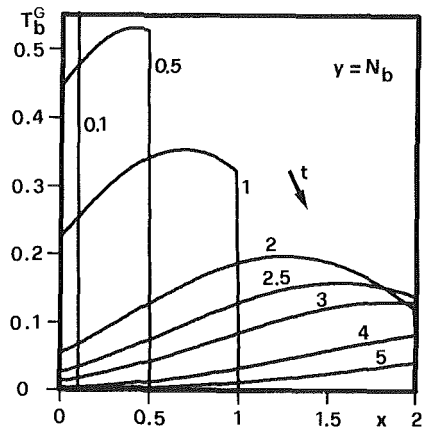


Fig. 4 Secondary fluid temperature distribution in the exit section, for various times and $V_b = 0.01$

These expressions for T_a^G have been used to check the numerical integrations of equations (17), with quite satisfactory results.

Results and Concluding Remarks

While in the previous sections the analysis has been carried out using the three parameters N_a , N_b , and R (together with V_a and V_b) in order to avoid the double formalism connected to NTU, the numerical results are here presented using the more common parameters E , R , and NTU. The general solutions in equations (10) are dependent on five physical parameters together with the inlet temperature (which can simulate any perturbation and can be given as an analytical function or a data set deduced by experimental tests). It will be the aim of more specific work to investigate deeply and emphasize the different particular applications relevant to industrial practice, which can be characterized by governing parameters varying in a wide range and by the most different inlet perturbations. Hence this section deals only with the investigation of the exchanger temperature distributions following a deltalike perturbation in the inlet primary temperature, expressed by equations (17).

The fluid temperature distributions in the exit sections are reported in Figs. 1 and 2, for various times, assuming all the governing parameters (E , R , NTU, V_a , V_b) to be unity. Consequently the parameters N_a and N_b are equal to 2. The perturbation reaches the exit section of the primary fluid at $t = V_a N_a$ and then is slowly flattened, more rapidly near the section $y=0$, where the cold secondary fluid enters the ex-

changer. When t is small enough, occurrence of intervals on the y axis in which T_a^G is constant, as discussed in the previous section, is apparent. Of course $T_a^G \rightarrow 0$ for any y when $t \rightarrow \infty$. The secondary fluid temperature distribution in the exit section is characterized by a sudden, but continuous, increase near the inlet section of the primary fluid, then after the wave front has propagated all over the length N_a , the location of the maximum value moves toward the exit section, until eventually the temperature slowly decreases to zero, everywhere. It must be born in mind that T_b^G experiences the effects of the main wave front (propagating in the x direction with speed $1/V_a$ and with a jump discontinuity $\exp(-x)$ for T_w^G , or a deltalike discontinuity for T_a^G) only in an indirect way, since the secondary fluid, flowing in the y direction at a speed R/V_b , can get energy only from a previously heated solid wall. The occurrence of a maximum in Fig. 2 is explained in terms of the competing effects of a larger section of the interval $0 < y < N_b$ contributing to warm up the secondary fluid, and of the decrease of the wall temperature after the passage of the main wave front.

To stress the role played by the finite wall heat capacitance, the mean exit temperatures are shown in Figs. 3–6 for the case when V_a and V_b are varied from unity, in order to see the effects of different heat capacity ratios, and thus of different propagation speeds.

In Figs. 3 and 4 V_b is taken equal to 10^{-2} , while E , R , NTU, and V_a remain unity (in a certain sense, the secondary fluid behaves like a gas, and the secondary wave front is much faster than the primary one). As is apparent from the reported curves of $T_a^G(N_a, y, t)$ and $T_b^G(x, N_b, t)$, a consequence of

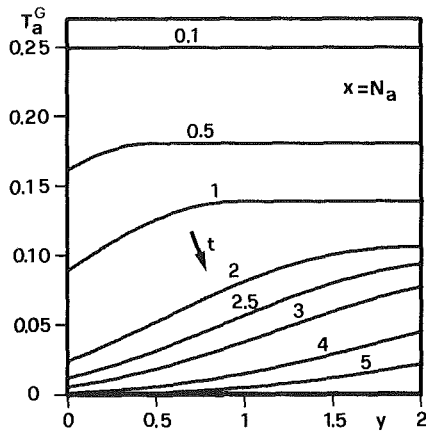


Fig. 5 Primary fluid temperature distribution in the exit section, for various times and $V_a = 0.01$

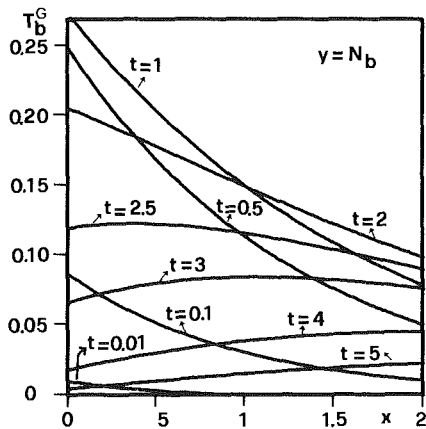


Fig. 6 Secondary fluid temperature distribution in the exit section, for various times and $V_a = 0.01$

the above features is that the secondary fluid is very sensitive to all variations of the primary fluid, and tends to follow them very closely; in fact, intervals on the y axis in which T_a^G is constant have almost disappeared, and T_b^G versus x , though still continuous, exhibits very sharp variations in a small neighborhood of the main propagating wave front at $x = t/V_a$. The complementary situation in which V_a is equal to 10^{-2} with unit values for E , R , NTU and V_b is sketched in Figs. 5 and 6. Now the primary wave front is in turn much faster, and therefore the results for the same outlet temperatures as before are much closer to those of a gas-to-gas exchanger, discussed in Spiga and Spiga (1987), with only a considerable time lag of T_b^G variations with respect to T_a^G variations; both of them are however very smooth after time $V_a N_a$, and the slope of $T_b^G(x, N_b, t)$ versus x changes slowly from everywhere negative to everywhere positive when t increases.

At last, an overall view of the two-dimensional temperature fields is provided by Fig. 7, where the core wall temperature is shown for different values of time, again with all governing parameters E , R , NTU , V_a , and V_b set equal to one. The

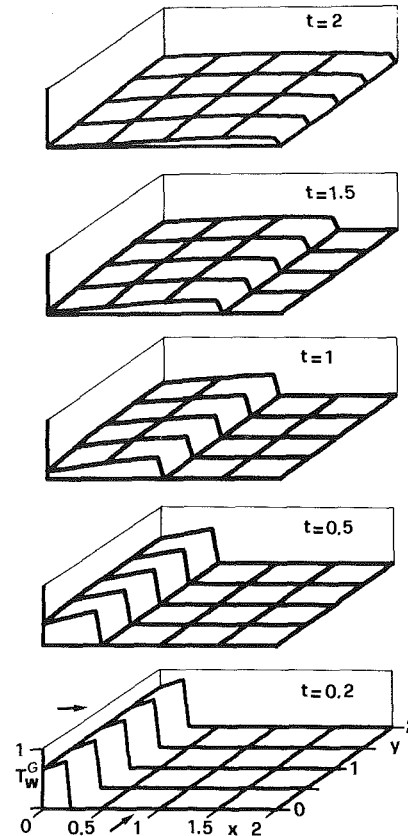


Fig. 7 Transient temperature field in the core wall, for various times

propagation of the wave front, its jump discontinuity, and the flattening following the delta pulse at the inlet of the primary fluid are quite clear.

Acknowledgments

This work was financially supported by the Italian Ministry of Public Education and the National Research Council.

References

- Baclic, B. S., and Heggs, P. J., 1985, "On the Search for New Solutions of the Single-Pass Crossflow Heat Exchanger Problem," *International Journal of Heat Mass Transfer*, Vol. 28, pp. 1965-1976.
- Gvozdenac, D. D., 1986, "Analytical Solution of the Transient Response of Gas-to-Gas Crossflow Heat Exchanger with Both Fluids Unmixed," *ASME JOURNAL OF HEAT TRANSFER*, Vol. 108, pp. 722-727.
- Mullisen, R. S., and Loehrke, R. I., 1986, "A Transient Heat Exchanger Evaluation Test for Arbitrary Fluid Inlet Temperature Variation and Longitudinal Core Conduction," *ASME JOURNAL OF HEAT TRANSFER*, Vol. 108, pp. 370-376.
- Romic, F. E., 1983, "Transient Response of Gas-to-Gas Crossflow Heat Exchangers With Neither Gas Mixed," *ASME JOURNAL OF HEAT TRANSFER*, Vol. 105, pp. 563-570.
- Spiga, G., and Spiga, M., 1987, "Two-Dimensional Transient Solutions for Crossflow Heat Exchangers With Neither Gas Mixed," *ASME JOURNAL OF HEAT TRANSFER*, Vol. 109, pp. 281-286.
- Yamashita, H., Izumi, R., and Yamaguchi, S., 1978, "Analysis of the Dynamic Characteristics of Crossflow Heat Exchangers With Both Fluids Unmixed," *JSME Bulletin*, Vol. 21, pp. 479-485.

Thermal Effectiveness of Multiple Shell and Tube Pass TEMA E Heat Exchangers

A. Pignotti

TECHINT S. A.,
1001 Buenos Aires, Argentina

P. I. Tamborenea

Fundación Hermanos
Agustín y Enrique Rocca,
1054 Buenos Aires, Argentina

The thermal effectiveness of a TEMA E shell-and-tube heat exchanger, with one shell pass and an arbitrary number of tube passes, is determined under the usual simplifying assumptions of perfect transverse mixing of the shell fluid, no phase change, and temperature independence of the heat capacity rates and the heat transfer coefficient. A purely algebraic solution is obtained for the effectiveness as a function of the heat capacity rate ratio and the number of heat transfer units. The case with M shell passes and N tube passes is easily expressed in terms of the single-shell-pass case.

Introduction

The thermal problem for the TEMA E exchanger has been analyzed for several different configurations, using the following simplifying assumptions: no phase change, no heat losses, perfect transverse mixing of the shell and tube fluids, and no temperature dependence of the heat capacity rates, or of the heat transfer coefficient.

For the 1- N geometry (one shell pass and N tube passes), the cases of $N=1$ and $N \rightarrow \infty$ are trivial, the former coinciding with either countercurrent or parallel current geometries, and the latter with the mixed-mixed crossflow exchange (Stevens et al., 1957).

The 1-2 and 1-4 cases were solved long ago (Nagle, 1933; Underwood, 1934; Bowman, 1936) and, more recently, the 1- N geometry has been solved for even N up to $N=12$ (Kraus and Kern, 1965). Common practice is to use the $N=2$ results for arbitrary even values of N , although previous results (Kraus and Kern, 1965; Crozier and Samuels, 1977) and the asymptotic limit $N \rightarrow \infty$ show that, for even N , the effectiveness decreases slightly as N increases. It should be pointed out that, when the number of tube passes is even, it is immaterial whether the shell and tube outlets are at the "same end" or "opposite ends" of the exchanger. This is an immediate consequence of flow-reversibility (Pignotti, 1984).

For odd N , the same-end and opposite-end configurations are, of course, not equivalent. The case of $N=3$ has been analyzed by Fischer (1938), who obtained an equation for the mean temperature difference with the opposite-end geometry, which he proceeded to solve by iteration. More recently, Crozier and Samuels (1977) used a numerical procedure to integrate the differential equations for even and odd values of N , and showed an example of N dependence up to $N=15$. Very recently, one of us obtained an analytical solution for the effectiveness in the 1-3 case (Pignotti, 1986), and the same approach is generalized here to arbitrary values of N . This result, coupled to the known expression for the effectiveness of series assemblies of heat exchangers (Domingos, 1969), provides a purely algebraic solution for the most general M - N configuration.

Formulation

We proceed in two stages in the formulation of the problem and, for concreteness, we consider the opposite-end 1- N case, for odd N . In the first stage, an auxiliary problem, in which the connections between successive tube passes are severed, is

solved. The geometry of this problem, in which there are $N+1$ inlet and $N+1$ outlet streams, is shown in Fig. 1. In the approximation used, the $N+1$ temperatures at the $z=1$ end of the exchanger are related to the $N+1$ temperatures at the $z=0$ end by the matrix equation

$$\begin{bmatrix} T_1(1) \\ \cdot \\ \cdot \\ \cdot \\ T_N(1) \\ t(1) \end{bmatrix} = H \begin{bmatrix} T_1(0) \\ \cdot \\ \cdot \\ \cdot \\ T_N(0) \\ t(0) \end{bmatrix} \quad (1)$$

where H is an $(N+1) \times (N+1)$ temperature-independent matrix. The first step in our solution is precisely the determination of this matrix H . The constraints on the tube fluid temperatures at $z=0$ and $z=1$, which follow from the fact that the tube streams so far considered are actually the successive passes of a single tube stream, are enforced in the second stage. After this is accomplished, the effectiveness of the exchanger can be readily obtained as a function of the heat capacity rate ratio R and the number of heat transfer units N_{tu} .

First Stage

The shell and tube fluid temperatures $t(z)$ and $T_i(z)$ satisfy a set of coupled equations which, in matrix form, can be written as

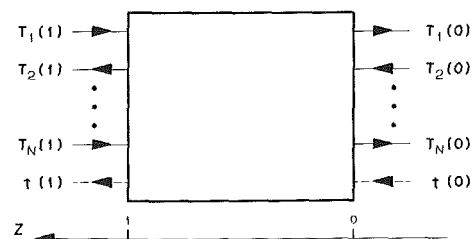


Fig. 1 Configuration used for the "opposite end" 1-odd N case.

Contributed by the Heat Transfer Division for publication in the JOURNAL OF HEAT TRANSFER. Manuscript received by the Heat Transfer Division July 10, 1986.

$$\frac{N}{N_{tu}} \frac{d}{dz} \begin{bmatrix} T_1(z) \\ \vdots \\ T_N(z) \\ t(z) \end{bmatrix} = D \begin{bmatrix} T_1(z) \\ \vdots \\ T_N(z) \\ t(z) \end{bmatrix}$$

with

$$D = \begin{bmatrix} R & 0 & \cdot & \cdot & \cdot & 0 & -R \\ 0 & -R & \cdot & \cdot & \cdot & 0 & R \\ \cdot & \cdot & \cdot & \cdot & \cdot & \cdot & \cdot \\ \cdot & \cdot & \cdot & \cdot & \cdot & \cdot & \cdot \\ 0 & 0 & \cdot & \cdot & \cdot & R & -R \\ 1 & 1 & \cdot & \cdot & \cdot & 1 & -N \end{bmatrix}$$

In order to diagonalize the matrix D , thereby decoupling the $N+1$ equations, the following z -independent linear transformation B is introduced:

$$\begin{bmatrix} T_1(z) \\ \vdots \\ T_N(z) \\ t(z) \end{bmatrix} = B \begin{bmatrix} \tau_1(z) \\ \vdots \\ \tau_N(z) \\ \tau(z) \end{bmatrix}$$

Hence, equation (2) can be written for the τ variables as

$$(2) \quad \frac{N}{N_{tu}} \frac{d}{dz} \begin{bmatrix} \tau_1(z) \\ \vdots \\ \tau_N(z) \\ \tau(z) \end{bmatrix} = B^{-1} D B \begin{bmatrix} \tau_1(z) \\ \vdots \\ \tau_N(z) \\ \tau(z) \end{bmatrix} = \Lambda \begin{bmatrix} \tau_1(z) \\ \vdots \\ \tau_N(z) \\ \tau(z) \end{bmatrix} \quad (5)$$

(3) The reader is referred to Appendix A for details on the determination of B , and the diagonal matrix Λ .

Equation (5) can now be easily integrated and gives

$$\begin{bmatrix} \tau_1(z) \\ \vdots \\ \tau_N(z) \\ \tau(z) \end{bmatrix} = e^{N_{tu} \Lambda z / N} \begin{bmatrix} \tau_1(0) \\ \vdots \\ \tau_N(0) \\ \tau(0) \end{bmatrix} \quad (6)$$

From equations (1), (4), and (6) we obtain

$$(4) \quad H = B \exp(N_{tu} \Lambda / N) B^{-1} \quad (7)$$

This is the desired expression for the matrix H . The corresponding matrix elements required for the determination of the effectiveness are given explicitly in Appendix B.

Second Stage

In order to use the above results for the problem under consideration, we now have to introduce the requirement that the

Nomenclature

A = heat transfer surface area, m^2	referred to the shell fluid	x'_i = auxiliary variable introduced in equation (12)
B = matrix relating the τ variables to stream temperatures	N_{tui} = number of heat transfer units of a single shell pass	X_i = auxiliary quantities defined in equation (B3)
b_j = j th column of the B matrix	P = $(t' - t)/(T - t)$ = shell fluid thermal effectiveness	z = longitudinal coordinate along the shell axis
c, C = shell and tube fluid specific heats, $J/kg^\circ C$	P_i = effectiveness of a single shell pass	α, β, γ = auxiliary quantities defined in equation (16)
D = matrix defined in equation (3)	R = $c_w / C W$ = shell-to-tube heat capacity rate ratio	δ = auxiliary quantity defined in equation (B4)
F = logarithmic mean temperature difference correction factor	t, t' = inlet and outlet shell fluid temperatures, $^\circ C$	λ_i = i th eigenvalue of the D matrix
H = matrix which relates left-hand to right-hand temperatures in equation (1)	T, T' = inlet and outlet tube fluid temperatures, $^\circ C$	Λ = diagonalized D matrix
M = number of shell passes	T_i, T'_i = inlet and outlet temperatures for the i th tube stream, $^\circ C$	ξ, η = auxiliary quantities defined in equation (16)
N = total number of tube passes	U = overall heat transfer coefficient, $W/^\circ C m^2$	τ, τ_i = linear combinations of shell and tube temperature variables introduced in equation (4), $^\circ C$
n = number of tube passes per shell pass	w, W = shell and tube fluid mass flowrates, kg/s	χ = function of R and P defined in equation (21)
N_{tu} = UA/c_w = number of heat transfer units	x_i = auxiliary variables introduced in equations (8) and (10)	

outlet temperature of a given tube pass, is equal to the inlet temperature of the following one, i. e.,

$$\begin{aligned} T_1(0) &= T_2(0) = x_1 T \\ T_2(1) &= T_3(1) = x_2 T \\ T_3(0) &= T_4(0) = x_3 T \\ &\cdot \\ &\cdot \\ &\cdot \\ T_{N-1}(1) &= T_N(1) = x_{N-1} T \end{aligned} \quad (8)$$

where we have introduced auxiliary dimensionless variables x_i . In addition, we identify the inlet and outlet temperatures of the 1- N exchanger as

$$t = t(0), \quad T = T_1(1), \quad t' = t(1), \quad T' = T_N(0) \quad (9)$$

Without loss of generality, we choose $t=0$, which, using the definition of P and the relation $R = (T - T') / (t' - t)$, implies

$$T' = (1 - RP)T = x_N T \quad (10)$$

The first N rows of equation (1) can now be used to write a system of N linear equations for the unknowns x_1, \dots, x_N , the coefficients of which are only functions of the elements of the matrix H . The solution of these equations for $x_N = 1 - RP$ can be written as a quotient of two determinants. From it, the effectiveness is obtained as

$$P = (1 - x_N) / R \quad (11)$$

“Same End” and Even- N Cases

For the 1- N exchanger, the configuration of the same-end case can be obtained from that of the opposite-end case by just the inversion of the direction of flow of the tube fluid. This introduces only minor changes in the treatment described above, which lead to the expression

$$P = (1 - x'_1) / R \quad (12)$$

with

$$x'_1(R, N_{tu}) = 1 / x_N(-R, N_{tu}) \quad (13)$$

where x_N is the solution obtained above for the opposite-end case.

The same procedure used for odd N is applied for even N , with minor changes in the eigenvalues and boundary conditions.

Explicit 1-3 and 1-5 Solutions

The solution obtained in the previous sections for the effectiveness in terms of R and N_{tu} is purely algebraic, and involves matrix operations such as determinants and matrix products. The order of these matrices increases with N , and, therefore, the explicit expressions obtained from the expansion of these products and determinants become more complex as N increases. It is, however, straightforward to write a program that performs these operations numerically for arbitrary values of N .

As examples of explicit expressions that follow from the expansion of the solution for $N=3$ and $N=5$, we write below the formulas obtained in terms of the matrix elements of H , which are given in Appendix B.

For $N=3$ we find

$$x_3 = (H_{22} - H_{13} - 2H_{12}) / [H_{13}(H_{22} - H_{13} - 2H_{12}) + (H_{11} + H_{12})^2] \quad (14)$$

whereas for $N=5$ we obtain

$$x_5 = (\alpha\gamma - \beta^2) / [(\alpha\gamma - \beta^2)H_{13} + \alpha\xi^2 + \gamma\eta^2 - 2\beta\xi\eta] \quad (15)$$

where

$$\begin{aligned} \alpha &= H_{24} - H_{11} - 2H_{12} \\ \beta &= H_{22} - H_{11} - 2H_{12} \\ \gamma &= H_{24} - H_{13} - 2H_{12} \\ \xi &= H_{11} + H_{12} \\ \eta &= H_{13} + H_{12} \end{aligned} \quad (16)$$

In the opposite-end case, the effectiveness P is immediately obtained from equation (11) and the above expressions for x_3 or x_5 . In the same-end case, equations (12) and (13) must be used.

Two or More Shell Passes

A configuration with M shell passes, each one with n tube passes, is equivalent to a series assembly of M single-shell-pass exchangers. The effectiveness P of such an assembly, in terms of the effectivenesses P_i of each component, has been written by Domingos (1969). Assuming overall countercurrent connection, the effectiveness is given by

$$P = \{1 - [(1 - P_i R) / (1 - P_i)]^M\} / \{R - [(1 - P_i R) / (1 - P_i)]^M\} \quad \text{for } R \neq 1 \quad (17)$$

and

$$P = 1 / [1 + (1 - P_i) / MP_i] \quad \text{for } R = 1 \quad (18)$$

Here, R is the heat capacity rate ratio, which is the same for the individual components, as for the overall assembly. On the other hand, P_i can be obtained as shown in the previous sections for the single-shell-pass case, with the corresponding value of N_{tu} given by

$$N_{tu} = N_{tu} / M \quad (19)$$

In the practical examples of exchangers considered below, when n is odd, we still use the same-end and opposite-end notation; this does not refer to the location of the outlets of the exchanger as a whole but, rather, to the location of the tube and shell outlets of any given shell pass (see Figs. 2 and 3).

Discussion of Results

For two or more tube passes per shell pass, the effectiveness of an M - N exchanger is determined, in a first approximation, by the number of shell passes M , and increases with M . In the following, we discuss the differences that arise in the region of practical interest, for a given M , as N varies.

For this purpose, we introduce the LMTD correction factor F , such that

$$F(R, P) = \frac{\chi(R, P)}{N_{tu}} \quad (20)$$

where

$$\chi(R, P) = \begin{cases} \frac{1}{R-1} \ln\left(\frac{1-P}{1-RP}\right) & R \neq 1 \\ \frac{P}{1-P} & R = 1 \end{cases} \quad (21)$$

For each configuration and R value, N_{tu} is increased from zero in adequate steps, the effectiveness is obtained with the formulas of the previous sections, and F is calculated from equations (20) and (21). As N_{tu} increases, F decreases. The process is stopped when F decreases below the value of 0.7, which is considered the boundary of the region of practical applications. The analysis is also restricted to $0.1 \leq R \leq 10.0$. When we quote percentage differences between two configura-

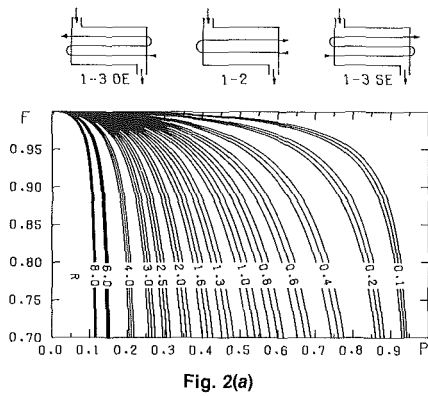


Fig. 2(a)

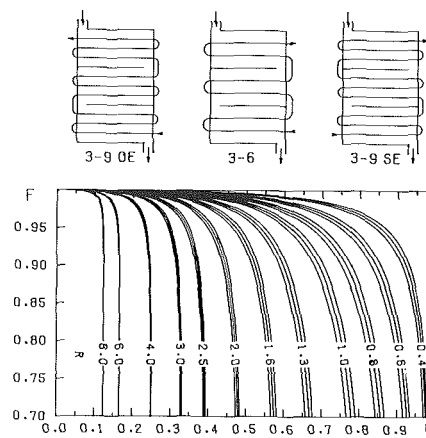


Fig. 2(c)

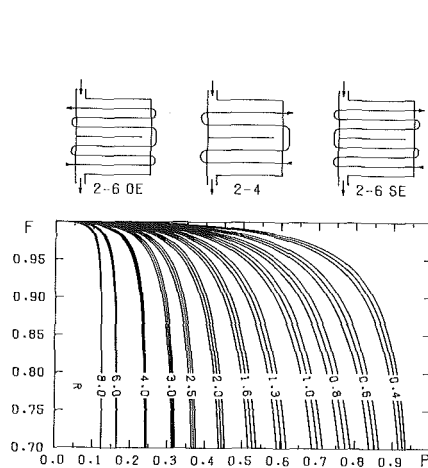


Fig. 2(b)

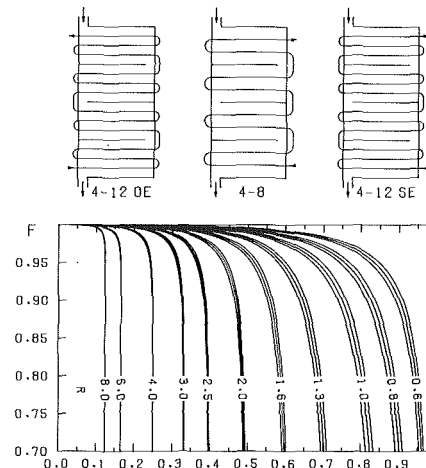


Fig. 2(d)

Fig. 2 LMTD correction factor F for M - $3M$ exchangers: (a) $M = 1$; (b) $M = 2$; (c) $M = 3$; (d) $M = 4$. For each value of R , the upper curves correspond to the "opposite end" configuration (left-hand diagram), the lower curves, to the "same end" configuration (right-hand diagram), and the middle curves to the M - $2M$ geometry, which is shown for comparison (central diagram).

tions in the discussion below, we refer to F values computed for the same values of R and P within this region, such as shown in Figs. 2 and 3.

We begin with the analysis of the 1-even N case. For $N = 2$, the effectiveness is given by the well-known expression

$$P = 2 / \{ 1 + R + (1 + R^2)^{1/2} \coth[(1 + R^2)^{1/2} N_{tu} / 2] \} \quad (22)$$

This expression is also often used for even $N \geq 4$. Our results show, however, that in such cases it is preferable to use the $N \rightarrow \infty$ formula

$$P = N_{tu} \left\{ \frac{RN_{tu}}{1 - \exp(-N_{tu}R)} + \frac{N_{tu}}{1 - \exp(-N_{tu})} - 1 \right\} \quad (23)$$

rather than equation (22), for two reasons: (a) It is a better approximation to the correct value; and (b) it is a conservative approximation, whereas using equation (22) is not on the safe side. The largest percentage difference between F_{1-2} and $F_{1-\infty}$ in the region explored occurs for $R = 1.09$ and $P = 0.511$. The corresponding F values are $F_{1-2} = 0.718$, $F_{1-4} = 0.705$, $F_{1-6} = 0.702$, $F_{1-\infty} = 0.700$. The relative errors introduced when using F_{1-2} instead of F_{1-4} or F_{1-6} are +1.8 and +2.2 percent, respectively, whereas if $F_{1-\infty}$ is used, they are -0.7 and -0.3 percent. This shows that, even for $N = 4$, the $N \rightarrow \infty$ limit is a better and safer approximation than the $N = 2$ case.

The above results are consistent with those of Kraus and Kern (1965), who compare values of P at the same R and N_{tu} , whereas here we quote differences in F at the same R and P values. The larger differences found by these authors are due to the fact that they do not put constraints on the F values considered.

As explained in the previous section, exchangers with two or more shell passes are evaluated as coupled single-shell-pass exchangers. Therefore, the considerations given above for the 1-even N case, apply to "multiples" of these exchangers, i. e., M - nM configurations with even n .

More important effects are found in the 1-odd N geometries. Our expressions are in agreement with the numerical results of Crozier and Samuels (1977) and Fischer (1938), and make it possible to perform a systematic search for the largest percentage differences between the 1-2 and 1-odd N cases. For $N = 3$ we find the following results

$$R = 10.0 \quad P = 0.0937 \quad F_{1-3,oe} = 0.804 \\ F_{1-2} = 0.700 \quad (-12.9 \text{ percent})$$

$$R = 10.0 \quad P = 0.0921 \quad F_{1-3,se} = 0.700 \\ F_{1-2} = 0.793 \quad (+13.3 \text{ percent})$$

The corresponding F curves are shown in Fig. 2(a) for several

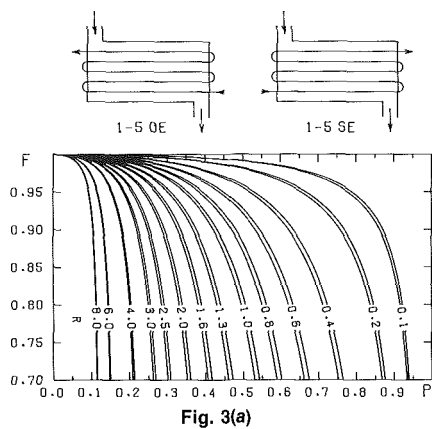


Fig. 3(a)

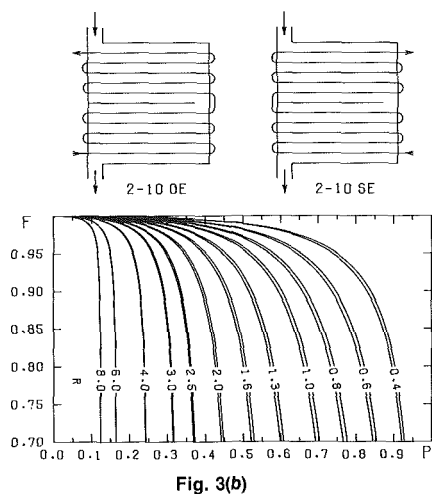


Fig. 3(b)

Fig. 3 LMTD correction factor F for (a) 1-5 exchanger; (b) 2-10 exchanger. The upper curves correspond to "opposite end" configurations (left-hand diagrams), and the lower ones to the "same end" configurations (right-hand diagrams).

values of R . They show that substantial differences between F_{1-2} and F_{1-3} are present, not only for large values of R , but also throughout the region of practical interest. A comparison of the 2-6 and the 2-4 configurations shows similar results (see Fig. 2b), and the effect is even larger for the 3-9 and 4-12 geometries, when compared to the 3-6 and 4-8 configurations, respectively (Figs. 2c and 2d).

The opposite-end 1-5 exchanger, with three counterflow and two parallel-flow tube passes, is expected to show a pattern similar to that of the 1-3 exchanger, but attenuated. Indeed, the 1-5 and 2-10 opposite-end exchangers are found to differ from the 1-2 and 2-4 cases, respectively, by up to nearly 6 percent. Comparisons between the opposite-end and same-end configurations for the 1-5 and 2-10 exchangers are shown in Figs. 3(a) and 3(b).

Concluding Remarks

We have shown that the effectiveness for arbitrary M - N TEMA E configuration can be written explicitly as a function of the dimensionless variables R and N_{tu} . In doing so, we have taken advantage of the matrix formalism, which is particularly suited to the linear nature of the problem under consideration, and of the fact that the secular equation factorizes in the simple form of equation (A1).

As N increases, the solution obtained becomes more complicated, but, as it rapidly approaches a simple asymptotic

limit, there is no point in carrying the analysis to large values of N . On the other hand, the complexity of the solution found originates from the expansion of determinants of degree N . If these determinants are evaluated numerically rather than expanded, no additional complication arises in going to higher values of N .

As expected, the larger improvements from the usual 1-2 configuration are found first in the 1-3, and then in the 1-5 opposite-end geometries. Therefore, it is comparatively advantageous to use these arrangements. It is well known that there may be constructive drawbacks when using an odd number of tube passes, but these disappear, and full advantage may be taken of the higher effectiveness of the 1-3 or 1-5 arrangements, when even "multiples" of these units, such as 2-6, 4-12, or 2-10 exchangers, are used.

References

- Bowman, R. A., 1936, "Mean Temperature Difference Correction in Multipass Exchangers," *Ind. and Eng. Chem.*, Vol. 28, pp. 541-544.
- Crozier, R. Jr., and Samuels, M., 1977, "Mean Temperature Difference in Odd-Tube-Pass Heat Exchangers," *ASME JOURNAL OF HEAT TRANSFER*, Vol. 99, pp. 487-489.
- Domingos, J. D., 1969, "Analysis of Complex Assemblies of Heat Exchangers," *Int. J. Heat and Mass Transfer*, Vol. 12, pp. 352-360.
- Fischer, F. K., 1938, "Mean Temperature Difference Correction in Multipass Exchangers," *Ind. and Eng. Chem.*, Vol. 30, pp. 377-383.
- Kraus, A. D., and Kern, D. Q., 1965, "The Effectiveness of Heat Exchangers With One Shell Pass and Even Number of Tube Passes," ASME Paper No. 65-HT-18.
- Nagle, W. M., 1933, "Mean Temperature Differences in Multipass Heat Exchangers," *Ind. and Eng. Chem.*, Vol. 25, pp. 604-609.
- Pignotti, A., 1984, "Flow Reversibility of Heat Exchangers," *ASME JOURNAL OF HEAT TRANSFER*, Vol. 106, pp. 361-368.
- Pignotti, A., 1986, "Analytical Solution for the Thermal Effectiveness of a 1-3 TEMA E Shell-and-Tube Heat Exchanger," *Proceedings of the 2nd Latin American Conference on Heat and Mass Transfer*, Sao Paulo, Brazil, Vol. 1, pp. 254-265.
- Stevens, R. A., Fernández, J., and Woolf, J. R., 1957, "Mean Temperature Difference in One, Two, and Three-Pass Crossflow Heat Exchangers," *Trans. ASME*, Vol. 79, pp. 287-297.
- Underwood, A. J. V., 1934, "The Calculation of the Mean Temperature Difference in Multi-pass Heat Exchangers," *J. Inst. Pet. Technol.*, Vol. 20, pp. 145-158.

APPENDIX A

The elements λ_j of the diagonal matrix Λ are the eigenvalues of the matrix D , i. e., the roots of the secular equation, which can be written in the form

$$\lambda(R - \lambda)^{(N-1)/2}(-R - \lambda)^{(N-3)/2}$$

$$[-\lambda^2 - N\lambda + R(R-1)] = 0 \quad (A1)$$

valid for odd $N \geq 3$. Therefore, we obtain

$$\lambda_{1,2} = -\frac{N}{2} \pm \left[\frac{N^2}{4} + R(R-1) \right]^{1/2}$$

$$\lambda_{3,5,\dots,N} = R \quad (A2)$$

$$\lambda_{4,6,\dots,N-1} = -R \quad (\text{not present for } N=3)$$

$$\lambda_{N+1} = 0$$

From equation (5) it follows that \mathbf{b}_j , the j th column of the matrix B , is an eigenvector of D , with eigenvalue λ_j , so that it satisfies the equation

$$D\mathbf{b}_j = \lambda_j \mathbf{b}_j \quad (A3)$$

From this equation, the eigenvectors \mathbf{b}_j can be calculated up to an arbitrary normalization constant, which cancels out in the final expression of equation (7).

APPENDIX B

The elements of the matrix H can be obtained from equation (7), and the expressions for B and Λ from Appendix A.

Because of the symmetries of the problem considered, not all the elements of H are independent, and, at most, five need to be calculated. We choose them to be H_{11} , H_{12} , H_{13} , H_{22} , and H_{24} . The remaining ones can be obtained through the following relations, valid for $1 \leq i \leq N$, $1 \leq j \leq N$:

$$\begin{aligned}
 H_{ij} &= H_{11} \text{ for } i=j=\text{odd} \\
 &= H_{22} \text{ for } i=j=\text{even} \\
 &= H_{13} \text{ for } i=\text{odd}, \\
 &\quad j=\text{odd} \neq i \\
 &= H_{12} \text{ for } i=\text{odd}, \\
 &\quad j=\text{even} \\
 &= H_{24} \text{ for } i=\text{even}, \\
 &\quad j=\text{even} \neq i \\
 &= -H_{12} \text{ for } i=\text{even}, \\
 &\quad j=\text{odd}
 \end{aligned} \tag{B1}$$

The expressions obtained are, for odd N

$$\begin{aligned}
 H_{11} &= \begin{cases} \frac{(R+\lambda_1)(R-\lambda_2)}{(N+1)\lambda_1\delta} X_1 - \frac{(R-\lambda_1)(R+\lambda_2)}{(N+1)\lambda_2\delta} X_2 + \frac{N-1}{N+1} X_3 + \frac{1}{1-R} & \text{for } R \neq 1 \\ \frac{2N-1+N_{tu}}{N^2} + \frac{1-N}{(N+1)N^2} X_2 + \frac{N-1}{N+1} X_3 & \text{for } R = 1 \end{cases} \\
 H_{12} &= \begin{cases} \frac{(R+\lambda_1)(R+\lambda_2)}{(N-1)\lambda_1\delta} X_1 - \frac{(R+\lambda_1)(R+\lambda_2)}{(N-1)\lambda_2\delta} X_2 - \frac{1}{1-R} & \text{for } R \neq 1 \\ \frac{1-N_{tu}}{N^2} - \frac{1}{N^2} X_2 & \text{for } R = 1 \end{cases} \\
 H_{13} &= \begin{cases} \frac{(R+\lambda_1)(R-\lambda_2)}{(N+1)\lambda_1\delta} X_1 - \frac{(R-\lambda_1)(R+\lambda_2)}{(N+1)\lambda_2\delta} X_2 - \frac{1}{N+1} X_3 + \frac{1}{1-R} & \text{for } R \neq 1 \\ \frac{2N-1+N_{tu}}{N^2} + \frac{1-N}{(N+1)N^2} X_2 - \frac{2}{N+1} X_3 & \text{for } R = 1 \end{cases} \tag{B2} \\
 H_{22} &= \begin{cases} \frac{(R-\lambda_1)(R+\lambda_2)}{(N-1)\lambda_1\delta} X_1 - \frac{(R+\lambda_1)(R-\lambda_2)}{(N-1)\lambda_2\delta} X_2 + \frac{N-3}{N-1} X_4 - \frac{1}{1-R} & \text{for } R \neq 1 \\ \frac{2N+1-N_{tu}}{N^2} + \frac{1+N}{(N-1)N^2} X_2 + \frac{N-3}{N-1} X_4 & \text{for } R = 1 \end{cases} \\
 H_{24} &= \begin{cases} \frac{(R-\lambda_1)(R+\lambda_2)}{(N-1)\lambda_1\delta} X_1 - \frac{(R+\lambda_1)(R-\lambda_2)}{(N-1)\lambda_2\delta} X_2 - \frac{2}{N-1} X_4 - \frac{1}{1-R} & \text{for } R \neq 1 \\ \frac{2N+1-N_{tu}}{N^2} + \frac{1+N}{(N-1)N^2} X_2 - \frac{2}{N-1} X_4 & \text{for } R = 1 \end{cases}
 \end{aligned}$$

where

$$X_i = \exp(\lambda_i N_{tu}/N) \tag{B3}$$

and

$$\delta = \lambda_1 - \lambda_2 \tag{B4}$$

Shellside Waterflow Pressure Drop Distribution Measurements in an Industrial-Sized Test Heat Exchanger

H. Halle

Argonne National Laboratory,
Argonne, IL
Mem. ASME

J. M. Chenoweth

Heat Transfer Research Inc.,
Alhambra, CA
Mem. ASME

M. W. Wambsganss

Argonne National Laboratory,
Argonne, IL
Mem. ASME

Throughout the life of a heat exchanger, a significant part of the operating cost arises from pumping the heat transfer fluids through and past the tubes. The pumping power requirement is continuous and depends directly upon the magnitude of the pressure losses. Thus, in order to select an optimum heat exchanger design, it is as important to be able to predict pressure drop accurately as it is to predict heat transfer. This paper presents experimental measurements of the shellside pressure drop for 24 different segmentally baffled bundle configurations in a 0.6-m (24-in.) diameter by 3.7-m (12-ft) long shell with single inlet and outlet nozzles. Both plain and finned tubes, nominally 19-mm (0.75-in.) outside diameter, were arranged on equilateral triangular, square, rotated triangular, and rotated square tube layouts with a tube pitch-to-diameter ratio of 1.25. Isothermal water tests for a range of Reynolds numbers from 7000 to 100,000 were run to measure overall as well as incremental pressure drops across sections of the exchanger. The experimental results are given and correlated with a pressure drop versus flowrate relationship.

1 Introduction

Along with the capacity to transfer heat, the pressure drop across a heat exchanger is a very important parameter. This is because the pressure drop is proportional to the energy required to pump the heat-transferring fluids through the heat exchanger; consequently, the operating cost throughout the life of the exchanger depends on the pressure losses. One of the goals of heat exchanger design is to optimize the relationships of heat transfer, pressure drop, and cost. This task has been greatly facilitated by development of comprehensive computer programs that permit more precise thermal and hydraulic design for the use of the industry. e.g., HTRI (Heat Transfer Research, Inc., 1982).

This paper presents pressure drop measurements of shellside flow of water through industrial-sized shell-and-tube heat exchanger configurations. Data are reported for 24 different configurations obtained by appropriate assembly of the test exchanger specially designed and fabricated to provide the versatility required for this effort. The test configurations comprise different combinations of tube layout patterns, number of crosspasses, size of inlet/outlet nozzles, and plain or finned tubes.

The measurements taken include the overall inlet-to-outlet pressure drop as well as the pressure drop distribution through various sections of the segmentally baffled test heat exchangers. It appears that there is surprisingly little information available in the open literature on the shellside pressure drop of actual, operating heat exchangers. There is no incremental pressure drop information for the limited overall pressure drop data. The current data in conjunction with the given descriptions of the tested exchanger configurations are expected to be useful for comparison, input, and perhaps even retrofitting of computer programs for industrial heat exchanger design and for the sophisticated flow distribution mapping such as the program applied by Wambsganss et al. (1984).

Work supported by the U.S. Department of Energy, Energy Conversion and Utilization Technologies Program, under Contract No. W-31-109-ENG-38.

Contributed by the Heat Transfer Division and presented at the 22nd National Heat Transfer Conference, Niagara Falls, NY, August 1984. Manuscript received by the Heat Transfer Division September 10, 1984.

The experimental results are correlated with a relationship involving the exponential change of pressure drop as a function of flowrate. Ideally one prefers to relate pressure drop to a velocity rather than a flowrate. This presents a problem for the shell side of shell-and-tube heat exchangers. The velocity is constantly changing in magnitude and direction, is accelerating and decelerating, and is typically not uniform along the length of any tube span. There is no general agreement at this time as to how an "effective" velocity is defined nor has it been measured. As a result, the authors have chosen to present the data in a more general form that can be transformed into whatever "effective" velocity may prove to be appropriate. The definition may well come with the application of three-dimensional flow distribution codes such as the one used by Wambsganss et al. (1984) to compute an effective crossflow velocity for predicting fluid-elastic instability thresholds.

Finally, a preliminary method is devised to estimate the total, i.e., combined inlet and outlet nozzle pressure losses.

The pressure drop measurements were undertaken as part of a Heat Exchanger Tube Vibration Program as reported by Halle et al. (1983, 1984). The objective of this program is to contribute to the development and evaluation of new and improved vibration prediction methods and, ultimately, to the cost-effective and energy efficient design of shell-and-tube heat exchangers capable of operating without flow-induced vibration damage.

2 Test Exchanger Configurations

The test exchanger is a segmentally baffled shell-and-tube exchanger, representative of an industrial heat exchanger. It has a removable tube bundle with component tubesheets, baffles, and tubes that are rearranged or replaced to provide different test configurations readily. All tests are run under isothermal conditions. There is no flow on the tubeside, and the tube ends are open to permit observation or instrumentation readily. The shell is piped to a large water loop that is part of Argonne's Flow-Induced Vibration Test Facility (FIVTF) as shown in Fig. 1. Figure 2 shows the tube bundle, in a no-

tubes-in-window configuration, on a specially built transporter prior to insertion into the shell, seen in the left background.

The general features, dimensions, and specifications of the test exchanger are given in Tables 1 and 2. It is configured with eight or six crosspasses, having seven or five equally spaced single segmental baffles, as shown on Figs. 3 and 4 schematically. The finned tubes are plain at the ends and at five lands where they contact the baffles.

Table 3 explains the configuration code used throughout this paper for an abbreviated description of all the configurations tested and listed on tables further below. Several of the associated tube layout patterns are shown on Fig. 5. The small dots on Fig. 5 show the positions of smaller diameter tie bars that space and secure the baffle plates.

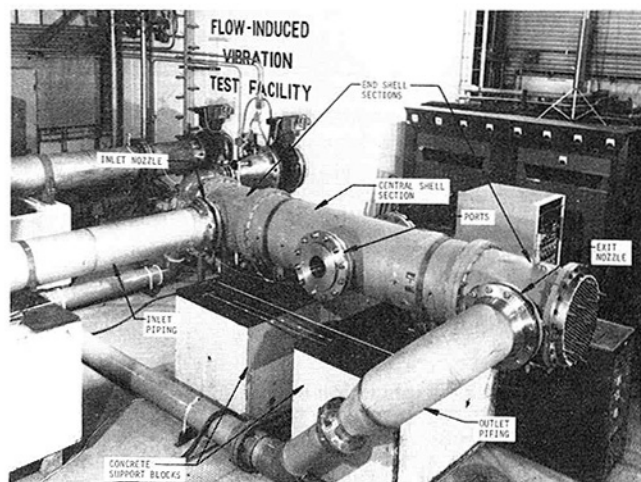


Fig. 1 Test exchanger installed in Flow-Induced Vibration Test Facility (FIVTF)

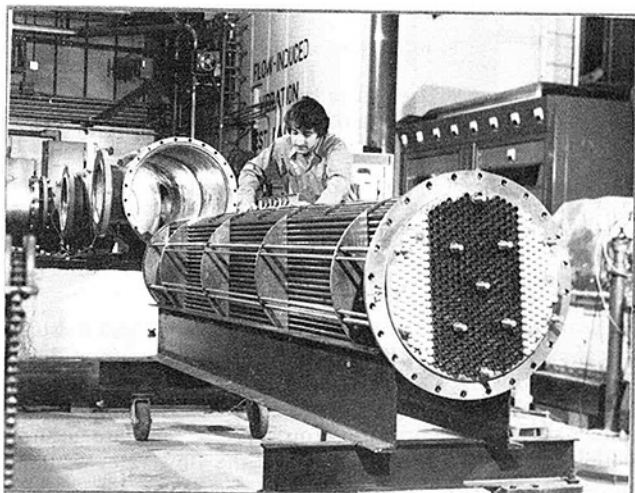


Fig. 2 Test exchanger in no-tubes-in-window configuration (30 deg triangular pattern, eight-crosspass tube bundle)

Table 1 General features and basic dimensions of test exchanger

Shellside fluid	Water
Tubeside	No fluid, open tubes
Shell (stainless steel), i.d.	0.59 m (23.25 in.)
Shell, inside length (tubesheet spacing)	3.58 m (140.75 in.)
Nozzles, inlet and outlet	Insertion of piping to reduce inside diameter permits nominal sizes: inside diameters 14-in. size: 337 mm (13.25 in.) i.d. 10-in. size: 241 mm (9.500 in.) i.d.
Nozzles at shell midspan	Observation ports
Tube bundle	Removable unit, ready assembly/disassembly
Tie bars	Secure and space baffle plates, 12.7 mm (0.5 in.) overall o.d., eight locations, tied to outlet tubesheet

In accordance with industrial practice, the baffle cut was slightly increased for the six-crosspass configuration tests performed subsequent to the eight-crosspass tests of the 30 and 90 deg layout tube bundles. The 45 and 60 deg layout bundles were tested with widely different baffle cuts to investigate the effect of such baffle cut; the smaller one of these is more conventional for no-tubes-in-window (NTIW) configurations. The NTIW configurations comprise a design obtained by removing all tubes in the baffle window flow-turnaround regions. Since these tubes include those most susceptible to vibration, the NTIW bundles contain only the remaining well-supported central tubes. Naturally, the removal of the tubes alters the heat transfer/pressure drop relationship. For the subject tests, the window areas of the baffles were fitted with metal plates to cover the unused baffle holes. The unused tubesheet holes were plugged and sealed.

3 Flow Tests

3.1 Test Procedure. Shellside pressure drop measurements were taken for all configurations tested with room temperature water as the shellside fluid. Figure 6 schematically shows the location of the pressure taps for the eight and six-crosspass configurations. Figure 7 shows details of the size and locations of the pressure taps A and I in the inlet and outlet nozzles. The inlet connection (left center of photo on Fig. 1) provides more than 12 diameters of straight pipe to reduce extraneous prior-to-entrance effects. Both nozzles were of the same nominal 14-in. diameter pipe size. The nominal 10-in. size was provided by placing inserts into both the inlet (maintaining a long approach) and outlet steel pipe (Fig. 7b). The central observation ports, built to serve as nozzles in the future, have essentially the same construction as the inlet/outlet nozzles. The windows are contoured with transparent acrylic plastic to provide a continuous surface at the internal shell diameter. Figure 7(c) indicates the sheltered location of the central tap E, to which pressure is transmitted through a narrow annular gap around the periphery of the window insert. The pressure taps drilled into the shell had a diameter of 9.5 mm (0.375 in.) to be able also to accommodate other instrumentation.

Nomenclature

Q = flowrate

α = exponential variation of pressure drop with flowrate (equation (1))

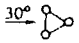
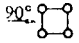
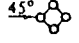
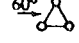
γ = overall (inlet-to-outlet) pressure drop at the reference flowrate of 0.06309 m³/s (1000 gal/min)

Δp = pressure drop

Δp_k = pressure drop in "core" region of exchanger

Δp_n = pressure drop in nozzle regions

Table 2 Tube and tube bundle specifications

Tube, plain (Admiralty brass)		
o.d.		19.1 mm (0.750 in.)
wall thickness		1.2 mm (0.049 in.)
Tube, finned (Admiralty brass), 748 fins/m (19 fins/in.)		
o.d.		19.1 mm (0.750 in.)
i.d., unfinned plain tube at end or land		15.7 mm (0.620 in.)
root diameter, finned section		15.9 mm (0.625 in.)
i.d., finned section		13.8 mm (0.541 in.)
o.d. of equivalent plain tube having same weight/unit length as finned section		1.69 mm (0.666 in.) est.
Tube layout patterns		
30 deg triangular		One side of equilateral triangle normal to flow
90 deg square		Sides parallel and normal to flow
45 deg rotated square		Sides oriented 45 deg to flow
60 deg triangular		One side of equilateral triangle parallel to flow
Tube pitch-to-diameter ratio		1.25
Number of crosspasses		8 (i.e., seven baffles) 6 (i.e., five baffles)
Number of tubes (not counting eight tie bars and, in NTIW bundles, four tube positions in window regions)		
30 deg triangular layout		499, full tube bundle 333, NTIW, eight crosspass 293, NTIW, six crosspass
90 deg square layout		421, full tube bundle 283, NTIW, eight crosspass 245, NTIW, six crosspass
45 deg rotated square layout		421, full tube bundle 365, NTIW, six crosspass, 16 percent baffle cut
60 deg triangular layout		499, full tube bundle 425, NTIW, six crosspass, 16 percent baffle cut 275, NTIW, six crosspass, 30 percent baffle cut
Outer tube limit (O.T.L.), maximum diametral dimension of tube bundle		568 mm (22.374 in.), 30 and 60 deg layouts 562 mm (22.128 in.), 90 deg and 45 deg layouts
Baffle spacing		448 mm (17.6 in.) approx., eight crosspass 597 mm (23.5 in.) approx., six crosspass
Baffle (brass)		
o.d.		587 mm (23.109 in.)
thickness		9.5 mm (0.375 in.)
Tube/baffle hole diametral clearance		0.4 mm (0.016 in.) minimum

The overall inlet-to-outlet pressure drop was measured between the taps designated A and I by means of a differential pressure transducer. The transducer usually employed for this program had a ± 690 kPa (100 lb/in.²) differential pressure range. The signal output was obtained by means of a bridge conditioner, routed through a resistance-capacitance network to attenuate signal fluctuations, and displayed on a digital voltmeter. The system is calibrated end-to-end. The pressure

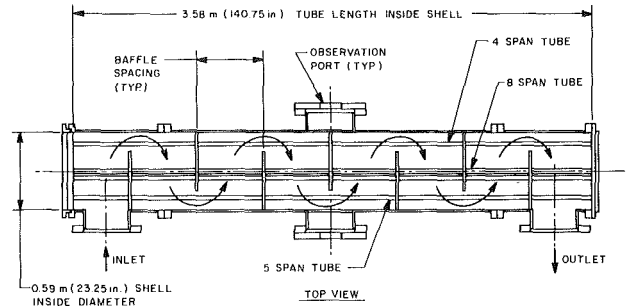


Fig. 3 Test heat exchanger, eight-crosspass configuration

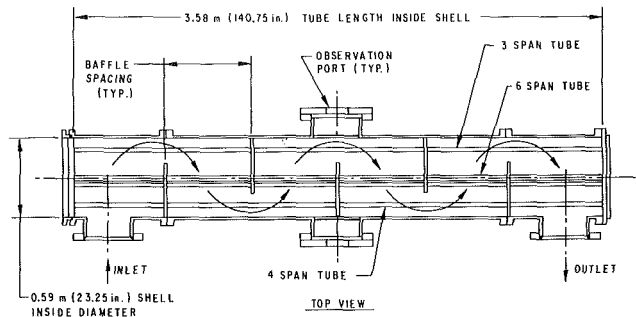


Fig. 4 Test heat exchanger, six-crosspass configuration

Table 3 Explanation of configuration code

Position	Symbols	Definition
1st letter	F N	Full tube bundle No-tubes-in-window (NTIW) bundle
2nd letter	P E	Plain tube Finned (enhanced surface) tube
1st number	6 or 8	Number of crosspasses
2nd number	10 or 14 in.	Nominal size of nozzles
3rd number	30 to 90 deg	Tube layout pattern
Last item	16 to 30 percent	Baffle cut as percentage ¹ of inside shell diameter

¹To three significant figures: 16 percent = 15.5 percent, 26 percent = 25.5 percent, 29 percent = 28.9 percent, and 30 percent = 29.6 percent except for 45 deg when 29.8 percent.

level of the exchanger outlet was measured also, and it usually remained at less than 240 kPa (35 lb/in.²) above atmospheric. The waterflow rate through the test exchanger was measured with turbine flowmeters mounted in the upstream piping. It is anticipated that the pressure drop measurements are accurate within ± 1.4 kPa (0.2 lb/in.²) and the flow rates ± 0.002 m³/s (30 gal/min).

3.2 Overall Pressure Drop. When the overall pressure drop Δp (taps A to I) is plotted as a function of flowrate Q on log-log paper, the data can be correlated with a straight line (Fig. 8). This implies that the overall pressure drop can be correlated by a power function relationship of the general form

$$\Delta p = \gamma Q^\alpha \quad (1)$$

where γ and α are constants for a particular tube bundle configuration.

In this paper the above equation will be expressed with US units as

$$\Delta p(\text{lb/in.}^2) = \gamma(\text{lb/in.}^2) \left\{ \frac{Q(\text{gal/min})}{1000} \right\}^\alpha \quad (2)$$

or, with SI units

$$\Delta p(\text{kPa}) = \gamma(\text{kPa}) \left\{ \frac{Q(\text{m}^3/\text{s})}{0.06309} \right\}^\alpha \quad (3)$$

For the pressure drop data obtained from each of the various test configurations, equation (2), after taking logarithms on both sides, was employed to determine the constants γ and α by means of linear regression analysis. Table 4 indicates the range of flowrates from which the data were taken, summarizes the results of the linear regression analysis computations, and lists the constants α and γ . Statistical examination indicated that 95 percent of all data points varied less than 5 percent from the computed curves, and no points varied more than 10 percent. Note that γ represents the overall pressure drop at 0.063 m³/s (1000 gal/min). The Reynolds numbers listed have been computed by means of the HTRI (1982) program based on the average velocity of the flow passing through the available crossflow area at the central tube row between the baffle plates of the test exchanger, using the tube diameter as the characteristic dimension. The Reynolds numbers are given only for general guidance; the HTRI (1982) program accounts for leakage flows that comprise about 30 to 45 percent of the total. Figure 8 shows the pressure drop

curves for the configurations with the smallest and largest α values encountered.

3.3 Pressure Distribution. The pressure distribution through various sections of the test exchanger was determined by taking pressure drop measurements between taps B through H and the outlet tap I of the exchanger with the differential pressure transducer (Fig. 6). The connections were made by switching with a valve system.

To determine the normalized fractional distribution, the overall pressure drop was set equal to unity and the fractional drops (remaining to the outlet tap) were calculated for each flowrate tested and averaged. The data are listed on Table 5. As indicated on Fig. 6, taps C, D, E (center), F, and G are located in different positions for the eight and six-crosspass configurations. Figure 9 presents typical examples of fractional pressure distributions in graphic form, with the tap locations B through H plotted approximately scaled according to their axial location along the shell.

4 Analysis and Interpretation of Results

4.1 Comparison of Overall Pressure Drop. At the same flowrate the overall pressure drop varied as expected with respect to certain test parameters when comparing otherwise corresponding test configurations. The overall pressure drop was always higher for the 10-in. nozzles than for 14-in. nozzles, higher for eight than for six crosspasses, and higher for the 30 deg than the less densely occupied 90 deg tube layout pattern.

Comparison of the pressure drop across the full tube bundle, 29 or 30 percent baffle cut configurations, indicates that the drop across the 60 and 45 deg layout bundles is about 10 percent less than across the corresponding 30 and 90 deg bundles. A probable contributing factor is the maximum mean gap crossflow velocity through the gap between the tubes. When computed with very much idealized assumptions (e.g., pure and uniform crossflow in the plane of the paper of Fig. 5), for a given flowrate the maximum mean gap flow velocities are the same for 30 and 90 deg layouts, but reduced to 87 and 71 percent in corresponding 60 and 45 deg layouts for a 1.25 pitch-to-diameter ratio. This may explain why a 45 deg layout with a seemingly more arduous flowpath has a smaller

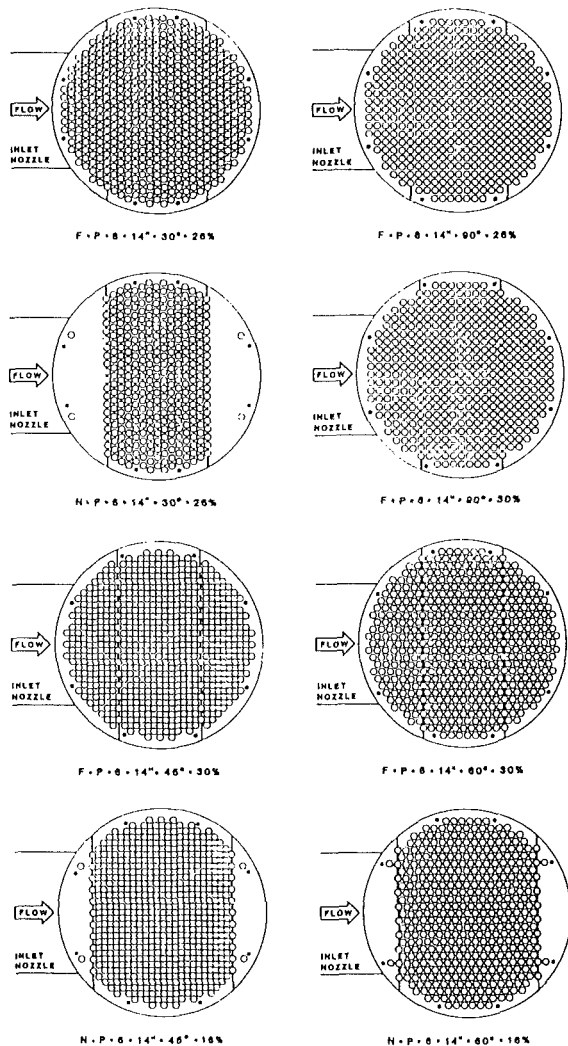
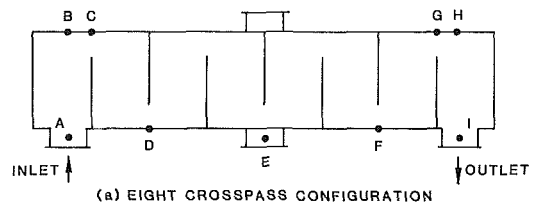
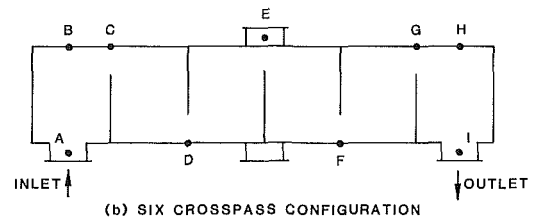


Fig. 5 Schematics of typical test configurations



TOP VIEWS



Taps - A, E, and I: on bottom of nozzles

B, C, D, F, G, and H: on shell in horizontal plane of flow

Fig. 6 Location of pressure taps on shell: (a) eight-crosspass configuration; (b) six-crosspass configuration

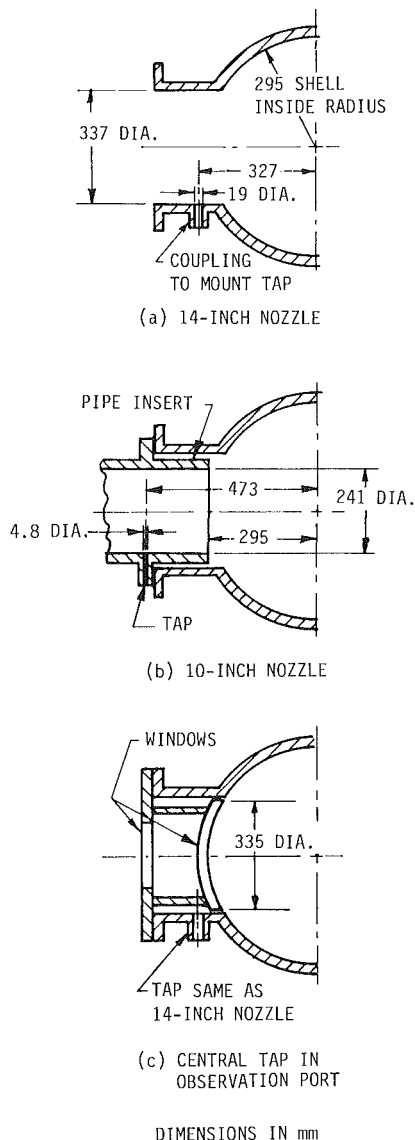


Fig. 7 Details of nozzles and pressure tap locations

pressure drop than a 90 deg bundle. It may be noted that in the 30 and 90 deg bundles the gaps with the maximum mean flow velocity are oriented perpendicular to the basic crossflow direction (Fig. 5), while in the 45 and 60 deg bundles these gaps are inclined to it. Observations made during the vibration tests indicate that actual flow conditions are far from uniform. Leakage and bypass flows may create high flow velocities through low resistance paths and conditions in which the flow actually encounters a changed pattern, for instance a 90 deg layout orientation in a 45 deg layout tube bundle.

Only 30 and 90 deg tube layout bundles were comparison tested with finned tubes, which were substituted for plain tubes in otherwise identical bundles. It may be noted that flow in the two principal flow directions, transverse and parallel to the tubes, results in opposite effects on the pressure drop. When subjected to cross (transverse) flow, the gaps between the tubes are increased by the area between the fins and as a consequence the pressure drop is reduced. When subjected to parallel flow, both plain and finned tubes, having identical outside diameters, provide the same flow channel area; however, the presence of the fins increases the surface

roughness of the flow channel and thus results in an increased pressure drop. Since the flow winding through an actual heat exchanger is in most places oriented at an angle to the tubes, the combination of the transverse and parallel flow can be expected to provide a mixed effect on the pressure drop. The experimental results showed that for 90 deg layouts the pressure drop of finned tube bundles is less than for plain tubes, indicating that the transverse flow effect dominated over the parallel flow effect. For the 30 deg layouts the pressure drop for plain and finned tube bundles was found to be nearly the same as the above effects apparently balanced each other.

4.2 Comparison of Exponential Variation of Pressure Drop Versus Flowrate Function.

Customary friction factor versus Reynolds number graphs (Moody's diagram) indicate that for internal pipe flow the exponent α (equation (1)) increases with flow velocity (Reynolds number) as well as with surface roughness. This is corroborated by two examples for commercial water pipe, taken from an industrial source (Crane Co., 1969), and included on Table 4 to provide a comparison with the subject test data, which appear to show similar tendencies. The exponents in Table 4 were calculated in a consistent manner for all test cases and the two examples on the basis of being constant at all flowrates. There was some scatter in the results of the values of α , which were determined by regression analysis techniques. Some interesting trends that can be observed from examining the data are discussed below.

Comparison of the no-tubes-in-window (NTIW) configuration data indicated all NTIW bundles resulted in a lower exponent than for the corresponding full bundle. This is because the window areas void of tubes permit the flow to slow down to a lowered flow velocity for a substantial part of its path through the exchanger.

With closer baffle spacing producing higher flow velocities, the eight-crosspass configurations can be expected to have higher exponents than the comparative six-crosspass configurations. This was found experimentally with the exception of two pairs of test cases where nozzle loss effects may have dominated.

For all test cases the exponent was higher for the finned tubes than for the plain tubes, even though the finned bundle has, at least in the crossflow regions, larger gaps, and lower velocities. Apparently the additional roughness dominates to increase the exponent.

The small (16 percent) baffle cut configurations tested with the 45 and 60 deg layout pattern resulted in larger exponents than the corresponding tests with the 30 percent baffle cuts. Apparently the higher flow velocities in the window flow-turnaround regions were a factor.

4.3 Pressure Distribution. With regard to the distribution of pressure drop through the various sections of the exchanger (Table 5 and Fig. 9), it appears that the pressure drop measurements are affected by the flow velocity at the measurement location. The small or sometimes negative difference between taps G and H suggests that the velocity of the flow passing tap G at the window is larger than at tap H which is somewhat bypassed by the main flow; thus the pressure at taps H appears to recover to offset any losses between taps G and H. The same phenomenon working in the opposite direction apparently exaggerates the measured pressure drop between taps B and C. There is apparently also some effect on the central tap E, which is in a sheltered location on the observation port, not directly on the internal shell wall (Fig. 7c). It is noted that the measured drop E to F is usually larger than the drop D to E for almost all tests; this probably indicates some pressure recovery at tap E.

4.4 Nozzle Losses. A method was devised to estimate the total, i.e., combined inlet and outlet nozzle losses. Perhaps en-

Table 4 Overall pressure drop versus flowrate

Configuration code ¹	Measurement range			Exponent α	γ , basic Δp	
	m ³ /s	Flowrate, Q gal/min	Reynolds number ² 1000's		at 0.063 m ³ /s kPa	at 1000 gal/min lb/in. ²
F•P•8•14"•30°•26%	0.049–0.201	770–3190	20.3–85.3	1.93	37.4	5.43
F•P•8•10"•30°•26%	0.050–0.189	800–3000	21.4–80.2	1.91	41.4	6.01
F•P•8•14"•90°•26%	0.063–0.164	1000–2600	26.7–70.4	1.93	28.9	4.19
F•P•8•10"•90°•26%	0.063–0.215	1000–3400	27.1–92.1	1.93	31.9	4.62
F•P•6•14"•30°•29%	0.067–0.135	1060–2140	20.9–42.1	1.87	23.3	3.38
F•P•6•10"•30°•29%	0.073–0.205	1160–3250	22.9–64.0	1.83	27.5	3.99
F•P•6•14"•90°•30%	0.050–0.189	800–3000	15.9–59.7	1.87	17.4	2.53
F•P•6•10"•90°•30%	0.078–0.176	1230–2790	24.5–55.5	1.95	19.1	2.77
F•P•6•14"•45°•16%	0.050–0.174	790–2760	11.9–41.6	1.98	39.1	5.67
F•P•6•14"•45°•30%	0.050–0.151	800–2400	11.2–33.7	1.91	15.9	2.30
F•P•6•14"•60°•16%	0.050–0.140	790–2220	14.4–40.5	1.94	45.4	6.59
F•P•6•14"•60°•30%	0.066–0.157	1050–2490	17.9–42.4	1.90	20.4	2.96
N•P•8•14"•30°•26%	0.100–0.316	1580–5010	42.4–134.5	1.79	20.2	2.93
N•P•8•10"•30°•26%	0.074–0.251	1180–3980	31.7–100.8	1.78	21.4	3.11
N•P•8•14"•90°•26%	0.064–0.251	1010–3980	27.3–107.7	1.89	18.0	2.61
N•P•6•10"•30°•29%	0.102–0.262	1620–4150	32.0–82.0	1.80	10.2	1.48
N•P•6•10"•90°•30%	0.037–0.251	590–3990	11.7–79.4	1.85	9.17	1.33
N•P•6•14"•45°•16%	0.050–0.177	800–2800	12.1–42.3	1.95	22.7	3.29
N•P•6•14"•60°•16%	0.054–0.189	850–2990	15.5–54.6	1.91	23.0	3.33
N•P•6•14"•60°•30%	0.051–0.203	810–3220	13.6–54.8	1.81	8.06	1.17
F•E•6•10"•30°•29%	0.038–0.164	600–2600	7.2–31.4	1.92	27.9	4.04
F•E•6•10"•90°•30%	0.064–0.203	1020–3220	12.4–39.3	2.03	16.4	2.38
N•E•6•10"•30°•29%	0.063–0.394	1000–6250	12.1–75.6	1.90	9.17	1.33
N•E•6•10"•90°•30%	0.050–0.332	790–5270	9.6–64.2	1.95	6.90	1.00
6-in. pipe ³	0.063–0.126	1000–2000	-	1.94	18.5	2.68
12-in. pipe ³	0.063–0.126	1000–2000	-	1.90	0.62	0.09

¹Refer to Table 3.

²Crossflow Reynolds number.

³Examples, 30.48 m (100 ft) of U.S. Schedule 40 pipe (Crane Co., 1969).

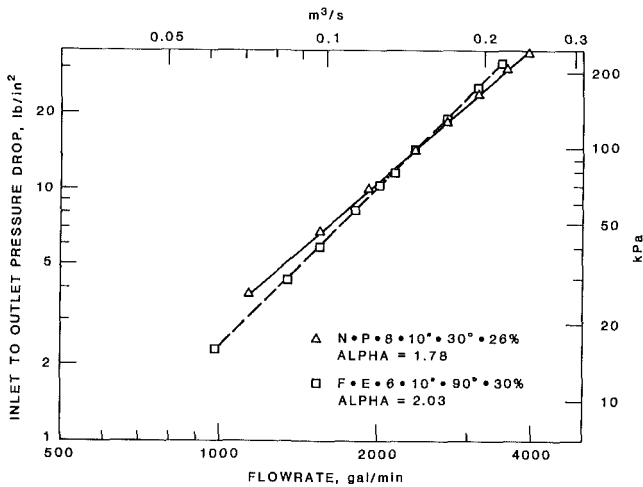


Fig. 8 Overall pressure drop versus flowrate of two test configurations

trance and exit would be more accurate terms, because the combined inlet/outlet flow effects extend well beyond the immediate nozzle region into the tube bundle. A simplified computational method was developed from those pairs of comparative test cases with both 10 and 14-in. size nozzles. Two sets of cases for each 30 and 90 deg full bundles and one set for a 30 deg NTIW bundle were available. On the basis of these limited data, the following assumptions were made to estimate the extent of the nozzle losses.

The overall pressure drop Δp is the sum of two components: the nozzle region pressure drop Δp_n , and the "core" pressure drop Δp_k , for the rest of the heat exchanger. It is assumed that for comparable heat exchangers where only the nozzle size has been changed, the Δp_k will be the same. Therefore, any difference in Δp is due to differences in Δp_n . Further, the relative values of Δp_n for nozzles of different size at the same flow rate would be proportional to the value of the velocity of the flow in the nozzles squared. Since flow area of the 14-in. nozzle is 1.945 times that for the 10-in. nozzle, the pressure drop for the 10-in. nozzle region would be 3.783 times that for the 14-in. nozzle. From these assumptions, it is possible to calculate the fraction of the overall pressure drop represented by the nozzles of the different sizes.

The results for the five data sets, expressed as a percentage of the overall pressure drop, are tabulated in Table 6 for a 0.063 m³/s (1000 gal/min) flowrate. On the average, the 14-in. nozzles accounted for about 4.5 percent of the overall pressure drop compared to 15 percent for the 10-in. nozzles on full bundles. On the other hand, the 14-in. nozzles only accounted for about 2 percent of the overall pressure drop and 8 percent for the 10-in. nozzles for the cases with the NTIW bundle. These differences were not unexpected due to the considerable differences in geometry in the region of the bundle under the nozzles. Based upon the results using the approach outlined above, one would anticipate that geometry plays a significant role in the prediction of shellside nozzle pressure drop.

5 Concluding Remarks

Systematic tests were run on 24 typical configurations of industrial-sized shell-and-tube heat exchangers to obtain both vibrational and pressure drop information for waterflow on the shellside. The vibration data are reported elsewhere, e.g., Halle et al. (1984), while this paper presents the results of the

Table 5 Pressure drop distribution

Listed is the fraction of the pressure drop between the tap indicated and the outlet tap to the overall inlet/outlet pressure drop. Note that, as explained in the text, the location of taps C through G is different for the eight and six-crosspass configurations; see Fig. 6.

Configuration code ¹	Tap	Fractional Pressure Drop							
		A	B	C	D	E	F	G	H
F•P•8•14"•30°•26%	1	0.906	0.869	0.729	0.518	0.289	0.180	0.167	
F•P•8•10"•30°•26%	1	0.882	0.846	0.714	0.510	0.295	0.191	0.181	
F•P•8•14"•90°•26%	1	0.891	0.864	0.748	0.554	0.312	0.202	0.195	
F•P•8•10"•90°•26%	1	0.873	0.846	0.743	0.563	0.341	0.243	0.239	
F•P•6•14"•30°•29%	1	0.871	0.810	0.639	0.505	0.361	0.214	0.219	
F•P•6•10"•30°•29%	1	0.854	0.796	0.652	0.542	0.426	0.301	0.309	
F•P•6•14"•90°•30%	1	0.881	0.821	0.664	0.539	0.401	0.250	0.257	
F•P•6•10"•90°•30%	1	0.840	0.790	0.670	0.560	0.450	0.320	0.330	
F•P•6•14"•45°•16%	1	0.961	0.865	0.663	0.507	0.337	0.144	0.108	
F•P•6•14"•45°•30%	1	0.902	0.837	0.666	0.528	0.380	0.227	0.239	
F•P•6•14"•60°•16%	1	0.943	0.847	0.641	0.507	0.339	0.154	0.123	
F•P•6•14"•60°•30%	1	0.881	0.819	0.659	0.523	0.383	0.232	0.238	
N•P•8•14"•30°•26%	1	0.914	0.890	0.746	0.517	0.274	0.155	0.159	
N•P•8•10"•30°•26%	1	0.923	0.899	0.768	0.548	0.317	0.209	0.213	
N•P•8•14"•90°•26%	1	0.904	0.877	0.747	0.529	0.275	0.153	0.155	
N•P•6•10"•30°•29%	1	0.904	0.864	0.699	0.583	0.440	0.296	0.315	
N•P•6•10"•90°•30%	1	0.914	0.882	0.711	0.583	0.445	0.288	0.302	
N•P•6•14"•45°•16%	1	0.954	0.861	0.643	0.497	0.318	0.128	0.137	
N•P•6•14"•60°•16%	1	0.935	0.839	0.629	0.492	0.317	0.139	0.171	
N•P•6•14"•60°•30%	1	0.893	0.852	0.662	0.518	0.354	0.185	0.209	
F•E•6•10"•30°•29%	1	0.880	0.820	0.660	0.540	0.420	0.290	0.260	
F•E•6•10"•90°•30%	1	0.880	0.824	0.665	0.548	0.415	0.271	0.255	
N•E•6•10"•30°•29%	1	0.930	0.880	0.700	0.570	0.440	0.280	0.300	
N•E•6•10"•90°•30%	1	0.950	0.893	0.718	0.588	0.443	0.281	0.315	

¹Refer to Table 3.

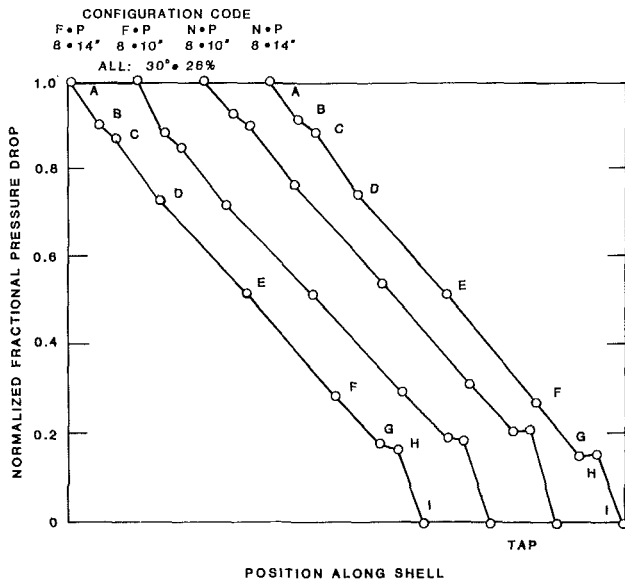


Fig. 9 Fractional distribution of pressure drop averaged and normalized to overall pressure drop

pressure drop measurements. The pressure drop data are unique as surprisingly few other data have been reported for these geometries in spite of the fact that there are so many shell-and-tube heat exchangers in service. Not only the overall pressure drop was measured, but also incremental pressure drop was obtained. The tests are described in detail and the basic data presented in such a way that they can be used by future researchers. The data not only permit a direct comparison of the performance of several different configurations, but also provide the basis for the evaluation of various pressure drop prediction models. One example of this applica-

tion of these data is the paper by Kistler and Chenoweth (1988).

A topical report by Halle and Wambsganss (1983) covering the pressure drop work includes testing of special design and field fix bundles and presents additional evaluations, but does not include the 45 and 60 deg layout test data presented in this update paper.

Pressure drop and distribution data from additional tests are presented by Halle et al. in topical reports that included seven-crosspass and double-segmentally baffled (1985) and pitch-to-diameter ratio 1.42 (1986) configurations.

Acknowledgments

This work was performed as part of a Heat Exchanger Tube Vibration Program which is sponsored by the U.S. Department of Energy, Office of Energy Systems Research, under the Energy Conversion and Utilization Technologies (ECUT) Program (Contract W-31-109-ENG-38), and represents a U.S. contribution to the International Energy Agency (IEA) Program of Research and Development on Energy Conservation in Heat Transfer and Heat Exchangers. Heat Transfer Research, Inc. (HTRI), an applications-oriented research organization, provided consultation, cooperation, and assistance to the program. The continuing encouragement and support of M. E. Gunn, W. H. Thielbahr, and J. J. Eberhardt of the US/DOE and J. Taborek, formerly of HTRI, are gratefully appreciated.

References

Crane Co., 1969, "Flow of Fluids Through Valves, Fittings, and Pipe," Tech Paper No. 410, New York.
 Halle, H., and Wambsganss, M. W., 1983, "Shellside Waterflow Pressure Drop and Distribution in Industrial Size Test Heat Exchanger," ANL Report ANL-83-9, Argonne National Laboratory, Argonne, IL.
 Halle, H., Chenoweth, J. M., and Wambsganss, M. W., 1984, "Flow-Induced Tube Vibration Thresholds in Heat Exchangers From Shellside Water Tests," *Proc. Symposium on Flow-Induced Vibrations*, Vol. 3, Vibration in Heat Exchangers, ASME G00269, pp. 17-32.
 Halle, H., Chenoweth, J. M., and Wambsganss, M. W., 1985, "Tube Vibra-

Table 6 Combined inlet/outlet nozzle region pressure drop losses at 0.063 m³/s (1000 gal/min) flowrate

Configuration code ²	Overall pressure drop ¹ Δp		"Core" loss Δp_k		Nozzle loss Δp_n		Nozzle loss, percent
	kPa	lb/in. ²	kPa	lb/in. ²	kPa	lb/in. ²	
F•P•8•14"•30°•26%	37.4	5.43	36.0	5.22	1.43	0.208	3.83
F•P•8•10"•30°•26%	41.4	6.01	36.0	5.22	5.43	0.787	13.1
F•P•8•14"•90°•26%	28.9	4.19	27.9	4.04	1.01	0.154	3.68
F•P•8•10"•90°•26%	31.9	4.62	27.9	4.04	4.02	0.583	12.6
F•P•6•14"•30°•29%	23.3	3.38	21.8	3.16	1.51	0.219	6.48
F•P•6•10"•30°•29%	27.5	3.99	21.8	3.16	5.72	0.829	20.8
F•P•6•14"•90°•30%	17.4	2.53	16.8	2.44	0.59	0.0862	3.41
F•P•6•10"•90°•30%	19.1	2.77	16.8	2.44	2.25	0.326	11.8
N•P•8•14"•30°•26%	20.2	2.93	19.8	2.87	0.45	0.0647	2.21
N•P•8•10"•30°•26%	21.4	3.11	19.8	2.87	1.69	0.245	7.87

¹ Δp is also γ for this flowrate.

²Refer to Table 3.

tion in Industrial Size Test Heat Exchanger (22 Additional Configurations)," ANL Report ANL-85-66, Argonne National Laboratory, Argonne, IL.

Halle, H., Chenoweth, J. M., and Wambsganss, M. W., 1986, "Tube Vibration in Industrial Size Test Heat Exchanger (Pitch-to-Diameter Ratio 1.42)," ANL Report ANL-86-53, Argonne National Laboratory, Argonne, IL

Heat Transfer Research, Inc., 1982, "Design or Rating of Shell-and-Tube Heat Exchangers," HTRI Computer Program ST-4, Alhambra, CA.

Kistler, R. S., and Chenoweth, J. M., 1988, "Heat Exchanger Shellside Pressure Drop: Comparison of Predictions With Experimental Data," ASME JOURNAL OF HEAT TRANSFER, Vol. 110, this issue.

Wambsganss, M. W., Yang, C. I., and Halle, H., 1984, "Fluidelastic Instability in Shell and Tube Heat Exchangers—A Framework for a Prediction Method," *Proc. Symposium on Flow-Induced Vibrations*, Vol. 3, Vibration in Heat Exchangers, ASME G00269, pp. 103-118.

Heat Exchanger Shellside Pressure Drop: Comparison of Predictions With Experimental Data

R. S. Kistler

J. M. Chenoweth

Mem. ASME

Heat Transfer Research, Inc.,
Alhambra, CA

A unique set of heat exchanger shellside pressure drop experimental data has become available from experiments at Argonne National Laboratory as a part of an ongoing research program in flow-induced vibration. These data provide overall pressure drop for a number of typical industrial heat exchanger configurations in addition to incremental pressure drop measurements along the shellside path. The test program systematically varied the baffle spacing, the tube field pattern, and nozzle size for a series of isothermal water tests for segmentally baffled bundles. Also recently a comprehensive method has been published in the Heat Exchanger Design Handbook (HEDH) for the prediction of bundle shellside pressure drops. A search of the literature failed to reveal a complementary method for predicting the shellside nozzle pressure losses. This paper compares the predicted with the measured data and validates the adequacy and limitations of the HEDH method for full bundles of plain tubes. It further applies an extension to the method for no-tubes-in-the-window bundles. Adjustments were indicated to improve the predictions for finned tubes and methods were developed to predict shellside nozzle pressure drops. Overall pressure drop predictions were within plus or minus 20 percent.

Introduction

The understanding of the behavior of the flow on the shellside of a shell-and-tube heat exchanger has progressed dramatically since the original work of Tinker (1952). The extensive research work at the University of Delaware summarized by Bell (1963) furthered this understanding, and led to a manual procedure for predicting the shellside pressure drop and heat transfer. Heat Transfer Research, Inc., later supplemented the data from the University of Delaware taken on small units with data on industrial-sized heat exchangers, and developed the computer-based Stream Analysis Method (1969). Recently, Taborek (1982) in the *Heat Exchanger Design Handbook* (HEDH) updated the work from the University of Delaware and published an extended method for shellside heat transfer and pressure drop. This method has several attractive features. It does not require extensive iteration to determine the shellside heat transfer and pressure drop; it is set up for both hand calculation and microcomputer application; and it provides an explanation of some of the behavior noticed in the Delaware Project in terms of the different leakage streams present in the exchanger.

However, there is no published method that deals with the pressure drop contribution due to the existence of the nozzles on the shellside of the exchanger. More surprising, no pressure drop data for industrial-sized units have been available in the open literature to evaluate the predictions by published methods.

Recently, as a part of the ongoing flow-induced vibration project conducted at Argonne National Laboratory, a large set of data on shellside isothermal pressure drop with water as the shellside fluid was published by Halle et al. (1984). These data are unique, as they represent the first-ever systematic study of the effect of shellside geometry on the onset of vibration in industrial sized heat exchangers. In addition, pressure drops were measured at various positions along the shell, in an attempt to see the effect of the onset of vibration on the

pressure drop. Thus, there are now data that can be used to test shellside pressure drop by predictive methods.

This paper presents comparisons of the prediction of the HEDH method with the experimental measurements from Argonne for different full plain and finned tube bundles with segmental baffles. It further presents complementary methods to account for nozzle pressure drops so that overall pressure drops can be compared. Finally, the HEDH method is extended to handle no-tubes-in-window bundles on the basis of the Argonne data.

Pressure Drop Measurements

Description of Test Apparatus. The test apparatus was an industrial-sized heat exchanger shell into which bundles of various configurations could be inserted. The test fluid was room-temperature water circulating in a closed loop through the shell side of the test exchanger. There was no fluid flowing on the tube side and there were no end covers permitting visual observation of the vibrating tubes, making of movies of the vibration, and insertion of instrumentation. Pressure taps were located at strategic locations from nozzle to nozzle so that local pressure drop measurements could be made. Figure 1 shows the location and designation of these pressure taps for the two different baffle spacings tested. By changing tubesheets, baffles, tubes, and tie rods, different bundle configurations could be produced. Easy disassembly and reassembly was facilitated by holding the tubes between dual tubesheets with O-ring seals. Figure 2 shows a picture of one of the no-tubes-in-window (NTIW) bundles used as a part of these tests. The nozzle diameter could be reduced by the use of plastic inserts. A full description of the apparatus and the pressure drop measurements has been published by Halle and Wambsganss (1983).

The diameter of the shell in the research unit is 590.55 mm (23.25 in.) and the overall tube length is 3.66 m (12 ft). The baffled tube length inside the tubesheets is 3.58 m (11.75 ft). The tube outside diameter is 19.05 mm (0.75 in.). Two different equal baffle spacings were investigated. The first with six crosspasses results in tube spans in the baffle windows ap-

Contributed by the Heat Transfer Division and presented at the 22nd National Heat Transfer Conference, Niagara Falls, New York, August 1984. Manuscript received by the Heat Transfer Division September 10, 1984.

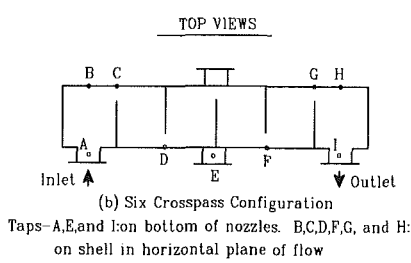
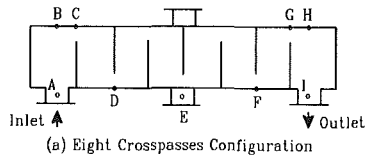


Fig. 1 Location of pressure taps for test heat exchanger

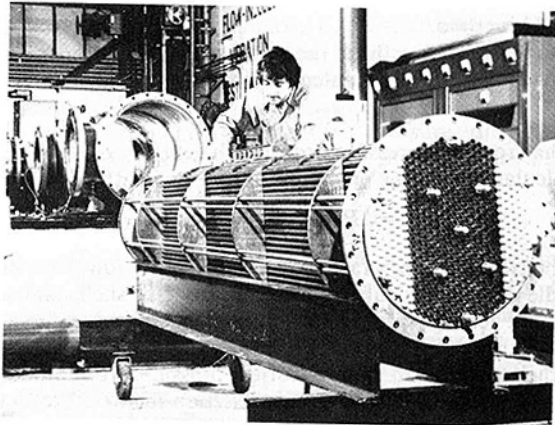


Fig. 2 Test exchanger no-tubes-in-window bundle configuration for 30 deg pattern and eight crosspasses

proximately equal to the TEMA maximum unsupported span (1978). The second with eight crosspasses results in approximately three-quarters of the TEMA maximum span. All usual tube patterns were investigated, and both plain and low-finned tubes with 748 fins/m (19 fin/in.) were investigated. Both full bundles with segmental baffles and no-tubes-in-the-window

Table 1 Pressure drop data cases for the Argonne tests

Tube Pattern, deg.	Number of Crosspasses	Baffle Cut, %	Nozzle Diameter, mm	Case Number	Configuration Code (Halle et al., 1983)
Full Bundle with Plain Tubes					
30	8	25.5	336.55	1	F·P·8·14°·30°·26%
30	8	25.5	241.30	3	F·P·8·10°·30°·26%
30	6	28.9	336.55	6	F·P·6·14°·30°·29%
30	6	28.9	241.30	7	F·P·6·10°·30°·29%
90	8	25.5	336.55	17	F·P·8·14°·90°·26%
90	8	25.5	241.30	16	F·P·8·10°·90°·26%
90	6	28.9	336.55	19	F·P·6·14°·90°·30%
90	6	28.9	241.30	20	F·P·6·10°·90°·30%
45	6	29.6	336.55	29	F·P·6·14°·45°·30%
45	6	15.5	336.55	27	F·P·6·14°·45°·16%
60	6	29.6	336.55	32	F·P·6·14°·60°·30%
60	6	15.5	336.55	30	F·P·6·14°·60°·16%
Full Bundles with Finned Tubes					
30	6	28.9	241.30	15	F·E·6·10°·30°·29%
90	6	28.9	241.30	25	F·E·6·10°·90°·30%
No-Tubes-in-Window Bundles with Plain Tubes					
30	8	25.5	336.55	4	N·P·8·10°·30°·26%
30	8	25.5	241.30	5	N·P·8·14°·30°·26%
30	6	28.9	241.30	13	N·P·6·10°·30°·29%
90	8	25.5	336.55	18	N·P·8·14°·90°·26%
90	6	28.9	241.30	23	N·P·6·10°·90°·30%
No-Tubes-in-Window Bundles with Finned Tubes					
30	6	28.9	241.30	14	N·E·6·10°·30°·29%
90	6	28.9	241.30	26	N·E·6·10°·90°·30%

bundles with segmental baffles were tested. Cases to be used for development and comparisons are summarized in Table 1.

Test Results. The pressure drops measured were reported by Halle et al. (1984) in equation form, which was shown to represent the data extremely well (95 percent of the data predicted within ± 5 percent). For each case, the values for the constants, α and γ in equation (1) below, were given to calculate the overall nozzle-to-nozzle pressure. This pressure drop, ΔP_{total} , the pressure drop between taps A and I of the

Nomenclature

A_{baff} = crossflow area at the baffle tip, mm^2
 A_{escape} = flow area into the shell between the shell and bundle along the nozzle diameter, mm^2
 A_{slot} = flow area between the tubes for entering the bundle directly below the nozzle, mm^2
 A_{nz} = nozzle flow area, mm^2
 D_{of} = tube diameter over the finned portion, mm
 D_{req} = "flattened" equivalent tube diameter for finned tubes, mm
 D_{fr} = fin root diameter for finned tubes, mm
 f_i = isothermal shellside crossflow friction factor
 F_i = predicted fraction of flow entering the bundle

through the slots below the nozzle
 F_{ci} = correction factor for F_i
 F_o = predicted fraction of flow leaving the bundle through the slots below the nozzle
 F_{co} = correction factor for F_o
 K_{ent} = number of velocity heads lost in the inlet nozzle for no-tubes-in-the-window baffles
 K_{ex} = number of velocity heads lost in the outlet nozzle for no-tubes-in-the-window
 K_c = contraction coefficient for flow exiting the bundle for no-tubes-in-the-window baffles
 L_{fh} = fin height for low-finned tubes, mm

L_{fs} = average fin thickness for low-finned tubes, mm
 M_w = window flow mass velocity, $kg/m^2 s$
 M_s = shellside crossflow mass velocity based on average crossflow area
 S_m , $kg/m^2 s$
 N_f = number of fins per unit length for low-finned tubes, 1/m
 N_b = number of baffles in the exchanger
 N_{tcc} = number of tube rows crossed in one baffle spacing between the baffle tips
 N_{tcw} = number of tube rows crossed in one baffle window

experimental unit (see Fig. 1), was correlated by the following equation:

$$\Delta P_{\text{total}} = \gamma(Q/0.06309)^\alpha \quad (1)$$

where the flow rate Q is given in cubic meters per second and the pressure drop ΔP_{total} is calculated in kPa. Halle et al. (1984) also gave the fraction of the overall pressure drop from the inlet to each of the intermediate pressure taps. In this way, the local pressure drop can be calculated. For example, the central bundle pressure drop can be determined by the pressure drop between taps C and G.

Six different flow rates were used for each case. These are 44.1, 63.1, 94.6, 126.2, 157.7, and 189.3 kg/s. These cover the range of tested flow rates for all cases except the no-tubes-in-the-window bundle. However, even for that bundle style, this range covers shellside velocities currently used in normal design practice. For the units with eight crosspasses, this range of flow rates represents nominal shellside Reynolds numbers (Re_s) of 15,000 to 64,000 and nominal shellside velocities (based on area S_m) of 0.76 to 3.28 m/s (2.49 to 10.76 ft/sec). For the units with six crosspasses, this range of flow rates represents nominal shellside Reynolds numbers (Re_s) of 11,000 to 48,000 and nominal shellside velocities (based on area S_m) of 0.57 to 2.44 m/s (1.87 to 8.00 ft/sec).

Among the most important features of the pressure drop measurements were the incremental shellside pressure taps. These taps allowed comparison of the bundle pressure drop with the analytical method, as well as the development of a model for calculating the entry and exit nozzle pressure drops. The location of these taps is shown in Fig. 1. Notice that, for both the six and eight-crosspass bundles, pressure taps are available before and after the end zones. These taps are labeled C and G. For the six-crosspass configuration, the pressure drop from taps C to G represents four central zone crosspasses and four window pressure drops. For the eight crosspass unit, the pressure drop from taps C to G represents six central pressure drops and six window pressure drops. The pressure drop from tap A to C may be interpreted as the inlet nozzle pressure drop plus the inlet zone pressure drop plus one-half of a window pressure drop. Similarly, the pressure drop from tap G to I may be interpreted as the sum of one-half of a window pressure drop plus the outlet zone pressure drop

plus the outlet nozzle pressure drop. The pressure drops between all taps are reported as a part of the Argonne research work, allowing a unique chance to analyze the shellside pressure drop and its components.

Shellside Pressure Drop Prediction Method

One of the outstanding features of the HEDH method for calculating shellside heat transfer and pressure drop is its completeness. With the exception of rotated triangular (60 deg) tube patterns and nozzles, all of the necessary equations and correction factors for shellside pressure drops are presented and discussed in detail. Graphs for hand calculations and equations for computer applications are given. The reader is referred to Section 3.3 of the HEDH for further information. Since all the data from Argonne were isothermal, only the shellside pressure drop method can be compared with the HEDH method.

In the HEDH method, the total shellside pressure drop excluding nozzles, ΔP_s , is calculated by

$$\Delta P_s = \Delta P_c + \Delta P_w + \Delta P_e \quad (2)$$

The crossflow pressure drop for the entire exchanger, ΔP_c , is calculated from the pressure drop for one baffle spacing by

$$\Delta P_c = \Delta P_{bi} (N_b - 1) (R_b) (R_l) \quad (3)$$

The two correction factors, R_b and R_l , are functions of the bundle cross flow, tube-to-baffle, bundle-to-shell, and shell-to-baffle leakage areas. The calculation of these factors is discussed in detail by Taborek (1982), and equations are given for their calculation. The crossflow pressure drop in one baffle space, ΔP_{bi} , is calculated from friction factor curve-fit constants for ideal tube banks that are presented in the HEDH method. The equation is

$$\Delta P_{bi} = 0.002 f_i N_{\text{tcc}} M_s^2 / \rho_s \phi_s^{-r} \quad (4)$$

The isothermal friction factor, f_i , is based on the nominal shellside Reynolds number, Re_s , and is evaluated from charts given with the HEDH method assuming full shellside flow across the nominal crossflow area at the shell diameter S_m . N_{tcc} is the number of tube rows crossed between baffle tips, and M_s is the shellside mass velocity. Calculation of the

Nomenclature (cont.)

Q = shellside flow rate, m^3/s	S_d = downstream flow area for pressure drop, m^2	
r = exponent for shellside viscosity correction for pressure drop in equation (4)	S_b = bypass flow area between the bundle diameter and the shell, mm^2	pressure drop for all windows in the exchanger, kPa
R_b = bundle bypass pressure drop correction factor	S_{tb} = tube-to-baffle-hole leakage area, mm^2	ΔP_e = predicted crossflow pressure drop for both end zones, kPa
R_l = baffle leakage correction factor	V_u = upstream flow velocity, m/s	ΔP_{bi} = predicted crossflow pressure drop for one baffle without corrections, kPa
Re_s = shellside Reynolds number based on area S_m	α = constant equation (1), determined from experimental data	ΔP_{total} = nozzle-to-nozzle pressure drop, kPa
R_s = end zone baffle spacing correction factor for pressure drop	γ = constant in equation (1), determined from experimental data	ΔP_{nzi} = inlet nozzle pressure drop, kPa
S_m = crossflow area (nominal) at the bundle center line, mm^2	ΔP_s = predicted shellside pressure drop, kPa	ΔP_{nzo} = outlet nozzle pressure drop, kPa
S_w = net longitudinal flow area in the window, mm^2	ΔP_c = predicted crossflow pressure drop for the entire exchanger excluding the end zones, kPa	ρ_s = average shellside fluid density, kg/m^3
S_u = upstream flow area for pressure drop, m^2	ΔP_w = predicted window	ρ = shellside fluid density, kg/m^3
		ϕ_s = shellside viscosity ratio

viscosity correction factor, ϕ_s , and its exponent r are described in the method.

The total pressure drop for all baffle windows, ΔP_w , is calculated by equation (5) for turbulent flow where the shellside Reynolds number is greater than 100. For lower flow rates, a different equation is used. However, all of the Argonne data are well into turbulent flow.

$$\Delta P_w = N_b [(2 + 0.6 N_{tcw}) (M_w^2 / [2 \rho_s]) 10^{-3}] R_l \quad (5)$$

The constant 0.6 in equation (5) was found to overpredict the window pressure drop for the 60 deg layouts. For that layout, a value of 0.346 was used in place of the 0.6. The value of 0.346 was obtained by multiplying the value of 0.6 by the ratio of the distances between tube rows in the direction of the shellside flow of the 60 deg layout to the 30 deg layout. The window mass velocity, M_w , is based on the geometric average flow area for window flow and cross flow

$$M_w = M_s / (S_m S_w)^{0.5} \quad (6)$$

The leakage correction factor, R_l , is the same as used in equation (3) and is a function of the bundle-to-shell and cross-flow areas. The number of rows crossed in the window, N_{tcw} , is the total number of rows in the window.

The final term in the shellside pressure drop, ΔP_e , represents the pressure drop for both end zones in the exchanger. It is calculated by

$$\Delta P_e = \Delta P_{bi} (1 + N_{tcw} / N_{icc}) R_b R_s \quad (7)$$

Notice that the leakage correction, R_l , is not applied in the end zones, as might be expected. The correction factor R_s is the unequal end baffle spacing correction factor and is also used to correct equation (2) so that it calculates the pressure drop for both end zones. Since the Argonne data were taken with the central spacing equal to the end zone spacing, $R_s = 2$ for all cases. If the end zone spacing had been greater than the central spacing, R_s would be less than 2. Similarly, if the end spacings are smaller than the central spacing, R_s would be greater than 2.

In order to use the method, all details of the shellside geometry are necessary. Fortunately, all the necessary details were available in the Argonne research report (Halle and Wambsganss, 1983) except for the baffle diameter, the bundle diameters, and the relative heights under the inlet and outlet nozzles. These could be easily calculated with a small computer program from the drawings of the bundles included in the report and by personal communication with the research engineers at Argonne (Halle, 1983).

Analysis Procedure

In order to make the large number of calculations necessary for evaluating the method and comparing the results with the Argonne data, a series of programs were written in Microsoft BASIC for use on an Atari 1200XL Computer system. The program was verified using an example problem given with the method. The computer program was further verified with hand calculations for several selected cases.

The remainder of the paper will be used to describe the application of the method to the experimental cases tested at Argonne including the development of the necessary extensions to represent the data. It is preferable to divide the cases according to the several different bundle styles. First, the full bundles with segmental baffles with plain and finned tubes, the nozzle predictions, and the overall pressure drop comparisons are presented. Then the no-tubes-in-window bundles will be presented in the same sequence. Finally, the conclusions and recommendations will follow.

Full Bundles With Segmental Baffles

The portion of the overall pressure drop predicted by the

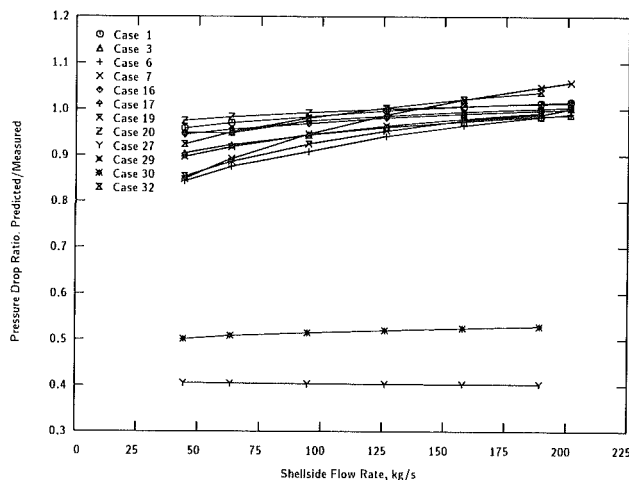


Fig. 3 Bundle pressure drop ratio for full bundle of plain tubes with segmental baffles

method is that exclusive of that for the nozzles and is the shellside pressure, ΔP_s , in equation (2). If the end zone pressure drop, ΔP_e , is subtracted, the bundle pressure drop equivalent to that measured between taps C and G for the Argonne tests remains.

Bundle Pressure Drop for Plain Tubes. There are twelve cases with segmental baffles and plain tubes, representing four different tube patterns (30, 90, 45, and 60 deg) in the Argonne data. These are cases 1, 3, 6, 7, 16, 17, 19, 20, 27, 29, 30, and 32. The comparison of the measured pressure drop between taps C and G with the bundle pressure drops by the method are shown in Fig. 3. In general, the predictions are quite good, averaging approximately plus or minus 10 percent, although most of the data are underpredicted. The exceptions are Cases 27 and 30 with extremely small (15.5 percent) baffle cuts. For these cases, the method predicts about one-half of the measured pressure drop.

All the cases except for Cases 27 and 30 have bundles of good designs with the longitudinal flow area in the window approximately equal to the crossflow area. Thus the window velocity is approximately equal to the crossflow velocity, a good design criterion for shell-and-tube heat exchangers. However, the window flow area for Cases 27 and 30 is approximately one-third smaller than that of the other cases, resulting in a window velocity approximately three times the crossflow velocity. This will produce an acceleration pressure drop in the window. However, the method does not contain any acceleration components to account for the added pressure drop, and, as a result, underpredicts the bundle pressure drop.

Bundle Pressure Drop for Finned Tubes. As given in the HEDH method, the modifications to the method for finned tubes are relatively simple. The tube diameter over the fins, D_{of} , is used to calculate the free longitudinal flow area in the window and the tube-to-baffle-hole leakage area S_{tb} . The crossflow area, S_m , is calculated based on an equivalent diameter, D_{req} , a "flattened" equivalent tube diameter as defined in the method as shown in equation (8). This diameter is also used in the calculation of the shellside Reynolds number used to calculate the isothermal shellside friction factor f_i .

$$D_{req} = D_{fr} + 2L_{fh} N_f L_{fs} (0.001) \quad (8)$$

Finally, Taborek recommends that the isothermal friction factor, f_i , be multiplied by an empirically determined factor of 1.4 to account for the "added frictional pressure drop due to the flow over the fins." It should be noted that this procedure results in a lower pressure drop in the window, since the

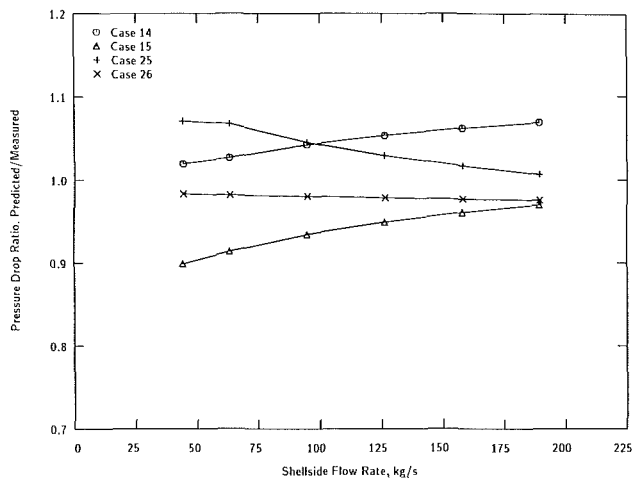


Fig. 4 Bundle pressure drop ratios for finned tube bundles

crossflow velocity will be lower will finned tubes as D_{req} is less than the tube plain end outside diameter. Note that no adjustment to the window pressure drop for the roughness of the fins is included in the method.

In the Argonne data, there are only four cases with finned tubes: Cases 15 and 25 with segmental baffles, and Cases 14 and 26 with no-tubes-in-the-window bundles. Although the data are insufficient to develop a new method for finned tubes, they are sufficient to test the method, since it does contain specific recommendations for finned tubes.

The computer program was modified with the changes described above and the bundle pressure drop for Cases 15 and 25 calculated. The method underpredicted the measured bundle pressure drops by approximately 30 percent for Case 15 and 20 percent for Case 25 based on the pressure drop from taps C to G. A modification of the method was therefore indicated to improve accuracy of the predictions. The modification was developed as follows:

Since the window pressure drop method should be identical for no-tubes-in-the-window bundles whether the tubes are plain or finned, the two no-tubes-in-the-window cases, Cases 14 and 26, were used to determine what factor could be used to replace the 1.4 recommended in the method. The required factor was determined to be 2.0. The segmental baffle data, Cases 15 and 25, were then used with this multiplication factor to determine the necessary multiplication factor for the window pressure drop. Based on these two cases, the window multiplication factor for segmentally baffled exchangers was found to be 1.3 for the single fin geometry studied at Argonne.

A comparison of the pressure drop from taps C to G with the modifications discussed above is given in Fig. 4. As can be seen in this figure, the agreement between the measured and predicted pressure drop is quite good, as all the data are predicted within plus or minus 10 percent. However, extreme caution should be taken when using these modifications. There are only four cases involved in the development, and all cases have six crosspasses, approximately the same baffle cut, and the same 748 fin/m (19 fin/in.) tubes.

Nozzle Pressure Drops for Full Bundles. Although the nozzle pressure drops were not directly measured as a part of the Argonne experiments, they can be back-calculated from the basic data if you have a method that can be used to predict the shellside pressure drop. Since the HEDH method predicted the bundle pressure drop well, it was assumed that the end zone pressure drops calculated by the method were correct. The procedure for calculating the nozzle pressure drops is the following. To determine the inlet nozzle pressure drop from the pressure drop between the inlet tap A and tap C, subtract one-half of a window pressure drop and the calculated end

zone pressure drop. Similarly, the outlet nozzle pressure drop was calculated by determining the pressure drop between tap G and the exit tap I, then subtracting one-half of a window pressure drop and the end zone pressure drop. It should be noted that the method does not give separate recommendations for the inlet and outlet zone pressure drops, but gives equation (7) for both end zones combined. In this development, the total end zone pressure drop was allocated equally between the inlet and outlet.

When the nozzle pressure drops are back-calculated using the above procedure, the nozzle pressure drops are higher at the outlet of the exchanger than at the inlet. This is not surprising, and may be attributed to the more complex flows at the outlet where the various flow streams (Palen and Taborek, 1969) must combine to exit from the exchanger. At the inlet, the flow patterns are developing and the flow sees a simpler path into the bundle.

In order to estimate the total pressure loss in the exchanger, a method is needed for predicting the pressure drop in the inlet and outlet nozzles. The nozzle pressure drop may not be dismissed as unimportant, since, for some of the Argonne cases, over 40 percent of the total pressure drop in the exchanger is in the end zones and nozzles. The method in HEDH does not include a procedure for calculating nozzle pressure drops.

However, Henry (1982) in Section 2.2.7 of the HEDH does make specific recommendations for tubeside inlet and exit nozzles. These were tried for the shellside nozzles, but proved to be inadequate. This is not surprising, since the tubeside entrance is a free expansion and the exit is a contraction. This is easier to predict than the complex flow in the region of the shellside nozzles.

A recommendation is also made by Henry (1982) that equation (9) be used for the shellside entry pressure drop if an impingement plate is present. It is further stated that, if an impingement plate is absent, the same equation can be used if the velocity is based on the flow area between the tubes.

$$\Delta P_{nzi} = \rho_s (S_u/S_d + 0.3) V_u^2 \quad (9)$$

Unfortunately, equation (9) failed to predict the shellside inlet nozzle pressure drop adequately.

To predict the nozzle pressure drops, a simplified model was developed. Based on flow visualization studies of the entry region presented by HTRI (1965), a model was postulated that assumes that only part of the entering flow passes through the slots between the tubes. Preliminary investigations showed that this model could be used in combination with standard pressure drops for sudden contractions and expansions in pipes published by the Crane Company (1969). All calculations are based on the fraction of the entering stream that flows into the bundle through the slots between tubes. However, in order to be used it is necessary to predict correctly the fraction of the total flow flowing through the bundle. That required pressure balancing the flow bypassing the bundle with that flowing through the bundle. Due to the differences in the physical situation at the inlet and outlet of the exchanger, the assumptions at the inlet and outlet of the exchanger are slightly different.

Inlet Nozzle Pressure Drop. The method used to calculate the fraction entering the bundle through the slots below the nozzle assumes that the entering flow divides into two separate parts. The first part is the fraction that enters the bundle. The second part enters the nozzle, makes a turn, then enters the bypass flow area for flow between the bundle and the shell. The pressure drops for both streams are assumed to be equal. Therefore, the individual equations for the pressure drop for each stream can be written, set equal, and solved for the fraction of the flow that enters the bundle. The inlet nozzle

pressure drop can then be calculated from either stream. The equation that must be solved at the inlet is given by

$$0.5 \rho (0.75) \left[\frac{(1-F_i)M_s}{A_{\text{escape}}} \right]^2$$

(turning of bypass stream)

$$+ 0.5 \rho \left[1 - \frac{S_b}{A_{\text{escape}}} \right] \left[\frac{(1-F_i)M_s}{S_b} \right] = \Delta P_{\text{nzi}} =$$

(contraction of bypass stream)

$$0.5 \rho \left[1 - \frac{A_{\text{slot}}}{(A_{\text{nz}})(F_i)} \right] \left[\frac{(F_i)(M_s)}{A_{\text{slot}}} \right]^2 \quad (10)$$

(friction loss for stream entering bundle)

The stream bypassing the bundle is represented on the left-hand side of equation (10). The first term represents the pressure loss due to the turning of the stream. The second term represents a contraction from the escape area below the nozzle into the bundle-to-shell clearance area. The term on the right-hand side of equation (10) represents the pressure loss for the stream entering the bundle. Notice that the shell fluid density and flow rate can be canceled in equation (10), leaving terms that are a function of the shellside geometry that can be solved for F_i . However, because of the complexity of equation (10), it is most easily solved for F_i using a computer program for the iterative calculations.

Although the solution to equation (10) did not predict the nozzle pressure drop adequately, it did give the proper trends. It was therefore necessary to introduce a correction factor, F_{ci} , as shown in equation (11), to increase the accuracy of the prediction. The form of the correction factor F_{ci} is shown in equation (12). The constants in equation (12) were determined using regression analysis techniques, and the constants were adjusted to give slightly conservative inlet pressure drop predictions.

$$\Delta P_{\text{nzi}} = 0.5 \rho \left[1 - \frac{A_{\text{slot}}}{(A_{\text{nz}})(F_i)} \right] \left[\frac{(F_i)(M_s)}{A_{\text{slot}}} \right]^2 F_{ci} \quad (11)$$

$$F_{ci} = 4.4 \left[\frac{A_{\text{escape}}}{S_m} \right]^{-0.12} \left[\frac{S_b}{S_m} \right]^{0.89} \quad (12)$$

The inlet nozzle pressure drops predicted by equation (12) are within plus or minus 50 percent of the back-calculated inlet nozzle pressure drops. This represents significant scatter. However, the largest scatter occurs at the lowest flow rates where the measured pressure drops are small, and the effect on the overall pressure drop prediction is also small.

Outlet Nozzle Pressure Drop. The method used at the outlet of the exchanger is similar to that for the inlet, except that more items need to be considered. The flow leaving the bundle is treated the same as the inlet, except for the form of the pressure loss K value. The bypass stream is assumed to leave the bundle, impinge on the shell, turn, contract from the bundle-to-shell flow area into the escape area, and finally turn to exit through the nozzle. As with the inlet, the pressure drops for the two streams are set equal and solved for the fraction flowing out through the bundle. The equation that must be solved at the outlet is given by

$$0.5 \rho (1.00) \left[\frac{(1-F_o)(M_s)}{S_m} \right]^2$$

(bypass stream impingement)

$$+ 0.5 \rho (0.75) \left[\frac{(1-F_o)(M_s)}{S_b} \right] +$$

(turning of bypass stream)

$$0.5 \rho \left[1 - \frac{S_b}{A_{\text{escape}}} \right]^2 \left[\frac{(1-F_o)(M_s)}{S_b} \right]$$

(bypass stream expansion)

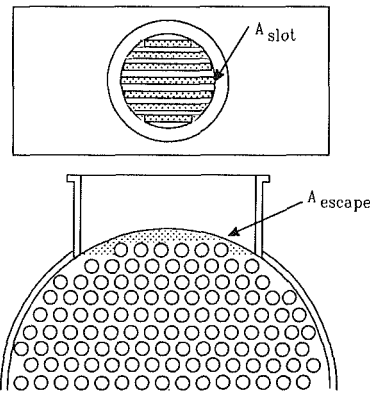


Fig. 5 Sketch of nozzle flow area definitions

$$+ 0.5 \rho (0.75) \left[\frac{(1-F_o)(M_s)}{A_{\text{escape}}} \right] =$$

(bypass stream nozzle flow)

$$\Delta P_{\text{nzo}} = \left[1 - \frac{A_{\text{slot}}}{(A_{\text{nz}})(F_o)} \right]^2 \left[\frac{(F_o)(M_s)}{A_{\text{slot}}} \right]^2 \quad (13)$$

(friction loss for stream exiting bundle)

The stream bypassing the bundle is represented on the left-hand side of equation (13). The first term represents the impingement of the bypass stream on the shell. The second term represents the turning of the stream. The third term represents the expansion from the bypass stream flow area into the escape area. The final term represents the turning of the stream to flow out through the nozzle. The term on the right-hand side of equation (13) represents the pressure loss for the stream exiting the bundle. Notice that the shell fluid density and flow rate can be cancelled in equation (13), leaving an equation which can be solved for F_o in terms that are a function of the shellside geometry only. As with equation (10), equation (13) cannot be solved directly. An iterative technique must be used to solve for the fraction F_o flowing out from the bundle.

As with equation (10), equation (13) gave the proper trends but did not predict the nozzle pressure drop adequately. A correction factor F_{co} , as shown in equation (14), was introduced to increase the accuracy of the predicted pressure drop. The form of the correction factor F_{co} is shown in equation (15). As with equation (12), the constants in equation (15) were determined using regression analysis techniques and were adjusted to give slightly conservative outlet nozzle pressure drops.

$$\Delta P_{\text{nzo}} = \left[1 - \frac{A_{\text{slot}}}{(A_{\text{nz}})(F_o)} \right]^2 \left[\frac{(F_o)(M_s)}{A_{\text{slot}}} \right]^2 F_{co} \quad (14)$$

$$F_{co} = 2.8 \left[\frac{A_{\text{escape}}}{S_m} \right]^{0.06} \left[\frac{S_b}{S_m} \right] \quad (15)$$

The outlet nozzle pressure drops predicted by equation (14) are within plus or minus 30 percent of the back-calculated values from the Argonne data.

Flow Area Calculations for Nozzle Pressure Drop Calculations. During the development of the pressure drop method for the nozzles, it quickly became apparent that it was not possible to develop any correlation with inaccurate flow areas. Initially, several simplifying assumptions were made in the calculation of the flow areas. However, it was not possible to develop a correlation with approximate flow areas. Finally, the drawings of the bundle included in the report by Halle (1983) were consulted. The flow areas were then determined by numerical integration. The definition of the flow areas used in the correlations are indicated in Fig. 5 by shading.

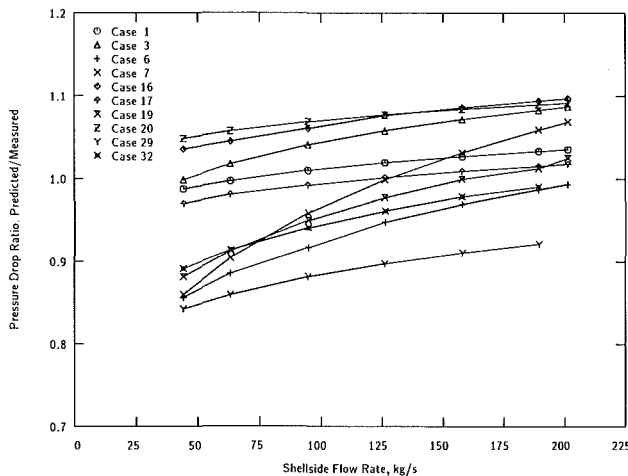


Fig. 6 Nozzle-to-nozzle pressure drop ratios for full bundle with segmental baffles

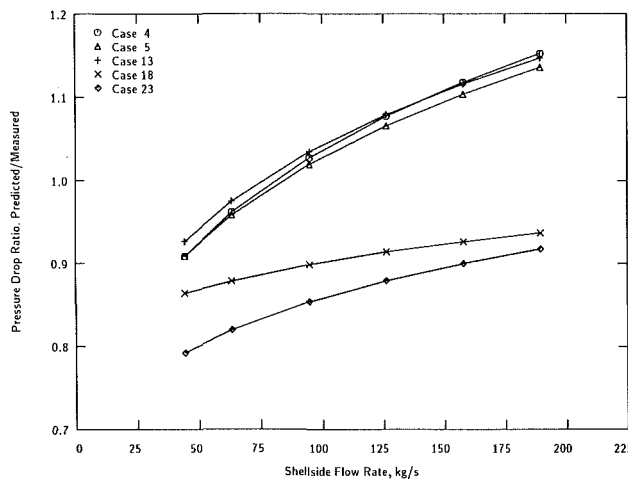


Fig. 7 Bundle pressure drop ratios for no-tubes-in-the-window bundles of plain tubes with segmental baffles

Nozzle-to-Nozzle Pressure Drop Predictions. The overall nozzle-to-nozzle pressure drop predictions are the result of summing the bundle pressure drop and the end zone pressure drops predicted by the HEDH method and the inlet and outlet pressure drops predicted by the methods above. These are normalized with the measured pressure drops and plotted in Fig. 6 versus the flow rate.

Although the predictions of the nozzle pressure drop appear to have considerable scatter, the effect of the predicted nozzle pressure drops on the nozzle-to-nozzle pressure drop is far more important. As can be seen in Fig. 6, the predicted pressure drops are not as good as the bundle pressure drops shown in Fig. 3, but the predictions of the combined methods are still within plus or minus 15 percent. This represents extremely good agreement between the measured and predicted pressure drops. The only exceptions are Cases 27 and 30 with the very small baffle cuts which were not predicted well by the method and so are not included in Fig. 6.

No-Tubes-in-the-Window Bundles With Segmental Baffles

The only recommendation made for no-tubes-in-the-window bundles in the HEDH method is that the pressure drop in the window be approximately equal to two velocity heads based on the longitudinal velocity in the window. It is also stated that the changes necessary in the method are "logical engineering extensions, but should be compared to

data for verification." Further details of the necessary modifications to the method are not given.

No-Tubes-in-the-Window Bundle Pressure Drop for Plain Tubes. In order to adapt the method for no-tubes-in-the-window bundles, several minor changes are required. First, the number of rows crossed in the window will be zero ($N_{tcw} = 0$). Second, the flow area in the window must be modified to reflect the absence of tubes in the window. The final change is to remove the bypass correction, R_b , from the window pressure drop equation. Then the equation for window pressure drop, ΔP_w , is

$$\Delta P_w = N_b(2) \left[\frac{M_w^2}{2 \rho_s} \right] 10^{-3} \quad (16)$$

Since the method predicted the pressure drop from taps C to G correctly for segmental baffles, it is assumed that the crossflow pressure drop, ΔP_c , is correct for no-tubes-in-the-window bundles. Therefore, any difference between the predicted pressure drop and the measured pressure drop is assumed to be due to the window pressure drop. If the bundle bypass correction, R_b , is included in equation (16), the pressure drop from taps C to G is predicted 20 to 45 percent low. However, if the bypass correction is excluded, the predictions are plus or minus 20 percent between taps C and G as shown in Fig. 7. Although this is not as good for full bundles with segmental baffles, the prediction is well within acceptable limits.

A word of caution should be given, however. The no-tubes-in-the-window bundles tested are not typical. They were created by removing the tubes from the baffle windows of bundles originally designed as segmental baffled exchangers and plugging the holes left in the baffles and tubesheets (see Fig. 2). As a result, the baffle cut is considerably larger than usually used for no-tubes-in-the-window bundles. Typically, a baffle cut of 15 to 20 percent would be used for no-tubes-in-the-window bundles in liquid service, rather than the 25 and 29 percent tested. This would result in a window velocity two or three times higher than crossflow. The bundles tested have a window velocity that is less than the crossflow velocity due to the large baffle cut. It may be possible to account for baffle cut variation by basing the velocity heads lost in the window on the actual window velocity. However, this would require additional data for verification.

Bundle Pressure Drop for Finned Tubes. The bundle pressure drop for finned tubes was presented earlier in the section that described the full bundle results. For reference, see Fig. 4 for the ratio of predicted to measured pressure drops. The limited data for Cases 15 and 25 were used to adjust the method for a reasonable fit.

Nozzle Pressure Drop for No-Tubes-in-Window Bundles. The nozzle pressure drops were back-calculated from the data using the same procedure used for segmental baffles. The back-calculated values showed pressure recovery at the inlet and a pressure loss at the outlet. Since this agrees with the expected behavior for the tubeside nozzles (Henry, 1982) a similar approach was tried. The inlet nozzle of a no-tubes-in-the-window bundle is similar to that of the inlet on the tubeside, with an expansion from the inlet nozzle area to the flow area at the baffle tip. Similarly, the outlet is similar to the tubeside outlet with the flow contracting from the flow area at the baffle tip to the area of the nozzle.

The K values for the inlet and outlet nozzles, K_{ent} and K_{ex} , are given in equations (17) and (18), respectively.

$$K_{ent} = \left[1 - \frac{A_{nz}}{A_{baff}} \right]^2 + \left[\frac{A_{nz}}{A_{baff}} \right] - 1 \quad (17)$$

$$K_{ex} = K_c + 1 - \left[\frac{A_{nz}}{A_{baff}} \right] \quad (18)$$

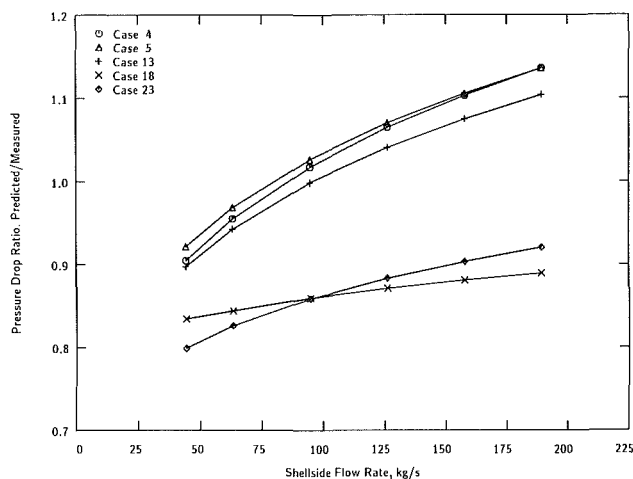


Fig. 8 Nozzle-to-nozzle pressure drop ratios for no-tubes-in-the-window bundle with segmental baffles

The contraction coefficient, K_c , curve presented graphically in the Crane Technical Paper was fit with a polynomial.

$$K_c = 0.570 + 0.0139 \left[\frac{A_{nz}}{A_{baff}} \right] - 1.463 \left[\frac{A_{nz}}{A_{baff}} \right]^2 + 0.868 \left[\frac{A_{nz}}{A_{baff}} \right]^3 \quad (19)$$

The pressure drop in the inlet and outlet nozzles is then calculated by multiplying the K value determined by equation (17) or (18) by the velocity head based on the velocity in the inlet or outlet nozzle, respectively. Although the calculation of the nozzle flow area, A_{nz} , is straightforward, the calculation of the flow area at the baffle tip, A_{baff} , requires an explanation. It was determined by consulting the drawings of the bundle included with the report by Halle and Wambsganss (1983). The number of tubes in the row at the baffle tip was first determined from the drawing of the bundle. This determined the number of tube gaps along the baffle, and, therefore, the area in the slots between the baffles. To this area, the area between the outside tube row on each side of the shell was added. Therefore, the area A_{baff} represents the nominal flow area at the baffle tip.

These relationships assumed that the flow in the nozzle is turbulent, and that the exit nozzle may be treated as a sharp-edged exit. The reader is referred to Henry (1982) for further details.

Nozzle-to-Nozzle Pressure Drop Predictions for No-Tubes-in-Window Bundles. The overall nozzle-to-nozzle pressure drop predictions are the result of summing the bundle pressure drop and the end zone pressure drops predicted by the method and the inlet and outlet pressure drops predicted by the methods above. These are normalized with respect to the measured pressure drops and plotted in Fig. 8 versus the flow rate. The trends are approximately the same as for the bundle pressure drop shown in Fig. 7. The overall pressure drops are predicted within plus or minus 20 percent.

Conclusions and Recommendations

The pressure drop data from Argonne have been used to evaluate the HEDH method (Taborek, 1982) for predicting shellside pressure drop in shell-and-tube heat exchangers. The evaluations of the method with the data were possible with the writing of programs for a microcomputer. The following conclusions and recommendations can be made when the extensions to the method developed in this paper have been made

for nozzles and finned tubes for full bundles and no-tubes-in-window bundles with segmental baffles:

- The method for full bundles with segmental baffles predicts the Argonne bundle pressure drop data well for typically designed bundles. However, if the window flow area is considerably less than the crossflow area, the method underpredicts the pressure drop, and should be used with extreme caution. Addition of a window acceleration pressure drop to the method should be considered by the author of the method.
- The recommendations in the method for low-finned tubes underpredicted the Argonne pressure drop data by up to 30 percent, and should be used with caution. Recommendations made in this paper to increase the crossflow pressure drop multiplying factor from 1.4 to 2.0 and introduce a window pressure drop multiplying factor of 1.3 dramatically improve the predictions. However, the changes should be used with caution, as they are based on only four cases, all with the same baffle cut and baffle spacing.
- The modifications presented in this paper extend the method presented in HEDH to predict the pressure drop for no-tubes-in-the-window bundles with segmental baffles. With the modifications, the shellside pressure drop data are predicted within plus or minus 10 percent. However, the geometry of the bundles tested is not typical, as the baffle cut is larger than would typically be used in liquid service. With a small baffle cut, the method would underpredict the shellside pressure drop.
- The two simplified models developed in this paper for nozzle pressure drop with either full bundles with segmental baffles or no-tubes-in-the-window bundles predict well the nozzle pressure drop for the Argonne data. However, the reader is cautioned about the following items:

- 1 The methods were developed using data from isothermal tests with water. The methods have not been tested for compressible fluids, two-phase mixtures, or liquids other than water.
- 2 The methods are limited to bundles with baffle cuts perpendicular to the center line of the nozzle. They will most probably require modifications before they work well for bundles with the baffle cuts parallel to the center line of the nozzles.
- 3 The modifications presented complement the HEDH method for prediction of shellside pressure drop. They should not be expected to work if another method is used.
- 4 Accurate flow areas were found to be essential for successful pressure drop predictions. These should be determined from drawings of the bundle if at all possible. Approximations of the slot area below the nozzle (A_{slot}) and the escape area (A_{escape}) were tried and failed to produce satisfactory estimations of the nozzle pressure drops with the methods described in this paper.

Acknowledgments

The authors wish to acknowledge the careful experimental studies conducted in the Components Technology Laboratory at Argonne National Laboratory by Henry Halle and Martin Wambsganss, who provided the basic data that made this study possible. No HTRI proprietary information has been used and the developed relationships and equations do not reflect HTRI recommendations. Permission by the Management of HTRI to publish the results of this independent study is greatly appreciated by the authors. Further, the authors wish to thank Jerry Taborek for providing us with insights into HEDH pressure drop method, the starting point for this study.

References

- Bell, K. J., 1963, "Final Report of the Cooperative Research Program on Shell and Tube Heat Exchangers," Bulletin No. 5, University of Delaware Engineering Experiment Station, Newark, DE.
- Crane Company, 1969, "Flow of Fluids Through Valves, Fittings, and Pipe," Technical Paper No. 410, Crane Company, New York.
- Halle, H., 1983, Personal correspondence.
- Halle, H., Chenoweth, J. M., and Wambsganss, M. W., 1984, "Shellside Waterflow Pressure Drop Distribution Measurements in an Industrial-Sized Test Heat Exchanger," *A Reappraisal of Shellside Flow in Heat Exchangers*, HTD Vol. 36, pp. 37-48.
- Halle, H., and Wambsganss, M. W., 1983, "Shellside Waterflow Pressure Drop and Distribution in Industrial Size Test Heat Exchanger," Report ANL-83-9, Argonne National Laboratory, Argonne, IL.
- Heat Transfer Research, Inc. (HTRI), 1965, "Shell-and-Tube Heat Exchangers," Movie HTRI-1, Heat Transfer Research, Inc., Alhambra, CA (36-minute color and sound movie).
- Henry, J. A. R., 1982, "Headers, Nozzles, and Turnarounds," *Heat Exchanger Design Handbook*, Hemisphere, New York, Section 2.2.7.
- Palen, J. W., and Taborek, J., 1969, "Solution of Shell Side Flow Pressure Drop and Heat Transfer by Stream Analysis Method," *Chemical Engineering Progress Symposium Series*, Vol. 65, No. 92, pp. 53-63.
- Taborek, J., 1982, "Shell-and-Tube Heat Exchangers: Single-Phase Flow," *Heat Exchanger Design Handbook*, Hemisphere, New York, Section 3.3.
- Tinker, T., 1952, "Shell Side Characteristics of Shell and Tube Heat Exchangers, Parts, I, II, and III," *Proceedings of the General Discussion on Heat Transfer*, Institution of Mechanical Engineers and American Society of Mechanical Engineers, London, pp. 89-116.
- Tubular Exchanger Manufacturers Association (TEMA), 1978, "Standards of Tubular Exchanger Manufacturers Association," 6th ed., The Tubular Exchanger Manufacturers Association, Inc., New York.

The Effect of Condensible Impurities in the Working Fluid on the Performance of Cryogenic Regenerators

R. K. Sahoo

Department of Mechanical Engineering,
Regional Engineering College,
Rourkela—769 008, India

S. Sarangi

Cryogenic Engineering Centre,
Indian Institute of Technology,
Kharagpur—721302, India

In many cryogenic regenerator applications the working fluid contains a small quantity of condensible impurity, which undergoes condensation/evaporation along its sublimation curve due to pressure cycling. The governing differential equations for such a system have been formulated in terms of conventional dimensionless parameters. Numerical solution of these equations is presented for several combinations of fluid flow parameters using nitrogen as the working fluid and carbon dioxide as the impurity. The model indicates that: (a) as long as there is no net accumulation of frost a higher pressure ratio has a negligible effect on the thermal performance of the regenerator; (b) a larger reduced period affects the thermal performance of the regenerator in the presence of a condensible impurity to a greater extent than in the absence of it; (c) the matrix temperature profile undergoes a much larger swing in the presence of a condensible component; and (d) since the exit impurity concentration is a function of reduced length, reduced period, and inlet composition, arbitrarily chosen regenerator parameters cannot be used to purify a warm process stream.

Introduction

Regenerator-based compact cryorefrigerators with various operating cycles are becoming increasingly popular for production of low temperatures. Due to their superior effectiveness, compactness, and economy compared to recuperative heat exchangers, they have also replaced the latter in many process applications. In addition to these, one of the major advantages of the regenerator is that it is relatively insensitive to plugging by condensible impurities. Hence a regenerator can be used not only as an efficient and compact exchanger of sensible heat but also for the exchange of mass between two streams under certain conditions. Small amounts of a condensible component in the hot process stream will condense on the matrix surface, and will be picked up by the dry return stream. If the pressure ratio between the two streams is sufficiently high the quantity condensed during the hot blow period will be fully evaporated during the cold blow period, permitting continuous cyclic operation of the regenerator. This is possible because at reduced pressure the specific volume of the fluid is high even at a slightly lower temperature of the return stream, and it can contain a larger fraction of the condensible component at the latter's saturation vapor pressure. Hence, as far as mass transfer is concerned the unit acts as a short cycled pressure swing gas adsorption unit where the impurity is adsorbed at high pressure and desorbed at low pressure in the presence of a revert gas, which may be all or part of the purified gas stream.

This mechanism can be used: (a) for the purification of a high-pressure process stream where the revert gas is composed of another low-pressure waste gas, (b) in open-cycle refrigeration/liquefaction systems where the simultaneous heat exchange and purification of the high-pressure stream is achieved before the fluid enters the expansion machinery, and (c) in closed-cycle refrigeration systems where undesirable impurities in the working fluid are frozen out before entering the critical stage heat exchangers.

The presence of condensible components in the working

fluid, however, can adversely affect the thermal performance of regenerator: (a) by adding an additional heat load associated with the latent heat of the condensible components; (b) by reducing the local heat transfer coefficient due to the deposition of frost on the matrix surface; and (c) by blocking the passages and thus increasing the pressure drop.

In this paper, only the first of the above three effects, i.e., thermal performance deterioration due to the additional heat load of the condensible component, has been investigated theoretically. The revert gas constitutes the whole of the purified gas stream resulting in a balanced operation of the regenerator. Based on the above facts the governing differential equations and boundary conditions are developed in terms of the reduced length Λ , reduced period Π , and other relevant parameters [1, 2]. Numerical solution of these equations for a particular system consisting of nitrogen as the working fluid and carbon dioxide as the impurity illustrates the role of the condensation/evaporation process.

Heat transfer in rotary heat exchangers has been analyzed by several authors in connection with gas turbine regenerator applications. Holmberg [3] and van Leersum and Ambrose [4] have analyzed the heat and moisture recovery in a rotary regenerator used in air conditioning applications. Holmberg's formulation also provides for both liquid and solid condensates with two latent heats. In this analysis, it has been felt unnecessary for low impurity concentration and for a cryogenic environment to include the liquid phase. Hence, the phase transformation takes place only across the sublimation line.

Governing Equations

An idealized model of the regenerator, first proposed by Schumann [5], is considered, the only exception being the presence of a condensible component in the working fluid. It is further assumed that evaporation and condensation of the impurity are strictly controlled by the matrix temperature.

The governing partial differential equations can be derived by considering the conservation of mass and energy over a differential control volume (Fig. 1) along with relevant transport equations.

Contributed by the Heat Transfer Division for publication in the JOURNAL OF HEAT TRANSFER. Manuscript received by the Heat Transfer Division August 5, 1985.

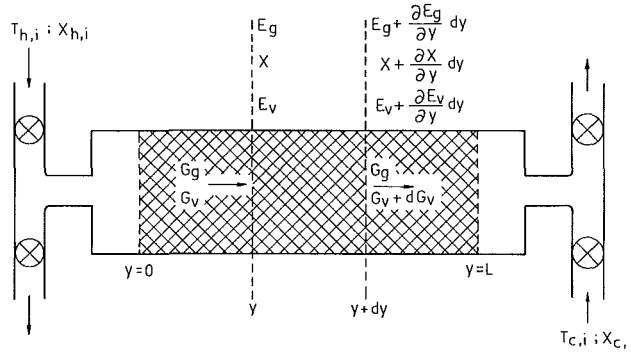


Fig. 1 Mass and energy balance over a differential control volume of the regenerator

The energy balance for the fluid (gas + vapor) is

$$\frac{\partial}{\partial y} (G_g E_g + G_v E_v) + \frac{\partial}{\partial t} \{ F(\rho_g U_g + \rho_v U_v) \} + hA(T_g - T_m) + \rho_g h_x A (X_{sat} - X) E_v = 0 \quad (1)$$

where y = length coordinate along the axis of the regenerator; t = time coordinate; G = fluid (gas or vapor) mass velocity; E = enthalpy of the fluid (gas or vapor); U = internal energy of the fluid (gas or vapor); ρ = density of fluid (gas or vapor), matrix or frost; A = heat/mass transfer area per unit volume of the matrix; T = temperature; h = heat transfer coefficient; X = impurity mass concentration; and the subscripts m, g, v , and s refer to the matrix, gas, vapor, and frost, respectively. ρ_g and ρ_v refer to the true density of the gas and vapor, respectively, whereas ρ_m and ρ_s refer to the densities of the matrix and frost with respect to the total matrix volume.

In equation (1) the first term refers to the difference between inlet and exit enthalpy flow rates, the second term is the time rate of change of internal energy in the control volume,

the third term is the heat transfer to the matrix, and the last term refers to the energy transfer associated with condensation/evaporation of the minor component.

The energy balance for matrix with frost is

$$\rho_m C_m \frac{\partial T_m}{\partial t} + \frac{\partial}{\partial t} (\rho_s U_s) + hA(T_m - T_g) - \rho_g h_x A (X_{sat} - X) E_v = 0 \quad (2)$$

The mass balance for the condensate only is

$$\frac{\partial \rho_s}{\partial t} + \rho_g h_x A (X_{sat} - X) = 0 \quad (3)$$

The mass balance for condensible species (vapor + condensate) is

$$\frac{\partial G_v}{\partial y} + F \frac{\partial \rho_v}{\partial t} + \frac{\partial \rho_s}{\partial t} = 0 \quad (4)$$

Equations (1)–(4) are the basic governing equations of a regenerator in the presence of a condensible component in the working fluid. They can be further simplified in the following manner.

By neglecting the change of mass and internal energy of the gas and vapor contained within the regenerator and by using equations (3) and (4) and the constant fluid property criterion ($dE = C_p dT$), equation (1) reduces to

$$G_g C_{p,g} \frac{\partial T_g}{\partial y} + G_v C_{p,v} \frac{\partial T_g}{\partial y} + hA(T_g - T_m) = 0 \quad (5)$$

Similarly, by combining equations (2)–(4) and neglecting terms containing $\rho_s C_s / \rho_m C_m$ and $\partial \rho_v / \partial t$, we get

$$\rho_m C_m \frac{\partial T_m}{\partial t} + hA(T_m - T_g) + r \frac{\partial G_v}{\partial y} = 0 \quad (6)$$

where $r = E_v - U_s$ is the latent heat of vaporization of the impurity; the energy change of the impurity vapor during its

Nomenclature

A = heat/mass transfer area per unit volume, m^2/m^3
 a_{1-3} = intermediate variables defined in appendix
 $A_{1,2}$ = intermediate variables defined in appendix
 B_{1-5} = intermediate variables defined in appendix
 b = intermediate variable defined in appendix
 c = intermediate variable defined in appendix
 $C_{1,2}$ = specific heat, J/kg K
 C_p = specific heat at constant pressure, J/kg K
 $C_{1,2}$ = intermediate variables defined in appendix
 D_{1-4} = intermediate variables defined in appendix
 E = enthalpy, J/kg
 \bar{E} = mean exit enthalpy, J/kg
 F = void fraction in the matrix
 f, g = grid indices during cold blow period
 G = fluid mass velocity, kg/m^2s
 h = heat transfer coefficient, W/m^2K

h_x = mass transfer coefficient, s^{-1}
 i, j = grid indices during hot blow period
 K_{1-4} = intermediate variables defined in appendix
 L = length of the regenerator
 M = molecular weight
 $N, N_{1,2,3}$ = number of grid divisions
 Le = Lewis number
 P = total period of a cycle, s
 pr = pressure
 r = latent heat of condensation/evaporation, J/kg
 $r_1 = r/C_{p,g}$, K
 S = dimensionless density of frost = $2\rho_s L/G_g P$
 t = time, s
 T = temperature, K
 \bar{T} = mean exit temperature, K
 U = internal energy, J/kg
 X = impurity mass concentration
 y = distance coordinate, m
 z = dimensionless distance coordinate = y/L
 α = specific heat ratio = $C_{p,v}/C_{p,g}$

ϵ = effectiveness
 θ = integer part of temperature T , K
 Λ = reduced length = $hAL/G_g C_p$
 Π = reduced period = $hAP/2\rho_m C_m$
 ρ = density, kg/m^3
 σ = constant used in convergence criterion
 τ = dimensionless time coordinate = $2t/P$
 $\phi_j, \bar{\phi}$ = dummy variables

Subscripts

av = average
 c = cold
 E = enthalpy
 g = working fluid
 h = hot
 i = inlet
 m = matrix
 o = outlet
 s = solid or frost
 sat = saturation
 T = temperature
 v = vapor
 x = impurity

transport across the boundary layer is negligible. By neglecting $\partial\rho_v/\partial t$ terms, equations (3) and (4) reduce to

$$\frac{\partial\rho_s}{\partial t} + \rho_g h_x A (X_{\text{sat}} - X) = 0 \quad (7)$$

and

$$\frac{\partial G_v}{\partial y} + \frac{\partial\rho_s}{\partial t} = 0 \quad (8)$$

The following dimensionless parameters are defined to reduce equations (5)–(8) to dimensionless form

$$\alpha = \frac{C_{p,v}}{C_{p,g}}, \quad X = \frac{G_v}{G_g} = \frac{\rho_v}{\rho_g}, \quad z = \frac{y}{L},$$

$$\tau = \frac{2t}{P}, \quad S = \frac{2\rho_s L}{G_g P}$$

Also, from the Lewis relation the heat and mass transfer coefficients are related as

$$\text{Le} = \frac{h}{\rho_g h_x C_{p,g}}$$

The saturation mass fraction X_{sat} is computed from the saturation vapor pressure pr_{sat} by the relation

$$X_{\text{sat}} = \frac{M_v}{M_g} \frac{pr_{\text{sat}}}{pr_g}$$

where M_g and M_v are the molecular weights of gas and vapor, respectively. The saturation vapor pressure pr_{sat} for various gases is normally available in literature as a function of temperature.

The governing equations (5)–(8) can be expressed in terms of the above dimensionless parameters as

$$\frac{\partial T_g}{\partial z} = \frac{\Lambda}{1 + \alpha X} (T_m - T_g) \quad (9)$$

$$\frac{\partial T_m}{\partial \tau} = -(1 + \alpha X) \frac{\Pi}{\Lambda} \frac{\partial T_g}{\partial z} - r_1 \frac{\Pi}{\text{Le}} (X_{\text{sat}} - X) \quad (10)$$

$$\frac{\partial S}{\partial \tau} = -\frac{\Lambda}{\text{Le}} (X_{\text{sat}} - X) \quad (11)$$

and

$$\frac{\partial X}{\partial z} = -\frac{\partial S}{\partial \tau} \quad (12)$$

where $r_1 = r/C_{p,g}$ has the dimension of temperature.

The term $(1 + \alpha X)$ in equations (9) and (10) accounts for the increase in mass flow rate of the fluid due to the vapor over that of dry gas. This term is close to unity for small impurity concentrations. Still, determination of X at every point in the innermost loop of the computer program significantly increases the computation time. Therefore this term may be replaced by a constant $(1 + \alpha X_{av})$, where $X_{av} = (X_{h,i} + X_{c,i})/2$, in all calculations, without introducing significant error. Equations (9)–(12) can now be expressed in a form suitable for numerical solution.

Equations (9)–(12) are the governing differential equations for hot and cold blow periods. The boundary, initial and cyclic conditions may be stated as follows:

Boundary conditions:

$$T_g(\tau, z=0) = T_{h,i} \quad \text{for } 0 < \tau \leq 1.0$$

$$X(\tau, z=0) = X_{h,i} \quad \text{for } 0 < \tau \leq 1.0$$

$$T_g(\tau, z=1) = T_{c,i} \quad \text{for } 1.0 < \tau \leq 2.0$$

and

$$X(\tau, z=1) = X_{c,i} \quad \text{for } 1.0 < \tau \leq 2.0$$

Initial condition:

$$S(\tau=0, z)=0$$

This is true for all cycles if there is complete scavenging of the condensible component. If complete scavenging is not taking place this condition is valid only for the first cycle when impurity is added to an otherwise steady-state system.

Cyclic condition:

$$T_m(\tau, z) = T_m(\tau + 2, z)$$

$$S(\tau, z) = S(\tau + 2, z)$$

Governing equations for the case of sensible heat transfer alone may be deduced from equations (9)–(12) by dropping the terms related to mass transfer. The resulting equations are the same as those already available in the literature for dry working fluids.

Numerical Scheme

The numerical scheme used in this paper is similar to that of Holmberg [3] and van Leersum and Ambrose [4], which, in turn, is a modification of Lambertson's [6] scheme for a sensible heat regenerator. The spatial and temporal grid arrays for the numerical solution are given in Fig. 2.

Using standard representation of the variables and the derivatives equations (9)–(12) may be written in a finite difference form

$$T_g(i+1, j) = A_1 T_g(i, j) + A_2 \{T_m(i, j) + T_m(i, j+1)\} \quad (13)$$

$$T_m(i, j+1) = B_1 T_g(i, j) + B_2 T_m(i, j) + B_3 X(i, j) + B_4 \{X_{\text{sat}}(i, j) + X_{\text{sat}}(i, j+1)\} \quad (14)$$

$$S(i, j+1) = S(i, j) + C_1 X(i, j) + C_2 \{X_{\text{sat}}(i, j) + X_{\text{sat}}(i, j+1)\} \quad (15)$$

$$X(i+1, j) = X(i, j) + c \{S(i, j) - S(i, j+1)\} \quad (16)$$

The coefficients A , B , and C are given in the appendix. Simultaneous solution of the set of equations (13)–(16) gives T_g , T_m , S , and X at all values of position and time.

The saturation concentration of vapor $X_{\text{sat}}(i, j)$ is a function only of the matrix temperature $T_m(i, j)$. This makes equation (14) an implicit equation and an iterative loop is re-

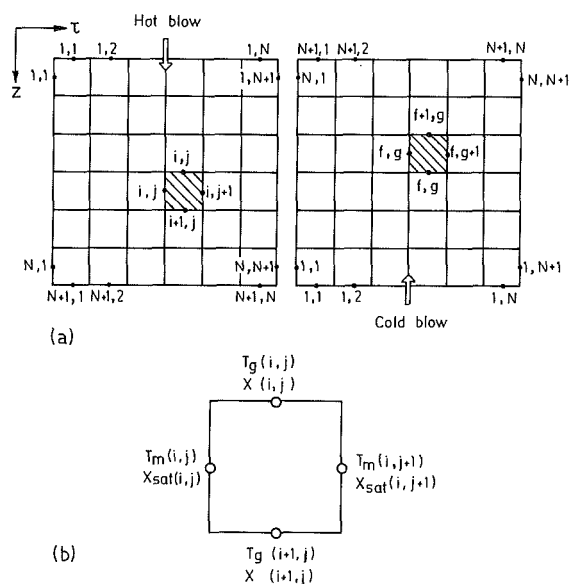


Fig. 2 (a) Grid array for numerical solution; (b) a typical grid element

quired to calculate the values of T_m and X_{sat} simultaneously at the same grid location (i, j) . This calculation in the innermost loop of the program needs a large amount of computing. The following method results in considerable saving in computing time.

The saturation vapor pressure data are stored as an array whose θ th element gives the saturation concentration at a temperature θ K, θ being an integer. So X_{sat} at a matrix temperature T_m can be written as:

$$X_{\text{sat}}(i, j) = X_{\text{sat}}\{\theta_m(i, j)\} + \{X_{\text{sat}}(\theta_m(i, j+1)) - X_{\text{sat}}(\theta_m(i, j))\} \cdot \{T_m(i, j) - \theta_m(i, j)\} \quad (17)$$

$\theta_m(i, j)$ is the integer part of the matrix temperature $T_m(i, j)$. Using equation (17), equation (14) can be written as

$$\begin{aligned} T_m(i, j+1) = & D_1 T_g(i, j) + D_2 T_m(i, j) + D_3 X(i, j) \\ & + D_4 X_{\text{sat}}(\theta_m(i, j)) + D_4 [\{X_{\text{sat}}(\theta_m(i, j+1)) - X_{\text{sat}}(\theta_m(i, j))\} \cdot \{T_m(i, j) - \theta_m(i, j)\} \\ & + X_{\text{sat}}(\theta_m(i, j+1)) - \{X_{\text{sat}}(\theta_m(i, j+1)) + 1\} \\ & - X_{\text{sat}}(\theta_m(i, j+1))\} \cdot \theta_m(i, j+1)] \quad (18) \end{aligned}$$

where D_1 through D_4 are a set of constants defined in the appendix.

Equation (18) still requires an iterative process to determine $\theta_m(i, j+1)$, but θ_m has to converge only within 1 K which requires about 1 cycle.

The above equations (18), (13), (15), and (16) are the finite difference equations for the estimation of matrix temperature, gas temperature, solid (frost) density, and impurity concentration, respectively. However, under certain constraints the equations may be slightly altered. Two constraints that must be observed are that: (a) the amount of frost on the matrix cannot be negative and (b) the impurity concentration in the fluid cannot be negative.

(a) Negative Frost Density on Matrix. During the evaporation process, if $S(i, j)$ is already small, application of equation (15) may result in $S(i, j+1) < 0$, which is physically impossible. In this case $S(i, j+1)$ is set equal to zero. For this step equations (18), (15), and (16) are modified as

$$T_m(i, j+1) = B_1 T_g(i, j) + B_2 T_m(i, j) - \frac{B_4}{C_2} S(i, j) \quad (18a)$$

$$S(i, j+1) = 0 \quad (15a)$$

$$X(i+1, j) = X(i, j) + c S(i, j) \quad (16a)$$

Equation (13) for the fluid temperature remains unchanged.

(b) Negative Impurity Concentration in Fluid. During a condensation process, particularly when the grid size is large (small value of N) it may happen that $X(i+1, j)$ computed from equation (16) becomes negative, which is absurd. In this case $X(i+1, j)$ is set equal to zero. For this step equations (18), (15), and (16) are modified as

$$T_m(i, j+1) = B_1 T_g(i, j) + B_2 T_m(i, j) + \left(B_3 + \frac{B_4(1-cC_1)}{cC_2}\right) X(i, j) \quad (18b)$$

$$S(i, j+1) = S(i, j) + X(i, j)/c \quad (15b)$$

$$X(i+1, j) = 0 \quad (16b)$$

Equation (13) for fluid temperature remains unchanged.

The boundary and cyclic conditions expressed in numerical form are as follows. For the hot blow period

$$\begin{aligned} T_g(1, j) &= T_{h,i}, & j &= 1, 2, \dots, N \\ X(1, j) &= X_{h,i}, & j &= 1, 2, \dots, N \\ S(i, 1) &= S(f, N+1) = 0, & i &= 1, 2, \dots, N \\ & & & \text{and } f = N+1-i \\ T_m(i, 1) &= T_m(f, N+1), & i &= 1, 2, \dots, N \\ & & & \text{and } f = N+1-i \end{aligned}$$

For cold blow period

$$\begin{aligned} T_g(1, g) &= T_{c,i}, & g &= 1, 2, \dots, N \\ X(1, g) &= X_{c,i}, & g &= 1, 2, \dots, N \\ S(f, 1) &= S(i, N+1), & f &= 1, 2, \dots, N \\ & & & \text{and } i = N+1-f \\ T_m(f, 1) &= T_m(i, N+1), & f &= 1, 2, \dots, N \\ & & & \text{and } i = N+1-f \end{aligned}$$

i, j are grid indices in distance and time coordinates, respectively, in the hot blow period and f, g are the corresponding indices in the cold blow period.

Solution Procedure

The solution procedure to the numerical equations is similar to that given in [7]. Starting with an arbitrary initial matrix temperature profile the case of "dry working fluid" is solved. When a cyclically steady temperature condition is reached, the matrix temperature profile at the end of a cold blow period serves as the corresponding initial condition for the case of condensible impurities. The solution procedure in the latter case is also similar to that for the dry working fluid except for the additional variables, equations, and constraints. The convergence criterion for ensuring a cyclically steady condition is based upon the average exit enthalpy

$$\frac{(\bar{E}_{h,o})_k - (\bar{E}_{h,o})_{k-1}}{(\bar{E}_{h,o})_k - (\bar{E}_{c,o})_k} \leq \sigma \quad (19a)$$

$$\frac{(\bar{E}_{c,o})_k - (\bar{E}_{c,o})_{k-1}}{(\bar{E}_{h,o})_k - (\bar{E}_{c,o})_k} \leq \sigma \quad (19b)$$

σ is the convergence parameter (taken as 0.001 in this analysis), and the subscript k refers to the k th cycle. Following Willmott [8], the mean parameters (temperature, enthalpy, or concentration) over a half cycle are determined, using the Gregory formula

$$\begin{aligned} \bar{\phi} = & \frac{1}{(N-1)} \left\{ \frac{1}{2} \phi_1 + \sum_{j=2}^{N-1} \phi_j + \frac{1}{2} \phi_N \right. \\ & - \frac{1}{12} (\nabla \phi_N - \Delta \phi_1) - \frac{1}{24} (\nabla^2 \phi_N + \Delta^2 \phi_1) \\ & \left. - \frac{19}{120} (\nabla^3 \phi_N - \Delta^3 \phi_1) \right\} \end{aligned}$$

where ϕ refers to the variables $T_g(N+1, j)$, $E(N+1, j)$, or $X(N+1, j)$. Δ and ∇ are the forward and backward differences, respectively.

The grid size in both space and time coordinates must be chosen to minimize the computing time needed, still maintaining the required precision. At the beginning a rather coarse grid is chosen. When the solution converges a new grid size is chosen that is half the previous value. The initial condition for the new grid size is determined by linear interpolation between the values obtained for the previous grid size. After a convergent solution is obtained for at least three grid sizes and the

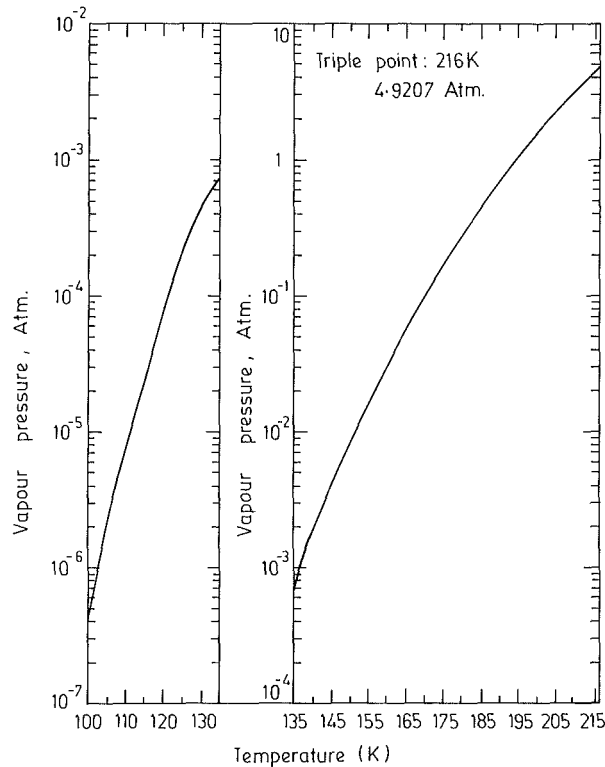


Fig. 3 Vapor pressure of carbon dioxide from 100 K to 216 K [10, 11]

difference between the last two effectiveness values is less than 0.001, the results are extrapolated to zero grid size by the following formula [9]:

$$\epsilon = \frac{\frac{N_1 - N_2}{N_3} \epsilon_3 + \frac{N_2 - N_3}{N_1} \epsilon_1 + \frac{N_3 - N_1}{N_2} \epsilon_2}{\frac{N_1 - N_2}{N_3} + \frac{N_2 - N_3}{N_1} + \frac{N_3 - N_1}{N_2}}$$

$N_{1,2,3}$ are the numbers of division in the z and τ axes for the three grid sizes. In this analysis the grid sizes on both the z and τ axes have always been taken as equal to each other.

Results

A regenerator is normally characterized by an effectiveness ϵ_E which is the ratio of the true time-averaged enthalpy change of the fluid to the maximum possible enthalpy change. For convenience another effectiveness ϵ_T based on the time-averaged exit temperature is sometimes used. In the presence of a condensible component in the working fluid, apart from the effectiveness ϵ_E and ϵ_T , there is an additional effectiveness ϵ_X which is based upon the time-averaged concentration at the exit

$$\epsilon_{X,h} = \frac{1}{P} \int_0^P \frac{X_{h,i} - X_{h,o}}{X_{h,i} - X_{c,i}} dt$$

and

$$X_{c,c} = \frac{1}{P} \int_P^{2P} \frac{X_{c,o} - X_{c,i}}{X_{h,i} - X_{c,i}} dt$$

In case of complete scavenging of frost, i.e., if no net mass deposition occurs, the two terms $\epsilon_{X,h}$ and $\epsilon_{X,c}$ are equal. Numerical equations developed in the last section were solved to obtain these three effectivenesses for several input parameters with nitrogen as the working fluid and carbon

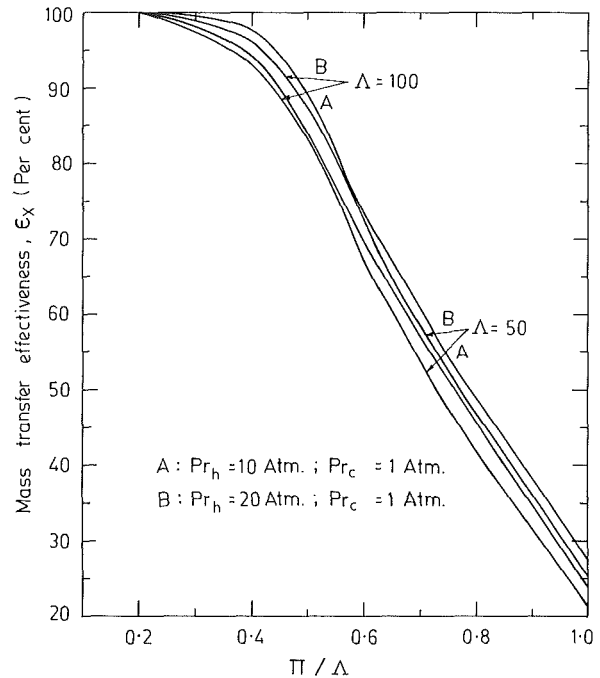


Fig. 4 Mass transfer effectiveness ϵ_X shown versus Π/Λ for $\Lambda = 50$ and 100 and for pressure ratio = 10 and 20. The inlet conditions are: $T_{h,i} = 300$ K, $T_{c,i} = 100$ K, $X_{h,i} = 0.10$, and $X_{c,i} = 0.00$

dioxide as the impurity. The vapor pressure data for CO_2 were taken from [10, 11] and are shown graphically in Fig. 3. The other physical parameters for the fluid systems are

$$\alpha = C_p(\text{CO}_2)/C_p(\text{N}_2) = 0.81$$

$$r_1 = r(\text{CO}_2)/C_p(\text{N}_2) = 300 \text{ K}$$

$$M_{\text{CO}_2}/M_{\text{N}_2} = 1.57 \text{ and } \text{Le} = 1.0$$

where r , C_p , and M refer to the latent heat of vaporization, specific heat, and molecular weight, respectively. The other input parameters are: temperature range: $T_{h,i} = 300$ K and $T_{c,i} = 100$ K; pressure range; $pr_h = 20$ atm, 10 atm, and $pr_c = 1$ atm.

It is observed from Fig. 4 that as long as a particular pressure ratio is sufficient to prevent the net deposition of frost, a higher pressure ratio has a negligible effect on the performance of the regenerator. Hence, in subsequent figures the results for pressure ratio 20 have been omitted.

Figures 5 and 6 show that the thermal effectiveness drops rapidly with reduced period. It is also true in the absence of impurities, but then the effect is much less pronounced. This is due to the additional heat load caused by the release of latent heat on condensation of the impurities and its absorption on evaporation, the quantity of heat increasing with duration. The matrix temperature profiles at the end of hot and cold blow periods are shown in Figs. 7 and 8 for different combinations of operating parameters. These are significantly different from their counterparts without condensation or evaporation. This is particularly so for the hot blow period and for large values of reduced period II. The condensing and later re-evaporating vapor creates some kind of isothermalizing effect, such that the temperature remains nearly constant in a particular section of the bed.

This observation is further supported by the concentration profiles shown in Fig. 9. At low values of Π , where ϵ_X approaches unity, the impurity concentration is always low, indicating complete drying. But at later times the matrix temperature rises, the frost re-evaporates and the exit gas con-

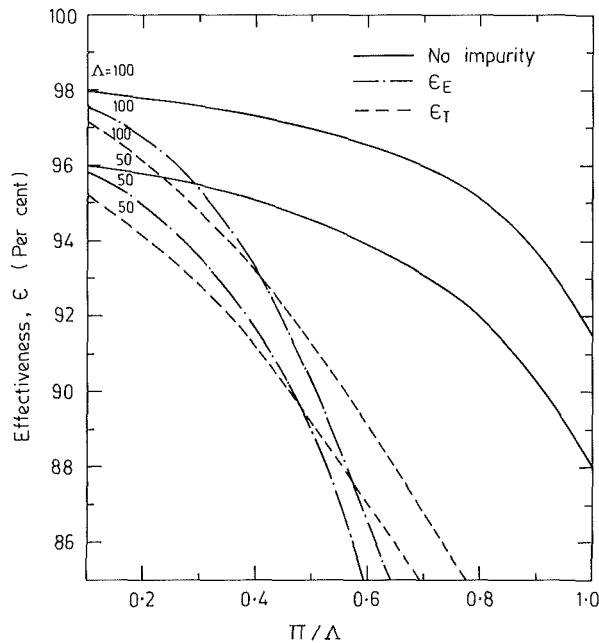


Fig. 5 Enthalpy and temperature effectivenesses ϵ_E and ϵ_T shown versus Π/Λ for $\Lambda = 50$ and 100 are compared with the case of no condensible impurity; $T_{h,i} = 300$ K, $T_{c,i} = 100$ K, $X_{h,i} = 0.10$, $X_{c,i} = 0.00$, $pr_h = 10$ atm, and $pr_c = 1$ atm

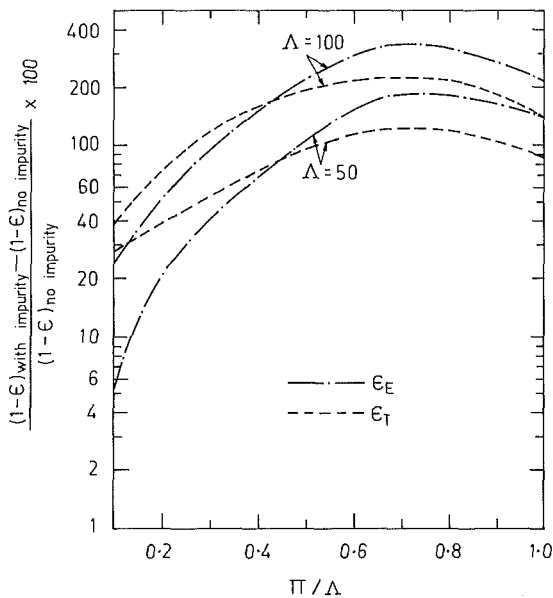


Fig. 6 Relative change of enthalpy and temperature ineffectivenesses shown versus Π/Λ ; $T_{h,i} = 300$ K, $T_{c,i} = 100$ K, $X_{h,i} = 0.10$, $X_{c,i} = 0.00$, $pr_h = 10$ atm, and $pr_c = 1$ atm

tains significant amount of vapor. Hence, if a regenerator has to be used to purify a warm process stream, the reduced period cannot be arbitrarily large.

There is a scarcity of experimental or empirical data on this subject, with which our results could be compared. Results with very small inlet concentration (approaching zero) agree with calculations of Bahnke and Howard in the absence of impurities [12]. Although calculations have been made for the specific case of the N_2/CO_2 system and computed results have been presented only for a few combinations of parameters, the theory and numerical procedures are sufficiently general to be applicable to any other similar system. Detailed programs have been given in [13].

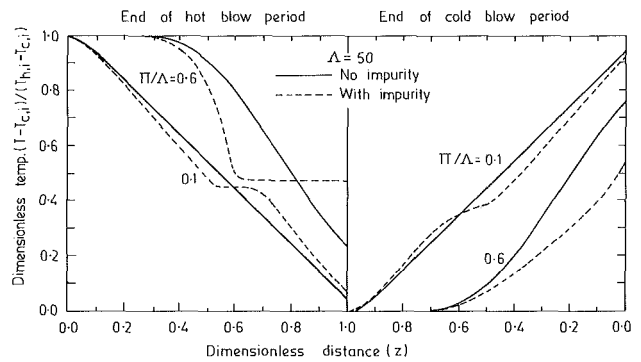


Fig. 7 Dimensionless matrix temperature profiles at the end of hot and cold blow periods are shown with and without impurity; $T_{h,i} = 300$ K, $T_{c,i} = 100$ K, $X_{h,i} = 0.10$, $X_{c,i} = 0.00$, $pr_h = 10$ atm, $pr_c = 1$ atm and $\Lambda = 50$

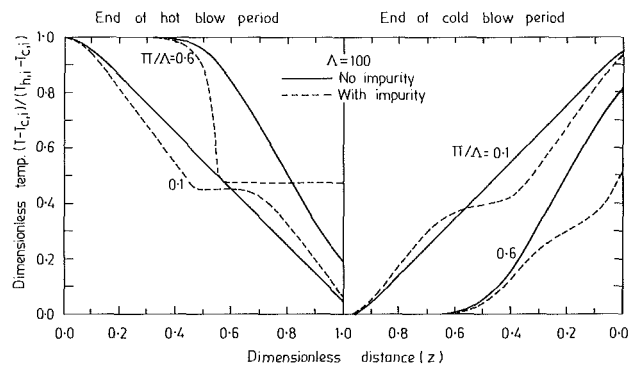


Fig. 8 Dimensionless matrix temperature profiles at the end of hot and cold blow periods are shown with and without impurity; $T_{h,i} = 300$ K, $T_{c,i} = 100$ K, $X_{h,i} = 0.10$, $X_{c,i} = 0.00$, $pr_h = 10$ atm, $pr_c = 1$ atm and $\Lambda = 100$

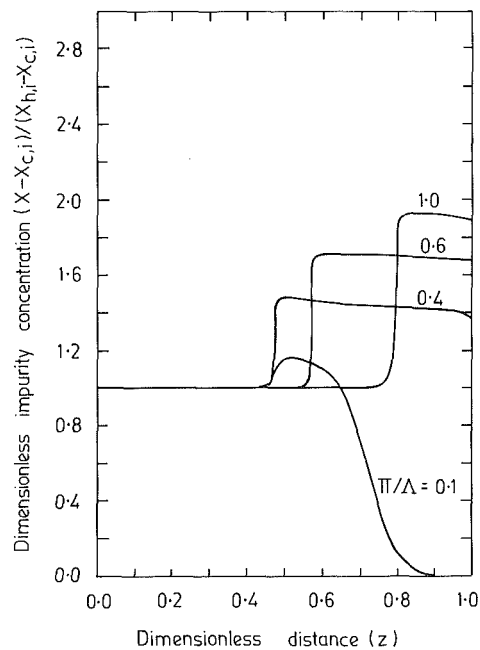


Fig. 9 Dimensionless impurity concentration profiles at the end of the hot blow period; $T_{h,i} = 300$ K, $T_{c,i} = 100$ K, $X_{h,i} = 0.10$, $X_{c,i} = 0.00$, $pr_h = 10$ atm, $pr_c = 1$ atm and $\Lambda = 100$

Acknowledgments

This work has been supported by the Department of Science and Technology, Government of India through a research grant entitled "Development of Recuperative and Regenerative Heat Exchangers for Cryogenic Applications."

References

- 1 Hausen, H., *Heat Transfer in Counterflow, Parallel Flow and Cross Flow*, McGraw-Hill, New York, 1983.
- 2 Schmidt, F. W., and Willmott, A. J., *Thermal Energy Storage and Regeneration*, Hemisphere, New York, 1981.
- 3 Holmberg, R. B., "Heat and Mass Transfer in Rotary Heat Exchangers With Nonhygroscopic Rotor Materials," *ASME JOURNAL OF HEAT TRANSFER*, Vol. 99, 1977, pp. 196-202.
- 4 van Leersum, J. G., and Ambrose, C. W., "Comparison Between Experiments and a Theoretical Model of Heat and Mass Transfer in Rotary Regenerators With Nonsorbing Matrices," *ASME JOURNAL OF HEAT TRANSFER*, Vol. 103, 1981, pp. 189-195.
- 5 Schumann, T. E. W., "Heat Transfer: A Liquid Flowing Through a Porous Prism," *J. Franklin Institute*, Vol. 208, 1929, pp. 405-416.
- 6 Lambertson, T. J., "Performance Factors of a Periodic-Flow Heat Exchanger," *Trans. ASME*, Vol. 80, 1958, pp. 586-592.
- 7 Sahoo, R. K., and Sarangi, S., "The Effect of Temperature Dependent Specific Heat of Working Fluid on the Performance of Cryogenic Regenerators," *Cryogenics*, Vol. 25, 1985, pp. 583-590.
- 8 Willmott, A. J., "Digital Computer Simulation of a Thermal Regenerator," *Int. J. Heat Mass Transfer*, Vol. 7, 1964, pp. 1291-1302.
- 9 Crandall, S. H., *Engineering Analysis*, McGraw-Hill, New York, 1956.
- 10 Hilsenrath, J., et al., *Tables of Thermodynamic and Transport Properties*, Pergamon Press, New York, 1960.
- 11 Honig, R. E., and Hook, H. O., "Vapor Pressure Data for Some Common Gases," *RCA Review*, Vol. 21, 1960, pp. 360-368.
- 12 Bahnke, G. D., and Howard, C. P., "The Effect of Longitudinal Heat Conduction on the Periodic Flow Heat Exchanger Performance," *Trans. ASME*, Vol. 86, 1964, pp. 105-119.
- 13 Sahoo, R. K., "Heat and Mass Transfer in Cryogenic Regenerators," Ph.D. Dissertation, Indian Institute of Technology, Kharagpur, 1984.

APPENDIX

$$a_1 = \frac{\Lambda \cdot \Delta z}{2}; \quad a_2 = \frac{a_1}{1 + \alpha X_{av}}; \quad a_3 = \frac{a_1}{Le};$$

$$b = \frac{\Pi \cdot \Delta \tau}{2}; \quad c = \frac{\Delta z}{\Delta \tau}$$

$$A_1 = \frac{1 - a_2}{1 + a_2}; \quad A_2 = \frac{a_2}{1 + a_2}; \quad c_1 = \frac{2a_3}{c(1 + a_3)};$$

$$C_2 = -C_1/2;$$

$$B_1 = \frac{2b}{1 + a_2 + b}; \quad B_2 = \frac{1 + a_2 - b}{1 + a_2 + b};$$

$$B_3 = \frac{2r_1 a_3 b(1 + a_2)}{a_1(1 + a_3)(1 + a_2 + b)}; \quad B_4 = -B_3/2;$$

$$B_5 = 1 - B_4 \{X_{\text{sat}}(\theta_m(i, j + 1) + 1) - X_{\text{sat}}(\theta_m(i, j + 1))\};$$

$$D_1 = B_1/B_5; \quad D_2 = B_2/B_5; \quad D_3 = B_3/B_5; \quad D_4 = B_4/B_5$$

$$K_1 = \frac{2b}{1 + a_1 + b}; \quad K_2 = \frac{1 + a_1 - b}{1 + a_1 + b}; \quad K_3 = \frac{1 - a_1}{1 + a_1};$$

$$K_4 = \frac{a_1}{1 + a_1}$$

Heat Transfer From a Flat Surface to an Oblique Impinging Jet

R. J. Goldstein

M. E. Franchett¹

Department of Mechanical Engineering,
University of Minnesota,
Minneapolis, MN 55455

Experiments are conducted to determine the heat transfer to a jet impinging at different oblique angles to a plane surface. The main portion of the test plate contains a composite sheet of temperature-sensitive liquid crystal, which is sandwiched between a thin metallic-foil heater and a specially designed liquid bath. The results indicate a displacement of the peak heat transfer from the geometric center of the jet origin, the displacement being a function primarily of impingement angle. Contours of constant heat transfer coefficient are obtained and correlated with an empirical equation that permits determination of average Nusselt numbers over areas of interest.

Introduction

Impinging jets are widely used to provide high local heat and/or mass transfer in a variety of applications including glass manufacturing, paper drying, and gas turbine cooling. They offer the potential of high heat transfer rate and relative ease of controlling specific areas to be cooled (heated or dried).

The present paper is concerned with heat transfer to a single impinging jet. A recent paper (Goldstein et al., 1968) reviews heat transfer studies of a single jet impinging normal to a surface. Studies of heat transfer from a jet impinging at an oblique angle to a surface are relatively rare. Perry (1954) made quasi-local measurements using a calorimeter that was approximately the same size as the jet diameter. The temperature of the jet was considerably above that of the ambient. Hollworth and Gero (1984) indicate the need for careful consideration of such temperature differences. Sparrow and Lovell (1978) measured local mass transfer to an oblique impinging jet at low (10,000 or less) Reynolds numbers. Studies of the flow field with an oblique impinging jet include the work of Donaldson and Snedeker (1971) and Donaldson et al. (1971) at very high (greater than 350,000) Reynolds numbers. Beltaos (1976) studied the flow of an oblique impinging jet with very large jet-to-plate spacing. Foss and Kleis (1976) examined the flow field of an oblique jet with jet angles that varied from 0 to 15 deg. Foss (1979) also examined the flow field of an oblique jet with a jet Reynolds number of 48,000, a jet spacing $L/D = 4.95$, and a jet angle of 45 deg. Other studies dealing with the flow of oblique jets include those of Lamont and Hunt (1980) and Rubel (1981). In these studies the stagnation point and/or peak heat transfer on the surface were found to be displaced from the intersection of the jet axis with the surface in the direction toward the location of the jet exit.

The present experiments are performed with a round jet formed from a square (orifice height equals orifice diameter) orifice impinging on a flat surface. The total temperature of the jet is held to within 0.2°C of the local ambient temperature. The minimum temperature difference between the heated surface and the impinging jet is 14°C . The surface is heated with a thin metallic foil through which an electric current passes. Isotherms on the plate surface are mapped using a temperature-sensitive liquid crystal. From these isotherms, contours of constant heat transfer coefficient could be determined. The jet Reynolds numbers studied are 10,000, 20,000, and 30,000, with a few tests at 35,000. The jet orifice-

to-plate spacings (L/D) are 4, 6, and 10, and the angle between the axis of the jet orifice and the plate surface is set at 30, 45, 60, or 90 deg.

Experimental Apparatus and Operational Procedure

Air for the jet flow is supplied by the building compressor. After filtering and regulation, the air is metered by a replaceable thin-plate orifice. An electric heater wrapped around the flow tube maintains the jet temperature at the room temperature. The air is delivered to the apparatus by a 100-mm o.d. flexible tube. It passes through a straight 28.4-mm i.d., 1.75-m-long tube before entering the jet orifice. The jet orifice is square-edged with both height and diameter equal to 10 mm. The jet orifice and delivery tube are held in place by a pivoting bridge, which allows the jet to be set at different angles. The jet temperature is measured by a thermocouple 250 mm upstream of the jet orifice.

The test section (Fig. 1) has a transparent constant-temperature guard bath, a sheet of liquid crystal, and a stainless-steel electric shim heater. The test section is held vertically in the test stand. The liquid crystal sheet is sandwiched between the stainless steel shim and the guard bath. This allows the liquid crystal colors to be viewed from the back side of the apparatus, through the bath. The guard bath is constructed by lexan and plexiglass. Water from a constant-temperature circulator passes through the guard bath to maintain it at a constant temperature. The temperature of the water is set at the temperature of the red liquid crystal isotherm. A cross section of the top surface composite is illustrated in Fig. 1. The test section is 485 mm high, 305 mm wide, and has a depth of 26 mm.

The liquid crystal used in this experiment is Cholesteric liquid crystal purchased from Liquid Crystal Application of Clark, NJ. The manufacturer paints liquid crystal on a mylar sheet and applies a background color with black ink. The mylar sheet is 0.127 mm thick and the ink and liquid crystal combined are 0.073 mm thick. This particular liquid crystal goes through its entire color display between 41.0 and 43.0°C . The isotherms of the red color band are recorded by photographing the liquid crystal through a red filter with black and white film. An example of several of these photographs is illustrated in Fig. 2. Using the filter, the red band has a width of 0.36°C and a temperature resolution of 0.18°C is achieved.

With the temperature difference between the jet and liquid isotherm fixed, different Nusselt number contours are determined by varying the heat flux. Eight to twelve isotherms (each corresponding to a different heat flux) are photographed to record the local contours under an oblique impinging jet. The locations on each isotherm are digitized following a pro-

¹Present address: General Motors Technical Center, Advanced Product Manufacturing and Engineering, Warren, MI 48090.

Contributed by the Heat Transfer Division for publication in the JOURNAL OF HEAT TRANSFER. Manuscript received by the Heat Transfer Division July 2, 1986.

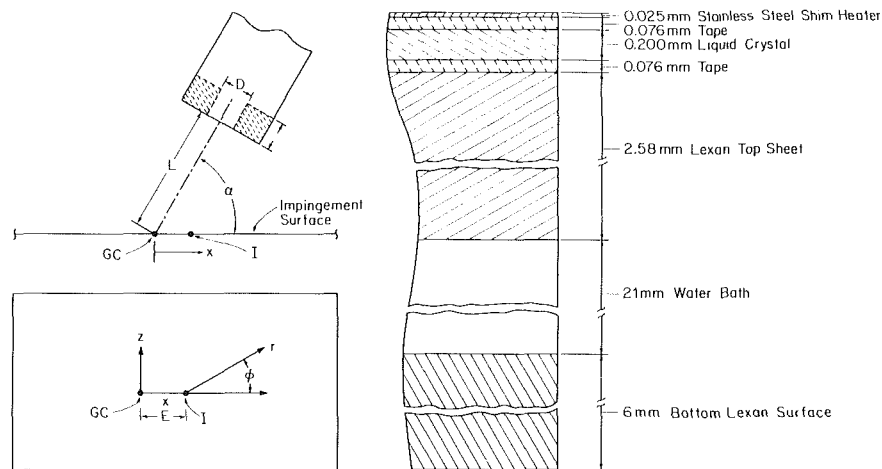


Fig. 1 Coordinate system and top surface cross section

jection of the photographic image on a digitizing pad. Coordinates of the contours of constant temperature obtained at different heat fluxes (different heating currents) are used to determine contours of constant convective heat transfer coefficient with modest corrections for radiation and conduction in the plate assembly. Several measurements were taken to ensure uniform dissipation in the resistance. The width and thickness of the shim heater were both checked and found to vary by less than 2 percent. The voltage drop along the surface of the shim heater was also checked in the direction of current flow and was found to be linear.

The constant-temperature bath behind the liquid crystal serves several functions. Being transparent, it permits viewing the liquid crystal through the plastic container and the bath. Keeping the bath at the color temperature (red) of the crystal drastically reduces any conduction heat loss normal to the test surface near the location in which measurements of the isotherms are to be made, and significantly reduces lateral conduction through the plate. The bath is particularly helpful in systems, such as the present, in which a large range of heat transfer coefficients occur; thus, even when isotherms are taken near the region of peak heat transfer coefficient, which requires a relatively large heat flux, the outer regions of the plate and liquid crystal are not overheated.

Consider the thermal boundary condition of the test plate. The constant-temperature bath drives the plate toward a boundary condition of constant temperature, while the uniform energy dissipation in the heating foil tends to drive it toward a constant heat flux boundary condition. An axisymmetric two-dimensional control volume analysis is used to determine the thermal condition of the test plate's top layers: heating foil, two layers of tape, liquid crystal, and lexan sheet (Fig. 1). The boundary conditions at the top surface are calculated assuming heat transfer for a normal impinging jet.

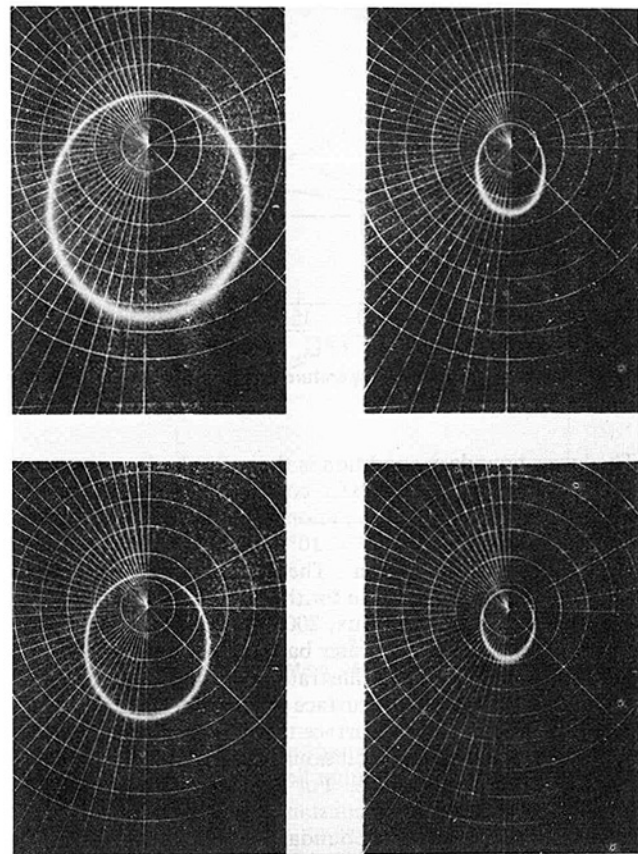


Fig. 2 Contours of constant temperature in liquid crystal obtained at different heat fluxes; $Re = 20,000$, $L/D = 6$, and $\alpha = 45$ deg

Nomenclature

A = correlation magnitude coefficient
 B = first correlation shape coefficient
 C = second correlation shape coefficient
 D = jet diameter = 10 mm in present experiment
 E = correlation offset; displacement of I from GC (dimensionless r/D)
 GC = geometric center of the jet (axis) on the impingement surface

h = local heat transfer coefficient
 I = location of peak heat transfer coefficients at effective center of impingement
 k = thermal conductivity
 L = distance from jet orifice (jet-axis) exit to heat transfer surface
 m = power of (r/D) in correlation
 $Nu = hD/k$ = Nusselt number
 q = convective heat flux from the wall

$Re = UD/\nu$ Reynolds number
 T_c = liquid crystal isotherm temperature
 T_j = jet (total) temperature
 T_w = wall surface temperature
 U = jet mean velocity
 x, y, z = Cartesian coordinates, see Fig. 1
 r, Φ = cylindrical coordinates for correlation of contours of constant Nu , see Fig. 1
 α = jet angle from surface = 90 deg for normal jet
 ν = kinematic viscosity

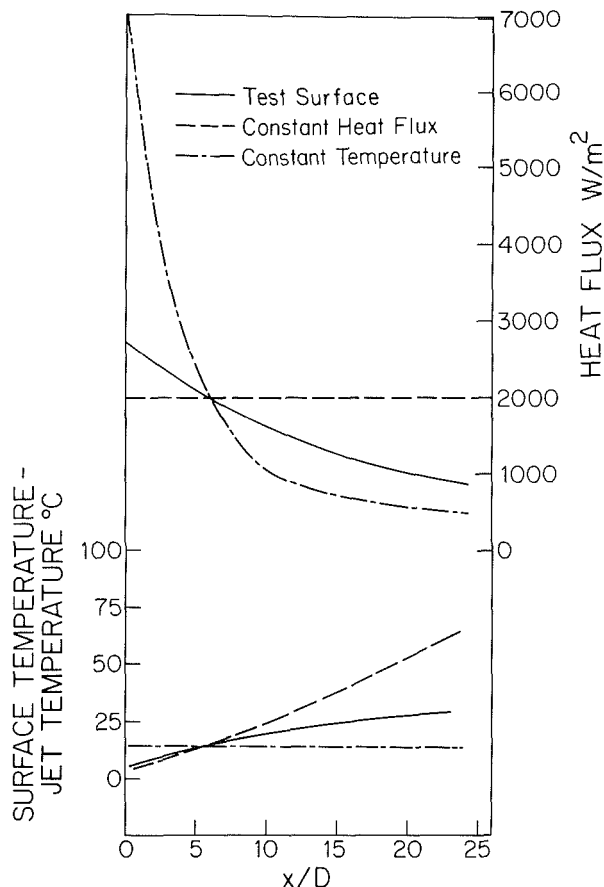


Fig. 3 Calculated surface temperature and heat transfer distribution for a normal jet

The lower boundary condition is the water bath temperature, 41.5°C, and the heat transfer coefficients for the turbulent water bath. The energy dissipation, input as the source term in the heating foil layer, is $80 \times 10^6 \text{ W/m}^3$, which is equivalent to a heat flux of 2000 W/m². The solid lines on Fig. 3 are the calculated thermal condition for the top surface of the test section. The particular heat flux, 2000 W/m², places the surface temperature equal to the water bath temperature at $r/D = 6$. The dashed lines in Fig. 3 illustrate calculated surface thermal conditions for a constant surface temperature and a uniform heat flux. The calculated surface thermal condition of the test plate falls between the conditions of constant heat flux and constant wall temperature. For turbulent flows, the heat transfer coefficients for a constant heat flux boundary and a constant wall temperature boundary should be very close. The results of the test plate control volume heat balance illustrate the thermal boundary condition of the test surface used to determine the heat transfer coefficients in the present tests.

The isotherms shown in Fig. 2 are obtained with the red filter to define a specific isotherm. The grid represents constant angles and radial lines, and is centered at the intersection of the geometric axis of the jet on the front surface of the heating plate. Note that the isotherms appear to be in near-elliptical form. The figures shown are for $L/D = 6$, $Re = 20,000$, and $\alpha = 45$ deg.

The liquid crystal color temperature used is 41.5°C, some 14°C above the highest jet temperature in any of the experiments. At the highest Reynolds number the dynamic temperature of the air in the jet is about 1.2°C. Thus, the correction for a recovery factor slightly different from unity is not critical in calculating the Nusselt number. As noted earlier, the contours of constant heat transfer coefficient are not directly equivalent to the isotherms, as measured from the

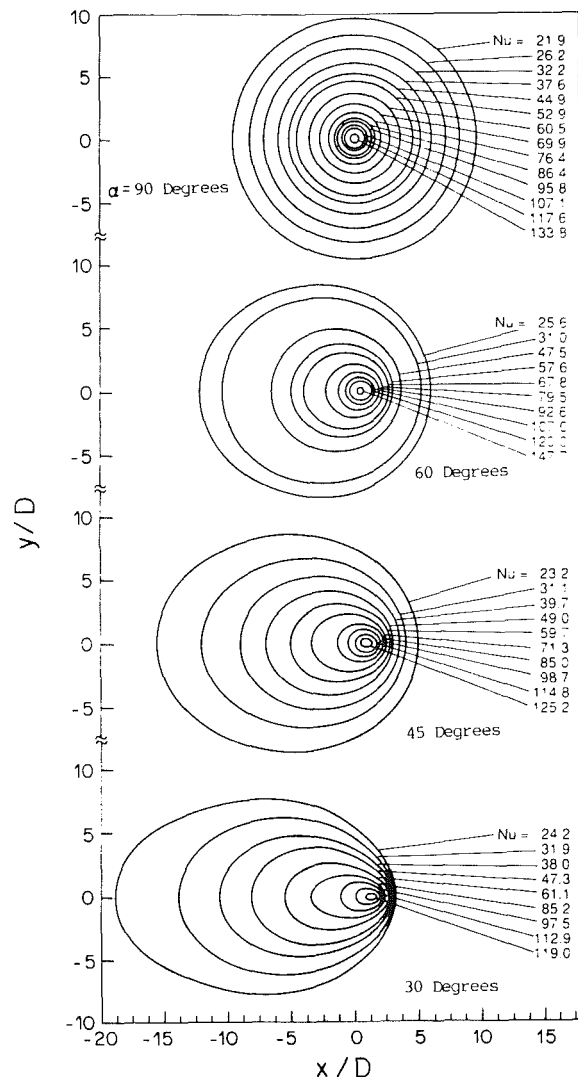


Fig. 4 Contours of constant Nusselt number; $L/D = 6$, $Re = 20,000$

photographs. They are determined after taking into account thermal conduction in the plate, radiation from the surface, and other corrections, the key one being the lateral conduction. This correction is typically about 4 percent of the net flux. The wall temperature is shown by the (filtered) colored line; the difference between the temperature of the metallic foil and the liquid crystal is negligible with the constant-temperature water bath. The largest measurement uncertainty occurs in the near-peak region ($0 < r/D < 1$), where the effects of dynamic temperature are greatest. The uncertainties of Nu in this region for the tests at Reynolds numbers 30,000, 20,000, and 10,000 are respectively 6.9, 5.5, and 4.9 percent. The uncertainty outside this peak heat transfer coefficient region is about 3.2 percent independent of Reynolds number.

The experimental results are presented in terms of a local Nusselt number

$$Nu = hD/k$$

The local heat transfer coefficient is determined from

$$h = q / (T_w - T_j)$$

where q is the convection heat flux, T_w is the wall temperature [the liquid crystal (red) isotherm temperature], and T_j is the jet (total) temperature.

The exact location of the peak heat transfer is difficult to determine. In the data reduction process, the point midway within the (red) isotherm is the location digitized as the posi-

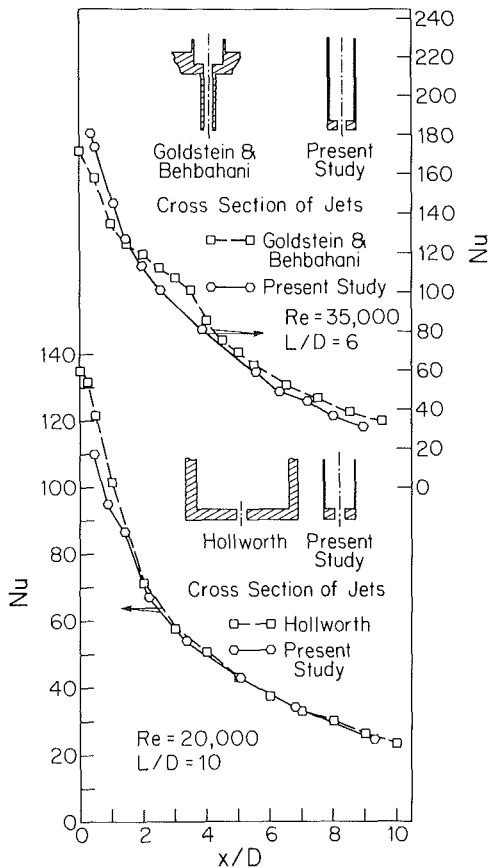


Fig. 5 Heat transfer measurements for a normal jet compared with those from earlier studies

tion of the liquid crystal isotherm temperature. At the peak heat transfer point, the diffuse region observed does not allow the middle of the isotherm to be defined. The local heat transfer coefficients, in most cases, are measured to within a quarter jet diameter of the peak heat transfer location.

Results

Figure 4 shows results in terms of contours of constant heat transfer coefficient (Nusselt number) for $L/D = 6$, a Reynolds number of 20,000, and four different jet angles. For the normal jet the contours of constant Nusselt number are circular. As the jet is inclined closer and closer to the surface the contours become quasi-elliptical with greater elongation as the jet is inclined further.

For the normal jet the local distributions of the Nusselt number at spacings of $L/D = 4$ and $L/D = 6$ are very similar (compare Figs. 6 and 8). The local Nusselt numbers near the peak for a spacing of $L/D = 10$ are about 20 percent less (see Fig. 10) than the values measured for the spacings of 4 and 6. The distribution of the Nusselt numbers is essentially independent of Reynolds number when presented as $Nu/Re^{0.7}$. This is discussed in greater detail below.

Figure 5 compares the results for the normal jet with those from earlier studies (Hollworth and Gero, 1984; Goldstein and Behbahani, 1982) that used more conventional heat transfer and temperature instrumentation. Excellent agreement is found except very close to the peak heat transfer point, where the results are very sensitive to the geometry of the jet orifice.

The local heat transfer results for an oblique jet are described in three parts: the near-peak region ($0 < r/D < 1$), the x -axis profile, and the y -axis profile. The near-peak Nusselt numbers for the x -axis profile and the y -axis profile are similar. The distribution of the local Nusselt number in the

Table 1

α	Correlation Coefficients							
	A			B	C	E		
	$L/D = 4$	$L/D = 6$	$L/D = 10$			$L/D = 4$	$L/D = 6$	$L/D = 10$
90°	0.159	0.155	0.123	0.37	0.0	0.0	0.0	0.0
60°	0.163	0.152	0.115	0.40	0.12	0.8	0.6	0.9
45°	0.161	0.146	0.107	0.47	0.23	1.2	1.0	1.5
30°	0.136	0.124	0.091	0.54	0.34	1.5	1.4	1.9

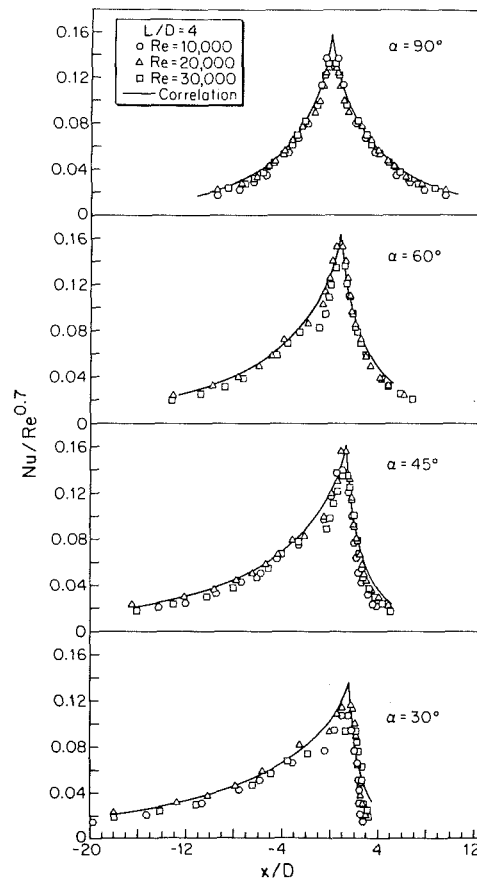


Fig. 6 Comparison of correlation with measured Nusselt numbers along the x axis for $L/D = 4$

near-peak region is nearly independent of ϕ . Outside the near-peak region, the local Nusselt numbers are strongly dependent on the direction ϕ .

As the impinging jet is moved from normal, the local Nusselt numbers in the near-peak region change. The rate at which these local Nusselt numbers vary with jet angle is dependent on the orifice-to-plate spacing. For the smaller spacings, the near-peak Nusselt numbers are not significantly affected by the initial decreases in the jet angle.

The near-peak Nusselt numbers for $L/D = 4$ are not significantly affected by changes in jet angle until the angle is 30 deg (see Fig. 6). At 30 deg, the average of the near-peak Nusselt numbers is 23 percent less than that with a normal jet. For $L/D = 6$, the near-peak Nusselt numbers are not affected by the decrease in jet angle until the jet is at 45 deg (Fig. 8). At 45 deg and $L/D = 6$, the average of the near-peak Nusselt number is 11 percent less than the value with the normal jet. At a jet angle of 30 deg and $L/D = 6$, the average of the near-peak Nusselt numbers is 22 percent less than that with the normal jet at equal spacing. The near-peak Nusselt numbers for the jet spacing $L/D = 10$ decrease with the initial change in jet angle (see Fig. 10). The average near-peak value for a jet angle

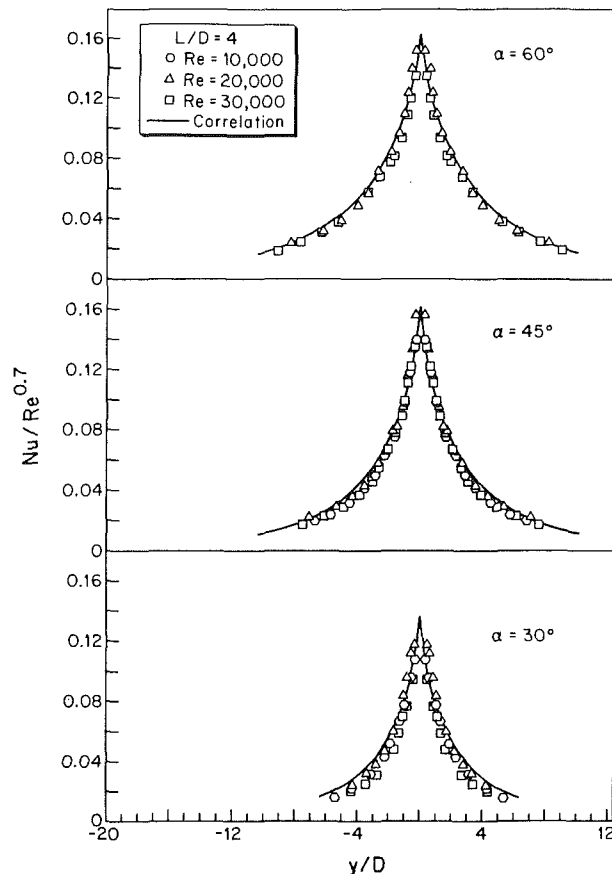


Fig. 7 Comparison of correlation with measured Nusselt numbers along the y axis for $L/D = 4$

of 60 deg is 5 percent less than that with the normal jet. The average value for a jet angle of 45 deg is 17 percent less than that with the normal jet and for the jet angle of 30 deg the average near-peak value is 30 percent less than that with the normal jet.

The overall shape of the local Nusselt number x -axis profile is influenced by both the jet orifice-to-plate spacing and the jet angle. For a given L/D , the slope of the local Nusselt number variation on the upstream of the x -axis profile ($x/D > 0$) increases with decreasing jet angle. The slope on the downstream of the profile ($x/D < 0$) decreases with decreasing jet angle. The rate at which the x -axis profile is altered with decreasing jet angle is dependent on L/D . The x -axis distribution of the local Nusselt numbers is more dependent on the jet angle for the smaller spacings ($L/D = 4$ and 6) (Figs. 6 and 8). The x -axis profile at the smaller spacings varies to a greater degree from jet angle to jet angle than do the x -axis profiles at the larger spacing $L/D = 10$ (Fig. 10).

All of the y -axis Nusselt number profiles have the same general characteristic shape. The profiles with smaller orifice-to-plate spacing and smaller jet angle have steeper profiles than the profiles with larger spacing and larger angles. The y -axis profiles for all three spacings are independent of the decrease in the jet angle from 90 to 60 deg, but are altered as the jet angle is decreased from 60 to 45 deg and to 30 deg.

Comparisons with the mass transfer results (Sparrow and Lovell, 1978) for an oblique jet are dependent on the Prandtl (Schmidt) number influence on the Nusselt (Sherwood) number. Using the dependence recommended in that study, the results are similar, although the equivalent mass transfer values are about 10 percent lower than the Nusselt number in the present studies at $Re = 10,000$ and $L/D = 10$.

A correlation of the local Nusselt numbers was sought. This

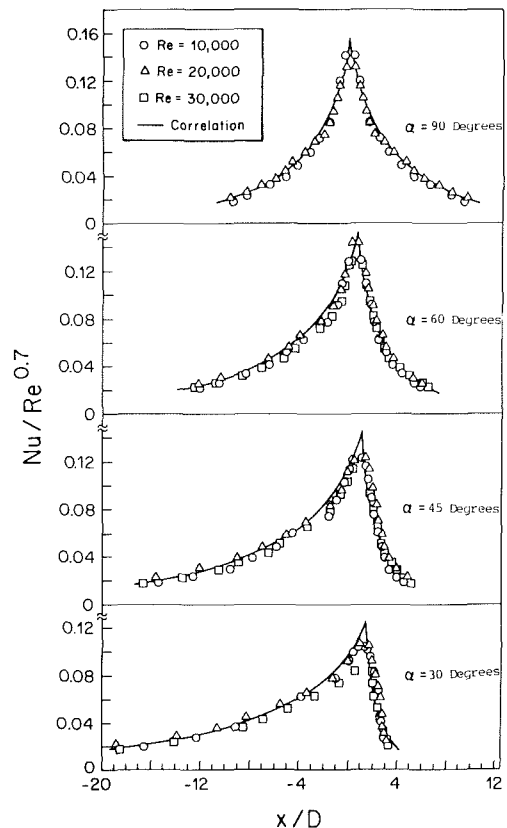


Fig. 8 Comparison of correlation with measured Nusselt number along the x axis for $L/D = 6$

can be used for interpolation as well as calculation of area-averaged heat transfer. As noted earlier, local Nusselt numbers are found to be independent of Reynolds number when divided by the Reynolds number raised to the power 0.7. Note that this exponent is lower than the value 0.76 recently found (Goldstein et al., 1986) in a parallel study. This exponent is clearly a function of Re and at the lower Re a smaller exponent would be expected. The distribution of the local values, $Nu/Re^{0.7}$, is correlated by an offset exponential, which varies in the r and Φ directions

$$Nu/Re^{0.7} = A e^{-(B+C \cos \Phi)(r/D)^m}$$

The measured near-peak Nusselt numbers were found to be offset from the geometric intersection of the jet axis and the plate surface. The correlation accounts for this offset by shifting the origin of the cylinder coordinate system a distance E along the X axis from the geometric intersection of the jet (point GC) to point I (Fig. 1).

The coefficients A , B , C , the coordinate shift E , and the power m are determined from a least-squares fit of the local Nusselt numbers for each Reynolds number, jet angle, and jet-to-plate spacing. It was observed in the initial fits of the data that m for each range of conditions was close to 0.75. To simplify the correlation, the power of r is fixed at 0.75 and A , B , C , and E are determined from the least-squares fit. The coefficient A , which determines the magnitude of $Nu/Re^{0.7}$, is a function of both the jet angle and L/D . The coefficients B and C determine how the exponential varies in the Φ direction. B and C are functions only of the jet angle. The coordinate shift E is a function of both the jet angle and L/D . The coefficients are presented in Table 1. These are, strictly speaking, only valid within the range of the parameters of the present tests.

Figures 6–11 compare the correlation equation with measured values along the x axis and y axis for all spacings

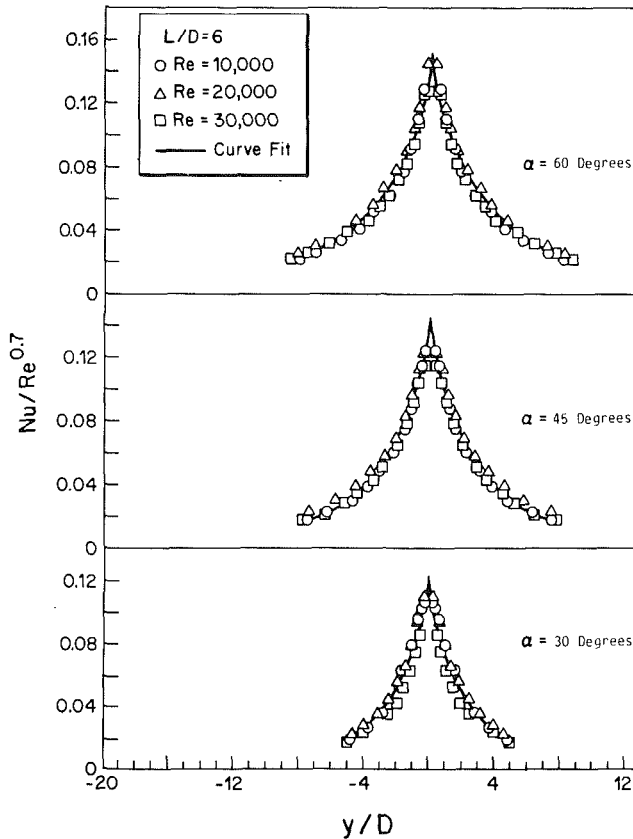


Fig. 9 Comparison of correlation with measured Nusselt number along the y axis, $L/D = 6$

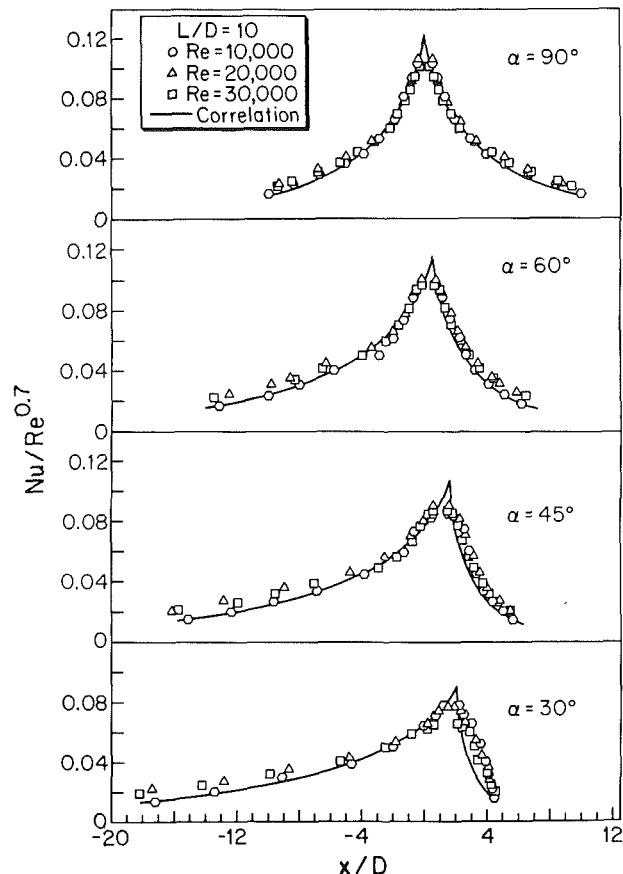


Fig. 10 Comparison of correlation with measured Nusselt numbers along the x axis for $L/D = 10$

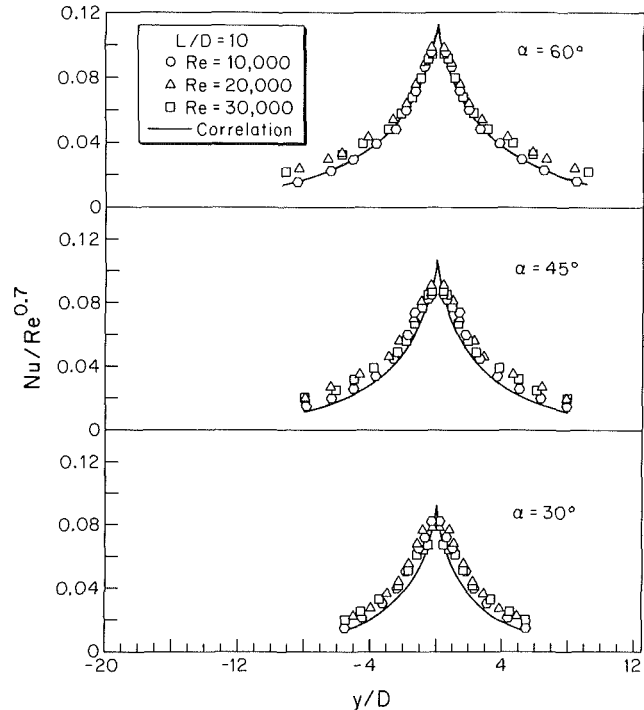


Fig. 11 Comparison of correlation with measured Nusselt numbers along the y axis for $L/D = 10$

and angles. The agreement is quite good. At a spacing $L/D = 10$ the curves are not as steep as the distribution of local values for spacings of 6 and 4. The correlation does not predict the local Nusselt numbers near the peak for $L/D = 10$ as accurately as predicted for smaller jet spacings. The blunter profiles for the larger spacings are difficult to fit with the exponential function. The peak values are predicted by the correlation from extrapolation of measured near-peak data.

Summary and Conclusions

Local measurements have been made of the heat transfer coefficients on a flat surface on which a jet impinges. The angle between the jet axis and the surface is varied from 90 to 30 deg. The distance of the jet orifice to the plate varies from four to ten orifice diameters. The jet Reynolds numbers is between 10,000 and 30,000.

The heat flux is provided by passing an electric current through a thin metallic foil. The actual convection surface boundary condition is between that of constant wall temperature and constant heat flux. The temperature distribution is observed using a sheet of liquid crystals. Recent tests using such systems had insulation on the back face of the heater to prevent heat loss and also to minimize lateral conduction. A variation on this technique is used; a constant temperature bath, set at the liquid crystal temperature, is placed behind the crystal. The bath permits the liquid crystal to be viewed from the rear through a colored filter while the jet impinges directly on the heated surface. The bath also reduces the influence of conduction in the plate and permits measurements over a large range of heat fluxes.

The isotherms are photographed and digitized. The digitized positions of the isotherms, along with the temperature and heat flux data, are used to calculate the local heat transfer coefficients under the oblique impinging jet. The local heat transfer coefficients, when the jet is normal to the surface, agree well with previous studies. For an oblique jet the location of the peak heat transfer is displaced somewhat from the intersection of the geometric axis of the jet with the plate sur-

face. Empirical equations are used to correlate the distribution of the local Nusselt number. The equations can be used to determine the average Nusselt number over different regions on the plate.

Acknowledgments

The research was supported by a grant from the Engineering Research Program of the Office of Basic Energy Science, and the US Department of Energy. Mark Schneider and Bob Hain provided significant assistance in setting up the experiment.

References

- Beltaos, S., 1976, "Oblique Impingement of Circular Turbulent Jets," *Journal of Hydraulic Research*, Vol. 14, pp. 17-36.
- Donaldson, C. D., and Snedeker, R. S., 1971, "A Study of Free Jet Impingement, Part I, Mean Properties of Free Impinging Jets," *Journal of Fluid Mechanics*, Vol. 45, Part 2, pp. 281-319.
- Donaldson, C. D., Snedeker, R. S., and Margolis, D. P., 1971, "A Study of Free Jet Impingement, Part II, Free Jet Turbulent Structure and Impingement Heat Transfer," *Journal of Fluid Mechanics*, Vol. 45, Part 3, pp. 477-512.
- Foss, J. F., 1979, "Measurement in a Large-Angle Oblique Jet Impingement Flow," *AIAA Journal*, Vol. 17, p. 801.
- Foss, J. F., and Kleis, S. J., 1976, "Mean Flow Characteristics for the Oblique Impingement of an Axisymmetric Jet," *AIAA Journal*, Vol. 14, p. 705.
- Goldstein, R. J., and Behbahani, A. I., 1982, "Impingement of a Circular Jet With and Without Cross Flow," *International Journal of Heat and Mass Transfer*, Vol. 25, No. 9, pp. 1377-1382.
- Goldstein, R. J., Behbahani, A. I., and Kieger Heppelman, K. K., 1986, "Streamwise Distribution of the Recovery Factor and the Local Heat Transfer Coefficient to an Impinging Circular Air Jet," *International Journal of Heat and Mass Transfer*, Vol. 29, pp. 1227-1235.
- Hollworth, B. R., and Gero, L. R., 1984, "Entrainment Effects on Impingement Heat Transfer, Part 2: Local Heat Transfer Measurement," ASME Paper No. 84-WA/HT-20.
- Lamont, P. J., and Hunt, B. L., 1980, "The Impingement of Underexpanded, Axisymmetric Jets on Perpendicular and Inclined Flat Plates," *Journal of Fluid Mechanics*, Vol. 100, Part 3, pp. 471-511.
- Perry, K. P., 1954, "Heat Transfer by Convection From a Hot Gas Jet to a Plane Surface," *Proceedings of the Mechanical Engineering Institute*, Vol. 168, pp. 775-784.
- Rubel, A., 1981, "Computations of the Oblique Impingement of Round Jets Upon a Plane Wall," *AIAA Journal*, Vol. 19, pp. 863-871.
- Sparrow, E., and Lovell, B. J., 1980, "Heat Transfer Characteristics of an Obliquely Impinging Wall Jet," ASME JOURNAL OF HEAT TRANSFER, Vol. 102, pp. 202-209; cf. Lovell, B. J., 1978, *Local Transfer Coefficients for Impingement of an Axisymmetric Jet on an Inclined Flat Plate*, M.S. Thesis, M.E. Department, University of Minnesota.

Local Heat/Mass Transfer Distributions Around Sharp 180 deg Turns in Two-Pass Smooth and Rib-Roughened Channels

J. C. Han

Associate Professor.

P. R. Chandra

Graduate Assistant.

S. C. Lau

Assistant Professor.

Department of Mechanical Engineering,
Texas A&M University,
College Station, TX 77843

The detailed mass transfer distributions around the sharp 180 deg turns in a two-pass, square, smooth channel and in an identical channel with two rib-roughened opposite walls were determined via the naphthalene sublimation technique. The top, bottom, inner (divider), and outer walls of the test channel were naphthalene-coated surfaces. For the ribbed channel tests, square, transverse, brass ribs were attached to the top and bottom walls of the channel in alignment. The rib height-to-hydraulic diameter ratios (e/D) were 0.063 and 0.094; the rib pitch-to-height ratios (P/e) were 10 and 20. Experiments were conducted for three Reynolds numbers of 15,000, 30,000, and 60,000. Results show that the Sherwood numbers on the top, outer, and inner walls around the turn in the rib-roughened channel are higher than the corresponding Sherwood numbers around the turn in the smooth channel. For both the smooth and the ribbed channels, the Sherwood numbers after the sharp turn are higher than those before the turn. The regional averages of the local Sherwood numbers are correlated and compared with published heat transfer data.

Introduction

In modern gas turbine blades, as depicted in Fig. 1, cooling air is circulated through internal cooling passages to remove heat from the blade external surfaces that are exposed to high-temperature gas flows. A typical cooling passage can be modeled as a straight or a multipass rectangular channel with a pair of opposite walls with rib turbulators. Han et al. (1984, 1985, 1986) investigated systematically the effects of rib height, rib pitch, rib angle of attack, and channel aspect ratio on the heat transfer and the pressure drop in uniformly heated, straight, rectangular channels with two opposite ribbed walls. In a multipass rectangular channel, in addition to the rib turbulators, the flow separation and recirculation in the turnaround regions and the flow redevelopment downstream of the sharp 180 deg turns are expected to have significant effects on the distribution of the local heat transfer coefficient and on the overall channel heat transfer.

Metzger and Sahn (1985) studied the effects of the channel geometry (the before-turn and after-turn channel aspects ratios, and the turn clearance) and the flow Reynolds number on the heat transfer in smooth rectangular channels with sharp 180 deg turns. The test channels were constructed of 17 separate copper segments, each with its individually controlled heater to maintain the interior walls of the test channel at uniform temperatures. The regionally averaged heat transfer coefficients of the top, bottom, and outer walls around the turns were obtained. The results showed that the maximum regionally averaged heat transfer coefficients, which were about two to three times the fully developed values, were obtained in regions immediately downstream of the turns.

Sparrow and Tao (1983, 1984) used the naphthalene sublimation technique to determine the local mass transfer distributions in straight rectangular channels of large aspect ratios with rib turbulators of circular cross section. In their experiments, they attached metallic drill rods onto the naphthalene-coated walls of the test channels. The highly

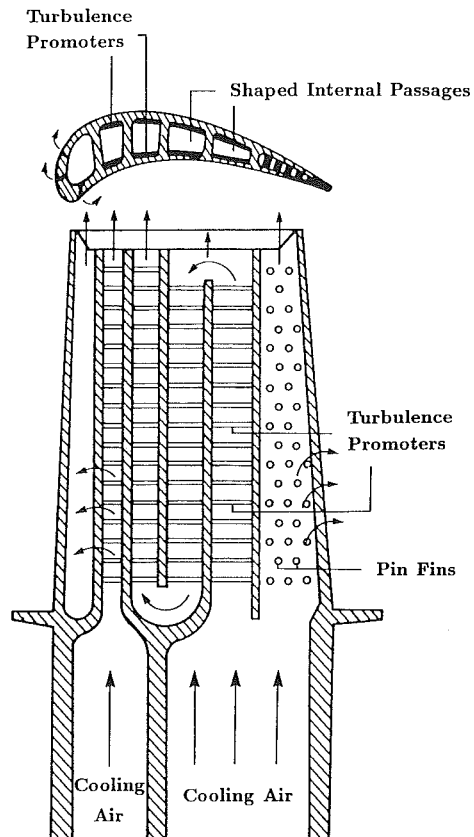


Fig. 1 Cooling concepts of a modern multipass turbine blade

detailed distributions of the mass transfer coefficient on the exposed channel wall between adjacent ribs were reported. The mass transfer coefficients on the ribs were not determined, however, since the ribs were not naphthalene-coated surfaces.

Boyle (1984) studied the heat transfer in both smooth and rib-roughened square channels with sharp 180 deg turns, which simulated turbine blade cooling passages. The top and

Contributed by the Heat Transfer Division and presented at the 31st International Gas Turbine Conference and Exhibit, Düsseldorf, Federal Republic of Germany, June 8-12, 1986. Manuscript received by the Heat Transfer Division October 27, 1986. Paper No. 86-GT-114.

bottom walls of the test channels were heated uniformly by passing current through 0.05-mm (0.002-in.)-thick Inconel foils; the other two walls were not heated. The experimental results showed that the heat transfer coefficients at the turns in the smooth channel and the ribbed channel were about two to three times and three to four times the corresponding fully developed values, respectively. Since the test channels for the study were sparsely instrumented with thermocouples, the detailed distributions of the heat transfer coefficient around the sharp 180 deg turns were not determined.

To investigate the effect of conductive and nonconductive ribs on the surface heat transfer distributions, Boyle (1984) repeated the experiments with glued-on Bakelite ribs. He found that the corresponding distributions of the local heat transfer coefficient in channels with integral foil-ribs and glued-on Bakelite ribs were within 10 percent of each other. He concluded that the augmented heat transfer in the rib-roughened channels was the result of the turbulence promoted by the ribs, and not the result of the fin effect – an increase of about 20 percent in the heat transfer surface area with the installation of the ribs. The use of Bakelite ribs instead of foil ribs in Boyle's (1984) heat transfer experiments is analogous to the use of drill rods instead of naphthalene-coated rods in the mass transfer experiments of Sparrow and Tao (1983, 1984).

Experimental data on the detailed distributions of the heat transfer coefficient around sharp 180 deg turns in multipass channels are important for two reasons: (1) They help design engineers understand the effect of sharp 180 deg turns on the surface heat transfer in multipass channels. Knowledge of the flow field and heat transfer characteristics in multipass channels facilitates the design of effectively cooled turbine blades that are not susceptible to structural failure from uneven thermal stresses. (2) Detailed local heat transfer results provide a data base for researchers and engineers to develop numerical models to predict the flow field and heat transfer characteristics in multipass channels of various geometries.

In the present investigation, the detailed distributions of the local mass transfer coefficient around sharp 180 deg turns in a smooth channel and in a rib-roughened channel were measured via the naphthalene sublimation technique. The test section was a two-pass square channel that modeled turbine blade cooling passages. The top, bottom, outer, and inner (divider) walls of the test channel were all naphthalene-coated plates. For ribbed channel tests, brass ribs (with surfaces from which no mass was transferred) were placed on the top and bottom walls of the naphthalene-coated channel so that the corresponding ribs on the two walls were directly opposite each other. The rib height-to-hydraulic-diameter ratios (e/D) were 0.063 and 0.094. The rib pitch-to-height ratios (P/e) were 10 and 20. The rib angle of attack (α) was 90 deg. In both the smooth channel and the ribbed channel experiments, the highly detailed distributions of the mass transfer coefficient

Table 1 Test conditions for the present investigation

Case No.	Channel Condition	e/D	P/e	Re
1	smooth	0	0	15,000
2	smooth	0	0	30,000
3	smooth	0	0	60,000
4	rib-roughened	0.063	10	15,000
5	rib-roughened	0.063	10	30,000
6	rib-roughened	0.063	10	60,000
7	rib-roughened	0.063	20	30,000
8	rib-roughened	0.094	10	30,000

on the top, outer, and inner walls around the sharp 180 deg turn in the test channel were determined for three Reynolds numbers of 15,000, 30,000, and 60,000. Eight test runs were performed. The test conditions of the runs are given in Table 1.

The boundary conditions on the naphthalene-coated channel walls with brass ribs in the present mass transfer experiments are identical to those on the channel walls with metallic ribs made of drill rods in Sparrow and Tao (1983, 1984). They are also analogous to the boundary conditions on the channel walls with Bakelite ribs in Boyle (1984). Based on Boyle's results, the use of brass ribs instead of naphthalene-coated ribs may result in an error of about 10 percent in the distribution of the mass transfer coefficient between adjacent ribs in the present study.

Note that the total rate of mass transferred from the channel walls is the sum of the rates of mass transferred from the ribs and from the exposed surfaces of the channel walls. In the present investigation, attention is focused on the detailed distribution of the local mass transfer coefficient on the exposed rib-roughened walls between adjacent ribs and the smooth walls. In addition to obtaining information for better understanding of the flow and heat transfer characteristics in rib-roughened channels with sharp 180 deg turns, the present study provides detailed local heat/mass transfer data on the exposed channel walls for researchers to test numerical models for the predictions of the local heat transfer coefficients in these channels.

Experimental Apparatus and Procedure

The main components of the test apparatus are the test section, a settling chamber, a calibrated orifice flow meter, a control valve, and a centrifugal blower. The entire apparatus, including the measuring instruments, is in an air-conditioned laboratory, which was maintained at a temperature 21°C (70°F) throughout the tests.

Nomenclature

D = channel width; also hydraulic diameter	Re = Reynolds number based on channel hydraulic diameter	t = thickness of the inner (divider) wall
\bar{D} = diffusion coefficient, equation (5)	Sc = Schmidt number for naphthalene	Δt = duration of the test run
e = rib height	Sh = local Sherwood number, equation (5)	X = axial distance from channel entrance
h_m = local mass transfer coefficient, equation (2)	\bar{Sh} = average Sherwood number on each surface of the test channel	α = rib angle of attack
\dot{m}'' = local mass transfer rate per unit area, equation (1)	\overline{Sh} = overall average Sherwood number before the turn, in the turn, or after the turn	ν = kinematic viscosity of pure air
Nu = Nusselt number	Sh ₀ = Sherwood number for fully developed turbulent tube flow	ρ_b = bulk naphthalene vapor density in the flow passage
P = rib pitch		ρ_s = density of solid naphthalene
Pr = Prandtl number for air		ρ_w = local naphthalene vapor density at wall

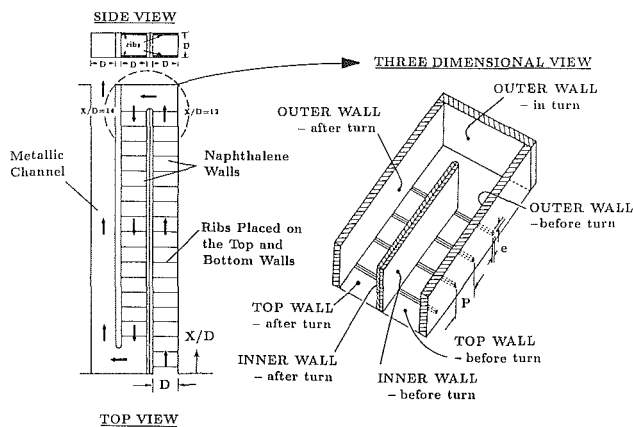


Fig. 2 Sketch of the test section

Test Section. Figure 2 is a schematic diagram of the test section, a multipass channel with a 2.54-cm (1-in.) square cross section. The top, bottom, and outer walls of the channel were constructed of 0.95-cm (0.375-in.) thick aluminum plates. The inner (divider) wall was constructed of two 0.325-cm (0.125-in.) thick aluminum plates, bonded together back-to-back with double-sided tape. The clearance at the tip of the divider wall was 2.54 cm (1 in.). To simulate actual turbine cooling passages, the ratio of the before-turn (and also after-turn) channel length to the channel width, X/D , and the ratio of the divider wall thickness to the channel width, t/D , were kept at 13 and 0.25, respectively.

All the aluminum plates that made up the walls of the test channel were hollowed out and filled with naphthalene by casting against a highly polished stainless steel plate. As a result, all the interior surfaces of the test channel were smooth naphthalene surfaces. For the roughened channel experiments, brass ribs with a 0.159-cm (0.063-in.) or 0.238-cm (0.094-in.) square cross section were glued periodically to the top and bottom naphthalene surfaces of the two straight sections of the test channel. The rib pitch-to-height ratio was 10 or 20. There was no rib in the turn region. The rib height-to-hydraulic-diameter ratios corresponding to the two types of ribs were 0.063 and 0.094. The glue thickness was estimated to be less than 0.0127 mm (0.005 in.).

A relatively large metallic baffle was attached to the inlet of the test section to provide a sudden contraction flow entrance condition. During a test run, air from the naphthalene-free laboratory was drawn through the test section and ducted to the outside of the building.

Instrumentation. The most important part of any naphthalene sublimation experiment is the instrumentation used to measure the highly detailed distributions of the local mass transfer on the naphthalene surfaces. In this investigation, a Starrett electronic depth gage with an accuracy of 0.00001 in./0.0001 mm determined the contours of the various naphthalene surfaces before and after a test run. The depth gage consisted of an electronic amplifier and a lever-type gaging head. The naphthalene plate, whose contour was to be measured, was mounted firmly on a coordinate table. The coordinate table facilitated the traversing of the naphthalene plate in two perpendicular directions tangential to the plate surface. The gaging head was affixed to a stand mounted on the stationary base of the coordinate table and hung over the naphthalene plate to be measured.

To measure the elevation at a point on the naphthalene surface, the platform of the coordinate table was moved so that the gaging head rested against the naphthalene surface at the measurement point. The deflection of the tip of the gaging head was converted to an electrical signal (d-c voltage) by the amplifier. The signal was recorded with a Texas Instruments

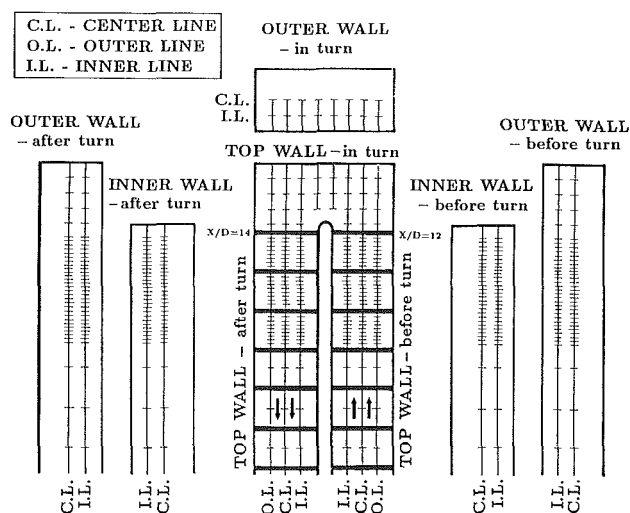


Fig. 3 Measurement points before, in, and after the turn for a typical test run

Professional Computer connected to the amplifier through an A/D converter. The elevation measurement stations for a typical ribbed channel experiment are shown in Fig. 3.

Five, 36-gage, copper-constantan thermocouples were used with a digital temperature indicator to measure the temperature of the flowing air and the temperatures at four stations on the naphthalene surfaces during a test run.

Procedure. After all the naphthalene plates were prepared under a fume hood, they were tightly sealed individually in plastic bags to prevent sublimation. They were then left in the laboratory for 6–8 h to attain thermal equilibrium. Before a test run, the surface contours of all the naphthalene plates were measured and recorded. In a ribbed channel test run, ribs were glued to the appropriate naphthalene surfaces. The test section was then assembled and attached to the rest of the test rig.

To initiate the test run, the blower was switched on for air to flow through the test channel at a predetermined rate. During the test run, the air temperature, the temperatures at the four stations on the naphthalene surfaces, the pressure drop across the orifice, the static pressure upstream of the orifice, and the atmospheric pressure were recorded periodically. A typical run lasted about 30 min. At the completion of the test run, the contours of the naphthalene surfaces were measured again. From the corresponding before-run and after-run surface contours, the depth change at each measurement station on the naphthalene surfaces was calculated.

Separate tests were conducted to determine the mass losses from the various naphthalene surfaces due to natural convection while the surface contours were being measured and while the ribs were being glued onto the appropriate naphthalene surfaces. The total mass loss by natural convection was no more than 4 percent of the total mass transfer during any test run. In calculating the local Sherwood numbers, these losses of mass from the various naphthalene surfaces were taken into account accordingly.

Data Reduction

The mass flux \dot{m}'' at any measurement point is calculated by the following equation:

$$\dot{m}'' = \rho_s \Delta Z / \Delta t \quad (1)$$

where ρ_s is the density of solid naphthalene; ΔZ is the measured change of elevation at the measurement point; and Δt is the duration of the test run.

The local mass transfer coefficient h_m is given by

$$h_m = \dot{m}'' / (\rho_w - \rho_b) \quad (2)$$

where ρ_w and ρ_b are the naphthalene vapor density at the measurement point and the bulk naphthalene vapor density, respectively. The local vapor density ρ_w is determined by the perfect gas law in conjunction with Sogin's (1958) vapor pressure-temperature relationship and the measured surface temperature

$$\rho_w = P_w / (R_v T_w) \quad (3)$$

$$\log_{10} P_w = A - B/T_w \quad (4)$$

where R_v , A , B are given in Sogin (1958). The bulk naphthalene vapor density ρ_b is the cumulative mass transferred from the naphthalene surfaces to the airstream divided by the air volumetric flow rate.

The local Sherwood number is defined as

$$Sh = h_m D / \bar{D} = h_m D / (\nu / Sc) \quad (5)$$

where the Schmidt number Sc for naphthalene is 2.5 according to Sogin (1958), and ν is the kinematic viscosity of pure air.

The local Sherwood number can be converted to the corresponding local Nusselt number by using the heat and mass transfer analogy (Sogin, 1958)

$$Nu = (Pr/Sc)^{0.4} Sh \quad (6)$$

where the Prandtl number Pr is about 0.707 for air at room temperature.

The Nusselt number for fully developed turbulent tube flow correlated by McAdams

$$Nu_0 = 0.023 Re^{0.8} Pr^{0.4} \quad (7)$$

was the reference for comparison. By combining equations (5), (6), and (7), the experimentally determined local Sherwood number can be normalized by the Sherwood number for fully developed turbulent tube flow as follows:

$$Sh/Sh_0 = (h_m D / \bar{D}) / [0.023 Re^{0.8} Pr^{0.4} (Sc/Pr)^{0.4}] \quad (8)$$

Uncertainties in Data Reduction. For a 0.56 °C (1 °F) variation in the naphthalene surface temperature, there was a 6 percent change in the local naphthalene vapor density, according to equations (3) and (4). In the present study, the naphthalene surface temperatures were measured at two stations in each of the two straight sections of the test channel. The variation of the four temperatures for any test run was never more than 0.28 °C (0.5 °F). Therefore, the uncertainties in the local vapor density (ρ_w) calculations were relatively small although not all surface temperatures at all elevation measurement stations were measured.

Since the surface contours were measured at discrete points along one, two, or three axial lines on the naphthalene surfaces, errors were introduced into the calculations of the bulk naphthalene vapor densities (ρ_b) when they were determined from the cumulative mass transferred into the airstream. The values of the bulk vapor density (ρ_b) were generally much smaller than those of the local naphthalene vapor density (ρ_w) because of the relatively short test channel and the high air flow rates used in the experiments. The bulk vapor density, whose value was maximum at the end of the second straight section downstream of the sharp turn, never exceeded 10 percent of ρ_w . Consequently, even if naphthalene ribs had been used in the experiments and the mass transferred from the additional 20 percent naphthalene rib surface to the airstream included in the ρ_b calculation, the maximum value of ρ_b would still have been only about 12 percent of ρ_w . Since ρ_b is much smaller than ρ_w , the error introduced into the calculation of the local mass transfer coefficient on the exposed channel walls by the use of brass ribs instead of naphthalene ribs should be small (about 2 percent).

The maximum uncertainty in the calculations of ($\rho_w - \rho_b$) was estimated to be 6 percent. Other uncertainties in the

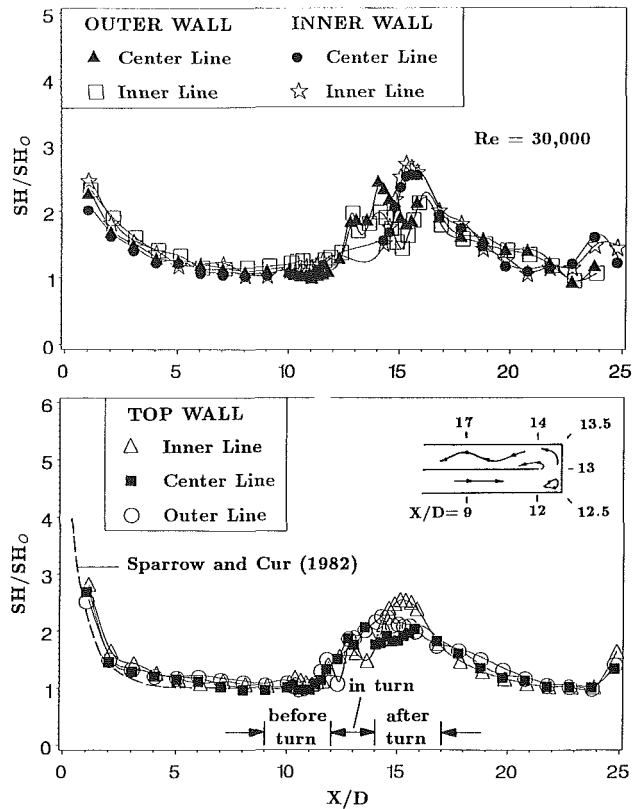


Fig. 4 Local Sherwood number ratio for a smooth channel with $Re = 30,000$

calculations of the density of solid naphthalene (ρ_s), the contour measurement (ΔZ), and the duration of the test run (Δt) were estimated to be 2, 4, and 3 percent, respectively. The uncertainty estimation method of Kline and McClintock (1953) determined a maximum uncertainty in the calculated local Sherwood numbers of less than 8 percent.

Results and Discussion

The local mass transfer results are presented in this section as the axial distributions of a normalized Sherwood number ratio Sh/Sh_0 , as given in equation (8). For each set of data, the Sherwood number ratios along the inner line, the center line, and the outer line (Fig. 3) on the top wall are plotted separately from those along two axial lines (inner line and center line) on the inner and outer walls. Along the axial lines, the Sh/Sh_0 data are unevenly distributed. For the smooth channel test runs, there are more data points around the turn than along the straight sections of the channel. For the ribbed channel runs, there are many data points between adjacent ribs on the top wall to illustrate the axially periodic nature of the Sh/Sh_0 distributions. The "before-turn" and "after-turn" regions refer to the sections of the test channel between $X/D = 9$ and 12, and $X/D = 14$ and 17 (three times the hydraulic diameter upstream and downstream of the turn), respectively.

Results for Smooth Channel. Typical results of the local Sherwood number ratios for the smooth channel are shown in Fig. 4 for $Re = 30,000$ (case 2). Attention is first focused on the Sh/Sh_0 distribution on the top wall in Fig. 4. In the entrance section, the Sherwood number ratio decreases monotonically with increasing axial distance until it attains the value of one at $X/D \cong 10$. The Sh/Sh_0 distribution compares well with that for a straight smooth channel of large aspect ratio by Sparrow and Cur (1982).

Entering the turn region, Sh/Sh_0 increases with a rapid in-

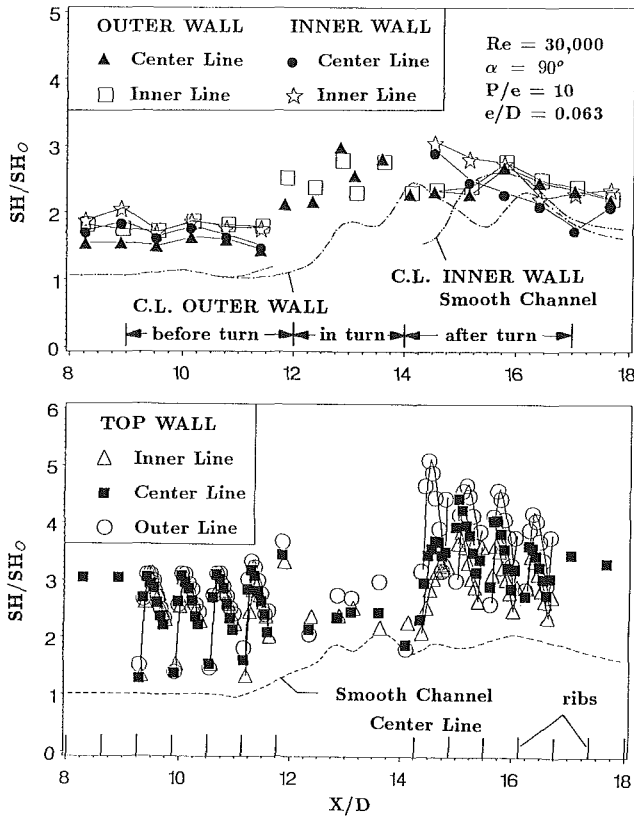


Fig. 5 Local Sherwood number ratio for a ribbed channel with $e/D = 0.063$, $P/e = 10$, and $Re = 30,000$

crease along the outer line. The increase is believed to be the result of secondary flow induced by the turn. The dip in the Sh/Sh_0 distribution along the outer line at $X/D \approx 12.5$ indicates that there is a low mass transfer zone at the outside corner of the turn region. The outer-line Sh/Sh_0 then increases gradually and reaches a maximum at the end of the turn ($X/D \approx 14.5$). The large Sh/Sh_0 values near the outer wall at the end of the turn are caused by the flow being forced outward by the sharp turn.

The low Sherwood number ratios along the inner line at $X/D \approx 13.5$ are due to the flow separation at the tip of the inner wall. The downturn of the Sh/Sh_0 distribution along the center line at $X/D \approx 14$ can also be attributed to the flow separation. The large values of Sh/Sh_0 at $X/D \approx 15$ along the inner line are due to the flow reattachment and the flow being pushed back toward the inner wall after the turn. In general, the top-wall Sh/Sh_0 values in the after-turn region are much higher than those in the before-turn region.

Leaving the after-turn region, the top-wall Sh/Sh_0 drops gradually. The flow becomes almost redeveloped near the end of the second straight section of the test channel.

Attention is now turned to the Sh/Sh_0 distributions on the inner wall and on the outer wall. In the before-turn region, the values of Sh/Sh_0 on both the inner and outer walls are about one. In the turn region, the outer-wall Sh/Sh_0 increases gradually around the turn. In the after-turn region, the Sh/Sh_0 along the outer wall is high at $X/D \approx 14$. The flow is being forced toward the outer wall at the end of the turn. Farther downstream, the outer-wall Sh/Sh_0 reaches a minimum at $X/D \approx 15$ and then a peak at $X/D \approx 16$, showing that the flow is being pushed away from the outer wall and then back toward the outer wall.

The effect of the flow separation (at the tip of the inner wall) and reattachment on the flow field can be seen clearly in the inner-wall Sh/Sh_0 distribution in the after-turn region.

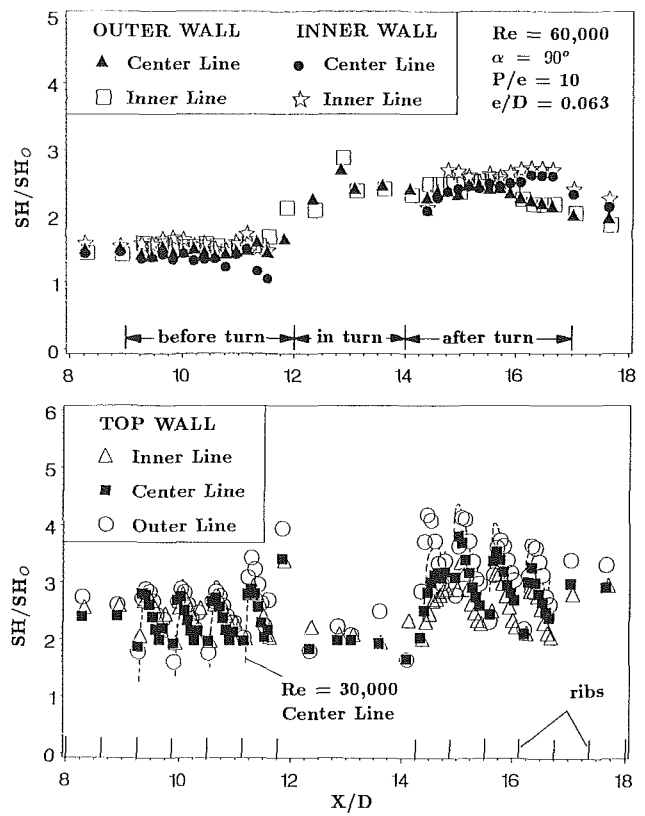


Fig. 6 Local Sherwood number ratio for a ribbed channel with $e/D = 0.063$, $P/e = 10$, and $Re = 60,000$

The inner-wall Sh/Sh_0 distribution is initially very low at $X/D \approx 14.5$ and has a high peak at $X/D \approx 15.5$.

The inner-wall and outer-wall Sh/Sh_0 values in the after-turn region are generally higher than those in the before-turn region. Downstream of the after-turn region, the Sh/Sh_0 drops gradually as the effect of the turn on the flow diminishes. In the downstream straight section of the test channel, the criss-crossing pattern of the Sh/Sh_0 distribution shows that the flow is being pushed toward the inner wall and the outer wall alternately.

Results for Rib-Roughened Channel. The experimental results for the rib-roughened channel with $e/D = 0.063$, $P/e = 10$ are shown in Fig. 5 for $Re = 30,000$ (case 5). The center-line Sherwood number ratios in the case of the smooth channel and $Re = 30,000$ are included for comparison. In the before-turn region of the test channel, the axial Sh/Sh_0 distribution on the top wall settles into a periodic pattern with a small spanwise variation, just before entering the sharp turn. In the periodic region, the maximum Sh/Sh_0 value between adjacent ribs is approximately equal to 3. The axial location where the value of Sh/Sh_0 is maximum (due to flow reattachment) is about four times the rib height downstream of a rib.

In the turn region, the top-wall Sh/Sh_0 is relatively low since there is no rib in the region. In the after-turn region, the top-wall Sh/Sh_0 distribution is generally higher than that in the before-turn region. There is an increase in the Sh/Sh_0 in the spanwise direction toward the outer wall. Farther downstream of the turn, the peak between adjacent ribs in the Sh/Sh_0 distribution decreases gradually and the spanwise variation becomes smaller.

The distributions of the Sherwood number ratio on the inner wall and the outer wall, separately from that on the top wall, are shown in Fig. 5. In the before-turn region, the Sh/Sh_0 distribution on the inner wall is about the same as that

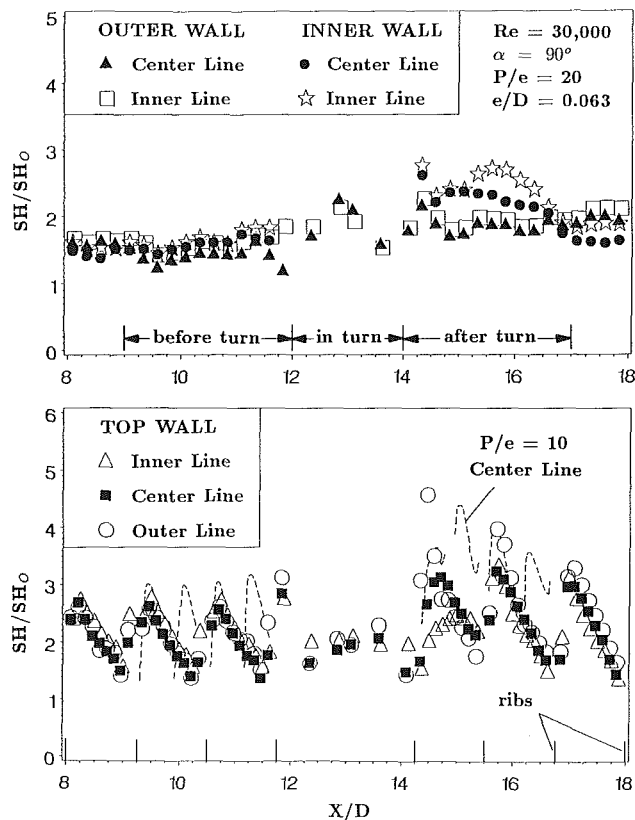


Fig. 7 Local Sherwood number ratio for a ribbed channel with $e/D = 0.063$, $P/e = 20$, and $Re = 30,000$

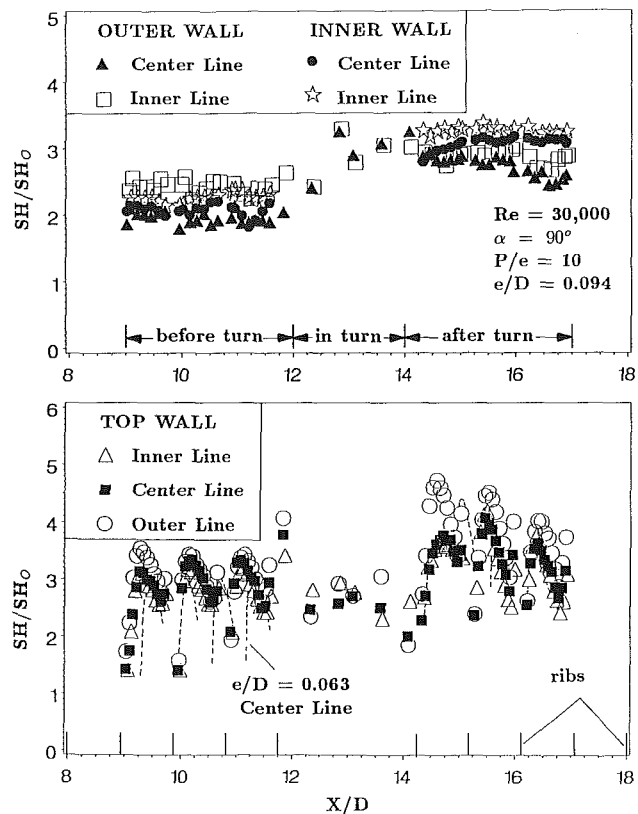


Fig. 8 Local Sherwood number ratio for a ribbed channel with $e/D = 0.094$, $P/e = 10$, and $Re = 30,000$

on the outer wall, with the inner-line Sh/Sh_0 values on each wall slightly higher than the corresponding center-line Sh/Sh_0 values (due to the proximity of the ribs on the top wall to the inner line on each wall). The outer-wall Sherwood number ratios in the turn region are generally higher than those in the before-turn region. After the turn, the side-wall Sherwood number ratios remain as high as those in the turn region and decrease gradually in the main flow direction.

Effect of Reynolds Number. The experimental results for the ribbed channel with $e/D = 0.063$, $P/e = 10$ are shown in Fig. 6 for $Re = 60,000$ (case 6). The center-line Sherwood number ratios for case 5 ($e/D = 0.063$, $P/e = 10$, and $Re = 30,000$) are included for comparison. The Sherwood number ratio distributions for $Re = 60,000$ and $Re = 30,000$ exhibit similar trends. On the top wall, the flow tends to reattach at a shorter distance downstream of the point of separation at $Re = 60,000$, about two times the rib height, than at $Re = 30,000$, about four times the rib height. In general, the Sherwood number ratio decreases slightly with increasing Reynolds number. The spanwise Sh/Sh_0 variation in the after-turn region also decreases slightly with increasing Reynolds number. For both Reynolds numbers, the after-turn top-wall Sherwood number ratios near the outer wall are higher than those near the inner wall.

Effect of Rib Spacing. The experimental results for a ribbed channel with $e/D = 0.063$ and $P/e = 20$ are shown in Fig. 7 for $Re = 30,000$ (case 7). In Fig. 7, the center-line Sherwood number ratios for case 5 ($e/D = 0.063$, $P/e = 10$, and $Re = 30,000$) are also given so the effect of varying the rib spacing on the Sh/Sh_0 distribution can be examined.

The effect of increasing the rib spacing (P/e) on the Sh/Sh_0 distribution around a sharp 180 deg turn is the overall lower Sh/Sh_0 values as a result of the longer and thicker concentration boundary layer downstream of flow reattachment when

the rib spacing is large. In the before-turn region, the top-wall Sh/Sh_0 distribution is axially periodic with a relatively small spanwise variation. The after-turn, top-wall Sh/Sh_0 distribution is generally higher than that in the before-turn region with the larger values of the Sh/Sh_0 along the outer line. As the peak between adjacent ribs in the after-turn Sh/Sh_0 distribution drops gradually with increasing axial distance, the spanwise variation decreases. The peak in the outer-line, top-wall Sh/Sh_0 distribution for $P/e = 20$ drops in the streamwise direction slightly faster than that for $P/e = 10$.

Effect of Rib Height. The effect of the rib height on the heat transfer around a sharp turn is studied by examining Fig. 8, in which the Sh/Sh_0 distributions for $e/D = 0.063$ and 0.094 (cases 5 and 8, respectively) are shown. The top-wall Sh/Sh_0 distribution for $e/D = 0.094$ is slightly higher than that for $e/D = 0.063$ around the sharp turn. In both cases, the peaks in the top-wall Sh/Sh_0 distributions in the after-turn region drop with increasing axial distance at about the same rate.

The spanwise variation of the after-turn top-wall Sh/Sh_0 for ribs with a large e/D is smaller than that for ribs with a small e/D . On the inner and outer walls, the Sh/Sh_0 distributions for $e/D = 0.094$ are again higher than those for $e/D = 0.063$ around the turn.

Average Sherwood Number Ratios and Correlations. The local Sherwood number ratios were averaged over various segments of the interior channel surfaces in the before-turn region, in the turn region, and in the after-turn region. The averaging of the local Sherwood number ratios was area-weighted. A typical set of \bar{Sh}/Sh_0 results for $Re = 30,000$ is given in Fig. 9. In the figure, the top-wall, outer-wall, and inner-wall average Sherwood number ratios for the smooth and roughened channel cases studied are shown in three separate charts.

Figure 9 shows that the present \bar{Sh}/Sh_0 data for the smooth

Table 2 Numerical values of the coefficients a , b , m , and n in equation (9)

Region	Surface	a	b	m	n
before turn, smooth channel	top wall	2.02	-0.06	0	0
	outer wall	2.10	-0.06	0	0
	inner wall	2.08	-0.06	0	0
in turn, smooth channel	top wall	3.21	-0.06	0	0
	outer wall	3.23	-0.06	0	0
after turn, smooth channel	top wall	3.84	-0.06	0	0
	outer wall	3.45	-0.06	0	0
	inner wall	4.07	-0.06	0	0
before turn, ribbed channel	top wall	7.2	-0.1	0.22	-0.3
	outer wall	4.6	-0.1	0.69	-0.11
	inner wall	4.6	-0.1	0.53	-0.15
in turn, ribbed channel	top wall	6.7	-0.1	0.23	-0.31
	outer wall	7.0	-0.1	0.31	-0.52
after turn, ribbed channel	top wall	9.3	-0.1	0.13	-0.49
	outer wall	6.7	-0.1	0.4	-0.30
	inner wall	7.3	-0.1	0.68	-0.14

channel are always lower than those for the rib-roughened channel. For instance, the top-wall \bar{Sh}/Sh_0 values for the smooth channel in the before-turn region, the turn region, and the after-turn region are 1.1, 1.7, and 2.05, respectively. The corresponding \bar{Sh}/Sh_0 values for a typical roughened channel with $P/e = 10$ and $e/D = 0.063$ are 2.6, 2.55, and 3.5. Increasing the rib height results in a higher \bar{Sh}/Sh_0 around the turn due to the higher turbulence level in the flow for the larger rib case. Increasing the rib pitch lowers the \bar{Sh}/Sh_0 around the turn because of the longer boundary layer between adjacent ribs downstream of the reattachment zone.

The after-turn \bar{Sh}/Sh_0 values are always higher than the corresponding before-turn values as a result of the sharp turn. For the smooth channel, the top-wall \bar{Sh}/Sh_0 in the turn region is more than 50 percent higher than that in the before-turn region. For the roughened channel cases, the top-wall \bar{Sh}/Sh_0 values in the turn region are slightly lower than the respective before-turn \bar{Sh}/Sh_0 values because there is no rib on the top-wall in the turn region.

In all cases studied, the values of the outer-wall \bar{Sh}/Sh_0 in the turn region are only slightly different from the corresponding after-turn values.

The \bar{Sh}/Sh_0 data for both the smooth and roughened channels were correlated well by the following equation:

$$\bar{Sh}/Sh_0 = a Re^b [(e/D)/0.063]^m [(P/e)/10]^n \quad (9)$$

with the numerical values of a , b , m , and n listed in Table 2. Equation (9) correlates all of the \bar{Sh}/Sh_0 data of the present investigation within ± 6 percent. Note that equation (9) applies only to a smooth channel or a ribbed channel with a rib angle-of-attack of 90 deg. Correlations for other angle-of-attack cases are in Chandra et al. (1987) and Han and Chandra (1987). In Fig. 10, the present top-wall \bar{Sh}/Sh_0 data in the before-turn and after-turn regions for both the smooth and roughened channels are plotted against the flow Reynolds number with the correlation of equation (9).

Comparison With Heat Transfer Data. The results of the present study are compared with published heat transfer data for smooth and roughened channels. The present smooth channel data are presented in Fig. 11(a) with the heat transfer data for a smooth, two-pass, rectangular channel with an aspect ratio of 0.4 reported by Metzger and Sahm (1985). In Fig. 11(a), the present overall Sherwood number ratio in the before-turn, turn, or after-turn region, \bar{Sh}/Sh_0 , is the area-weighted average of the \bar{Sh}/Sh_0 values on the top and side walls in the respective region. The heat transfer data are based on the Nusselt number-Reynolds number correlations in regions 2, 3, and 4 given by Metzger and Sahm (1985). The Nusselt numbers are converted to the corresponding Sherwood numbers by equation (6).

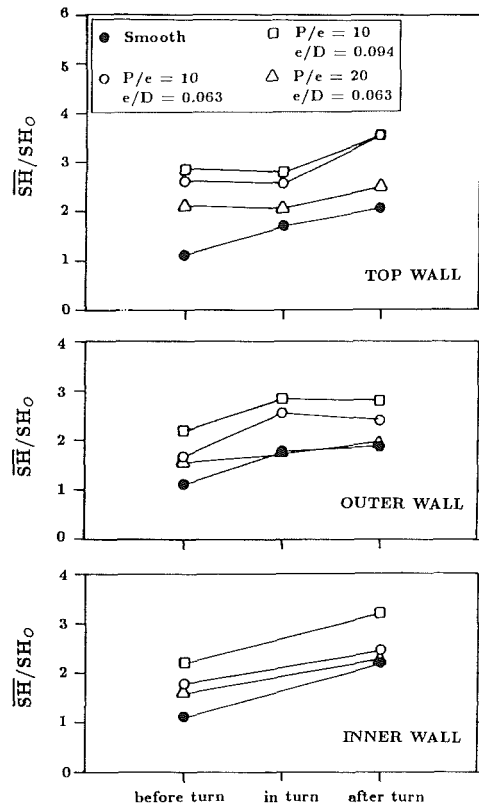


Fig. 9 Average Sherwood number ratio on each of the channel surfaces with $Re = 30,000$

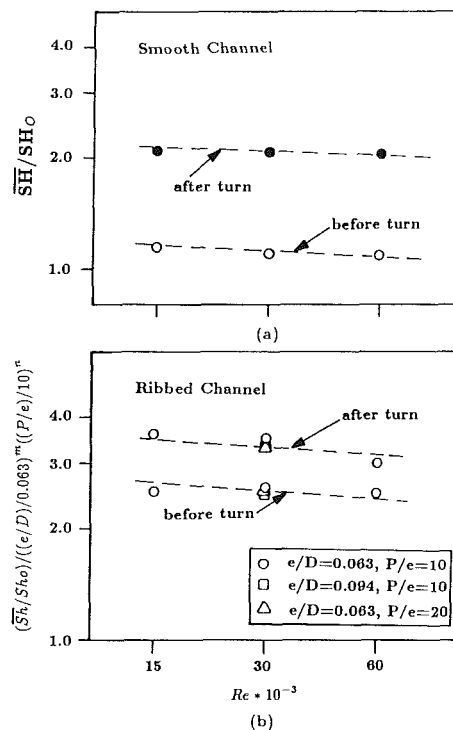


Fig. 10 Correlations of the average Sherwood number ratio on the top wall

Both the present mass transfer data and the heat transfer data show that, for all three Reynolds numbers, the average Sherwood number ratios in the after-turn region and in the turn region are successively higher than those in the before-turn region. In addition, both the present average Sherwood

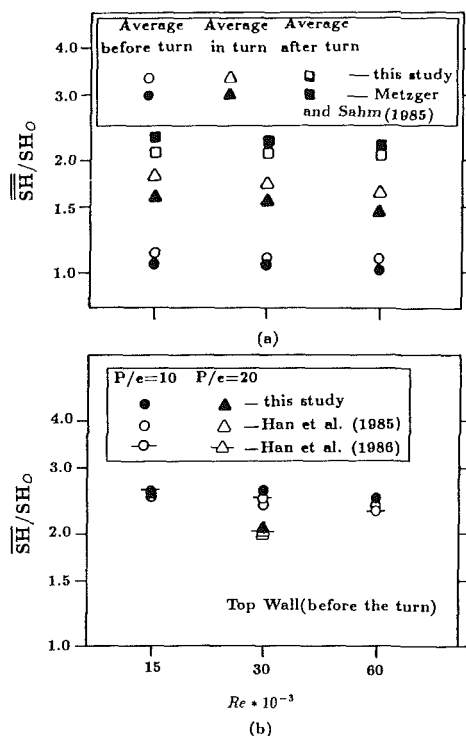


Fig. 11 Comparison between the present results and published heat transfer data

number ratios and those of Metzger and Sahn (1985) decrease slightly with increasing Reynolds number.

For the typical case of $Re = 30,000$, the present mass transfer data in the before-turn region and in the turn region are about 4 and 12 percent higher than the corresponding heat transfer data; the present \overline{Sh}/Sh_0 in the after-turn region is about 9 percent lower. Considering the differences in the channel aspect ratios and in the channel surfaces over which the data are averaged in the two studies, the agreement between the present data and those by Metzger and Sahn (1985) is acceptable.

In Fig. 11(b), the present ribbed channel data are compared with the heat transfer data by Han et al. (1985, 1986). The heat transfer data are for the fully developed flow of air in a uniformly heated, straight, square channel with two opposite ribbed walls, and with the same values of e/D , P/e , and Re as those of the present study. The fully developed Nusselt numbers on the ribbed walls are converted to their corresponding Sherwood numbers by equation (6). They are then plotted with the before-turn, top-wall \overline{Sh}/Sh_0 data of the present study for the three Reynolds numbers of 15,000, 30,000, and 60,000. Figure 11(b) shows that the present mass transfer data are slightly higher (by up to 10 percent) than the heat transfer data. This may be due to the effect of the turn on the top-wall \overline{Sh}/Sh_0 at the end of the before-turn region, or the use of brass ribs instead of naphthalene ribs as turbulence promoters.

Concluding Remarks

Conclusions from the study of the detailed mass transfer distributions around the sharp 180 deg turns in a smooth channel and in a rib-roughened channel are:

1 For the smooth channel, the mass transfer around the turn is influenced by the flow separation at the tip of the divider (inner) wall and the secondary flow induced by the centrifugal force at the turn. The mass transfer after the turn is higher than that before the turn. The mass transfer in the turn

is also high compared with that before the turn except at the first outside corner of the turn.

2 For the rib-roughened channel, the mass transfer around the turn is influenced not only by the flow separation and the secondary flow at the turn, but also by the presence of repeated ribs on the top and bottom walls. The mass transfer coefficients on the smooth side walls and on the rib-roughened top and bottom walls around the turn are larger than the corresponding coefficients for the smooth channel. The axially periodic distribution of the top-wall mass transfer coefficient after the turn is higher than that before the turn with a more noticeable spanwise variation. The inner-wall and outer-wall mass transfer coefficients after the turn are higher than the respective before-turn coefficients.

3 For the range of Reynolds number studied, the average Sherwood number ratios around the sharp turns in the smooth and rib-roughened channels decrease slightly with increasing Reynolds number. For the ribbed channel, the spanwise variation of the top-wall Sherwood number ratio in the after-turn region decreases with increasing Reynolds number.

4 The mass transfer around the turn in the ribbed channel decreases with increasing rib spacing and increases with increasing rib height.

5 The average Sherwood number ratios for individual wall segments around the turns in the smooth and ribbed channels can be correlated by equation (9) to within ± 6 percent.

6 The published heat transfer results for straight rib-roughened channels can be applied to the design of the straight section before the first sharp turn in a multipass ribbed cooling passage in a turbine blade.

Acknowledgments

The investigation was supported in part by the NASA-Lewis Research Center through Contract NAS 3-24227 and by the NSF through Grant MEA-8205234. Very special thanks are due to Dr. C. P. Lee of General Electric-Aircraft Engine Business Group for his suggestions and discussions at the beginning of this study.

References

- Boyle, R. J., 1984, "Heat Transfer in Serpentine Passages With Turbulence Promoters," ASME Paper No. 84-HT-24.
- Chandra, P. R., Han, J. C., and Lau, S. C., 1987, "Effect of Rib Angle on Local Heat/Mass Transfer Distribution in a Two-Pass Rib-Roughened Channel," ASME Paper No. 87-GT-94; ASME *Journal of Turbomachinery*, in press.
- Han, J. C., 1984, "Heat Transfer and Friction in Channels With Two Opposite Rib-Roughened Walls," ASME *JOURNAL OF HEAT TRANSFER*, Vol. 106, pp. 774-781.
- Han, J. C., Park, J. S., and Lei, C. K., 1985, "Heat Transfer Enhancement in Channels With Turbulence Promoters," ASME *Journal of Engineering for Gas Turbines and Power*, Vol. 107, pp. 628-635.
- Han, J. C., Park, J. S., and Ibrahim, M. Y., 1986, "Measurement of Heat Transfer and Pressure Drop in Rectangular Channels With Turbulence Promoters," NASA CR-4015; USAAVSCOM-TR-86-C-25.
- Han, J. C., and Chandra, P. R., 1987, "Local Heat/Mass Transfer and Pressure Drop in a Two-Pass Rib-Roughened Channel for Turbine Airfoil Cooling," NASA CR-179635; AVSCOM-TR-87-C-14.
- Kline, S. J., and McClintock, F. A., 1953, "Describing Uncertainties in Single-Sample Experiments," *Mechanical Engineering*, Vol. 75, pp. 3-8.
- Metzger, D. E., and Sahn, M. K., 1985, "Heat Transfer Around Sharp 180 Degree Turns in Smooth Rectangular Channels," ASME Paper No. 85-GT-122.
- Sogin, H. H., 1958, "Sublimation From Disks to Air Streams Flowing Normal to Their Surfaces," *Trans. ASME*, Vol. 80, pp. 61-69.
- Sparrow, E. M., and Cur, N., 1982, "Turbulent Heat Transfer in a Symmetrically or Asymmetrically Heated Flat Rectangular Duct With Flow Separation at Inlet," ASME *JOURNAL OF HEAT TRANSFER*, Vol. 104, pp. 82-89.
- Sparrow, E. M., and Tao, W. Q., 1983, "Enhanced Heat Transfer in a Flat Rectangular Duct With Streamwise-Periodic Disturbances at One Principal Wall," ASME *JOURNAL OF HEAT TRANSFER*, Vol. 105, pp. 851-861.
- Sparrow, E. M., and Tao, W. Q., 1984, "Symmetric vs. Asymmetric Periodic Disturbances at the Walls of a Heated Flow Passage," *International Journal Heat Mass Transfer*, Vol. 27, pp. 2133-2144.

P. K. Sarma

Department of Mechanical Engineering.

T. Subrahmanyam

Department of Mechanical Engineering.

V. Dharma Rao

Department of Chemical Engineering.

College of Engineering,
Andhra University,
Visakhapatnam 530 003 India

Natural Convection From a Vertical Heat-Generating Fin—a Conjugate Problem

The problem of natural convection from a vertical heat-generating fin is solved by coupling the equation of thermal diffusion in the fin to the constitutive equations of the ambient medium under laminar flow conditions. The analysis is accomplished by employing an integral method. For the range of values of the fin parameter and the strength of the heat source considered in the analysis, the numerical results are rendered into a correlation equation for the average Nusselt number as a function of the fin parameter and the strength of the heat source.

Introduction

Natural convection is a very widely investigated field and many reviews, such as Raithby and Hollands (1975), Ede (1967), and Jaluria (1980) exist depicting the state of the art in this particular area. Heat transfer studies on fins are important in connection with the development of low-power-output electronic devices. Lock and Gunn (1968) developed a similarity solution from a tapered fin in a fluid of infinite Prandtl number. The analysis of Sparrow and Acharya (1981) treated the problem of natural convection from a fin coupling the constitutive equations of the medium with that of the process of thermal diffusion in the material. The flow of the medium adjacent to the fin is due to the resultant buoyant forces arising from the thermal potential between the medium and the fin. The analysis of Sparrow and Acharya (1981) indicated that the heat transfer coefficient along the length of the fin is not uniform but is nonmonotonically varying with the spatial distance measured from its base. Kuehn et al. (1983) presented a similarity solution for the conjugate free convective heat transfer from a vertical fin of infinite length. Himasekhar (in press) extended that analysis for a long vertical fin with variable thermal conductivity and variable thickness.

The purpose of this study is to investigate the performance of the fin with a heat-generating source in the constitutive equations. In practice, the fin can be a component for a low-powered electronic circuit in which Joulean heating occurs. For such cases the dissipation of the heat to the medium is represented by the inclusion of the source term in the equation of thermal diffusion in the fin material. Thus, this special case of the conjugate problem of the fin with internal heat generation, not tackled earlier, is solved and the efficacy of the integral method applied to the conjugate problem is tested.

Formulation

The fin configuration is shown as the inset in Fig. 1. The fin is situated in a quiescent medium, with a temperature less than that at the base of the fin. In addition, the fin is generating a source of q' due to the passage of electric current. The flow adjacent to the fin is caused by the buoyant forces under laminar flow conditions. For the configuration and the coordinate system chosen, the problem is governed by the steady-state one-dimensional heat conduction equation in a thin fin with $(\delta_f/L) \ll 1$.

$$\frac{d^2 T_w}{dx^2} - \frac{Pq}{k_w A} + \frac{q'}{k_w} = 0 \quad (1)$$

where $q(x)$ is the flux of heat removal at the lateral surface of the fin, given by

$$q(x) = -k_L \frac{dT}{dy} \Big|_{y=0}$$

Further, the equations of conservation of mass, momentum, and energy in the ambient medium can be written, respectively, as

$$\frac{\partial u}{\partial x} + \frac{\partial v}{\partial y} = 0 \quad (2)$$

$$u \frac{\partial u}{\partial x} + v \frac{\partial u}{\partial y} = \nu \frac{\partial^2 u}{\partial y^2} + g\beta(T - T_\infty) \quad (3)$$

$$u \frac{\partial T}{\partial x} + v \frac{\partial T}{\partial y} = \alpha \frac{\partial^2 T}{\partial y^2} \quad (4)$$

The boundary conditions are

$$\begin{aligned} y=0, u=v=0, \text{ and } T=T_w \text{ where } T_w=T_w(x) \text{ for } 0 < x < L \\ y=\delta, u=0, \text{ and } T=T_\infty \\ x=L, T=T_{w,L} \end{aligned} \quad (5)$$

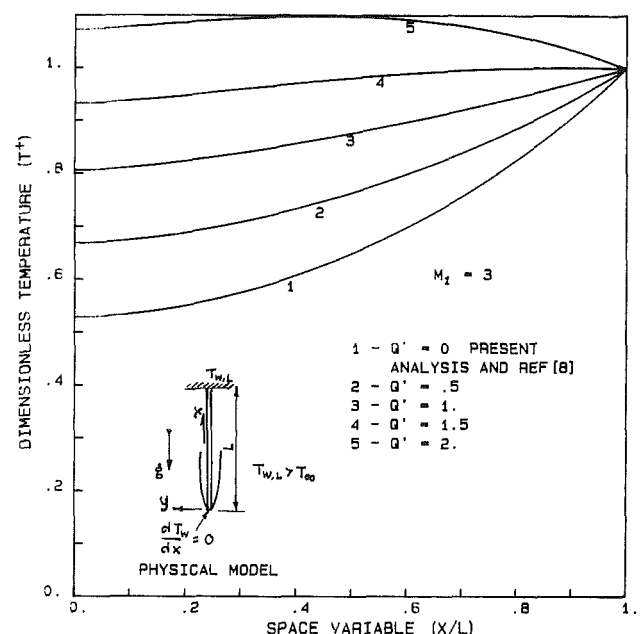


Fig. 1 Variation of temperature in the fin as a function of Q' for $M_1 = 3$

Contributed by the Heat Transfer Division for publication in the JOURNAL OF HEAT TRANSFER. Manuscript received by the Heat Transfer Division November 10, 1986.

$$x=0, \frac{dT_w}{dx}=0 \text{ (adiabatic condition of heat flow at the tip)} \quad (6a)$$

The results are also obtained for another possible boundary condition at the tip of the fin, i.e., the condition of prescribed temperature, as expressed below:

$$x=0, T_w = T_{w,0} = \text{const} \quad (6b)$$

Further, if $T_w = T_{w,0} = 0$ and $dT_w/dx = 0$ at $x=0$, the problem corresponds to the case of an infinitely long fin. From a mathematical point of view, equation (1), the second-order differential equation satisfying three boundary values, one at the base and two at the tip, would necessarily impose a constraint on the magnitude of the independent variable, i.e., the length of the fin.

The following velocity and temperature profiles are assumed in the ambient medium adjacent to the fin:

$$\frac{u}{u_i} = (y/\delta)(1 - y/\delta)^2$$

where $u_i = u_i(x)$

$$\frac{T - T_\infty}{T_w - T_\infty} = (1 - y/\delta)^2 \quad (7)$$

Equations (2)–(4) are transformed into integral form (not shown for the sake of brevity) with the aid of the boundary conditions, equation (5). The resulting integral equations are evaluated making use of the velocity and temperature profiles, equation (7), to obtain the constitutive differential equations given below:

$$\frac{d^2 T^+}{d\eta^2} - 2M^{4/3} \frac{T^+}{f} + Q' = 0 \quad (8)$$

$$\frac{1}{105} \frac{d}{d\eta} (\phi^2 f) = \text{Pr} M^{4/3} \left(\frac{f T^+}{3} - \frac{\phi}{f} \right) \quad (9)$$

$$\frac{d}{d\eta} (\phi f T^+) = 60 M^{4/3} \frac{T^+}{f} \quad (10)$$

where f and ϕ are the nondimensional boundary layer

thickness, δ , and characteristic velocity, u_i , respectively defined as

$$f(\eta) = \frac{\delta}{L} \left[\frac{k_w A}{k_L P L} \right]^{-1/3} \text{Ra}^{1/3} \quad (11)$$

$$\phi(\eta) = \frac{u_i L}{\alpha} \left[\frac{k_w A}{k_L P L} \right]^{-2/3} \text{Ra}^{-1/3} \quad (12)$$

The transformed boundary conditions for solving equations (8)–(10) are as follows:

$$\begin{aligned} f = \phi = 0 & \text{ at } \eta = 0 \\ T^+ = 1 & \text{ at } \eta = 1 \end{aligned} \quad (13)$$

$$\frac{dT^+}{d\eta} = 0 \text{ at } \eta = 0 \text{ (short fin with adiabatic condition at the tip)} \quad (14a)$$

$$T^+ = T_{w,0}^+ \text{ at } \eta = 0 \text{ (short fin with finite temperature at the tip)} \quad (14b)$$

$$T^+ = \frac{dT^+}{d\eta} = 0 \text{ at } \eta = 0 \text{ (long fin)} \quad (14c)$$

The selection of the boundary conditions depends on the physical problem to be solved.

Either the adiabatic condition of heat flow, equation (14a), or the condition of prescribed tip temperature, equation (14b), is to be used. Application of the condition, i.e., equation (14c), would result in fixing up the critical length of the fin. In other words the critical value of the fin parameter is to be evaluated iteratively for each assumed value of Q' .

Another important observation can be made from the list of equations (8)–(10) for $\text{Pr} \gg 1$. In equation (9), the term on the left-hand side represents inertial forces and the two terms within brackets on the right-hand side represent shear and buoyancy terms. For $\text{Pr} \gg 1$ the term representing the inertial forces can be neglected in comparison with the terms representing the other two forces to obtain

$$\phi = \frac{f T^+}{3} \quad (15)$$

Nomenclature

A = cross-sectional area of fin, m^2	Nu = local Nusselt number	u_i = characteristic velocity appearing in the velocity profile, equation (7)
E = fin efficiency defined in equation (20)	$= hL/k_L$	
f = dimensionless thickness of the boundary layer, equation (11)	Nu_m = average Nusselt number	u, v = x and y components of velocity, respectively
g = acceleration due to gravity	$= h_m L/k_L$	x, y = position coordinates
Gr = Grashof number	P = perimeter of fin, m	α = thermal diffusivity, m^2/s
$= g\beta(T_{w,L} - T_\infty)L^3/\nu^2$	Pr = Prandtl number of ambient medium	β = coefficient of thermal expansion, K^{-1}
h = local heat transfer coefficient, $\text{W}/\text{m}^2\text{-}^\circ\text{C}$	q = flux of heat removal at lateral surface of fin, equation (1), W/m^2	δ = thickness of the boundary layer, m
h_m = average heat transfer coefficient, $\text{W}/\text{m}^2\text{-}^\circ\text{C}$	q' = strength of the heat source, W/m^3	δ_i = thickness of the fin, m
\bar{h}_{iso} = average heat transfer coefficient for isothermal plate when $T_w = T_{w,L}$ for $0 < x < L$, $\text{W}/\text{m}^2\text{-}^\circ\text{C}$	Q' = dimensionless strength of the heat source	η = dimensionless space variable = (x/L)
k = thermal conductivity, $\text{W}/\text{m}\text{-}^\circ\text{C}$	$= q' L^2/k_w(T_{w,L} - T_\infty)$	ν = kinematic viscosity, m^2/s
L = length of fin, m	Q_{fin} = heat dissipation at the base of the fin, i.e., at $x=L$	ϕ = dimensionless characteristic velocity, equation (12)
M = fin parameter = $(k_L P L/k_w A) \text{Ra}^{1/4}$	Q_{iso} = heat removal at the lateral surface of the fin under isothermal conditions	
M_1 = fin parameter = $(k_L P L/k_w A) \text{Gr}^{1/4}$	Ra = Rayleigh number = $(\text{Gr} \cdot \text{Pr})$	Subscripts
M^* = critical fin parameter	T = temperature	$W,0$ = tip of the fin, $x=0$
	T^+ = dimensionless temperature = $(T_w - T_\infty)/(T_{w,L} - T_\infty)$	∞ = medium
		L = fluid
		W = wall
		W,L = base of the fin, $x=L$

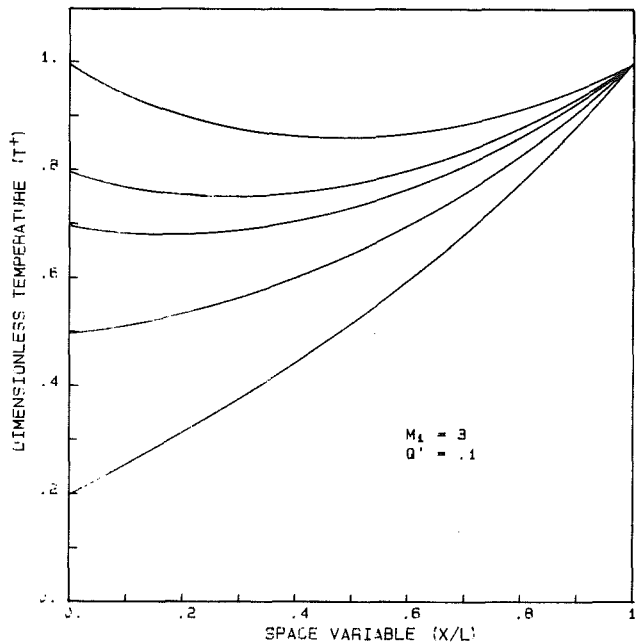


Fig. 2 Variation of temperature in the fin for different tip temperatures for $M_1 = 3$ and $Q' = 0.1$

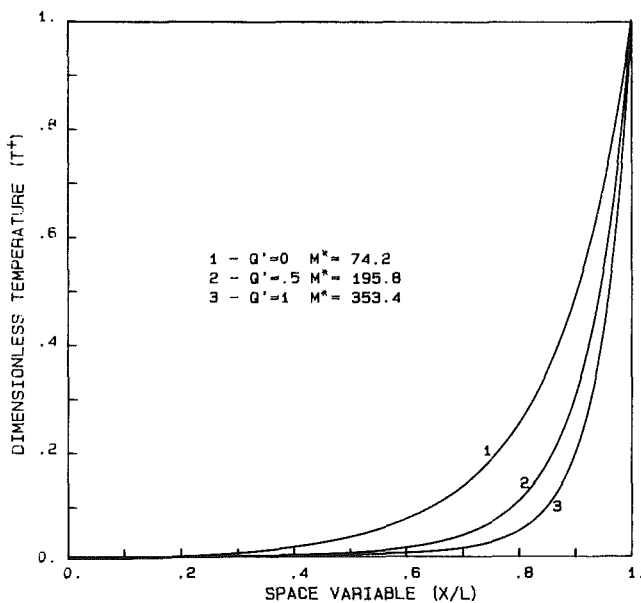


Fig. 3 Effect of Q' on the temperature distribution along a long fin

Equations (8), (10), and (15) can be manipulated to yield a single differential equation in T^+ as follows

$$\frac{d^2 T^+}{d\eta^2} - 2M^{4/3} \frac{T^{+5/3}}{90^{1/3}} (dT^+/d\eta)^{-1/3} + Q' = 0 \quad (16)$$

The boundary conditions are

$$\frac{dT^+}{d\eta} = 0 \text{ at } \eta = 0 \text{ and } T^+ = 1 \text{ at } \eta = 1 \quad (16a)$$

Equation (16) suggests that for high Prandtl numbers, the temperature field is a function of the fin parameter for a given Q' .

Local and Mean Heat Transfer Coefficients. The local heat transfer coefficients are evaluated from the equation

$$h = 2 \frac{k_L}{\delta} \quad (17)$$

Equation (17), when expressed in dimensionless form, gives the local Nusselt number as

$$\frac{Nu}{Ra^{1/4}} = \frac{2M^{1/3}}{f} \quad (18)$$

The average Nusselt number is obtained by integrating equation (18) within the limits for η , from 0 to 1, to give

$$\frac{Nu_m}{Ra^{1/4}} = 2M^{1/3} \int_0^1 \frac{d\eta}{f(\eta)} \quad (19)$$

Fin Efficiency. In problems related to fins, estimation of the fin efficiency is an important feature. Efficiency is defined as the ratio of the rate of heat dissipation from the base into the fin to the rate of heat removal by the medium at the lateral surface of the fin if the fin were to be at the base temperature all along its length

$$E = \frac{Q_{fin}}{Q_{iso}} = \frac{k_w A}{\bar{h}_{iso} (T_{w,L} - T_{\infty}) PL} \left. \frac{dT_w}{dx} \right|_{x=L} \quad (20)$$

In dimensionless form

$$E = \frac{1.476}{M} \left. \frac{dT^+}{d\eta} \right|_{\eta=1} \quad (20a)$$

Results and Discussion

Equations (8)–(10) are simultaneously solved numerically subject to the boundary conditions, equations (13)–(14c), for $Pr = 0.7$. The case of the fin for the adiabatic condition at its tip with no source term is first solved and the results for $Q' = 0$ are compared with the solution of Sparrow and Acharya (1981) in Fig. 1 and for the sake of comparison the fin parameter M is transformed to M_1 according to the definition adopted by them. A close agreement is observed between their results and the results of the present analysis, indicating the efficacy of the integral method of analysis for conjugate problems. Further, Fig. 1 shows the temperature variation along the fin for the fin parameter, $M_1 = 3$, and for values of the nondimensional strength of the heat source Q' from 0 to 3.5. The tendency for the fin is to assume higher values of temperature with an increase in the value of the fin parameter M_1 . As can be expected, an increase in Q' , the strength of the heat source, has resulted in an increase in the temperature all along the fin. Also, it can be observed that the temperature derivative at the base of the fin can be positive, zero, or negative implying the direction of heat flow at the base. The values of M and Q' profoundly influence the temperature profile in the fin and hence its performance. The problem is also solved for the second type of boundary condition at the tip, i.e., the condition of prescribed tip temperature, given by equation (14b). The temperature profiles in the fin are shown in Fig. 2 for different values of prescribed temperature at the tip, i.e., at $(x/L) = 0$. This particular case would lead to definite temperature gradients at both the tip and the base. In Fig. 3, typical temperature profiles for various values of Q' in a long fin are shown plotted. As pointed out earlier for the case of a long fin, each value of Q' has a corresponding critical value of the fin parameter M^* . It is observed that as Q' increases, the value of M^* also increases.

The next part of the analysis corresponds to the case of a short fin with negligible heat dissipation at its tip. The effect of M_i and Q' on local Nusselt numbers is presented in Fig. 4. It is interesting to note that in the region of the tip of the fin the local Nusselt numbers increase with an increase in Q' . At the base of the fin a reverse trend is observed, i.e., the local Nusselt numbers decrease with an increase in Q' . The fin efficiency as a function of M and Q' is shown plotted in Fig. 5, and the results can be represented by the following expression:

$$E = C - DQ' \quad (21)$$

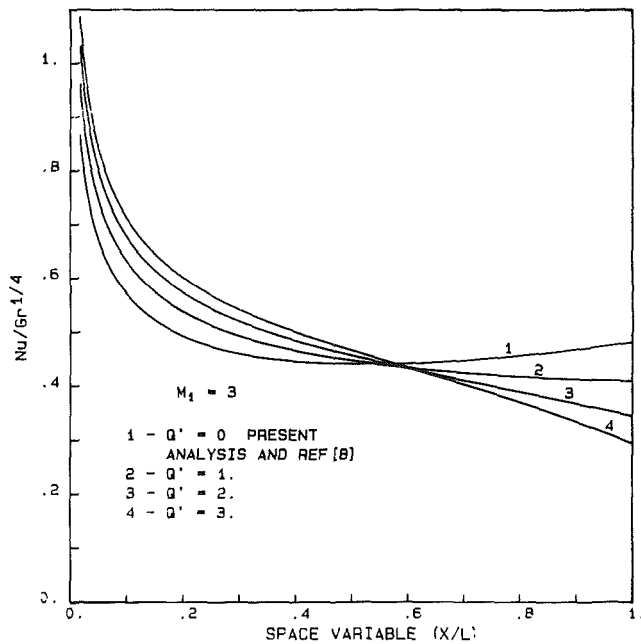


Fig. 4 Variation of local heat transfer coefficients along the fin for different values of Q' for $M_1 = 3$

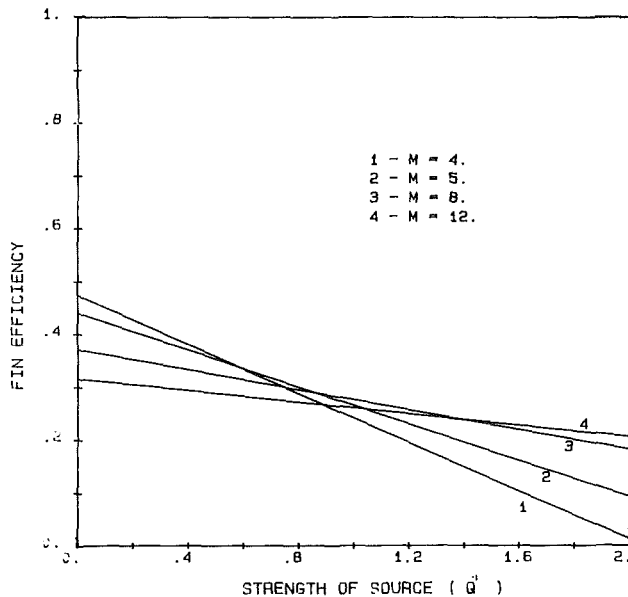


Fig. 5 Variation of fin efficiency as a function Q' for $4 < M < 12$

where C and D are functions of the fin parameter M as given by the regression analysis adopted to the numerical results derived from the computer.

$$C = 0.85M^{-0.4} \text{ and } D = 2.2M^{-1.6} \quad (22)$$

As one would expect, the fin efficiency decreases as Q' increases. For the range of the parameters $4 < M < 12$, and $0.6 < Q' < 1$, the variation in the fin efficiency is marginal.

In Fig. 6, the variation of the average Nusselt number with the strength of the source is shown for $1 < M < 20$. It is observed that the mean Nusselt variation, which is more or less linear, can be approximated by the following functional relationship:

$$Nu_m = 0.547Ra^{1/4} \exp(AQ' - BM) \quad (23)$$

where $A = 0.0122$, $B = 0.0034$; $0 < M < 24$ and $0 < Q' < 2$.

The average deviation of the expression from the numerical results is ± 0.17 percent, indicating the utility of equation (23)

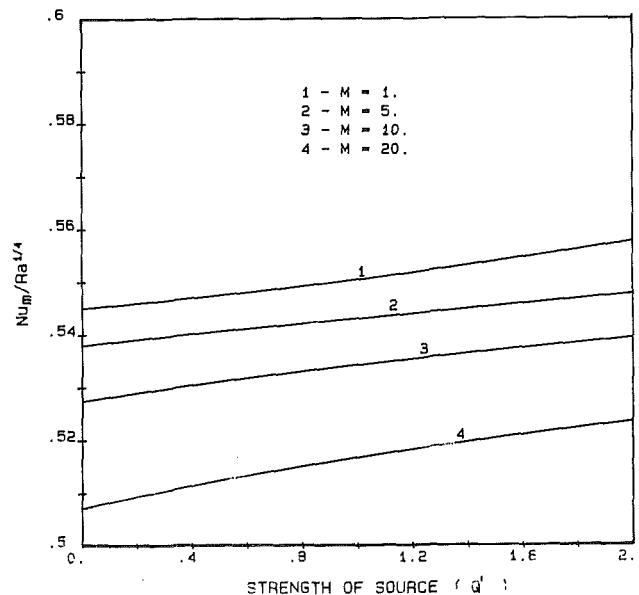


Fig. 6 Effect of Q' , the strength of the heat source, on average Nusselt number for $1 < M < 20$

in predicting the average Nusselt number as a function of the fin parameter and the strength of the source. Another aspect is also obvious, that for both M and Q' tending to zero the fin problem tends to the case of an isothermal plate maintained throughout at a temperature $T_{w,L}$. Equation (23) for $M = Q' = 0$ coincides with the expression given by Eckert and Drake (1972) for an isothermal plate.

Conclusions

The analysis establishes the influence of Q' on the performance of the fin in a quiescent medium. It is observed that the integral technique employed in the analysis is accurate enough (at least for $Pr = 0.7$) in predicting the thermal fields along the fin in as much the values agree well with those of Sparrow and Acharya (1981). Equation (21) can be employed to estimate the rate of heat removal at the base of the fin for given values of M and Q' . Equation (23) can be used for predicting the average heat transfer coefficients.

Acknowledgments

The authors thank the University Grants Commission, New Delhi for the financial support provided under Departmental Research Support Programme.

References

- 1 Eckert, E. R. G., and Drake, R. M., Jr., *Analysis of Heat and Mass Transfer*, McGraw-Hill Kogakusha, Ltd., International Student ed.
- 2 Ede, A. J., 1967, "Advances in Free Convection," *Advances in Heat Transfer*, Vol. 4, pp. 1-64.
- 3 Himasekhar, K., (in press), "Integral Analysis of Conjugate Natural Convection Heat Transfer From a Long Vertical Fin," *Int. J. Heat Mass Transfer*.
- 4 Jaluria, Y., 1980, *Natural Convection Heat and Mass Transfer*, Pergamon Press, New York, p. 73.
- 5 Kuehn, T. H., Kwon, S. S., and Tolpadi, A. K., 1983, "Similarity Solution for Conjugate Natural Convection Heat Transfer From a Long Vertical Plate Fin," *Int. J. Heat Mass Transfer*, Vol. 26, pp. 1718-1721.
- 6 Lock, G. S. H., and Gunn, J. C., 1968, "Laminar Free Convection From a Downward-Projecting Fin," *ASME JOURNAL OF HEAT TRANSFER*, Vol. 90, pp. 63-70.
- 7 Raithby, G. D., and Hollands, K. G. T., 1975, "A General Method of Obtaining Approximate Solutions to Laminar and Turbulent Free Convection Problems," *Advances in Heat Transfer*, Vol. 11, Academic Press.
- 8 Sparrow, E. M., and Acharya, S., 1981, "A Natural Convection Fin With Solution-Determined Non-monotonically Varying Heat Transfer Coefficients," *ASME JOURNAL OF HEAT TRANSFER*, Vol. 103, pp. 218-225.

Natural Convection Along Slender Vertical Cylinders With Variable Surface Temperature

H. R. Lee

T. S. Chen

Fellow ASME

B. F. Armaly

Fellow ASME

Department of Mechanical and Aerospace
Engineering,
University of Missouri-Rolla,
Rolla, MO 65401

Natural convection in laminar boundary layers along slender vertical cylinders is analyzed for the situation in which the wall temperature $T_w(x)$ varies arbitrarily with the axial coordinate x . The governing boundary layer equations along with the boundary conditions are first cast into a dimensionless form by a nonsimilar transformation and the resulting system of equations is then solved by a finite difference method in conjunction with the cubic spline interpolation technique. As an example, numerical results were obtained for the case of $T_w(x) = T_\infty + ax^n$, a power-law wall temperature variation. They cover Prandtl numbers of 0.1, 0.7, 7, and 100 over a wide range of values of the surface curvature parameter. Representative local Nusselt number as well as velocity and temperature profiles are presented. Correlation equations for the local and average Nusselt numbers are also given.

Introduction

Heat transfer by natural convection along a vertical cylinder has been analyzed rather extensively. Elenbaas (1948) used Langmuir's stagnant film model to evaluate the heat transfer coefficient for a vertical cylinder with uniform wall temperature. Sparrow and Gregg (1956) also used the stagnant film model along with a series expansion to solve the isothermal cylinder problem. Subsequently, the power series expansion method was used by Kuiken (1968) and by Fujii and Uehara (1970) in their studies of natural convection along vertical cylinders with axial variations in wall temperature and surface heat flux. However, owing to the truncation nature and the uncertain convergence characteristics of power series, their series solutions are expected to be valid only for small values of the cylinder curvature parameter; that is, for cylinders with large radius that do not deviate significantly from a vertical flat plate. To analyze the problems of slender cylinders, Cebeci and Na (1969, 1970), and Narain and Uberoi (1972) employed the similarity solution method and obtained results for the cases of uniform wall temperature and uniform surface heat flux, respectively. Later, Minkowycz and Sparrow (1974) used the local nonsimilarity solution method to re-examine the case of isothermal vertical cylinders and were able to obtain numerical results for a Prandtl number of 0.733 that cover a wider range of curvature parameter, $0 \leq \xi \leq 10$. More recently, Chen and Yuh (1980) included the effect of mass transfer and obtained results for $Pr = 0.7$ and 7 covering large values of the curvature parameter for both uniform wall temperature and uniform surface heat flux cases.

From the above discussion it is clear that no study has been conducted for laminar natural convection along vertical slender cylinders or needles that have nonuniform surface temperature. This has motivated the present study in which the problem is formulated for an arbitrary variation of the wall temperature. Numerical solutions are carried out for the case of power-law variation of the wall temperature, $T_w(x) = T_\infty + ax^n$, for slender cylinders and needles having curvature parameter ξ as large as 70 by an efficient finite difference method (Lee et al., 1986a) together with the cubic spline interpolation scheme (Burden and Fairs, 1985).

Numerical results of interest, such as the local and average Nusselt numbers, velocity distributions, and temperature

distributions, are presented for a range of Prandtl numbers $0.1 \leq Pr \leq 100$ covering the curvature parameter in the range of $0 \leq \xi \leq 70.71$. The effects of the cylindrical curvature ξ and the power-law exponent n on the surface heat transfer rate are also examined. Finally, correlation equations for the local and average Nusselt numbers are presented.

Analysis

Consider a vertical cylinder of radius r_0 which is aligned in a quiescent ambient fluid at temperature T_∞ . The x coordinate is measured upward (or downward) in the axial direction from the leading edge of the cylinder when $T_w(x) > T_\infty$ (or when $T_w(x) < T_\infty$) and the r coordinate is measured in the radial direction from the axis of the cylinder. The surface of the cylinder is subjected to an arbitrary wall temperature variation $T_w(x)$. The gravitational acceleration g is acting downward. In addition, the fluid properties are assumed to be constant except for the density variation which induces the buoyancy force. By employing laminar boundary layer flow assumptions and the Boussinesq approximation, the governing conservation equations can be written as

$$\frac{\partial}{\partial x}(ru) + \frac{\partial}{\partial r}(rv) = 0 \quad (1)$$

$$u \frac{\partial u}{\partial x} + v \frac{\partial u}{\partial r} = \nu \frac{1}{r} \frac{\partial}{\partial r} \left(r \frac{\partial u}{\partial r} \right) + g\beta(T - T_\infty) \quad (2)$$

$$u \frac{\partial T}{\partial x} + v \frac{\partial T}{\partial r} = \alpha \frac{1}{r} \frac{\partial}{\partial r} \left(r \frac{\partial T}{\partial r} \right) \quad (3)$$

where u and v are the velocity components in the x and r directions, T is the fluid temperature; and β , ν , and α are, respectively, the volumetric coefficient of thermal expansion, kinematic viscosity, and thermal diffusivity of the fluid.

The associated boundary conditions are

$$\begin{aligned} u = v = 0, & \quad T = T_w(x) & \text{at } r = r_0 \\ u \rightarrow 0, & \quad T \rightarrow T_\infty & \text{as } r \rightarrow \infty \\ u = u_\infty, & \quad T = T_\infty & \text{at } x = 0, r \geq r_0 \end{aligned} \quad (4)$$

In writing the last two boundary conditions, it is assumed that both the flow and the thermal boundary layer thickness are zero at the leading edge ($x=0$).

As a prelude to obtain solutions, the governing equations (1)–(4) are first transformed into a dimensionless form. To do

Contributed by the Heat Transfer Division for publication in the JOURNAL OF HEAT TRANSFER. Manuscript received by the Heat Transfer Division November 18, 1986.

this, one introduces a pseudo-similarity variable $\eta(x, r)$ and a dimensionless axial coordinate $\xi(x)$ as

$$\eta = [(r^2 - r_0^2)/2r_0x](Gr_x/4)^{1/4}, \quad \xi = (2x/r_0)(Gr_x/4)^{-1/4} \quad (5)$$

along with a reduced stream function $f(\xi, \eta)$ and a dimensionless temperature $\theta(\xi, \eta)$ in the form

$$f(\xi, \eta) = \psi/[4\nu r_0(Gr_x/4)^{1/4}], \\ \theta(\xi, \eta) = (T - T_\infty)/[T_w(x) - T_\infty] \quad (6)$$

In the above equations, the stream function $\psi(x, r)$ satisfies the mass conservation equation (1) with $u = (1/r)\partial\psi/\partial r$ and $v = -(1/r)\partial\psi/\partial x$, and the local Grashof number is defined as $Gr_x = g\beta[T_w(x) - T_\infty]x^3/\nu^2$.

Next, by substituting equations (5) and (6) into equations (2)–(4) one can arrive at the following system of equations:

$$(1 + \xi\eta)f''' + \xi f'' + (\Omega + 3)ff'' - 2(\Omega + 1)f'^2 + \theta \\ = (1 - \Omega)\xi(f' \partial f' / \partial \xi - f'' \partial f / \partial \xi) \quad (7)$$

$$(1 + \xi\eta)\theta'' + \xi\theta' + Pr(\Omega + 3)f'\theta' - 4\Omega Pr f' \theta \\ = Pr(1 - \Omega)\xi(f' \partial \theta / \partial \xi - \theta' \partial f / \partial \xi) \quad (8)$$

$$f'(\xi, 0) = 0, \quad \theta(\xi, 0) = 1 \\ (\Omega + 3)f'(\xi, 0) + (1 - \Omega)\xi \partial f(\xi, 0) / \partial \xi = 0 \quad (9)$$

$$f'(\xi, \infty) = 0, \quad \theta(\xi, \infty) = 0$$

where the parameter Ω has the expression

$$\Omega = \frac{d[T_w(x) - T_\infty]}{dx} \frac{x}{[T_w(x) - T_\infty]} \\ = \frac{(1 - \Omega)}{4} \frac{d[T_w(x) - T_\infty]}{[T_w(x) - T_\infty]} \frac{\xi}{d\xi} \quad (10)$$

In equations (7)–(9) the primes stand for partial derivatives with respect to η and Pr is the Prandtl number. The system of equations (7)–(9) constitutes a general mathematical form for natural convection in laminar boundary layer along vertical cylinders with an arbitrary wall temperature variation expressed by the parameter Ω . When $T_w(x)$ is specified, Ω becomes known and the system of equations (7)–(9) can be solved.

To facilitate numerical computations, a modified curvature parameter $\lambda(x)$ is introduced such that

$$\xi(x) = C\lambda^2(x) \quad (11)$$

where C is an arbitrary constant. Thus, the domain of computations can be greatly reduced by replacing $\xi(x)$ with $\lambda(x)$ as the dimensionless axial coordinate if C is chosen to be larger than one. For example, the range of $0 \leq \lambda \leq 5$ corresponds to $0 \leq \xi \leq 25C$.

With the introduction of $\lambda(x)$ along with $\Omega(x)$, equations (7)–(9) can be rewritten as

$$(1 + a_1\eta)f''' + a_1f'' + a_2ff'' + a_3f'^2 + a_4\theta \\ = a_5(f'' \partial f / \partial \lambda - f' \partial f' / \partial \lambda) \quad (12)$$

$$(1 + a_1\eta)\theta'' + a_1\theta' + a_2Prf'\theta' + a_6Prf'\theta \\ = a_5Pr(\theta' \partial f / \partial \lambda - f' \partial \theta / \partial \lambda) \quad (13)$$

$$f'(\lambda, 0) = 0, \quad \theta(\lambda, 0) = 1, \quad a_2f(\lambda, 0) - a_5 \partial f(\lambda, 0) / \partial \lambda = 0 \\ f'(\lambda, \infty) = 0, \quad \theta(\lambda, \infty) = 0 \quad (14)$$

where

$$a_1 = C\lambda^2, \quad a_2 = \Omega + 3, \quad a_3 = -2(\Omega + 1), \quad a_4 = 1, \\ a_5 = (\Omega - 1)\lambda/2, \quad a_6 = -4\Omega \quad (15)$$

It is appropriate to note that when the curvature parameter ξ or λ approaches zero (i.e., $x < r_0$), the flow configuration approaches that for pure free convection along a vertical flat plate.

The physical quantities of interest include the local and average Nusselt numbers, the local wall shear stress, the axial velocity distributions, and the temperature distributions. The first four quantities are expressible as

$$Nu_x(Gr_x/4)^{-1/4} = -\theta'(\lambda, 0) \quad (16)$$

$$\overline{Nu}(Gr_L/4)^{-1/4} = \{8\lambda_L^{-6}/[T_w(L) - T_\infty]\} \\ \cdot \int_0^{\lambda_L} \{-\theta'(\lambda, 0)\lambda^5 [T_w(x) - T_\infty]/(1 - \Omega)\} d\lambda \quad (17)$$

$$\tau_w = 4(\mu\nu/x^2)(Gr_x/4)^{3/4}f''(\lambda, 0) \quad (18)$$

$$ux/\nu = 4(Gr_x/4)^{1/2}f'(\lambda, \eta) \quad (19)$$

The average Nusselt number \overline{Nu} is defined as $\overline{Nu} = \bar{h}L/k$, where \bar{h} is the average heat transfer coefficient over an arbitrary length of the cylinder L , and $\lambda_L = \lambda(x)$ at $x = L$.

In this paper, as an example, numerical calculations were performed for the case of power-law variation of the wall temperature

Nomenclature

f = reduced stream function = $(\psi/4\nu r_0)(Gr_x/4)^{-1/4}$
 g = $\partial f / \partial \eta$ or gravitational acceleration
 Gr_x = local Grashof number = $g\beta[T_w(x) - T_\infty]x^3/\nu^2$
 Gr_L, Gr_0 = Grashof numbers defined, respectively, as $g\beta[T_w(L) - T_\infty]L^3/\nu^2$ and $g\beta[T_w(r_0) - T_\infty]r_0^3/\nu^2$
 h = local heat transfer coefficient = $q_w/[T_w(x) - T_\infty]$
 \bar{h} = average heat transfer coefficient
 k = thermal conductivity of the fluid
 L = an arbitrary length of cylinder
 n = exponent in the power-law variation of the wall temperature
 Nu_x = local Nusselt number = hx/k
 \overline{Nu} = average Nusselt number = $\bar{h}L/k$
 Pr = Prandtl number = ν/α
 r = radial coordinate
 r_0 = radius of the cylinder
 T = fluid temperature

u = axial velocity component
 v = radial velocity component
 x = axial coordinate
 α = thermal diffusivity
 β = volumetric coefficient of thermal expansion
 η = pseudo-similarity variable = $[(r^2 - r_0^2)/(2r_0x)](Gr_x/4)^{1/4}$
 θ = dimensionless temperature = $(T - T_\infty)/[T_w(x) - T_\infty]$
 λ = modified curvature parameter = $[(x/r_0)^{1-n}/Gr_0]^{1/8}$
 ν = kinematic viscosity
 ξ = curvature parameter = $(2x/r_0)(Gr_x/4)^{-1/4}$
 τ_w = local wall shear stress
 ψ = stream function
 Ω = dimensionless parameter defined by equation (10)

Subscripts

p = for a flat plate
 w = condition at the wall
 ∞ = condition at the free stream

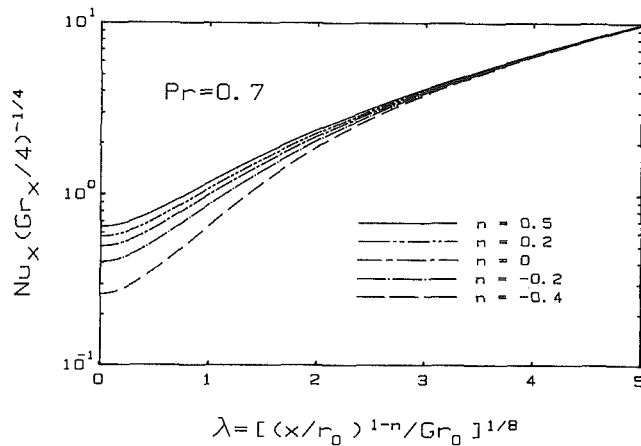


Fig. 1 Local Nusselt number results, $Pr=0.7$

$$T_w(x) = T_\infty + ax^n \quad (20)$$

in which a is a dimensional constant and n is a constant exponent. With the $T_w(x)$ variation given by equation (20), the parameter Ω appearing in equation (10) reduces to

$$\Omega = n = \text{const} \quad (21)$$

In addition, if the modified curvature parameter $\lambda(x)$ is defined as

$$\lambda(x) = [(x/r_0)^{1-n}/Gr_0]^{1/8} \quad (22)$$

where $Gr_0 = g\beta[T_w(r_0) - T_\infty]r_0^3/\nu^2$, with $[T_w(r_0) - T_\infty] = ar_0^n$, the constant C in equation (11) becomes $2^{3/2}$ and thus $\xi(x) = 2^{3/2}\lambda^2(x)$.

Method of Solution

Equations (12)–(14) constitute a system of coupled, nonlinear, partial differential equations in the (λ, η) coordinates, with Pr and Ω as parameters. For large values of λ , the coefficient $a_1 = C\lambda^2$ in equations (12) and (13) becomes very large. As a result, the ratio $a_1/(1 + a_1\eta)$ becomes very large at $\eta \approx 0$ and very small as $\eta \rightarrow \infty$. Equation (12) will thus behave as a second-order equation and equation (13) as a first-order equation in the region adjacent to the wall, but will retain their respective third-derivative term and second-derivative term in the region away from the wall to the free stream. That is, equations (12) and (13) become stiff when the values of the surface curvature parameter λ are large. Equation (13) will also become stiff when Prandtl number is large. To solve stiff differential equations by the finite-difference method, an upwind scheme or its equivalent is required.

In the present study the finite-difference method based on a weighting function scheme proposed by Lee et al. (1986b) was employed to obtain numerical results. The details of this numerical solution method are omitted here to conserve space. It suffices to mention some of its highlights. The first step in solving the system of equations (12)–(14) is to convert the partial differential equations (12) and (13) into quasi-linear ordinary differential equations. These quasi-linear differential equations along with the boundary conditions, equation (14), are then cast into finite difference equations with the proper use of weighting factors. This enables the numerical scheme to shift automatically from the central difference algorithm to the upwind difference algorithm, and vice versa. The resulting system of algebraic equations is then solved numerically by the Gaussian elimination method in conjunction with the cubic spline interpolation procedure (see, for example, Burden and Fairs, 1985). This solution method has been found to yield rapid convergence and numerical results of high accuracy (Lee et al., 1986b, 1987).

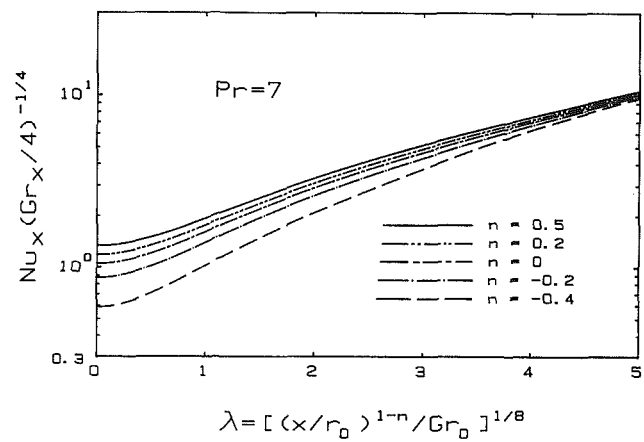


Fig. 2 Local Nusselt number results, $Pr=7$

Results and Discussion

Typical numerical results for the case of power-law variation of the wall temperature, $T_w(x) - T_\infty = ax^n$, were obtained for Prandtl numbers of 0.1, 0.7, 7, and 100 over the range of modified curvature parameter $0 \leq \lambda \leq 5$ (i.e., $0 \leq \xi \leq 70.71$). In the numerical calculation, a step size of $\Delta\eta = 0.0125$ was found to be necessary to provide accurate results for large values of the modified curvature parameter λ . For small values of λ , $\Delta\eta = 0.025$ was found to be sufficient. Thus, to obtain accurate results over the entire range of the modified curvature parameter $0 \leq \lambda \leq 5$, a step size of $\Delta\eta = 0.0125$ was used in the present calculation for all values of λ . As an example to illustrate the numerical accuracy, it is mentioned here that for the case of $Pr = 0.7$ and $n = 0$ (uniform wall temperature), the value of $-\theta'(\lambda, 0)$ at $\lambda = 5$ (or $\xi = 70.71$) was found to be 22.744 for $\Delta\eta = 0.035$ as compared to 9.8035 for $\Delta\eta = 0.0125$, with an error of over 100 percent on the high side. The values of the exponent n were limited to $-0.4 \leq n \leq 0.5$ in the numerical calculations because physical realism for the power-law case is limited to $-0.6 \leq n < 1.0$ (Gebhart, 1971).

Numerical results from the present analysis will now be presented. Figures 1 and 2 show representative local Nusselt number results in terms of $Nu_x(Gr_x/4)^{-1/4}$ as a function of the modified curvature parameter $\lambda = [(x/r_0)^{1-n}/Gr_0]^{1/8}$ for two Prandtl numbers $Pr = 0.7$ and 7, with exponent values $n = 0.5, 0.2, 0, -0.2$ and -0.4 . Curves for $Pr = 0.1$ and 100 are similar in shape and are not shown to conserve space. The case of $n = 0$ corresponds to the uniform wall temperature (UWT), and for a flat plate $\lambda = 0$ (or $\xi = 0$). From Figs. 1 and 2 it can be seen that for a given Prandtl number and a given exponent n , the local Nusselt number increases with increasing value of the modified curvature parameter λ . That is, the surface heat transfer rate increases as the curvature of the cylinder is increased. In addition, the effect of the exponent n on the local Nusselt number is felt most strongly for a vertical plate ($\lambda = 0$), with a larger n providing a larger surface heat transfer rate, and diminishes as λ becomes larger, as one can see from Figs. 1 and 2 that all curves for different n values merge to form a single line as λ increases. This is particularly true for small Prandtl numbers. For large values of λ (i.e., very large values of ξ), except for Pr values that are very large, the first two terms of the energy equation (13), i.e., the $(1 + 2^{3/2}\lambda^2\eta)\theta''$ and $2^{3/2}\lambda^2\theta'$ terms, become dominant and thus its solution becomes independent of the exponent n . Physically, it can be seen that the effect of λ (or ξ) on the local heat transfer rate becomes more important than the exponent n as λ (or ξ) becomes large, especially for small Prandtl numbers.

A comparison between Figs. 1 and 2 reveals that for given values of n and λ , fluids with larger Prandtl numbers yield

Table 1 Local Nusselt number ratio $Nu_x/Nu_{x,p}$

λ	ξ	$Nu_x/Nu_{x,p}$															
		Pr = 0.1				Pr = 0.7				Pr = 7				Pr = 100			
		n				n				n				n			
		-0.4	0	0.2	0.5	-0.4	0	0.2	0.5	-0.4	0	0.2	0.5	-0.4	0	0.2	0.5
0.0	0.0000	1.0000	1.0000	1.0000	1.0000	1.0000	1.0000	1.0000	1.0000	1.0000	1.0000	1.0000	1.0000	1.0000	1.0000	1.0000	1.0000
0.5	0.7071	2.1233	1.5932	1.5204	1.4567	1.5220	1.2928	1.2611	1.2330	1.2534	1.1472	1.1323	1.1190	1.1245	1.0733	1.0661	1.0595
1.0	2.8284	5.3403	3.1332	2.8435	2.5976	2.8047	2.0237	1.9152	1.8187	1.9176	1.5401	1.4870	1.4393	1.4687	1.2785	1.2516	1.2273
1.5	6.3640	10.460	5.4970	4.8562	4.3160	4.6251	3.0526	2.8339	2.6405	2.8538	2.1033	1.9975	1.9024	1.9744	1.5851	1.5299	1.4801
2.0	11.314	17.032	8.5889	7.4955	6.5713	7.0581	4.3603	3.9887	3.6636	3.9858	2.7906	2.6218	2.4701	2.6013	1.9699	1.8803	1.7993
2.5	17.678	24.933	12.361	10.725	9.3388	10.245	5.9751	5.3969	4.8963	5.2736	3.5775	3.3378	3.1224	3.2293	2.4203	2.2911	2.1742
3.0	25.456	34.167	16.804	14.538	12.613	14.210	7.9263	7.0859	6.3627	6.7084	4.4586	4.1399	3.8533	4.1512	2.9312	2.7575	2.6004
3.5	34.648	44.790	21.942	18.954	16.412	18.880	10.232	9.0797	8.0890	8.3412	5.4523	5.0410	4.6712	5.0686	3.5033	3.2801	3.0783
4.0	45.255	56.941	27.839	24.029	20.782	24.203	12.913	11.404	10.105	10.295	6.5993	6.0714	5.5987	6.0908	4.1423	3.8643	3.6129
4.5	57.276	70.883	34.620	29.867	25.816	30.254	16.015	14.103	12.451	12.735	7.9534	7.2740	6.6702	7.2358	4.8604	4.5213	4.2147
5.0	70.711	87.043	42.488	36.646	31.656	37.232	19.626	17.253	15.194	15.799	9.5743	8.7015	7.9320	8.5350	5.6785	5.2708	4.9020

higher local Nusselt numbers when the values of λ (or ξ) are small, but the local Nusselt number tends to become independent of Prandtl number for large values of λ (or ξ). These trends are to be expected physically, because a larger Prandtl number gives rise to a larger wall temperature gradient and hence a larger surface heat transfer rate. This can also be seen from energy equation (13). When the values of λ are very large, equation (13) can be approximated by

$$(1 + a_1 \eta) \theta'' + a_1 \theta' = 0 \quad (23)$$

where $a_1 = C\lambda^2$ with $C = 2^{3/2}$. Integration of equation (23) subject to the boundary conditions $\theta(\lambda, 0) = 1$ and $\theta(\lambda, \infty) = 0$ yields the local Nusselt number expression for very large values of λ as

$$Nu_x(Gr_x/4)^{-1/4} = -\theta'(\lambda, 0) = a_1 [\ln(1 + a_1 \eta_\infty)]^{-1} \quad (24)$$

which is independent of Prandtl number. For $\lambda = 5$ and $\eta_\infty = 30$ (as in the present calculations), one can obtain from equation (24) that $Nu_x(Gr_x/4)^{-1/4} = 9.2308$. This value agrees within 10 percent of the actual calculations for $0.1 \leq Pr \leq 7.0$ and $-0.4 \leq n \leq 0.5$.

To observe better the effect of curvature on the local Nusselt number, the local Nusselt number ratio $Nu_x/Nu_{x,p}$, where $Nu_{x,p}$ is the local Nusselt number for a vertical flat plate, was calculated and the results are listed in Table 1. It is evident from Table 1 that the $Nu_x/Nu_{x,p}$ ratio is equal to unity at $\lambda = \xi = 0$ and that this ratio increases as λ or ξ increases. That is, for given n and Pr , the smaller the radius of the cylinder, the larger is the local Nusselt number. Also, it is seen that as n increases the Nusselt number ratio becomes smaller.

The effect of n on the local Nusselt number can be seen from the local Nusselt number ratio $Nu_x/Nu_{x,UWT}$, where $Nu_{x,UWT}$ is the local Nusselt number for the uniform wall temperature case (UWT) with $n = 0$, listed in Table 2. It is seen from Table 2 that the ratio $Nu_x/Nu_{x,UWT}$ is less than 1 when $n < 0$, but larger than 1 when $n > 0$. Another interesting feature is that for $n < 0$ the ratio starts with a value much less than 1 at $\lambda = \xi = 0$ and approaches 1 as $\xi \rightarrow \infty$, whereas for $n > 0$ it starts with a value much larger than 1 and again approaches 1 as ξ becomes very large. This behavior clearly shows that the effect of n on the local Nusselt number diminishes as ξ becomes very large, as has been mentioned. Table 2 also exhibits the characteristic observed earlier that the local Nusselt number becomes independent of the Prandtl number when ξ becomes very large.

The present local Nusselt number results are compared with those of the earlier study by Fujii and Uehara (1970) in Table 3 in the form of $Nu_x/Nu_{x,p}$ as a function of λ (or ξ) for $Pr = 1$ with $n = 0$ and 0.1 and $Pr = 100$ with $n = 0$. The results of Fujii and Uehara were from their power series solutions containing the quadratic terms of ξ^2 . As can be seen from such a com-

parison, the power series solutions are good only for small values of ξ ($\xi < 1$). Thus, the results of Fujii and Uehara are good only for cylinders having large diameters that do not deviate significantly from a vertical flat plate. On the other hand, the present results apply well to slender cylinders and needles.

The average Nusselt number over a length L of the cylinder was calculated from equation (17). The behavior of the resulting $\bar{Nu}(Gr_L/4)^{-1/4}$ versus λ_L (or ξ_L) curves is similar to those described for the local Nusselt numbers and they are thus not presented.

Representative velocity and temperature profiles are shown, respectively, in Figs. 3 and 4 for $Pr = 0.7$. Only curves of $n = -0.4, 0$, and 0.5 for each modified curvature parameter $\lambda = 0, 2$, and 5 are illustrated. To conserve space, profiles for $Pr = 0.1, 7$ and 100 are not presented. From Figs. 3 and 4 one can see that both the dimensionless momentum boundary layer thickness and the dimensionless thermal boundary layer thickness increase as the modified curvature parameter λ (or ξ) increases. This can be explained as follows. Let $y = r - r_0$ be designated as the radial distance measured outward from the surface of the cylinder. Then the η coordinate in equation (5) can be rewritten as

$$\eta = (y/x)(Gr_x/4)^{1/4} [(1 + r/r_0)/2] \quad (25)$$

In addition, from the ξ and η definitions in equation (5), it follows that

$$r/r_0 = (1 + \xi \eta)^{1/2} \quad (26)$$

Thus, for large values of ξ , r/r_0 may be substantially much larger than one and the factor $(1 + r/r_0)/2$ that appears in equation (25) acts to increase the range of η for $\xi > 0$. However, as can be seen from equation (25), this increase in the range of η does not mean that the range of $(y/x)(Gr_x/4)^{1/4}$, which is a more accurate measure of the boundary-layer thickness, has increased. Indeed, the range of this quantity could even decrease with increasing ξ , but the η value still increases because of the large increase in the factor $(1 + r/r_0)/2$. Therefore, in addition to the adequately small step size in η coordinate, a sufficiently large η_∞ value is also required in the numerical calculations.

For practical applications, the local and average Nusselt number results from the present calculations in the ranges of $0 \leq \xi \leq 70$, $0.1 \leq Pr \leq 100$, and $-0.4 \leq n < 1$ can be correlated by the following respective expressions:

$$\begin{aligned} \ln[Nu_x(Gr_x/4)^{-1/4}] &= R_1(\xi) + \{ \ln[(Nu_{x,p})_{UWT}(Gr_x/4)^{-1/4}] - R_1(0) \\ &\quad + 0.97031n - 1.22087n^2 + 0.64755n^3 \} \\ &\quad \cdot \exp[-p_1 \xi^{1/2} (1 - 0.39086n + 0.51011n^2 - 0.25295n^3)] \end{aligned} \quad (27)$$

Table 2 Local Nusselt number ratio $Nu_x/Nu_{x,UWT}$

λ	ξ	$Nu_x/Nu_{x,UWT}$															
		Pr = 0.1				Pr = 0.7				Pr = 7				Pr = 100			
		n				n				n				n			
		-0.4	-0.2	0.2	0.5	-0.4	-0.2	0.2	0.5	-0.4	-0.2	0.2	0.5	-0.4	-0.2	0.2	0.5
0.0	0.0000	0.4876	0.7890	1.1600	1.3435	0.5234	0.8095	1.1413	1.3017	0.5571	0.8269	1.1270	1.2708	0.5696	0.8331	1.1219	1.2600
0.5	0.7071	0.6499	0.8572	1.1070	1.2284	0.6162	0.8467	1.1133	1.2415	0.6087	0.8469	1.1124	1.2395	0.5968	0.8435	1.1144	1.2439
1.0	2.8284	0.8312	0.9307	1.0528	1.1138	0.7254	0.8908	1.0800	1.1698	0.6936	0.8799	1.0881	1.1876	0.6543	0.8656	1.0983	1.2096
1.5	6.3640	0.9280	0.9692	1.0247	1.0549	0.7930	0.9183	1.0595	1.1260	0.7559	0.9041	1.0702	1.1494	0.7095	0.8867	1.0829	1.1766
2.0	11.314	0.9670	0.9836	1.0123	1.0279	0.8473	0.9399	1.0440	1.0937	0.7957	0.9196	1.0588	1.1248	0.7522	0.9031	1.0709	1.1509
2.5	17.478	0.9915	0.9960	1.0065	1.0084	0.9383	0.9744	1.0309	1.0667	0.8213	0.9296	1.0515	1.1092	0.7835	0.9152	1.0620	1.1319
3.0	25.456	0.9955	0.9978	1.0020	1.0049	0.9658	0.9850	1.0203	1.0449	0.8382	0.9364	1.0464	1.0983	0.8067	0.9242	1.0554	1.1178
3.5	34.648	0.9974	0.9987	1.0012	1.0029	0.9810	0.9912	1.0079	1.0186	0.8523	0.9422	1.0419	1.0887	0.8241	0.9310	1.0505	1.1072
4.0	45.255	0.9984	0.9992	1.0008	1.0018	0.9888	0.9946	1.0050	1.0120	0.8691	0.9492	1.0368	1.0781	0.8375	0.9362	1.0466	1.0990
4.5	57.276	0.9990	0.9995	1.0005	1.0009	0.9929	0.9966	1.0033	1.0078	0.8920	0.9582	1.0307	1.0657	0.8480	0.9402	1.0437	1.0927
5.0	70.711	0.9990	0.9995	1.0005	1.0009	0.9929	0.9966	1.0033	1.0078	0.9194	0.9682	1.0243	1.0528	0.8561	0.9434	1.0414	1.0877

Table 3 Comparison of local Nusselt number ratio $Nu_x/Nu_{x,p}$

λ	ξ	Pr = 1, n = 0		Pr = 1, n = 0.1		Pr = 100, n = 0	
		Present study	Fujii and Uehara (1970)	Present study	Fujii and Uehara (1970)	Present study	Fujii and Uehara (1970)
		0.0	0.0000	1.0000	1.0000	1.0000	1.0000
0.2	0.1131	1.0440	1.0440	1.0414	1.0413	1.0119	1.0116
0.4	0.4525	1.1705	1.1694	1.1603	1.1590	1.0472	1.0453
0.6	1.0182	1.3666	1.3558	1.3447	1.3338	1.1047	1.0985
0.8	1.8102	1.6195	1.5693	1.5829	1.5339	1.1825	1.1665
1.0	2.8284	1.9197	1.7625	1.8659	1.7146	1.2785	1.2428
1.2	4.0729	2.2607	1.8746	2.1874	1.8186	1.3905	1.3191
1.4	5.5437	2.6389	1.8310	2.5438	1.7756	1.5169	1.3852
1.6	7.2408	3.0525	1.5437	2.9332	1.5028	1.6563	1.4290
1.8	9.1641	3.5017	0.9111	3.3553	0.9045	1.8076	1.4368
2.0	11.314	3.9880	-0.1819	3.8112	-0.1278	1.9699	1.3928
2.5	17.478	5.3826	-5.8062	5.1119	-5.4335	2.4203	0.9359
3.0	25.456	7.0660	-17.530	6.6720	-16.486	2.9312	-0.2852
3.5	34.648	9.0689	-38.261	8.5230	-36.025	3.5033	-2.6681
4.0	45.255	11.413	-71.441	10.691	-67.291	4.1423	-6.6829
4.5	57.276	14.134	-121.03	13.213	-114.02	4.8604	-12.872
5.0	70.711	17.308	-191.54	16.160	-180.45	5.6785	-21.849

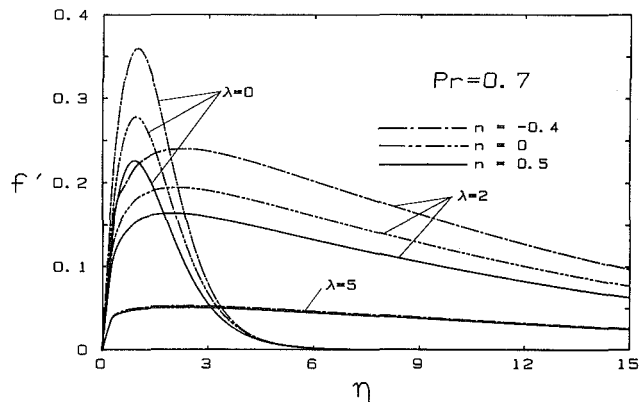


Fig. 3 Representative velocity profiles, Pr = 0.7

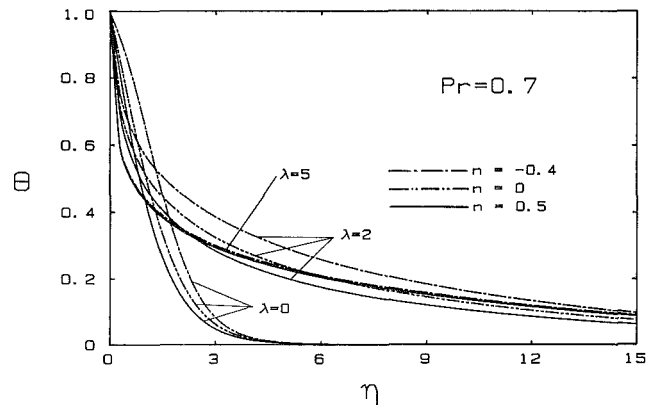


Fig. 4 Representative temperature profiles, Pr = 0.7

$$\ln[\bar{Nu}(Gr_L/4)^{-1/4}] = R_2(\xi_L) + \{ \ln[3(n+3)^{-1}(\bar{Nu}_p)_{UWT}(Gr_L/4)^{-1/4}] - R_2(0) + 0.97034n - 1.22080n^2 + 0.64746n^3 \} \quad (28)$$

$$\cdot \exp[-p_2 \xi_L^{1/2} (1 - 0.24592n + 0.45745n^2 - 0.25153n^3)]$$

where

$$R_1(\xi) = -2.92620 + 1.66850\xi^{1/2} - 0.21909\xi + 0.011308\xi^{3/2}$$

$$R_2(\xi_L) = -2.92620 + 1.66850\xi_L^{1/2} - 0.21909\xi_L + 0.011308\xi_L^{3/2} \quad (29)$$

$$p_1 = 0.34181 + 0.36050Pr^{-0.24563}$$

$$p_2 = 0.29369 + 0.32635Pr^{-0.19305} \quad (30)$$

$$(Nu_{x,p})_{UWT}(Gr_x/4)^{-1/4} = (3/4)(2Pr)^{1/2} [2.5(1 + 2Pr^{1/2} + 2Pr)]^{-1/4} \quad (31)$$

and

$$(\bar{Nu}_p)_{UWT}(Gr_L/4)^{-1/4} = (2Pr)^{1/2} [2.5(1 + 2Pr^{1/2} + 2Pr)]^{-1/4} \quad (32)$$

It is interesting to note that for natural convection along an isothermal vertical flat plate (i.e., $\xi = 0$ and $n = 0$) the correlation equations (27) and (28) can be reduced, respectively, to equations (31) and (32). The correlation equation (31) for the local Nusselt number $(Nu_{x,p})_{UWT}(Gr_x/4)^{-1/4}$ over an isothermal vertical flat plate was taken from Ede (1967), and the corresponding correlation equation (32) for the average Nusselt number was derived in accordance with its definition $\bar{Nu} = hL/k$. The maximum errors in equations (27) and (28) are about 10 percent and occur when $\lambda > 4$ (or $\xi > 45$).

Conclusion

In this paper, natural convection in laminar boundary layer flow along slender vertical cylinders and needles has been investigated analytically for arbitrary wall temperature variation. A finite difference method in conjunction with cubic spline interpolation scheme is used in the numerical solutions to remove some difficulties which arise from large values of the curvature parameter ξ . Numerical results were obtained for the case of power-law variation in wall temperature. Local Nusselt number results are presented for $0.1 \leq Pr \leq 100$ covering $-0.4 \leq n \leq 0.5$ and $0 \leq \lambda \leq 5$ (i.e., $0 \leq \xi \leq 70.71$). Correlation equations for Nu_x and \bar{Nu} are also given. The major findings from the present study can be summarized as follows:

- 1 For the power-law variation in wall temperature, the local surface heat transfer rate increases with increasing value

of the curvature parameter λ (or ξ) for given values of the exponent n and the Prandtl number Pr .

2 For given curvature parameter λ (or ξ) and Prandtl number Pr , the local surface heat transfer rate increases with increasing exponent n , especially when the values of the curvature parameter are small and the values of Prandtl number are large.

3 The local surface heat transfer rate increases with increasing Prandtl number for given exponent n and curvature parameter λ (or ξ).

Acknowledgments

The present study was supported in part by a grant from the National Science Foundation (NSF MEA 83-00785).

References

- Burden, R. L., and Fairs, J. D., 1985, *Numerical Analysis*, 3rd ed., Prindle, Weber and Schmidt Publishers, Boston, MA, pp. 117–129.
- Cebeci, T., and Na, T. N., 1969, "Laminar Free-Convection Heat Transfer From a Needle," *The Physics of Fluids*, Vol. 12, pp. 463–465.
- Cebeci, T., and Na, T. N., 1970, "Erratum: Laminar Free-Convection Heat Transfer From a Needle," *The Physics of Fluids*, Vol. 13, p. 536.
- Chen, T. S., and Yuh, C. F., 1980, "Combined Heat and Mass Transfer in Natural Convection Along a Vertical Cylinder," *International Journal of Heat and Mass Transfer*, Vol. 23, pp. 451–461.
- Ede, A. J., 1967, "Advances in Free Convection," in: *Advances in Heat Transfer*, Vol. 4, pp. 1–64.
- Elenbaas, W., 1948, "The Dissipation of Heat by Free Convection From Vertical and Horizontal Cylinders," *Journal of Applied Physics*, Vol. 19, pp. 1148–1154.
- Fujii, T., and Uehara, H., 1970, "Laminar Natural Convection Heat Transfer From the Outer Surface of a Vertical Cylinder," *International Journal of Heat and Mass Transfer*, Vol. 13, pp. 607–615.
- Gebhart, B., 1971, *Heat Transfer*, 2nd ed., McGraw-Hill, New York, p. 340.
- Kuiken, H. K., 1968, "Axisymmetric Free Convection Boundary Layer Flow Past Slender Bodies," *International Journal of Heat and Mass Transfer*, Vol. 11, pp. 1141–1153.
- Lee, S. L., Chen, T. S., and Armaly, B. F., 1986a, "New Finite Difference Solution Methods for Wave Instability Problems," *Numerical Heat Transfer*, Vol. 10, pp. 1–18.
- Lee, S. L., Chen, T. S., and Armaly, B. F., 1986b, "Mixed Convection Along Isothermal Vertical Cylinders and Needles," *Proceedings of the Eighth International Heat Transfer Conference*, Vol. 3, pp. 1425–1432.
- Lee, S. L., Chen, T. S., and Armaly, B. F., 1987, "Mixed Convection Along Vertical Cylinders and Needles With Uniform Surface Heat Flux," *ASME JOURNAL OF HEAT TRANSFER*, Vol. 109, pp. 711–716.
- Minkowycz, W. J., and Sparrow, E. M., 1974, "Local Nonsimilar Solutions for Natural Convection on a Vertical Cylinder," *ASME JOURNAL OF HEAT TRANSFER*, Vol. 96, pp. 178–183.
- Narain, J. P., and Uberoi, M. S., 1972, "Laminar Free Convection From Vertical Thin Needles," *The Physics of Fluids*, Vol. 15, pp. 928–929.
- Raju, M. S., Liu, X. Q., and Law, C. K., 1984, "A Formulation of Combined Forced and Free Convection Past Horizontal and Vertical Surface," *International Journal of Heat and Mass Transfer*, Vol. 27, pp. 2215–2224.
- Sparrow, E. M., and Gregg, J. L., 1956, "Laminar Free Convection Heat Transfer From the Outer Surface of a Vertical Circular Cylinder," *Trans. ASME*, Vol. 78, pp. 1823–1829.

Heat Transfer by Natural Convection of Helium Between Horizontal Isothermal Concentric Cylinders at Cryogenic Temperature

E. H. Bishop

Department of Mechanical Engineering,
Clemson University,
Clemson, SC 29631

An experimental study was performed of the heat transfer by natural convection of helium between horizontal isothermal concentric cylinders at cryogenic temperatures. Time-averaged temperature profiles at various locations in the annulus and overall heat transfer rates were measured as the Rayleigh number was varied from 6×10^6 to 2×10^9 and the expansion number from 0.20 to 1.0 for a constant Prandtl number of 0.688 and diameter ratio of 3.36. It was found that the heat transfer rate depends on the magnitude of the expansion number as well as on the magnitude of the Rayleigh number. With gas properties evaluated at a volume-weighted reference temperature, a correlation equation is presented that correlates the heat transfer data with maximum deviations of -8.2 and $+8.5$ percent. The results of this study are compared with previously published studies of other investigators.

Introduction

The natural convection of gases between horizontal isothermal concentric cylinders has been studied by many previous investigators and much information is available in the literature on this problem. However, there appear to have been no studies reported on where the surface temperatures of the cylinders are in the cryogenic temperature region.

There have been a number of experimental studies in other geometries of natural convection at cryogenic temperatures. Threlfall (1975) presents the results of a study of the free convection of helium in a cylindrical vessel with differentially heated ends, where temperatures as low as 4 K were obtained. Clausing and Kempka (1981) performed experiments to determine the influence of property variations on natural convection from vertical surfaces by employing a cryogenic environment to obtain large ratios of wall temperature to ambient temperature. The cryogenic ambient environment was nitrogen gas that had been cooled in a cryogenic wind tunnel and then allowed to reach a quiescent state after the fans had been shut off. Clausing et al. (1984) performed experiments in this same cryogenic wind tunnel to determine the combined convection heat transfer from a short vertical cylinder in crossflow. The cryogenic facility enables simultaneous generation of large Rayleigh numbers and large Reynolds numbers as well as large values of the temperature ratio. Radiation effects are negligibly small at these low temperatures.

At cryogenic temperature levels (around 77 K) the expansion number $\beta \Delta T$ could easily range in magnitude from 0.2 to 1.0 without an exceptionally large temperature difference. Since these magnitudes are significantly greater than the values of the expansion number of the experimental tests on horizontal isothermal concentric cylinders reported on in the literature (around 0.1), it is reasonable to question whether the correlation equations now in use for this geometry would be valid at these temperature levels. Also, since the magnitudes of the transport properties for gases such as helium at liquid nitrogen temperature are much different from those of air or

nitrogen at room temperatures and above, the question of an appropriate reference temperature needs to be addressed.

The first basic study of natural convection in cylindrical annuli was carried out by Beckmann (1931) and extended by Kraussold (1934) to include Prandtl number variations. Since that time other investigators have determined more precisely the effect of the diameter ratio and the influence of the Prandtl number on the overall heat transfer coefficient. Most of the work prior to 1966 was limited to Rayleigh numbers less than 10^6 , or in the laminar flow regime. Lis (1966) extended this maximum Rayleigh number to around 10^{10} by using pressurized nitrogen and sulfur hexafluoride in the annulus. Actually, the only data on the overall heat transfer rate reported in the literature for Rayleigh numbers greater than about 5×10^7 are from Lis and represent nearly all of the information in this geometry where the flow is turbulent. Raithby and Hollands (1975) and Kuehn and Goldstein (1976a) presented correlating equations, obtained by using a conduction layer model, for the overall heat transfer rate, which correlated the available data over reasonably significant ranges of the Prandtl and Rayleigh numbers.

Kuehn and Goldstein (1976a) showed that the data of a number of investigators in both the laminar and the turbulent regions are well correlated by their model. In a later study, Kuehn and Goldstein (1976b) used a Mach-Zender interferometer to determine temperature distributions and local heat transfer coefficients for water and air for one diameter ratio over a small range of values of Rayleigh number (up to approximately 10^6). Then in 1978 Kuehn and Goldstein utilized optical methods to obtain instantaneous and time-averaged temperature distributions and local heat transfer coefficients for pressurized nitrogen up to Rayleigh numbers in the 10^7 range. They modified slightly the equation they presented earlier to correlate the heat transfer results and presented interferograms and a detailed description of the flow behavior as the flow became unsteady and apparently turbulent. No comparisons were made with the results obtained by Bishop et al. (1968) who presented detailed descriptions and quantitative information concerning the

Contributed by the Heat Transfer Division for publication in the JOURNAL OF HEAT TRANSFER. Manuscript received by the Heat Transfer Division December 3, 1986.

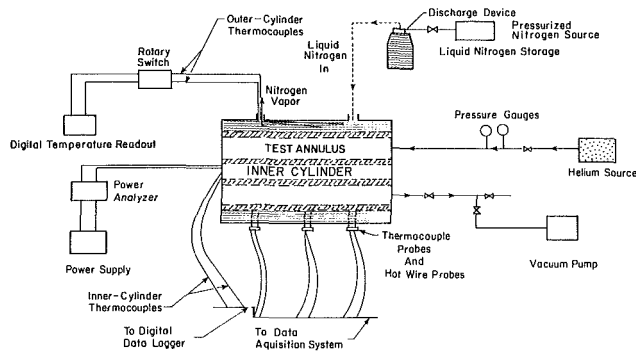


Fig. 1 Schematic diagram of experimental setup

characteristics of an oscillatory flow that has its inception from a previously stable flow. Empirical equations are presented that give the amplitude, period, and wavelength of the oscillatory flow as well as the value of the Grashof number at inception of the oscillation.

This paper presents the results of a detailed experimental study of high Rayleigh number natural convection of helium between isothermal concentric cylinders at cryogenic temperatures with $D_o/D_i = 3.36$, $Pr = 0.688$, and with values of the expansion number up to 1.10 and temperature ratios $(T_i - T_o)/T_o$ up to 1.57. The inner cylinder is maintained at temperatures higher than the outer cylinder in all tests. With these temperature difference conditions, the directions of the temperature gradient and the gravity vector are the same at the top of the annulus, normal at the horizontal diameter and opposing at the bottom of the annulus. At the top of the annulus the helium will be thermally unstable while at the bottom it will be stable. The experimental results are presented in the following manner: mean temperature profiles for selected annulus locations and values of expansion number and Rayleigh number; an overall correlation equation for heat transfer in terms of Rayleigh number and expansion number; and a plot of heat transfer data for selected values of the expansion number and along with the equations of Lis (1966), Raithby and Hollands (1975), and Kuehn and Goldstein (1978).

Apparatus and Procedures

Figure 1 is a schematic diagram of the experimental setup. The basic test apparatus consists of a 0.0603-m-o.d., heated,

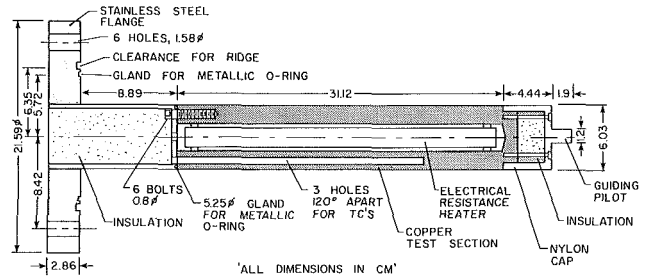


Fig. 2 Detail drawing of inner cylinder

copper inner test cylinder supported concentrically in a 0.203-m-i.d., cooled, stainless-steel outer test cylinder whose inside surface had been honed to a smooth finish. These two cylinders are in turn supported concentrically in a larger diameter stainless-steel cylinder that is insulated on its outside surface with at least 10 cm of fiberglass. The annular space between the outer test cylinder and this cylinder is used as a cooling jacket for maintaining the outer test cylinder at a constant temperature. The cooling jacket fluid could be either water or liquid nitrogen; however for the results presented in this paper the cooling fluid was liquid nitrogen. The stainless-steel outer test cylinder and the cooling jacket cylinder are both welded to stainless-steel end plates. The end plates were maintained at close to liquid nitrogen temperature by passing liquid nitrogen through heat exchangers that were attached to the plates at both ends of the apparatus. The end plates were insulated by 10 cm of fiberglass. The inner test cylinder is secured concentrically in the outer test cylinder by a bolt-flange arrangement at the left end plate with a metal "o"-ring seal to permit pressurization or evacuation of the annulus for control of the test-gas pressure. The annulus was pressurized by connecting it to a pressurized bottle of helium through a pressure regulator or it was evacuated by a vacuum pump. The flange was cooled by passing liquid nitrogen through a coil of copper tubing wrapped around the flange. The liquid nitrogen charging system consists of three 50 liters dewars with liquid discharge devices connected in series and capable of being pressurized by nitrogen gas up to 5 psig. The charge line was connected to the end plate and flange heat exchangers and to the cooling jacket.

The construction details of the inner cylinder are shown in Fig. 2. The actual test cylinder is the 31.12-cm-long, 6.03-cm-

Nomenclature

A, C = constants in equation (3)

D = cylinder diameter

D_i = inner-cylinder diameter

D_o = outer-cylinder diameter

g = acceleration due to gravity

h = convection coefficient

k = thermal conductivity

k_{eff} = effective thermal conductivity = $(q/l)_{\text{conv}} \ln(r_o/r_i) / 2\pi (T_i - T_o)$

K_{eq} = equivalent thermal conductivity = k_{eff}/k

L = gap thickness = $(r_o - r_i)$

m = constant in equation (3)

Pr = Prandtl number = ν/α

r = radial coordinate

r_i = inner-cylinder radius

r_o = outer-cylinder radius

r_{avg} = average radius = $(r_o + r_i)/2$

Ra_L = Rayleigh number = $gL^3\beta\Delta T/\nu\alpha$

T = temperature

\bar{T} = time-averaged temperature

T_i = inner-cylinder temperature

T_o = outer-cylinder temperature

T_{ref} = reference temperature

q_{loss} = rate of heat loss from inner cylinder by radia-

tion and longitudinal conduction

$(q/l)_{\text{conv}}$ = rate of convection heat transfer from inner cylinder, per unit length

ΔT = temperature difference = $T_i - T_o$

α = thermal diffusivity

β = coefficient of thermal expansion

$\beta\Delta T$ = expansion number

θ = angular coordinate, measured clockwise from the upward vertical, $\theta = 0$

μ = dynamic viscosity

ν = kinematic viscosity

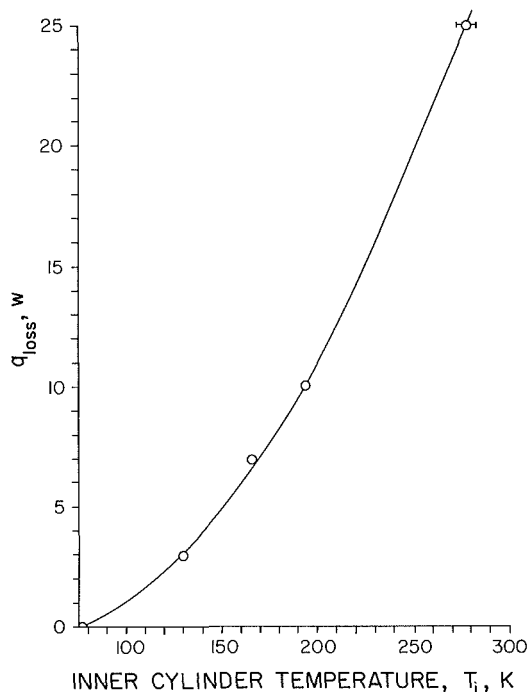


Fig. 3 Calibration curve giving heat transfer by radiation and longitudinal conduction (q_{loss} versus T_i)

dia, 1.75-cm-thick copper section of the inner cylinder. The primary purpose here is to ensure a test annulus where end-plate effects on the flow around the inner cylinder have been minimized and to provide means whereby the longitudinal conduction could be reduced and controlled. The right end of the cylinder is capped with a hollow nylon cylinder filled with fiberglass insulation and the left end is attached through a metal "o"-ring seal to a stainless steel cylinder, which is welded to the flange and inside of which is placed fiberglass insulation. The temperature of the inner cylinder was controlled by varying the power input to an electrical resistance heater embedded in alumina and supported along the axis of the copper cylinder by teflon spacers. The temperature of the cylinder was measured at nine locations by copper-constantan thermocouples affixed to the cylinder at the quarter-, mid-, and three-quarter planes at 120 deg intervals. Three, 0.476-cm-dia holes, 120 deg apart, were drilled parallel to the axis of the cylinder and the thermocouples were inserted to the proper longitudinal depth and epoxied to the surface. Alumina was packed in the holes after each thermocouple was in place. The cylinder temperature was taken to be the arithmetic average of these nine thermocouples. The maximum difference between any of the nine measured temperatures was 5°C, and this was for tests at the highest temperature difference ($\Delta T = 123$ K). All thermocouple wires and electrical leads were contained within the inner cylinder and brought out through the flange end of the cylinder.

Temperature probe passages were located at the center plane of the annulus at the top and every 30 deg measured downward from the upward vertical. Special probe holders were designed that permitted probing while the annulus was under pressure. The probes were specially modified TSI model 1248 hot-wire anemometer probes, which were used in a constant current circuit with the voltage drop across the sensing element being monitored. The probes were traversed across the annulus using a "Unislide" traversing mechanism with a least count of 0.001 cm. A mounting bracket was used to connect the traverse to the probe passages. The voltage output was measured and stored on a Digital Equipment Corporation MINC 1103 data acquisition computer. The uncertainty in the

measurement of the helium temperatures is estimated to be $\pm 1^\circ\text{C}$.

Since only heat transfer by natural convection was being sought, it was necessary to determine the radiation transfer and longitudinal conduction loss through the inner cylinder to the end plates. These heat transfer rates were experimentally determined by evacuating the gap between the cylinders to a pressure of about 15 N/m². At this pressure and at the maximum inner-cylinder temperature to be used for the convection tests of 200 K the Rayleigh number is less than 10^{-1} and thus convection is essentially suppressed. At this pressure gap conduction is reduced, and by maintenance of a constant outer-cylinder temperature at 77 K for the calibration, the sum q_{loss} of the radiation and longitudinal conduction becomes a function of the temperature of only the inner cylinder and is essentially equal to the total power input to the electrical resistance heater. The power input to the heater was set to a sufficient number of values to permit plotting a calibration curve over a range of inner-cylinder temperatures from about 100 K to 300 K with variances of ± 1 K and ± 5 K, respectively. About 20 h were allowed for each calibration point to assure steady-state conditions. Figure 3 is a plot of q_{loss} versus inner-cylinder temperature.

About 70 heat transfer runs were conducted with helium at pressures from 1.5 to 18 atm in the annulus. Since the primary objective of the experiments was to determine the effects of varying the expansion number on the heat transfer, it was necessary to hold this parameter constant at several values while varying the Rayleigh number. This required that the inner-cylinder temperature not change while the Rayleigh number was changed by increasing or decreasing the pressure of the helium in the annulus. The inner-cylinder temperature was kept constant as the pressure was changed by adjusting the power input to the inner cylinder heater either up or down depending upon whether the pressure was increased or decreased. Normally 2–3 h were allowed for establishment of a steady state before each run. Steady state was assumed after the nine inner-cylinder thermocouples indicated less than 0.10° change in temperature over a 15-min period of time. The outer cylinder was maintained at the same temperature as that used for the calibration so that the curves of Fig. 3 could be used to predict q_{loss} at a variety of inner-cylinder temperatures. For the heat transfer runs q_{loss} varied from about 2 to 7 percent of the total power input to the heater. At selected values of the Rayleigh number and expansion number temperature traverses were made utilizing the resistance probes.

Temperature Distribution

Measurements of the temperature T at various radial positions for selected angular positions and magnitudes of the Rayleigh number and expansion number were made. Since the smallest Rayleigh number magnitude achievable on the test setup (6×10^6) was greater than the value at which unsteady flow is known to occur (Bishop et al., 1968) temperature fluctuations were expected. The temperature measuring system as described in the Apparatus and Procedure section was designed to detect and record these fluctuations.

Profiles of the time-averaged temperature \bar{T} versus radial position for selected values of the Rayleigh number and expansion number are presented in Figs. 4–6. Each temperature point \bar{T} is the average of 1024 data points taken over a 20.48 s time period at a 50 Hz sampling frequency. The value of the expansion number given in Figs. 4–6 is the average over a range of values and does not necessarily represent the exact value at which the specific profile was measured. For a value of 0.25 the range is 0.22 to 0.28, for 0.50 the range is 0.46 to 0.53, and for 1.0 the range is 0.96 to 1.02. Even though the

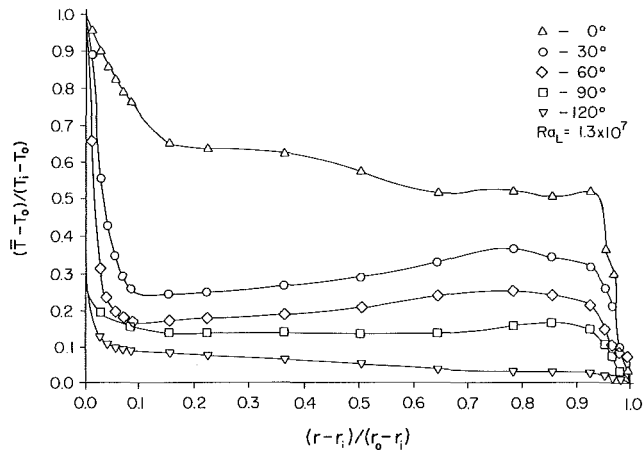


Fig. 4 Dimensionless time-averaged temperature profile for $Ra_L = 1.31 \times 10^7$ and $\beta \Delta T = 1.0$

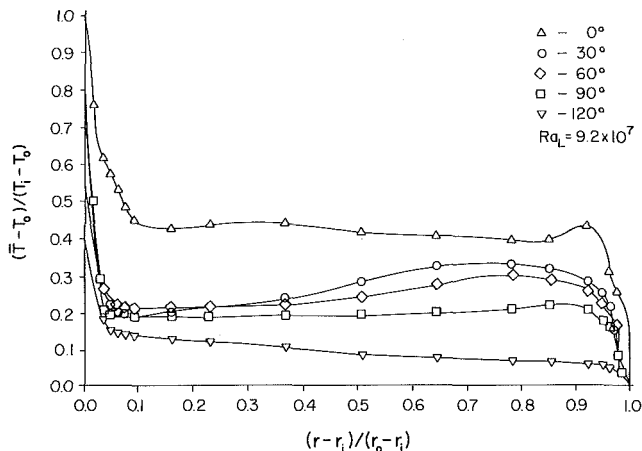


Fig. 5 Dimensionless time-averaged temperature profile for $Ra_L = 9.21 \times 10^6$ and $\beta \Delta T = 0.25$

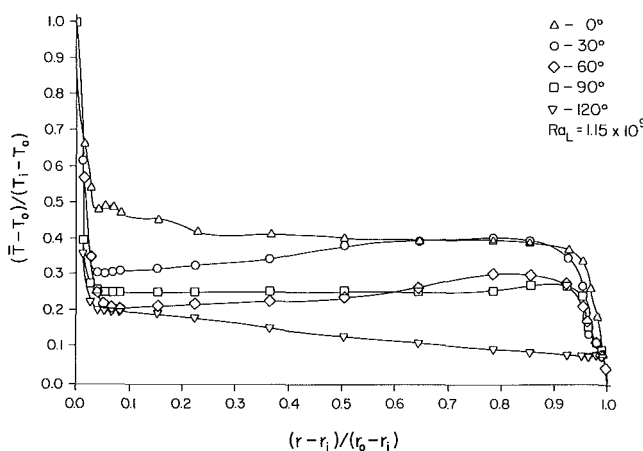


Fig. 6 Dimensionless time-averaged temperature profile for $Ra_L = 1.15 \times 10^9$ and $\beta \Delta T = 0.50$

value of the expansion number is not identical for each of the profiles, the general form of the profiles for a given Rayleigh number and the changes in the profiles observed as the Rayleigh number is increased are not affected because of this. The effect of changing the expansion number on the temperature profiles for a given Rayleigh number will be presented later.

A direct comparison of the temperature profiles shown in Figs. 4 and 6 with published information is not possible since

none is currently available. There are trends however that do agree with existing data, which are for Rayleigh number magnitudes less than those of this study. Because of the steep temperature gradients, it is clear that thin high-speed boundary-layer-like flows exist adjacent to both the inner-cylinder surface and to the outer-cylinder surface, which is in agreement with Kuehn and Goldstein (1978). Also, in the central portion of the annulus a temperature inversion exists where the fluid near the cooled surface is warmer than fluid closer to the heated surface. This inversion has been observed previously by Kuehn and Goldstein (1976b) and Mahony et al. (1986) and is caused by the strong recirculating flow. As the Rayleigh number is increased from 1.31×10^7 to 1.15×10^9 , the gradients near the cylinder surfaces at all angular positions become steeper and temperatures in the plume region begin to approach those at an angular position of 30 deg. These changes are as expected when the strength of the flow becomes such that turbulence is occurring. As shown in Fig. 6 for $Ra_L = 1.15 \times 10^9$, for each angular position the temperature profile is relatively flat throughout the region $0.1 \leq (r - r_i)/(r_o - r_i) \leq 0.9$, with at most a 10 percent change in the time-averaged temperature.

The effect on the time-averaged temperature profiles of varying the expansion number for a fixed magnitude of the Rayleigh number is shown in Figs. 7-10. As can be seen in Figs. 7 and 8 for a Rayleigh number of approximately 1×10^7 , as the magnitude of the expansion number is increased from about 0.25 to 1.0 the temperature gradients adjacent to the inner- and outer-cylinder surfaces become steeper and there is a general lowering of the temperature in the annulus. Figures 9 and 10 for a Rayleigh number of about 1×10^8 show the same trends; however, they are not nearly as pronounced. Based on these mean temperature profile results, it can be anticipated that for a fixed value of the Rayleigh number the heat transfer rate will increase with increasing magnitudes of the expansion number. Also, the general form of the profiles and their relative ordering with respect to angular position appear to be independent of the magnitude of the expansion number.

Heat Transfer

The overall heat transfer results are presented in dimensionless form in terms of an equivalent thermal conductivity, which is defined as

$$K_{eq} = k_{eff}/k \quad (1)$$

where $k_{eff} = (q/l)_{conv} \ln(r_o/r_i)/2\pi(T_i - T_o)$ and k is the thermal conductivity of the annulus gas. Alternately, the results could be expressed in terms of a Nusselt number, which is defined in the standard manner as

$$hD/k = (q/l)_{conv}/\pi(T_i - T_o)k \quad (2)$$

The Nusselt number in terms of the equivalent thermal conductivity is

$$Nu = (2/\ln(r_o/r_i))K_{eq} \quad (3)$$

Previous investigators, for example, Lis (1966) and Raithby and Hollands (1975), have shown that the heat transfer depends on the following dimensionless parameters: D_o/D_i , $Ra_L = g\beta L^3(T_i - T_o)/\nu\alpha$, and $Pr = \nu/\alpha$; however, in all of these previous studies the expansion number $\beta \Delta T$ was less than 0.20, and in most studies, less than 0.1. It has been shown by Hellumns and Churchill (1961) that the expansion number may be neglected when its magnitude is much less than 1.0. If the outer cylinder is maintained at 77 K, which is the boiling temperature of liquid nitrogen at atmospheric pressure, it is possible to achieve magnitudes of the expansion number of over 1.0 with a temperature difference between the cylinders of only 125 K. Thus, in the cryogenic temperature range, the

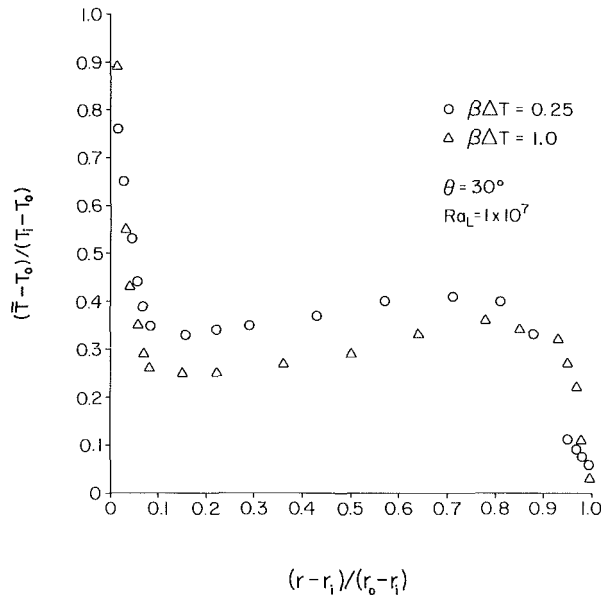


Fig. 7 Dimensionless time-averaged temperature profiles for $\theta = 30$ deg; $Ra_L = 1 \times 10^7$, $\beta \Delta T = 0.25$, and $\beta \Delta T = 1.0$

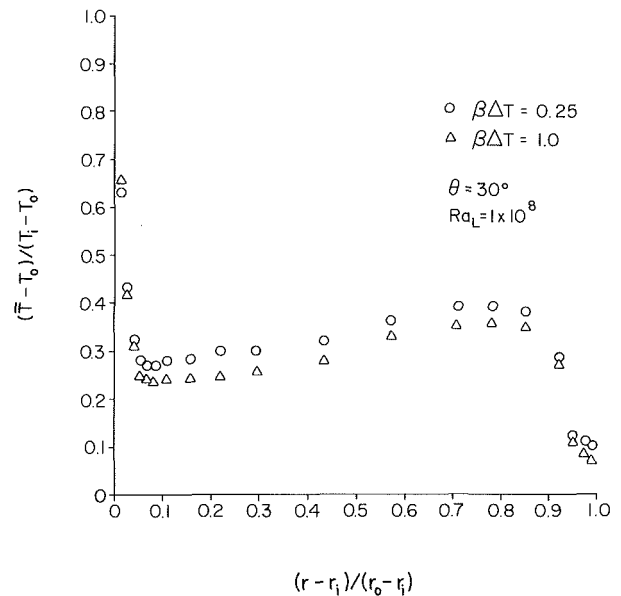


Fig. 9 Dimensionless time-averaged temperature profiles for $\theta = 30$ deg; $Ra_L = 1 \times 10^8$, $\beta \Delta T = 0.25$, and $\beta \Delta T = 1.0$

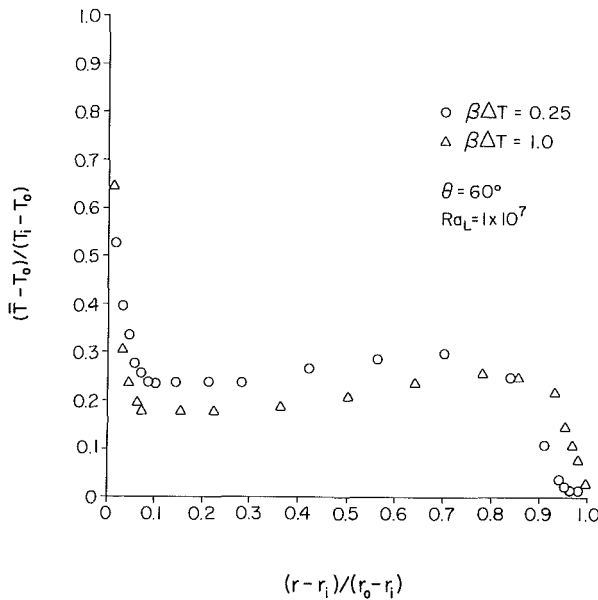


Fig. 8 Dimensionless time-averaged temperature profiles for $\theta = 60$ deg; $Ra_L = 1 \times 10^7$, $\beta \Delta T = 0.25$, and $\beta \Delta T = 1.0$

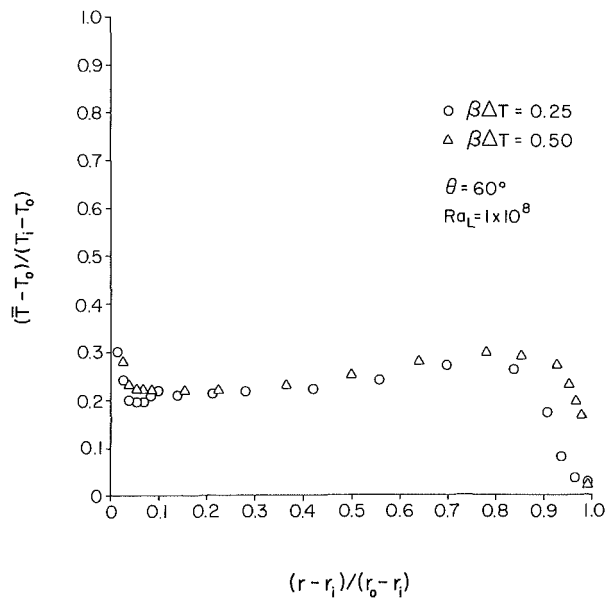


Fig. 10 Dimensionless time-averaged temperature profiles for $\theta = 60$ deg; $Ra_L = 1 \times 10^8$, $\beta \Delta T = 0.25$, and $\beta \Delta T = 0.50$

magnitude of the expansion number could be ten times larger than the maximum magnitude of existing studies. It is the purpose of this study to determine whether the expansion number must be considered as an independent parameter and if so, how it enters into the prediction equation for the heat transfer. Since the diameter ratio was kept constant at 3.36 and the Prandtl number of helium is constant at 0.688 over the temperature range (77 K to 200 K) used in this study, the following functional relationship is sought:

$$K_{eq} = f(Ra_L, \beta(T_i - T_0)) \quad (4)$$

Reference Temperature. To reduce the raw data and present them in an appropriate dimensionless form, it is necessary to define a reference temperature at which the properties of helium are evaluated. Since the magnitude of the viscosity μ and thermal conductivity k of helium increase by approximately 85 percent from $T_0 = 77$ K to $T_i = 200$ K, the choice

of a reference temperature will have a significant effect on the magnitudes of the equivalent thermal conductivity and the Rayleigh number at a specific data point (and, subsequently, the form of the correlating equation).

In all previously published experimental studies the inner and outer-cylinder surface temperatures were equally weighted (arithmetic average) to determine property values. Since in most other studies, for example Kuehn and Goldstein (1978), the transport properties did not vary appreciably over the temperature ranges investigated, the choice of reference temperature was not a critical matter. In a previous numerical study by this author of the variable property problem in this geometry (Mahony et al., 1986) a volume-weighted mean reference temperature was found to collapse all of the heat transfer rates to a single curve for temperature difference ratios $(T_i - T_0)/T_0 \leq 3$ and for Rayleigh number magnitudes less than about 10^5 . Based on this and the fact that

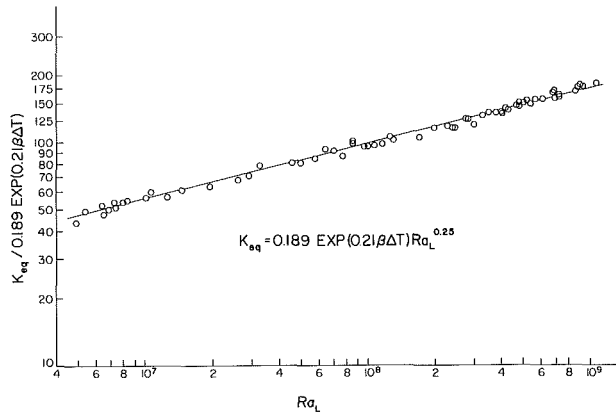


Fig. 11 Overall correlation of heat transfer data

the maximum temperature difference ratio obtained in this study was approximately 1.60, a logical choice for the reference temperature to reduce the data would be a volume-weighted mean temperature defined as

$$T_{ref} = ((r_{avg}^2 - r_i^2)/(r_o^2 - r_i^2))T_i + ((r_o^2 - r_{avg}^2)/(r_o^2 - r_i^2))T_o \quad (5)$$

This definition of reference temperature allows for greater weight to be assigned to the outer-cylinder temperature as the diameter ratio is increased. For the cylinder combination of this study, the volume-weighted mean temperature is

$$T_{ref} = 0.363T_i + 0.637T_o \quad (6)$$

The time-averaged temperature profiles shown in Figs. 4–6 support the volume-weighted mean temperature given by equation (6) as a reasonable choice for the reference temperature for all values of the Rayleigh number. It is felt that by using the reference temperature of equation (6) to evaluate the transport properties, any variations found in the heat transfer rate at a given Rayleigh number for different magnitudes of the expansion number would be due principally to changes in the expansion number.

Heat Transfer Results. To determine the effect of varying the expansion number on the convection heat transfer rate, it was necessary to hold the expansion number constant while varying the Rayleigh number, and repeat this for several values of the expansion number. The expansion number was held constant at a number of different average values in the range 0.20 to 1.0 and the Rayleigh number was varied from the lowest achievable value to the maximum achievable value for a given expansion number (all Rayleigh number values fell within the range 6×10^6 to 2×10^9). These parameter ranges are based on using the volume-weighted mean temperature of equation (6) as the reference temperature for property value evaluation.

From the time-averaged temperature profiles shown in Figs. 7–10, it can be observed that as the magnitude of the expansion number is increased for a given magnitude of the Rayleigh number the temperature gradients at the cylinder surfaces become steeper and thus, the heat transfer rate should increase. In analyzing the experimental heat transfer data, it was observed that plots of K_{eq} versus Rayleigh number for fixed values of the expansion number gave straight lines when plotted on log-log coordinates. It was further noted that plots of K_{eq} versus expansion number for fixed values of the Rayleigh number using semi-log coordinates gave straight lines. It was also observed from these semi-log plots that for each value of the Rayleigh number the slopes of the lines were roughly the same. Thus, the form of the correlating equation was assumed to be

$$K_{eq} = C \exp(A \beta \Delta T) (Ra_L)^m \quad (7)$$

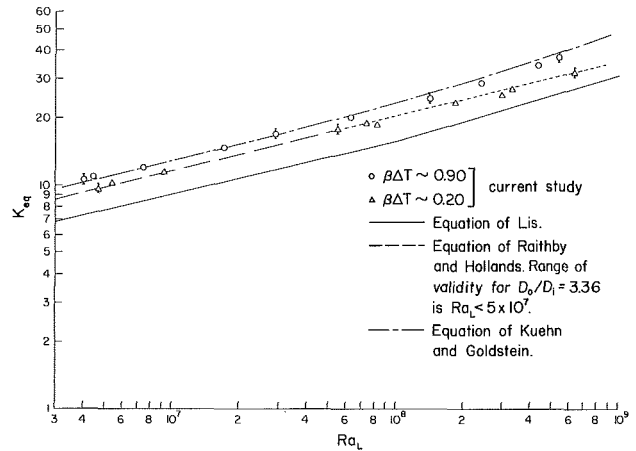


Fig. 12 Heat transfer data at $\beta \Delta T \approx 0.20$ and ≈ 0.90 compared to Lis equation, to Raithby and Hollands equation, and to Kuehn and Goldstein equation

By means of a least-squares technique, the constants C , A , and m were determined, and the following equation resulted:

$$K_{eq} = 0.189 Ra_L^{0.25} \exp(0.21 \beta \Delta T) \quad (8)$$

Equation (8) is valid for the following ranges of the pertinent variables:

$$D_o/D_i = 3.36, \quad Pr = 0.688, \quad 0.20 \leq \beta \Delta T \leq 1.0, \\ \text{and } 6 \times 10^6 \leq Ra_L \leq 2 \times 10^9$$

Applied to all of the data, equation (8) gave deviations ranging from -8.2 percent to $+8.5$ percent, where deviation is defined by

$$\text{Deviation} = [(K_{eq})_{equation} - (K_{eq})_{data}] / (K_{eq})_{data} \quad (9)$$

The maximum deviations occurred at the smallest values of $\beta \Delta T$, which were at the lowest values of ΔT for which small experimental errors are magnified in the final determination of both K_{eq} and Ra_L . Equation (8) is shown plotted along with all of the data in Fig. 11.

The exponential form of the $\beta \Delta T$ dependence was not expected; however, due to the accuracy and repeatability of the experiments, it should be a true representation of the physical phenomenon and not just represent a “best fit” of data using a guessed form of the equation. The uncertainties in the experimental measurements and in the transport property values combine to give errors in the calculation of Rayleigh number and the equivalent thermal conductivity of ± 11 and ± 5 percent, respectively. The data presented in this paper were obtained over a period of two years utilizing three different persons each employing slightly different startup procedures. Each succeeding person added data to existing data at each $\beta \Delta T$ value, as well as obtaining data at additional, new $\beta \Delta T$ values. In all cases new data were totally consistent with the old data, which supports the conclusion that the experimental results were repeatable.

A comparison of the results of this study for $\beta \Delta T$ values of ≈ 0.20 and ≈ 0.90 with the equations recommended by Lis (1966), Kuehn and Goldstein (1978), and Raithby and Hollands (1975), is shown in Fig. 12.

Lis equation:

$$\log K_{eq} = 0.0794 + 0.0625 \log X + 0.0154(\log X)^2$$

where $X = Ra_{D_i} [1 - (D_i/D_o)]^{6.5}$, $Re_{D_i} = (g\beta D_i^3 \Delta T) / (\nu\alpha)$, and $2 \leq D_o/D_i \leq 4$; $0.645 \leq Pr \leq 1.32$; $4 \times 10^4 \leq Ra_{D_i} \leq 4.7 \times 10^{10}$.

Raithby and Holland equation:

$$K_{eq} = 0.386 \left(\frac{\text{Pr}}{0.861 + \text{Pr}} \right)^{1/4} (\text{Ra}_L^*)^{1/4}$$

where $\text{Ra}_L^* = [(\ln D_o/D_i)^4/L^3 (D_i^{-3/5} + D_o^{-3/5})^5] \text{Ra}_L$ and $10^2 \leq \text{Ra}_L^* \leq 10^7$.

The equation of Kuehn and Goldstein is too involved to repeat here. Since Lis (1966), Raithby and Hollands (1975), and Kuehn and Goldstein (1978) used an arithmetic mean temperature as the reference temperature for property evaluation, for comparison purposes, the data of this study have been reduced also using an arithmetic mean temperature. As can be seen in Fig. 12, the equation of Lis underpredicts the heat transfer at all values of Rayleigh number at both $\beta \Delta T$ extremes; an average of 30 percent at $\beta \Delta T \approx 0.9$ and an average of 20 percent at $\beta \Delta T \approx 0.20$. Even though the results of this study are restricted to one diameter ratio (3.36), they do raise serious questions as to the accuracy of the correlation equation recommended by Lis. However, the equation proposed by Raithby and Hollands fits the data for $\beta \Delta T \approx 0.2$ quite well, even beyond the Ra_L value for which it is stated to be valid for this diameter ratio. The equation does, however, underpredict the heat transfer rate by an average of ~ 12 percent for $\beta \Delta T \approx 0.90$ for $\text{Ra}_L < 5 \times 10^7$. The equation given by Kuehn and Goldstein fits the data for $\beta \Delta T \approx 0.9$ reasonably well but overpredicts the heat transfer rate by as much as 30 percent for $\beta \Delta T \approx 0.2$ at the higher values of Ra_L .

Conclusions

The experimental results presented in this paper for a diameter ratio of 3.36 clearly show that the expansion number is an important parameter, along with the Rayleigh number, in the prediction of heat transfer rates between two isothermal horizontal concentric cylinders. The exponential part of equation (8), which accounts for the expansion number effect, varies from 1.021 for $\beta \Delta T = 0.1$ to 1.234 for $\beta \Delta T = 1.0$. For most of the past studies reported on in the literature, the $\beta \Delta T$ value was under 0.1, and therefore, could be neglected in the final correlation of the heat transfer results.

A volume-weighted mean temperature was used to evaluate the gas properties and the time-averaged temperature profiles obtained in the study support this choice for a reference temperature. These time-averaged temperature profiles are also consistent with the experimentally observed increase in K_{eq} for a fixed Rayleigh number as the expansion number is increased. The correlation equation of Lis (1966) was shown significantly to underpredict the heat transfer rate for $0.2 \leq \beta \Delta T \leq 1.0$, $6 \times 10^6 \leq \text{Ra}_L \leq 10^9$, and for a diameter ratio of 3.36. Its use is not recommended in this range of the pertinent

variables. The equation of Raithby and Hollands (1975) fits the data quite well for $\beta \Delta T \approx 0.20$ and $\text{Ra}_L \leq 5 \times 10^7$ but underpredicts K_{eq} for $\beta \Delta T \approx 0.90$ while the equation of Kuehn and Goldstein (1978) fits the data at $\beta \Delta T \approx 0.90$ but overpredicts at the lower $\beta \Delta T$ values.

Acknowledgments

The author wishes to acknowledge that this material is based upon work supported by the National Science Foundation under Grant No. CBT-8403467 and in part on data collected by Mr. Steve Brandon, an M.S. degree student. The author would like to acknowledge that the work was carried out in the Thermal/Fluids Science Research Laboratory, which was made possible by a grant from the National Science Foundation under the EPSCoR Program.

References

- Beckmann, W., 1931, "Die Wärmeübertragung in Zylindrischen Gasschichten bei natürlicher Konvektion," *Forsch. Geb. Ing. Wes.*, Vol. 2, No. 5, pp. 165-178, 213-217, 407.
- Bishop, E. H., Carley, C. T., and Powe, R. E., 1968, "Natural Convective Oscillatory Flow in Cylindrical Annuli," *International Journal of Heat and Mass Transfer*, Vol. 11, pp. 1741-1752.
- Clausing, A. M., and Kempka, S. N., 1981, "The Influences of Property Variations on Natural Convection From Vertical Surfaces," *ASME JOURNAL OF HEAT TRANSFER*, Vol. 103, pp. 609-612.
- Clausing, A. M., Wagner, K. C., and Skaidra, R. J., 1984, "An Experimental Investigation of Combined Convection From a Short Vertical Cylinder in a Crossflow," *ASME JOURNAL OF HEAT TRANSFER*, Vol. 106, pp. 558-562.
- Hellums, J. D., and Churchill, S. W., 1900, "Dimensional Analysis and Natural Circulation," *Chemical Engineering Progress Symposium Series on Heat Transfer—Buffalo*, No. 32, 57, pp. 75-80.
- Kraussold, H., 1934, "Wärmeabgabe von zylindrischen Flüssigkeitsschichten bei natürlicher Konvektion," *Forsch. Geb. Ing. Wes.*, Vol. 5, No. 4, pp. 186-191.
- Kuehn, T. H., and Goldstein, R. J., 1976a, "Correlating Equations for Natural Convection Heat Transfer Between Horizontal Circular Cylinders," *International Journal of Heat and Mass Transfer*, Vol. 19, pp. 1127-1134.
- Kuehn, T. H., and Goldstein, R. J., 1976b, "An Experimental and Theoretical Study of Natural Convection in the Annulus Between Horizontal Concentric Cylinders," *Journal of Fluid Mechanics*, Vol. 74, pp. 695-719.
- Kuehn, T. H., and Goldstein, R. J., 1978, "An Experimental Study of Natural Convection Heat Transfer in Concentric and Eccentric Horizontal Cylindrical Annuli," *ASME JOURNAL OF HEAT TRANSFER*, Vol. 100, pp. 635-640.
- Lis, J., 1966, "Experimental Investigation of Natural Convection Heat Transfer in Simple and Obstructed Horizontal Annuli," *Third International Heat Transfer Conference*, Vol. 2, pp. 196-204.
- Mahony, D. N., Kumar, R., and Bishop, E. H., 1986, "Numerical Investigation of Variable Property Effects on Laminar Natural Convection of Gases Between Two Horizontal Isothermal Concentric Cylinders," *ASME JOURNAL OF HEAT TRANSFER*, Vol. 108, pp. 783-789.
- Raithby, G. D., and Hollands, K. G. T., 1975, "A General Method of Obtaining Approximate Solutions to Laminar and Turbulent Free Convection Problems," *Advances in Heat Transfer*, Vol. 11, pp. 265-315.
- Threlfall, D. C., 1975, "Free Convection in Low Temperature Gaseous Helium," *Journal of Fluid Mechanics*, Vol. 67, pp. 17-28.

Transient Natural Convection Between Two Zones in an Insulated Enclosure

P. A. Litsek

A. Bejan

Mem. ASME

Department of Mechanical Engineering
and Materials Science,
Duke University,
Durham, NC 27706

The natural convection flow and heat transfer between two enclosures that communicate through a vertical opening is studied by considering the evolution of an enclosed fluid in which the left half is originally at a different temperature than the right half. Numerical experiments show that at sufficiently high Rayleigh numbers the ensuing flow is oscillatory. This and other features are anticipated on the basis of scale analysis. The time scales of the oscillation, the establishment of thermal stratification, and eventual thermal equilibrium are determined and tested numerically. At sufficiently high Rayleigh numbers the heat transfer between the communicating zones is by convection, in accordance with the constant-Stanton-number trend pointed out by Jones and Otis (1986). The range covered by the numerical experiments is $10^2 < Ra < 10^7$, $0.71 < Pr < 100$, and $0.25 < H/L < 1$.

Introduction

Despite considerable research conducted during the last ten years, one controversial topic that persists in the field of natural convection is the problem of heat transfer across a divided enclosure. The need for rethinking in this area was stated most eloquently by Jones and Otis (1986), who began by questioning the "natural convection" shape of an original correlation proposed by Brown and Solvason (1962). They showed that the Grashof-number notation was introduced artificially in that correlation, and that the correlation amounts to the simple statement that the Stanton number is constant.

The same problem was tackled in a wide-ranging theoretical and experimental study by Scott et al. (1986). These authors showed that there are two distinct regimes for natural convection heat transfer between two zones that communicate through a vertical opening: (1) the flow driven by the bulk density difference that exists between the two zones, and (2) the aperture jet counterflow driven by the vertical boundary layers that line the extreme (differentially heated) walls of the enclosure. The critical aperture area for which the flow switches from one regime to the other was determined.

The objective of the present study is to isolate Scott et al.'s first regime from the second regime, in order to analyze in detail its flow and heat transfer characteristics. With regard to these two regimes we note that the one that has attracted the most attention by far is the second; review, for example, the literature on enclosures heated from the side (Kakac et al., 1985). For this reason in this paper we isolate the first regime by considering the time-dependent flow and heat transfer between two distinct zones of an enclosure, which are allowed to communicate suddenly. The walls of the enclosure are insulated, and the flow is driven by the bulk density difference between the original two zones.

Mathematical Formulation

The system that forms the subject of this study is the two-dimensional rectangular cavity sketched in Fig. 1. The cavity contains a Newtonian and Boussinesq-incompressible fluid whose coefficient of volumetric thermal expansion is β . The four walls of the cavity are modeled as impermeable, no-slip and adiabatic. Initially, a vertical partition located at $x = L/2$

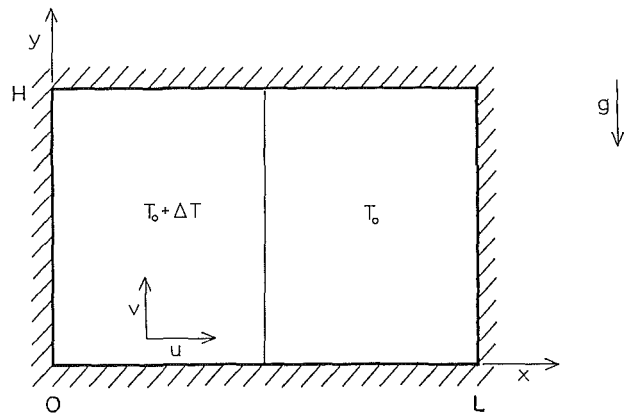


Fig. 1 Two adjacent enclosures that communicate suddenly through an H -tall opening (the vertical midplane)

divides the cavity into two compartments at different temperatures, T_0 and $T_0 + \Delta T$. The fluid is motionless and isothermal on each side of the partition.

The focus of this study is on the transient flow and heat transfer processes that are triggered by the sudden removal of the partition. Of special interest is the time scale of approach to thermal equilibrium throughout the cavity. The dimensionless form of the conservation equations for mass, momentum, and energy in two dimensions is

$$\frac{\partial u_*}{\partial x_*} + \frac{\partial v_*}{\partial y_*} = 0 \quad (1)$$

$$\frac{1}{Pr} \left(\frac{\partial u_*}{\partial t_*} + u_* \frac{\partial u_*}{\partial x_*} + v_* \frac{\partial u_*}{\partial y_*} \right) = -\frac{\partial P_*}{\partial x_*} + \nabla^2 u_* \quad (2)$$

$$\frac{1}{Pr} \left(\frac{\partial v_*}{\partial t_*} + u_* \frac{\partial v_*}{\partial x_*} + v_* \frac{\partial v_*}{\partial y_*} \right) = -\frac{\partial P_*}{\partial y_*} + \nabla^2 v_* + Ra \left(T_* - \frac{1}{\beta \Delta T} \right) \quad (3)$$

$$\frac{\partial T_*}{\partial t_*} + u_* \frac{\partial T_*}{\partial x_*} + v_* \frac{\partial T_*}{\partial y_*} = \nabla^2 T_* \quad (4)$$

where Pr is the Prandtl number ($= \nu/\alpha$) and Ra the Rayleigh number based on the initial temperature difference and on cavity height,

Contributed by the Heat Transfer Division for publication in the JOURNAL OF HEAT TRANSFER. Manuscript received by the Heat Transfer Division January 16, 1987.

$$Ra = \frac{g\beta H^3 \Delta T}{\alpha \nu} \quad (5)$$

The dimensionless variables denoted by the subscript ()_{*} have been defined as follows:

$$x_* = \frac{x}{H}, y_* = \frac{y}{H}, t_* = \frac{t}{H^2/\alpha} \quad (6)$$

$$u_* = \frac{u}{\alpha/H}, v_* = \frac{v}{\alpha/H}, P_* = \frac{P}{\mu\alpha/H^2}, T_* = \frac{T-T_0}{\Delta T} \quad (7)$$

where the physical quantities without subscript are defined in the Nomenclature. The governing equations (1)-(4) are based on the constant property model and the assumption that the density can be treated as constant everywhere except in the buoyancy term of the momentum equation. Throughout the numerical experiments described in this paper, the value of $\beta\Delta T$ in equation (3) was set equal to 0.1 (the $\beta\Delta T$ value does not affect the flow and temperature fields).

The dimensionless form of the boundary and initial conditions alluded to in the first paragraph of this section is

$$u_* = v_* = 0 \text{ at } x_* = 0, x_* = \frac{L}{H}, y_* = 0, y_* = 1 \quad (8)$$

$$\frac{\partial T_*}{\partial x_*} = 0 \text{ at } x_* = 0, x_* = \frac{L}{H} \quad (9)$$

$$\frac{\partial T_*}{\partial y_*} = 0 \text{ at } y_* = 0, y_* = 1 \quad (10)$$

and, respectively,

$$u_* = v_* = 0 \text{ throughout } \left(0 \leq x_* \leq \frac{L}{H}, 0 \leq y_* \leq 1\right) \quad (11)$$

$$T_* = 1 \text{ throughout } \left(0 \leq x_* \leq \frac{L}{2H}, 0 \leq y_* \leq 1\right) \quad (12)$$

$$T_* = 0 \text{ throughout } \left(\frac{L}{2H} \leq x_* \leq \frac{L}{H}, 0 \leq y_* \leq 1\right) \quad (13)$$

Graphic displays of the flow field are produced by first solving for (u_*, v_*) , and then calculating the streamfunction ψ_* by solving the Poisson-type equation

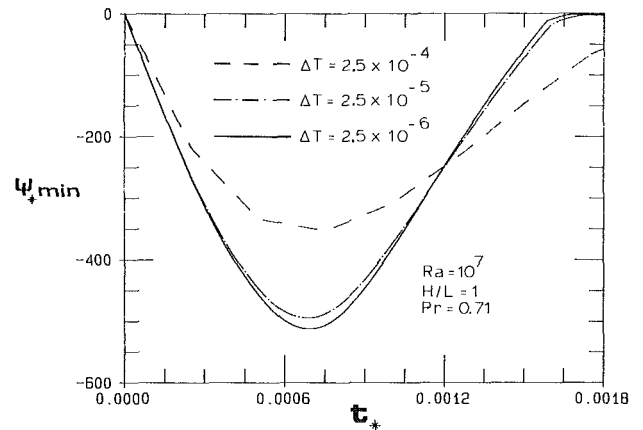
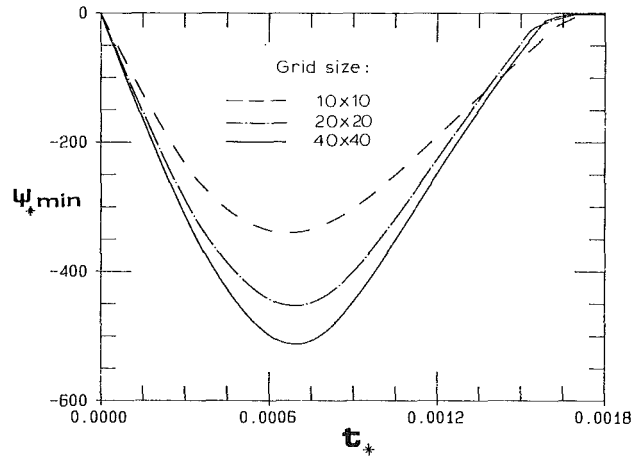


Fig. 2 Numerical accuracy tests showing the effect of grid fineness (top graph) and the effect of time step size (bottom graph)

$$\nabla^2 \psi_* = \frac{\partial u_*}{\partial y_*} - \frac{\partial v_*}{\partial x_*} \quad (14)$$

where $\psi_* = \psi/\alpha$, and

$$u = \frac{\partial \psi}{\partial y} \text{ and } v = -\frac{\partial \psi}{\partial x} \quad (15)$$

Nomenclature

c_p = specific heat at constant pressure, J/kg/K
 g = gravitational acceleration, m/s²
 Gr = Grashof number = Ra/Pr
 H = height, m
 k = thermal conductivity, W/m/K
 L = length, m
 P = pressure, N/m²
 Pr = Prandtl number
 q = convection heat transfer scale, W/m
 q_0 = conduction heat transfer scale, W/m

Ra = Rayleigh number
 St = Stanton number scale = $q/(H\Delta T\rho c_p u)$
 t = time, s
 T = temperature, K
 T_0 = reference temperature (Fig. 1), K
 T_L = average temperature of the left half of the enclosure
 T_R = average temperature of the right half of the enclosure
 T_c = temperature of the geometric center of the enclosure, dimensionless
 u, v = velocity components (Fig. 1) m/s

x, y = Cartesian coordinates (Fig. 1), m
 α = thermal diffusivity, m²/s
 β = coefficient of thermal expansion, 1/K
 μ = viscosity, kg/m/s
 ν = kinematic viscosity, m²/s
 ρ = density, kg/m³
 τ = scale of wall shear stress, N/m²
 ψ = stream function
 $\Delta()$ = difference
 $()_*$ = dimensionless variables, equations (6) and (7)

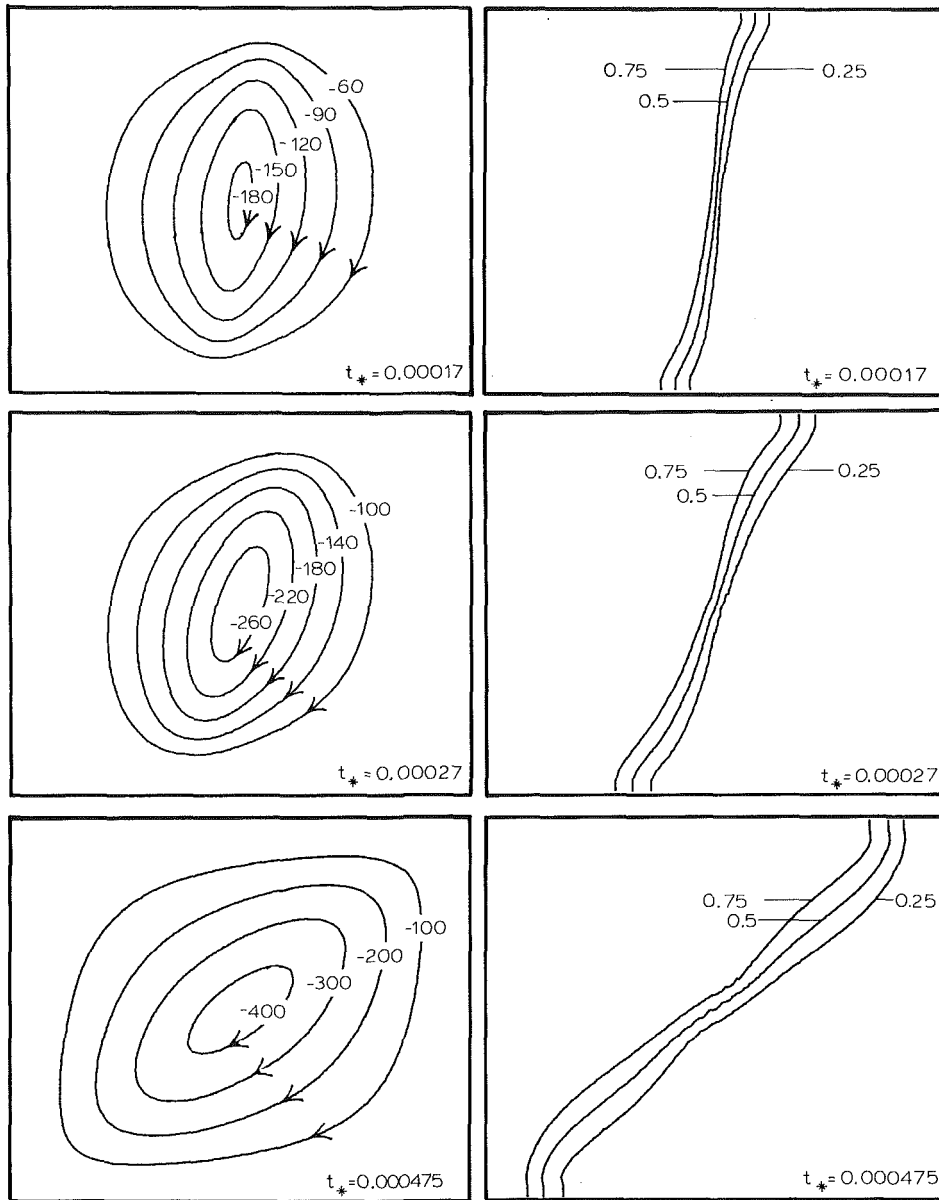


Fig. 3 Streamlines and isotherms during the first turning over of the temperature field, at a relatively high Rayleigh number ($Ra = 10^7$, $Pr = 0.71$, $H/L = 1$)

Numerical Experiments

The dimensionless equations were solved on a square mesh, using Van Doormaal and Raithby's (1984) variation of the control volume formulation developed by Patankar (1980). One advantage of this variation (known as SIMPLEC) is that it removes the need for one of the two relaxation factors required in the SIMPLE algorithm. The convergence of the SIMPLEC method depends on the choice of only one relaxation factor. This alternative method was shown to be faster, hence, less expensive.

The power law scheme was used to calculate all the fluxes across the boundaries of each control volume. To solve the Poisson-type equation (14) for stream function we used a standard finite difference scheme (SOR). The velocity values at the nonstaggered grid points were calculated based on linear interpolation (recall that the SIMPLE algorithm uses a staggered grid to solve the momentum equations).

Flow and temperature field solutions were obtained as a

function of t_* . At each time step t_* the solution was considered converged when

$$p_{\text{prime}} < \text{res} \quad (16)$$

for all x_* and y_* , where p_{prime} is Patankar's (1980) "pressure correction" and res is a number small enough so that the newly determined pressure field produces a velocity field that satisfies the continuity equation ($\text{res} = 0.0001$ in these calculations).

The numerical results exhibited in this paper were all obtained using uniform grids. The number of horizontal lines counted in the vertical direction was fixed at 40. The number of lines counted in the horizontal direction was set equal to 40 times the shallowness ratio (L/H). The goodness of this uniform grid size was established on the basis of accuracy tests of the kind shown in Fig. 2. In that figure we see a relatively small change in the history of the total flowrate of the natural circulation (ψ_{min}) as the grid fineness changes from 20×20 to 40×40 (note that $L/H = 1$).

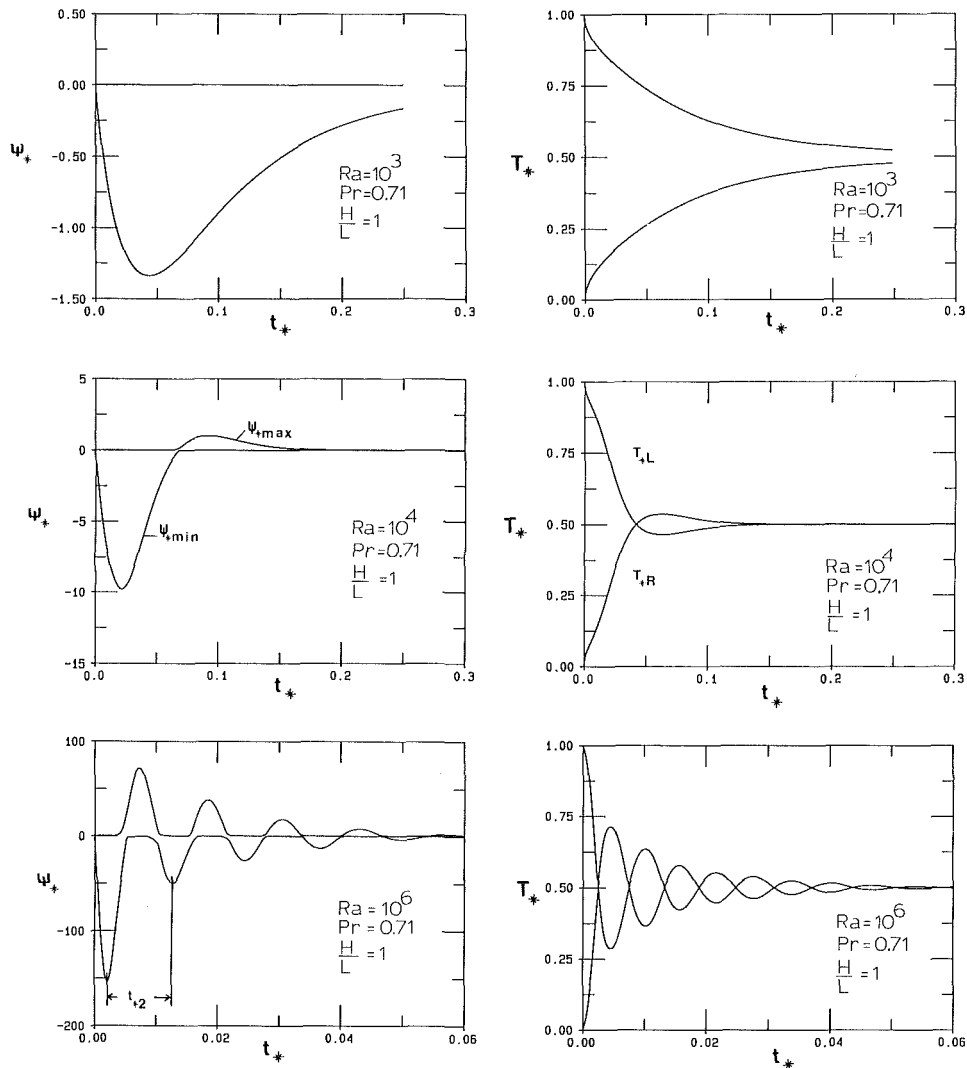


Fig. 4 The effect of Rayleigh number on the oscillatory behavior of the flow ($Pr = 0.71$, $H/L = 1$). Left side: ψ_{*min} and ψ_{*max} . Right side: T_{*L} and T_{*R} .

Numerical accuracy tests were conducted in order to determine also the proper size of the time step Δt_* . One such test is illustrated in Fig. 2, again in terms of the effect registered on ψ_{*min} . A summary of the time steps used for numerical experiments in a square enclosure is presented below:

Ra	Pr	Δt_*
10^2	0.71	10^{-4}
10^3		10^{-4}
10^4		10^{-4}
10^5		5×10^{-5}
10^6		5×10^{-6}
10^7		2.5×10^{-6}
10^5	7	5×10^{-5}
10^5	100	10^{-5}

Scale Analysis

There are at least two ways in which to study numerically the convection phenomenon that follows from the initial conditions sketched in Fig. 1. One way is to document the flow

and temperature field throughout their history (i.e., en route to equilibrium), and to repeat these runs while changing Ra, Pr, and H/L enough times, so that, it is hoped, a coherent albeit incomplete picture of the phenomenon will emerge. A first step in this extensive documentation effort might be Fig. 3, which shows how the warm fluid slips over the cold fluid in the earliest stages of a "high Rayleigh" number flow.

Another way to study the phenomenon is first to predict its main features theoretically, and then rely on numerical experiments only to test and, perhaps, extend the theory. We chose this second approach because (1) it is more challenging, (2) given the same journal space, it allows us to cover a greater territory and to paint a considerably more complete picture than if we did only numerical experiments, and (3) we find it more interesting to combine two methodologies (in this case, scaling theory + numerical experiments) than to employ a single methodology all the way through, for example, numerical experiments that remain unexplained, or theoretical predictions that remain untested.

The flow is initially driven by the mismatch between the hydrostatic pressure fields existing on the two sides of the vertical midplane (Fig. 1). The vertical pressure gradients on the left and right sides of the vertical midplane are $(\rho - \Delta\rho)g$ and

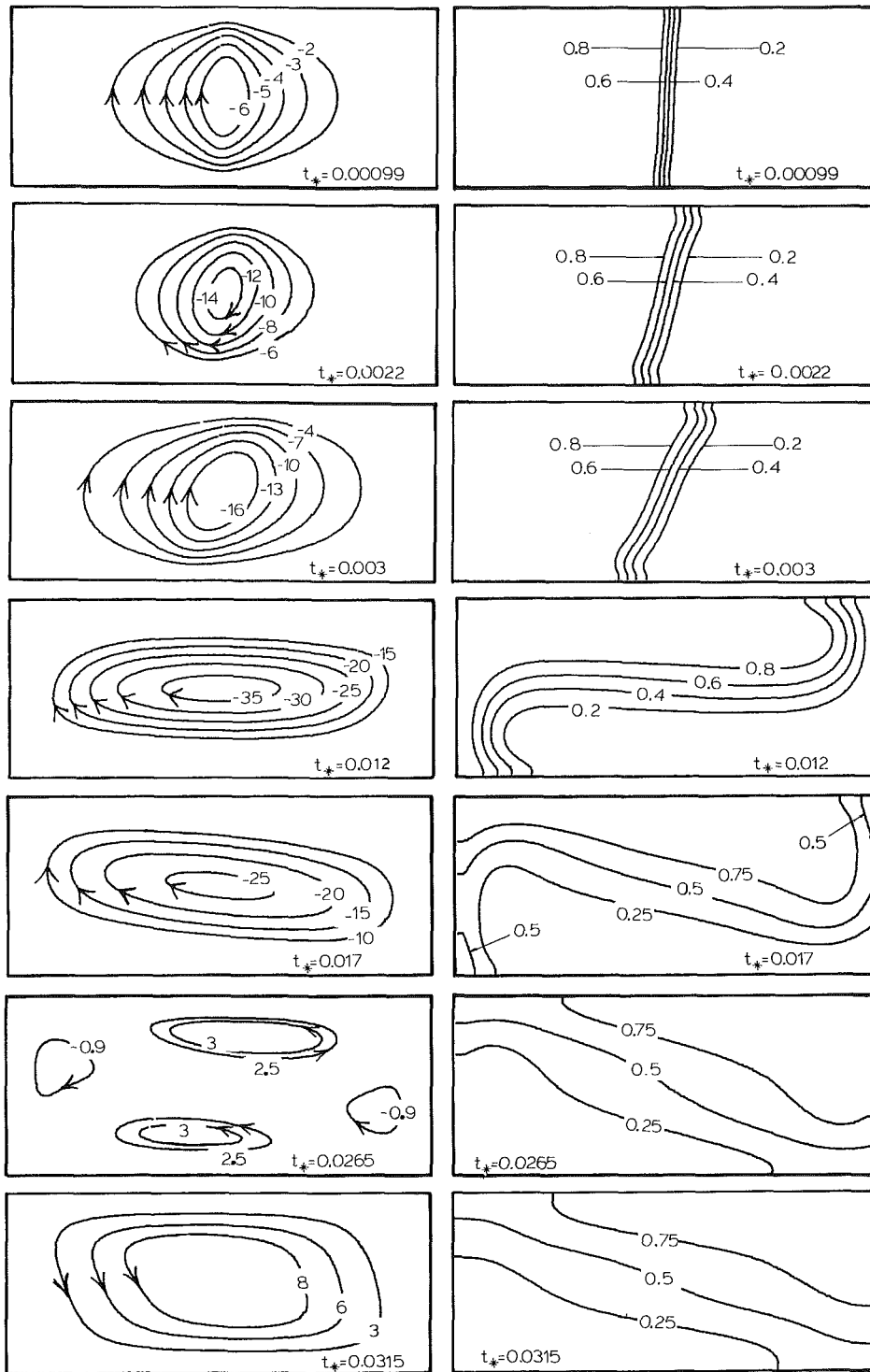


Fig. 5 Streamlines and isotherms in a shallow enclosure ($Ra = 10^5$, $Pr = 0.71$, $H/L = 0.5$)

ρg , respectively (note that $\Delta\rho = \rho\beta\Delta T$). This mismatch accounts for a pressure difference in the horizontal direction

$$\Delta P \sim \rho g H \beta \Delta T \quad (17)$$

The horizontal counterflow driven by ΔP is initially the result of the balance between ΔP and inertia (ρu^2); from this balance we deduce the horizontal velocity scale

$$u \sim (gH\beta\Delta T)^{1/2} \quad (18)$$

The effect of viscous diffusion propagates vertically away

from the horizontal walls, and across the middepth interface between the two branches of the counterflow. The penetration depth of this effect grows as $(\nu t)^{1/2}$. Therefore, the H -thick counterflow is fully penetrated by viscous diffusion at a time of order

$$t_1 \sim \frac{H^2}{\nu} \quad (19)$$

In the meantime, the inviscid flow (18) completes the layering (turning over) of the fluid at a time of order $t_2 \sim L/u$, i.e.,

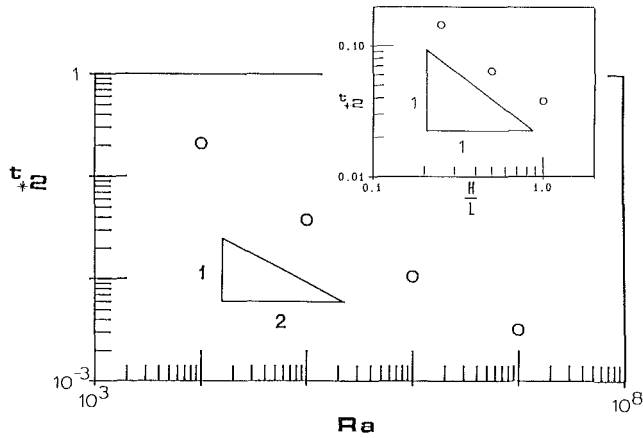


Fig. 6 Effect of Rayleigh number on the oscillation period ($Pr = 0.71$, $H/L = 1$). Inset: effect of aspect ratio on the oscillation period ($Ra = 10^5$, $Pr = 0.71$).

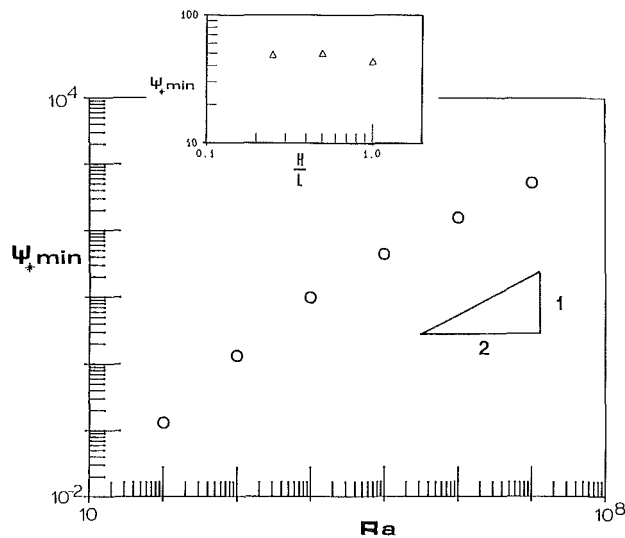


Fig. 7 Effect of Rayleigh number on stream function ($Pr = 0.71$, $H/L = 1$). Inset: insensitivity of stream-function amplitude to changes in H/L ($Ra = 10^5$, $Pr = 0.71$).

when the counterflow reaches the vertical ends of the enclosure. This happens provided $t_2 < t_1$, which translates into the following criterion for "inviscid" behavior during the first L -long sweep of the enclosure

$$Gr^{1/2} > \frac{L}{H} \quad (20)$$

The inviscid-flow criterion (20) is met by all the numerical experiments exhibited in this paper. We continue to assume that viscous diffusion is negligible even as t exceeds t_2 . The counterflow that just placed the heavy (cold) fluid at the bottom of the enclosure continues its clockwise motion due to its own inertia. The cold fluid rises into the left half of the enclosure, only to be slowed down and brought to rest by the effect of gravity. This completes the first half of the period of an oscillation in which the light and heavy portions of the fluid inventory trade sides until the effects of viscous and thermal diffusion take over. The period of the oscillation is of order t_2 , or in dimensionless notation

$$t_{*2} \sim \frac{L}{H} Ra^{-1/2} Pr^{-1/2} \quad (21)$$

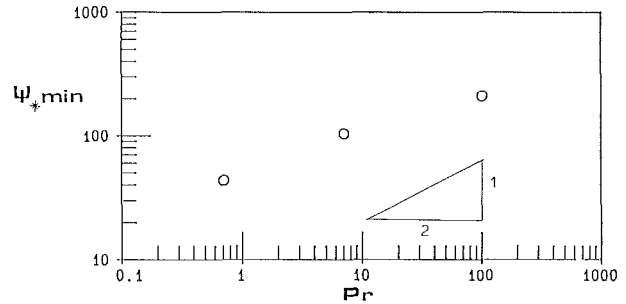


Fig. 8 Effect of Prandtl number on stream function ($Ra = 10^5$, $H/L = 1$)

The oscillatory flow is confirmed by numerical experiments (the flow sequence of Fig. 3 shows only the first quarter of the first period of the oscillation). A concise summary of the oscillatory behavior is presented in Fig. 4, whose left side shows the history of the stream-function minimum (clockwise flow) and stream-function maximum (counterclockwise flow). The circulation changes its sense periodically; however, the fluid does not come to a complete stop. For short intervals of time around the half-period points, the enclosure is inhabited by weak flows that rotate in both senses. Streamlines and isotherms that correspond to a flow of this kind are shown in the sixth frame of Fig. 5.

The right side of Fig. 4 shows the history of average temperatures calculated over the left half and right half of the enclosure, respectively,

$$T_{*L} = 2 \frac{H}{L} \int_{x_* = 0}^{L/2H} \int_{y_* = 0}^1 T_* dx_* dy_* \quad (22)$$

$$T_{*R} = 2 \frac{H}{L} \int_{x_* = L/2H}^{L/H} \int_{y_* = 0}^1 T_* dx_* dy_* \quad (23)$$

The slope of the $T_{*L}(t_*)$ curve indicates the direction and size of the total heat transfer rate out of the left side, across the vertical midplane. The times of flow reversal ($\psi_{*min,max} \approx 0$) on the left side of Fig. 4 correspond to times of maximum heat transfer across the vertical midplane (Fig. 4, right side).

The validity of the t_{*2} scale predicted by equation (21) is demonstrated in Fig. 6. The numerical t_{*2} values were obtained by measuring the t_* distance between the first two stream-function minima (Fig. 4, left side). The two graphs of Fig. 6 show that the calculated t_{*2} values vary as $Ra^{-1/2}$ and as L/H .

The preceding analysis allows also an estimate of the flowrate of the oscillatory circulation. Writing $\psi \sim uH$ and $\psi_* = \psi/\alpha$ yields

$$\psi_* \sim Ra^{1/2} Pr^{1/2} \quad (24)$$

This scaling law is tested in Figs. 7 and 8. The numerical ψ_* values plotted in these figures represent the absolute values of the first stream-function minimum seen on the left side of Fig. 4. The stream-function scale increases as $Ra^{1/2}$ (Fig. 7), especially in the high Rayleigh number limit indicated by criterion (20). The stream-function increases also as $Pr^{1/2}$ when the Rayleigh number is fixed (Fig. 8). Finally, when both Ra and Pr are held constant, the aspect ratio H/L appears to have no discernible effect on $|\psi_{*min}|$ (see Fig. 7, inset).

The time when the inertial flow dies out due to viscous diffusion can be estimated based on the following energy balance. The kinetic energy of the inviscid flow ($\rho u^2 H L$) is in time dissipated by the work of overcoming the viscous shear forces that line the two horizontal walls (τL). The shear stress scale is time dependent,

$$\tau \sim \mu \frac{u}{(\nu t)^{1/2}} \quad (25)$$

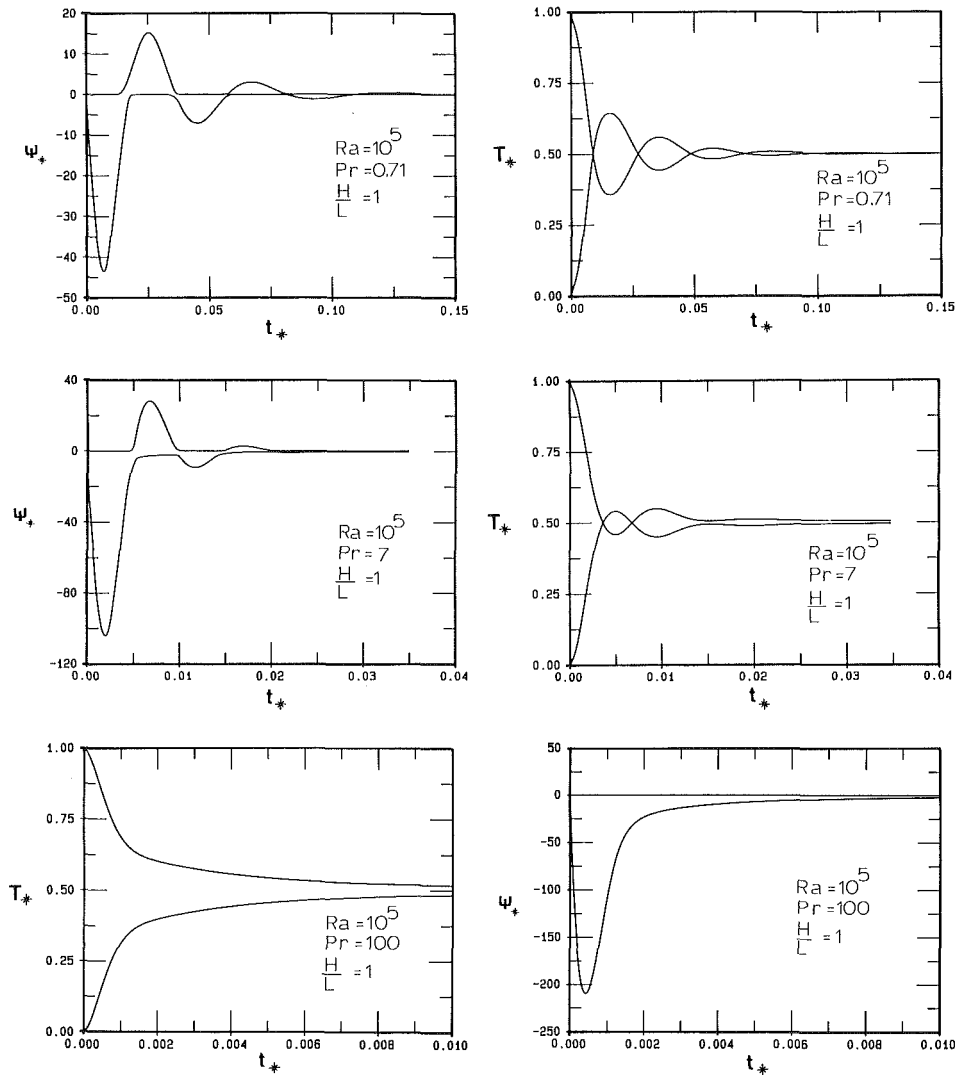


Fig. 9 Effect of Prandtl number on the oscillatory behavior of the flow ($Ra = 10^5$, $H/L = 1$). Left side: ψ_{*min} and ψ_{*max} . Right side: T_{*L} and T_{*R} .

and so is the dissipated work $(\tau L)(u)(t)$. The balance $\rho u^2 HL \sim \tau L u t$ yields the time of viscous decay $t_1 \sim H^2/\nu$, in other words

$$t_{*1} \sim Pr^{-1} \quad (26)$$

Figure 9 shows the effect of Pr on the oscillatory flow, specifically, how the life of the flow becomes shorter as Pr increases. When $Pr=100$ the oscillation is almost absent, because the viscous decay time t_1 becomes comparable with the oscillation period t_2 . A representative set of streamlines, isotherms, and heatlines of this last case is shown in Fig. 10. The flow is always clockwise. At the end of the sequence, $t_* = 0.0029$, when the flowrate has dropped to less than one tenth of its maximum value (Fig. 9, lower left corner), the warm fluid occupies the upper half of the enclosure. Thermal diffusion downward through the horizontal midplane continues beyond the time t_1 , until the temperature becomes uniform throughout the enclosure.

Heat Transfer

On top of the flow studied until now rides the phenomenon of heat transfer between the original left and right halves of the enclosure. Two heat transfer questions may be formulated at this point. From a thermal comfort perspective, we may

wish to know the time when the fluid becomes stagnant (e.g., stably stratified). From the point of view of understanding better the controversy reviewed in the Introduction, we may wish to study the net heat transfer rate through the vertical midplane of the enclosure. The answers to both questions are already contained in the flow scales that were derived and tested in the preceding section.

In the high-Rayleigh-number regime the heat transfer through the vertical midplane is dominated by convection. Writing q and q_0 for the horizontal convection and conduction scales, we have

$$q \sim \rho c_p u H \Delta T \quad (27)$$

$$q_0 \sim k H \frac{\Delta T}{(\alpha t)^{1/2}} \quad (28)$$

and

$$\frac{q}{q_0} \sim (Ra Pr t_*)^{1/2} \quad (29)$$

We see that q exceeds q_0 provided t_* is greater than $(Ra Pr)^{-1}$. Comparing this time scale with the shortest time scale uncovered until now, t_{*2} , we conclude that the heat transfer dur-

ing the oscillatory flow is by convection when q dominates from the beginning of the oscillation, i.e., when

$$t_2^* > (\text{RaPr})^{-1} \quad (30)$$

or

$$(\text{RaPr})^{1/2} > \frac{H}{L} \quad (31)$$

The convection scale (27) can be rewritten as

$$\frac{q/H\Delta T}{\rho c_p u} \sim 1 \quad (32)$$

which is precisely Jones and Otis' (1986) observation that the Stanton number ($St \sim q/H\Delta T/\rho c_p u$) must be a constant.

The constant- St scaling law can be tested numerically by first recognizing

$$q \sim \rho c_p H L \left| \frac{dT_{L,R}}{dt} \right| \quad (33)$$

and then

$$St \sim \frac{L}{H} \left| \frac{dT_{*L,R}/dt_*}{\psi_*} \right| \quad (34)$$

The right-hand side of this last expression can be evaluated using the type of information displayed in Figs. 4 and 9. The results are illustrated in Fig. 11, where the St values plotted on the ordinate represent the value obtained for the right-hand side of equation (34). For the ψ_* denominator of equation (34) we used the $(-\psi_{*min})$ and ψ_{*max} values read sequentially off plots like on the left side of Fig. 4. In the short time intervals in which circulation of both signs exists in the enclosure (e.g., the "pinch" points where both ψ_{*min} and ψ_{*max} approach zero in Fig. 4), the ψ_* denominator was set equal to the greater of the two values $(-\psi_{*min})$ and ψ_{*max} .

Figure 11 shows that the Stanton number is consistently of order one, in accordance with Jones and Otis' (1986) argument. The short time intervals in which St is seen to drop

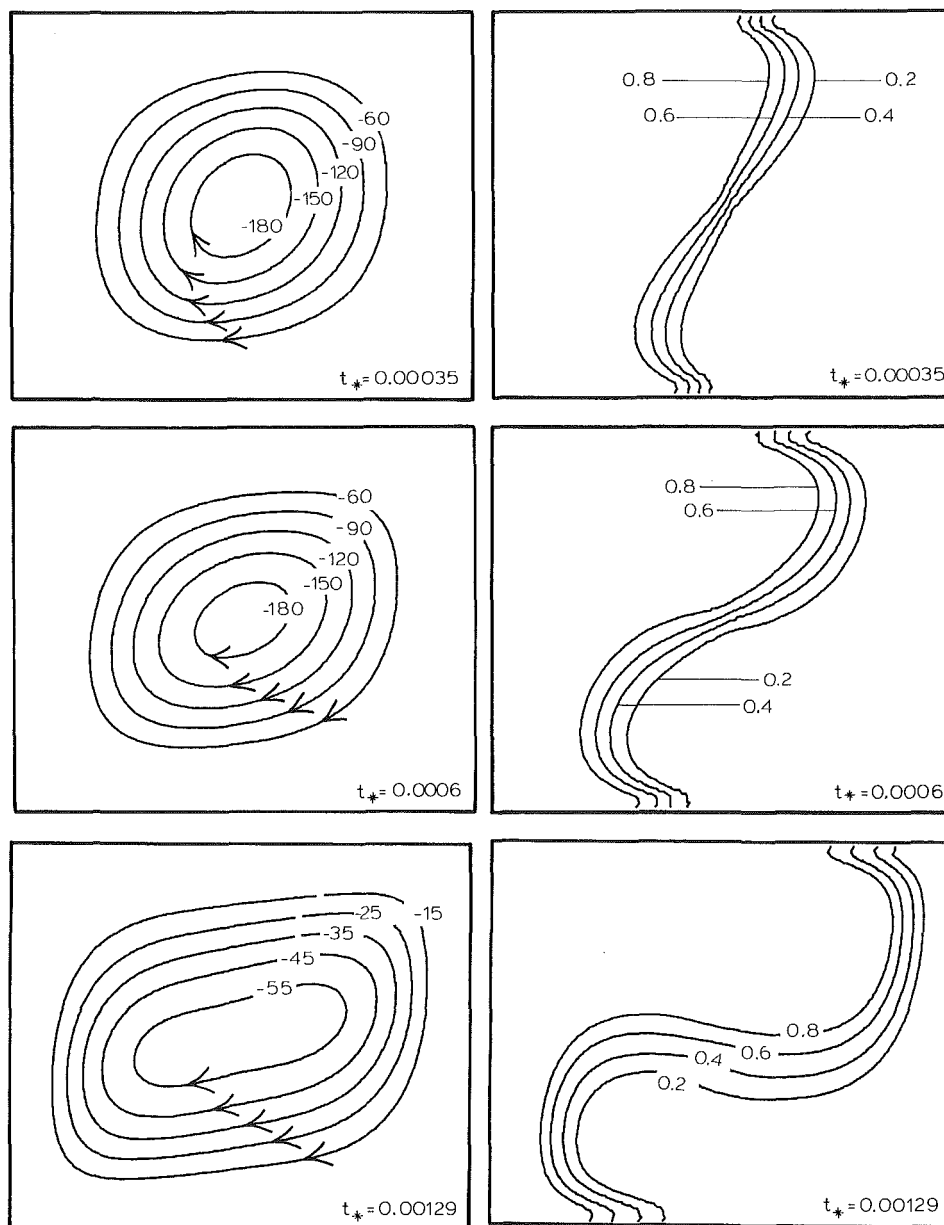


Fig. 10 Streamlines and isotherms showing the disappearance of oscillations in the high Prandtl number limit ($Pr = 100$, $Ra = 10^5$, $H/L = 1$)

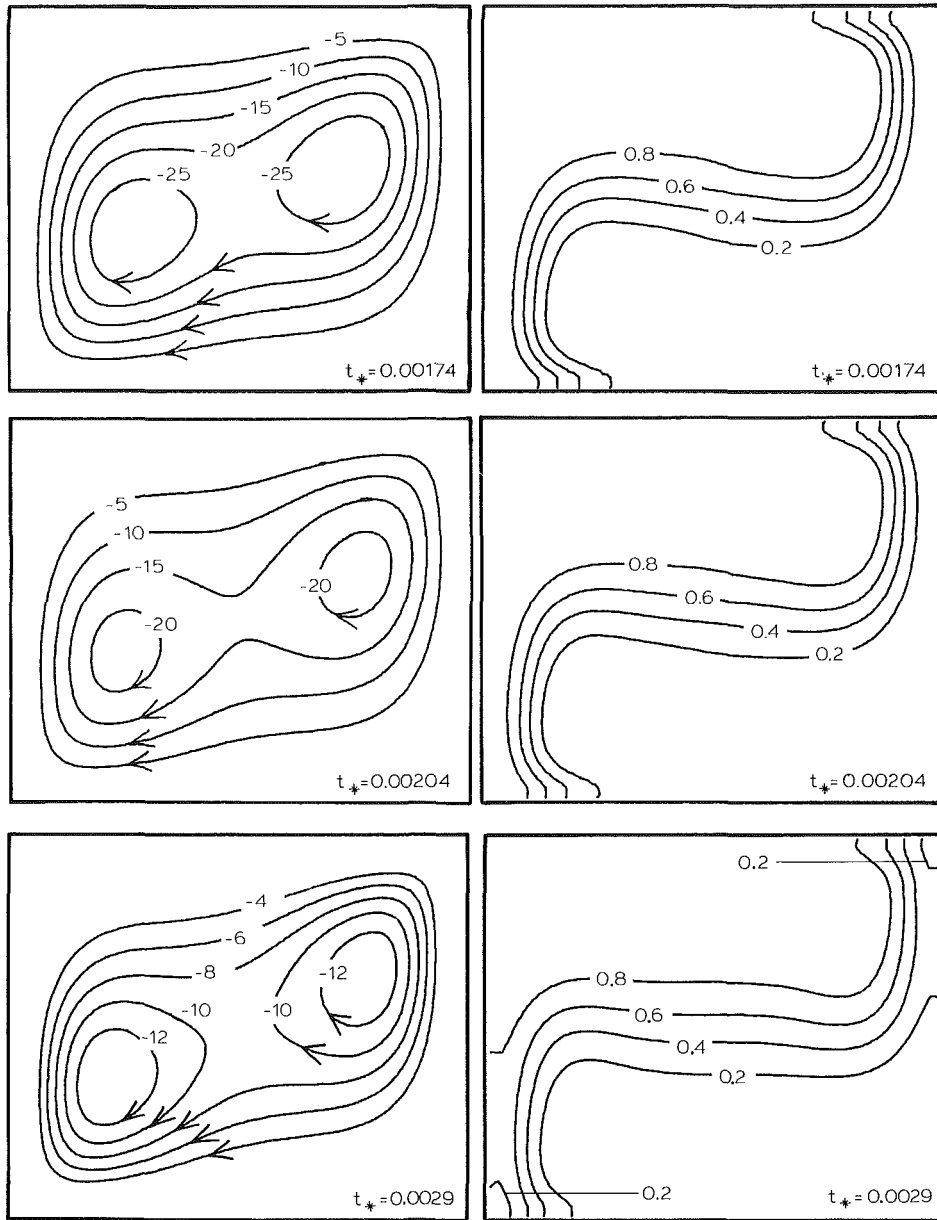


Fig. 10 (cont.)

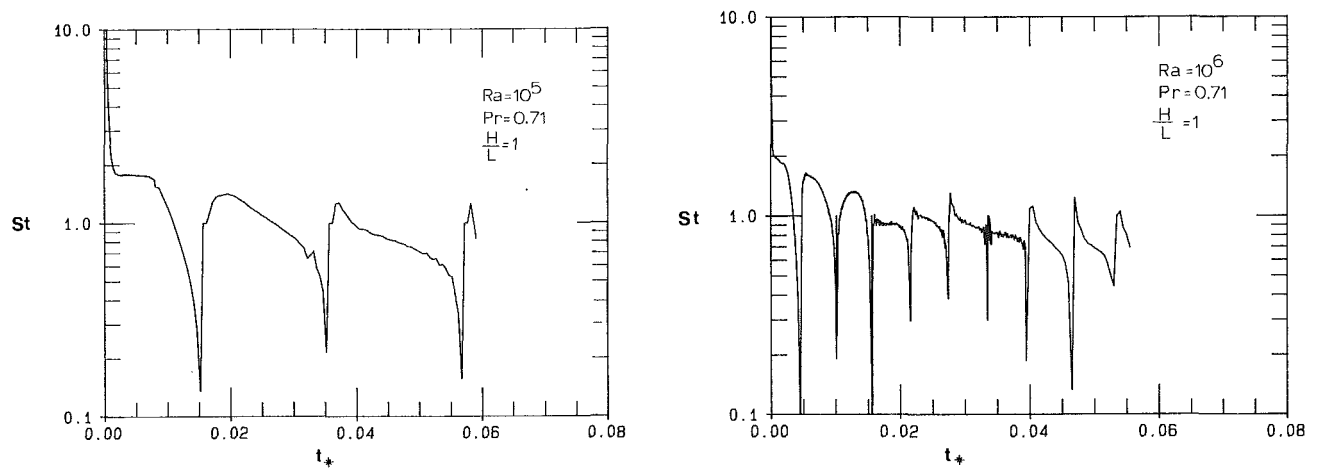


Fig. 11 Stanton number for convective heat exchange between the two zones of the enclosure, and validity of the $St \sim 1$ scaling law

abruptly to zero are related to the times of zero-slope in the $T_{*L}(t_*)$ and $T_{*R}(t_*)$ curves of Fig. 4. The calculated St value drops to zero momentarily because, as explained in the preceding paragraph, the ψ_* denominator of equation (34) is always finite. Increasing the Rayleigh number does not change the plateau of the St traces; this move only increases the frequency of the oscillation in accordance with the scaling law (21). Graphs similar to those sampled in Fig. 11 (not shown here for the sake of brevity) demonstrate that St continues to be of order one as Pr increases at constant Ra. The scaling law (32) is therefore an integral part of the convection-dominated regime of the two-enclosure transient interaction. The calculated St deviates from 0(1) as $t_* \rightarrow 0$, because in that limit the left→right heat transfer is by pure conduction, not by convection.

Acknowledgments

Both authors acknowledge the support received from the Electric Power Research Institute (contract No. RP 8006-4) and from Duke University. P. A. Litsek acknowledges also the

support received from the American Chamber of Commerce for Brazil in the form of a Fulbright fellowship, and from his home company Promon Engenharia, S.A.

References

- Brown, W. G., and Solvason, K. R., 1962, "Natural Convection Through Rectangular Openings in Partitions," *International Journal of Heat and Mass Transfer*, Vol. 5, pp. 859-868.
- Jones, G. F., and Otis, D. R., 1986, "On the Correlation of Natural Convection Heat Transfer in Divided Enclosures," *International Communications in Heat and Mass Transfer*, Vol. 13, pp. 109-113.
- Kakac, S., Aung, W., and Viskanta, R., 1985, *Natural Convection: Fundamentals and Applications*, Hemisphere, Washington, DC.
- Patankar, S. V., 1980, *Numerical Heat and Fluid Flow*, McGraw-Hill, New York.
- Scott, D., Anderson, R., and Figliola, R. S., 1986, "Blockage of Natural Convection Boundary Layer Flow in a Multizone Enclosure," presented at the AIAA/ASME Heat Transfer and Thermophysics Conference, Boston, MA, June 2-4.
- Van Doormaal, J. P., and Raithby, G. D., 1984, "Enhancements of the Simple Method for Predicting Incompressible Fluid Flows," *Numerical Heat Transfer*, Vol. 7, pp. 147-163.

Turbulent Thermal Convection in an Enclosure With Internal Heat Generation

B. Farouk

Associate Professor,
Mechanical Engineering and
Mechanics,
Drexel University,
Philadelphia, PA 19104

Numerical results are presented for turbulent thermal convection, driven by uniform volumetric energy sources for two-dimensional flows in a rectangular enclosure. Rigid adiabatic sides and a rigid isothermal upper surface are considered. For the rigid bottom surface, zero heat flux boundary conditions are used. Computations are carried out for Prandtl number = 6.5 and Rayleigh number (based on enclosure depth L) range of 10^6 to 10^{10} . The aspect ratio (L/X) of the enclosure was maintained at 0.5 for all cases. The turbulence model used in this study is a k - ϵ model, which characterizes turbulence through the kinetic energy and its volumetric rate of dissipation. Buoyancy effects on the turbulence structure are accounted for. Results show the transition from well-ordered multicellular flow to fully turbulent flow within the enclosure as the Rayleigh number increases.

Introduction

Natural convection flows in enclosures with internal heat generation are of interest in a variety of environmental, geophysical, astrophysical, and nuclear engineering heat transfer problems. The problem of convective heat transfer at the surface of a horizontally infinite or shallow heat generating fluid layer bounded from below either by a perfectly insulating or an isothermal surface and from above by a constant temperature surface (same as that of the bottom surface) has been studied by a number of investigators (Tritton and Zarraga, 1967; Thirlby, 1970; Schwiderski and Schwab, 1971; Cheung, 1977; Kulacki and Emara, 1977; Kulacki and Goldstein, 1972, 1974; Catton and Suo-Antilla, 1974). In such systems, the nature of the mean temperature and velocity profiles and the distribution of quantities relating to the level of turbulence are of interest to both analysts and experimentalists. However, very little activity has been reported on turbulent thermal convection with heating from within.

Heat transfer measurements and horizontally averaged temperature profiles for turbulent thermal convection with uniform volumetric energy sources were used by Kulacki and Goldstein (1974) to deduce the mean eddy heat flux in fluid layers bounded by two rigid isothermal planes of equal temperature. Emara and Kulacki (1980) presented finite difference solutions of the equations governing laminar thermal convection driven by uniform volumetric energy sources in a finite rectangular domain. The side walls and the bottom surface were considered adiabatic and rigid, while both rigid and free isothermal upper surfaces were considered.

Steinberner and Reineke (1978) applied the k - ϵ turbulence model for predicting turbulent buoyancy-driven convection heat transfer with internal heat sources in a rectangular cavity. In this case, the top and bottom walls were considered adiabatic and the vertical walls were cooled. Only heat transfer results were presented and the flow and the turbulence characteristics were not discussed. The averaged Nusselt numbers of the numerical calculations were in good agreement with the experimentally obtained values. The k - ϵ model has also been successfully used in predicting recirculating buoyancy-driven turbulent flows (Farouk and Guceri, 1982; Fraikin et al., 1980).

Recently, Kulacki and Richards (1985) have reviewed the

state of knowledge of natural convection in enclosures wherein buoyancy is produced by distributed volumetric energy sources. Enclosures having adiabatic side walls (plane layers) and adiabatic top and bottom walls (cavities) were considered. A detailed account of the past work on stability of thin heat-generating fluid layers (cooled on the top and insulated on the bottom) is also given. For convection at large Rayleigh number (thick layers), when it is apparently not possible to predict analytically either flow structure or heat transfer, numerical methods and/or experiments are the only resort.

The present study is undertaken to apply a k - ϵ turbulence model to calculate the time-dependent high Rayleigh number natural convection flows in a confined heat generating fluid layer with adiabatic rigid side walls. The upper surface is rigid and maintained at a constant temperature. The bottom surface is considered insulated. The ratio of vertical depth to the horizontal extent of the fluid layer is 0.5 for the results presented here. Buoyancy effects on the turbulence structure are accounted for. Local and average Nusselt numbers, time-averaged temperature profiles, and streamlines, along with turbulent characteristics in the flow domain, are presented and compared with those from previous investigations whenever possible. The model (with modifications) gives realistic predictions and reproduces the essential features of the flow observed experimentally. It may be pointed out here that Cheung (1977) had earlier successfully applied an eddy viscosity model to give heat transfer predictions for the above problem.

Governing Equations

The computational approach considered casts the governing nonlinear partial differential equations in the stream function-vorticity form and seeks solutions for turbulent convection in terms of the turbulent viscosity. Various authors have proposed closure models for turbulent flows in an attempt to predict the turbulent shear stresses accurately. Due to its demonstrated success in calculating a wide variety of forced and natural flows, the k - ϵ model of Jones and Launder (1972) was chosen for calculating the flow in this study. In the turbulence model employed, time-averaged values of the temperature \bar{T} , stream function $\bar{\psi}$, and vorticity $\bar{\omega}$ are used. The mean motion is considered to be two dimensional; however, fluctuating components of velocities in all three dimensions are taken into account. The turbulent heat fluxes

Contributed by the Heat Transfer Division for publication in the JOURNAL OF HEAT TRANSFER. Manuscript received by the Heat Transfer Division November 11, 1986.

are obtained by using the turbulent Prandtl number approach (Rodi, 1979).

The length scale is chosen as the layer thickness L .

Using the nondimensional variables

$$x^* = \frac{x}{L}; \quad y^* = \frac{y}{L}; \quad \bar{T}^* = \frac{\bar{T} - T_{\text{ref}}}{HL^2/2\lambda}$$

$$\bar{\psi}^* = \frac{\bar{\psi}}{\rho\alpha}; \quad \bar{\omega}^* = \frac{L^2}{\alpha} \bar{\omega} \quad \text{where} \quad \alpha = \frac{\lambda}{\rho c_p}$$

$$v_x^* = \frac{L}{\alpha} v_x, \quad v_y^* = \frac{L}{\alpha} v_y, \quad t^* = \frac{t\alpha}{L^2} \quad (= \text{Fo})$$

and

$$k^* = \frac{L^2 k}{\alpha^2}; \quad \epsilon^* = \frac{L^4 \epsilon}{\alpha^3}; \quad \mu_t^* = \frac{\mu_t}{\mu}$$

the following closed system of five equations describing time-dependent turbulent, buoyancy-driven two-dimensional flow in a heat generating fluid is obtained:

$$\frac{\partial}{\partial x^*} \left[\frac{\partial \bar{\psi}^*}{\partial x^*} \right] + \frac{\partial}{\partial y^*} \left[\frac{\partial \bar{\psi}^*}{\partial y^*} \right] = -\bar{\omega}^* \quad (1)$$

$$\begin{aligned} & \frac{1}{\text{Pr}} \frac{\partial \bar{\omega}^*}{\partial t^*} + \frac{1}{\text{Pr}} \left\{ \frac{\partial}{\partial x^*} \left[\bar{\omega}^* \frac{\partial \bar{\psi}^*}{\partial y^*} \right] - \frac{\partial}{\partial y^*} \left[\bar{\omega}^* \frac{\partial \bar{\psi}^*}{\partial x^*} \right] \right\} \\ & - \frac{\partial}{\partial x^*} \left[\frac{\partial \{ (1 + \mu_t^*) \bar{\omega}^* \}}{\partial x^*} \right] - \frac{\partial}{\partial y^*} \left[\frac{\partial \{ (1 + \mu_t^*) \bar{\omega}^* \}}{\partial y^*} \right] \\ & = \text{Ra} \frac{\partial \bar{T}^*}{\partial x^*} \end{aligned} \quad (2)$$

$$\begin{aligned} & \frac{\partial \bar{T}^*}{\partial t^*} + \frac{\partial}{\partial x^*} \left[\bar{T}^* \frac{\partial \bar{\psi}^*}{\partial y^*} \right] - \frac{\partial}{\partial y^*} \left[\bar{T}^* \frac{\partial \bar{\psi}^*}{\partial x^*} \right] - \frac{\partial}{\partial x^*} \\ & \left[\left(1 + \frac{\mu_t^*}{\sigma T} \right) \frac{\partial \bar{T}^*}{\partial x^*} \right] - \frac{\partial}{\partial y^*} \left[\left(1 + \frac{\mu_t^*}{\sigma T} \right) \frac{\partial \bar{T}^*}{\partial y^*} \right] = 2 \end{aligned} \quad (3)$$

$$\begin{aligned} & \frac{1}{\text{Pr}} \frac{\partial k^*}{\partial t^*} + \frac{1}{\text{Pr}} \left\{ \frac{\partial}{\partial x^*} \left[k^* \frac{\partial \bar{\psi}^*}{\partial y^*} \right] - \frac{\partial}{\partial y^*} \left[k^* \frac{\partial \bar{\psi}^*}{\partial x^*} \right] \right\} \\ & - \frac{\partial}{\partial x^*} \left[\left(1 + \frac{\mu_t^*}{\sigma_k} \right) \frac{\partial k^*}{\partial x^*} \right] - \frac{\partial}{\partial y^*} \left[\left(1 + \frac{\mu_t^*}{\sigma_k} \right) \frac{\partial k^*}{\partial y^*} \right] = S'_k \end{aligned} \quad (4a)$$

where

$$\begin{aligned} S'_k = & \mu_t^* \left[2 \left(\frac{\partial v_x^*}{\partial x^*} \right)^2 + 2 \left(\frac{\partial v_y^*}{\partial y^*} \right)^2 + \left(\frac{\partial v_x^*}{\partial y^*} + \frac{\partial v_y^*}{\partial x^*} \right)^2 \right] \\ & - \text{Pr} \cdot \text{Ra} \frac{\mu_t^*}{\sigma_T} \left[\frac{\partial \bar{T}^*}{\partial y^*} \right] - \epsilon^* / \text{Pr} - 2 \left[\left(\frac{\partial k^{*1/2}}{\partial x^*} \right)^2 \right. \\ & \left. + \left(\frac{\partial k^{*1/2}}{\partial y^*} \right)^2 \right] \end{aligned} \quad (4b)$$

and

$$\begin{aligned} & \frac{1}{\text{Pr}} \frac{\partial \epsilon^*}{\partial t^*} + \frac{1}{\text{Pr}} \left\{ \frac{\partial}{\partial x^*} \left[\epsilon^* \frac{\partial \bar{\psi}^*}{\partial y^*} \right] - \frac{\partial}{\partial y^*} \left[\epsilon^* \frac{\partial \bar{\psi}^*}{\partial x^*} \right] \right\} \\ & - \frac{\partial}{\partial x^*} \left[\left(1 + \frac{\mu_t^*}{\sigma_\epsilon} \right) \frac{\partial \epsilon^*}{\partial x^*} \right] - \frac{\partial}{\partial y^*} \left[\left(1 + \frac{\mu_t^*}{\sigma_\epsilon} \right) \frac{\partial \epsilon^*}{\partial y^*} \right] = S'_\epsilon \end{aligned} \quad (5a)$$

where

$$\begin{aligned} S'_\epsilon = & C_1 \mu_t^* \frac{\epsilon^*}{k^*} \left[2 \left(\frac{\partial v_x^*}{\partial x^*} \right)^2 + 2 \left(\frac{\partial v_y^*}{\partial y^*} \right)^2 \right. \\ & \left. + \left(\frac{\partial v_x^*}{\partial y^*} + \frac{\partial v_y^*}{\partial x^*} \right)^2 \right] - \text{Pr} \cdot \text{Ra} C_3 \frac{\mu_t^*}{\sigma_T} \frac{\epsilon^*}{k^*} \\ & \times \left[\frac{\partial \bar{T}^*}{\partial y^*} \right] - C_2 \frac{\epsilon^{*2}}{k^*} \cdot \frac{1}{\text{Pr}} (1 - 0.3 \exp - \text{Re}_t^2) \\ & + 2 \text{Pr} \cdot \mu_t^* \left[\left(\frac{\partial^2 v_x^*}{\partial x^{*2}} \right)^2 + \left(\frac{\partial^2 v_x^*}{\partial y^{*2}} \right)^2 \right. \\ & \left. + \left(\frac{\partial^2 v_y^*}{\partial x^{*2}} \right)^2 + \left(\frac{\partial^2 v_y^*}{\partial y^{*2}} \right)^2 \right] \end{aligned} \quad (5b)$$

Nomenclature

C_μ, C_1, C_2, C_3 = empirical turbulence model constants
 c_p = specific heat at constant pressure
 Fo = Fourier number = $t\alpha/L^2$
 H = volumetric heat generation rate
 g = gravitational acceleration
 k = turbulent kinetic energy = $1/2 (\overline{v_x'^2 + v_y'^2 + v_z'^2})$
 ℓ = characteristic length scale of turbulence
 L = vertical depth of enclosure
 Pr = Prandtl number = ν/α
 Ra = Rayleigh number = $(g\beta/\alpha\nu)(HL^3/2\lambda)$

Ra_c = critical Rayleigh number (from linear stability theory)
 Re_t = turbulence Reynolds number = $\rho k^2/\mu\epsilon$
 t = time
 T = temperature = $\bar{T} + T'$
 T_{ref} = reference temperature of the upper wall
 v_x = horizontal velocity component = $\bar{v}_x + v_x'$
 v_y = vertical velocity component = $\bar{v}_y + v_y'$
 v_z = velocity component in z direction = $0 + v_z'$
 x = horizontal coordinate

X = horizontal extent of the enclosure
 y = vertical coordinate
 α = thermal diffusivity
 β = thermal coefficient of volume expansion
 ϵ = volumetric dissipation rate of turbulent kinetic energy
 λ = thermal conductivity
 μ = molecular viscosity
 μ_t = turbulent viscosity
 ρ = density
 σ = turbulent Prandtl number
 ψ = stream function
 ω = vorticity

Table 1 Constants used in the turbulence model

C_μ	C_1	C_2	C_3	σ_k	σ_ϵ	σ_T
0.09	1.44	1.92	1.44	1.0	1.3	1.0

with

$$\bar{v}_x^* = \frac{\partial \bar{\psi}^*}{\partial y^*}; \quad \bar{v}_y^* = -\frac{\partial \bar{\psi}^*}{\partial x^*}$$

The terms on the right-hand side of the k^* equation are the energy production and/or dissipation terms. The sum of these terms in turn determines the description of turbulence. The turbulent viscosity is given by the expression

$$\mu_t = \frac{C_\mu \rho k^2 \exp[-2.5/(1 + \text{Re}_t/50)]}{\epsilon} \quad (6)$$

where C_μ is a constant of proportionality; Re_t is the turbulence Reynolds number. The model contains other empirical constants in the preceding expressions. σ_T , σ_k , and σ_ϵ are the turbulent Prandtl numbers for T , k , and ϵ , respectively. Numerical values for C_μ , C_1 , C_2 , σ_T , σ_k , and σ_ϵ are taken as recommended by Jones and Launder (1972). The constant C_3 is applicable only for buoyancy-driven flows. Its value can be chosen to be equal to C_1 , implying similar contributions from buoyant and gradient production on the scale and intensity of the turbulence. A sensitivity study was undertaken (Farouk and Guceri, 1982), for the above constant in buoyancy-driven recirculating flows. It was found that the effect of variation of C_3 (within ± 20 percent of the value of C_1) was small on the heat transfer and streamline values, but the effects were larger on the turbulence quantities. However, $C_3 > C_1$ is not recommended for this problem as horizontal boundary layers are encountered at the top and bottom surfaces. The values of the constants used here are shown in Table 1.

It should be noted that both the molecular viscosity and the laminar Prandtl number have been taken into account in the turbulent form of the equations. Thus, the equations are valid throughout laminar, semilaminar, and turbulent regions of the field (Launder and Jones, 1972). This is also necessary because of the type of flow considered and the range of Rayleigh number for which solutions are obtained.

For the turbulence model employed in this study, the Reynolds stresses are linearly related to the mean rate of strain via the scalar turbulent viscosity (Launder and Jones, 1972) as

$$-\bar{v}_x'^2 = 2\nu_t \frac{\partial \bar{v}_x}{\partial x} - \frac{2}{3} k \quad (7)$$

$$-\bar{v}_y'^2 = 2\nu_t \frac{\partial \bar{v}_y}{\partial y} - \frac{2}{3} k \quad (8)$$

$$-\bar{v}_x'v_y' = \nu_t \left(\frac{\partial \bar{v}_x}{\partial y} + \frac{\partial \bar{v}_y}{\partial x} \right) \quad (9)$$

Using the turbulent Prandtl number approach we obtain

$$-\bar{v}_y'T' = \frac{\nu_t}{\sigma_T} \frac{\partial \bar{T}}{\partial y} \quad (10)$$

Boundary Conditions

The entire flow domain is considered for the computations and no symmetry plane is assumed. This is necessary for the present problem as (shown in the later sections) the flow patterns mutate from a symmetric multicellular structure to a unicellular flow as the Rayleigh number increases. The time-averaged stream function is set equal to zero on all four boundary walls. An expression for the vorticity boundary conditions on the rigid walls can be obtained by expanding the

stream function near the wall, using a three-term Taylor series and making use of the continuity and the no-slip condition. Thus, on all boundaries

$$\bar{\psi}^* = 0; \quad \bar{\omega}^* = -\frac{2\bar{\psi}_p^*}{(\Delta r^*)^2} \quad (11)$$

where $\bar{\psi}_p^*$ is the value of the stream function at the nearest node (Δr^*) into the fluid. At the upper wall $T^* = 0$ and

$$\frac{\partial T^*}{\partial x^*} = 0$$

for the side walls. For a zero heat flux bottom, $\partial T^*/\partial y^*$ is set equal to zero at that surface.

The near-wall region poses some special problems in the numerical computation of turbulent flows. Close to a wall the variations of the properties are so steep that a very fine grid is required in the region for accurate calculations. In order to predict the behavior of the flow near the wall, particularly in the viscous sublayer, the effects of nonisotropic dissipation (if the value of dissipation is set equal to zero at the wall) and molecular viscosity must be taken into account. The latter has been done by the inclusion of the molecular viscosity in the diffusive terms in all of the transport equations. The recommended modification of Jones and Launder (1972) consists of including a destruction term $-2\mu[(\partial k^{1/2}/\partial x)^2 + (\partial k^{1/2}/\partial y)^2]$ to the k equation, including a generation term (see equation 5(b)) to the ϵ equation and replacing C_μ and C_2 with $C_\mu \exp[-2.5/(1 + \text{Re}_t/50)]$ and $C_2(1 - 0.3 \exp - \text{Re}_t)$, respectively. The values of k^* and ϵ^* are both set equal to zero on the walls. The present model (with the modifications) is able to handle transitional as well as fully turbulent flow situations.

Solution Procedure

The governing equations (1)-(5) are transformed into finite difference equations by using a control volume-based finite difference method. The finite difference procedure adopts a hybrid difference treatment of the convective-diffusive terms and the difference equations are solved by a line-by-line tridiagonal matrix algorithm. The hybrid scheme is known to reduce the numerical diffusion error (Patankar, 1980). A fully implicit transient scheme is used to obtain the time-dependent results.

A grid is established by dividing the region in the x and y directions. A 51×31 grid is considered for the computations for the lower Rayleigh numbers considered in this study (10^6 to 10^8). Higher grid numbers (71×41) are used as the Rayleigh number increases. Since the thermal boundary layers tend to become very thin at the high Rayleigh numbers, the grid points have to be closely placed near the wall surfaces. The spacings in the x and y direction progressively increase according to the relation

$$r = B_1 \tan(B_2 W) / \tan(B_2) \quad (13)$$

where r can be either x or y , B_1 and B_2 are constants that determine the nonuniformity of spacing of grids, and W is the number of grid divisions. The values of B_1 and B_2 were chosen such that the ratio of the maximum to minimum grid sizes was about ten. To check for grid independency, additional sample calculations were carried out with 61×41 and 81×51 meshes for the lower and higher Rayleigh number cases. No significant changes in the results were observed with the finer mesh sizes. Due to the relatively large variations of the source terms of the k^* and ϵ^* equations, underrelaxation had to be used in the iterative calculations.

The local Nusselt number at the upper boundary is defined in terms of the local maximum temperature difference within the layer \bar{T}_0^* , where

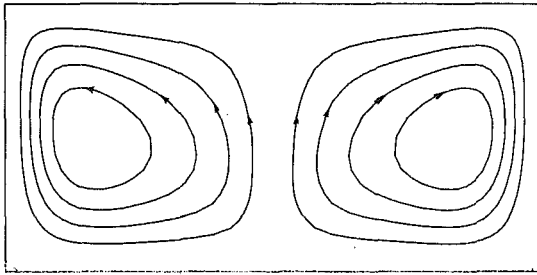


Fig. 1 Streamline patterns for $Ra = 10^6$, $\Delta\psi^* = \pm 5.23$

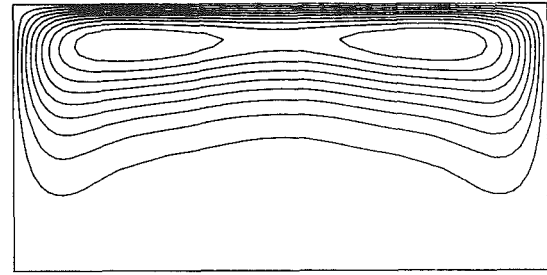


Fig. 3 Turbulent kinetic energy (k^*) contours, $Ra = 10^6$, $\Delta k^* = 2217$

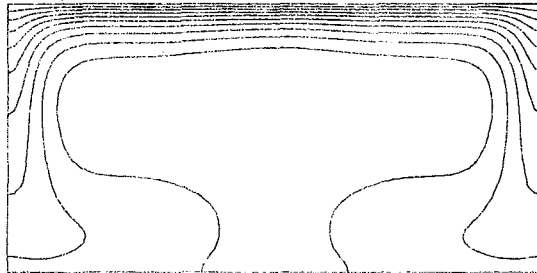


Fig. 2 Isotherms for $Ra = 10^6$, $\Delta T^* = 0.022$

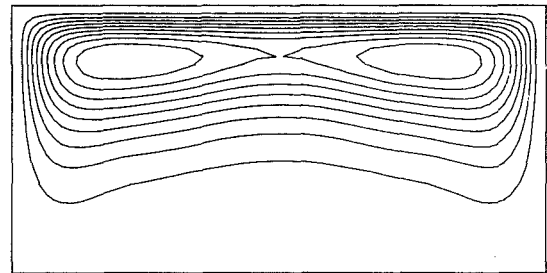


Fig. 4 Normalized turbulent viscosity (μ_{\dagger}^*) contours, $Ra = 10^6$, $\Delta\mu_{\dagger}^* = 0.112$

$$\bar{T}_0^* = \frac{\bar{T}_{\max} - T_{\text{ref}}}{HL^* / 2\lambda}$$

and the local gradient of temperature at the upper surface. Hence,

$$Nu(x) = \left(\frac{\partial \bar{T}^*}{\partial y^*} \right)_w / \bar{T}_0^* \quad (14)$$

\bar{T}_{\max} is the maximum horizontally averaged layer temperature. The local gradient of temperature at the upper surface is calculated by using a three-point Taylor series expansion of the temperature. For the converged solutions an energy balance was satisfied to within 1 percent for all results presented here. The average Nusselt number at the upper boundary is obtained by numerical integrations of the local values using the trapezoidal rule.

Results

All results presented in this section are for $Pr = 6.5$ and aspect ratio of $1/2$ for the flow domain. In order to study the applicability of the numerical scheme for the present study a series of computations was first made for the laminar convection in an enclosure with a heat-generating fluid. Experiments on the planform of the motion in a layer with isothermal top and adiabatic bottom boundary conditions (Tritton and Zaragoza, 1967) show that turbulent motion begins at approximately $80 \cdot Ra_c$ ($Ra_c = 1386$) (Kulacki and Emara, 1977). Results are presented in this study for the Rayleigh number range of 10^6 to 10^{10} (Ra/Ra_c range of 7.21×10^2 to 7.21×10^6) with a constant $L/X = 0.5$.

Flow and temperature field predictions for the enclosure geometry were obtained for the Rayleigh number range of 10^4 to 10^5 without using any turbulence model. The features of the flow and temperature fields and the Nusselt number predictions in the above Rayleigh number range agreed well with those given by an earlier study by Emara and Kulacki (1980) for the same aspect ratio of the enclosure. The major difference between the laminar Rayleigh-Benard convection and the present (laminar) problem becomes apparent from these results. They are, however, not shown in this paper. In the former (Rayleigh-Benard convection), heat transfer at the two boundaries is governed by boundary layers on both, and in the latter thermals rise or fall to enhance convective transport. In

the present problem, warm fluid from the interior of the layer must rise via a type of bulk convective process to reach the only thermal boundary layer at the top.

Although the transient forms of the governing equations were employed, results are only presented for the cases (large Fourier number) where the mean Nusselt number had reached a steady-state value. Starting with an isothermal fluid layer, the Nusselt number was found to reach a steady-state value at Fourier number values between 0.5 and 0.75. The overall flow patterns and temperature profiles, however, never reached steady-state situations (for $Ra > 10^7$) as the Fourier number was increased during the fully implicit calculations. Similar observations were also made by Emara and Kulacki (1980) for laminar flow prediction in a heat generating fluid layer.

Time-averaged results for stream function, temperature, turbulent kinetic energy, and turbulent viscosity are shown in Figs. 1-4 for Ra (based on layer width L) = 10^6 . Steady-state results were obtained at the Fourier number of 0.55. The aspect ratio considered was $1/2$ and the flow is essentially symmetric. Thin boundary layers form around the walls, in particular, the vertical ones. The time-averaged isotherms indicate a large isothermal core with sharp gradients near the upper wall. The turbulent kinetic energy and the turbulent viscosity are high near the two upper corners as shown in Figs. 3 and 4. The turbulence level in $Ra = 10^6$ is relatively low for the entire domain and the maximum turbulent viscosity is found to be only three times the molecular viscosity. The flow is mostly laminar at the bottom region and at the midsection of the flow domain. The turbulent heat flow is modeled here as being proportional to the vertical temperature gradient. Both buoyancy and shear contribute to the production of turbulence in the upper corners of the flow domain.

Similar distributions for $\bar{\psi}^*$, \bar{T}^* , k^* , and μ_{\dagger}^* are shown in Figs. 5-8 for $Ra = 10^7$ and $Fo = 0.61$. The boundary layers continue to thin down near the upper surface at the high Rayleigh number. As the Rayleigh number increases, the value of the turbulence viscosity becomes higher in the flow domain. The high turbulent viscosity at the upper corners causes mixing and the effect of that is evident in Fig. 8. The location of the maximum value of the stream function continues to move toward the bottom corners as the Rayleigh number increases. The multicellular flow observed at lower Rayleigh number is retained.

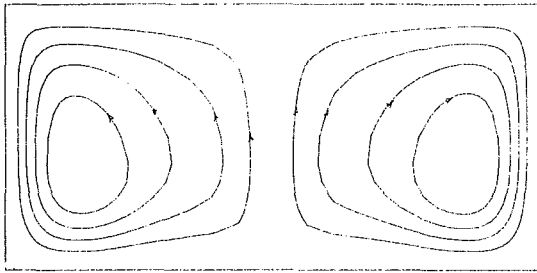


Fig. 5 Streamline patterns for $Ra = 10^7$, $\Delta\psi^* = \pm 17.91$

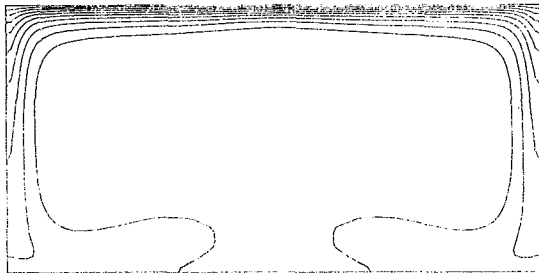


Fig. 6 Isotherms for $Ra = 10^7$, $\Delta T^* = 0.016$

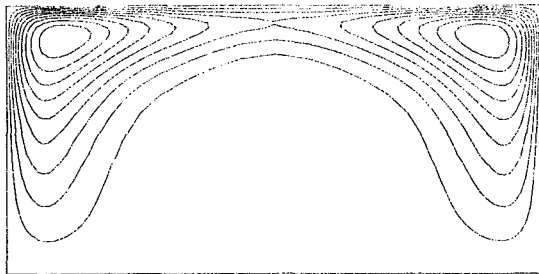


Fig. 7 Turbulent kinetic energy (k^*) contours, $Ra = 10^7$, $\Delta k^* = 18.046$

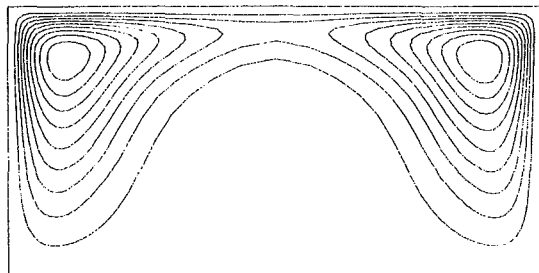


Fig. 8 Normalized turbulent viscosity (μ_t) contours, $Ra = 10^7$, $\Delta\mu_t^* = 0.299$

At higher Rayleigh numbers, the above regularity of the streamline patterns is lost. Isotherm patterns at these Rayleigh numbers indicate that thermals released from the thermal boundary layer at the upper surface can have a length scale of the order of the layer depth and can penetrate almost the entire depth of the layer. These in turn have significant effect on the turbulence quantities in the flow field.

Figures 9, 10, and 11 display the streamlines, isotherms, and turbulent kinetic energy contours, respectively, for $Ra = 10^8$. The flow field undergoes a reversal in the center of the enclosure and four counterrotating rolls are formed. A thin thermal boundary is formed on the upper surface, with broad regions of upflow and corresponding narrow jetlike downflows. The downward thermal generates high levels of turbulent kinetic energy near the central region of bottom insulated surface. The mean Nusselt number reached a steady-state value near $Fo = 0.7$. The large-scale motions in the fluid

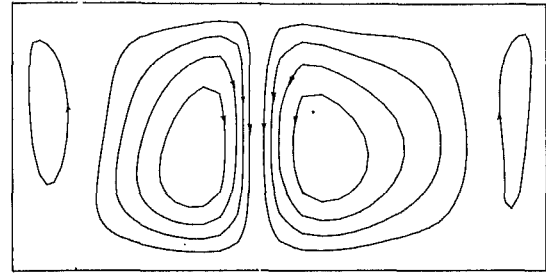


Fig. 9 Streamline patterns for $Ra = 10^8$, $+\Delta\psi^* = 39.39$, $-\Delta\psi^* = 32.73$

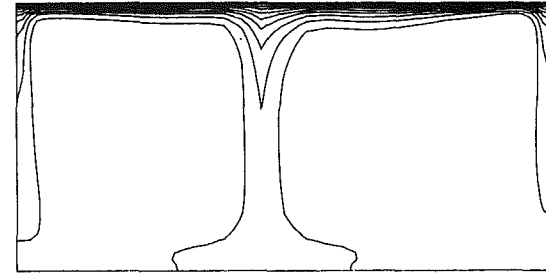


Fig. 10 Isotherm for $Ra = 10^8$, $\Delta T^* = 7.6 \times 10^{-3}$

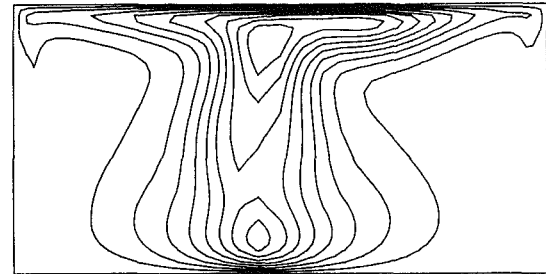


Fig. 11 Turbulent kinetic energy (k^*) contours, $Ra = 10^8$, $\Delta k^* = 51,125$

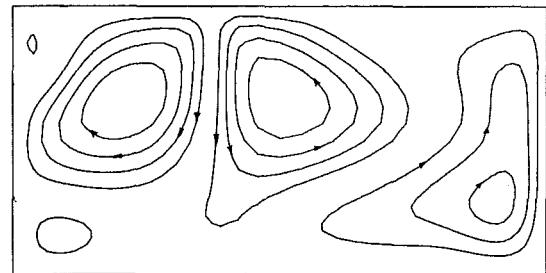


Fig. 12 Streamline patterns for $Ra = 10^9$, $+\Delta\psi^* = 63.10$, $-\Delta\psi^* = 78.45$

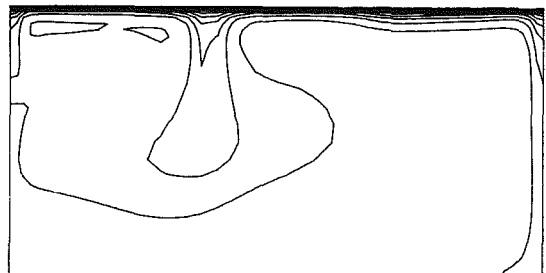


Fig. 13 Isotherms for $Ra = 10^9$, $\Delta T^* = 4.8 \times 10^{-3}$

layer, however, did not reach a steady-state condition even for Fo as large as 5.0.

At still larger Rayleigh numbers, the above features of streamlines and isotherm patterns become more pronounced. The streamline and isotherm patterns at $Ra = 10^9$ are shown in Figs. 12 and 13 at $Fo = 5.0$. The thermal boundary layer at the

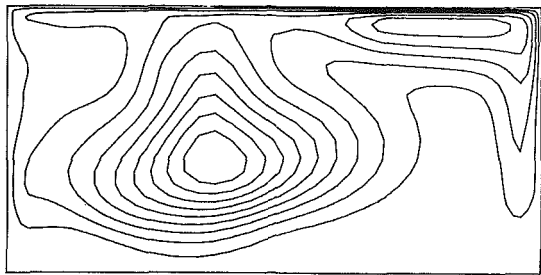


Fig. 14 Turbulent kinetic energy (k^*) contours, $Ra = 10^9$, $\Delta k^* = 105,709$

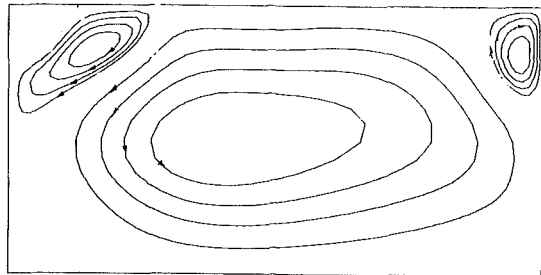


Fig. 15 Streamline patterns for $Ra = 10^{10}$, $+\Delta\psi^* = 455.3$, $-\Delta\psi^* = 49.55$

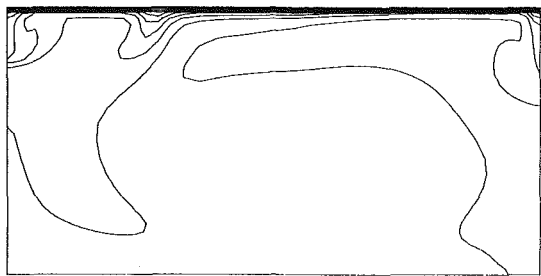


Fig. 16 Isotherms for $Ra = 10^{10}$, $\Delta T^* = 2.81 \times 10^{-3}$

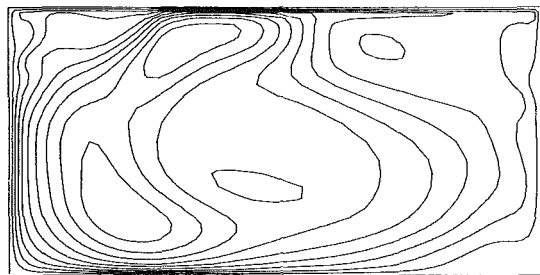


Fig. 17 Turbulent kinetic energy (k^*) contours, $Ra = 10^{10}$, $\Delta k^* = 219,750$

upper surface is thin, signifying high heat transfer rate, but the hydrodynamic boundary condition at the upper surface has minimal influence on the large-scale motion within the enclosure. The large-scale motion continues to vary with time (as also experienced in experimental studies) but the mean Nusselt number reaches a steady-state value. The turbulent kinetic energy field at $Ra = 10^9$ is shown in Fig. 14. Due to the large thermal gradients at the upper surface (see equation (10)) high levels of turbulent kinetic energy are predicted near the upper surface. The turbulent viscosity is, however, higher near the central core of the enclosure because of large-scale motions induced by the thermals.

In Figs. 15 and 16 streamline and isotherm patterns are presented for a Rayleigh number of 10^{10} at $Fo = 5.5$. The multicellular flow is almost replaced by a unicellular turbulent flow pattern. Multiple thermals are discharged from the upper surface where the thermal boundary layer continues to be thin. It is conjectured that at even higher Rayleigh numbers, more

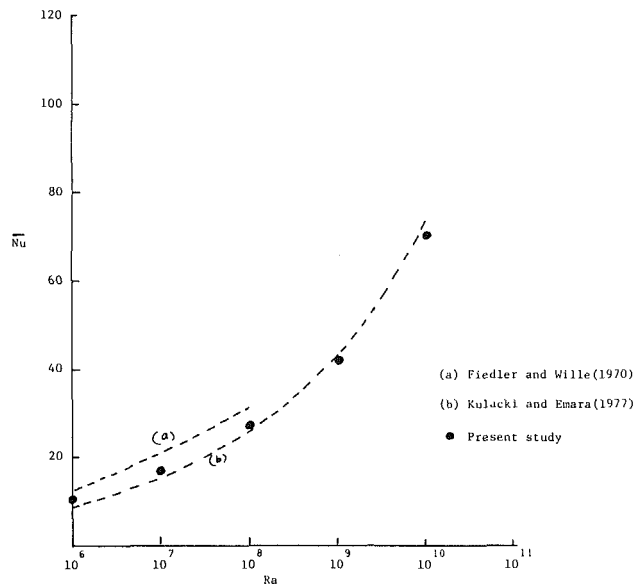


Fig. 18 Heat transfer from the upper surface of the fluid layer

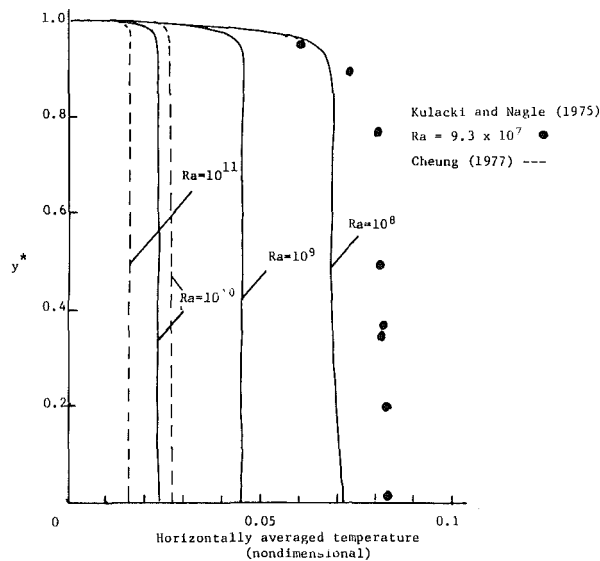


Fig. 19 Horizontally averaged temperature profiles across the enclosure depth

thermals will be discharged from the upper surface and the turbulent core flow will be essentially unicellular. The corresponding k^* contour lines at $Ra = 10^{10}$ are shown in Fig. 17. Although the turbulent kinetic energy levels are high near the upper and lower surfaces, the turbulent viscosity is found to be high near the central and bottom regions of the enclosure.

Average Nusselt numbers at the upper boundary of the enclosure have been computed by integrating the local Nusselt number values evaluated according to equation (14). The mean Nusselt number values are plotted as a function of the Rayleigh number in Fig. 18. The experimental results of Fiedler and Wille (1970) and Kulacki and Emara (1977) are also shown in the same figure. The experimental results of Kulacki and Emara were obtained for $1.89 \times 10^3 \leq Ra \leq 2.17 \times 10^{12}$ and $0.025 \leq L/X \leq 0.50$. In this study, however, L/X was set equal to 0.5 for all cases. Despite the discrepancy, the agreement of our predictions with the results of Kulacki and Emara is very good.

The aspect ratio effect for the present problem (insulated bottom and isothermal top surface) has not been studied in

detail. It has, however, been shown (Lambha et al., 1978) that for the vertical cavity problem (isothermal side walls and insulated top and bottom), the aspect ratio has negligible effect on the heat transfer characteristics.

Horizontally averaged mean temperature distribution across the enclosure depth are given in Fig. 19 for the Rayleigh number range of 10^8 to 10^{10} . The results agree well with predictions of Cheung (1977), who applied a phenomenological model of eddy heat transport to the above problem. The temperature profiles are found to be essentially flat except in the region near the upper surface. There is practically no thermal sublayer at the lower wall region. The predictions of Cheung (1977) based on a phenomenological model of eddy heat transport are shown for Rayleigh numbers of 10^{10} and 10^{11} . The measurements of Kulacki and Nagle (1975) at $Ra = 9.3 \times 10^7$ and presumably at a different aspect ratio than 0.5 are also shown in the same figure. Qualitatively, good agreement is obtained, particularly near the wall.

Conclusions

Natural convection in a volumetrically heated fluid layer at high Rayleigh numbers is treated numerically by application of a two-equation turbulence model. The model enables the determination of the boundary heat fluxes, the mean turbulent temperature and flow fields, the distribution of turbulent kinetic energy, and the turbulent viscosity. At high Rayleigh number, the structured multicellular flow pattern breaks down and the flow is characterized by the discharge of downward thermals and large-scale motions. The mean temperature is, however, found to be essentially constant throughout the depth of the enclosure except in a sublayer region near the upper wall. Production of turbulent kinetic energy is high near the upper surface for the symmetric multicellular flows (for lower Rayleigh numbers). For the higher Rayleigh number cases, the production is dictated by the discharge of the thermals.

References

Catton, I., and Suo-Antilla, A. J., 1974, "Heat Transfer From a Volumetrically Heated Horizontal Fluid Layer," *Proc. 5th International Heat Transfer Conference*, Tokyo, Paper No. NC2.7.

Cheung, F. B., 1977, "Natural Convection in a Volumetrically Heated Fluid Layer at High Rayleigh Numbers," *International Journal of Heat and Mass Transfer*, Vol. 20, pp. 499-506.

Emara, A. A., and Kulacki, F. A., 1980, "A Numerical Investigation of Thermal Convection in a Heat Generating Fluid Layer," *ASME JOURNAL OF HEAT TRANSFER*, Vol. 102, pp. 531-537.

Farouk, B., and Guceri, S. I., 1982, "Laminar and Turbulent Natural Convection in the Annulus Between Horizontal Concentric Cylinders," *ASME JOURNAL OF HEAT TRANSFER*, Vol. 104, pp. 631-636.

Fiedler, H. E., and Wille, R., 1970, "Turbulente Freie Konvektion in Einer Horizontale Flüssigkeitsschicht mit Volumen-Wärmequelle," *Proceedings 4th International Heat Transfer Conference*, Paris, Paper No. NC4.5.

Fraikin, M. P., Portier, J. J., and Fraikin, C. J., 1980, "Applications of a $k-\epsilon$ Turbulence Model to an Enclosed Buoyancy Driven Recirculating Flow," *ASME Paper No. 80-HT-68*.

Jones, W. P., and Launder, B. E., 1972, "The Prediction of Laminarization With a 2-Equation Model of Turbulence," *International Journal of Heat and Mass Transfer*, Vol. 15, pp. 301-314.

Kulacki, F. A., and Goldstein, R. J., 1972, "Thermal Convection in a Horizontal Fluid Layer With Uniform Volumetric Energy Sources," *Journal of Fluid Mechanics*, Vol. 55, part 2, pp. 271-287.

Kulacki, F. A., and Goldstein, R. J., 1974, "Eddy Heat Transfer in Thermal Convection With Volumetric Energy Sources," *Proceedings Fifth International Heat Transfer Conference*, Tokyo, Vol. 3, pp. 64-68.

Kulacki, F. A., and Nagle, M. E., 1975, "Natural Convection in a Horizontal Fluid Layer With Volumetric Energy Sources," *ASME JOURNAL OF HEAT TRANSFER*, Vol. 91, pp. 204-211.

Kulacki, F. A., and Emara, A. A., 1977, "Steady and Transient Thermal Convection in a Fluid Layer With Uniform Volumetric Energy Sources," *Journal of Fluid Mechanics*, Vol. 83, pp. 375-395.

Kulacki, F. A., and Richards, D. E., 1985, "Natural Convection in Plane Layers and Cavities With Volumetric Energy Sources," in: *Natural Convection, Fundamentals and Applications*, S. Kakac, W. Aung, and R. Viskanta, eds., Hemisphere Publishing Corporation, Washington, DC, pp. 179-258.

Lambha, N. K., Korpela, S. A., and Kulacki, F. A., 1978, "Thermal Convection in a Cylindrical Cavity With Uniform Volumetric Energy Generation," *Proceedings Sixth International Heat Transfer Conference*, Toronto, Aug., pp. 311-316.

Patankar, S. V., 1980, *Numerical Heat Transfer and Fluid Flow*, McGraw-Hill, New York.

Peckover, R. S., and Hutchinson, J. H., 1974, "Convective Rolls Driven by Internal Heat Sources," *Physics of Fluids*, Vol. 17, pp. 1369-1371.

Rodi, W., 1979, "Influence of Buoyancy and Rotation on Equations for the Turbulent Length Scale," *2nd Symposium on Turbulent Shear Flows*, Imperial College, London, pp. 10.37-10.42.

Schwiderski, E. W., and Schwab, J. H. A., 1971, "Convection Experiments With Electrolytically Heated Fluid Layers," *Journal of Fluid Mechanics*, Vol. 48, pp. 703-719.

Steinberner, U., and Reineke, H. H., 1978, "Turbulent Buoyancy Convection Heat Transfer With Internal Heat Sources," *Heat Transfer Conf.*, Toronto, Vol. 2, pp. 305-310.

Thirby, R., 1970, "Convection in an Internally Heated Fluid Layer," *Journal of Fluid Mechanics*, Vol. 44, pp. 673-693.

Tritton, D. J., and Zarraga, M. N., 1967, "Convection in Horizontal Fluid Layers With Heat Generation Experiments," *Journal of Fluid Mechanics*, Vol. 41, pp. 21-32.

Tveitereid, M., and Palm, E., 1976, "Convection Due to Internal Heat Sources," *Journal of Fluid Mechanics*, Vol. 76, part 3, pp. 481-499.

Non-Darcy Natural Convection in a Saturated Horizontal Porous Annulus

K. Muralidhar¹

F. A. Kulacki

Department of Mechanical Engineering,
Colorado State University,
Fort Collins, CO 80523

A computational study of free convective flow and heat transfer in a saturated porous horizontal annulus is reported. Both isothermal and constant heat flux boundary conditions have been considered on the inner walls while the outer wall is held at a constant temperature. The calculation of the flow field involves consideration of non-Darcy effects, such as inertial and viscous forces, and also the variation of porosity near the walls. While the literature shows that Darcy flow model is inadequate in predicting average Nusselt numbers, the present study examines whether non-Darcy effects, and in particular the presence of the boundary, could play a significant role in explaining this discrepancy. Average Nusselt numbers have been obtained for Rayleigh-Darcy numbers from 20 to 4000 for the case of isothermal boundaries, and 20 to 20,000 for the case of constant heat flux on the inner wall. Radius ratio has been varied from 1.1 to 3. Over this range of parameters, inertia and viscous friction in the fluid phase have been found to produce a small effect on the Darcy flow. The effect of including variable porosity near a boundary is seen to produce channeling near the wall which in turn substantially increases the heat transfer coefficient.

Introduction

One of the unique features of calculating flow and heat transfer in a saturated porous medium is the choice of the governing equations. The use of Darcy's law has now become commonplace, though its validity for all geometric configurations and flow regimes, even within the context of buoyancy-drive flows, remains far from completely ascertained. As such, it has become necessary to consider standard geometries and their orientation with respect to the gravity vector, case by case, and compare the results of analysis with experiments. The present study deals with natural convection in a horizontal porous annulus with constant temperature or heat flux condition on the inner wall and an isothermally cooled outer wall. This geometry permits an evaluation of the interrelation of Rayleigh number and radius ratio effects with respect to the traditional Darcy flow model. From a technological perspective, buoyancy-driven flow in a horizontal porous annulus can occur in the backfill about buried canisters of nuclear waste, convection around buried pipelines or electrical conduits, as well as in a variety of thermal insulation systems.

Problems involving vertical porous layers bounded by parallel walls have been extensively studied and a detailed review has been written by Cheng (1978). Prasad (1983) has studied convection in a vertical annulus by both experiments and numerical analysis using the Darcy flow assumption. Kulkarni (1983) has experimentally treated a constant heat flux inner wall boundary condition. Kimura and Bejan (1985) have analyzed natural convection in a stably heated corner where Darcy flow is driven by competing thermal gradients. Recently, problems related to double-diffusive flow which combine heat and mass transfer have been addressed by Bejan and Khair (1985) and Kumari et al. (1985). Prasad et al. (1985) have experimentally studied convection in a vertical porous annulus comprising various combinations of ball sizes and fluids. The absence of a unique relation between Nusselt and Rayleigh numbers has been traced to the improper definition

of effective thermal conductivity. This has been interpreted to be a Prandtl number dependence by Catton (1985). Vafai and Tien (1981) have studied boundary and inertia effects on flow and heat transfer in the wall region of a porous medium. Vafai (1984) has studied channeling effects arising from variable porosity near a solid boundary, using the method of matched asymptotic expansions. Vafai et al. (1985) have investigated experimentally the non-Darcian effects arising in forced convection heat transfer in flat beds. The published work which comes closest to the present study is that of Caltagirone (1976), which also deals with convection between two concentric horizontal cylinders. This paper presents an extensive parametric analysis with respect to radius ratio, to obtain the Nusselt number dependence on Rayleigh number, under a traditional Darcy flow assumption. Further, Caltagirone considers the stability of two-dimensional base flow before it becomes three-dimensional and also analyzes the post-stability behavior of the flow system. However, comparison with experiments is limited and the differences with the analytical results have been attributed to flow perturbations rather than non-Darcy effects.

The objective of the present work is to analyze free convective flow and heat transfer in a horizontal annulus filled with a fluid-saturated porous material. The solid phase consists of packed spheres of uniform diameter with a liquid phase filling the void region. It is assumed that the flow pattern reaches steady state at every Rayleigh number and radius ratio. Rao et al. (1985) have reported transient calculations for a fluid-filled annulus, where the flow becomes multicellular as Ra is increased. The possibility of unsteadiness does not form the scope of the present work. A finite-difference scheme is used in the present work to solve the system of governing equations. The formulation is general enough to include non-Darcy effects. As implied in this work, factors leading to the breakdown of Darcian flow arise from inertial forces, viscous friction in the liquid phase, and variable porosity near the solid boundary.

Mathematical Formulation

Figure 1 shows the physical system and the coordinates

¹Presently at Indian Institute of Technology—Kanpur.

Contributed by the Heat Transfer Division and presented at the ASME/AIAA Thermophysics Conference, Boston, Massachusetts, June 2-4, 1986. Manuscript received by the Heat Transfer Division June 3, 1986.

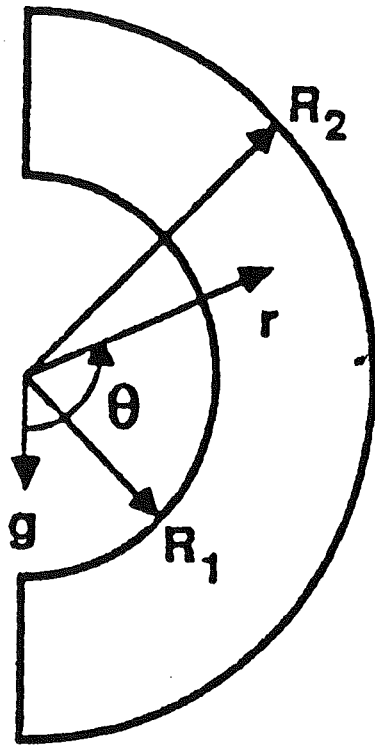


Fig. 1 Flow configuration and coordinate system

employed to describe the flow field. Two-dimensional, steady, incompressible flow is assumed, and body forces are included via the Boussinesq approximation. The governing equations have been written in terms of stream function and temperature variables, as given below, where ϕ can represent either of these variables (Vafai and Tien, 1981)

Table 1 Coefficients of equation (1) for momentum and energy equations

ϕ	a	b	S
ψ	0	$\frac{\epsilon}{K} + \frac{F\epsilon^2\bar{u}}{\text{Pr}} \sqrt{\frac{\text{Da}}{K}}$	S_ψ
T	ϵ	1	0

$$a^\phi \left[\frac{\partial}{\partial \theta} \left(\phi \frac{\partial \psi}{\partial r} \right) - \frac{\partial}{\partial r} \left(\phi \frac{\partial \psi}{\partial \theta} \right) \right] - \left[\frac{\partial}{\partial \theta} \left(\frac{b^\phi}{r} \frac{\partial \phi}{\partial \theta} \right) + \frac{\partial}{\partial r} \left(b^\phi r \frac{\partial \phi}{\partial r} \right) \right] = S^\phi \quad (1)$$

The quantities a , b , and S depend on the choice of ϕ and are given in Table 1. Here

$$S_\psi = S_1 + S_2, \quad S_1 = -r\text{Ra}(\sin \theta \frac{\partial T}{\partial r} + \frac{\cos \theta}{r} \frac{\partial T}{\partial \theta}) \quad (1a)$$

$$S_2 = \frac{\text{Da}}{\bar{\epsilon}\text{Pr}} \left(\frac{\partial}{\partial \theta} (\nabla^2 v) - \frac{\partial}{\partial r} (r \nabla^2 u) \right); \quad \bar{u} = (u^2 + v^2)^{1/2} \quad (1b)$$

The quantities ϵ and K appearing in Table 1 are normalized values with respect to $\bar{\epsilon}$, the measured mean porosity, and \bar{K} , the mean permeability given as (Bear, 1972)

$$\bar{K} = \frac{\bar{\epsilon}^3 d_p^2}{180(1-\bar{\epsilon})^2} \quad (2)$$

The factor F arises as an empirical constant when the inertia terms are represented by the square of the local velocity. For a bed of packed spheres, F is given by (Vafai, 1984)

Nomenclature

- a, b = coefficients appearing equation (1)
- C = empirical constant in equation (5)
- c_p = specific heat, J/kgK
- d_p = ball diameter relative to gap width
- Da = Darcy number = \bar{K}/D_{gap}^2
- D_{gap} = gap width between cylinders, m; also, characteristic dimension
- F = empirical constant in inertia term
- g = acceleration due to gravity, m/s²
- k_e = effective thermal conductivity, W/mK
- K = normalized permeability
- \bar{K} = mean permeability, m²
- Nu_i = inner Nusselt number = $-\partial T/\partial r|_{R_1}/R_1 \ln(R_2/R_1)$ (isothermal); = $1/T(R_1)$ (constant flux)
- $\text{Nu}_{o\theta}$ = outer Nusselt number = $-\partial T/\partial r|_{R_2}/R_2 \ln(R_2/R_1)$ (isothermal); or $-\partial T/\partial r|_{R_2}/(R_2/R_1)$ (constant flux)

- Nu_i = average inner Nusselt number
- Nu_o = average outer Nusselt number
- p = pressure, N/m²
- q_w = inner wall heat flux, W/m²
- r = dimensionless radial coordinate
- R_1, R_2 = dimensionless inner and outer radii of the annulus
- Ra = Rayleigh number = $g\beta\Delta T\bar{K}D_{\text{gap}}/\nu\alpha$
- S = source terms in equation (1)
- T = dimensionless temperature
- ΔT = characteristic temperature difference, $K = T_h - T_c$ (isothermal); or $q_w D_{\text{gap}}/k_e$ (constant flux)
- u = tangential component of velocity = $-\partial\psi/\partial r$
- v = radial component of velocity = $\partial\psi/\partial\theta$
- \mathbf{v} = filtration velocity vector with components u and v
- \mathbf{v}_i = interstitial velocity vector
- α = thermal diffusivity = $k_e/(\rho C_p)_f$, m²/s

- β = volumetric expansion coefficient, K⁻¹
- γ = empirical constant in equation (6)
- δ = boundary-layer thickness
- $\bar{\epsilon}$ = mean porosity of the annulus
- ϵ = local porosity of an elementary control volume
- θ = angular coordinate
- μ = dynamic viscosity, kg/ms
- ν = Kinematic viscosity, m²/s
- ρ = density, kg/m³
- ϕ = generic variable (ψ or T)
- ψ = dimensionless stream function scaled by α

Subscripts

- c = cold
- d = dynamic value
- e = effective value
- f = fluid
- h = hot
- max = maximum value
- o = outer flow
- v = viscous

Table 2 Comparison of results of present study with Caltagirone (1976); radius ratio-2; isothermal boundary conditions

	Ra	\bar{Nu}	Nu _i		ψ_{\max}
			min	max	
Ref.	10	1.0172	0.759	1.266	1.177
Present	10	1.025	0.759	1.27	1.17
Ref.	200	2.625	0.062	5.23	15.86
Present	200	2.74	0.173	5.25	16.4

$$F = \frac{1.75}{\sqrt{150\epsilon^{3/2}}} \quad (3)$$

Further, for most materials (Veavers and Sparrow, 1969), $0.014 < F < 1$. Also, it must be mentioned at this point that the velocity referred to in equation (1) is the filtration velocity, and is related to the interstitial (fluid) velocity v_i by the expression

$$\mathbf{v} = \bar{\epsilon} \mathbf{v}_i \quad (4)$$

The variation of porosity near the inner wall is assumed to be represented by a formula

$$\epsilon = 1 + C \exp\left[\frac{-\gamma(r-R_1)}{d_p}\right] \quad (5)$$

A similar formula is applicable in the vicinity of the outer wall. Here, C and γ are adjustable constants to be determined from experiments. The specific form of equation (5) is motivated from the experimental work of Benenati and Brosilow (1962). The fluctuations their results show in the porosity distribution are taken to the inside of the representative control volume (REV) for which the differential equations are taken as valid. In this manner, only the envelope of the pointwise distribution of porosity is important. Since $\bar{\epsilon} < 1$, C must always be so chosen that $\epsilon < 1/\bar{\epsilon}$. The variation of porosity near a solid boundary leads to a change in permeability, as given by equation (2). The values of C and γ are effected by curvature of the bounding wall and the particle diameter (in this case, ball diameter) of the porous material. However, only parametric studies with respect to these quantities have been reported in the present study.

Boundary Conditions

The thermal boundary conditions imposed on the physical system are uniform with respect to the angular coordinate, and hence the plane which splits the annulus into equal halves is a plane of symmetry. The computational domain thus comprises one half of the annulus over which the following boundary conditions are applied:

$$\begin{aligned} \psi &= 0 \text{ on all boundaries} \\ r &= R_1, T=1 \text{ or } \frac{\partial T}{\partial r} = -1 \\ r &= R_2, T=0 \\ \theta &= 0 \text{ or } \pi, \frac{\partial T}{\partial \theta} = 0 \end{aligned} \quad (6)$$

Solution

Equations (1) and associated boundary conditions given by equation (6) have been solved by a finite difference scheme (Gosman et al., 1969). Success with this scheme has been reported by Farouk (1985) and others for nonporous problems and by Prasad and Kulacki (1984) for free convection in a vertical porous annulus. Upwind differencing of the second kind

has been used for the convective terms in the energy equations and the inertia terms in the momentum equation have been locally linearized between successive iterations. A convergence criterion of 0.01 percent relative error anywhere in the flow field has been used. As the Rayleigh number is increased, a variable grid with nodal concentration near the solid walls is used to maintain an upper limit on the excess energy balance at about 3 percent. This limit is reached in non-Darcy flow especially as the wall influence is made progressively stronger, and is much smaller for the Darcian case even at high Rayleigh numbers. All results have been obtained on a grid which discretizes the r and θ directions into 21×41 nodal points. The computer code developed to implement the numerical procedure has been verified by repeating the calculations of Caltagirone (1976) for Darcy flow. The comparison is given in Table 2. Despite differences in the numerical schemes, and the reduced number of nodal points used here, the agreement for Nusselt numbers is quite good.

Even for the highest Rayleigh number treated in the present computations, the inertia terms do not pose convergence problems. Their influence on the results further decreases as the Prandtl number is increased.

Results

Numerical results for Darcy flow can be recovered from equation (1) by setting F to zero and ignoring boundary effects on the porosity variation, i.e., $C=0$ (equation (5)). Since in many practical instances Da is very small, viscous effects within the liquid phase have been entirely ignored in all the calculations. This amounts to setting S_2 to zero in equation (1).

The magnitude of the Darcy number in the present study is of the order 10^{-5} . This value is expected to be realized in a uniformly fractured porous medium, and is much smaller when the system is unfractured. The inertial terms are proportional to \sqrt{Da} , and are not necessarily small. These terms have not been dropped. The viscous terms in the fluid phase, being proportional to Da , can be justifiably ignored. However, very close to the wall ($r-R_1 \approx \sqrt{Da}$), the formation of a boundary layer is likely to affect heat transfer. This has been analyzed in the Appendix. The consequence of including inertial terms is to reduce consistently the values of Nusselt number on the inner wall below the Darcy model. This difference is however too small (less than 2 percent) to be graphically represented. Inertia terms further become insignificant as Pr is increased. In the absence of viscous terms, Pr appears only in the inertial terms and hence the present calculations do not exhibit a formal dependence of heat transfer on Pr . In the present study, inertial terms have been retained in all non-Darcy flow calculations.

The most important factor that causes the solution to deviate from that of Darcy flow is the presence of the boundary, for the range of parameters studied here. Besides the radius ratio, Rayleigh number, and mean porosity of the annulus, these parameters include the wall-related quantities C and γ appearing in equation (5) and also the boundary condition imposed on the inner wall. Both constant temperature and constant heat flux cases have been studied in the present work. The characteristic temperature difference is based on the wall temperatures in the former, while it is based on heat flux in the second problem.

Table 3 presents results of a parametric study of mean inner Nusselt number as a function of Rayleigh number for a radius ratio of 1.1 and constant temperature boundaries. This difference is also larger than the reduction caused by retaining inertial terms in the formulation. For a fixed value of γ , increasing C increases Nu_i beyond the Darcy value for any Rayleigh number. For a fixed value of C , increasing γ reduces Nu_i . Since γ can be interpreted as the decay coefficient of porosity,

Table 3 Values of Nu_i , as a function of the parameters C and D ; $R_2/R_1 = 1.1$; isothermal walls; $d_p = 0.05$

		$\bar{\epsilon} = .3$			$\bar{\epsilon} = .4$		
Ra	$\gamma = 2.0$	C = .5			$\gamma = 2.0$		
		C = 0	.15	.50	$\gamma = 5.0$	C = .15	.50
20	1.0045	1.0049	1.0062	1.0051	1.005	1.0067	
100	1.05	1.0557	1.073	1.0589	1.0568	1.0798	
250	1.2219	1.2475	1.3261	1.2622	1.2523	1.3565	
500	1.591	1.657	1.8629	1.6963	1.6692	1.9404	
1000	2.267	2.4112	2.8659	2.5006	2.4376	3.0354	
2000	3.927	3.5834	4.4875	3.7727	3.6364	4.8378	
4000	4.789	5.3208	6.2675	5.7022	5.4269	7.7715	

increasing it amounts to reducing the region where wall effects are seen. AS expressed by equation (5), the solid wall provides a domain of increased porosity which allows increased levels of heat transfer. The effect of increasing d_p can be interpreted via changes in the value of γ , which suitably changes the extent of porosity (and hence permeability) variation near the wall. Table 3 also shows the effect of increasing the mean porosity of $\bar{\epsilon}$ of the annulus from 0.3 to 0.4. Based on Darcy model, this would show no increase in Nu_i for a given Ra. However, including boundary effects, Nu_i increases with mean porosity for given values of C and γ .

Figure 2 shows a Nu_i -Ra plot for a radius ratio of 2 with and without non-Darcy parameters. These are seen to be important over the full range of Ra, although they are more so at higher values of Ra. Vafai (1984) has suggested that the main effect of varying porosity is to cause a channeling phenomenon, which can increase heat transfer rates. This has been confirmed in the present study. Figure 3 shows velocity profiles at various angular locations for both Darcy and non-Darcy flow. The increase in the magnitude of u near the walls signifies the channeling effect, and arises from increased permeability; of the medium. Plots in this figure use values from the numerical calculation, except at the boundaries. Instead of extrapolating the velocity profile to the wall, thus making it non-zero, the figure shows the fluid coming to rest on a stationary surface, thus identifying properly the viscous layer in the annulus. It is this region which has been analyzed in the Appendix.

Figure 4 shows the temperature profiles in the annulus. The non-Darcy effects can be seen here to increase wall temperature gradients. This figure also shows the existence of a stagnation region near the bottom ($\theta = 18$ deg) and a plume region near the top ($\theta = 162$ deg), as is commonly observed in annulus without a porous structure. Figure 5 shows the distribution of inner and outer local Nusselt numbers as a function of the angular position, for both Darcy and non-Darcy flow. The critical regions of heat transfer are seen to be strongly affected by the presence of the boundary. For the inner cylinder, this is closer to $\theta = 0$ deg, where boundary layers are thin, and for the outer cylinder, it is closer to $\theta = 180$ deg, where a considerable portion of the energy is rejected. Figure 6 shows the Nu_i -Ra plot for a radius ratio of 3, for various values of C . For Darcy flow, values of Nu_i are higher than for the systems having lower radius ratio. However, the wall effect leads to an increase in Nu_i , that is almost independent of curvature of the boundary.

Caltagirone (1976) has noted a systematic discrepancy between measured data and computations using Darcy law for the horizontal annulus with a constant temperature inner wall. This has been reproduced in Fig. 7. For Rayleigh numbers

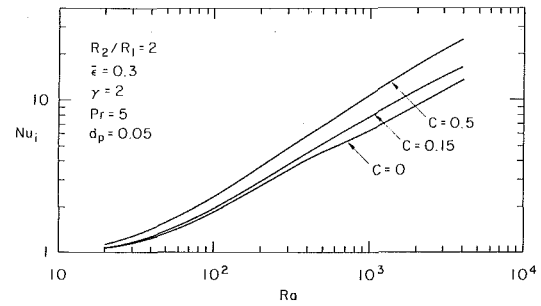


Fig. 2 Average inner Nusselt number as a function of Rayleigh number; isothermal boundaries

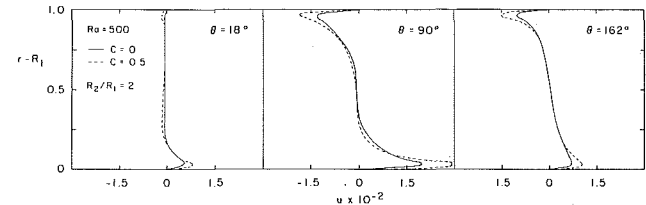


Fig. 3 Velocity profile in the annulus, with isothermal walls; effect of variation of porosity near a boundary

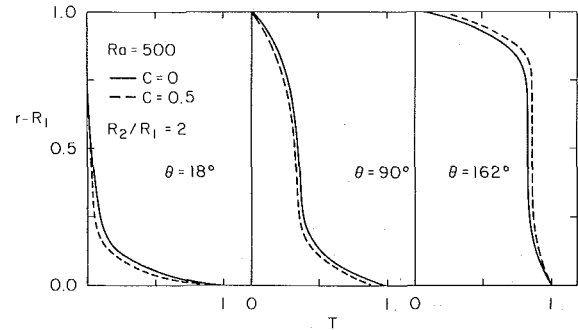


Fig. 4 Temperature profiles in the annulus with isothermal walls

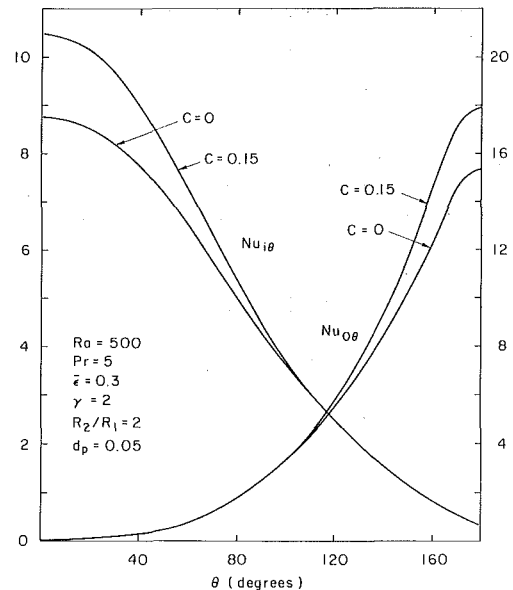


Fig. 5 Local Nusselt number distribution number distribution in the annulus; isothermal walls

beyond the conduction regime, i.e., $Ra > 10$, the experimental data are consistently above the numerically generated curve. The difference has been traced to the possibility of instability,

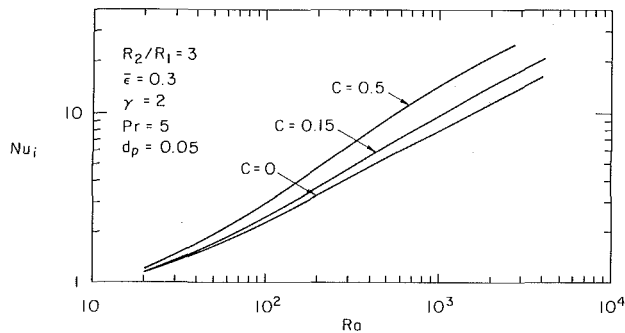


Fig. 6 Inner Nusselt number as a function of Rayleigh number; isothermal boundaries

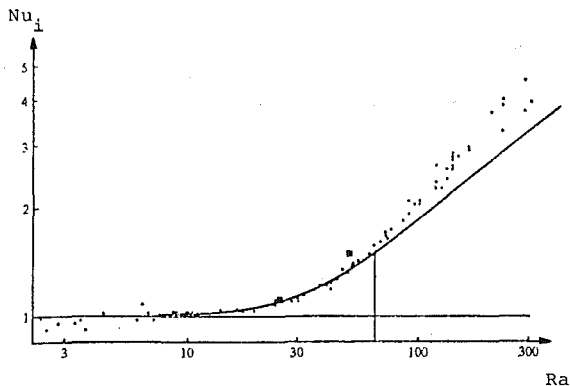


Fig. 7 Comparison of experimental data with Darcy model (-); from Caltagirone (1976)

and in particular, the onset of three-dimensional flow from an initially two-dimensional base flow. Increased levels of heat transfer are then expected to occur due to small perturbations being sustained by mean flow. Such an explanation has not been borne out in a recent set of experiments under similar conditions, except for constant heat flux boundary conditions on the inner wall (Baunchalk, 1985). It has been noticed that end losses decrease rapidly with increasing Ra, thus invalidating the hypothesis of three-dimensional flow. Furthermore, results obtained with nonporous problems show that the effect of a transition (as described above) is to reduce Nusselt numbers rather than increase it. Owing to these arguments, an alternative approach has been sought to explain the discrepancy between theory and experiments. Including variable porosity near a solid boundary provides this explanation.

Figure 8 shows local Nusselt number distribution in the annulus, when the inner wall is a constant heat flux boundary. Figure 9 is a comprehensive plot of Nu_i versus Ra for three radius ratios, for this inner wall boundary condition. The Nusselt number increases with radius ratio, whereas (as for the constant temperature case) the wall effect is only a weak function of this quantity.

Conclusion

There is increasing evidence that boundary-layer flow in porous media could be significantly altered by inertial and viscous effects, even for moderately large values of Darcy number. This issue has been studied in the context of buoyancy-driven flow in a horizontal annulus, in the present work. The consequence of including these terms in the formulation is consistently to reduce the Nusselt number below the Darcian value. For Darcy numbers of the order of 10^{-5} , the inertial terms reduce heat transfer by 2 percent, based on a numerical solution of the extended Darcy law. The viscous ef-

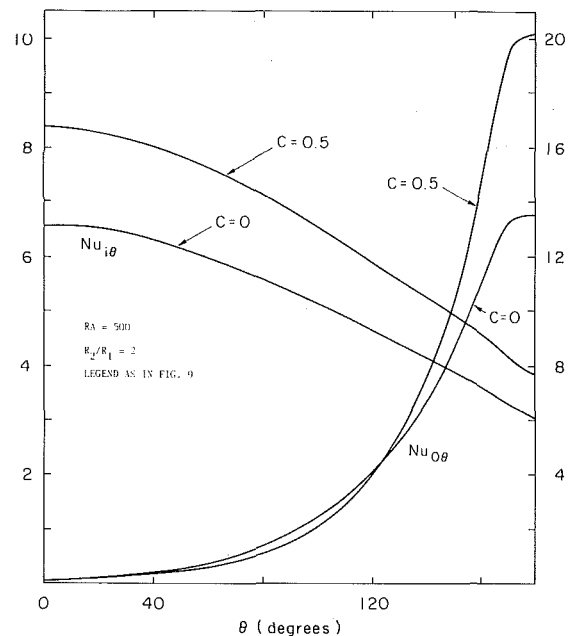


Fig. 8 Local Nusselt number distribution in the annulus; constant heat flux on the inner wall

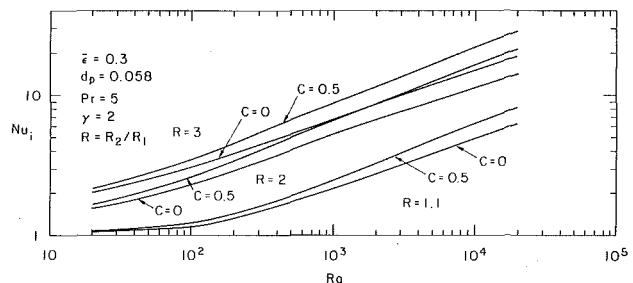


Fig. 9 Average Nusselt number as a function of Rayleigh number; constant heat flux on the inner wall

fects reduce heat transfer up to 4 percent, based on a numerical solution of the extended Darcy law. The viscous effects reduce heat transfer up to 4 percent, based on an integral analysis within the boundary layer. These values can be expected to be larger for higher values of the Darcy number, which are, however, not encountered frequently in practice. None of the mechanisms referred to above explains increase in heat transfer beyond the Darcy value observed in the experiments. It is proposed in this study that the variation of porosity near a solid boundary causes channeling of flow, thus increasing heat transfer. This variation has been modeled as an exponential decay of porosity, with two adjustable parameters. For moderate values of these parameters ($C=0.5$, $\gamma=2$), it amounts to restricting the wall effect to about two ball diameters and maximum porosity to 1.5 times mean value. The augmentation in heat transfer due to this factor alone is seen to be larger than the combined effect of inertial and viscous terms in the governing equations.

References

- Bauchalk, R. A., 1985, "Experimental Study of Free Convection in a Horizontal Porous Annulus," M.M.A.E. Thesis, University of Delaware, Newark, DE.
- Bear, J., 1972, *Dynamics of Fluids in Porous Media*, Elsevier, New York.
- Beavers, G. S., and Sparrow, E. M., 1969, "Non-Darcy Flow Through Fibrous Porous Media," *ASME Journal of Applied Mechanics*, Vol. 136, pp. 711-714.
- Bejan, A., and Khair, K. R., 1985, "Heat and Mass Transfer by Natural Con-

vection in a Porous Medium," *International Journal of Heat and Mass Transfer*, Vol. 28, pp. 909-918.

Beninati, R. F., and Brosilow, C. B., 1962, "Void Fraction Distribution of Beds of Spheres," *AIChE Journal*, Vol. 8, pp. 359-361.

Caltagirone, J., 1976, "Thermoconvective Instabilities in a Porous Medium Bounded by Two Concentric Horizontal Cylinders," *Journal of Fluid Mechanics*, Vol. 76, pp. 337-362.

Catton, I., 1985, "Natural Convection Heat Transfer in Porous Media," *Proceedings, NATO Advanced Study Institute on Natural Convection*, W. Aung, S. Kakac, and R. Viskanta, eds., Hemisphere, New York, pp. 514-547.

Cheng, P., 1978, "Heat Transfer in Geothermal Systems," *Advanced in Heat Transfer*, J. Hartnett and T. F. Irvine, eds., Academic Press, Vol. 14, pp. 1-105.

Farouk, B., 1985, "Mixed Convective Flows Around a Slowly Rotating Sphere," *ASME JOURNAL OF HEAT TRANSFER*, Vol. 107, p. 431-438.

Gosman, A. D., Pun, W. M., Runchal, A. K., Spalding, D. B., and Wolfstein, M., 1969, *Heat and Mass Transfer in Recirculating Flows*, Academic Press, New York.

Kimura, S., and Bejan, A., 1985, "Natural Convection in a Stably Heated Corner Filled With Porous Medium," *ASME JOURNAL OF HEAT TRANSFER*, Vol. 107, pp. 293-298.

Kulkarni, A. V., 1983, "Experimental Studies on Convective Heat Transfer in a Vertical Porous Annulus With Constant Heat Flux on the Inner Wall," M.M.A.E. Thesis, University of Delaware, Newark, DE.

Kumari, M., Pop, I., and Nath, G., 1985, "Non-Darcy Natural Convection From a Heated Vertical Plate in Saturated Porous Media With Mass Transfer," *International Communications in Heat and Mass Transfer*, Vol. 12, pp. 337-346.

Prasad, V., 1983, "Natural Convection in Porous Media-Experimental and Numerical Study for Vertical Annular and Rectangular Enclosures," Ph.D. Thesis, University of Delaware, Newark, DE.

Prasad, V., Kulacki, F. A., and Keyhani, M., 1985, "Natural Convection in Porous Media," *Journal of Fluid Mechanics*, Vol. 150, pp. 89-119.

Prasad, V., and Kulacki, F. A., 1984, "Natural Convection in a Vertical Porous Annulus," *International Journal of Heat and Mass Transfer*, Vol. 27, pp. 207-219.

Rao, Y., Miki, Y., Fukuda, K., Takata, Y., and Hasegawa, S., 1985, "Flow Patterns of Natural Convection in Horizontal Cylindrical Annuli," *International Journal of Heat and Mass Transfer*, Vol. 28, pp. 705-714.

Vafai, K., and Tien, C. L., 1981, "Boundary and Inertia Effects of Flow and Heat Transfer in Porous Media," *International Journal of Heat and Mass Transfer*, Vol. 24, pp. 195-203.

Vafai, K., 1984, "Convective Flow and Heat Transfer in Variable Porosity Media," *Journal of Fluid Mechanics*, Vol. 147, pp. 233-259.

Vafai, K., Alkire, R. L., and Tien, C.L., 1985, "An Experimental Investigation of Heat Transfer in Variable Porosity Media," *ASME JOURNAL OF HEAT TRANSFER*, Vol. 107, pp. 642-647.

APPENDIX

Effect of Viscous Friction on Free Convective Heat Transfer From a Horizontal Cylinder

While the viscous effects in a porous medium are of the order $O(Da)$, they are $O(\sqrt{Da})$ in the region just adjacent to an impermeable wall. The effect of this viscous layer on heat transfer can be determined by performing a boundary layer analysis, where the outer flow is simply Darcian. For the case of a horizontal cylinder embedded in an unbounded porous medium, the problem is one of a viscous layer overlaid by a Darcian boundary layer.

Outer Flow Analysis. Using the approximations of $u \gg v$ and $\partial/\partial\theta \ll \partial/\partial r$, Darcy's law can be stated as

$$\frac{\partial}{\partial r}(ru) = r Ra \frac{\partial T}{\partial T} \sin \theta \quad (A1)$$

The energy equation is

$$\frac{\partial}{\partial\theta}(uT) + \frac{\partial}{\partial r}(vrT) = \frac{\partial}{\partial r}\left(r \frac{\partial T}{\partial r}\right) \quad (A2)$$

In equations (A1) and (A2), the cylinder radius R is used as the characteristic dimension. For a constant heat flux boundary condition, T can be approximated as

$$T = \frac{\delta}{2} \left(1 - \frac{(r-1)}{\delta}\right)^2 \quad (A3)$$

Hence

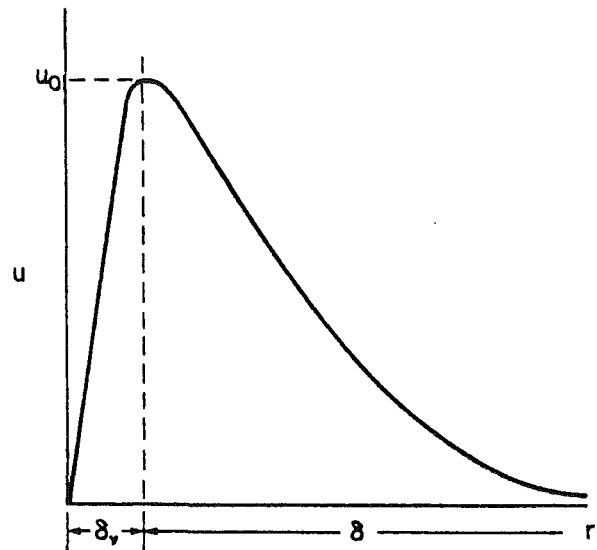


Fig. A1 Model of flow near an impermeable boundary

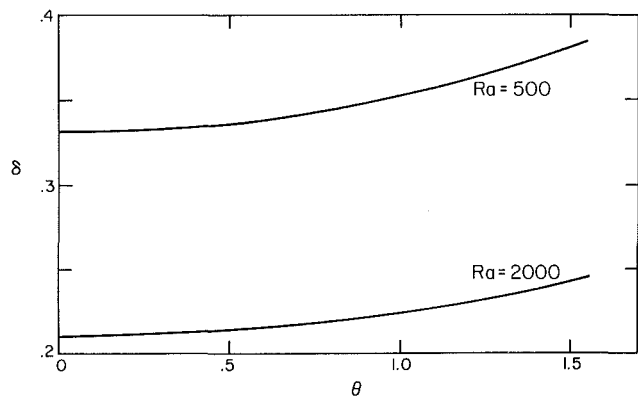


Fig. A2 Boundary layer growth over a single cylinder buried in a porous medium

$$u = \frac{Ra \sin \theta}{r} \left[\frac{(r^3 - (1+\delta)^3)}{3\delta} - \frac{1}{2} \left(\frac{1+\delta}{\delta}\right) (r^2 - (1+\delta)^2) \right] \quad (A4)$$

Here δ is the thickness of the boundary layer in which Darcy's law is valid. δ can be obtained by using the integral version of equation (A2). This leads to

$$\int_1^{1+\delta} F(r, \delta, \theta) dr = \theta \quad (A5)$$

where $F = u(r - (1+\delta))/2\delta$. δ has been extracted from equation (A5) for prescribed values of θ by a Newton-Raphson scheme. Note that the wall temperature is given as $T_0 = \delta/2$. Figure A2 shows a plot of $\delta(\theta)$ for two values of Ra .

Inner Flow Analysis. A model of flow near a solid boundary is shown in Fig. A1, where the no-slip condition is satisfied. To obtain the thickness of the viscous layer δ_v it is assumed that the following conditions prevail:

- 1 constant radial heat flux
- 2 constant shear stress

The temperature profile is then given as

$$T = T_0 + \ln \frac{(1+\delta_v)}{r} \quad (A6a)$$

Table 4 Comparison of Nusselt numbers using Darcy and Brinkman models; for case B, $Da/\epsilon = 10^{-5}$

θ	Ra = 500		2000	
	Nu(D)	Nu(B)	Nu(D)	Nu(B)
.1	6.012	5.855	9.451	9.069
.5	5.934	5.780	9.327	8.954
1.0	5.687	5.547	8.936	8.594
1.5	5.269	5.148	8.274	7.979

and

$$u = u_o \frac{(r-1)}{\delta_v}, \quad 1 < r < 1 + \delta_v \quad (\text{A6b})$$

T_o is the wall temperature calculated from outer flow considerations alone.

The Brinkman equations in r - θ coordinates are

$$\frac{-\partial p}{\partial r} = -\rho g \cos \theta \approx -\rho_o g \cos \theta \quad (\text{A7a})$$

$$\frac{-\partial p}{r\partial \theta} - \rho g \sin \theta - \frac{\mu}{K} u + \frac{\mu}{\epsilon} \nabla^2 u = 0 \quad (\text{A7b})$$

Defining a dynamic pressure $p_d = p - \rho_o g \cos \theta r$, equation (A7a) shows that $\partial p_d / \partial r = 0$. Hence

$$\frac{-\partial p_d}{r\partial \theta} - (\rho - \rho_o) g \sin \theta - \frac{\mu}{K} u + \frac{\mu}{\epsilon} \nabla^2 u = 0$$

and in particular, at the outer edge of the viscous layer,

$$\frac{-\partial p_d}{r\partial \theta} + \frac{\mu}{K} u_o + 0$$

Combining these equations and nondimensionalizing, one obtains

$$u_o \delta_v - \frac{u_o \delta_v}{2} = \frac{Da}{\epsilon} \frac{u_o}{\delta_v} \quad (\text{A8})$$

where $\ln(1 + \delta_v)$ is taken as δ_v . Hence

$$\delta_v = \sqrt{\frac{2Da}{\epsilon}} \quad (\text{A9a})$$

$$T_w = T_o + \ln(1 + \delta_v) \quad (\text{A9b})$$

and

$$Nu = \frac{1}{T_w}$$

Table 4 gives values of Nu for both Darcy and Brinkman equations. Clearly viscous effects can be seen to reduce heat transfer.

Asymptotic Solution for Thermocapillary Flow at High and Low Prandtl Numbers Due to Concentrated Surface Heating

C. L. Chan¹

M. M. Chen

J. Mazumder

Laser Aided Materials Processing
Laboratory,
Department of Mechanical and Industrial
Engineering,
University of Illinois at Urbana-Champaign,
Urbana, IL 61801

Thermocapillary convection due to nonuniform surface heating is the dominant form of fluid motion in many materials processing operations. The velocity and temperature distributions for the region adjacent to the area of peak surface heating are analyzed for the limiting cases of large and small Prandtl numbers. For a melt pool whose depth and width are large relative to the thermal and viscous boundary layers, it is shown that the most important parameter is the curvature (i.e., $\nabla^2 q$) of the surface heat flux distribution. The solutions of the temperature and stream functions are presented, some of which are in closed form. Simple, explicit expressions for the velocity and maximum temperature are presented. These results are found to be quite accurate for realistic Prandtl number ranges, in comparison with exact solutions for finite Prandtl numbers. Besides being more concise than exact results, the asymptotic results also display the Prandtl number dependence more clearly in the respective ranges.

1 Introduction

When a free surface is heated by a concentrated heat source, the resulting temperature distribution causes a nonuniform surface tension distribution. Typically, surface tension is a decreasing function of temperature. Thus the fluid layer on the surface experiences a shear force pulling the fluid from the warmer central region to the cooler outer region. This outward thermocapillary flow entrains fluid toward the surface at the center, forming a stagnation-type flow field and temperature field if the fluid is deep enough. This is the common feature in the melt pools of a number of industrial processes, including welding [1], cutting, and alloying using concentrated energy beams [2], such as arcs, electron beam, or lasers. Similar situations also occur in zone melting crystal growth [3].

The present paper presents solutions for the flow near the center of the heated surface for the limiting cases of small and large Prandtl numbers, assuming the viscous and conductive boundary layer thicknesses to be small relative to the depth and width of the pool. It will be shown that the flow depends primarily on the curvature of the heat flux distribution at the surface. Explicit expressions for the maximum temperature and velocity are given for $Pr \ll 1$ and $Pr \gg 1$. These results are shown to be approximately applicable for $Pr \leq 1$ and $Pr \geq 1$, respectively.

A number of numerical and theoretical analyses of thermocapillary flows can be found in the literature [3-8]. Ostrach [3] presented a general formulation of the phenomenon, and discussed the basic nondimensionalization and boundary layer scaling. His results clarified the scaling for fluids of $Pr \sim 1$. Separately, he and his co-worker also obtained numerical solutions for thermocapillary flow relevant to zone melting crystal growth [6]. Cowley and Davis [7] performed an asymptotic analysis for flows induced by a heated surface adjacent to an adiabatic free surface, for high Prandtl numbers. Their flow is thus associated with the nonuniform surface temperature distribution caused by interior convective cooling, and not by nonuniform surface heating.

In a recent paper [8], the present authors solved the stagna-

tion thermocapillary flow problem near the central region of a nonuniformly heated surface. The scaling and nondimensionalization, however, are based on a fluid with Prandtl number near unity. Although Prandtl number-dependent coefficients for nonunity Prandtl number have been computed, the results do not yield the simple and explicit Prandtl number dependence obtainable with asymptotic analyses for large and small Prandtl numbers. It may be recalled that in forced and free convection, the asymptotic relationships $Nu = C_1 Re^{1/2} Pr^{1/3}$, $Nu = C_2 Ra^{1/4}$ for $Pr \gg 1$, and $Nu = C_3 Pe^{1/2}$, $Nu = C_4 Gr^{1/4} Pr^{1/2}$ for $Pr \ll 1$ are not only approximately valid for the wide ranges $Pr \geq 1$ and $Pr \leq 0.1$, respectively, but are much more convenient and illuminating than the basic dimensional results $Nu = \phi_1(Pr) Re^{1/2}$ and $Nu = \phi_2(Pr) Gr^{1/4}$, where ϕ_1 and ϕ_2 denote the functional dependence of Nu on Pr . Similar results for thermocapillary convection for $Pr \gg 1$ and $Pr \ll 1$ can thus be expected to be applicable for all nonmetallic and metallic liquids, respectively. The purpose of the present paper is to obtain these asymptotic results and show that they are approximately valid for most materials of interest.

2 Mathematical Formulation

The physical model is shown in Fig. 1. Both the two-dimensional and axisymmetric cases are considered. The two-dimensional case represents the limiting case of the flows encountered in zone melting crystal growth when the heat source dimension is small with respect to the radius of the crystal-

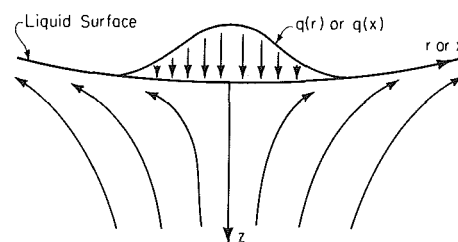


Fig. 1 Schematic diagram of physical model

¹Presently at the Department of Aerospace and Mechanical Engineering, University of Arizona, Tucson, AZ.

Contributed by the Heat Transfer Division and presented at the ASME Winter Annual Meeting, Miami Beach, Florida, November 1985. Manuscript received by the Heat Transfer Division September 19, 1985.

lizing rod. The axisymmetric case represents the limiting case of the flows encountered in welding and laser surface alloying when the scanning velocity is small relative to the velocity of the thermocapillary motion. The governing equations are:

Continuity equation:

$$\frac{\partial}{\partial r}(r^{n-2}u_r) + \frac{\partial}{\partial z}(r^{n-2}u_z) = 0 \quad (1)$$

r-momentum equation:

$$u_r \frac{\partial u_r}{\partial r} + u_z \frac{\partial u_r}{\partial z} = -\frac{1}{\rho} \frac{\partial p}{\partial r} + \nu \left[\frac{\partial^2 u_r}{\partial r^2} + \frac{\partial}{\partial r} \left(\frac{u_r^{n-2}}{r^{n-2}} \right) + \frac{\partial^2 u_r}{\partial z^2} \right] \quad (2)$$

z-momentum equation:

$$u_r \frac{\partial u_z}{\partial r} + u_z \frac{\partial u_z}{\partial z} = -\frac{1}{\rho} \frac{\partial p}{\partial z} + \nu \left[\frac{1}{r^{n-2}} \frac{\partial}{\partial r} r^{n-2} \frac{\partial u_z}{\partial r} + \frac{\partial^2 u_z}{\partial z^2} \right] \quad (3)$$

Energy equation:

$$u_r \frac{\partial T}{\partial r} + u_z \frac{\partial T}{\partial z} = \kappa \left[\frac{1}{r^{n-2}} \frac{\partial}{\partial r} r^{n-2} \frac{\partial T}{\partial r} + \frac{\partial^2 T}{\partial z^2} \right] \quad (4)$$

The boundary conditions on the free surface are

$$z=0; \quad \mu \frac{\partial u_r}{\partial z} = -\gamma \frac{\partial T}{\partial r}, \quad u_z=0, \quad -k \frac{\partial T}{\partial z} = q''(r) \quad (5)$$

The dimensionless parameter governing the pressure boundary condition is the Weber number

$$We = \frac{\rho u^2 D}{\gamma} \quad (6)$$

For large Weber numbers pressure variations due to surface tension associated with surface curvature are of the order γ/D , and hence much smaller than the dynamic pressure ρu^2 . In other words, the small pressure variation at the surface due to surface tension has little influence in the momentum equations. For typical welding and surface alloying applications $We = O(10^4)$. Hence the pressure boundary condition will be

$$\frac{\partial p}{\partial r} = 0 \text{ at } z=0 \quad (7)$$

The first boundary condition in equation (5) represents the balance of the surface shear to the surface tension gradient.

This is the characteristic of thermocapillary flow where the flow is driven by the temperature gradient. This is also where the coupling of the momentum and energy equations occurs. Finally, at a distance far away from the surface

$$z \rightarrow \infty; \quad u_r \rightarrow 0, \quad T \rightarrow T_\infty \quad (8)$$

Near the center, the surface heat flux distribution can be represented as a truncated power series

$$q''(r) = q_0 + q_1 r^2 \quad (9)$$

It can be seen that q_1 is the lowest order term responsible for temperature nonuniformity. Hence a two-term series is the simplest nontrivial representation. The present study will be restricted to the two-term representation. It can be shown by substitution and matching the boundary conditions that the solution can be expanded in the following forms:

$$T - T_\infty = \frac{q_0}{k} g_0(z) + \frac{q_1}{k} g_1(z) r^2 \quad (10)$$

$$u_r = \frac{2\gamma q_1}{k\mu} f_1'(z) r \quad (11)$$

$$u_z = -(n-1) \frac{2\gamma q_1}{k\mu} f_1(z) \quad (12)$$

where g_0 , g_1 , and f_1 are functions of z only. Equations (10) and (12) may also be considered the leading terms of a series expansion.

Substituting these expansions into the governing equations, equations (1)–(5) and (8), a set of coupled ordinary differential equations is obtained. The viscous length scale can be obtained from the momentum equation. As it turns out the present system can be decoupled by introducing an unknown variable, which can be determined separately. This mathematical manipulation of decoupling the system means that the coupling between the energy and momentum equations is similar in terms of the scales introduced. The scalings are as follows:

$$\tilde{z} = \frac{z}{\left(\frac{k\mu\nu}{2\gamma q_1} \right)^{1/4} [\tilde{g}_1(0)]^{-1/4}}$$

$$\tilde{f} = \frac{f_1}{\left(\frac{k\mu\nu}{2\gamma q_1} \right)^{3/4} [\tilde{g}_1(0)]^{1/4}}$$

Nomenclature

C_p = heat capacity
 f_1 = stream function, see equation (11)
 \tilde{f}_∞ = value of the universal stream function at infinity
 \tilde{f}'_{10} = slope of the universal stream function at $\tilde{z} = 0$
 g_0 = temperature function defined in equation (10)
 g_1 = temperature function defined in equation (10)
 k = thermal conductivity
 n = dimensionality index = 2 for two-dimensional plane; 3 for axisymmetric

p = pressure
 Pr = Prandtl number
 q = nonuniform heat flux distribution
 q_0, q_1 = coefficients of heat source expansion, see equation (9)
 r = radial axis, see Fig. 1
 T = temperature
 T_∞ = temperature at infinity
 u_r = velocity in radial direction
 u_z = velocity in z direction
 z = depth axis, see Fig. 1
 γ = temperature coefficient of surface tension
 δ_κ = thermal boundary layer

δ_ν = viscous boundary layer
 κ = thermal diffusivity
 μ = dynamic viscosity
 ν = kinematic viscosity
 ρ = density

Superscripts

' = derivative with respect to the independent variable
 $*$ = dimensionless quantities
 \sim = scaled dimensionless quantities
 o = stretched variables for the case of $Pr \rightarrow 0$
 i = stretched variables for the case of $Pr \rightarrow \infty$

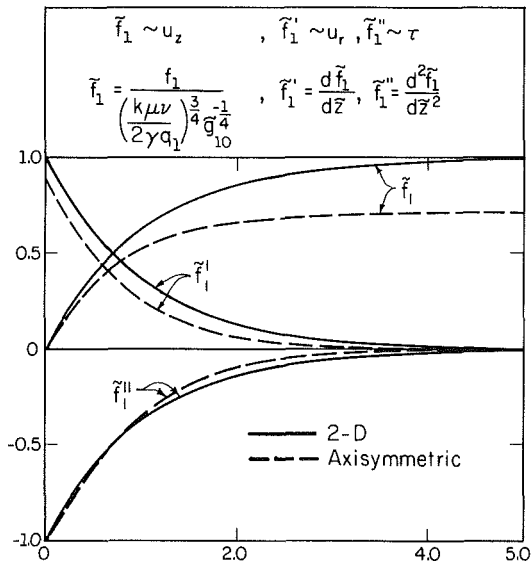


Fig. 2 Graphs of the stream functions f_1 , velocity profiles f_1' , and shear stress f_1'' versus depth

$$\bar{g}_0 = \frac{g_0}{\left(\frac{k\mu\nu}{2\gamma q_1}\right)^{1/4} [\bar{g}_1(0)]^{-1/4}}$$

$$\bar{g}_1 = \frac{g_1}{\left(\frac{k\mu\nu}{2\gamma q_1}\right)^{1/4} [\bar{g}_1(0)]^{-1/4}} \quad (13)$$

The dimensionless equations become

$$\bar{f}_1''' + (n-1)\bar{f}_1\bar{f}_1'' - \bar{f}_1'^2 = 0 \quad (14)$$

$$\bar{g}_0'' + \text{Pr}(n-1)\bar{f}_1\bar{g}_0' = 0 \quad (15)$$

$$\bar{g}_1'' + \text{Pr}[(n-1)\bar{f}_1\bar{g}_1' - 2\bar{f}_1'\bar{g}_1] = 0 \quad (16)$$

subject to the boundary conditions

$$\bar{z} = 0; \quad \bar{f}_1 = \bar{f}_1'' + 1 = \bar{g}_0' + 1 = \bar{g}_1' + 1 = 0 \quad (17)$$

$$\bar{z} \rightarrow \infty; \quad \bar{f}_1 = \bar{g}_0 = \bar{g}_1 = 0 \quad (18)$$

The boundary condition is no longer coupled. Solution of \bar{f}_1 can be obtained first. The result is then used to solve \bar{g}_0 and \bar{g}_1 . Analytical closed-form solutions are possible for some cases. Numerical solutions using fourth-order Runge-Kutta method are obtained for others. These results were presented in [8]. The dimensionless stream functions, which are required to carry out the asymptotics of high and low Prandtl numbers, are plotted in Fig. 2.

3 Asymptotic Limit of $\text{Pr} \rightarrow 0$

(i) **Formulation.** The physical implication as the Prandtl number tends to zero is that the thermal boundary layer, within which most of the heat transfer occurs, is much thicker than the viscous boundary layer. Therefore, the pertinent velocity field for the convective heat transfer is actually the velocity field beyond the viscous boundary layer. The fact that the governing equations are decoupled allows this asymptotic limit to be analyzed using the energy equations with the appropriate velocity field. In the case of small Prandtl number, the velocity field is given by the universal stream functions at large \bar{z} . The stream functions are constants of order 1 in this region (see Fig. 2). These constant values \bar{f}_∞ for plane two-dimensional and axisymmetric cases are tabulated in Table 1.

Table 1 Asymptotic limits of stream function at large and small \bar{z}

	Functional Form	Plane 2-D	Axisymmetric
$\bar{z} \rightarrow 0$	$\bar{f}_1 = \bar{f}_{10}\bar{z}$	$\bar{f}_{10} = 1.0$	$\bar{f}_{10} = 0.89872$
$\bar{z} \rightarrow \infty$	$\bar{f}_1 = \bar{f}_\infty$	$\bar{f}_\infty = 1.0$	$\bar{f}_\infty = 0.71242$

We shall now rescale the variables so that as $\text{Pr} \rightarrow 0$ all the terms in the governing equations are of order one in the thermal boundary layer. The surface heat flux condition equation (17) requires that \bar{z} , \bar{g}_0 , and \bar{g}_1 should be stretched identically. The energy equations, (15) and (16) require the stretching to be Pr^{-1} in order to balance all the terms. Accordingly, we introduce the following stretched variables:

$$\bar{z}^o = \bar{z} \text{Pr}$$

$$\bar{g}_0^o(\bar{z}^o) = \bar{g}_0(\bar{z}) \text{Pr}$$

$$\bar{g}_1^o(\bar{z}^o) = \bar{g}_1(\bar{z}) \text{Pr} \quad (19)$$

Here the superscript o indicates that these are the outer variables, since the thermal boundary layer represents the outer solution relative to the viscous boundary layer which is the inner solution.

The governing equations therefore become

$$\bar{g}_0^{o''} + (n-1)\bar{f}_\infty\bar{g}_0^{o'} = 0 \quad (20)$$

$$\bar{g}_1^{o''} + (n-1)\bar{f}_\infty\bar{g}_1^{o'} - 2\bar{f}_\infty\delta(\bar{z}^o)\bar{g}_1^o = 0 \quad (21)$$

where $\delta(\bar{z}^o)$ is the Dirac delta function and $\bar{f}_\infty = \bar{f}_1(\infty)$ is a constant and listed in Table 1. The derivation of these equations is presented in the Appendix.

The boundary conditions are:

$$\bar{z}^o = 0, \quad \bar{g}_0^{o'} = \bar{g}_1^{o'} = -1$$

$$\bar{z}^o \rightarrow \infty, \quad \bar{g}_0^o = \bar{g}_1^o = 0 \quad (22)$$

The effect of Pr number, which appears explicitly in equations (15) and (16), is now embedded in the stretched variables so that one solution represents the whole range of small Prandtl numbers. The term involving the Dirac delta function in equation (21) represents convection in the r direction. Its existence is due to the fact that the velocity in the r direction is nonzero on the surface. The conventional forced convection over the flat plate has zero velocity at the surface. This difference is also reflected in the structure of the thermal boundary layer. The rescaling in equation (19) implies that the ratio of the viscous and thermal layers is $\delta_v/\delta_t = \text{Pr}^{-1}$ as compared to the conventional forced convection where $\delta_v/\delta_t = \text{Pr}^{-1/2}$.

(ii) **Analytical Solutions.** The system governed by equations (20) and (21) and subject to the boundary conditions equation (22) can be solved analytically. The solutions are found to be

$$\bar{g}_0^o(\bar{z}^o) = \frac{1}{(n-1)\bar{f}_\infty} \exp[-(n-1)\bar{f}_\infty\bar{z}^o] \quad (23)$$

and

$$\bar{g}_1^o(\bar{z}^o) = \frac{1}{(n+1)\bar{f}_\infty} \exp[-(n-1)\bar{f}_\infty\bar{z}^o] \quad (24)$$

The constants $\bar{g}_0^o(0)$ and $\bar{g}_1^o(0)$ can now be evaluated and are listed in Table 2.

4 Asymptotic Limit of $\text{Pr} \rightarrow \infty$

(i) **Formulation.** The physical implication as Prandtl number goes to infinity is that the thermal boundary layer is much thinner than the viscous boundary layer. The velocity field responsible for the convection is the one confined within the thermal boundary layer. The stream functions in this region behave linearly. The slopes of these linear functions for

Table 2 Asymptotic limits of surface temperature

		Plane two-dimensional	Axisymmetric
Pr → 0	B ≡ g ₀ ⁱ (0)	1.0	0.70185
	C ≡ g ₁ ⁱ (0)	0.33333	0.35093
Pr → ∞	D ≡ g ₀ ⁱ (0)	1.25333	0.93484
	E ≡ g ₁ ⁱ (0)	0.62666	0.59514

both plane two-dimensional and axisymmetric cases are tabulated in Table 1. Again, by balancing the terms in the surface heat flux condition and the energy equations, it can be shown easily that the coordinate stretching is

$$\begin{aligned} \tilde{z}^i &= \tilde{z} \text{Pr}^{1/2} \\ \tilde{g}_0^i(\tilde{z}^i) &= \tilde{g}_0(\tilde{z}) \text{Pr}^{1/2} \\ \tilde{g}_1^i(\tilde{z}^i) &= \tilde{g}_1(\tilde{z}) \text{Pr}^{1/2} \end{aligned} \quad (25)$$

Here, the superscript *i* indicates that these are the inner variables relative to the outer variables of the viscous boundary layer. Upon substitution, the equations become

$$\tilde{g}_0^{i''} + (n-1)\tilde{f}'_{10}\tilde{z}^i\tilde{g}_0^i = 0 \quad (26)$$

$$\tilde{g}_1^{i''} + (n-1)\tilde{f}'_{10}\tilde{z}^i\tilde{g}_1^i - 2\tilde{f}'_{10}\tilde{g}_1^i = 0 \quad (27)$$

where $\tilde{f}'_{10} \equiv \tilde{f}'_1(0)$ is a constant tabulated in Table 1. The boundary conditions are

$$\begin{aligned} \tilde{z}^i = 0; \quad \tilde{g}_0^i &= \tilde{g}_1^i = -1 \\ \tilde{z}^i \rightarrow \infty; \quad \tilde{g}_0^i &= \tilde{g}_1^i = 0 \end{aligned} \quad (28)$$

The rescaling in equation (25) implies that $\delta_x/\delta_\nu = \text{Pr}^{-1/2}$, which is the same as the case of conventional forced convection as Pr goes to zero. The nonzero velocity on the surface gives rise to a linear term for the stream function. Consequently, the limiting term (large Pr) of the velocity in the *r* direction is a constant. In this large Pr limit, the problem becomes convection in uniform flow field which is identical to the conventional forced convection as Pr → 0. Finally, it should be remarked that $\delta_x/\delta_\nu = \text{Pr}^{-1/3}$ for the conventional forced convection as Pr → ∞.

(ii) **Analytical and Numerical Solutions.** A closed-form solution for \tilde{g}_0^i is possible, and it can be expressed in terms of the complementary error function as

$$\tilde{g}_0^i(\tilde{z}^i) = \frac{1}{2} \left(\frac{2\pi}{(n-1)\tilde{f}'_{10}} \right)^{1/2} \text{erfc} \left[\left(\frac{(n-1)\tilde{f}'_{10}}{2} \right)^{1/2} \tilde{z}^i \right] \quad (29)$$

The numerical solution for \tilde{g}_1^i is obtained by using the fourth-order Runge-Kutta method. The constants $\tilde{g}_0^i(0)$ and $\tilde{g}_1^i(0)$ are evaluated from the solutions and listed in Table 2.

5 Results

(i) **Small Prandtl Number Results.** The dimensionless functions $\tilde{g}_0^i(\tilde{z}^i)$ and $\tilde{g}_1^i(\tilde{z}^i)$ are plotted in Fig. 3. This asymptotic analysis provides explicit formulae for the Prandtl number effect on the scaling laws. In the following equations, constants *B* and *C* are tabulated in Table 2. The scaling introduced for $\tilde{g}_1^i(\tilde{z})$ in equation (25) implies that the length scale of the viscous boundary layer is

$$\delta_\nu = C^{-1/4} \left(\frac{k\mu\nu}{2\gamma q_1} \right)^{1/4} \text{Pr}^{1/4} \quad (30)$$

This can be rewritten as

$$\begin{aligned} \delta_\nu &= C^{-1/4} \left(\frac{\rho k}{2\gamma q_1} \right)^{1/4} \frac{\nu^{3/4}}{\kappa^{1/4}} \\ &= C^{-1/4} \left(\frac{\rho^2 C_p}{2\gamma q_1} \right)^{1/4} \nu^{3/4} \end{aligned} \quad (31)$$

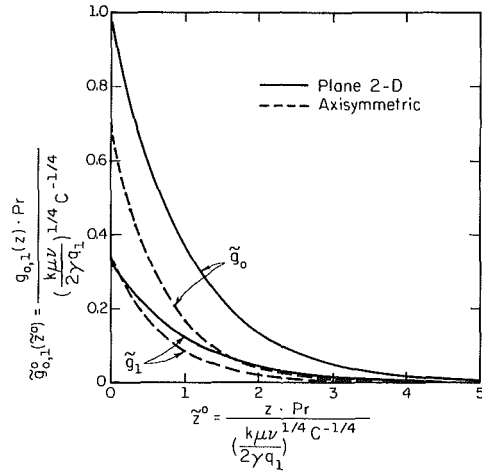


Fig. 3 Temperature profile for the limiting case of small Prandtl number

Thus, the viscous boundary layer thickness is proportional to $\nu^{3/4}$. The rescaling of the length scale equation (25) implies that the ratio of the length scale of the thermal boundary layer to that of the viscous boundary layer is

$$\delta_x/\delta_\nu = \text{Pr}^{-1} \quad (32)$$

so that

$$\begin{aligned} \delta_x &= C^{-1/4} \left(\frac{k\mu\nu}{2\gamma q_1} \right)^{1/4} \text{Pr}^{-3/4} \\ &= C^{-1/4} q_1^{-1/4} k \left(\frac{1}{2\rho^2 C_p^3 \gamma \nu} \right)^{1/4} \end{aligned} \quad (33)$$

Similarly, Prandtl number dependence is found for the temperature. In particular, the maximum temperature difference which occurs on the surface at the center can be obtained by setting $r = 0, z = 0$ in equation (10). Substituting the scaling for g_0 , we have

$$\begin{aligned} \Delta T_{\max} &= B C^{-1/4} \frac{q_0}{k} \left(\frac{k\mu\nu}{2\gamma q_1} \right)^{1/4} \text{Pr}^{-3/4} \\ &= B C^{-1/4} \frac{q_0}{q_1^{1/4}} \left(\frac{1}{2\rho^2 C_p^3 \gamma \nu} \right)^{1/4} \end{aligned} \quad (34)$$

The temperature gradient on the surface in the radial direction is the driving force of the thermocapillary flow and can be expressed as

$$\begin{aligned} \frac{\partial T}{\partial r} &= C^{3/4} \frac{2q_1}{k} \left(\frac{k\mu\nu}{2\gamma q_1} \right)^{1/4} \text{Pr}^{-3/4} r \\ &= C^{3/4} 2q_1^{3/4} \left(\frac{1}{2\rho^2 C_p^3 \gamma \nu} \right)^{1/4} r \end{aligned} \quad (35)$$

The velocity in the radial direction can be examined closely by substituting the scaling into equation (11), yielding

$$\begin{aligned} u_r &= C^{1/2} \left(\frac{2\gamma q_1}{k\mu\nu} \right)^{1/2} \nu \text{Pr}^{-1/2} r \tilde{f}'_1(\tilde{z}) \\ &= C^{1/2} q_1^{1/2} \left(\frac{2\gamma}{\rho^2 \nu C_p} \right)^{1/2} r \tilde{f}'_1(\tilde{z}) \end{aligned} \quad (36)$$

It is interesting to note that the viscous length scale, the maximum temperature, the surface temperature gradient, and the velocity scale (see equations (31), (34), (35), and (36)) do not depend on the thermal conductivity. The vertical velocity u_z can be derived from the continuity equation

$$u_z = \frac{(n-1)\nu \text{Pr}^{-1/4}}{\left(\frac{k\mu\nu}{2\gamma q_1}\right)^{1/4} C^{-1/4}} \tilde{f}'_1(\tilde{z}) \quad (37)$$

$$= (n-1)C^{1/4}q_1^{1/4}\left(\frac{2\gamma\nu}{\rho^2 C_p}\right)^{1/4} \tilde{f}'_1(\tilde{z})$$

The shear stress can be obtained by differentiating u_r with respect to z in equation (11)

$$\mu \frac{\partial u_r}{\partial z} = C \mu \nu \left(\frac{k\mu\nu}{2\gamma q_1}\right)^{-3/4} \text{Pr}^{-3/4} r \quad (38)$$

$$= C q_1^{3/4} \mu \left(\frac{2\gamma\nu}{\rho^2 C_p}\right)^{3/4} r$$

(ii) **Large Prandtl Number Results.** The dimensionless functions $\tilde{g}'_0(\tilde{z}')$ and $\tilde{g}'_1(\tilde{z}')$ for plane two-dimensional and axisymmetric cases are plotted in Fig. 4. The solutions behave as expected, attaining their maximum on the surface and decreasing very rapidly downward.

Similarly, this asymptotic limit provides explicit formulae for the effect of Prandtl number on the scaling laws for large Pr. The constants, D and E , are tabulated in Table 2. The length scale of the viscous boundary layer is

$$\delta_\nu = E^{-1/4} \left(\frac{k\mu\nu}{2\gamma q_1}\right)^{1/4} \text{Pr}^{1/8} \quad (39)$$

$$= E^{-1/4} \frac{1}{q_1^{1/4}} \left(\frac{k\mu^2\nu^3\rho C_p}{4\gamma^2}\right)^{1/8}$$

The ratio of the length scale of the thermal boundary layer and that of the viscous boundary layer is

$$\frac{\delta_\kappa}{\delta_\nu} = \text{Pr}^{-1/2} \quad (40)$$

so that

$$\delta_\kappa = E^{-1/4} \left(\frac{k\mu\nu}{2\gamma q_1}\right)^{1/4} \text{Pr}^{-3/8} \quad (41)$$

$$= C^{-1/4} \frac{1}{q_1^{1/4}} \left(\frac{k^5\mu^2}{4\gamma^2\nu\rho^3 C_p^3}\right)^{1/8}$$

The maximum temperature difference is found to be

$$\Delta T_{\max} = \frac{D}{E^{1/4}} \frac{q_0}{k} \left(\frac{k\mu\nu}{2\gamma q_1}\right)^{1/4} \text{Pr}^{-3/8} \quad (42)$$

$$= \frac{D}{E^{1/4}} \frac{q_0}{q_1^{1/4}} \left(\frac{\nu}{4\rho k^3 C_p^3 \gamma^2}\right)^{1/8}$$

The surface temperature gradient is

$$\frac{\partial T}{\partial r} = E^{3/4} \frac{2q_1}{k} \left(\frac{k\mu\nu}{2\gamma q_1}\right)^{1/4} \text{Pr}^{-3/8} \quad (43)$$

$$= E^{3/4} 2q_1^{3/4} \left(\frac{\nu}{4k^3\rho\gamma^2 C_p^3}\right)^{1/8}$$

The radial velocity is

$$u_r = E^{1/2} \frac{2\gamma q_1}{k\mu} \left(\frac{k\mu\nu}{2\gamma q_1}\right)^{1/2} \text{Pr}^{-1/4} r \tilde{f}'_1(\tilde{z}) \quad (44)$$

$$= E^{1/2} q_1^{1/2} \left(\frac{4\gamma^2}{\rho^3 C_p k\nu}\right)^{1/4} r \tilde{f}'_1(\tilde{z})$$

The vertical velocity is

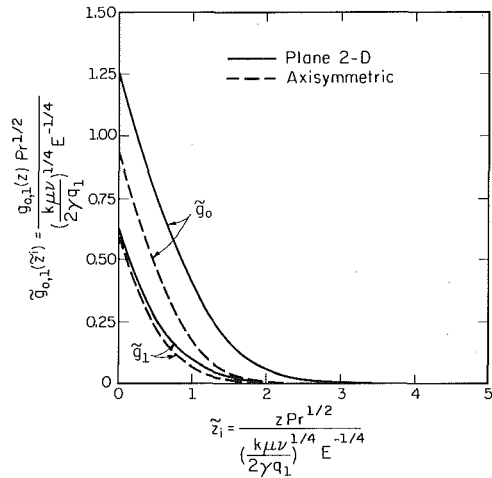


Fig. 4 Temperature profile for the limiting case of large Prandtl number

$$u_z = \frac{(n-1)\nu \text{Pr}^{-1/8}}{\left(\frac{k\mu\nu}{2\gamma q_1}\right)^{1/4} E^{-1/4}} \tilde{f}'_1(\tilde{z}) \quad (45)$$

$$= (n-1)E^{1/4}q_1^{1/4}\left(\frac{4\gamma^2\nu^3}{k\rho^3 C_p}\right)^{1/8} \tilde{f}'_1(\tilde{z})$$

Finally, the shear stress is

$$\mu \frac{\partial u_r}{\partial z} = E^{3/4} \mu \nu \left(\frac{k\mu\nu}{2\gamma q_1}\right)^{-3/4} \text{Pr}^{-3/8} r \quad (46)$$

$$= E^{3/4} q_1^{3/4} \mu \nu \left(\frac{4\gamma^2}{k\rho^3\nu^5 C_p}\right)^{3/8}$$

To examine the accuracy and usefulness of these asymptotic limits, the surface temperature and its curvature, $\tilde{g}_0(0)$ and $\tilde{g}_1(0)$, calculated from equations (15)–(18), and the two asymptotic analyses for both plane two-dimensional and axisymmetric are plotted against Pr in Figs. (5) and (6), respectively. The asymptotic limits appear as straight lines (log-log plot) of slopes, $-1/2$ and -1 . It can be observed that the exact solutions governed by equations (15)–(18) approach their asymptotic limits very rapidly. Consequently, the simple concise algebraic formulae can be used to estimate various quantities such as maximum temperature and velocities.

Another property of the parameters q_0 and q_1 is worth noting. Since q_0 is the peak heat flux and q_1 is the second derivative of the heat flux, $(q_0/q_1)^{1/2}$ is a length scale which characterizes the “spot size” of the nonuniform surface heat flux. For example, for the Gaussian distribution frequently employed for nonuniform heating calculations

$$q = 2q_a \exp\left(-\frac{2r^2}{r_0^2}\right)$$

where q_a is the average heat flux, and r_0 is the beam radius; $(q_0/q_1)^{1/2}$ is equal to $r_0/\sqrt{2}$. In other words, surface heating and hence thermocapillary effects are primarily confined in a region whose radius is of the order $(q_0/q_1)^{1/2}$. One may thus obtain a characteristic velocity by setting r equal to $(q_0/q_1)^{1/2}$ in equations (36) and (44)

$$u_c = E^{1/2} \tilde{f}'_1(0) \frac{2\gamma q_1}{k\mu} \left(\frac{k\mu\nu}{2\gamma q_1}\right)^{1/2} \text{Pr}^{-1/4} \left(\frac{q_0}{q_1}\right)^{1/2} \text{ for } \text{Pr} \gg 1 \quad (44)$$

$$u_c = C^{1/2} \tilde{f}'_1(0) \frac{2\gamma q_1}{k\mu} \left(\frac{k\mu\nu}{2\gamma q_1}\right)^{1/2} \text{Pr}^{-1/2} \left(\frac{q_0}{q_1}\right)^{1/2} \text{ for } \text{Pr} \ll 1$$

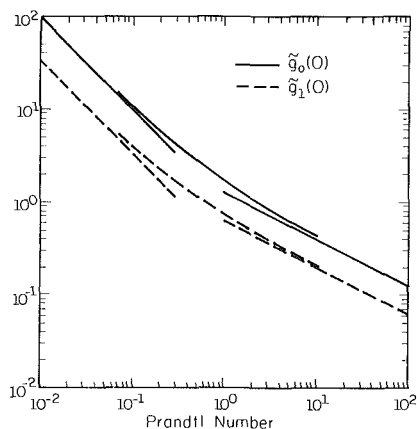


Fig. 5 Surface temperature and its curvature $\tilde{g}_{0,1}(0)$, versus Prandtl numbers for plane two-dimensional case

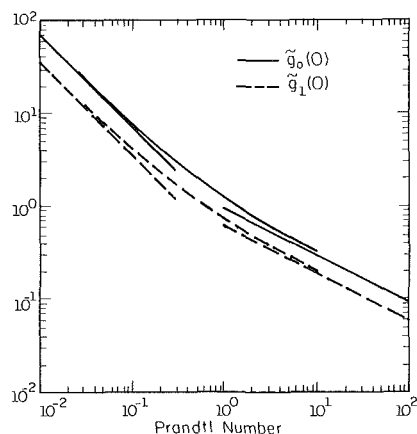


Fig. 6 Surface temperature and its curvature $\tilde{g}_{0,1}(0)$, versus Prandtl numbers for axisymmetric case

u_c is expected to be a good order-of-magnitude estimate of the maximum velocity due to thermocapillarity.

It may be recalled that for flows around blunt bodies of average proportions (i.e., excluding very slender or very oblate bodies), the stagnation flow essentially sets the tone for the viscous and thermal boundary layers for the rest of the body. For example, the heat transfer coefficient for the front half of a cylinder in cross flow is essentially equal to that at the stagnation point. Therefore, it is expected that the stagnation thermocapillary flow results obtained here could be a useful rough estimate for the thermocapillary flow associated with a more complex heat flux distribution.

It should be pointed out that the numerical values tabulated in Table 1 and Table 2 are obtained from the numerical solutions using the fourth-order Runge-Kutta method [9]. The step size used is 0.0125 in all cases. The error is of the order $(\Delta X)^5$ and therefore of the order 10^{-10} . The tabulated values are therefore to four significant figures.

6 Conclusions

Solutions of thermocapillary convection in the central region of a nonuniformly heated surface for the asymptotic limits of very small and very large Prandtl number have been presented. The model is valid when the viscous and thermal boundary layers are small as compared to the depth and width of the melt pool. The resulting temperature distributions are given in the form of simple functions. Furthermore, explicit expressions for maximum temperature and velocity are given in the previous section. These expressions explicitly display the dependence of maximum temperature and velocity on the

physical properties and the given parameters. It is interesting to note that the most important parameter is q_1 , which can be interpreted as the curvature of the surface heat flux distribution. In other words, the intensity of thermocapillary convection and the boundary layer thicknesses in the stagnation region depend primarily on the curvature of the heat flux distribution.

These asymptotic results are compared with the numerical solutions of [8] in Figs. 5 and 6. It is seen that for liquid metals, with Pr generally less than 0.15, the maximum error from using the zero Pr results is about 10 percent for the surface temperature at $r = 0$ (i.e., $\tilde{g}_0(0)$) and about 10 percent for the second derivative of the surface temperature (i.e., $\tilde{g}_1(0)$). For nonmetallic liquids with Pr greater than 10 the maximum error from using the large Pr limit is about 10 percent for surface temperature at $r = 0$ (i.e., $\tilde{g}_0(0)$) and 10 percent for the second derivative of the surface temperature (i.e., $\tilde{g}_1(0)$). Accordingly, the more concise results in the present paper can be used in place of the exact results for most problems of practical interest.

Acknowledgments

This work was made possible by a grant (N00014-84-K0135) from the office of Naval Research, Arlington, VA. Drs. Bruce McDonald and O. M. Arora are the technical monitors.

References

- Oreper, G. M., Eagar, T. W., and Szekeley, J., "Convection in Arc Weld Pools," *Welding Journal*, Vol. 63, 1983, pp. 307s-312s.
- Chande, T., and Mazumder, J., *Appl. Phys. Letter*, Vol. 61, 1982, pp. 973-1025.
- Ostrach, S., "Low-Gravity Fluid Flows," *Ann. Rev. Fluid Mech.*, Vol. 14, 1982, pp. 313-345.
- Chan, C. L., Mazumder, J., and Chen, M. M., "A Two-Dimensional Transient Model for Convection in Laser Melted Pool," *Metal. Trans. A*, Vol. 15A, 1984, pp. 2175-2183.
- Chan, C. L., Mazumder, J., and Chen, M. M., "Three-Dimensional Axisymmetry Model for Convection in Laser Melted Pools," *Materials Science and Technology*, Vol. 3, 1987.
- Fu, B., and Ostrach, S., "Numerical Solutions of Thermocapillary Flows in Floating Zones," *Transport Phenomena in Materials Processing*, ASME, PED, Vol. 10, HTD-Vol. 29, 1983.
- Cowley, S. J., and Davis, S. H., "Viscous Thermocapillary Convection at High Marangoni Number," *J. Fluid Mechanics*, Vol. 135, 1983, pp. 175-188.
- Chan, C. L., "Thermocapillary Convection During Laser Surface Heating," Ph.D. Thesis, University of Illinois at Urbana-Champaign, 1986.
- White, F. M., *Viscous Fluid Flow*, McGraw-Hill, New York, 1974.

APPENDIX

Substituting the coordinate stretching (equation (19)) into the energy equations (equations (15)-(18)), the systems of governing equations become

$$\tilde{g}_0'' + \tilde{f}_1(\tilde{z}^0/\text{Pr})\tilde{g}_0' = 0 \quad (\text{A1})$$

$$\tilde{g}_1'' + \tilde{f}_1(\tilde{z}^0/\text{Pr})\tilde{g}_1' - 2 \frac{\tilde{f}_1'(\tilde{z}^0/\text{Pr})}{\text{Pr}} \tilde{g}_1^0 = 0 \quad (\text{A2})$$

and the boundary conditions are

$$\tilde{z}^0 = 0, \quad \tilde{g}_0' = \tilde{g}_1' = -1$$

$$\tilde{z}^0 \rightarrow \infty, \quad \tilde{g}_0^0, \quad \tilde{g}_1^0 \rightarrow 0 \quad (\text{A3})$$

$\tilde{f}_1(\tilde{z}^0/\text{Pr})$ tends to $\tilde{f}_1(\infty)$ as Pr goes to zero. It can be shown that $\tilde{f}_1'(\tilde{z}/\text{Pr})/\text{Pr}$ behaves like a Dirac delta function. For the plane two-dimensional case

$$\tilde{f}_1 = 1 - e^{-\tilde{z}} \quad (\text{A4})$$

so that

$$\frac{\tilde{f}'_1(\tilde{z}^o/Pr)}{Pr} = \frac{e^{-\tilde{z}^o/Pr}}{Pr} \quad (A5)$$

Consider the definite integral

$$\int_0^{-Pr \log Pr} \frac{e^{-\tilde{z}^o/Pr}}{Pr} d\tilde{z}^o = 1 - Pr \quad (A6)$$

As Pr goes to zero, $-Pr \log Pr$ also goes to zero, but the integral goes to 1. Furthermore, the definite integral

$$\int_0^\infty \frac{e^{-\tilde{z}^o/Pr}}{Pr} d\tilde{z}^o = 1 \quad (A7)$$

The contribution of the function $\exp(-\tilde{z}^o/Pr)/Pr$ to the in-

tegral is confined in the narrow region $0 \leq \tilde{z}^o < -Pr \log Pr$. Thus, $\tilde{f}'_1(\tilde{z}^o/Pr)/Pr$ behaves like a Dirac delta function. A similar situation occurs for the axisymmetric case but with a different strength of the Dirac delta function. It can be shown easily for both plane two-dimensional and axisymmetric cases that

$$\frac{\tilde{f}'_1(\tilde{z}^o/Pr)}{Pr} = \tilde{f}_\infty \delta(\tilde{z}^o). \quad (A8)$$

Substituting $\tilde{f}_1(\tilde{z}^o/Pr) = \tilde{f}_\infty$ and $\tilde{f}'_1(\tilde{z}^o/Pr)/Pr = \tilde{f}_\infty \delta(\tilde{z}^o)$ into equations (A1) and (A2) will give the system equations (20)–(22).

Mixed Convection in a Liquid-Saturated Porous Medium

D. C. Reda

Sandia National Laboratories,
Albuquerque, NM 87185
Mem. ASME

An experimental and numerical investigation of mixed convection phenomena about a finite-length, vertical, cylindrical heat source in a uniform, liquid-saturated, porous medium was conducted. Buoyancy-induced upflow about the heat source was systematically altered by the superposition of vertical, pressure-driven flows which opposed the buoyancy-induced fluid motion. The evolution of the mixed convection velocity and thermal fields with increasing magnitude of the imposed-flow Peclet number are reported. The ratio of the natural convection Rayleigh number Ra to the imposed-flow Peclet number Pe is shown to be the nondimensional parameter that characterizes the relative influence of buoyancy-induced to pressure-driven fluid motion. Using total disappearance of buoyancy-induced upflow as the criterion, the transition from mixed to forced convection, for opposing flows, is numerically predicted to occur for $|Ra/Pe| \approx 1/2$, independent of the heat source length or power input.

Introduction

The subject of this paper is the study of nonisothermal, buoyancy-induced flows in a liquid-saturated porous medium subjected to superimposed, pressure-driven flows that oppose the buoyancy-induced fluid motion. The Reynolds number based on area-averaged superimposed pore velocity and average particle size always remains less than unity to ensure the applicability of Darcy's law.

Interest in this topic has increased in recent years due primarily to its impact on various engineering problems. Some notable examples include nuclear waste isolation in geologic repositories, geothermal energy extraction, thermal energy storage in underground aquifers, and thermal insulation effectiveness in the presence of leakage.

Natural convection in liquid-saturated porous media has been studied extensively, both experimentally, e.g., the references given by Reda (1983, 1986a) and Prasad (1985), and theoretically, e.g., the review articles by Combarous and Bories (1975) and Cheng (1978). On the contrary, the problem of mixed convection in liquid-saturated porous media remains virtually unexplored experimentally and investigated to only a limited extent theoretically.

Experimental investigations are limited to the works of Elder (1967), Combarous and Bia (1971), and Schrock and Laird (1976). Analytically, this problem has been studied by Wooding (1963), Burns et al. (1977), Cheng (1977a, 1977b, 1982), Troncoso and Kassoy (1983), Minkowycz et al. (1984), and Haajizadeh and Tien (1984). Numerical solutions to problems involving mixed convection in fluid-saturated porous media have been published by Elder (1967), Sutton (1970), Combarous and Bia (1971), Burns et al. (1977), Troncoso and Kassoy (1983), Haajizadeh and Tien (1984), and Ranganathan and Viskanta (1984). All of these investigators employed finite difference techniques to generate solutions. To date, no applications of finite element techniques to the stated problem area have been reported.

In the present work, a combined experimental and finite element numerical study was conducted using a vertically oriented annular geometry as the flow region of interest. Buoyancy-driven flow was induced by a constant heat flux applied along a section of the annulus inner boundary, while superimposed flows were forced vertically downward through

the annulus by a constant pressure gradient imposed over the vertical extent of the test region. Of special interest were those cases where the strengths of the buoyancy-induced upflow and the superimposed downflow were approximately matched (i.e., the ratio of Rayleigh number to Peclet number was order one) such that a closed, recirculating flow region formed adjacent to the heat source. The presence of trapped vortical cells formed in this manner, and the associated phenomena of pore flow "separation" from and "reattachment" to an impermeable boundary adjacent to a liquid-saturated porous medium, have not been previously investigated.

Experimental Approach and Test Conditions

The experimental investigation was carried out in an axisymmetric test vessel shown schematically in Fig. 1. The vertical annular region containing the saturated porous medium had a radial gap width of $\Delta r = 20.96$ cm and was bounded by

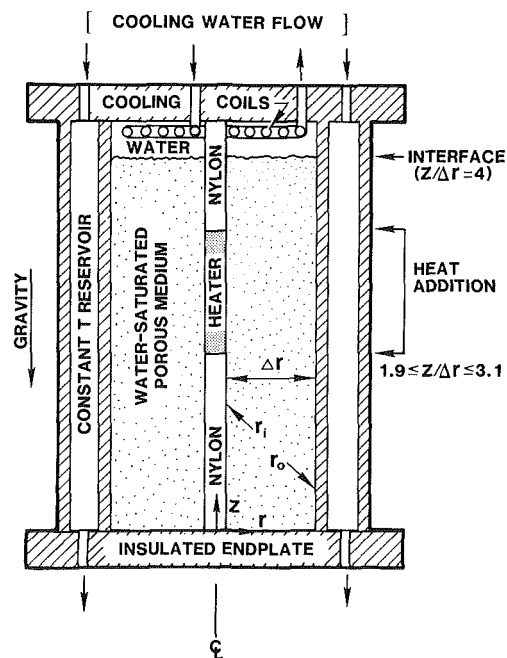


Fig. 1 Schematic of experimental apparatus

Contributed by the Heat Transfer Division for publication in the JOURNAL OF HEAT TRANSFER. Manuscript received by the Heat Transfer Division January 13, 1987.

an inner cylinder of radius $r_i = 0.95$ cm and a concentric outer cylinder of radius $r_o = 21.91$ cm. The height of the porous region was set at four times the gap width, $h = 83.84$ cm.

The inner cylinder was comprised of a resistance heater embedded in a steel jacket and supported above and below by nylon insulating sections. The heated section of the cylinder was located vertically between $1.9 \leq Z/\Delta r \leq 3.1$. Power input to the heater was measured by a wattmeter and maintained at a constant 50 W via a feedback loop incorporating a microcomputer and a stepping-motor-controlled variac. Power dissipation in the heater was $P = 198.8$ W/m.

A liquid layer was maintained above the porous region to provide a constant-pressure, permeable boundary condition. The fluid in this region was maintained at a constant temperature of 21.5°C through use of an immersed cooling coil linked, in a closed loop, to a constant-temperature bath. The outer circumference of the test vessel was surrounded by an annular reservoir, the temperature of which was also maintained at 21.5°C by the continual circulation of cooling water from a second constant-temperature bath.

Superimposed downflows within the porous region were created by introducing pressurized liquid (at 21.5°C) into the overlying fluid layer through ports in the upper boundary, while simultaneously withdrawing fluid from screen-covered bleed holes on the lower boundary. The superimposed volumetric flow rate Q was maintained constant with a pressure regulator on the inflow boundary and a micrometer-adjusted flow control valve immediately downstream of the exit boundary. Measurements of the volumetric flow rate through the apparatus were used to calculate the area-averaged superimposed pore velocity \bar{V}_p

$$\bar{V}_p = \frac{Q}{\pi(r_o^2 - r_i^2)\phi} \quad (1)$$

It should be noted that several cases involving superimposed upflows were also investigated and limited results for these cases are reported here. Hence, a sign convention is adopted, wherein negative values for \bar{V}_p denote superimposed downflow and positive values correspond to superimposed upflow.

The porous medium used in the present study consisted of solid glass beads (20 Mesh), essentially spherical in shape, with an average particle diameter $\bar{d} = 650$ μm . The diameter distribution for this matrix material was reported earlier by Reda (1986a). All properties of this medium, including porosity ($\phi = 0.34$), permeability ($k = 611 \times 10^{-12}$ m^2) and effective thermal conductivity ($K_e = 0.87$ $\text{W/m}\cdot^\circ\text{C}$) were measured. Distilled, deaerated water was used as the saturating fluid. Details of the instrumentation and data acquisition system are given by Reda (1983, 1986a).

In a supporting study, Reda (1986b) reported experimental results on transient and steady-state free convection

phenomena obtained with the described test facility. In these natural convection experiments, for a heater power level of $P = 198.8$ W/m, a Rayleigh number of 160 (based on Δr) or 7.25 (based on r_i) was measured. In the present work, this baseline natural convection flow was combined with a range of superimposed flow velocities to produce a spectrum of mixed convection flow fields. Average superimposed pore velocities from $\bar{V}_p = -391$ $\mu\text{m/s}$ to $+233$ $\mu\text{m/s}$ were used to produce Peclet numbers (based on r_i) from -17.9 to $+10.7$. The ratio (Ra/Pe) was thus varied from ∞ to -0.41 for superimposed downflows (12 cases) and from ∞ to $+0.68$ for superimposed upflows (3 cases). The maximum value for the Reynolds number $|\rho \bar{V}_{p,\text{max}} \bar{d}/\mu|$ was 0.26, assuring the existence of Darcy flow under all test conditions.

Modeling and Numerical Approach

The physical modeling and numerical approach used here are described by Reda (1986a) and are based on the extensive computational research of Gartling (1977), Hickox and Gartling (1981), and Gartling and Hickox (1982, 1985). Readers are referred to these sources for details.

Experimental Uncertainties and Numerical Accuracy

The three physical parameters measured during these experiments were power input to the heater, superimposed volumetric flow rate through the annular porous region, and temperatures throughout the annular porous region. Power input, measurable to ± 0.01 W, was held constant at a nominal level of 50 W, within limits of ± 0.1 W, for an accuracy of ± 0.2 percent. Superimposed volumetric flow rates were always ≥ 100 ml/min and were measurable to the nearest 1 ml/min, for an accuracy of ± 1 percent or better. Temperatures were monitored and recorded to the nearest 0.1°C , but data accuracy was limited to $\sim 1^\circ\text{C}$ by probe conduction effects.

The numerical simulations of the fluid flows and heat transfer within the annular porous region were carried out by using a finite element mesh of 543 elements; see Fig. 3 of Reda (1986b). The distribution of elements within the annular region was designed to produce increased resolution in the high-gradient regions near the heated cylinder. The final mesh configuration was the result of a mesh refinement study and is quite conservative in its ability to resolve the details of the fluid and thermal fields.

Results and Discussion

The results of the experimental and numerical work have been used in a complementary way to improve our understanding of the mixed convection problem. The experimental measurements provide basic information on the mixed convec-

Nomenclature

\bar{d} = average particle diameter	Δr = annular gap width $= (r_o - r_i)$	μ = viscosity
g = acceleration of gravity	Ra = Rayleigh number based on length $r_i = [g\beta k r_i \Delta T / \alpha \nu]$	ν = kinematic viscosity
h = test region height	T = temperature	ρ = density
k = permeability	ΔT = characteristic temperature difference $= (T_i - T_o)$	ϕ = porosity
K_e = effective thermal conductivity of fluid-solid mixture	ΔT_z = see equation (2)	
P = power per unit length	\bar{V}_p = area-averaged superimposed pore velocity; see equation (1)	Subscripts
Pe = Peclet number based on length $r_i = (\bar{V}_p r_i / \alpha)$	Z = vertical coordinate	i = at inner radius
Q = superimposed fluid volumetric flow rate	α = effective thermal diffusivity	max = maximum
r = radial coordinate	β = coefficient of thermal expansion	o = at outer radius
r_i = inner radius		r_i = based on r_i
r_o = outer radius		Δr = based on Δr
		TR = transition from mixed to forced convection

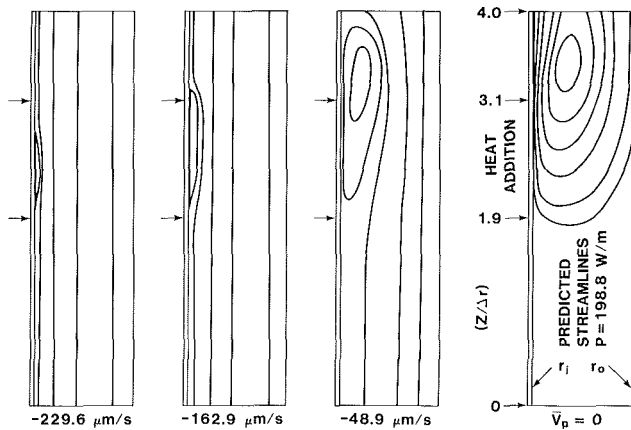


Fig. 2 Predicted streamline patterns, superimposed downflows

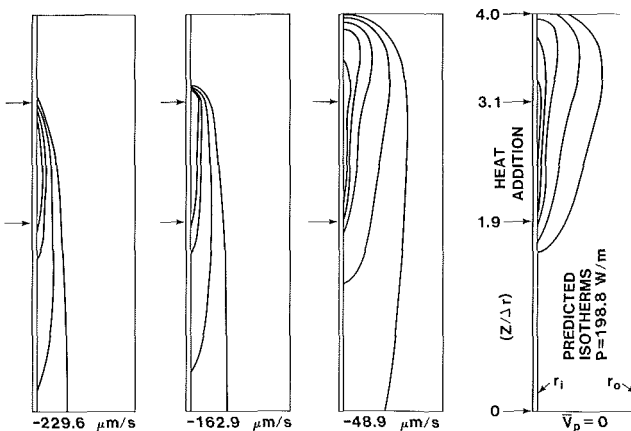


Fig. 3 Predicted isotherm patterns, superimposed downflows

tion thermal fields which develop within the porous medium. Direct comparison of measured temperature profiles with predictions then allows for verification of the mathematical model and numerical approach. The numerical results, in turn, provide detailed descriptions of the mixed convection velocity fields, results which would be most difficult to obtain experimentally. Evolution of mixed convection phenomena with increasing strength of the superimposed flow can thus be explored numerically with confidence, e.g., to investigate the transition from the mixed to the forced convection regime.

A visual summary of the present problem is obtained from Figs. 2 and 3, where plots of the stream function and isotherms generated by the numerical procedure are presented. The changing features of the velocity and thermal fields with variations in magnitude of the superimposed downflow pore velocity are quite evident. (Note: These plots are meant to provide visual overviews and relative comparisons only, hence individual contours are not labeled; quantitative results and comparisons of predictions with measurements will be given in subsequent figures.)

For the case of pure natural convection ($\bar{V}_p = 0$) the buoyancy-induced velocity field produces a series of streamlines that enter into and return from the overlying fluid layer. The thermal energy produced by the heat source is convected upward along the inner cylinder forming a plumelike thermal field. Detailed results for this baseline case were reported by Reda (1986b).

A complex evolution was observed in the mixed convection flow field as the strength of the imposed downflow was continually increased. The buoyancy-induced upflow along the inner cylinder was at first retarded, then stagnated, and

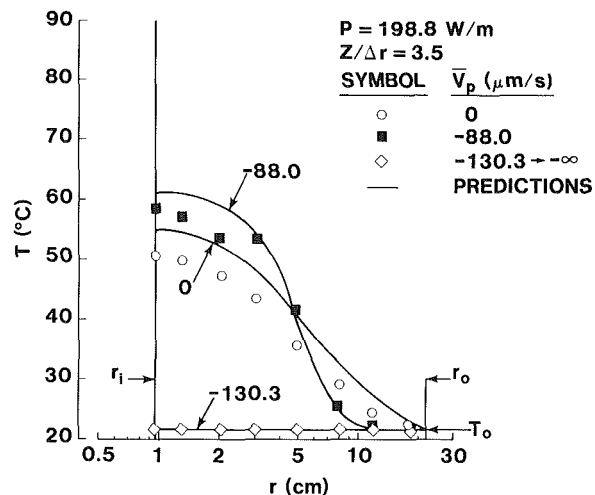


Fig. 4 Radial temperature profiles, $Z/\Delta r = 3.5$, superimposed downflows

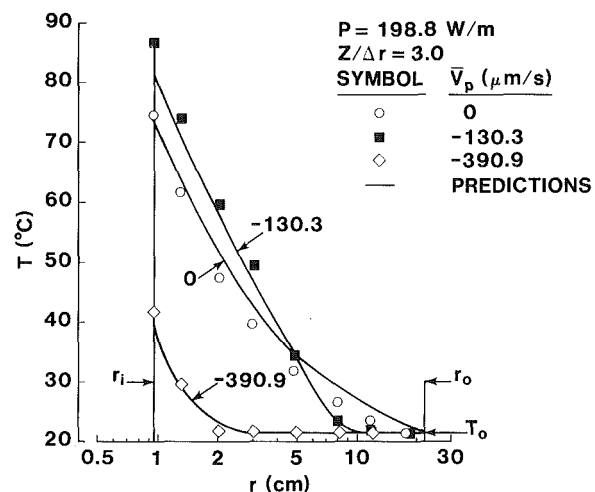


Fig. 5 Radial temperature profiles, $Z/\Delta r = 3$, superimposed downflows

ultimately suppressed. As a result, a closed recirculation region was predicted to form, the size of which decreased with increasing downflow Peclet number. For cases where a closed cell (bounded on one side by r_i) was predicted to exist, the Darcy-flow streamline along the r_i boundary was predicted to "separate" from this impermeable boundary at the uppermost extent of the cell and "reattach" to this same solid boundary at the lower extreme of the cell. In other words, the local pore velocity along the r_i boundary was predicted to change direction at each of two locations, upflow occurring along r_i between reattachment and separation, with downflow along r_i at all other elevations. The thermal fields for these cases showed an evolution from a plumelike field to a thermal boundary layer response, with the boundary layer developing downward along the inner cylinder. The occurrence of a recirculation cell for the $\bar{V}_p < 0$ flows provided a useful criterion for delimiting the mixed and forced convection regimes. This issue will be discussed in detail later in this section.

The quality and accuracy of the numerical results were assessed by comparisons with the measured temperature fields. Shown in Figs. 4–7 are radial temperature profiles, at each of four different vertical locations within the annulus, which illustrate the influence of superimposed downflow. In each figure, data are presented for the reference case of pure natural convection, for the case of a strong imposed downflow corresponding to a forced convection state, and for an in-

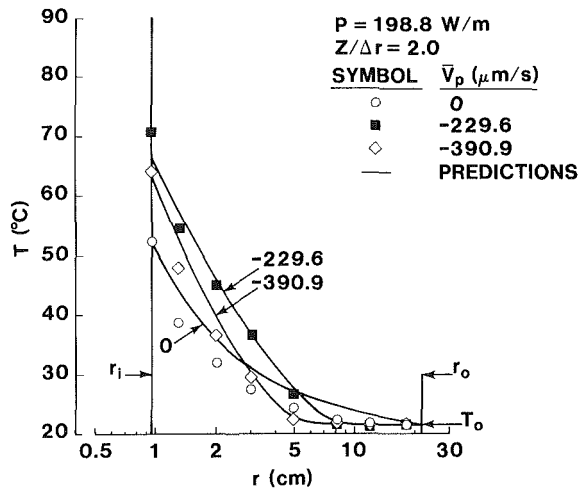


Fig. 6 Radial temperature profiles, $Z/\Delta r=2$, superimposed downflows

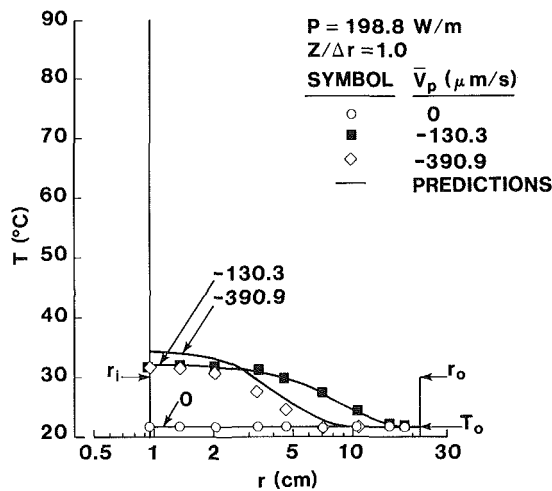


Fig. 7 Radial temperature profiles, $Z/\Delta r=1$, superimposed downflows

intermediate imposed flow corresponding to a mixed convection state. The intermediate \bar{V}_p value in each of these figures corresponds to the situation in which a local maximum of the inner cylinder surface temperature was attained; further increases in the magnitude of the imposed downflow caused the wall temperature to decrease (or, in the case of Fig. 7, no longer to increase).

Beginning with the $Z/\Delta r=3.5$ plane (above the heat source), it is apparent that as the imposed downflow velocity was changed from zero to a value of $\bar{V}_p = -88 \mu\text{m/s}$, temperatures at, and adjacent to, the inner cylinder boundary increased due to the retardation of the buoyancy-induced upflow. Simultaneously, the lateral extent of the thermally influenced region was reduced, i.e., the outer extremity of the convection cell was compressed inward as the imposed downflow bypassed this "obstacle" in its path to the lower boundary. A small additional increase in $|\bar{V}_p|$ beyond this state resulted in a rapid collapse of the thermal profile to a uniform temperature level equal to that of the injected liquid, an observation that clearly illustrates cell suppression to an elevation below the $Z/\Delta r=3.5$ plane.

Progressing downward to the $Z/\Delta r=3.0$ plane (near the top of the heated zone), we see in Fig. 5 a similar response of the radial temperature profile to increasing strength of the imposed downflow. Temperatures increased near the inner boundary under mixed convection conditions (indicating

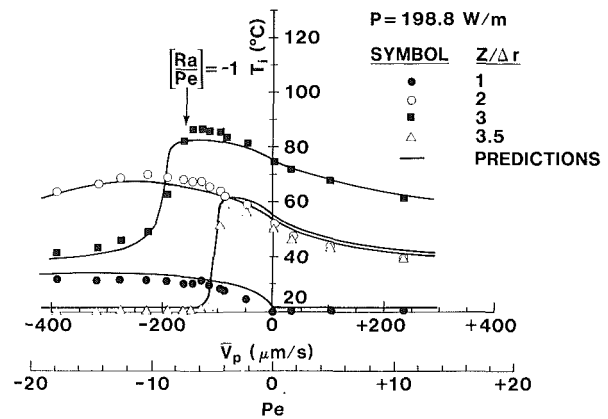


Fig. 8 Inner cylinder surface temperatures versus superimposed flow conditions

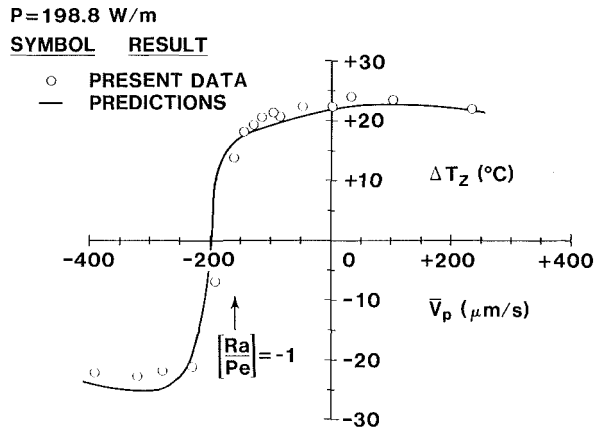


Fig. 9 Vertical temperature difference along heated surface as a function of superimposed pore velocity

upflow retardation), coupled with a corresponding reduction in the lateral extent of the thermally influenced region (indicating downflow bypass). In this instance, however, the thermal profile adjacent to the heated surface evolved into a thermal boundary layer profile of thickness approximately 1 cm under conditions of strong imposed downflow; this observation is consistent with upflow suppression to an elevation below the $Z/\Delta r=3.0$ plane. Figure 6 shows a like response at the $Z/\Delta r=2.0$ plane, near the bottom (downstream end) of the heated zone, the thermal boundary layer thickness having increased by a factor of approximately 4 for flow along the heated surface (top to bottom) under conditions of forced convection.

Figure 7 shows radial temperature profiles measured on the $Z/\Delta r=1.0$ plane, below the heat-addition region. Under natural convection conditions, temperature was constant across the annulus, equal to the value imposed at the outer boundary. Under mixed convection conditions, which resulted in the formation of a recirculating flow, or cell, above this plane, the temperature profile assumed the appearance of a broad thermal wake, indicative of flow bypass around a "heated obstacle," i.e., the cell. Under conditions of forced convection downflow, wherein no recirculating flow region existed above this plane, the radial temperature distribution evolved into a thermal wake of reduced lateral extent, consistent with the flow downstream of a heated cylinder immersed in, and aligned with, a uniform stream. Qualitative and quantitative agreement between numerical predictions and measurements is seen to be quite good for all cases.

We focus attention now on the evolution of the mixed convection thermal field along the inner (r_i) boundary. Figure 8 shows measured and predicted temperatures along the r_i boundary, at each of four vertical locations, as a function of superimposed flow conditions. (Note: Pe here is based on r_i as the length scale and $Pe = 4.57 \times 10^4 \bar{V}_p$ throughout, where \bar{V}_p in this conversion has the units of m/s.) Recall that $Z/\Delta r = 1$ is below the heat source, the $Z/\Delta r = 2$ and 3 stations are near the bottom and top of the heated region, respectively, and the $Z/\Delta r = 3.5$ station is above the heat source, essentially 1/2 the distance between the top of the heated zone and the permeable upper boundary.

For superimposed upflows, T_i values on the $Z/\Delta r = 1$ plane, upstream of the heated zone, were equal to the temperature of the injected liquid. For all positive Pe values, T_i values on the heated surface increased in the direction of flow, from the $Z/\Delta r = 2$ to the $Z/\Delta r = 3$ elevation. At all measurement stations adjacent to, and above, the heat-input region, T_i values decreased monotonically from their natural convection values as Pe was increased from zero, consistent with the increased convective cooling of a constant-flux source. Measured and predicted results are seen to be in good agreement.

For superimposed downflows, as the magnitude of the Peclet number was increased, T_i values at elevations above, and adjacent to, the heat source initially increased, reached maximum values, then decreased. To interpret these downflow results better, we view first the $Z/\Delta r = 3.5$ measurement station (above the heat source) then progress sequentially downward in the direction of the superimposed flow to other measurement locations.

For $Z/\Delta r = 3.5$, T_i steadily increased above its natural convection value as $|Pe|$ was increased from zero to ≈ 4 , indicating a retardation of the thermally driven upflow along the r_i boundary. A maximum T_i value was reached at this location for $|Pe| \approx 4$, at which point a small additional increase in $|Pe|$ caused an abrupt reduction in T_i to a temperature equal to that of the injected liquid. This response is clearly indicative of local upflow stagnation at this elevation, followed by suppression of the upflow stagnation point to a location below $Z/\Delta r = 3.5$. The attainment of a maximum T_i value at any elevation above the heat source could thus potentially serve as an indicator of downflow separation from the r_i boundary. (This point will be discussed in more detail later, with Fig. 10.)

At an elevation of $Z/\Delta r = 3.0$, the $T_{i,max}$ state was seen to occur at an absolute value of the downflow Peclet number ~ 6 , while at the lower elevation of $Z/\Delta r = 2.0$, this state was not achieved until the magnitude of the downflow Peclet number had been increased to ~ 10 . Temperatures near the top and bottom of the heat source "crossed over" just after the $(Ra/Pe) = -1$ condition was reached, indicating downflow along some, or all, of the heat-addition region. The T_i value at $Z/\Delta r = 1$ was seen to rise above the ambient level for all $Pe < 0$ states, indicating the formation of a thermal wake downstream of the heat-addition region. As can be seen in Fig. 8, numerically predicted results were found to be in good agreement with measured values over the complete \bar{V}_p range investigated, further corroborating the overall picture of upflow retardation, stagnation, and cell suppression given by the streamlines and isotherms of Figs. 2 and 3. (It should be noted that measured steady-state thermal fields were found to be path independent. In a transient test, the $\bar{V}_p = -229 \mu\text{m/s}$ state relaxed back to the previously measured $\bar{V}_p = 0$ state upon cessation of the superimposed downflow.)

Figure 9 expands on the results of Fig. 8. Here we see a plot of the vertical temperature difference along the heated surface

$$\Delta T_z = T_i(\text{at } Z/\Delta r = 3) - T_i(\text{at } Z/\Delta r = 2) \quad (2)$$

as a function of the superimposed average pore velocity. For $\bar{V}_p > 0$, ΔT_z was seen to be positive, reaching a maximum measured value of $+24^\circ\text{C}$ for weak superimposed upflow,

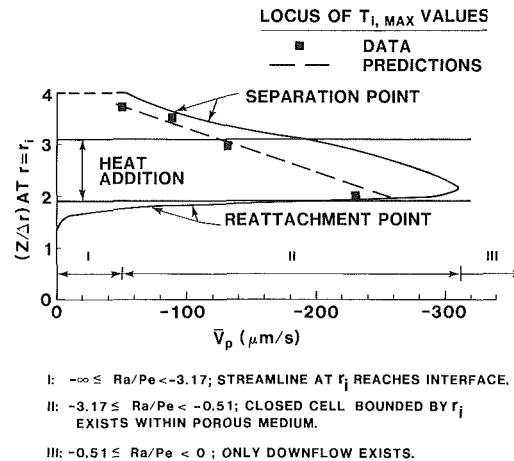


Fig. 10 Predicted flow reversal elevations along inner cylinder boundary as a function of superimposed pore velocity; definition of flow regimes and comparisons with thermal field results

where $(Ra/Pe) \approx 5$. For $\bar{V}_p < 0$, ΔT_z steadily decreased as $|\bar{V}_p|$ was increased. A rapid transition from positive to negative values for ΔT_z occurred just after the $(Ra/Pe) = -1$ condition was reached. A maximum negative value for ΔT_z of -23°C was measured for $(Ra/Pe) \approx -0.5$, essentially equal and opposite to the maximum upflow ΔT_z value.

In Fig. 10, we show the loci of predicted separation and reattachment point locations for the Darcy-flow streamline along the r_i boundary as a function of the superimposed downflow pore velocity. The vertical extent of the heat-addition region is shown for reference. Also shown is the locus of predicted maximum T_i "states," or values, in comparison with measured data. Each pairing of a \bar{V}_p value and a $Z/\Delta r$ elevation on this T_i locus corresponds to the attainment of the maximum T_i condition, at that particular elevation, as \bar{V}_p was varied from zero to minus infinity (recall Fig. 8).

Let us focus attention initially on the computed velocity field results. Three flow regimes, labeled I, II, and III, were found to exist. In the first regime, bounded by the conditions $-\infty \leq Ra/Pe < -3.17$, the upflow streamline along the r_i boundary reached the permeable interface at $Z/\Delta r = 4$, hence no separation point existed. Reattachment of a downflow streamline to the r_i boundary occurred everywhere within this regime, even for the natural convection case. (In the limit of $Pe = 0$, a very weak counterrotating cell, not shown in Fig. 2, was predicted to form below the heat-addition region.) In the second regime, given by $-3.17 \leq Ra/Pe < -0.51$, the upflow streamline along the r_i boundary stagnated somewhere below the permeable interface. In this regime, both a separation and a reattachment point were predicted to exist, i.e., a trapped, recirculating flow region was predicted to form immediately adjacent to the inner boundary. Throughout this regime, as $|Pe|$ was increased, the vertical distance between separation and reattachment was predicted to decrease. For $(Ra/Pe) = -1$, predicted separation and reattachment point locations approached the top and bottom of the heat-addition region, respectively. Cell height was driven to zero, at the $Z/\Delta r = 2.15$ location, as (Ra/Pe) approached a value of -0.51 . In the third regime, given by $-0.51 \leq Ra/Pe < 0$, only downflow was predicted to exist within the porous medium.

We now focus attention on the $T_{i,max}$ locus of Fig. 10 in an attempt to relate the thermal and velocity field results. Two general observations were made. First, this locus of $T_{i,max}$ states was predicted to be a linear function of \bar{V}_p , showing decreasing elevations as the magnitude of the superimposed pore velocity was increased, in good agreement with measured results. Second, this locus fell everywhere within the predicted recirculating flow region, but its location relative to the

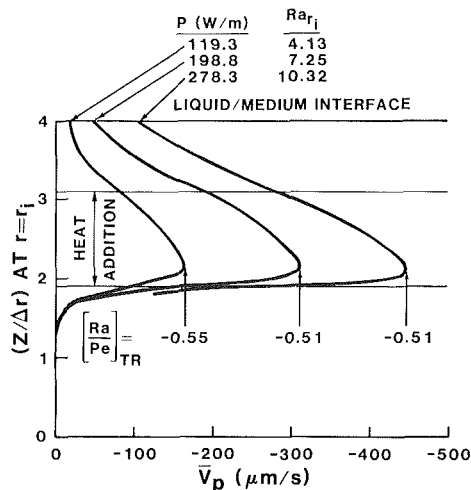


Fig. 11 Predicted flow reversal elevations along inner cylinder boundary as a function of superimposed pore velocity; finite length heated zone, Rayleigh number as the parameter

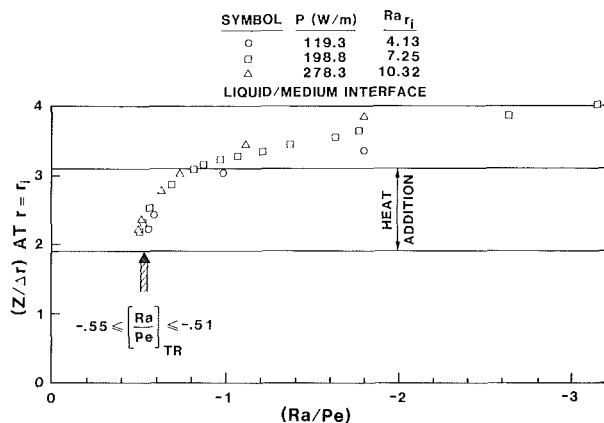


Fig. 12 Uppermost predicted flow reversal elevation along inner cylinder boundary as a function of Rayleigh-to-Peclet number ratio; finite length heated zone, Rayleigh number as the parameter

predicted separation and reattachment points was strongly dependent on the ratio of predicted cell height to heated length.

Expanding on this last point, we note that two distinct situations occurred within flow regime II. For any given \bar{V}_p value that resulted in the predicted separation point being *well above* the heat-addition region (cell height greater than heated length), the attainment of the $T_{i,max}$ condition was found to occur at an elevation just below separation. Intuitively, the vertical distance that the heated liquid was able to rise above its "origin" (the heat source), against the opposing flow, would be expected to be closely correlated with the upper extent of the cell. Hence, for such cases, measurement of the $T_{i,max}$ state could serve as a reasonable indicator of upflow stagnation, and thus of downflow separation.

On the other hand, for any \bar{V}_p value that resulted in the predicted separation point being *adjacent to* the heat-addition region (cell height less than heated length), attainment of the $T_{i,max}$ condition no longer occurred at an elevation in close proximity to separation. In fact, as $|\bar{V}_p|$ was increased, and the vertical dimension of the cell was reduced to an extent less than that of the heat-addition region, the attainment of the $T_{i,max}$ state (for each \bar{V}_p value) was seen to shift from the top to the bottom of the cell. In such cases, measurement of the $T_{i,max}$ state would not be a valid indicator of the downflow separation point.

Interpreting the predicted velocity field results in terms of the transition from mixed to natural convection is not straightforward. For opposing flows, mixed convection could be reasoned to exist throughout regime II and well into regime I. No precise definition of this transition, in terms of a limiting (Ra/Pe) value, can be given. Predicted cell disappearance, however, provides a clear demarcation of the transition from mixed to forced convection.

Having validated the physical modeling and numerical approach through detailed comparisons of predicted and measured thermal fields, it remains to apply this computational tool in order to: (1) show that the ratio (Ra/Pe) is, in fact, the correct dimensionless grouping for characterizing the relative influence of buoyancy-induced to pressure-driven fluid motion; and (2) demonstrate, using the cell-disappearance criterion, that the apparent limiting value of $(Ra/Pe) \approx -1/2$ is independent of both heat source strength and vertical physical extent. Radial temperature profiles measured adjacent to the heat source under mixed and forced convection conditions (Figs. 5 and 6) showed that lateral (or aspect-ratio) effects were clearly not important to these considerations.

In order to accomplish these final two objectives, extensive numerical computations were done for both the finite length heat source geometry studied here and the full-length heat source geometry of Reda (1983). For each geometry, three energy input levels were chosen, corresponding to cases wherein measurements of the Rayleigh number for pure natural convection had been made.

Figure 11 shows results for the finite length heat source. The ordinate and abscissa are the same as used in Fig. 10; power input is the parameter. The upper branch of each curve gives the locus of predicted separation point elevations as a function of superimposed pore velocity; the lower branch gives the locus of predicted reattachment point elevations. For a given power input, when these two branches converged to a single point, cell disappearance was predicted to occur. As expected, an increase in P , from 198 to 278 W/m, required a higher superimposed pore velocity to force all buoyancy-induced upflow to vanish; similarly, a reduction in P , from 198 to 119 W/m, required a lower superimposed pore velocity to achieve cell disappearance. However, in terms of the ratio $(Ra/Pe)_{TR}$, the transition from the mixed to the forced convection regime (denoted by the subscript TR) consistently occurred at a value of $\approx -1/2$.

For a given power input, Fig. 11 shows that the top of the convection cell was systematically suppressed in elevation as the strength of the superimposed downflow was increased, while the bottom of the cell remained essentially stationary, coincident with the bottom of the heat-addition region. Consequently, to test the hypothesis regarding the utilization of the ratio (Ra/Pe) to characterize mixed convection flows, we focus attention now on the upper branches of these three curves.

In Fig. 12, the predicted separation point elevations (shown here as individual symbols for clarity) are replotted as a function of the ratio (Ra/Pe) . As before, power input is the parameter. For all locations *adjacent to* the heat source, these results were found to collapse to a single curve. The top of the cell approached the top of the heat source when (Ra/Pe) was ≈ -1 , and cell disappearance occurred when (Ra/Pe) was $\approx -1/2$, independent of power input. (For elevations *above* the heat source, separation point locations were found to depend on power input, as discussed earlier with Fig. 10.)

Figures 13 and 14 show similar results for the case of a full-length heat source. For a given power input, the predicted separation point elevation was seen to be systematically suppressed toward the lower (outflow) boundary as the magnitude of the superimposed pore velocity was increased. Upflow, when present, was always predicted to originate at

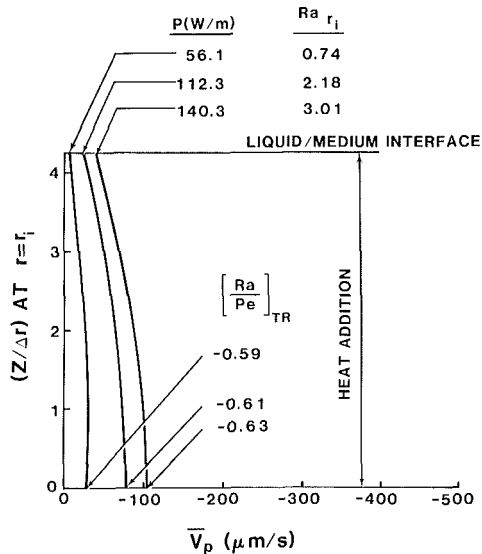


Fig. 13 Predicted flow reversal elevation along inner cylinder boundary as a function of superimposed pore velocity; full-length heated zone, Rayleigh number as the parameter

SYMBOL	P(W/m)	Ra r _i
○	56.1	0.74
□	112.3	2.18
△	140.3	3.01

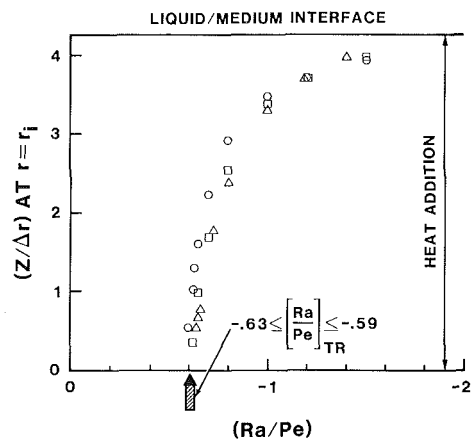


Fig. 14 Predicted flow reversal elevation along inner cylinder boundary as a function of Rayleigh-to-Peclet number ratio; full-length heated zone, Rayleigh number as the parameter

the bottom of the heated zone, itself coincident with the lower boundary, hence no reattachment point locations existed for this problem. As with the finite-length heat source, higher power input required a larger superimposed pore velocity to force the buoyancy-induced upflow to vanish. Cell disappearance, however, consistently occurred for $(Ra/Pe) \approx -1/2$. These full-length heat source results were also found to collapse to a single curve when plotted versus (Ra/Pe) , as shown in Fig. 14. Buoyancy-induced upflow reached the overlying liquid layer whenever the magnitude of the Rayleigh number was at least twice as large as the magnitude of the Peclet number. A rapid suppression of the top of the convection cell, downward along the heat source, was predicted to begin for the condition $(Ra/Pe) \approx -1$, followed by cell disappearance for $(Ra/Pe) \approx -1/2$, both observations being consistent with those noted in Fig. 12.

Figure 15 summarizes present findings. The transition from the mixed convection regime to the forced convection regime, for opposing flows about vertical, cylindrical heat sources in

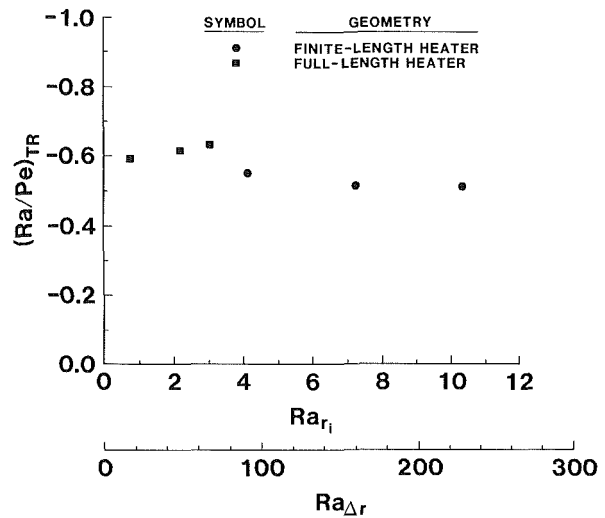


Fig. 15 Rayleigh-to-Peclet number ratio for predicted upflow disappearance as a function of Rayleigh number; definition of transition from mixed to forced convection

liquid-saturated permeable media, occurs for an absolute value of the ratio of Rayleigh number to Peclet number of approximately 0.5, independent of heat source length or power input.

The only other investigator to offer a quantitative definition for the transition from mixed to forced convection in uniform liquid-saturated porous media was Cheng (1977a). Based on predicted heat transfer rates, obtained from similarity solutions for opposing flows about *planar, inclined* surfaces, Cheng defined this transition in terms of a limiting Grashof-to-Reynolds number ratio (both dimensionless parameters based on an identical length scale); the limiting value of this ratio was found to be 0.15. It can be shown that Cheng's ratio of dimensionless parameters is identical to the (Ra/Pe) ratio invoked herein. Hence, the magnitude of Cheng's analytically derived limit (for planar, inclined surfaces) was found to be consistent with the magnitude of the numerically predicted limit (for vertical, cylindrical surfaces) presented here.

Conclusions

The problem of mixed convection in liquid-saturated porous media was investigated both experimentally and numerically. The geometry used in the present study was a vertical annular region bounded by coaxial cylinders. The annular region was filled with a liquid-saturated porous medium. The inner cylinder was comprised of a finite length, constant heat flux source mated above and below to insulating sections; the outer cylinder was maintained isothermal. The vertical boundaries of the annular test region were impermeable, while the horizontal boundaries were permeable. The buoyancy-induced upflow, which occurred adjacent to and above the heated zone, was systematically altered by the superposition of pressure-driven flows forced vertically downward through the annulus.

All experiments were conducted in the Darcy-flow (noninertial) regime, for a particle-to-heated cylinder diameter ratio of order 10^{-2} . Detailed measurements were made of the resultant steady-state thermal fields along the inner cylinder boundary and radially across the annulus under conditions of natural, mixed, and forced convection. A finite element computer code, based on the work of Gartling and Hickox (1982, 1985), was employed to predict numerically such flows and results were verified through comparisons of predicted and measured

thermal fields. Specific observations made during this research are outlined below:

1 In the presence of superimposed downflows, the mixed convection velocity fields showed the buoyancy-induced upflow to be at first retarded, then stagnated, and ultimately suppressed with increasing magnitude of the downflow Peclet number. The corresponding thermal fields showed an evolution from a plumelike response under natural convection conditions, to a suppressed plume with both upward and downward convection of thermal energy under mixed convection conditions, to a thermal boundary layer response under forced convection conditions, the thermal boundary layer thickness increasing in the downward direction.

2 Under superimposed downflow/mixed convection conditions, the occurrence of a maximum temperature at the inner cylinder boundary (at elevations above the heat source) was found to correlate with the prediction of buoyancy-induced upflow stagnation (i.e., with downflow separation).

3 The ratio of the Rayleigh number Ra to the Peclet number Pe was shown to be the nondimensional parameter that characterizes the relative influence of buoyancy-induced to pressure-driven fluid motion.

4 Using total disappearance of buoyancy-induced upflow as the criterion, the transition from mixed to forced convection, for opposing flows about vertical cylindrical heat sources in liquid-saturated porous media, was predicted to occur for $|Ra/Pe| \approx 1/2$, independent of the heat source length or power input.

Acknowledgments

This work was performed at Sandia National Laboratories, supported by the U.S. Department of Energy, under contract number DE-AC04-76DP00789.

References

Burns, P. J., Chow, L. C., and Tien, C. L., 1977, "Convection in a Vertical Slot Filled With Porous Insulation," *Int. J. Heat Mass Transfer*, Vol. 20, pp. 919-926.

Cheng, P., 1977a, "Combined Free and Forced Convection Flow About Inclined Surfaces in Porous Media," *Int. J. Heat Mass Transfer*, Vol. 20, pp. 807-814.

Cheng, P., 1977b, "Similarity Solutions for Mixed Convection From Horizontal Impermeable Surfaces in Saturated Porous Media," *Int. J. Heat Mass Transfer*, Vol. 20, pp. 893-898.

Cheng, P., 1978, "Heat Transfer in Geothermal Systems," *Advances in Heat Transfer*, Vol. 14, pp. 1-105.

Cheng, P., 1982, "Mixed Convection About a Horizontal Cylinder and a Sphere in a Fluid-Saturated Porous Medium," *Int. J. Heat Mass Transfer*, Vol. 25, pp. 1245-1247.

Combarous, M. A., and Bia, P., 1971, "Combined Free and Forced Convection in Porous Media," *Soc. Petroleum Eng. Journal*, Vol. 11, pp. 399-405.

Combarous, M. A., and Bories, S. A., 1975, "Hydrothermal Convection in Saturated Porous Media," *Advances in Hydroscience*, Vol. 10, pp. 231-307.

Elder, J. W., 1967, "Steady Free Convection in a Porous Medium Heated From Below," *J. Fluid Mechanics*, Vol. 27, pp. 29-48.

Gartling, D. K., 1977, "Convective Heat Transfer Analysis by the Finite Element Method," *Comp. Meth. Applied Mech. Eng.*, Vol. 12, pp. 365-382.

Gartling, D. K., and Hickox, C. E., 1982, "MARIAH—A Finite Element Computer Program for Incompressible Porous Flow Problems: Theoretical Background," Sandia National Laboratories Report SAND79-1622.

Gartling, D. K., and Hickox, C. E., 1985, "A Numerical Study of the Applicability of the Boussinesq Approximation for a Fluid-Saturated Porous Medium," *Int. J. Num. Meth. Fluids*, Vol. 5, pp. 995-1013.

Haajizadeh, M., and Tien, C. L., 1984, "Combined Natural and Forced Convection in a Horizontal Porous Channel," *Int. J. Heat Mass Transfer*, Vol. 27, pp. 799-813.

Hickox, C. E., and Gartling, D. K., 1981, "A Numerical Study of Natural Convection in a Horizontal Porous Layer Subjected to an End-to-End Temperature Difference," *ASME JOURNAL OF HEAT TRANSFER*, Vol. 103, pp. 797-802.

Minkowycz, W. J., Cheng, P., and Hirschberg, R. N., 1984, "Nonsimilar Boundary Layer Analysis of Mixed Convection About a Horizontal Heated Surface in a Fluid-Saturated Porous Medium," *Int. Comm. Heat Mass Transfer*, Vol. 11, pp. 127-141.

Prasad, V., Kulacki, F. A., and Keyhani, M., 1985, "Natural Convection in Porous Media," *J. Fluid Mechanics*, Vol. 150, pp. 89-119.

Ranganathan, P., and Viskanta, R., 1984, "Mixed Convection Boundary-Layer Flow Along a Vertical Surface in a Porous Medium," *Numerical Heat Transfer*, Vol. 7, pp. 305-317.

Reda, D. C., 1983, "Natural Convection Experiments in a Liquid-Saturated Porous Medium Bounded by Vertical Coaxial Cylinders," *ASME JOURNAL OF HEAT TRANSFER*, Vol. 105, pp. 795-802.

Reda, D. C., 1986a, "Natural Convection Experiments in a Stratified Liquid-Saturated Porous Medium," *ASME JOURNAL OF HEAT TRANSFER*, Vol. 108, pp. 660-666.

Reda, D. C., 1986b, "Natural Convection Experiments With a Finite-Length, Vertical, Cylindrical Heat Source in a Water-Saturated Porous Medium," *Nuclear and Chemical Waste Management Journal*, Vol. 6, pp. 3-14.

Schrock, V. E., and Laird, A. D. K., 1976, "Physical Modeling of Combined Forced and Natural Convection in Wet Geothermal Formations," *ASME JOURNAL OF HEAT TRANSFER*, Vol. 98, pp. 213-220.

Sutton, F. M., 1970, "Onset of Convection in a Porous Channel With Net Through Flow," *Physics of Fluids*, Vol. 13, pp. 1931-1934.

Troncoso, J., and Kassoy, D. R., 1983, "An Axisymmetric Model for the Charging of a Liquid-Dominated Geothermal Reservoir," *Int. J. Heat Mass Transfer*, Vol. 26, pp. 1389-1401.

Wooding, R. A., 1963, "Convection in a Saturated Porous Medium at Large Rayleigh Number or Peclet Number," *J. Fluid Mechanics*, Vol. 15, pp. 527-544.

M. Sugawara

Associate Professor,
Department of Mechanical Engineering,
Akita University,
Akita 010, Japan

H. Inaba

Associate Professor,
Department of Mechanical Engineering,
Kitami Institute of Technology,
Kitami 090, Japan

N. Seki

President,
Hokkaido Polytechnic College,
Zenibako 047-02,
Hokkaido, Japan

Effect of Maximum Density of Water on Freezing of a Water-Saturated Horizontal Porous Layer

This experiment simulates the freezing of water in a layer of earth by the use of a porous bead layer. The layer is cooled from above. The beads are 1, 5, and 11-mm-dia glass and 11-mm-dia steel. When the predominant heat transfer mode in an unfrozen layer is conduction, the freezing rate is not affected by the bead diameter. However, in natural convection the freezing rate is greatly affected by the maximum density of water at 4°C. An approximate numerical analysis which does not treat the maximum density effects predicts well the freezing rate in the range of 0°C < T₂ < 4°C and 26°C < T₂ (T₂ = the lower plate temperature).

Introduction

Understanding the freezing of water in a porous earth layer is of engineering and scientific importance. For example, freezing in soil around an LNG or LPG storage tank can often heave the tank, leading to its eventual destruction; or such freezing can result in the breakdown of a house or a road. In a positive light, freezing a moist soil has recently begun to be used as part of a new technique for underground digging.

Behavior of water movement in an unfrozen layer plays a key role in predicting the freezing rate. For the case of when water saturation is unity, i.e., when the pore fraction in a porous layer is fully saturated with water, it can be recognized generally that water moves in accordance with Darcy's law.

Frivik et al. [1] investigated the combined problem of water and heat flow for freezing water in soil around a cooled pipe analytically and experimentally. Okada [2] reported an analysis to approximate freezing in the porous media around two cooled pipes. Both of these freezing models are examples of freezing in porous media through which water moves with Darcy's flow producing forced convection. However, there is a paucity of work on freezing in porous media through which water moves with natural convection, except for the work of Weaver et al. [3].

This paper is concerned with the freezing of a water-saturated horizontal porous layer. This is cooled from above at -20°C, and its bottom surface temperature ranges from 0°C to 30°C. The present analytical approximations of the frozen layer thickness are compared with the experimental results, and also a limit of prediction applicability is determined by considering the effect of maximum density on natural convection in the unfrozen layer.

Experimental Apparatus and Procedure

Figure 1(a) shows the experimental apparatus and the freezing model schematically. A vessel for the porous layer with inner dimensions of 234 L × 100 W × 150 H mm is manufactured from 8-mm-thick Lucite plate. The 100-mm-deep porous layer is composed of glass or steel beads and saturated with distilled water. The upper cooling section circulating coolant is a heat sink to freeze water in the porous layer. The heating section forming a base surface under the unfrozen layer is used to produce the prescribed heating wall temperature T₂, and therefore the proper heat flux through the porous layer. Figure 1(b) is a detail of the heating section's lamination pat-

tern. Two thermocouples are embedded between a main heater and guard heater, which are made of 0.05-mm-thick stainless foil. When the temperature difference between the heaters reaches zero, the heat flux through the porous layer can be evaluated by measuring the output of the main heater. The lower cooling section is utilized only for the experimental runs where the lower heating surface temperature T₂ is at or near 0°C. The vertical temperature profile in the layer is kept at uniform temperature before the start of the experimental run. The cooling surface temperature T₁ is rigorously maintained at about -20°C during each of the runs except during a short period at the start of the run. Figure 1(c) shows the three-dimensional schematic view of the upper and lower cooling sections that are indicated in Fig. 1(a). The coolant inlets and outlets for the upper and the lower cooling sections are arranged diagonally to simulate isothermal surface conditions as nearly as possible. When natural convection occurs in the unfrozen layer under the frozen layer, the geometric shape of the interface between the frozen and the unfrozen layers may not be flat as illustrated in Fig. 1(a). Since it is generally difficult to measure precisely a local frozen layer thickness, in this experiment the mean value of the frozen layer thickness is evaluated by measuring the volume change caused by solidification. The ratio of pore fraction volume to total volume, i.e., the porosity, in this experiment is about 0.41.

Approximate Prediction for Frozen Layer Thickness

Assuming the shape of a particle composing the porous layer to be a sphere, the energy equation concerning the heat transfer between a bead and water or ice is as follows [4]:

$$(1 - \epsilon)C_s\rho_s \frac{\partial T_s}{\partial t} = 6(1 - \epsilon)\frac{\alpha}{d}(T_f - T_s) + (1 - \epsilon)\lambda_s \frac{\partial^2 T_s}{\partial y^2} \quad (1)$$

It may be surmised that the water flow through the pore fraction is considerably weak due to friction force between water and beads. Assuming that water is in a quiescent state, the Nusselt number indicating the heat transfer around a bead has a value of 2 [5]. As the bead diameter is very small in general, the ratio of heat transfer coefficient to bead diameter α/d has a large value. Therefore, it can be seen in the first term in the right-hand side of equation (1) that the temperature difference between a bead and the water may be very small. Based on these considerations, here heat transfer between the beads and water is neglected, and the porous layer composed of two substances (beads and water or ice) is assumed to be a single substance for simplification of the present analysis.

Contributed by the Heat Transfer Division for publication in the JOURNAL OF HEAT TRANSFER. Manuscript received by the Heat Transfer Division June 13, 1986.

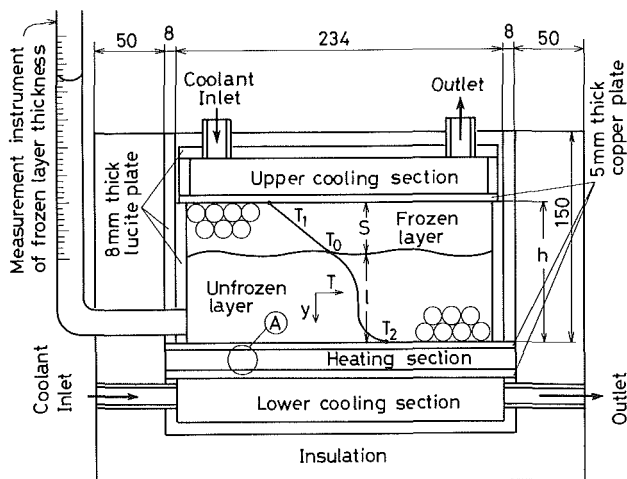


Fig. 1(a) Experimental apparatus and freezing model

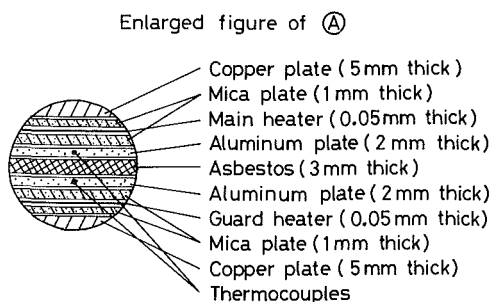


Fig. 1(b) Detail of heating section

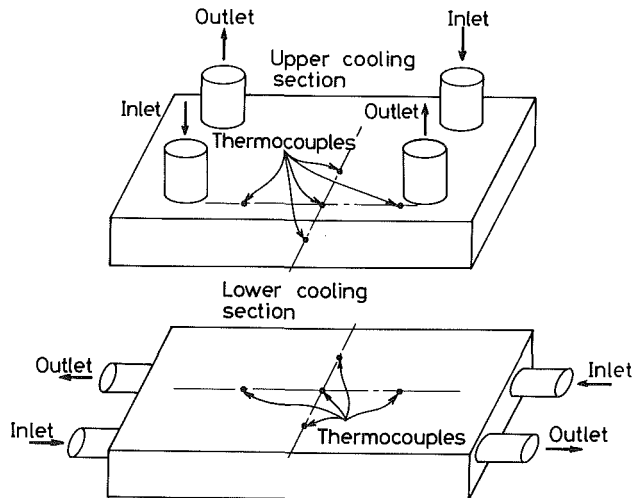


Fig. 1(c) Upper and lower cooling section

Conductive heat transfer

$$q = \lambda_{ew} \frac{T_0 - T_2}{l} \quad (3)$$

Convective heat transfer

$$q = \alpha_e (T_0 - T_2) \quad (4)$$

Effective thermal conductivities of both frozen and unfrozen layers are estimated from the relation by Yagi et al. [6]. Effective heat transfer coefficient α_e is evaluated from the following experimental results by Seki et al. [7]:

$$Nu_s = 0.064 Pr_e^{0.132} \left(\frac{d}{l}\right)^{-0.655} Ra_s^{0.5}, \quad 300 < Ra_s < 5000$$

$$Nu_s = 0.881 Pr_e^{0.132} \left(\frac{d}{l}\right)^{-0.655} Ra_s^{0.2}, \quad 5000 < Ra_s < 40000 \quad (5)$$

The critical point to change the heat transfer mode from conduction to convection can be determined from the following critical Rayleigh number by Katto et al. [8]:

$$(Ra_s)_c = 4\pi^2 \quad (6)$$

Nomenclature

C = heat capacity
 d = mean diameter of bead
 g = gravitational acceleration
 h = entire depth of porous layer
 k = permeability = $(d^2/150) \{ \epsilon^3 / (1 - \epsilon)^2 \}$
 K_e = thermal diffusivity of fluid and bead matrix = $\lambda_e / (\rho C)_f$
 l = thickness of unfrozen layer
 L = latent heat of freezing
 Nu = Nusselt number = $\alpha_e l / \lambda_{ew}$
 Nu_s = Nusselt number in equation (5) = $\alpha_e l / \lambda_{ef}$
 Pr_e = Prandtl number of porous layer = ν_f / K_e
 q = heat flux through unfrozen layer
 Ra = Rayleigh number = $g \beta l^3 (T_2 - T_0) / (\nu_f K_e)$

Ra_s = modified Rayleigh number = $\{ g \beta l^3 (T_2 - T_0) / (\nu_f K_e) \} (k / l^2)$
 Ra_m = modified Rayleigh number defined by equation (8)
 S = thickness of frozen layer
 t = time
 T = temperature
 T_0 = freezing temperature (= 0°C)
 T_1 = upper surface temperature of frozen layer (= cooling surface temperature)
 T_2 = lower surface temperature of unfrozen layer (= heating surface temperature)
 T_m = temperature at maximum density (= 4°C)
 y = coordinate

α = heat transfer coefficient
 α_e = effective heat transfer coefficient in porous layer
 β = coefficient of thermal expansion
 γ_1, γ_2 = constant
 ϵ = porosity
 λ = thermal conductivity
 λ_e = effective thermal conductivity of fluid-bead matrix or ice-bead matrix
 ν = kinematic viscosity
 ρ = density

Subscripts

c = critical
 f = fluid
 i = ice
 s = solid
 w = water

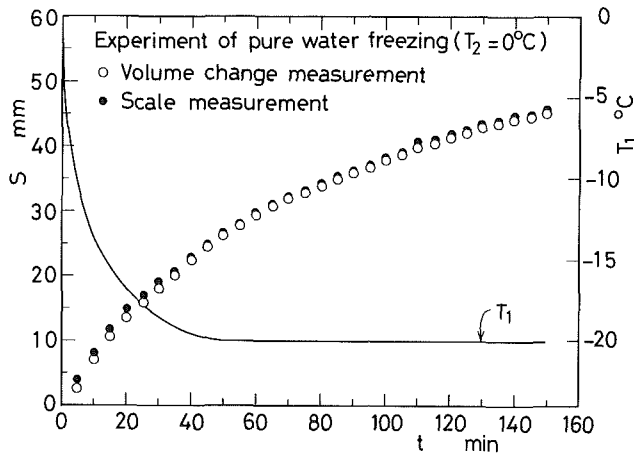


Fig. 2 Freezing of water layer without beads ($T_2 = 0^\circ\text{C}$)

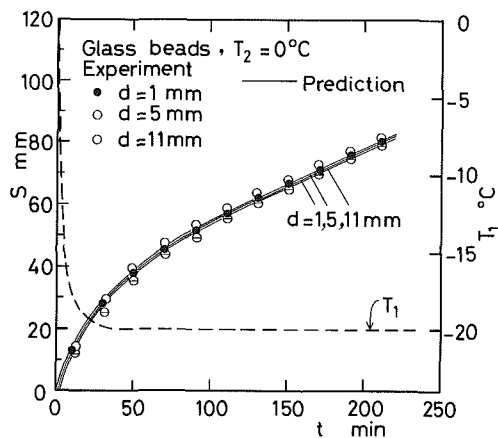


Fig. 3 Freezing of glass bead porous layer ($T_2 = 0^\circ\text{C}$)

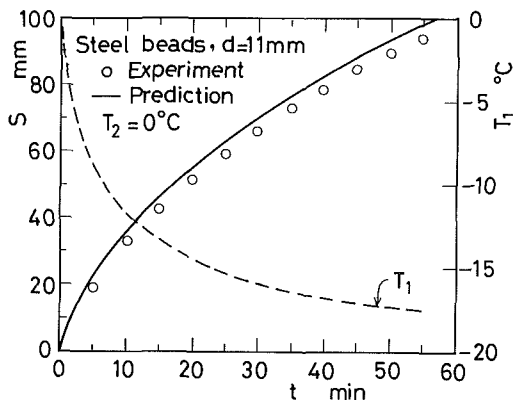


Fig. 4 Freezing of steel bead porous layer ($T_2 = 0^\circ\text{C}$)

Equation (2) can be solved numerically by using the Runge-Kutta-Gill method under the initial conditions $t = 0, S = 0$. For the case of $T_2 = 0$, i.e., no heat flux through the unfrozen layer, the analytical solution of the frozen layer thickness S can be obtained simply as follows:

$$S = \sqrt{-\frac{2\lambda_{ei}}{\epsilon\rho_i L} \int_0^t T_1(t) dt} \quad (7)$$

Results and Discussions

Freezing Behavior. Figure 2 shows the transient frozen layer

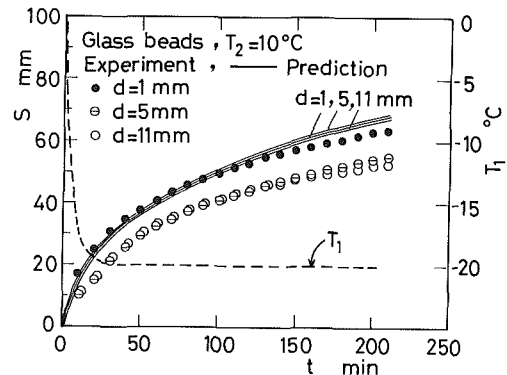


Fig. 5 Freezing of glass bead porous layer ($T_2 = 10^\circ\text{C}$)

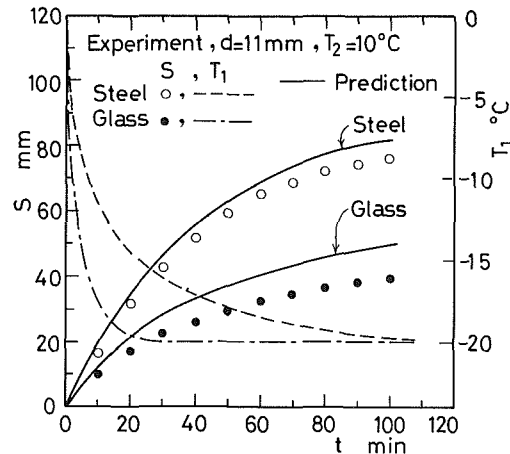


Fig. 6 Comparison of glass and steel porous layer ($T_2 = 10^\circ\text{C}$)

thickness of a water layer without beads, measured by both scale measurement and volume change (in which a scaled glass tube is installed vertically near the side of the experimental apparatus). By the close agreement between the two methods, that of volume change is proven accurate. It is used here because it gives a mean depth of frozen layer even when the freezing surface is uneven. The upper surface temperature of the frozen layer $T_1(t)$ is indicated by a solid line; it is represented by a polynomial expression in the numerical analysis.

Figure 3 (glass beads) and Fig. 4 (steel beads) demonstrate the transient behavior of the frozen layer thickness under the condition $T_2 = 0^\circ\text{C}$. The agreement between prediction and experiment is fairly good. The small deviation among the predictions (solid lines) corresponds to the small variation in the porosities of the bead bed. From the above freezing behavior, the frozen layer thickness is expected to be independent of the bead diameter given the same values of porosity. It should also be noted that the results ($T_2 = 0^\circ\text{C}$) may be applicable to the freezing of a snow layer in which water is saturated.

Figure 5 shows the results for $T_2 = 10^\circ\text{C}$ for glass beads of 1, 5, and 11 mm diameter. It is shown that the prediction for the case of 1 mm diameter is very close to the experimental results. However, the experimental results for the cases of 5 and 11 mm diameter deviate slightly from each of the predictions. Since these predictions are in the region of conduction, the above behavior may be understood by the fact that natural convection occurs in the unfrozen layer for the cases of 5 and 11 mm diameter. Experimental results of steel beads for $T_2 = 10^\circ\text{C}$ are in good agreement with the present prediction, as can be seen in Fig. 6. However, it is shown in Fig. 7 that the experimental results with steel beads for $T_2 = 15^\circ\text{C}$ deviate

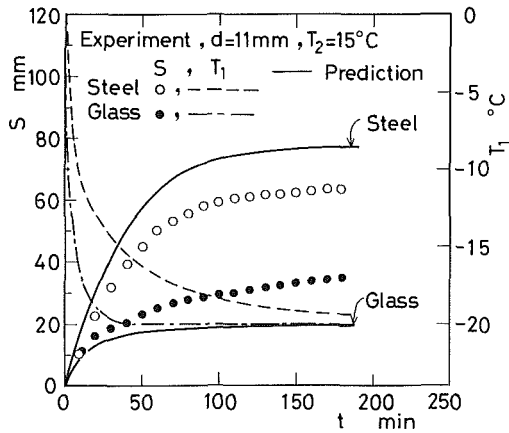


Fig. 7 Comparison of glass and steel porous layer ($T_2 = 15^\circ\text{C}$)

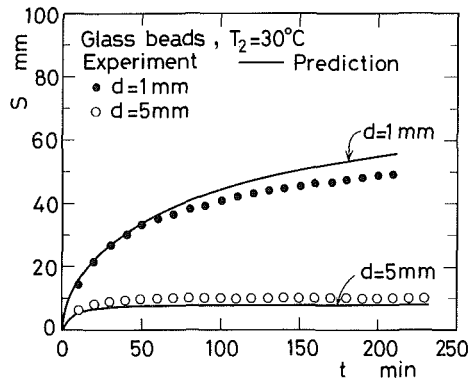


Fig. 8 Freezing of glass bead porous layer ($T_2 = 30^\circ\text{C}$)

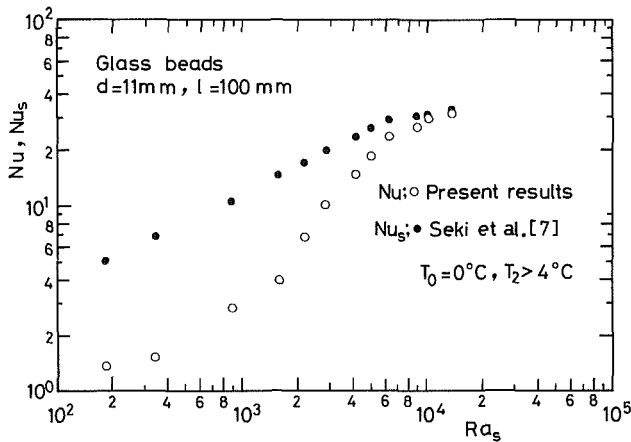


Fig. 9 Effect of maximum density on natural convection in glass bead porous layer

slightly from the prediction based on conduction. This means that heat transfer with steel beads in the unfrozen layer is dominated by natural convection when $T_2 = 15^\circ\text{C}$. In Fig. 7, the experimental results with glass beads are larger than the results predicted by natural convection. This behavior is different from the results with a steel bead porous layer. This curious outcome with glass beads may be explained by the fact that the actual heat flux through the unfrozen layer is smaller than the heat flux estimated from equation (4) because it excludes the effect of the maximum density of water at 4°C , as is explained next.

When the lower surface temperature is larger than 4°C , the water in the unfrozen layer is at maximum density. It is well

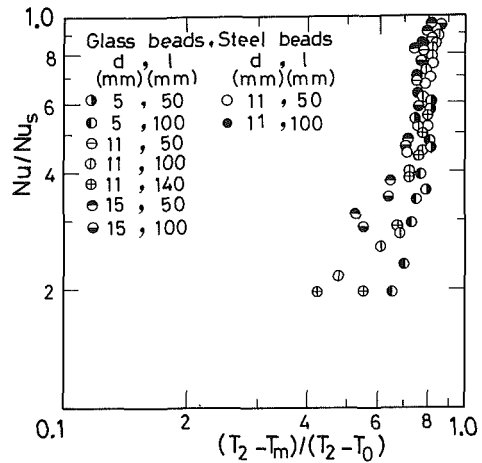


Fig. 10 Criterion of vanishing maximum density effect for natural convection

known that maximum density has significant effects on natural convection or the onset of convection in a horizontal water layer [9, 10]. However, in the present prediction the criterion for the onset of natural convection is based on the consideration of linear density variation with temperature. It is true that natural convection or the onset of convection in a water-saturated porous layer is also largely affected by the maximum density. Therefore, it could be concluded that most of the deviations between the experimental data and the present predictions may be caused by the effect of the maximum density of water.

Figure 8 shows the results for glass beads when $T_2 = 30^\circ\text{C}$. Agreement between the experiment and the prediction by conduction is comparatively good for the case of 1 mm bead diameter. It is also noteworthy that the prediction by convection for the case of 5 mm bead diameter is in good agreement with the experimental data in spite of exclusion of the maximum density effect. This result is mainly attributed to the fact that the effect of the maximum density vanishes due to a small value of $(T_m - T_0)/(T_2 - T_0)$. In other words, the stable layer thickness approximately denoted by the temperature difference $T_m - T_0$ becomes small compared with the thickness of the entire unfrozen layer.

Limit of Applicability for the Present Prediction

Since it can be recognized in the prior section that the present predictions are useful in cases of high T_2 (as shown in Fig. 8), next the limits of the prediction's usability must be examined. Figure 9 shows the relationship between Nusselt and Rayleigh numbers for the glass bead layer. Here the experimental results (open circle data points) are compared with other results (darkened circle data points) that do not include the effect of maximum density. Darkened circle data points are the results estimated from equation (5) presented by Seki et al. [7]. The thermal properties needed to evaluate the Rayleigh and Nusselt numbers are the values of $(T_2 + T_m)/2$. Since the porous layer depth is fixed at 100 mm, the increase in Rayleigh number corresponds to the increase in the temperature difference $T_2 - T_0$. The present data for Nu (open circle data points) including the maximum density effect are smaller than the value of Nus (darkened circle data points) estimated from equation (5). However the difference between them becomes small with increasing Rayleigh number, so that both results coincide at a Rayleigh number of about 10^4 .

Figure 10 shows the relation between the Nusselt number ratio Nu/Nus and the temperature difference ratio $(T_2 - T_m)/(T_2 - T_0)$ using several parameters of bead materials and diameters, and porous layer depth. Wide scatter of data

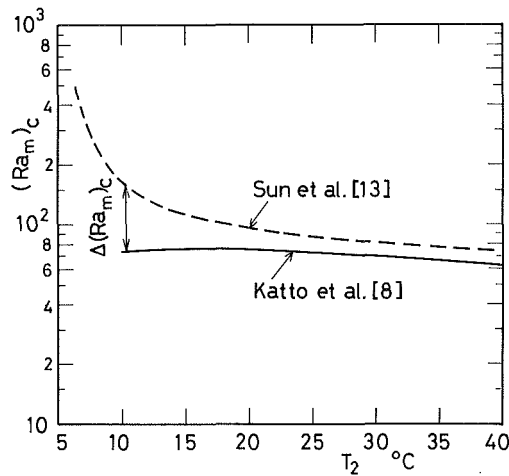


Fig. 11 Criterion of vanishing maximum density effect for onset of natural convection

points is found in the region of small temperature difference ratio. However, the scattering becomes small as the temperature difference ratio increases; the Nusselt number ratio finally converges to unity at a temperature difference ratio of about 0.85. This means that the effect of maximum density on natural convection in the porous layer vanishes when T_2 is higher than about 26°C.

One possible aid in setting limits is given by Blake et al. [11], who recently reported their numerical investigation of natural convection near 4°C in a water-saturated porous layer heated from below. However, since the base surface temperature in their paper is limited to the range of 4 ~ 8°C, the applicability limits of the present prediction cannot be developed from their numerical solution [11].

In addition, the onset of natural convection in a porous layer affected by maximum density can be discussed. The criterion for the onset of natural convection for a fluid having linear density variation with temperature is presented in equation (6) by Katto et al. [8], and the criterion considering the maximum density effect is presented by Yen [12]. That result is shown in Fig. 11 (dashed line); it is a derivative of the analytical prediction reported by Sun et al. [13]. Rayleigh number Ra_m defined by Sun et al. is as follows:

$$Ra_m = \frac{2lg\gamma_1(T_2 - T_0)(T_2 - T_m)}{\nu_f K_e} \left\{ 1 + (T_2 - T_m) \left(\frac{3\gamma_2}{2\gamma_1} \right) \right\} k \quad (8)$$

The criterion for onset in equation (6) can be recast as follows by using Rayleigh number Ra_m in equation (8)

$$(Ra_m)_c = \frac{2\gamma_1(T_2 - T_m)[1 + (T_2 - T_m)\{(3\gamma_2)/(2\gamma_1)\}]}{\beta} \cdot 4\pi^2 \quad (9)$$

The results of equation (9), which exclude the maximum density effect, are shown by the solid line in Fig. 11. The constants γ_1 and γ_2 in equation (9) are the constants for the relationship connecting density to temperature around 4°C. The information for density-temperature relationships have been presented by Gebhart and co-workers [14]. However, in this paper γ_1 and γ_2 are obtained by interpolation of the results given by Yen [12] and using the value for the coefficient of thermal expansion β value at the temperature $(T_2 + T_m)/2$. The critical Rayleigh number $(Ra_m)_c$ including the effect of maximum density [13] is considerably larger than $(Ra_m)_c$ calculated excluding the effect (as that of Katto et al. [8]), when T_2 is in a low-temperature range. This outcome may be

induced by a stable layer caused by the temperature difference $T_m - T_0$. However the difference between these results, $\Delta(Ra_m)_c$, becomes small with an increase in the base surface temperature T_2 , and approaches a constant value above about 26°C. This means that the effect of maximum density on the onset of natural convection diminishes in the range $T_2 > 26^\circ\text{C}$. It can be understood that the temperature 26°C is a reasonable value as a criterion, as mentioned above, considering the results of natural convection as shown in Fig. 10. It should be noted that a little difference between the results for the onset of natural convection in the range of $T_2 > 26^\circ\text{C}$ ($\Delta(Ra_m)_c \neq 0$) may be mainly attributed to physical properties such as the coefficient of thermal expansion.

It is found from the work of Yen [12] that the effect of maximum density on natural convection continues until a base surface temperature of about 55°C. However, in conclusion it should be clarified that for these results it is reasonable to consider that the maximum density effect continues until only 26°C.

Conclusions

The authors performed experimental investigations and analytical approximations concerned with freezing in a water-saturated horizontal porous layer cooled from above. As a summation of the results, the following conclusions can be drawn.

The analytical approximations presented in this paper are useful to predict transient frozen layer thickness under the conditions of base surface temperature in the range of $0^\circ\text{C} < T_2 < 4^\circ\text{C}$ in conductive and with $26^\circ\text{C} < T_2$ in fully convective heat transfer modes.

References

- 1 Frivic, P. E., and Comini, G., "Seepage and Heat Flow in Soil Freezing," *ASME JOURNAL OF HEAT TRANSFER*, Vol. 104, No. 2, 1982, pp. 323-328.
- 2 Okada, M., "Approximate Analysis of Freezing Around Two Cooled Pipes in Darcy Flow," *Refrigeration (Japan)*, Vol. 56, No. 639, 1981, pp. 3-13.
- 3 Weaver, J. A., and Viskanta, R., "Freezing of Water Saturated Porous Media in a Rectangular Cavity," *Int. Comm. Heat Mass Transfer*, Vol. 13, 1986, pp. 245-252.
- 4 Spiga, G., and Spiga, M., "Analytical Simulation in Heat Storage Systems," *Wärme- und Stoffübertragung*, Vol. 16, 1982, pp. 191-198.
- 5 Katto, Y., *Heat Transfer*, Yokendo, Japan, 1974, p. 163.
- 6 Yagi, S., and Kunii, D., *International Developments in Heat Transfer*, Part IV, 1961, pp. 742-750.
- 7 Seki, N., Fukusako, S., and Ariake, Y., "Consideration of Natural Convection in Horizontal Porous Layer," *Transactions of JSME (Japan)*, Ser. B, Vol. 45, No. 393, 1979, pp. 705-711.
- 8 Katto, Y., and Masuoka, T., "Criterion for the Onset of Convection Flow in a Fluid in a Porous Medium," *International Journal of Heat and Mass Transfer*, Vol. 10, No. 3, 1967, pp. 297-309.
- 9 Sugawara, M., Fukusako, S., and Seki, N., "Experimental Studies on the Melting of a Horizontal Ice Layer," *Bulletin of the JSME (Japan)*, Vol. 18, No. 121, 1975, pp. 714-721.
- 10 Sun, Z. S., Tien, C., and Yen, Y. C., "Thermal Instability of a Horizontal Layer of Liquid With Maximum Density," *AIChE Journal*, Vol. 15, No. 6, 1969, pp. 910-915.
- 11 Blake, K. R., Bejan, A., and Poulikakos, D., "Natural Convection Near 4°C in a Water Saturated Porous Layer Heated From Below," *International Journal of Heat and Mass Transfer*, Vol. 27, No. 12, 1984, pp. 2355-2364.
- 12 Yen, Y. C., "Effect of Density Inversion on Free Convective Heat Transfer in Porous Layer Heated From Below," *International Journal of Heat and Mass Transfer*, Vol. 17, No. 11, 1974, pp. 1349-1356.
- 13 Sun, Z. C., Tien, C., and Yen, Y. C., "Onset of Convection in a Porous Medium Containing Liquid With a Density Maximum," *Proceedings of Fourth International Heat Transfer Conference (Paris-Versailles)*, Vol. IV, 1972, NCA-11.
- 14 Gebhart, B., and Mollendorf, J. C., "Buoyancy-Induced Flow in Water Under Conditions in Which Density Extrema May Arise," *J. Fluid Mech.*, Vol. 89, Part 4, 1978, pp. 673-707.

Theoretical Analysis of Weld Pool Behavior in the Pulsed Current GTAW Process

C. L. Tsai

Associate Professor,
Department of Welding Engineering,
The Ohio State University,
Columbus, OH
Assoc. Mem. ASME

C. A. Hou

Assistant Professor,
Department of Mechanical Engineering,
Howard University,
Washington, DC

A general, three-dimensional, closed-form welding heat-flow solution, which is capable of analyzing thermal behavior of the weldment in its transient state and/or under time-dependent power change during welding, is presented. The analytical model utilizes the finite heat source theory with a Gaussian distribution and also considers the effects of finite plate thickness. The numerical values of the solution are calculated using the computational schemes on a minicomputer. In this paper the welding parameters of the pulsed current GTAW were studied using the solution. Two sets of pulsation parameters were analyzed and their sensitivity to the heat input control were evaluated.

Introduction

Gas tungsten arc welding (GTAW) is commonly used in the fabrication of heat-sensitive materials, thin gage joints, and dimensionally critical structures. Accurate control of the welding heat input is an important factor for success of the fabrication process. Pulsing the current during welding can change the energy input mode on a real time scale and formulate additional parameters for more flexible and accurate heat input control.

A number of investigators [1-17] have reported the effectiveness of the pulsed-current gas tungsten arc welding (PC-GTAW) process. Attempts have been made to establish a scientific approach for understanding the complex behavior of the material under pulsed current conditions. Concurrent with the experimental efforts, mathematical modeling of the physical phenomena of PC-GTAW has been of great interest to the investigators. Because of the time dependency of the welding current, a transient thermal model and analysis must be used. Unfortunately, literature on welding heat flow under transient conditions is scarce. This paper presents a general, closed-form solution capable of analyzing the thermal behavior of a weldment under transient conditions. The analytical model considers Gaussian distribution of the welding heat source and finite plate thickness. The numerical values of the solution are calculated using the computational schemes on a minicomputer. Numerical studies on two sets of pulsation parameters and their sensitivity to the heat input control are discussed.

Background

Many investigators have studied welding heat flow problems analytically, numerically, and experimentally [1, 18-33]. The majority of studies were concerned with the quasi-stationary thermal state. Lance and Martin [18], Rosenthal and Schmerber [19], and Rykalin [20] obtained, independently, an analytical temperature solution for the quasi-stationary state using a point or line heat source moving along a straight line on a semi-infinite body. A solution for plates of finite thickness was later obtained by many investigators using the imaged heat source method [20, 21]. Tsai [22], in 1977, derived an analytical solution for a model incorporating a welding heat source with a skewed Gaussian distribution and finite plate thickness. It was later called the "finite source theory" in his paper [23].

With the advancement of computer technology and such numerical techniques as finite difference and finite element methods, more precise welding thermal models were studied. The physical phenomena, such as nonlinear thermal properties, latent heat, surface heat loss, and various joint geometries, were considered in the studies. Tsai [22], Pavelic [24], Kou [25], Kogan [26], and Brody [1] simulated the welding thermal cycles using the finite difference scheme. Hibbitt and Marcal [27], Friedman [28], and Paley [29] made some progress in welding simulation by the finite element method.

Analytical solutions for transient welding heat flow in a plate were first studied by Naka [30], Rykalin [20], and Masubuchi and Kusuda [31] in the 1940s and 1950s. A point or line heat source, constant thermal properties and adiabatic boundary conditions were assumed. Tsai [32] extended the analytical solution, using the principle of superposition, to incorporate a Gaussian heat distribution. In this study, the analytical solution was used to investigate the welding parameters of the PC-GTAW process.

Pulsation Parameters and a Review

In the PC-GTAW process, the welding current follows a square wavelike shape and introduces four process variables. The welding current alternates between a high level, called the peak current I_p , and a low level, called the background current I_b . Other variables are durations of peak current and background current known as peak duration t_p and background time t_b . Figure 1 shows a schematic diagram of a square waveform current and some basic definitions.

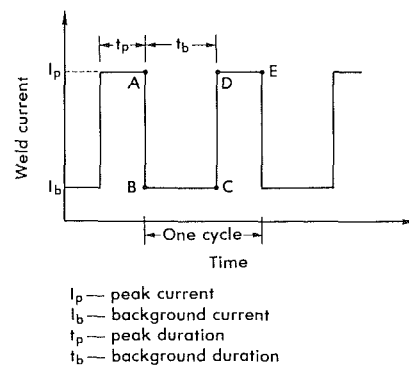


Fig. 1 Schematic diagram of an idealized square waveform current with basic definitions

Contributed by the Heat Transfer Division and presented at the ASME Winter Annual Meeting, Boston, Massachusetts, November 1983. Manuscript received by the Heat Transfer Division April 24, 1984.

Pulsing of the current results in discontinuous welding along the joint seam, observed as a series of overlapping spot welds. During the peak time, the peak current produces a large quantity of heat to melt the metal and form the weld puddle, while during the background time, the background current is employed to allow the weld to cool partially or solidify and to maintain a consistent arc. Controlling these pulsation parameters is the most efficient way of producing a high-quality weld. Therefore, the parameters are selected to achieve a desired weld penetration and bead width and, in conjunction with the welding speed and pulsing frequency, to produce a weld seam of overlapped spot welds.

The range of welding parameters used in the PC-GTAW process depends on the service requirements. The peak current can range from a few amperes to 400 A or more, depending on the type of material and thickness. In general, the peak current should be adjusted to at least twice that of the steady current GTAW that is normally used for the same job. The background current can be set to any value which is low compared with the peak current. Usually it is less than 15 percent of peak current and typically 5 to 10 A. The purpose of the background current is only to maintain a stable arc and its value is not critical. It has been reported that the background current has no significant effects on the geometry of weld pool and penetration [34, 35].

The peak time is, in practice, set to allow for the formation of the molten puddle which corresponds to the penetration desired. This may vary from 0.1 s to 3 s. The background time should be sufficiently long to allow the molten puddle to freeze partially.

These four parameters are called pulsation parameters because they are the primary variables involved in controlling heat input. For analytical purposes, modified parameters are sometimes used. They are the average current I_{av} , mark space ratio R , and pulsating frequency f , which are defined as follows:

$$I_{av} = (I_p t_p + I_b t_b) / (t_p + t_b) \quad (1)$$

$$R = t_p / t_b \quad (2)$$

$$f = 1 / (t_p + t_b) \quad (3)$$

The average current is a parameter used to represent the magnitude of the energy input rate and is the most important parameter in controlling penetration. The mark space ratio is defined as the ratio of peak duration to background duration. This ratio represents the severity of pulsing and is typically from 0.1 to 5 or more. A pulsing frequency of 0.1 to 10 Hz is used for most applications, while higher frequencies of over 200 Hz are being used for special cases, such as high-speed welding of aluminum to avoid hot cracking.

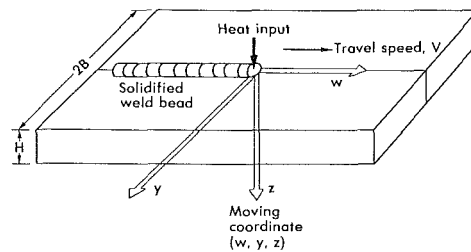


Fig. 2 Schematic diagram of welding thermal model with a Gaussian heat source distribution

In addition, welding speed V is another parameter which is chosen to determine the overlap for each of the individual welds formed by each pulse. The welding speed must be low enough to avoid discontinuities in the weld. A 45 to 80 percent overlap is usually used in the practical PC-GTAW applications. Equation (4) is a simple relationship for calculating the welding speed

$$V = W \times f \times (1 - b) \quad (4)$$

where W is pool width and b is percent of overlapping with respect to the pool width. The intensity of the welding heat input ($E I_{av} / V$) is also considered as a parameter for the purpose of comparison with the steady current arc welding.

Mathematical Model and Solution

The Welding Phenomenon. Figure 2 represents a physical model of the welding system. The Gaussian heat source moves at a constant speed along a straight path. The end effects resulting from either initiation or termination of the heat source cause a transient thermal state in the weldment. Some time after the initiation or before the termination of the heat source the temperature distribution is stationary with respect to the moving coordinates, which origin coincides with the center of the heat source. The intensive welding heat melts the metal and forms a molten pool. Some of the heat is conducted into the base metal and some is lost from the arc column or the metal surface to the environment surrounding the plate. Three metallurgical zones, weld metal WM, heat-affected zone HAZ, and base metal BM are formed in the plate upon completion of the thermal cycle. The peak temperature and the subsequent cooling rates determine the HAZ structures. Two additional parameters, thermal gradients and solidification rates across the liquid and solid pool boundary, determine the solidification structure of the WM zone. The size of the pool determines the amount of dilution and weld penetration.

Nomenclature

b = ratio of overlapping ($0 < b < 1$)	I_p = peak current, A	t_p = peak duration, s
B = half plate width, mm	K = thermal diffusivity, mm^2/s	V = welding speed, mm/s
C = shape constant for finite source distribu- tion, mm^{-2}	\dot{q} = heat input flux, W/mm^2	w, y, z = moving Cartesian coor- dinate, mm
C_p = specific heat, $\text{J}/\text{kg}\cdot^\circ\text{C}$	\dot{q}_e = internal heat generation rate, W/mm^3	W = pool width, mm
D = diameter of electrode, mm	\dot{q}_0 = heat flux at the source center, W/mm^2	δ = distance of the trailing edge movement during t_b
E = welding voltage, V	\dot{Q} = total heat input rate, W	θ = temperature, $^\circ\text{C}$
F = concentration factor	r = radial distance from the source center, mm	θ_0 = initial temperature, $^\circ\text{C}$
f = pulse frequency, Hz	R = mark space ratio	λ = thermal conductivity, $\text{W}/\text{mm}\cdot^\circ\text{C}$
H = plate thickness, mm	t = time, s	ρ = density, kg/mm^3
I_{av} = average current, A	t_b = background duration, s	ψ = angular coordinate, rad
I_b = background current, A		∇ = differential operator

Heat Conduction in Base Metal. The general heat flow equation for a differential element inside the conducting medium on the moving coordinates can be written as

$$\nabla \cdot (\lambda \nabla i) + \rho C_p V \frac{\partial \theta}{\partial w} + \dot{q}_e = \rho C_p \frac{\partial \theta}{\partial t} \quad (5)$$

λ , ρ , and C_p are, respectively, thermal conductivity, density, and specific heat of material. \dot{q}_e represents the internal heat generation rate in the material due to the welding current flow.

Arc Heat Distribution. Following the approach of Pavelic et al. [24], the heat transfer rate from the welding arc is, at any given time, assumed to be deposited on the surface of the weldment as a radially symmetric normal distribution function

$$\dot{q}(r) = \dot{q}_0 \exp(-Cr^2) \quad (6)$$

Two conditions are needed to determine the shape constant C and the heat flux at the arc center \dot{q}_0 . According to Apps and Milner [34], the total heat input rate \dot{Q} from an argon arc to a workpiece can be expressed as the sum of the concentrated arc heat and the diffused arc heat. The concentrated heat is distributed in the arc column and the diffused heat is dispersed around the column due to radiation, convection, and conduction. The shape constant can be obtained in terms of the arc column diameter D and the concentration factor F , which is defined as the ratio of the concentrated heat to the total welding heat input rate. By integrating equation (6) over the entire heat input domain, the heat flux at the source center can be determined as a function of the shape constant and the total heat input rate. The two constants are expressed as follows:

$$C = 4/D^2 \ln [1/(1-F)] \quad (7)$$

$$\dot{q}_0/\dot{Q} = C/\pi \quad (8)$$

Since the quantitative concentration factor for PC-GTAW was not available in the literature, a value was obtained by adjusting the factor to match the predicted stationary pool width with the experimentally measured bead width. The concentration factor was approximately 0.8.

Assumptions and Other Boundary Conditions. Some of the physical phenomena associated with the arc welding process were neglected in the derivation of the closed-form solution. They were: (a) Joule heating in the base metal; (b) physical phase changes; and (c) temperature dependence of material properties. Other boundary conditions used in the derivation were adiabatic surfaces, except the plate surface exposed to the welding arc and zero temperature response in the far-field areas.

Analytical Solution. The general solution for welding heat flow in a semi-infinite solid can be obtained by integrating the Green's function of the temperature responses of a material to an instantaneous point discharge liberated at a point on the surface and at a given instant [37]. By integrating the Green's function with respect to time and the appropriate space variables, the solution for the moving, finite source at a prescribed rate can be written as follows:

$$\theta - \theta_0 = \frac{1}{4\rho C_p (\pi K)^{3/2}} \int_0^t \frac{1}{(t-t')^{3/2}} \int_0^\infty \dot{q}r' \int_0^{2\pi} \exp \left\{ - \frac{[w + V(t-t') - r' \sin \psi]^2 + [y - r' \cos \psi]^2 + z^2}{4k(t-t')} \right\} dx dr' dt' \quad (9)$$

The solution for the plates of finite thickness with adiabatic surfaces can be modified from equation (9) using the image method. The solution is

Table 1 Experimental verification of the mathematical model (stainless 304L, 1-cm-thick plate)

Welding Condition:			
Peak Current	212 A		
Background Current	5 A		
Voltage	10 Volts		
Welding Speed	0.64 cm/s		
Frequency	3.3 Hz		
Peak Duration	0.15 s		
Material Property:			
Conductivity	0.043 Cal/s-cm-°C		
Diffusivity	0.05 cm ² /s		
Melting Temperature	1420 °C		
Welding Factor: 0.55			
	Measured	Computed	Remarks
Penetration	1.73 mm	1.73 mm	reference parameter
Bead Width	4.90 mm	4.06 mm	
Pool Length	3.92 mm	3.81 mm	trailing edge length
% Solidified	64 %	86%	

% Solidified is the ratio of the molten pool length at the end of the background duration to that at the end of the peak duration.

$$\theta - \theta_0 = \frac{1}{4\rho C_p (\pi k)^{3/2}} \left\{ - \iiint (w, y, z, t) + \sum_{m=0}^{\infty} \sum_{n=0}^{\infty} \left[\iiint (w, y_m, z_n, t) + \iiint (w, y'_m, z'_n, t) \right] \right\} \quad (10)$$

where the integrals are the same as those in equation (9), but the coordinate system of the integral function is changed.

$$\begin{aligned} y_m &= 2mB - y; & z_n &= 2nH - z \\ y'_m &= 2mB + y; & z'_n &= 2nH + z \end{aligned} \quad (11)$$

B and H are the width and thickness of the plate; m and n are integers which vary from zero to infinity.

Numerical Calculations and Experimental Verification

The thermal properties of the engineering materials are usually a temperature-dependent function. However, using the analytical solution, constant property values need to be selected for the numerical calculations. The selection is sometimes arbitrary. As an alternative, the thermal properties at any point of interest can be chosen at the current temperature through an iterative procedure. Thermal properties at a particular point are first assumed to be those at the specific temperature obtained from the previous calculation. A new temperature is then calculated. Taking the mean value of the new and the previous temperatures for the subsequent iteration, the solution converges to the situation with the thermal property values at the current temperature. Latent heat is treated as an increase or decrease in the specific heat of the material over the temperature range bonded by the solidus and liquidus temperatures.

The constant thermal properties can also be chosen as the average value of the material within a temperature range of interest. For the investigations of the weld pool behavior, melting temperature is of particular importance and the thermal properties are chosen at this temperature. Several computer runs using both alternatives showed a very small difference in the temperature solutions surrounding the pool. Therefore, the thermal properties at melting point were used for the parametric studies.

To verify the analytical solution for welding applications, numerical calculations were conducted to compare the results with the experimental data obtained by Barone [16] and Brody [1]. Table 1 shows the comparison of the weld pool dimensions, on a stainless steel 304L weldment, between the prediction and the measurement by Barone. Good agreement is shown, except that the predicted percent of solidification of the weld pool during the background duration is more than

Table 2 Experimental verification of the mathematical model (Fe-26Ni alloy, 0.08-cm-thick plate)

Welding Condition:	
Peak Current	120 A
Background Current	10 A
Voltage	10 Volts
Welding Speed	0.212 cm/s
Frequency	0.916 Hz
Peak Duration	0.208 s

Material Property:	
Conductivity	0.125 Cal/s-cm-°C
Diffusivity	0.111 cm ² /s
Melting Temperature	1456 °C

Welding Factor: 1.5

	Measured	Computed	Remarks
Pool Length	9.40 mm	7.87 mm	the entire length
Bead Width	7.10 mm	7.30 mm	reference parameter
Pool Area	55 mm ²	52 mm ²	

The measured data were taken by Brody.

the measured value. Since the exact amount of the arc energy reaching the plate is usually not known, a welding factor needs to be assumed and used as a correction factor to ensure the predicted results agree with the experimental values on a specific physical base. The welding factor used in this calculation was determined to be 0.55 on the base of equal penetration.

In a comparison with Brody's results on Fe-26Ni alloy, a welding factor of 1.5 was required to match the high-temperature data, but a factor of 1.7 was needed for the low-temperature data. By matching the high-temperature data, using the factor of 1.5, the predicted pool width and penetration agreed well with the measured pool dimensions, as shown in Table 2. Figure 3 shows the comparison of the solidification movement of the pool trailing edge during the background duration. While some variations were observed, the comparisons showed overall agreement in trend. The solution and the associated numerical schemes are suitable for the parametric investigations of the PC-GTAW process.

The welding factor used in the calculations is a value greater than unity. This factor, therefore, cannot be interpreted as the fraction of the energy reaching the plate. However, this factor should reflect the interactive effect of the welding energy and the other physical phenomena, such as latent heat and surface energy losses, not considered in the solution.

Parametric Study and Discussion

Computer Simulations. Twenty-three PC-GTAW simulations were made to conduct an analysis of weld pool dimensions. The welding conditions were simulated by making bead-on-plate welds on 10-mm-thick 304L stainless steel plate. The diameter of the arc column was assumed to be 1.6 mm, the same as the diameter of the tungsten electrode, and the concentration factor was assumed 0.8. The welding voltage was chosen as 10 V and fixed for all simulations.

Solidification Zones. Figure 4 shows the schematic diagram of overlap pools after one solidification and heating cycle. The pulsation of welding current is described in Fig. 1. At the end of each peak duration, the weld pool is at its maximum dimensions. The weld solidifies during t_b . The trailing edge of the pool moves inward by a distance of δ at the end of t_b . At this moment, the welding current returns to its peak value and a new pool forms and grows quickly. The old pool keeps solidifying during t_p until the two pools meet at a distance V/f from the trailing edge of the old pool's maximum dimensions. Four physical zones are formed during this cycle: a fast solidification zone which occurred during t_b , a slow solidification zone which occurred during t_p , a remelting zone and a liquid zone. Figure 5 shows the predicted temperature history at

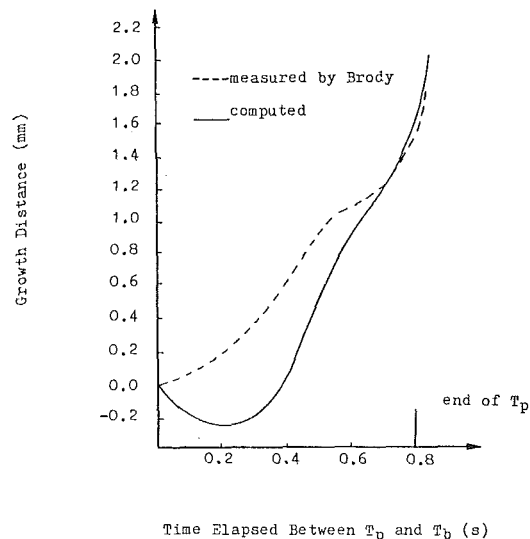


Fig. 3 Comparison between the computed and the measured [1] solidification movement of the pool trailing edge during the background duration

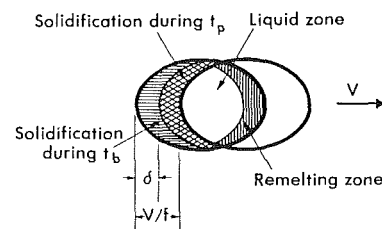


Fig. 4 Schematic diagram of solidification zones in pulsed current gas tungsten arc welding

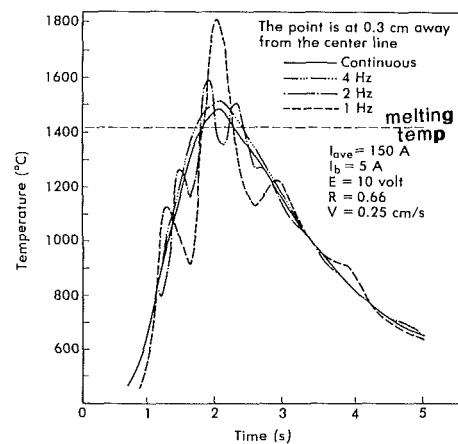


Fig. 5 Predicted temperature history at a point 3 mm from weld centerline under various pulsed current frequencies

a point 3 mm from the weld centerline. With a 2-Hz frequency, this point goes through a remelting process. The predictions of the surface solidification rates can be measured by the distance the pool interface traversed during the background time.

Solidification during the background duration differs significantly from that occurring during the peak duration, which closely resembles solidification during continuous current welding. For melting to occur along the front interface of the pool, the latent heat of fusion must be supplied by arc heating. Alternately, for solidification to occur along the real pool interface, the latent heat needs to be liberated into the

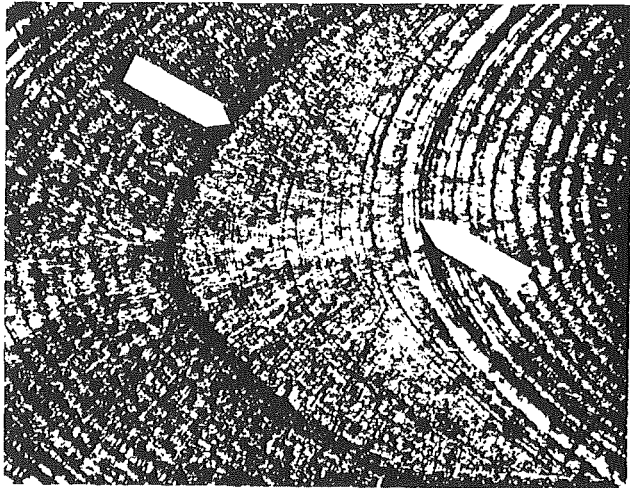


Fig. 6 Solidification zones occurred during peak duration (as marked by arrows) and background duration (unetched and unpolished weld surface, 37.5X) [16]; stainless steel 304L; pulsed-current gas tungsten arc welding; $I = 150$ A; $t_p = 295$ A; $I_b = 5$ A; arc voltage = 10. volts; frequency = 3.3 Hz; travel speed = 15.1 ipm (0.64 cm/s); $t_p = 0.15$ s; $t_b = 0.15$ s

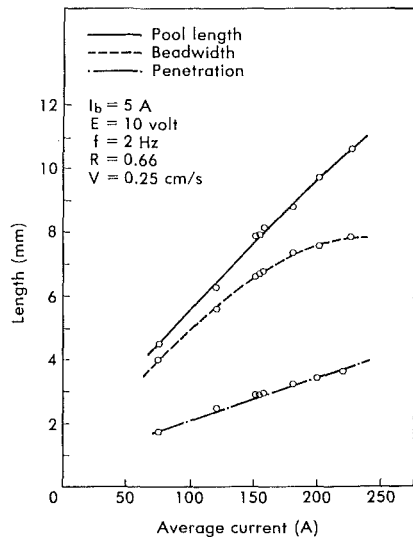


Fig. 7 Predicted correlations between the maximum pool dimensions and average current in pulsed current gas tungsten arc welding

base metal. This heat flow condition is true for continuous welding, but a different mechanism is apparent during pulsed welding. During peak current, essentially the same phenomena are occurring. When the peak current is terminated and the background current is initiated with negligible heat input, the latent heat of fusion is no longer supplied and therefore no additional melting occurs along the front interface. Since no melting is occurring, the region can behave in a manner similar to the real interface, and can become a region where the latent heat of fusion, supplied during the peak current, can escape. From the viewpoint of reduced heat input and increased area for latent heat to escape across the entire periphery of the weld pool, it is reasonable that the solidification rate during t_b is increased beyond that during t_p . Figure 6 shows these two distinct solidification structures [16].

Maximum Pool Dimensions. The weld bead produced by the PC-GTAW process constitutes a number of overlapped weld pools at their maximum dimensions. The degree of overlap, among other dimensions, is regulated by the magnitude and the duration of the pulsation parameters de-

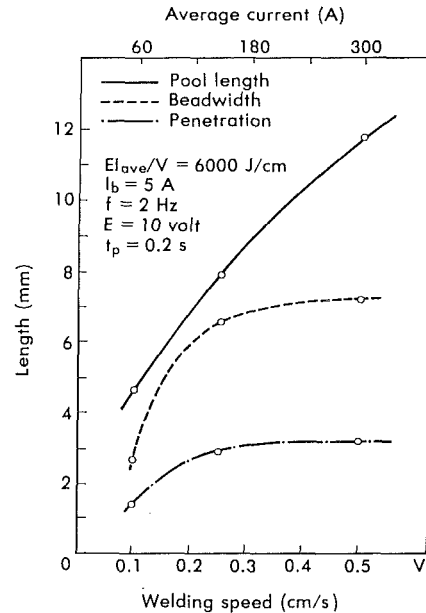


Fig. 8 Predicted variation of the maximum weld pool dimensions with respect to the proportional changes of welding speed and average current at a constant heat input intensity in pulsed current gas tungsten arc welding

finer in the previous section. With known maximum pool dimensions, frequency, and welding speed, a weld profile can be constructed by overlapping the pools. Variation in penetration and bead width along the joint length can be simulated. The quality of weldment can be evaluated.

Average Current. For a given welding speed, the maximum pool dimensions can be best correlated with respect to the average current. Figure 7 shows such correlations by curve fitting. From this we conclude that, regardless of the pulsation conditions, the maximum pool dimensions are a function of average current. A linear relationship is shown for all three pool dimensions, excepting bead width which approaches an asymptotic value when the average current is higher than 200 A. In a comparison between the various pulsation conditions and the steady current condition at 150 A of average current, the pulsing welding current increases all three pool dimensions. However, as the frequency becomes greater than 2 Hz, the increase in dimensions is negligible.

Heat Input Intensity (EI_{av}/V). Heat input intensity is often used as a parameter indicating thermal conditions, such as cooling rate in the weld HAZ, of weldments. Figure 8 shows the variation of maximum weld pool dimensions with respect to the proportional changes of welding speed and average current at a constant heat input intensity of 6000 J/cm. Both bead width and penetration of weld pool approach an asymptotic value when the welding speed is greater than 0.3 cm/s. Nevertheless, pool length increases almost linearly with the proportional increase of welding speed and average current. This result leads to the conclusion that, to obtain the same thermal condition in weldments, the welding speed can be increased with a proportional increase of average current to the capacity of the welding machine. With the addition of pulsation parameters, the amount of overlap at high-speed welding can be obtained by increasing the pulsing frequency since the travel distance of the pool trailing edge after each cycle is V/f . Although penetration and bead width of high-frequency welds are very similar to those produced under steady current with the same heat input intensity, the solidification structures can be controlled by adjusting the peak current and duration. As reported in [16], pulsing the welding current rounds off the

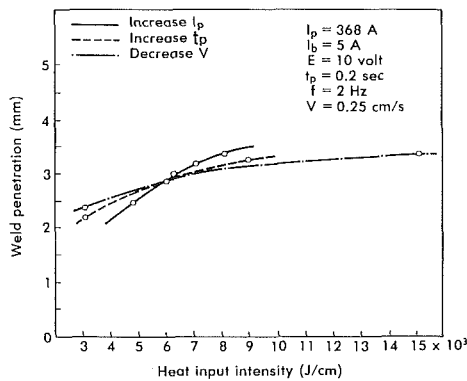


Fig. 9 Predicted weld penetration in pulsed current gas tungsten arc welding with various heat intensities by adjusting each individual pulsing parameter

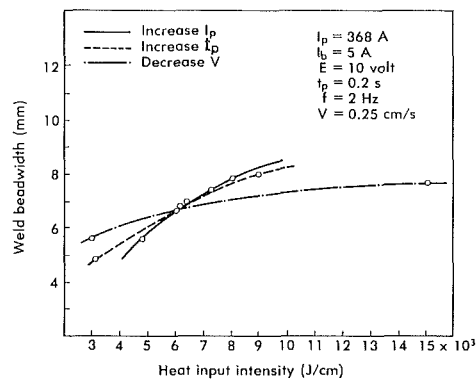


Fig. 10 Predicted bead width in pulsed current gas tungsten arc welding with various heat input intensities by adjusting each individual pulsing parameter

trailing edge of the pool and avoids the abrupt impingement of the growing columnar grains at the weld centerline and the control axial grain. The tendency toward centerline cracking is reduced.

With a given heat input intensity, weld pool dimensions may vary depending upon the pulsation conditions. Figures 9 and 10 show the difference in pool dimensions as a result of various heat input intensities affected by adjusting each individual pulsing parameter. The results indicate that peak current is the most effective parameter in controlling weld penetration and bead width because of its greater slope. Peak duration and welding speed are secondary in control of weld dimensions.

Concluding Remarks

High-speed PC-GTAW can be achieved by proportionally adjusting the speed and the pulse frequency. Penetration and bead width of pulsed welds may be no different from those produced under steady current. However, weld solidification structures can be controlled through the adjustment of peak current and duration.

Numerical simulation of the solidification phenomena is currently under study to assess quantitatively the effects of pulsing parameters on the weld solidification structures. Further experimental studies on solidification structures under pulsed conditions are recommended.

References

- 1 Ecer, G. M., Downs, M., Brody, H. D., and Gohkale, A., "Heat Flow Simulation of Pulsed Current Gas Tungsten Arc Welding," *Modeling of Casting and Welding Processes*, H. D. Brody and D. Apelian, eds., AIME, July 1981, pp. 139-160.

- 2 Anon, D., "Pulsed AC for TIG-Welding of Thin Non-ferrous Metals," *Elec. Review*, Vol. 188, June 1971, pp. 803-804.
- 3 Becker, D. W., and Adams, C. M., "Investigation of Pulsed GTA Welding Parameters," *Weld J.*, May 1978, pp. 134s-138s.
- 4 Becker, D. W., and Adams, C. M., "The Role of Pulsed GTA Welding Variables in Solidification and Grain Refinement," *Weld. J.*, May 1979, pp. 144s-152s.
- 5 Birman, U. I., and Petrov, A. V., "Influence of the Weld Metal Solidification Pattern on Hot Cracking Pulsed-Arc Tungsten Electrode Welding," *Weld. Prod.*, Vol. 18, 1971, pp. 22-26.
- 6 Gruzdev, B. L., and Nikiforov, G. D., "Some Aspects of the Crystal Structure of Weld Metals Deposited by the Pulsed-Arc Process With Non-consumable Electrodes," *Weld. Prod.*, Vol. 18, 1971, pp. 30-33.
- 7 Needham, J. C., "Pulsed Current Tungsten Arc Welding—An Introduction to the Process," Pulsed TIG-Welding Seminar handout, TWI, 1973, pp. 1-7.
- 8 Omal, A. A., and Lundin, C. D., "Pulsed Plasma-Pulsed GTA Arc: A Study of the Process Variables," *Weld. J.*, Apr. 1979, pp. 97s-104s.
- 9 Petrov, A. V., and Birman, U. I., "Solidification of Weld Metal in Pulsed TIG Welding," *Weld. Prod.*, Vol. 15, 1968, pp. 1-5.
- 10 Petrov, A. V., and Birman, U. I., "Conditions Under Which the Metal Pool Solidifies During Pulsed Arc Welding With a Tungsten Electrode," *Avt. Svarka*, Vol. 22, 1969, pp. 24-26.
- 11 Vagner, F. A., and Stepanov, V. V., "Choice of Weld Settings for Pulsed TIG Welding and Its Effect on Joint Properties," *Weld. Prod.*, Vol. 15, 1968, pp. 23-26.
- 12 Vilkas, E. P., "Pulsed Current and Its Application for Which Gas Tungsten Arc Welding Is Either Difficult or Not Applicable," *2nd International Conference on Materials Technology*, ASME, Aug. 24-27, 1970, pp. 389-398.
- 13 Vilkas, E. P., "Pulsed Current and Its Welding Applications," *Weld. J.*, Apr. 1970, pp. 255s-262s.
- 14 Bromberg, Y., "Defining Strategy for Choosing Optimal Welding Parameters for Pulsed Current Gas Tungsten Arc Welding," CWR Technical Report 529614-81-1, 1981.
- 15 Sonti, N., "Solidification in Pulsed Gas Tungsten Arc Spot Welds," CWR Technical Report 529502-82-3, 1982.
- 16 Barone, J. C., "Pulsed Current Gas Tungsten Arc Welding Effects on Weld Pool Geometry," CWR Technical Report 529502-82-1, 1982.
- 17 Tsai, C. L., and Albright, C. E., "An Investigation of Welding Solidification Under Time Dependent Power Variations," Final Report, CWR, 1983, pp. 37-72.
- 18 Boulton, N. S., and Lance-Martin, H. E., "Residual Stresses in Arc Welding Plates," *Pro. Inst. Mech. Eng.*, Vol. 33, 1963, pp. 295-339.
- 19 Rosenthal, D., and Schmerber, R., "Thermal Study of Arc Welding," *Weld. J.*, Apr. 1938, pp. 2s-8s.
- 20 Rykalin, N. N., *Calculations of Thermal Processes in Welding*, Mashgiz Publication, Moscow, 1951.
- 21 Masubuchi, K., *Analysis of Welded Structures*, Pergamon Press, New York, 1980.
- 22 Tsai, C. L., "Parametric Study on Cooling Phenomena in Underwater Welding," Ph.D. Thesis, MIT, 1977.
- 23 Tsai, C. L., "Finite Source Theory," *Modeling of Casting and Welding Process II*, Dantzig and Berry, eds., AIME, 1983, pp. 329-341.
- 24 Pavelic, R., Tanakuchi, R., Uehara, O. and Myers, P., "Experimental and Computed Temperature Histories in Gas Tungsten Arc Welding in Thin Plates," *Weld. J.*, July 1969, pp. 295-304s.
- 25 Kou, S., "Three-Dimensional Heat Flow During Fusion Welding," *Modeling of Casting and Welding Process*, H. D. Brody and D. Apelian, eds., AIME, 1981, pp. 129-138.
- 26 Kogan, P. G., "The Temperature Field in the Weld Zone," *Avt. Svarka*, Vol. 9, 1979, pp. 8-9.
- 27 Hibbitt, H., and Marcal, P., "A Numerical Thermomechanical Model for the Welding and Subsequent Loading of a Fabricated Structure," *Computer and Structures*, Vol. 3, 1973, pp. 1145-1174.
- 28 Friedman, E., "Thermomechanical Analysis of the Welding Process Using Finite Element Methods," *ASME Journal Pressure Vessel Technology*, Vol. 97, Aug. 1975, pp. 206-213.
- 29 Paley, Z., and Hibbert, P., "Computation of Temperature in Actual Weld Designs," *Weld. J.*, Nov. 1975, pp. 385s-392s.
- 30 Naka, T., "Temperature Distribution During Welding," *Journal of Japan Weld. Society*, Vol. 1, 1953, pp. 4-16.
- 31 Masubuchi, K., and Kusuda, T., "Temperature Distribution of Welded Plates," *Journal Japan Weld. Society*, Vol. 22, 1953, pp. 14-17.
- 32 Tsai, C. L., "Modeling of Thermal Behavior of Metals During Welding," *Trends in Welding Research in the USA*, S. A. David, ed., ASM, 1981, pp. 91-108.
- 33 Friedman, E., "Finite Element Analysis of Arc Welding," DOE Research and Development Report, WAPD-TV-1438, 1980.
- 34 Cary, H. B., *Modern Welding Technology*, Prentice-Hall, New York, 1979.
- 35 Dickens, R. G., and Pinfold, P. E., "Investigation in Pulsed Tungsten Inert Gas Welding," Pulsed TIG Welding Seminar handout, TWI, 1973.
- 36 Apps, R., and Milner, D., "Heat Flow in Argon-Arc Welding," *British Weld. J.*, Oct. 1955, pp. 475-485.
- 37 Carslaw, H. S., and Jaeger, J. C., *Conduction of Heat in Solids*, 2nd ed., Oxford Press, 1959.

Measurement of Total Hemispherical Emissivities of Metal Wires by Using Transient Calorimetric Technique

H. Masuda
Professor.

M. Higano
Research Assistant.

Institute of High Speed Mechanics,
Tohoku University,
Sendai 980, Japan

An application of the transient calorimetric technique was studied for measuring total hemispherical emissivities of metal wires. A unique idea of using guard wires, which have a function similar to usual guard heaters, was incorporated into the emissivity apparatus to reduce conduction heat losses through thermocouple leads suspending a specimen. Emissivity measurements were performed by using a copper wire as a specimen. The heat losses through the leads were analyzed in considering radiation heat transfer from the leads, and the effect of the guard wires on the heat losses was clarified. Temperature distributions in the specimen were also obtained analytically. From these results, it was found that an improved transient calorimetric technique in this work is applicable to the emissivity measurement on metal wires, and that the accuracy in the measurements is adequate.

1 Introduction

The requirements of the accurate radiative properties of metals have increased in connection with space applications, solar-energy utilization, and applications for low-temperature phenomena of superconductivity. The transient calorimetric technique has been evaluated as a method for measuring total hemispherical emissivities of metals in previous investigations (Ramanathan and Yen, 1977; Smalley and Sievers, 1978; Cheng, 1984). Most recently, an improved technique has been introduced by Masuda and Higano (1983, 1985). However, on metal wires, not on block-shaped metals as used in the above investigations, measurements of the emissivities have been carried out by a steady-state calorimetric technique, like the hot-wire method usually used (e.g., Chen and Saxena, 1973; Jody and Saxena, 1976; Taylor, 1981) or a unique heating method adopted by Brandt et al. (1960). The steady-state technique has some defects in that samples are very long in relation to the end effect and that the measurement requires a long time. If the transient calorimetric technique is applicable to the measurement on metal wires, these defects may be eliminated. In addition, the application of the technique to metal wires appears attractive as a relatively rapid measurement, especially in a low-temperature range below room temperature, because the cooling rates of wire-shaped specimens are considerably higher than those of block-shaped specimens.

The present work has been undertaken with a view to investigating whether the transient calorimetric technique can be applied to measurements of total hemispherical emissivities of metal wires. In applications to metal wires, there is need for an improvement on the commonly used transient calorimetric technique. In this work, a unique idea is adopted such that guard wires similar to guard heaters are fitted on the measuring section of the emissivity apparatus, to reduce conduction heat losses through thermocouple leads suspending a specimen. Measurements are made on a wire specimen. From the experimental data, the lead-wire heat losses are numerically determined, and then the total hemispherical emissivities of the wire specimen are obtained and compared with previous results obtained for block-shaped specimens. In order to estimate the accuracies of the emissivities obtained, the specimen temperatures are also analyzed.

2 Experiment

The transient calorimetric technique is used in this work. In our previous investigations (Masuda and Higano, 1983, 1985), we found that heat loss through thermocouple leads suspending a specimen considerably increases due to a cooling of the leads, as indicated in Fig. 1, by radiation heat transfer from the leads to the surroundings maintained at low temperature. In the present work, the measuring section of the apparatus used in our previous work is improved with a unique idea to reduce the heat loss.

2.1 Apparatus and Procedure. The apparatus developed for our research is shown schematically in Fig. 2. It consists of a vacuum chamber (1) equipped with upper and lower liquid-nitrogen-cooled baths (2 and 3) (about 490 mm in inner diameter and 540 mm in height) whose inner walls are painted with a 3 M black velvet coating, a specimen (4) supported at point A by an iron-constantan thermocouple (5) for measuring the specimen temperature, a terminal box (6) (about 5 mm \times 5 mm \times 30 mm) thermally controlling terminals (point D), which is provided to reduce heat loss through thermocouples, a support (7), a movable furnace (8) heated with an electric sheath heater, and a high-vacuum system.

In order to minimize the heat loss through the thermocouple leads (5), that is, to guard the heat leak by the thermocouple leads, a set of two pieces of metal wires was provided,

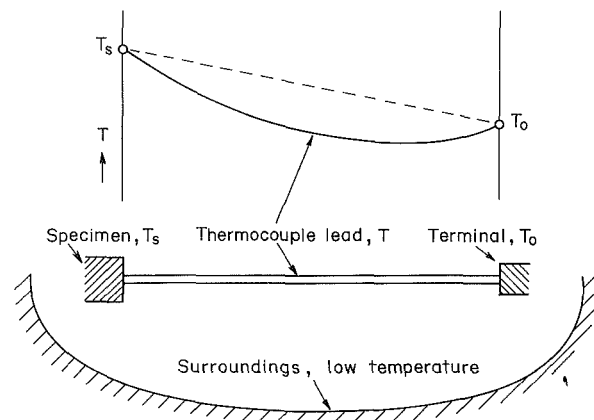


Fig. 1 Cooling of thermocouple lead by radiation

Contributed by the Heat Transfer Division for publication in the JOURNAL OF HEAT TRANSFER. Manuscript received by the Heat Transfer Division September 24, 1986.

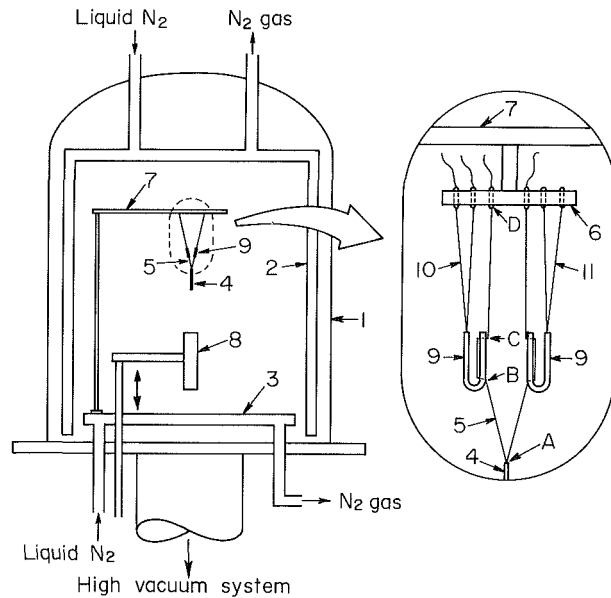


Fig. 2 Schematic drawing of emissivity apparatus: (1) vacuum chamber; (2) upper liquid-nitrogen bath; (3) lower liquid-nitrogen bath; (4) specimen; (5) thermocouple leads for specimen; (6) terminal box; (7) support; (8) furnace; (9) guard wires; (10) thermocouple leads for guard wire; (11) dummy thermocouple leads for guard wire

henceforth referred to as guard wires. As shown in Fig. 2, these two guard wires (9) of the same size were symmetrically attached with small pins to a pair of the thermocouple leads (5) passing through small holes drilled into the guard wires themselves at point B and C. In practice, the guard wires were transformed into a U-shape to shorten the total length of the heating section (the specimen and the guard wires). The temperatures of the guard wire were measured by a thermocouple (10) of the same kind as the thermocouple (5). Another thermocouple (11) was set as a dummy for the thermocouple (10). The iron and constantan leads of the thermocouples used were, respectively, 29 μm and 31 μm in diameter, which were the values measured by using a microscope.

The basic idea of the present technique by means of two guard wires is as follows: During the cooling process by the transient calorimetric technique, if parts of thermocouple leads suspending a specimen, near the specimen, have continually been maintained at about the same temperature as the specimen in some way, in other words, if the specimen and the two guard wires attached to two leads of the thermocouple as shown in Fig. 2, which are initially heated at the same temperature as the specimen in some way, have been allowed to cool at the same cooling rate, then the conduction heat loss

of the specimen through the leads can be kept very small. Here, the heating of the guard wires may be made together with the specimen by the furnace inside the vacuum chamber.

Eventually, such a pair of guard wires was carefully designed and made, and then they were fitted on the thermocouple leads.

For measuring temperatures of the specimen (or the guard wires), a thermocouple calibrated in our laboratory was used, and the junction was fixed into a smaller hole drilled into the tip of the specimen with a small pin of the same material. The chamber was evacuated, and the upper and lower baths were cooled by liquid nitrogen. After the specimen and the guard wires had been heated to an initial temperature required in the furnace, the furnace was turned off, moved downward, and then cooled in contact with the lower cooled bath. The cooling for the specimen and the guard wires was started at the same time, and both temperature decays were recorded on a digital data logger at intervals of 10–60 s. The measurements were carried out in the temperature range of 330–780 K in a vacuum of better than 7×10^{-5} Pa. The wall temperatures of the upper and lower cooled baths were measured by six thermocouples attached to the inner walls, and it was confirmed that their walls were kept at the liquid-nitrogen temperature (77.4 K). The terminals connecting thermocouple leads were maintained at a constant temperature (about 368 K) during all the measurements.

From the measured data, the time rate of change of specimen temperature, dT_s/dt , and the lead-wire heat loss Q_l may be calculated as described later. By using these values calculated, the total hemispherical emissivity of the specimen, $\epsilon_{h,s}$, can be obtained from the following equation (Smalley and Sievers, 1978) by assuming that the total hemispherical absorptivity $\alpha_{h,s}$ is equal to $\epsilon_{h,s}$ since $\alpha_{h,s}\sigma T_\infty^4 \ll \epsilon_{h,s}\sigma T_s^4$ and that the ambient wall is black:

$$\epsilon_{h,s}(T_s) = \frac{-m_s c_{p,s}(T_s) \frac{dT_s}{dt} \Big|_{T_s} - Q_l - Q_{\text{gas}}}{\sigma A_s (T_s^4 - T_\infty^4)} \quad (1)$$

where m , c_p , and A are, respectively, the mass, specific heat, and surface area, and the subscript s refers to the specimen. The surface area A_s is evaluated at T_s in consideration of the thermal expansion of the metal. T_∞ , σ , and Q_{gas} represent the ambient wall temperature (77.4 K in this work), the Stefan-Boltzmann constant, and the heat-loss rate through the residual gas in the vacuum chamber, respectively. The term Q_{gas} was neglected in the present work because the values (Nelson and Bevans, 1963) were always less than 0.1 percent of the total power loss of the specimen Q_s [$= -m_s c_{p,s}(dT_s/dt)$].

2.2 Specimen and Guard Wires. The specimen and the guard wires used in this work were made of copper wire of

Nomenclature

A = surface area
 c_p = specific heat
 D = wire diameter
 F = cross-sectional area
 k = thermal conductivity
 L = wire length
 m = mass
 Q_{gas} = conduction heat loss through the residual gas in vacuum chamber
 Q_s = total power loss of specimen
 $= -m_s c_{p,s}(dT_s/dt)$

Q_l = heat loss through the thermocouple leads suspending specimen
 q_r = radiative heat flux, equation (7)
 R = dimensionless heat loss, equation (6)
 T = temperature
 $T_{s,c}$ = temperature at center of wire specimen
 T_∞ = ambient wall temperature
 t = time

x = axial coordinate of wire
 α_h = total hemispherical absorptivity
 ϵ_h = total hemispherical emissivity
 ρ = density
 σ = Stefan-Boltzmann constant

Subscripts

g = guard wire
 s = specimen
 t = thermocouple

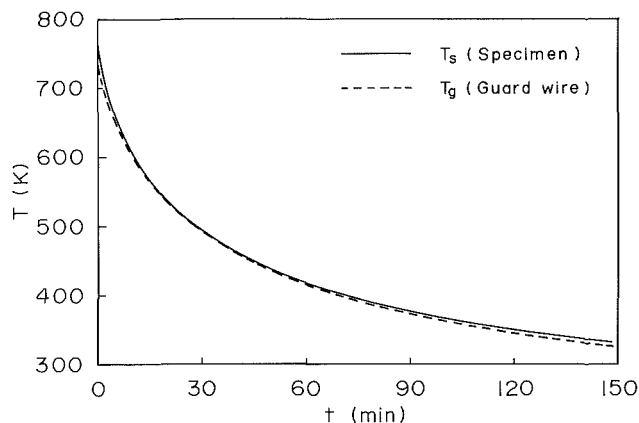


Fig. 3 Cooling curves of temperature versus time for the copper specimen and the guard wire

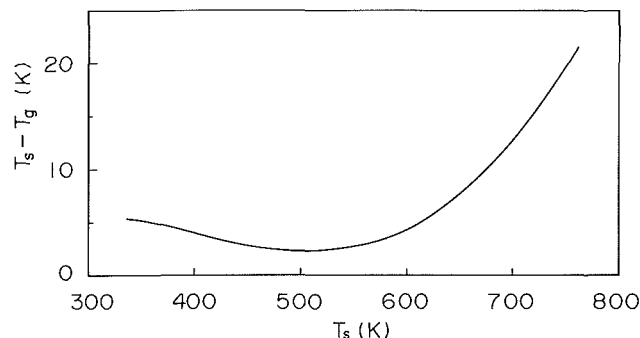


Fig. 4 Temperature difference between the copper specimen and the guard wire

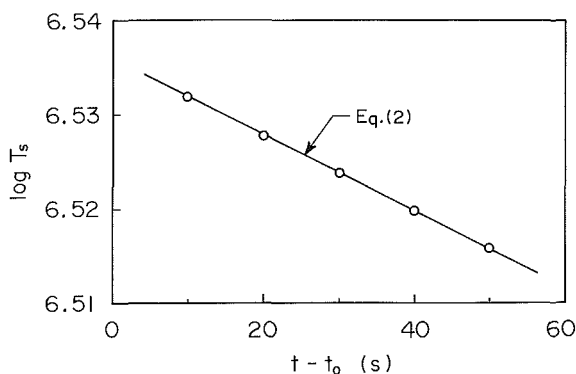


Fig. 5 Expression of the cooling curve for the specimen by an exponential function

99.95 percent purity. They were mechanically polished, cleaned with acetone, and then washed thoroughly with ultrasonic waves in distilled water. After this treatment they were dried in a vacuum chamber and carefully set up in the form shown in Fig. 2. The copper specimen had a mean diameter of 1.006 mm and a length of 49.95 mm at room temperature, and weighed 0.3510 g. The sizes of the guard wires were determined by taking into account the conduction heat losses through thermocouple leads connected with themselves, the radiation heat loss from themselves, and the data of some preliminary experiments. As a result, the copper guard wires were 1.28 mm in diameter and about 50 mm in length. The length of the thermocouple leads (5), indicated in Fig. 2, between A and B was about 20 mm (exactly 19.7 mm and 20.9 mm for the iron and constantan leads, respectively), and that between A and D was about 100 mm.

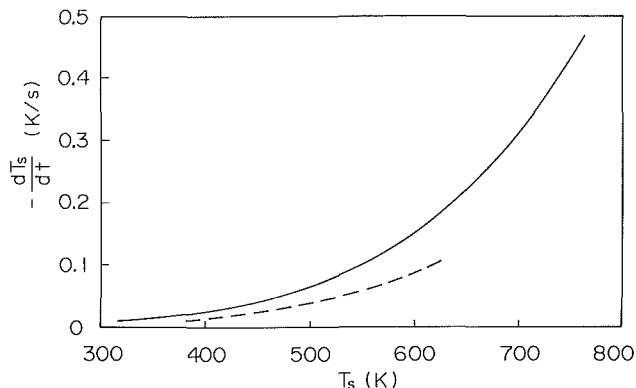


Fig. 6 Cooling rate ($-dT_s/dt$) versus temperature (T_s) curve for the copper specimens: solid line, present work, wire; dashed line, Masuda and Higano (1985), disk

3 Results and Discussion

3.1 Experimental Results. In Fig. 3 are shown T versus t curves obtained for the specimen and the guard wire. As expected, both the cooling curves for the specimen and the guard wire were in good agreement over the entire temperature range in the measurements. The temperature differences between the specimen and the guard wire at any time are shown more clearly in Fig. 4.

To obtain the value of $dT_s/dt|_{T_s}$, the specimen temperature T_s must be expressed as a function of t . The function $T_s(t)$ may be expressed by an exponential function as was done in the previous report (Masuda and Higano, 1985). In Fig. 5, an example of the experimental data is represented, in which t_0 is an arbitrarily fixed time. The function $T_s(t)$, therefore, was found to be given by

$$T_s(t) = a \exp(-bt) \quad (2)$$

and the constants a and b in the above equation were locally determined by using a least-squares method with a set of five adjacent experimental data. The deviation of equation (2) from T_s data was within 0.03 percent. Once the equation is determined, the derivative dT_s/dt can be obtained from the equation. The cooling rates for the specimen, obtained in this manner, are given by the solid line in Fig. 6. The dashed line in the figure indicates our previous results (Masuda and Higano, 1985) for the mechanically polished copper disk. It is of interest to note that the cooling rates of the wire specimen are much higher than those of the disk specimen. Besides, the cooling rate of wire becomes higher as the wire diameter is smaller.

3.2 Heat Loss Through Thermocouple Leads. In previous investigations in which the transient calorimetric technique was used, the lead-wire heat loss Q_l had mostly been evaluated by a simple analysis that is made by assuming steady state and by neglecting the term of radiation heat transfer in the heat-conduction equation (Estalote and Ramanathan, 1977; Wojcik et al., 1980). Recently, Masuda and Higano (1985) pointed out that the heat-loss results evaluated by this simple analysis include large errors, and presented a more exact analysis of the heat loss Q_l .

The heat loss Q_l must correctly be analyzed as a transient heat conduction. However, since the cooling rates of the specimen, the guard wires, and the thermocouple leads in the present experiment are very slow and the Q_l values obtained as a transient heat conduction are found to be almost equal to those obtained as a steady-state heat conduction as described later, the lead-wire heat loss is analyzed in this work as a steady-state and also as one-dimensional heat conduction because of fine wires.

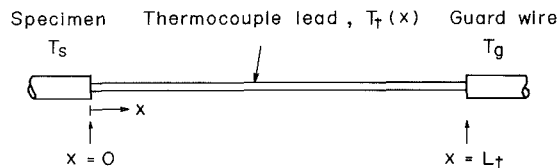


Fig. 7 Physical model for the thermocouple lead suspending the specimen

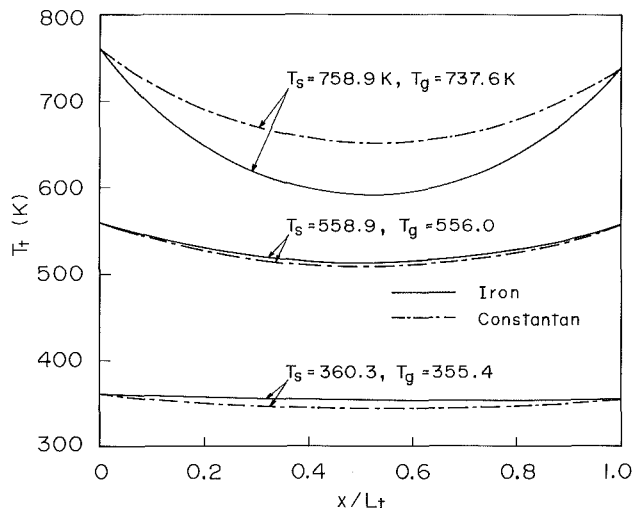


Fig. 8 Temperature distributions of the thermocouple leads between the specimen and the guard wire: $L_t = 20$ mm, $D_{t(\text{iron})} = 0.029$ mm and $D_{t(\text{constantan})} = 0.031$ mm

A thermal analysis is made on the thermocouple leads under the assumption that two leads of the thermocouple have no radiative interaction with each other, since their leads are very fine and have high reflectivity themselves. Figure 7 shows the physical model for one lead wire of the thermocouple. Let x be the coordinate along the lead and $T_t(x)$ be the temperature of the lead. T_g and L_t are the guard-wire temperature and the length of the thermocouple lead between the specimen and the guard wire, respectively. By neglecting the radiative interaction of the lead with the end surface of the specimen or the guard wire, and by assuming that thermal conductivity of the lead, k_t , is independent of temperature, the steady-state heat conduction equation may be written as

$$\frac{d^2 T_t}{dx^2} = \frac{4\epsilon_{h,t}\sigma(T_t^4 - T_\infty^4)}{D_t k_t} \quad (3)$$

where $\epsilon_{h,t}$ and D_t are the total hemispherical emissivity and the diameter of the lead, respectively. The boundary conditions for equation (3) are given by

$$\begin{aligned} T_t &= T_s & \text{at } x &= 0 \\ T_t &= T_g & \text{at } x &= L_t \end{aligned} \quad (4)$$

where for T_s and T_g at a prescribed time, the experimental data as expressed in Fig. 3 are used.

Once the solution of equation (3) is obtained, the heat loss $Q_{t(\text{iron})}$ of the iron lead, for instance, is calculated with the relation

$$Q_{t(\text{iron})} = -k_{t(\text{iron})} F_{t(\text{iron})} \left. \frac{dT_t}{dx} \right|_{x=0} \quad (5)$$

where $F_{t(\text{iron})}$ is the cross-sectional area of the iron lead.

We obtained the numerical solutions of equation (3), using a finite-difference method. On the thermophysical properties, iron's k value (Laubitz, 1960) and ϵ_h value (Davisson and Weeks, 1924), and constantan's k value (Sager, 1930) were evaluated at the mean temperature $T_m = [(T_s + T_g)/2]$. Here, Davisson and Weeks' expression for ϵ_h was used because the

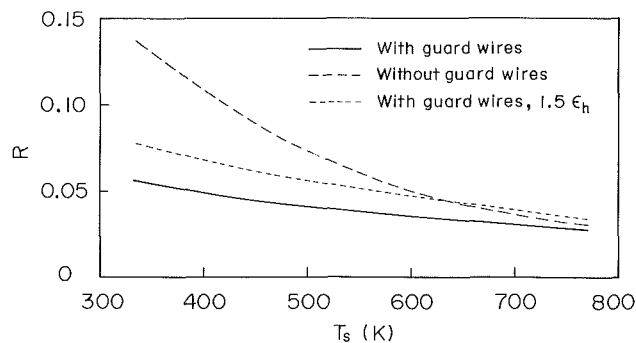


Fig. 9 Dimensionless heat loss R

expression was in good agreement with the experimental results for iron by Zuppardo and Ramanathan (1971). However, for constantan's ϵ_h the value of 0.059 (Barnes et al., 1947) was used, since the temperature dependence was not well known.

Figure 8 shows typical results of the temperature distributions obtained by the present analysis. The distribution curves hang downward because of the radiative heat loss from the lead, and the trend becomes stronger as the lead temperature is higher.

The lead-wire heat losses (two leads) calculated with the above solutions are shown by the solid line in Fig. 9 in terms of a ratio

$$R = Q_l / Q_s \quad (6)$$

where the total power losses Q_s have been calculated with our experimental data. As expected, the values of the heat loss obtained in the present work were quite satisfactory, since the maximum value of R in the previous work (Masuda and Higano, 1985) was about 0.13 at $T_s = 336$ K even for the block-shaped specimen. A comparison of the present result with the result obtained by supposing that guard wires are not used is given in Fig. 9. The dashed line in the figure indicates a result of a test without guard wires, which is predicted by assuming that the terminal box is maintained at the temperature of 368 K and that the length of the thermocouple leads is 100 mm. The comparison in Fig. 9 shows that the heat losses R brought out by an experimental technique without guard wires become much larger than those by our technique with guard wires, particularly at lower T_s . Such large values of R may not only largely contribute to the total error in $\epsilon_{h,s}$ to be measured, but cause nonuniform temperatures along the axis of the specimen to be unsatisfactory.

The above calculations for the heat loss were made by using iron's and constantan's ϵ_h values for highly polished surfaces. The real values of ϵ_h for the thermocouple leads used, however, might be much higher than those for highly polished surfaces because the thermocouple leads were so thin that it was difficult to polish them highly. So, we examined the effect of the ϵ_h values on the heat loss Q_l , assuming that the real values (both iron's and constantan's ϵ_h) are one and a half times as high as those used in the first calculations. The result obtained is also shown by the dotted line in Fig. 9. We find from the figure that R values obtained by the latter calculation are 1.3–1.4 times as large as those by the former. It should be noted that such a discrepancy between the heat-loss results occurs according to a magnitude of the ϵ_h values used in the calculations, although it is difficult to evaluate the lead-wire emissivities correctly.

The heat loss Q_l in this work has been evaluated for convenience by the analysis of steady-state heat conduction, not transient heat conduction. This evaluation must also be examined. Accordingly, we confirmed that the heat-loss results obtained by both the steady-state and the transient analysis in the mid-

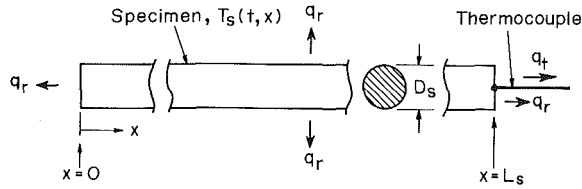


Fig. 10 Physical model for the specimen

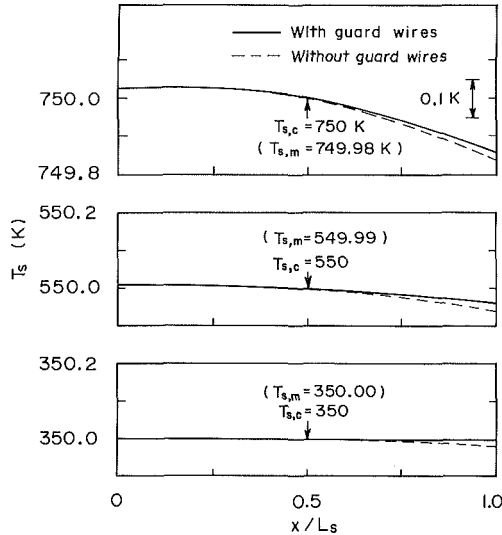


Fig. 11 Temperature distributions in the specimen

the temperature range in our experiment ($T_{t,x=0} = 600$ K) were in very good agreement with the difference within 1 percent.

3.3 Temperature Distributions in Specimen. In this work, the temperatures at one end of the specimen were measured, and they were used as specimen temperatures in the data analysis. So we must examine the temperature distributions in the specimen in the cooling process. An analysis of transient heat conduction for the specimen is made by taking the heat loss Q_t into account in the following.

The physical model is shown in Fig. 10. The coordinate along the axis of the specimen is x . The radiation heat flux from the specimen surface is q_r , and is given by

$$q_r = \epsilon_{h,s} \sigma (T_s^4 - T_\infty^4) \quad (7)$$

The specimen temperature T_s depends solely on time t and position x because the wire specimen is thin. By assuming that thermal conductivity of the specimen, k_s , is independent of temperature, the transient, one-dimensional heat conduction equation can be written as

$$\frac{\partial T_s}{\partial t} = \frac{k_s}{\rho_s c_{p,s}} \frac{\partial^2 T_s}{\partial x^2} - \frac{4\epsilon_{h,s} \sigma}{D_s \rho_s c_{p,s}} (T_s^4 - T_\infty^4) \quad (8)$$

where ρ is the density. With the initial temperature of the specimen, $T_{s(0)}$, heated in the furnace, the initial condition for equation (8) is as follows:

$$T_s(t, x) = T_{s(0)} \quad \text{for } t = 0 \quad (9)$$

The boundary condition for equation (8) at the left end surface of the specimen in Fig. 10 is

$$k_s \frac{\partial T_s}{\partial x} = \epsilon_{h,s} \sigma (T_s^4 - T_\infty^4) \quad \text{at } x = 0 \quad (10)$$

Another equation as boundary condition, at the right end surface ($x = L_s$), is introduced in the following. At this end surface, the boundary condition is

$$-k_s \frac{\partial T_s}{\partial x} = \epsilon_{h,s} \sigma (T_s^4 - T_\infty^4) + \frac{4Q_t}{\pi D_s^2} \quad \text{at } x = L_s \quad (11)$$

The heat loss Q_t in the above equation may be replaced by R . The total power loss Q_s can be approximated by

$$Q_s \approx \pi D_s L_s \epsilon_{h,s} \sigma (T_{s,c}^4 - T_\infty^4) \quad (12)$$

where $T_{s,c}$ is the temperature at the center of the specimen. Combining this equation with equation (6)

$$Q_t = \pi D_s L_s R \epsilon_{h,s} \sigma (T_{s,c}^4 - T_\infty^4) \quad (13)$$

Upon substituting equation (13) into equation (11), the following equation expressing the boundary condition can be obtained:

$$-k_s \frac{\partial T_s}{\partial x} = \epsilon_{h,s} \sigma (T_s^4 - T_\infty^4) + \frac{4L_s R \epsilon_{h,s} \sigma}{D_s} (T_{s,c}^4 - T_\infty^4) \quad (14)$$

Our data obtained in the present work may be applicable to the value R in this equation. The temperature distributions in the specimen may be found by combining equations (8)-(10) and (14).

The numerical solutions were obtained by using a finite-difference method. The calculations were made by dividing the measured range of T_s into parts at temperature intervals of 50 degrees and by assuming that the thermophysical property values and R values are constant in each divided T_s range. For $\epsilon_{h,s}$ and R , in the calculations, we used our data previously reported (Masuda and Higano, 1985) and the values indicated by the solid line in Fig. 9, respectively.

The numerical results are expressed by the solid lines in Fig. 11. In the figure, $T_{s,m}$ is the mean temperature of the wire specimen, which is defined as

$$T_{s,m} = \frac{1}{A_s} \int_{A_s} T_s dA_s \quad (15)$$

As seen in the figure, the temperature variations in the specimen are quite small; e.g., the maximum difference between the highest and the lowest local temperatures is only 0.18 K (top figure in Fig. 11). That is, the temperature drops, at the location where the thermocouple for measuring specimen temperatures is attached, due to the heat leak are extremely small, suggesting that the influence of the attached thermocouple on the temperature distributions in the specimen is negligible, at least for copper wire samples as used in this work. The error in $\epsilon_{h,s}$ caused by the temperature distributions is less than 0.1 percent. For reference, the temperature distributions in the absence of guard wires are also shown by dashed lines in Fig. 11. The influence of the attached thermocouple is similarly very small, if attention is directed only to temperature distribution in the specimen.

Furthermore, to ascertain whether or not the present technique is applicable to samples having low thermal conductivity, similar calculations were made for iron wire. In this case, the dimensionless heat loss R becomes about 0.006 to 0.014 because the emissivity of iron is so high that the radiation heat loss from the iron specimen grows about 4.5 times as large as that of a copper specimen of the same shape and size. As the numerical result, the maximum temperature differences in the iron specimen of the same shape as our copper specimen are found to be 1.3 K at $T_{s,c} = 750$ K and 0.05 K at $T_{s,c} = 350$ K. The error in the measurement of $\epsilon_{h,s}$, due to these temperature distributions, is estimated to be less than 1 percent. Our technique, therefore, may be applicable even to samples, such as iron wire, that have low thermal conductivity.

3.4 Temperature Distributions in Guard Wires. In the calculations of the heat loss Q_t , the temperatures measured at one end of the guard wire were used as guard-wire temperatures. Besides, the thermocouple leads for measuring specimen temperatures were fixed on each guard wire at two

Table 1 ϵ_h values obtained by the present work on copper wire

Temperature, K	ϵ_h , percent	Temperature, K	ϵ_h , percent	Temperature, K	ϵ_h , percent
758.9	2.28	599.5	1.80	439.2	1.42
741.5	2.23	580.0	1.77	420.3	1.35
718.4	2.14	558.9	1.71	400.4	1.31
698.6	2.10	539.2	1.67	380.0	1.23
681.2	2.01	519.5	1.63	360.3	1.17
660.8	1.99	499.9	1.58	340.0	1.15
639.3	1.88	480.1	1.51		
620.5	1.86	460.9	1.46		

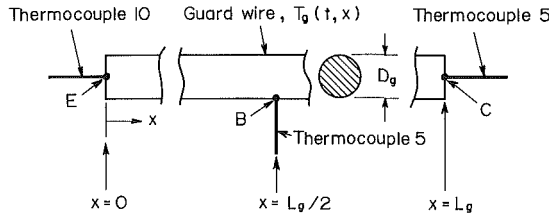


Fig. 12 Physical model for the guard wire

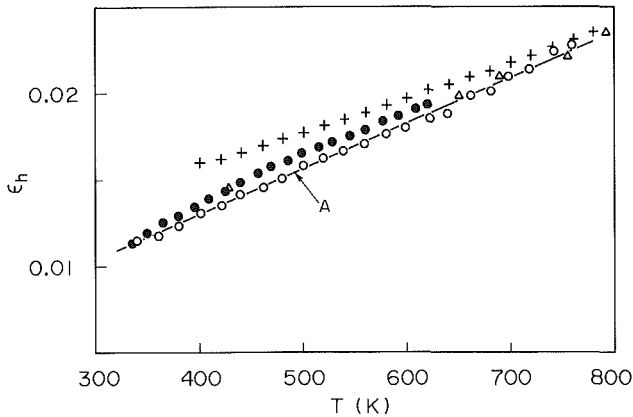


Fig. 13 Comparison of total hemispherical emissivity results for copper: \circ , present work, mechanically polished wire; line A, result by least squares for present data; \bullet , Masuda and Higano (1985), mechanically polished disk; $+$, Ramanathan and Yen (1977), mechanically polished sphere; Δ , Smalley and Sievers (1978), mechanically polished square plate

points, B and C, in Fig. 2. If the temperature variation in the guard wires at any instant is too large, problems may still remain on the calculated results of Q_l , and on a thermoelectric emf in the leads between points B and C. To clarify these, an analysis of the temperature of the guard wire was made.

The physical model is shown in Fig. 12. The guard wire is assumed to be straight for convenience. Points B and C in the figure correspond to B and C in Fig. 2, respectively, and point B is, as a matter of convenience, set at the center of the guard wire. Point E is the position where the thermocouple (10) shown in Fig. 2 is attached, and the subscript g used in symbols refers to the guard wire. All of the lead-wire heat loss through points B, C, or E can be obtained by calculations similar to those in subsection 3.2, since the temperature of the terminal box has also been measured. Once these three heat losses are found, the temperature distribution in the guard wire can be obtained in a manner similar to that for the specimen.

The results of the calculations showed that the uniformities of the guard-wire temperature were much better than those of the specimen because the diameter of the guard wire was larger than that of the specimen, although the figure expressing the results was omitted. For instance, the difference between local temperatures at points B and C was estimated to be only 0.03 K at $T_g \approx 760$ K, the highest temperature in the present ex-

periments, and, in that case, the difference between those at points B and E was 0.07 K. At lower T_g the differences were even smaller.

3.5 Total Hemispherical Emissivity of Copper Wire. The measured results of ϵ_h for copper wire, obtained in consideration of the thermal expansion of the metal, are listed in Table 1 and plotted as a function of temperature in Fig. 13. The thermal-expansion data used in the calculation are those recommended by Touloukian et al. (1975), and the specific-heat data are those of Lyusternik (1959) with an uncertainty of 1 percent. Straight line A in Fig. 13 represents the following expression obtained from our present data by a least-squares method:

$$\epsilon_h = 0.0024 + 2.65 \times 10^{-5} T \quad (16)$$

The ϵ_h values vary almost linearly over the temperature range of our experiments. A comparison of the present results is made with our previous results for a mechanically polished disk specimen (Masuda and Higano, 1985). As expected, both the results are in good agreement, with the mean difference being only 4 percent. In consequence, our transient calorimetric technique of using guard wires is considered to be quite satisfactory for measuring ϵ_h of metal wires, and its precision is also presumed to be sufficiently high.

The results of Ramanathan and Yen (1977) for a mechanically polished copper sphere are also plotted in Fig. 13 for comparison. Their data are higher than our present results by 1–22 percent, and the trend of deviation is larger at lower temperatures. It appears that the deviations are mainly due to the approximate evaluation of the heat loss Q_l by simple analysis. If the heat loss had more exactly been analyzed in consideration of the radiation heat transfer from the thermocouple leads, their data would have approached ours much more. On the other hand, the data of Smalley and Sievers (1978), plotted in Fig. 13, by an experimental technique similar to that of Ramanathan and Yen, agree well with ours, although their analysis of Q_l does not seem to be exact, and the details of their experiment are obscure.

The maximum absolute error in ϵ_h values measured in the present work, which is caused by temperature measurements, temperature distributions in the specimen, c_p data with an uncertainty of 1 percent, and so on, is estimated to be 3 percent. Furthermore, the examination of Q_l , made in subsection 3.2, reveals that supposing the correct values of the lead-wire emissivities are 1.5 times higher than those used in the present calculations, the results given in Table 1 are overestimated by 0.9 percent at the highest temperature and by 2.5 percent at the lowest temperature.

4 Concluding Remarks

In order to apply the transient calorimetric technique for measuring emissivities to the measurement on metal wires, the measuring section of the apparatus was specially designed with the idea of using the guard wires, and the measurement on copper wire were carried out. By using the guard wires, the heat loss through the thermocouple leads could be considerably reduced, i.e., by 60 percent at the maximum. From

the results obtained by the analyses of the lead-wire heat loss and of the temperature distribution in the specimen, it was clarified that the present technique of using the guard wires is applicable to the emissivity measurement on metal wires, especially to the measurement by very short specimens. Moreover, the accuracy in the measurement of the emissivity of metal wires by employing this technique is presumed to be sufficiently high. Emissivity measurements using metal wires by the transient calorimetric technique will be more useful and attractive in a low temperature range below room temperature, since the cooling rates for wire specimens are relatively high in comparison with those for block-shaped specimens.

References

- Barnes, B. T., Forsythe, W. E., and Adams, E. Q., 1947, "The Total Emissivity of Various Materials at 100–500°C," *J. Opt. Soc. Am.*, Vol. 37, pp. 804–807.
- Brandt, J. A., Irvine, T. F., Jr., and Eckert, E. R. G., 1960, "A Method of Measuring Total Hemispherical Emissivities at Low Temperatures – Results for Pure Iron From 300 to 500 Degrees Rankine," *Proceedings of the 1960 Heat Transfer and Fluid Mechanics Institute*, Stanford University Press, Stanford, CA, pp. 220–228.
- Chen, S. H. P., and Saxena, S. C., 1973, "Experimental Determination of Hemispherical Total Emittance of Metals as a Function of Temperature," *Ind. Eng. Chem. Fundam.*, Vol. 12, pp. 220–224.
- Cheng, S. X., 1984, "An Accurate Transient Calorimeter for Measuring the Total Hemispherical Emissivity of Metals and Alloys," *High Temperatures – High Pressures*, Vol. 16, pp. 459–468.
- Davison, C., and Weeks, J. R., Jr., 1924, "The Relation Between the Total Thermal Emissive Power of a Metal and Its Electrical Resistivity," *J. Opt. Soc. Am.*, Vol. 8, pp. 581–605.
- Estalote, E. A., and Ramanathan, K. G., 1977, "Low-Temperature Emissivities of Copper and Aluminum," *J. Opt. Soc. Am.*, Vol. 67, pp. 39–44.
- Jody, B. J., and Saxena, S. C., 1976, "Radiative Heat Transfer From Metal Wires: Hemispherical Total Emittance of Platinum," *Journal of Physics E: Scientific Instruments*, Vol. 9, pp. 359–362.
- Laubitz, M. J., 1960, *Can. J. Phys.*, Vol. 38, pp. 887–907; quoted by Y. S. Touloukian et al., *Thermophysical Properties of Matter*, Vol. 1, 1970, IFI/Plenum, New York, pp. 159, 165.
- Lyusternik, V. E., 1959, *Prib. Tekh. Eksp.*, Vol. 4, pp. 127–129; quoted by Y. S. Touloukian and E. H. Buyco, *Thermophysical Properties of Matter*, Vol. 4, 1970, IFI/Plenum, New York, pp. 52, 55.
- Masuda, H., and Higano, M., 1983, "A Transient Calorimetric Technique for Measuring Total Hemispherical Emissivities of Solid Materials – Estimation of Heat Losses by Thermocouple Leads," *Proceedings of the Fourth Japan Symposium on Thermophysical Properties*, Japan Society of Thermophysical Properties, pp. 5–8.
- Masuda, H., and Higano, M., 1985, "Transient Calorimetric Technique for Measuring Total Hemispherical Emissivities of Metals With Rigorous Evaluation of Heat Loss Through Thermocouple Leads," *J. Opt. Soc. Am. A*, Vol. 2, pp. 1877–1882.
- Nelson, K. E., and Bevans, J. T., 1963, "Errors of the Calorimetric Method of Total Emittance Measurement," *Measurement of Thermal Radiation Properties of Solids*, J. C. Richmond, ed., NASA SP-31, pp. 55–65.
- Ramanathan, K. G., and Yen, S. H., 1977, "High-Temperature Emissivities of Copper, Aluminum, and Silver," *J. Opt. Soc. Am.*, Vol. 67, pp. 32–38.
- Sager, G. F., 1930, Rensselaer Polytech. Inst., Eng. and Sci. Ser., Bull. 27, pp. 3–48; quoted by Y. S. Touloukian et al., *Thermophysical Properties of Matter*, Vol. 1, 1970, IFI/Plenum, New York, pp. 562, 566.
- Smalley, R., and Sievers, A. J., 1978, "The Total Hemispherical Emissivity of Copper," *J. Opt. Soc. Am.*, Vol. 68, pp. 1516–1518.
- Taylor, R. E., 1981, "Determination of Thermophysical Properties by Direct Electric Heating," *High Temperatures – High Pressures*, Vol. 13, pp. 9–22.
- Touloukian, Y. S., Kirby, R. K., Taylor, R. E., and Desai, P. D., 1975, *Thermophysical Properties of Matter*, Vol. 12, IFI/Plenum, New York, p. 77.
- Wojcik, L. A., Sievers, A. J., Graham, G. W., and Rhodin, T. N., 1980, "Total Hemispherical Emissivity of W(100)," *J. Opt. Soc. Am.*, Vol. 70, pp. 443–450.
- Zuppardo, G. L., and Ramanathan, K. G., 1971, "Anomalous Emissivities of Nickel and Iron Near Their Curie Temperatures," *J. Opt. Soc. Am.*, Vol. 61, pp. 1607–1612.

Structure and Radiation Properties of Luminous Turbulent Acetylene/Air Diffusion Flames

J. P. Gore
Research Fellow.

G. M. Faeth
Professor.
Fellow ASME

Department of Aerospace Engineering,
The University of Michigan,
Ann Arbor, MI 48109-2140

An experimental and theoretical study of the structure and radiation properties of luminous, round, turbulent acetylene/air diffusion flames is described. Measurements were made of mean and fluctuating velocities, mean concentrations, laser extinction (514 and 632.8 nm), spectral radiation intensities (1200–5500 nm), and radiative heat fluxes. The measurements were used to evaluate structure predictions based on the laminar flamelet concept, and radiation predictions based on a narrow-band model both ignoring and considering turbulence/radiation interactions. State relationships needed for the laminar flamelet concept were found from auxiliary measurements in laminar flames. Predictions were encouraging; however, quantitative accuracy was inferior to earlier findings for luminous flames. This is attributed to the large radiative heat loss fractions of acetylene/air flames (approaching 60 percent of the heat release rate); coupled structure and radiation analysis should be considered for improved results. The findings suggest significant turbulence/radiation interactions (increasing spectral intensities 40–100 percent from estimates based on mean properties); and that soot volume fractions may approximate universal fractions of mixture fraction in turbulent acetylene/air diffusion flames.

Introduction

This paper describes an extension of earlier work concerning the structure and radiation properties of turbulent diffusion flames (Gore and Faeth, 1987; Gore et al., 1987a, 1987b; Jeng and Faeth, 1984a, 1984b, and 1984c; Jeng et al., 1982, 1984). The objective was to determine whether theoretical methods developed by Gore and Faeth (1987) that were successful for luminous ethylene/air diffusion flames could be extended to more heavily sooting acetylene/air diffusion flames. Acetylene/air diffusion flames were studied since their soot concentrations are almost an order of magnitude higher than ethylene/air diffusion flames, providing a strong test of analysis. Acetylene/air diffusion flames are also interesting since they have received considerable attention by others (Becker and Liang, 1982, 1983; Beier et al., 1984; Kent and Bastin, 1984; Magnussen, 1975).

The scalar structure of flames must be known in order to estimate their radiation properties. The laminar flamelet concept for nonpremixed flames, proposed by Bilger (1977) and Liew et al. (1981) has been successful for estimating the scalar properties of nonluminous diffusion flames (Gore et al., 1987a, 1987b; Jeng and Faeth 1984a, 1984b). This concept is based on the observation that scalar properties in nonluminous laminar diffusion flames are nearly universal functions of mixture fraction (the fraction of mass at a point which originated from the injector), except near points of flame attachment. These functions have come to be called "state relationships" (Jeng and Faeth, 1984a). Turbulent flames are then viewed as wrinkled laminar flames having the same properties; thus, predictions of a single conserved scalar, like mixture fraction, provide a complete description of the scalar properties of the flow. When this approach is applicable, routine measurements or analysis of scalar properties in laminar flames essentially replace the complexities of flame chemistry in turbulent flames.

Extension of these ideas to luminous flames has been considered for ethylene/air diffusion flames (Gore and Faeth,

1987). The concentrations of major gas species were found to be nearly universal functions of mixture fraction, in spite of the presence of soot, in laminar ethylene/air diffusion flames. Furthermore, soot volume fractions, the main property needed to predict continuum radiation from soot, were also roughly correlated as a function of mixture fraction in laminar flames. Subsequent measurements suggested that universality of soot volume fraction as a function of mixture fraction was preserved for turbulent flames, providing a reasonably successful approach for predicting spectral absorption and emission by soot. In view of the added complexities of soot chemistry, this extension of the laminar flamelet concept is potentially quite valuable for finding the scalar structure and radiation properties of luminous flames, motivating the present study of the flamelet hypothesis for more heavily sooting acetylene/air flames.

A second issue concerning radiation from luminous turbulent flames involves effects of turbulence/radiation interactions, i.e., errors in radiation predictions based on mean scalar properties due to nonlinearities of radiation properties. This has been studied by comparing predictions based on mean scalar properties with results of a stochastic analysis which seeks to model effects of turbulent fluctuations (Gore and Faeth, 1987; Gore et al., 1987a, 1987b; Jeng and Faeth, 1984a, 1984b, 1984c; Jeng et al., 1982, 1984). Findings indicated relatively small effects (~20 percent) of turbulence/radiation interactions for carbon monoxide/air (Gore et al., 1987a) and methane/air (Jeng et al., 1984) diffusion flames. In contrast, hydrogen/air (Gore et al., 1987b) and ethylene/air (Gore and Faeth, 1987) diffusion flames exhibited very large effects (50–300 percent) of turbulence/radiation interactions. Since fuel type influences turbulence/radiation interactions, the phenomenon was also considered during the present investigation.

Earlier studies of turbulent acetylene/air diffusion flames, by Magnussen (1975), Kent and Bastin (1984), and Becker and Liang (1982, 1983), provide additional background for the present investigation. Magnussen (1975) measured Mie scattering from soot particles, finding that soot was confined to narrow regions associated with turbulent eddies, suggesting

Contributed by the Heat Transfer Division for publication in the JOURNAL OF HEAT TRANSFER. Manuscript received by the Heat Transfer Division February 18, 1987.

that this property is correlated with mixture fraction. Kent and Bastin (1984) used laser extinction measurements to study effects of residence time on soot concentrations. They observed that soot concentrations become relatively independent of residence time for sufficiently long residence times, pointing to quasi-equilibrium of soot properties for these conditions. Becker and Liang (1982, 1983) similarly find that the fraction of fuel carbon which is converted to soot, and is emitted from the flame, also becomes relatively independent of flame conditions for sufficiently long residence times. These observations all suggest potential for universality of the state relationship for soot volume fractions, at sufficiently long residence times, prompting further examination of this possibility during the present study.

The paper begins with a brief description of theoretical and experimental methods. Auxiliary measurements in laminar flames, to find state relationships, are then discussed. This is followed by comparison of structure predictions and measurements for the turbulent flames. Laser extinction measurements are then used to study soot volume fraction state relationships in turbulent flames. The paper concludes with consideration of predicted and measured radiant emission properties. The present discussion is brief, more details and a tabulation of data are provided by Gore (1986).

Experimental Methods

Apparatus. The turbulent flame apparatus was identical to past work, e.g., Gore and Faeth (1987). Acetylene was injected vertically upward from a water-cooled burner within a screened enclosure. The flames were attached at the burned exit using a small coflow of hydrogen.

The laminar flame apparatus was also identical to past work (Gore and Faeth, 1987). The burner involved vertical injection of acetylene (14.3-mm-dia port) in a concentric coflowing stream of air (102-mm-dia port) within a cylindrical enclosure.

Instrumentation. Instrumentation was generally similar to past work (Gore and Faeth, 1987). Streamwise mean and fluctuating velocities were measured across the burner exit ($x/d=2$) and along the axis of the turbulent flames, using a single-channel laser-Doppler anemometer (LDA). Radial velocity fluctuations were also measured at $x/d=2$, by rotating the beam plane of the LDA. These measurements were time averages with uncertainties (95 percent confidence) less than 5 percent for mean velocities and less than 10 percent for velocity fluctuations, largely governed by finite sampling times (Gore, 1986). Mean concentrations of gaseous species in the laminar and turbulent flames were measured by sampling and analysis with a gas chromatograph. A water-cooled probe, having an inlet diameter of 6.3 mm, was used for isokinetic sampling along the axis of the turbulent flames. A quartz microprobe, having an inlet diameter of 0.1–0.2 mm and operating with choked flow at the inlet, was used in the laminar flames. Both probes accumulated deposited soot and

tended to clog in regions having appreciable concentrations of soot; therefore, results for such locations are not reported in the following. Uncertainties in composition measurements (95 percent confidence) are less than 15 percent, largely governed by uncertainties in measuring gas chromatography peak areas (Gore, 1986).

Laser extinction measurements were used to study absorption by soot in the turbulent flames. Two wavelengths in the visible (514 and 632.8 nm) were used to determine whether the soot particles satisfied the small-particle Rayleigh-scattering limit, while minimizing effects of radiation emission by soot in the flames. A chopper, operated at 800 Hz, was used to improve signal-to-noise ratios by reducing effects of background and flame radiation. Uncertainties in these measurements (95 percent confidence) are estimated to be less than 10 percent, largely governed by finite sampling times (Gore, 1986).

Laser extinction measurements at 632.8 nm were used to measure soot volume fractions in the laminar flames, following the deconvolution technique reported by Santoro et al. (1983). Soot volume fractions were computed using the refractive-index correlation of Dalzell and Sarofim (1969). Uncertainties in the soot volume fraction measurements (95 percent confidence) are estimated to be less than 20 percent, largely governed by effects of finite sampling times and position accuracy in the build up of errors in the deconvolution procedure (Gore, 1986).

Spectral radiation intensities were measured with a monochromator, viewing roughly 10-mm-dia (1.2 deg field angle) horizontal paths through the flame axis. Various gratings and order-sorting filters were used for measurements in the 1200–5500 nm wavelength range (resolution of 8 percent at 1200 nm and 40 percent at 5500 nm). Uncertainties in intensity levels (95 percent confidence) are estimated to be less than 15 percent, largely governed by the finite sampling times (Gore, 1986).

Radiative heat fluxes were measured at points around the turbulent flames using a gas-purged, water-cooled radiometer (150 viewing angle with a sapphire window). Uncertainties (95 percent confidence) in these measurements were less than 10 percent, largely governed by uncertainties in sensor calibrations (Gore, 1986).

All measurements were repeatable within the uncertainty levels stated above during the course of the study.

Test Conditions. Table 1 is a summary of test conditions for the two turbulent flames studied. Initial Reynolds numbers were high enough to provide a reasonably turbulent flow, with residence times varying by roughly a factor of two for the two flames. Initial Richardson numbers were relatively low; however, effects of buoyancy were important near the tip of the flames (defined as the point where the fuel-equivalence ratio, in the mean, was unity along the axis). Radiative heat losses approach 60 percent of the chemical energy release rate in these flames. This is roughly twice the radiative heat loss

Nomenclature

a = acceleration of gravity
 d = burner exit diameter
 f = mixture fraction
 g = square of mixture fraction fluctuations
 I_λ = spectral radiation intensity
 k = turbulent kinetic energy
 m_o = burner mass flow rate

r = radial distance
 Re = burner Reynolds number
 u = streamwise velocity
 x = height above burner
 ϵ = rate of dissipation of turbulence kinetic energy
 ν = kinematic viscosity
 ρ = density

Subscripts

c = centerline quantity
 o = burner exit condition

Superscripts

$(\bar{\quad})$, $(\overline{\quad})$ = time- and Favre-averaged mean quantity
 $(\overline{\quad})'$, $(\overline{\quad})''$ = time- and Favre-averaged root-mean-square fluctuating quantity

Table 1 Summary of turbulent flame test conditions^a

Reynolds number ^b	5300	9200
Richardson number ^c × 10 ⁴	4.5	1.4
u_o (m/s) estimated	10.5	18.1
u_o (m/s) measured	11.8	20.6
$k_o^{1/2}/u_o$	0.13	0.13
Heat release rate (kW)	10.5	18.1
Radiative heat loss fraction (percent)	57.0	59.0
Fuel flow rate (mg/s)	217	376
Hydrogen flow rate (mg/s)	1.9	1.9

^aFlow directed vertically upward from a 5-mm-dia passage in still air at normal temperature and pressure. Commercial Grade acetylene, Detroit Welding Supply Co.

^bRe = $u_o d/\nu$ based on fuel-gas properties at burner exit.

^cRi = ad/u_o^2

fractions observed for luminous ethylene/air diffusion flames (Gore and Faeth, 1987). However, the present radiative heat loss fractions are similar to the findings of Becker and Liang (1982, 1983) for turbulent acetylene/air flames at comparable conditions.

Theoretical Methods

Flame Structure. Analysis of flame structure and radiation properties was identical to past work (Gore and Faeth, 1987; Gore et al., 1987a, 1987b; Jeng and Faeth, 1984a, 1984b, 1984c; Jeng et al., 1982, 1984) and will only be briefly described. Major assumptions of the structure analysis are as follows: low Mach number boundary-layer flow with no swirl; equal exchange coefficients of all species and heat; buoyancy only affects the mean flow; and negligible radiant energy exchange between various portions of the flame. Except for the last, these assumptions are either justified by the test conditions or by acceptable performance for similar diffusion flames. The present flames, however, lose an unusually large fraction of their chemical energy release by radiation (~60 percent), which is two to four times greater than flames analyzed earlier. This behavior suggests that there is significant radiant energy exchange within the present flames; thus, the last assumption is questionable. Nevertheless, the assumption is adopted, as a first approximation, in order to avoid the complexity and increased computation costs required for coupled structure and radiation analysis. Flow properties were found using a Favre-averaged k - ϵ - g turbulence model, proposed by Bilger (1977), with specific modifications and empirical constants due to Jeng and Faeth (1984).

Following Bilger (1977), the laminar flamelet approximation was used to relate scalar properties to the mixture fraction. State relationships for the concentrations of major gas species were obtained from the laminar flame measurements. The state relationship for soot volume fractions was found from laser extinction measurements in both laminar and turbulent flames, as described later. State relationships for temperature and density were computed, assuming that each flame lost 60 percent of its chemical energy release by radiation and using measured concentrations of major gas species from the state relationships. Thermochemical properties for these calculations were obtained from Gordon and McBride (1971).

Initial values of \bar{u} and k , needed for the calculations, were found by linear interpolation of measurements of mean and fluctuating velocities at $x/d=2$. k was estimated by assuming that radial and tangential velocity fluctuations were equal. The resulting values of k_o were relatively high, probably due to disturbances from the hydrogen slot within the burner. The boundary between the potential core and the shear layer was found from the measured profiles of \bar{u} and k . The initial mixture-fraction distribution was assumed to be the same as the normalized velocity profile. The initial value of ϵ in the

potential core was found by matching turbulent diffusivities of mixing-length and k - ϵ models at the exit. The value of g in the potential core was set equal to zero. Values of ϵ and g in the shear layer were found by assuming local equilibrium for these quantities.

Radiation Properties. The equation of radiative transfer was solved to find spectral intensities for radiation paths corresponding to the measurements. This involved a Goody statistical narrow-band model with the Curtis-Godson approximation for inhomogeneous gas paths, following Ludwig et al. (1973). The computer program RADCAL, developed by Grosshandler (1980), was used for the calculations, considering the gas bands of CO₂, CO, H₂O, and CH₄ as well as continuum radiation from soot at the small-particle limit, i.e., scattering was ignored.

Turbulence/radiation interactions were either ignored, by basing predictions on mean properties, or considered, by using a stochastic method. The mean-property method employed time-averaged mean scalar properties, found from the structure computations, along the radiation path. The stochastic method involved dividing the radiation path into dissipation-scale sized eddies which were assumed to have uniform properties at each instant. The probability density function of mixture fraction for each eddy was randomly sampled to provide a realization of scalar properties along the path, in conjunction with the state relationships. Spectral radiation intensities were then computed for each realization, similar to the mean-property method. Sufficient realizations were averaged to obtain statistically significant results.

Radiative heat fluxes were computed using the mean-property method, in conjunction with the discrete-transfer approach of Lockwood and Shah (1981). This involves summing spectral radiation intensities for various paths through the flame (120 to cover the field of view) and for the wavelength range having significant radiance (500–6000 nm), allowing for the cutoff of the sapphire window of the sensor (Gore, 1986).

Results and Discussion

State Relationships. Concentrations of O₂, N₂, CO₂, CO, CH₄, C₂H₆, H₂O, H₂, and C₂H₂, measured in the laminar flames, are plotted as a function of fuel-equivalence ratio (which is a single-valued function of mixture fraction) in Figs. 1 and 2. Three different axial stations and two fuel flow rates were considered; however, only the latter are identified to reduce clutter of the figures. Fuel-equivalence ratios were calculated based on the total carbon in all gas species and nitrogen, neglecting ambient carbon dioxide and water vapor, and assuming that the local carbon-to-hydrogen ratio was the same as the fuel. To reduce uncertainties in this procedure, positions involving significant concentrations of soot are not considered. However, soot particles do not diffuse like gas molecules; therefore, local carbon/hydrogen ratios could differ from the original fuel, even though soot concentrations are small. Uncertainties due to this effect are difficult to quantify; however, they are unlikely to exceed uncertainties in the concentration measurements themselves. Predictions based on the Gordon and McBride code (1971) (assuming thermodynamic equilibrium, no solid carbon present, and adiabatic combustion) also appear on the figures.

Measurements illustrated in Figs. 1 and 2 approximate local thermodynamic equilibrium for fuel-lean conditions, providing an immediate explanation for universal correlations of gas species concentrations in this region. Concentrations depart appreciably from equilibrium predictions for fuel-rich conditions; however, they still yield reasonably universal correlations as a function of fuel-equivalence ratio, satisfying the laminar flamelet approximation. Attainment of quasi-

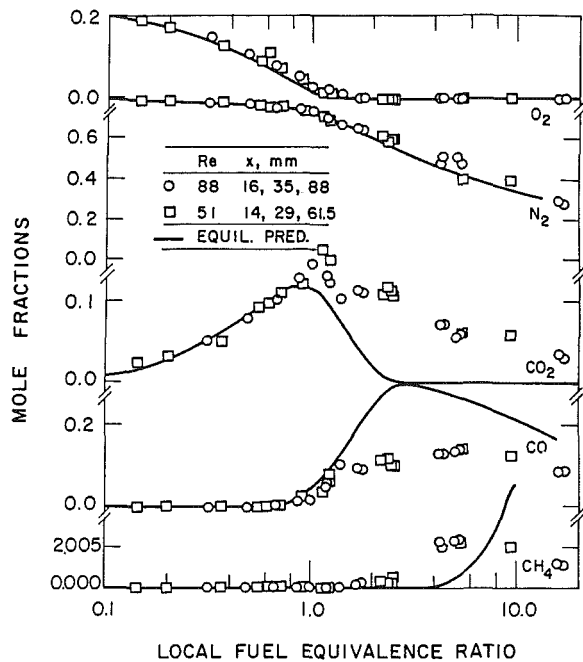


Fig. 1 State relationship for gas concentrations in acetylene/air diffusion flames

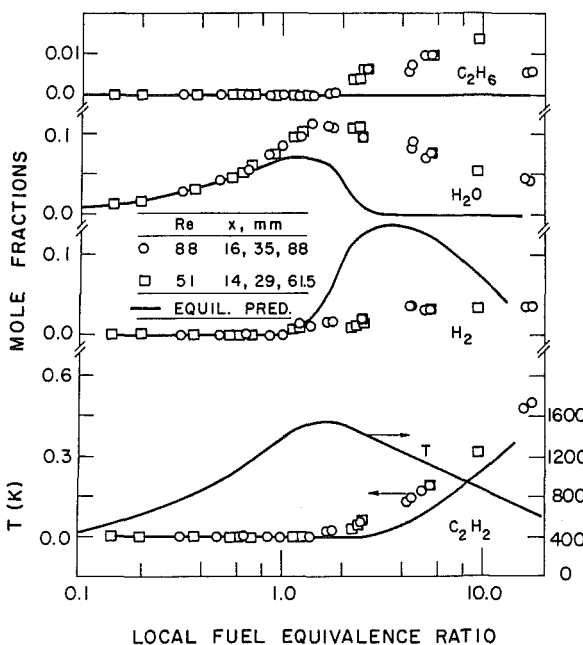


Fig. 2 State relationships for gas concentrations in acetylene/air diffusion flames (continued)

equilibrium for fuel-rich conditions is typical of other hydrocarbons that have been studied (Bilger, 1977; Gore and Faeth, 1987; Jeng and Faeth, 1984a; 1984b; Liew et al., 1981). Whether this behavior persists in regions having high concentrations of soot is unknown; however, results discussed next show that this involves a relatively narrow range of mixture fractions in any event.

Measurements of soot volume fractions for the laminar flame are plotted as a function of fuel-equivalence ratio in Fig. 3. As just noted, the highest concentrations of soot are confined to a relatively narrow range of fuel-equivalence ratios, just on the rich side of the diffusion flames. Species concentra-

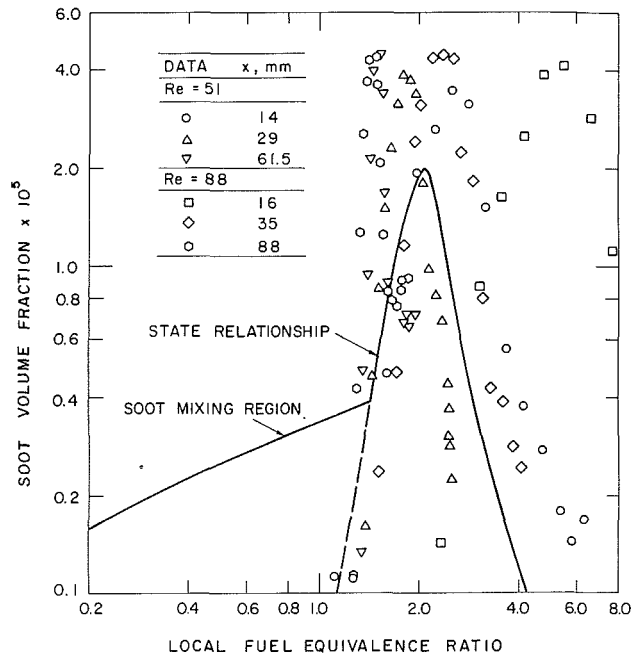


Fig. 3 State relationship for soot volume fraction in acetylene/air diffusion flames

tions could not be measured in this soot layer; therefore, fuel-equivalence ratios were estimated by interpolating plots of fuel-equivalence ratio as a function of distance for a given height above the burner, as described by Gore (1986). The uncertainty of this procedure is highest near the burner exit.

Results illustrated in Fig. 3 indicate that maximum soot volume fractions are relatively independent of burner flow rate and height above the burner. Only positions nearer the burner exit exhibit lower peak soot volume fractions, which are indicative of effects of finite-rate chemistry (Gore, 1986). Maximum soot volume fractions are roughly eight times larger than in ethylene/air diffusion flames. Except for the lowest traverse at the highest Reynolds number ($x/d=16$, $Re=88$), the results are crudely universal in view of potential uncertainties in estimations of fuel-equivalence ratios. However, there is a progressive shift in the location of the maximum soot volume fraction toward lower fuel-equivalence ratios with increasing distance above the burner that was not seen in the ethylene/air diffusion flames (Gore and Faeth, 1987). This behavior is probably due to convection since soot particles do not diffuse like gas molecules. The flow properties of the present laminar flames cause soot particles to be convected toward the flame axis near its base and away from the flame axis near its tip. Convection of soot particles by this motion would cause soot concentrations to shift toward rich conditions near the base of the flame and lean conditions near the tip, as seen in Fig. 3. Naturally, such hydrodynamic effects preclude exact universality of soot volume fractions in laminar flames, and effects of hydrodynamics are likely to be different in turbulent flames as well. Nevertheless, the divergence from universality for the laminar measurements illustrated in Fig. 3 is not large in comparison to other uncertainties concerning soot concentrations in turbulent flames; therefore, use of a soot volume fraction state relationship was pursued.

The soot volume fraction state relationship illustrated in Fig. 3 was constructed using the laminar measurements as well as laser extinction measurements in the turbulent flames, similar to the approach used earlier for ethylene/air diffusion flames (Gore and Faeth, 1987). The laminar and turbulent flames both emitted soot; therefore, the state relationship was extended into the fuel-lean region (the soot mixing region por-

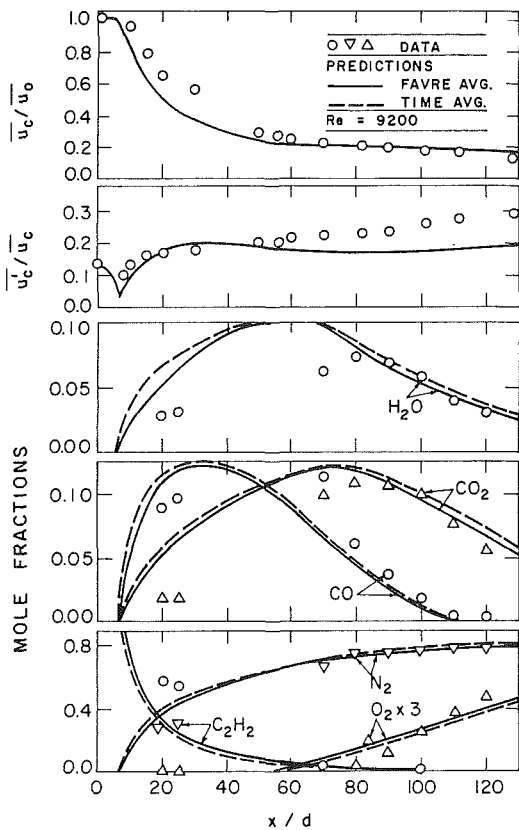


Fig. 4 Structure predictions and measurements along the axis of an acetylene/air diffusion flame: $Re = 9200$



Fig. 5 Light-sheet photograph of soot particles in an acetylene/air diffusion flame: $Re = 5300$

tion of the curve) to fit measurements of laser extinction above the flame tip. This portion was found by selecting a soot volume fraction at a fuel-equivalence ratio of 1.25 and computing values at leaner conditions using mixing analysis

neglecting any subsequent oxidation of soot. If the density of soot is taken to be 1100 kg/m^3 , based on recent findings of Newman and Steciak (1987), the present state relationship in the soot mixing region implies that roughly 21 percent of the original fuel carbon is emitted from the test flames as soot. Becker and Liang (1982, 1983) find that 5–20 percent of the fuel carbon is emitted as soot from turbulent acetylene/air flames having relatively long residence times; therefore, the present estimate seems reasonable. The maximum soot volume fraction and the width of the state relationship in the fuel-rich region were also somewhat optimized using the extinction measurements in the turbulent flames. The final result crudely resembles the laminar measurements in the fuel-rich region, but differs by allowing for soot emission in the fuel-lean region which does not occur near the base of the present laminar flames.

Flame Structure. Structure results for the two turbulent flames were similar; therefore, only the findings for the higher Reynolds number flame will be considered. Predicted and measured mean and fluctuating streamwise velocities and mean gas species concentrations along the axis are illustrated in Fig. 4. Time-averaged velocities were measured while the analysis only provides Favre-averaged velocities. Differences between these averages are typically less than 10 percent for mean velocities along the axis of turbulent diffusion flames (Faeth and Samuelson, 1986). However, time-averaged velocity fluctuations can be up to 40 percent greater than Favre averages near the tip of turbulent diffusion flames (roughly $x/d = 80$ in the present case) (see Faeth and Samuelson, 1986). Furthermore, the analysis only provides k ; therefore, \bar{u}'' has been estimated assuming isotropic turbulence ($\bar{u}''^2 = 2k/3$). Usual levels of anisotropy along the axis of turbulent diffusion flames would yield values roughly 20 percent higher (Faeth and Samuelson, 1986). In view of these observations, the comparison between predicted and measured velocities is reasonably good. However, velocity fluctuations are still somewhat underestimated in the region beyond the flame tip (and to even a greater degree in the lower Reynolds number flame, (Gore, 1986)). This behavior has been observed during all past evaluations of flame structure in this laboratory (Gore and Faeth, 1987; Gore et al., 1987a, 1987b; Jeng and Faeth, 1984b). The effect is attributed to neglecting turbulence/buoyancy interactions in the governing equations for turbulence quantities during the present formulation (Jeng et al., 1982).

The analysis provides both Favre- and time-averaged predictions of scalar properties; therefore, both are plotted in Fig. 4. The degree of density weighting of the measurements is unknown (Faeth and Samuelson, 1986); however, differences between these averages are not large for the concentrations of major gas species. Samples could not be obtained in regions having high soot concentrations; this accounts for the gaps in the data illustrated in Fig. 4. There is fair agreement between predictions and measurements, comparable to past evaluations of this approach (Gore and Faeth, 1987; Gore et al., 1987a, 1987b; Jeng and Faeth, 1984b); therefore, we proceed to the evaluation of radiation properties.

Spectral Absorption Properties. Soot properties of the turbulent flames were evaluated using light-sheet photographs as well as laser extinction predictions and measurements. The light-sheet photographs recorded Mie scattering from soot particles in the flames. They were obtained by sweeping the unfocused beam of a 4 W cw argon-ion laser (all-lines mode) in a vertical plane through the flame axis. Photographs were obtained with the camera shutter open for one sweep of the laser. Sweep speeds yielded illumination times on the order of $10 \mu\text{s}$ at each point in the flow, which effectively stopped the motion of the soot particles.

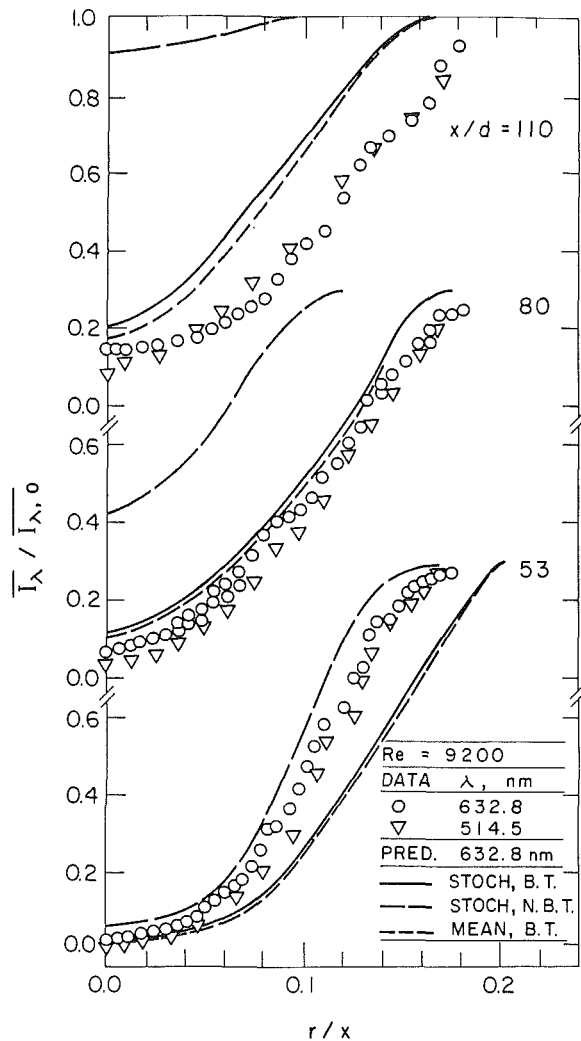


Fig. 6 Monochromatic transmittancies for an acetylene/air diffusion flame: $Re = 9200$

A typical light-sheet photograph appears in Fig. 5. The region seen is near the tip of the $Re = 5300$ flame, covering $x/d = 80-90$. This region was inside the luminous boundary of the flame at the instant that the photograph was obtained. The photograph shows that the soot is confined to streaks, probably associated with the eddy structure of the flame, similar to the earlier observations of Magnussen (1975). The results generally agree with the soot volume fraction state relationship illustrated in Fig. 3, with the finite-width streaks being associated with the narrow range of fuel-equivalence ratios where soot volume fractions are high enough to scatter appreciable amounts of light. Other photographs, having a larger field view and higher in the overfire region, show the streak pattern merging with broader regions of low-level scattering which is characteristic of the soot mixing region (Gore, 1986).

Predictions and measurements of laser extinction by soot for the two turbulent flames appear in Figs. 6 and 7. Measurements for the two laser wavelengths (514 and 632.8 nm) are consistent with the reciprocal-wavelength dependence of extinction coefficients at the small-particle limit, justifying this approximation in the analysis (Gore, 1986). Three sets of predictions for extinction at 632.8 nm appear on the figures, as follows: (1) the mean-property method with the complete state relationship for soot, denoted MEAN, BT; (2) the stochastic method with the complete state relationship for soot, denoted STOCH,BT; and (3) the stochastic method but

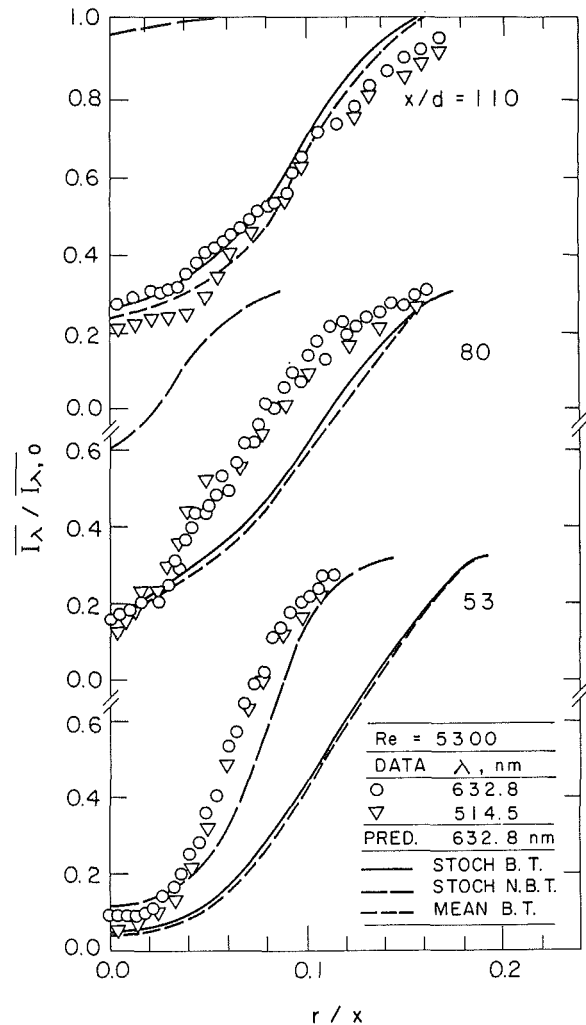


Fig. 7 Monochromatic transmittancies for an acetylene/air diffusion flame: $Re = 5300$

ignoring the soot mixing region of the soot state relationship, denoted STOCH,NBT.

Differences between the mean-property and stochastic predictions are not very significant in Figs. 6 and 7, indicating small effects of turbulence/radiation interactions for extinction. This finding is similar to earlier results for soot-containing ethylene/air diffusion flames (Gore and Faeth, 1987). The role of soot in the lean region can be seen by comparing results with and without the soot-mixing portion of the state relationships. Results for the upper positions show that neglecting the soot-mixing region causes substantial underestimation of extinction. In contrast, measurements at the lowest position are better represented by omitting the soot mixing region, although this might be fortuitous due to underestimation of flame widths (Gore, 1986). It is also plausible, however, that the flames do not emit much soot near their base, similar to findings for the laminar flames.

The absolute agreement between predictions using the complete state relationships for soot and the measurements is reasonably good in Figs. 6 and 7, aside from some overestimation of extinction at the lowest position, noted earlier. Results at the upper positions were fitted to some extent when the state relationship was constructed; therefore, good agreement is perhaps not very surprising. Nevertheless, it is encouraging that a single state relationship for soot volume fraction is able to treat effects of position and flow rate reasonably well, for present test conditions.

Radiation Emission Properties. Measurements and

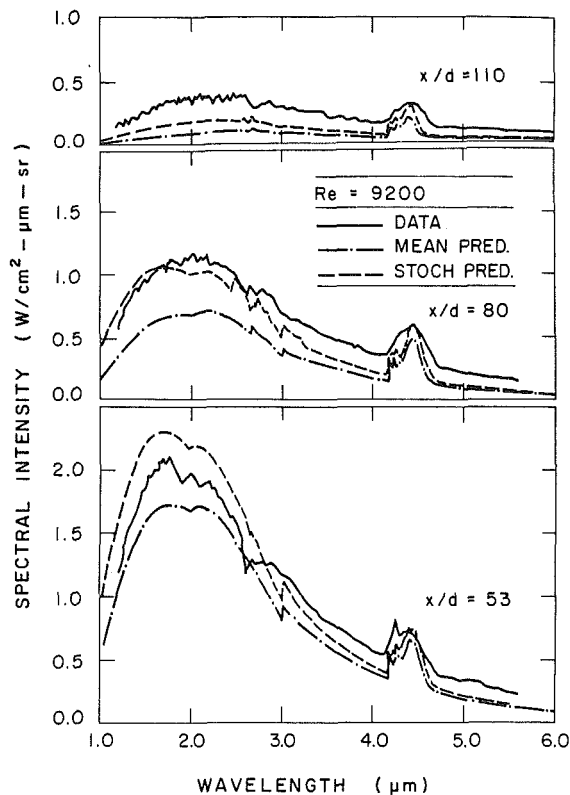


Fig. 8 Spectral radiation intensities for an acetylene/air diffusion flame: $Re = 9200$

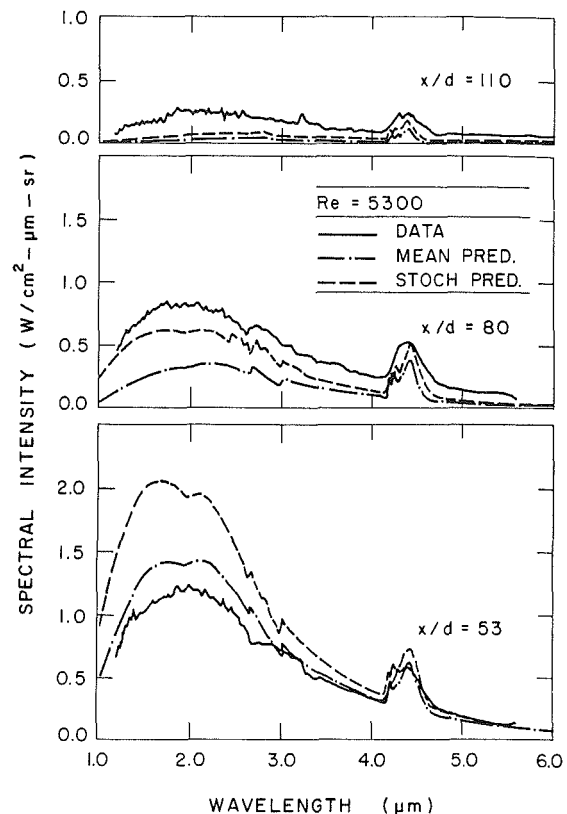


Fig. 9 Spectral radiation intensities for an acetylene/air diffusion flame: $Re = 5300$

predictions of spectral radiation intensities are illustrated in Figs. 8 and 9. Results are presented for three axial stations, representing locations before, near, and after the flame tip (which is at $x/d = 70-80$ for these flames). Predictions are based on the complete state relationship for soot volume fraction, both ignoring and considering effects of turbulence/radiation interactions.

The spectra in Figs. 8 and 9 are dominated by continuum radiation from soot; however, gas bands at 1140, 1870, 2700, and particularly 4300 nm can still be seen. Spectral intensities are highest at $x/d = 53$, which is somewhat before the tip of the turbulent flames. This differs from flames studied earlier where maximum spectral intensities have been generally associated with the flame tip (Gore and Faeth, 1987; Gore et al., 1987a, 1987b; Jeng et al., 1984a). One reason for this is that soot volume fractions, which strongly influence continuum radiation levels, peak at fuel-rich conditions, shifting peak radiation levels accordingly. Another factor could be reduced emission of soot in the lower portions of the flame, which was suggested by the laser extinction measurements. If this occurs, higher intensities in this region result from reduced absorption by soot particles in the lean portions of the flame. A third effect involves energy losses by radiation from the flame, tending to reduce temperatures near the flame tip. This behavior would be most noticeable for the present acetylene/air diffusion flames, due to their high radiative heat loss fractions, in comparison to flames considered earlier.

Differences between mean property and stochastic predictions illustrated in Figs. 8 and 9 suggest significant turbulence/radiation interactions (40–100 percent near peak continuum spectral intensities) for continuum radiation emission from the turbulent flames. Since extinction results were affected very little by turbulence/radiation interactions, the nonlinearity of the Planck function with temperature is probably the main cause of this behavior. This suggests similar

effects for other luminous flames having appreciable continuum radiation.

Predictions and measurements in Figs. 8 and 9 are qualitatively similar; however, quantitative agreement is poorer than for the luminous ethylene/air diffusion flames—particularly in continuum portions of the spectrum. Assuming that stochastic predictions are most realistic, major deficiencies are that spectral intensities are consistently underpredicted at the highest position ($x/d = 110$) and overpredicted at the lowest position ($x/d = 53$). Temperature predictions appear to be the most significant contributor to these difficulties, with these effects being greater for acetylene/air than ethylene/air flames, due to the higher radiative heat fluxes in the acetylene/air flames (reflecting their greater radiative heat loss fractions).

At the higher position, soot volume fraction (indicated by the laser extinction results of Figs. 6 and 7), and the extent of mixing (indicated by the species concentration results of Fig. 4) are predicted reasonably well and do not offer an obvious explanation of the underprediction of spectral intensities. Deficiencies in temperature predictions are a more likely source of the problem. This region is generally fuel lean for the entire optical path; therefore, the flow tends to absorb energy emitted from high-temperature regions of the flame, since it contains appreciable concentrations of soot and other absorbers in the infrared. Thus actual temperatures are probably greater than present predictions, where a uniform fraction of the chemical energy release is assumed to be lost from all portions of the flame. Furthermore, spectral intensities in the continuum region are very sensitive to flow temperatures in this region, e.g., a 5 percent temperature increase caused roughly a 50 percent increase in the spectral intensity at 1770 nm. Thus, radiant energy exchange within the flame provides a probable mechanism for underprediction of spectral intensities at $x/d = 110$, and probably in the rest of the overfire region as well.

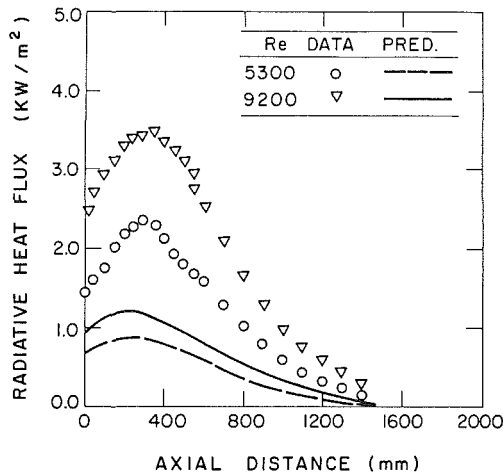


Fig. 10 Total radiative heat fluxes parallel to the axis of acetylene/air diffusion flames

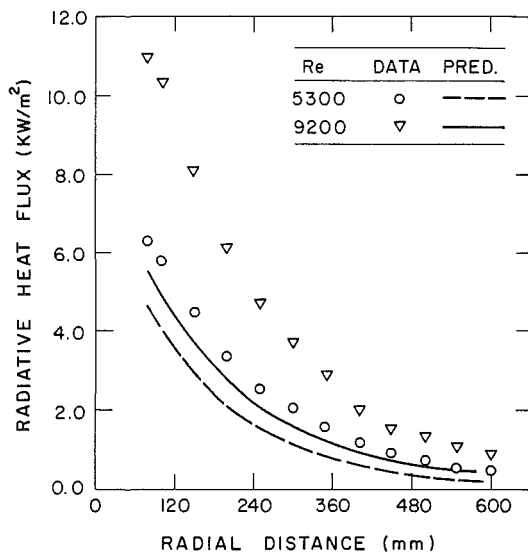


Fig. 11 Total radiative heat fluxes in the plane of the injector of acetylene/air diffusion flames

Internal radiant energy exchange is also a probable mechanism for overprediction of spectral intensities at $x/d=53$. At this position, the optical path traverses both fuel-rich and fuel-lean regions of the flow, although near-stoichiometric conditions are the largest contributors to spectral intensities. Thus, radiative energy transport from the highest temperature regions to other portions of the flame and the surroundings probably result in lower temperatures for these conditions than given by present predictions which assume a fixed radiative heat loss fraction. Furthermore, spectral intensities in this region are also sensitive to changes in flow temperatures, e.g., a 5 percent reduction in temperatures caused a 30 percent reduction in spectral intensities. These effects of internal radiant energy exchange seem sufficient to explain the problem with current predictions at this position as well. Based on this interpretation, the better agreement between predictions and measurements observed in Figs. 8 and 9 at $x/d=80$ is somewhat fortuitous, representing conditions where radiant energy losses from high-temperature regions are compensated by radiant energy gains for fuel-lean conditions.

Coupled structure and radiation analysis would be required to remove the deficiency in current predictions, by allowing

for radiant energy exchange between various portions of the flame. However, this is a challenging extension of the analysis due to both substantial increases in computation requirements and the strong sensitivity of spectral radiation intensity predictions to estimates of temperature in the flow.

Measurements and predictions of radiative heat flux distributions around the two turbulent flames are illustrated in Figs. 10 and 11. Predictions are based on the mean-property method. Figure 10 is an illustration of radiative heat fluxes for a transducer facing the flame axis and traversed vertically at a distance of 575 mm from the axis. The radiative heat fluxes reach a maximum for the flames at $x=300-350$ mm ($x/d=60-70$), which is slightly on the fuel-rich side of the flame tips ($x/d=70-80$). The predictions generally underestimate the measurements, consistent with the performance of the mean-property method for spectral intensities. The predictions generally treat effects of position and flow rate reasonably well, which is encouraging. However, effects of turbulence/radiation interactions and internal energy exchange within the flames, which were ignored for the heat flux predictions, are very significant for these flames, precluding close quantitative agreement between predictions and measurements.

Measured and predicted radiative heat fluxes for a transducer facing vertically upward, and traversing in the radial direction in the plane of the base of the flames, are illustrated in Fig. 11. In this case, the heat flux is a maximum near the injector and decreases monotonically with increasing radial distance. The comparison between predictions and measurements is similar to Fig. 10.

Conclusions

Major conclusions of the study are as follows:

- 1 Study of both laminar and turbulent acetylene/air diffusion flames suggests nearly universal state relationships for the concentrations of major gas species.

- 2 Soot volume fractions in the laminar flames were much less universal than gas concentrations. Nevertheless, universality of soot volume fractions in turbulent flames appears to be a useful concept, which circumvents the complexities of soot chemistry in turbulent environments. The concept should be investigated further.

- 3 Effects of turbulence/radiation interactions were significant for continuum radiation emission from soot (40–100 percent) but are not very important for absorption in the visible (514 and 632.8 nm). This suggests that turbulence/radiation interactions largely result from the strongly nonlinear dependence of the Planck function on temperature.

- 4 Radiation emission predictions were less satisfactory for the present acetylene/air diffusion flames than for earlier work with luminous ethylene air flames (Gore and Faeth, 1987). The main reason for this behavior is the much larger radiative heat loss fraction, approaching 60 percent of the chemical energy release, for the present flames. This implies significant radiative energy exchange within the flames; therefore, coupled structure and radiation analysis should be considered in an effort to reduce present deficiencies in predictions.

Acknowledgments

This research was supported by the Center for Fire Research of the National Bureau of Standards, Grant No. 60NANB5D0576, with Dr. B. J. McCaffrey serving as NBS Scientific Officer. The authors also wish to acknowledge the assistance of D. Hully during measurements of state relationships as well as useful discussions with Y. R. Sivathanu.

References

- Becker, H. A., and Liang, D., 1982, "Total Emission of Soot and Thermal Radiation by Free Turbulent Diffusion Flames," *Comb. Flame*, Vol. 44, pp. 305-318.
- Becker, H. A. and Liang, D., 1983, "Soot Emission, Thermal Radiation, and Laminar Instability of Acetylene Diffusion Flames," *Comb. Flame*, Vol. 52, pp. 247-256.
- Beier, R. A, Pagni, P. J., and Okoh, C. I., 1984, "Soot and Radiation in Combustion Boundary Layers," *Comb. Sci. and Tech.*, Vol. 39, pp. 235-262.
- Bilger, R. W., 1976, "Turbulent Jet Diffusion Flames," *Prog. Energy Combust. Sci.*, Vol. 1, pp. 87-109.
- Bilger, R. W., 1977, "Reaction Rates in Diffusion Flames," *Comb. Flame*, Vol. 30, pp. 277-284.
- Dalzell, W. H., and Sarofim, A. F., 1969, "Optical Constants of Soot and Their Application to Heat-Flux Calculations," *ASME JOURNAL OF HEAT TRANSFER*, Vol. 91, pp. 100-104.
- Faeth, G. M., and Samuelsen, G. S., 1986, "Fast-Reaction Nonpremixed Combustion," *Prog. Energy Combust. Sci.*, Vol. 12, pp. 305-372.
- Gordon, S., and McBride, B. J., 1971, "Computer Program for Calculation of Complex Chemical Equilibrium Compositions, Rocket Performance, Incident and Reflected Shocks, and Chapman-Jouget Detonations," NASA SP-273.
- Gore, J. P., 1986, "A Theoretical and Experimental Study of Turbulent Flame Radiation," Ph.D. Thesis, The Pennsylvania State University, University Park, PA.
- Gore, J. P., and Faeth, G. M., 1987, "Structure and Spectral Radiation Properties of Turbulent Ethylene/Air Diffusion Flames," *Twenty-First Symposium (International) on Combustion*, The Combustion Institute, Pittsburgh, in press.
- Gore, J. P., Jeng, S.-M., and Faeth, G. M., 1987a, "Spectral and Total Radiation Properties of Turbulent Carbon Monoxide/Air Diffusion Flames," *AIAA J.*, Vol. 25, pp. 339-345.
- Gore, J. P., Jeng, S.-M., and Faeth, G. M., 1987b, "Spectral and Total Radiation Properties of Turbulent Hydrogen/Air Diffusion Flames," *ASME JOURNAL OF HEAT TRANSFER*, Vol. 109, pp. 165-171.
- Grosshandler, W. L., 1980, "Radiative Heat Transfer in Nonhomogeneous Gases: A Simplified Approach," *Int. J. Heat Mass Trans.*, Vol. 23, pp. 1447-1459.
- Jeng, S.-M., and Faeth, G. M., 1984a, "Species Concentrations and Turbulence Properties in Buoyant Methane Diffusion Flames," *ASME JOURNAL OF HEAT TRANSFER*, Vol. 106, pp. 721-727.
- Jeng, S.-M., and Faeth, G. M., 1984b, "Predictions of Mean Scalar Properties in Turbulent Propane Diffusion Flames," *ASME JOURNAL OF HEAT TRANSFER*, Vol. 106, pp. 891-893.
- Jeng, S.-M., and Faeth, G. M., 1984c, "Radiative Heat Fluxes Near Turbulent Buoyant Methane Diffusion Flames," *ASME JOURNAL OF HEAT TRANSFER*, Vol. 106, pp. 886-888.
- Jeng, S.-M., Chen, L.-D., and Faeth, G. M., 1982, "The Structure of Buoyant Methane and Propane Diffusion Flames," *Nineteenth Symposium (International) on Combustion*, The Combustion Institute, Pittsburgh, pp. 349-358.
- Jeng, S.-M., Lai, M.-C., and Faeth, G. M., 1984, "Nonluminous Radiation in Turbulent Buoyant Axisymmetric Flames," *Comb. Sci. and Tech.*, Vol. 40, pp. 41-53.
- Kent, J. H., and Bastin, S. J., 1984, "Parametric Effects on Sooting in Turbulent Acetylene Diffusion Flames," *Comb. Flame*, Vol. 56, pp. 29-42.
- Liew, S. K., Bray, K. N. C., and Moss, J. B., 1981, "A Flamelet Model of Turbulent Non-premixed Combustion," *Comb. Sci. and Tech.*, Vol. 27, pp. 69-73.
- Lockwood, F. C., and Shah, N. B., 1981, "A New Radiation Solution Method for Incorporation in General Combustion Prediction Procedures," *Eighteenth Symposium (International) on Combustion*, The Combustion Institute, Pittsburgh, pp. 1405-1414.
- Ludwig, C. B., Malkmus, W., Reardon, J. E., and Thomson, J. A., 1973, *Handbook of Infrared Radiation from Combustion Gases*, NASA SP-3080.
- Magnussen, B. F., 1975, "An Investigation into the Behavior of Soot in a Turbulent Free Jet C_2H_2 -Flame," *Fifteenth Symposium (International) on Combustion*, The Combustion Institute, Pittsburgh, pp. 1415-1425.
- Newman, J. S., and Steciak, J., 1987, "Characterization of Particulates From Diffusion Flames," *Comb. Flame*, Vol. 67, pp. 55-64.
- Santoro, R. J., Semerjian, H. B., and Dobbins, R. A., 1983, "Soot Particle Measurements in Diffusion Flames," *Comb. Flame*, Vol. 51, pp. 203-218.

F. Takahashi

Department of Mechanical and
Aerospace Engineering,
Princeton University,
Princeton, NJ 08544
Mem. ASME

M. Mizomoto

S. Ikai¹

Department of Mechanical Engineering,
Keio University,
Yokohama, 223 Japan

Structure of the Stabilizing Region of a Laminar Jet Diffusion Flame

Velocity, temperature, and composition of major species were measured in the base region of a two-dimensional, laminar methane jet diffusion flame in unconfined still air under a low-velocity jetting condition. The velocity data showed acceleration near the flame zone caused primarily by thermal expansion and buoyancy. The heat flux vectors showed substantial heat flow from the flame base to both downstream and the burner wall. The premixed zone was formed in the dark space by convective penetration of oxygen and back-diffusion of methane. The molar flux vectors of methane and oxygen at the base pointed to the opposite directions, typical of diffusion flames.

Introduction

The structure of the base of diffusion flames and adjacent dark space, formed between the flame base and a burner or fuel surface, is of essential importance in various combustion phenomena, e.g., the lifting stability of gaseous fuel jet flames, the flame spread over solid materials and liquid fuels, or the instability of leading flame edge in the boundary layer combustion. Although a number of papers have been reported on the structure of jet diffusion flames, only a few examined the flame base region. Robson and Wilson (1969) first attempted to study the stability of laminar methane diffusion flames by means of flame structural measurements in the base region. Kawamura and Asato (1975) and Kawamura et al. (1980) followed their approach to study mainly the thermal structure by applying the structure analysis techniques, similar to those employed by Datta et al. (1971) and Datta and Reed (1972) for investigating the stabilizing region of premixed flames. The previous work has contributed to better understanding of the flame structure in the base region, yet relevant interpretations of the structure data in connection with the flame stability have remained unclear mainly because the mechanism of flame holding has not been discussed in an explicit manner.

It has been generally postulated (Gaydon and Wolfrhard, 1979) that at the very base of a jet diffusion flame, fuel and air form a small volume of premixed gases by interdiffusion and that the flame velocity at the base toward this premixed zone causes the combustion processes to propagate downward against the gas stream, thus preventing the flame from lifting. Based on the stability-limit data as functions of various parameters and types of fuels (Takahashi et al., 1980), the laser-Doppler velocity measurements in the stabilizing region of near-limit hydrogen flames (Takahashi et al., 1985), and the observation that the flame base remains laminar even in fully developed turbulent flames (Takahashi et al., 1982), we have recently (Takahashi, 1982; Takahashi et al. 1985) modeled and examined the lifting mechanism of free jet diffusion flames, following this concept (Gaydon and Wolfrhard, 1979). The velocity component of the stream entrained into the flame base in the direction along the flame zone correlated well with the maximum burning velocity obtainable by mixing the jet and external oxidant fluids, thus supporting the lifting mechanism proposed (Takahashi, 1982; Takahashi et al., 1985). However, if the jet velocity is very low as compared

with the critical value at lifting, the premixing may not necessarily be sufficient to produce the flame velocity and the flame holding may not depend on the propagation process. The purpose of this study is to reveal the flame structure of the stabilizing region of a laminar diffusion flame, in which the jet velocity is well below the lifting limit, as this relates to the flame holding mechanism, or the flame extinction phenomena near a cold surface.

Experimental Techniques

The burner, shown in Fig. 1, is a rectangular fuel channel of $2.2 \times 31 \times 310$ mm length provided with air channels (24×31 mm) adjacent to the fuel channel, placed vertically in still air, as described in detail elsewhere (Takahashi, 1975; Ikai et al., 1975). The air channels are open to the atmosphere 30 mm below the jet exit plane to allow free entrainment of the ambient air. The partition plate constituting the fuel channel is made of nickel-plated copper (0.2 mm thick) and sharp-edged at the tip on the outer surface with a slope of 1/10 to prevent recirculation in its wake. The end flame was extinguished by excluding ambient air by two Vicor-glass plates (50×50 mm) placed vertically along the short sides of the fuel channel above the position 5 mm below the exit, enabling observations of the planar diffusion flame. Methane (purity > 98 percent) was ejected at the average fuel jet velocity ($\bar{U}_j < 1.22$ m/s), well below (less than 1/8 of) the critical jet velocity at lifting. Unless otherwise noted, the results reported here were obtained at $\bar{U}_j = 1.22$ m/s.

The location of the visible flame zone was measured by projecting a direct time-exposure photograph on a screen with $50 \times$ magnification and by reading the coordinates of the traced boundary of the luminous zone with a cathetometer. Optical observations of the flame were made by the use of both the Schlieren technique and a Mach-Zehnder interferometer as well as direct photographs. A spark light source (~ 1 μ s duration) was used for the instantaneous Schlieren system and a helium-neon laser (15 mW) was used for the interferometer.

The velocity measurements were made by means of the particle track technique (Fristrom and Westenberg, 1965). Fine particles (typically < 5 μ m) of dried magnesium oxide were seeded into dry air from a high-pressure bottle with very low dew point and wind sieved while ascending slowly (1.7 cm/s) in the air channel, thereby eliminating agglomerated particles larger than the Stokes diameter (approximately 12 μ m) in principle. The air supply was minimized to achieve a "still" air condition and the number density of the particles was

¹Present address: Meisei University, Tokyo, Japan.

Contributed by the Heat Transfer Division and presented at the 2nd ASME-JSME Thermal Engineering Joint Conference, Honolulu, Hawaii, March 1987. Manuscript received by the Heat Transfer Division December 9, 1986.

minimized to avoid errors due to physical and chemical effects (Fristrom and Westenberg, 1965). A sheet of focused light from a high-pressure mercury lamp (500 W), which was chopped at 1200–1800 Hz by a rotating disk with 48 slits, illuminated the particles on the vertical plane crossing the center of the burner, perpendicular to the flame zone. Particle tracks were photographed on 35 mm film with $1.7\times$ magnification and projected on a screen with $50\times$ magnification to measure the dashed track length. The velocity was determined as a product of the particle track length and the illumination frequency. Based on the measured velocity profile along the streamline crossing the flame base, the error caused by slippage of the particle relative to the gas (Fristrom and Westenberg, 1965) was estimated for $5\ \mu\text{m}$ diameter as typically 1 percent for average acceleration and at most 6 percent near the flame zone where the acceleration was maximum.

The temperature was measured using a silica-coated (Fristrom and Westenberg, 1965; Kaskan, 1957) platinum/platinum–13 percent rhodium thermocouple (0.025 mm wire diameter by 29 mm length, 0.12 mm bead diameter after coating) to reduce the catalytic reaction error, inserted horizontally parallel to the flame sheet, i.e., the direction of uniformity, to eliminate the error due to conductive heat transfer through the wire. The output voltage was recorded on a chart and averaged over 1–3 min. Corrections were made for radiation heat losses by the use of the technique described by Friedman (1953), who assumed a spherical bead and Nusselt number 2, and the emissivity of the coated thermocouple (0.22) recommended by Kaskan (1957). The position of the thermocouple was determined using a cathetometer with a minimum reading of 0.01 mm.

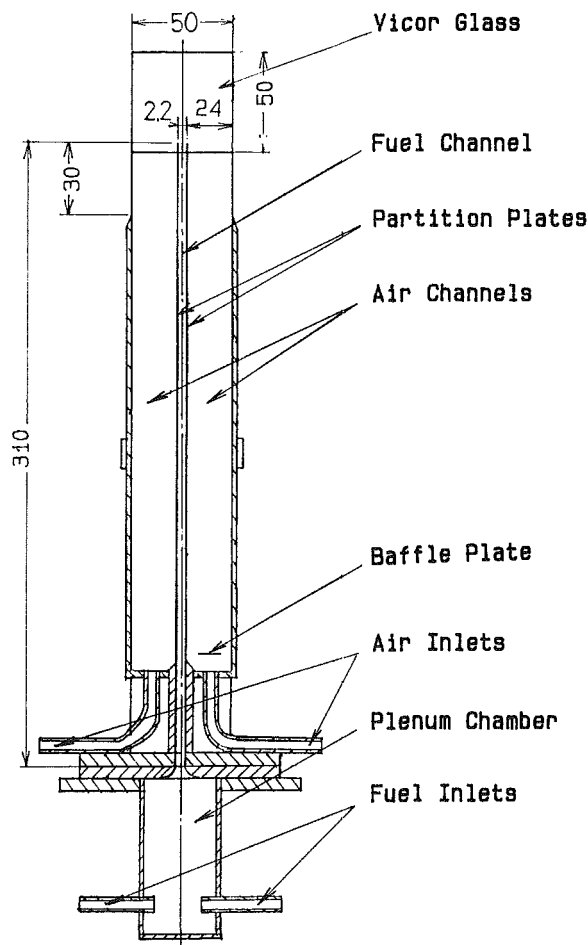


Fig. 1 Schematic drawing of burner; dimensions in mm

Gas sampling was made using a quartz microprobe (Fristrom and Westenberg, 1965) (0.028 mm throat diameter and 0.106 mm o.d.) with a 90 deg bend at 3 mm from the tip, enabling the rapid transit of the gas out from the high-temperature region to avoid further reactions inside the probe, which was inserted horizontally to withdraw gases parallel to the flame sheet, i.e., the direction of uniformity, to minimize disturbances on the flow and concentration fields. The flame was stable over the sampling period of 10–20 min. Major species (N_2 , O_2 , CO_2 , CO , CH_4) were analyzed by a gas chromatograph on a dry basis. The concentration of water vapor was calculated by assuming locally a constant C/H ratio (1/4) and the atomic mass conservation.

The analysis of the flame structure data is carried out by means of two-dimensional conservation equations of energy and species for a steady-state, constant-pressure system with no effects due to viscosity, radiation, external forces, the reciprocal thermal diffusion (Dufour effect), and the energy flux associated with molecular diffusion. The local heat flux vector (\mathbf{q}) is thus calculated using the following equation:

$$\mathbf{q} = \mathbf{i} \left[-\lambda \frac{\partial T}{\partial x} + \rho c_p U_x (T - T_e) \right] + \mathbf{j} \left[-\lambda \frac{\partial T}{\partial y} + \rho c_p U_y (T - T_e) \right] \quad (1)$$

Here, \mathbf{i} , \mathbf{j} , U_x , and U_y are unit vectors and velocity components in the x and y directions, respectively. The properties of nitrogen were used for calculating the thermal conductivity λ and density ρ at the local temperature T and the mean specific heat c_p between T and the ambient temperature T_e . The local species molar flux vector \mathbf{k}_i is calculated for methane and oxygen using the equation

$$\mathbf{k}_i = \mathbf{i} \left[\frac{\rho Y_i}{M_i} (U_x + u_{ix}) \right] + \mathbf{j} \left[\frac{\rho Y_i}{M_i} (U_y + u_{iy}) \right] \quad (2)$$

Here, Y_i and M_i are the mass fraction and molecular weight of the species i , respectively. The diffusion velocity vector of the species i is calculated from

$$\mathbf{u}_i = \mathbf{i} \left[-\frac{D_{ij}}{X_i} \frac{\partial X_i}{\partial x} \right] + \mathbf{j} \left[-\frac{D_{ij}}{X_i} \frac{\partial X_i}{\partial y} \right] \quad (3)$$

Here, X_i is the mole fraction of species i and D_{ij} is the binary diffusion coefficient, calculated using the expression in Hirschfelder et al. (1954) by regarding nitrogen as species j .

Results and Discussion

Optical Observations. Figure 2 shows direct, Schlieren, and interferometric photographs of the flame. In the direct photograph (Fig. 2a), a bright-blue flame zone is seen, which is fading off downstream (5–15 mm above the exit) where a yellow luminous zone appears in the fuel side of the blue flame zone, eventually superseding the blue flame zone. The base of the visible flame zone resides at a height slightly lower (0.46 mm) than the burner exit and 1.15 mm horizontally away from the partition plate in the air side, which is about half a minimum quenching distance (Anon., 1957) of the stoichiometric methane–air mixture, thus forming the dark space between the flame base and the burner wall. The spark Schlieren photograph (Fig. 2b), taken with a vertical knife edge, thus showing the horizontal gradient of the refractive index, which is primarily dependent on temperature, exhibits no turbulence except for low-frequency oscillation, seen downstream beyond 5 cm from the exit, due to the instability of the thermal boundary layer (Grant and Jones, 1975). This disturbance was suppressed by placing a V-shaped plate parallel to the burner slit far downstream to avoid the influence on the flame structure near the base. The flame zone, coincident with the peak temperature where the sign of the

temperature gradient changes, resides near the inner boundary of the dark region in the right half of the Schlieren picture or the bright region in the left, showing a relatively thick ($\approx 4\text{--}8$ mm) thermal layer in the air side of the flame zone. In the interferometric photograph (Fig. 2c) of the near-base region, which closely follows isotherms as will be shown later, the visible flame zone nearly coincides with the outer edge of the

wedge-shaped region surrounded by the innermost contour (compare Figs. 2a and 2c), and the thermal-layer thickness is approximately 2 mm around the flame-base region, spreading below the base.

Velocity Distributions. Figure 3 shows streamlines in the vicinity of the burner exit in both the ignited methane jet (Fig. 3a) and the isothermal air jet (Fig. 3b) at the same mean jet velocity ($\bar{U}_j = 1.22$ m/s). The coordinates x and y are vertical and horizontal distances, respectively, from the inner edge of

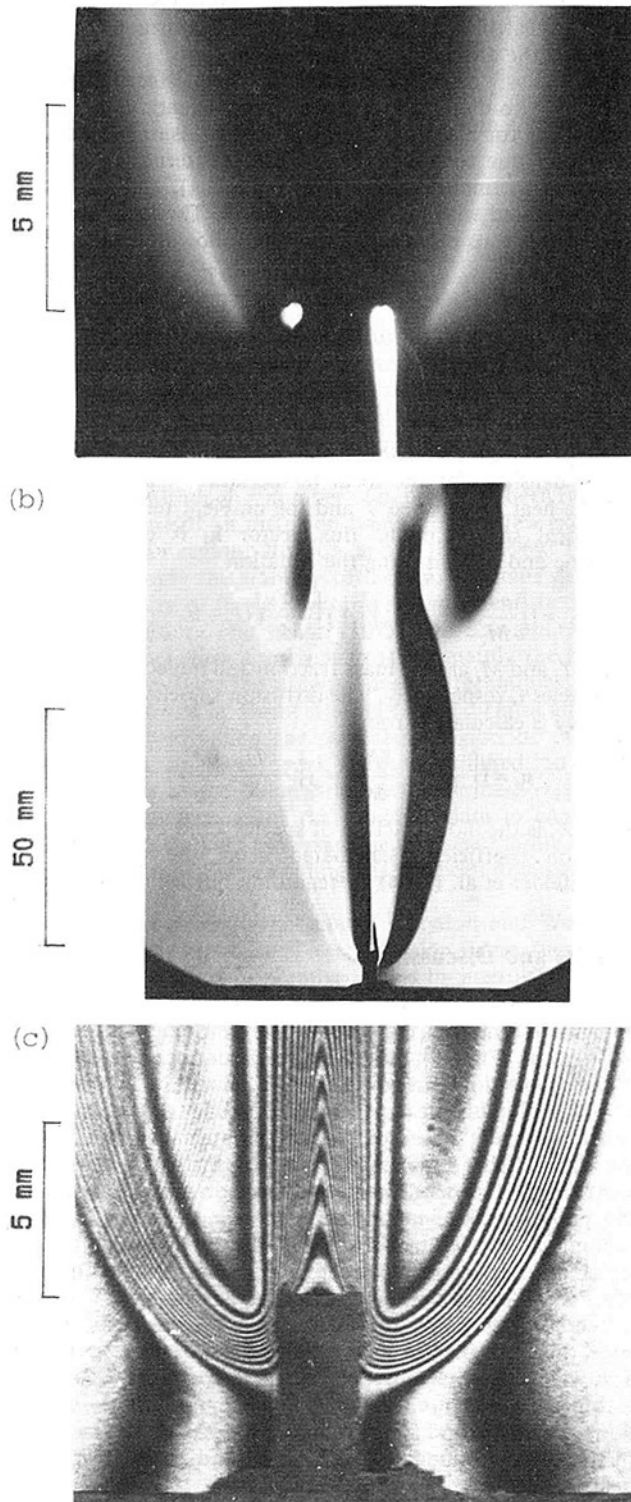


Fig. 2 Photographs of methane jet diffusion flames: (a) direct time exposure (1/60 s), $\bar{U}_j = 1.22$ m/s; (b) spark Schlieren photograph, $\bar{U}_j = 1.0$ m/s; (c) interferogram (1/125 s), $\bar{U}_j = 1.0$ m/s

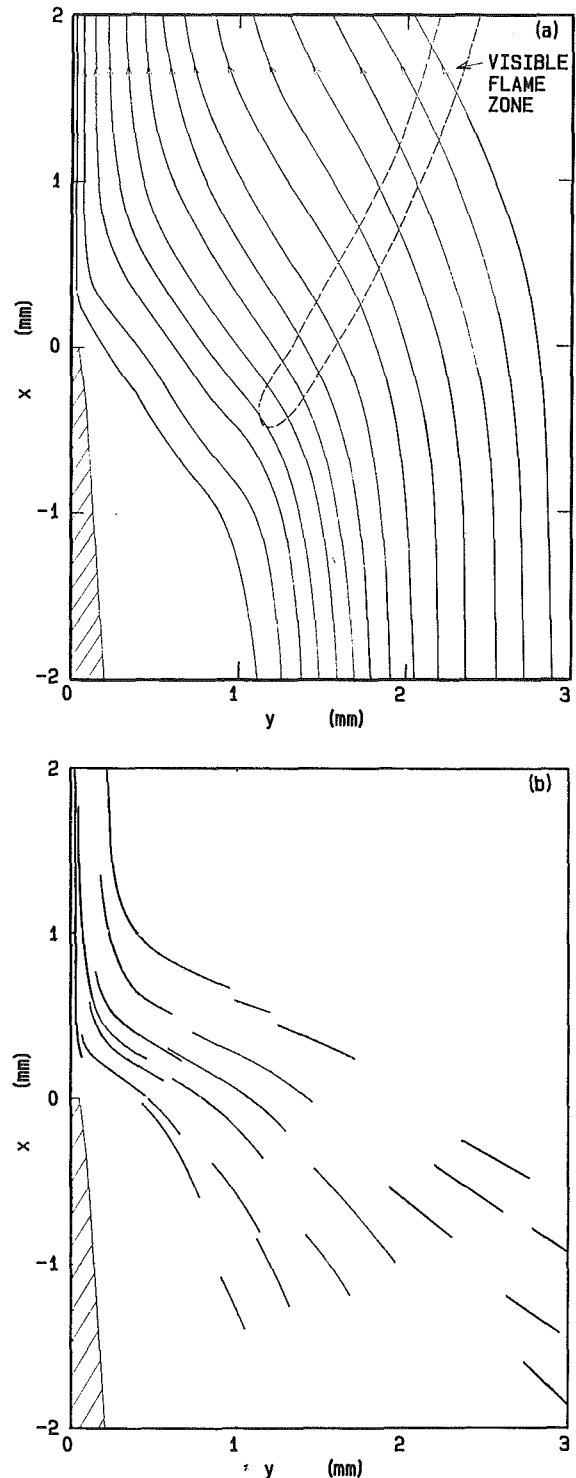


Fig. 3 Streamlines: (a) ignited methane jet; (b) isothermal air jet

the tip of the partition plate. A number of particle tracks (~ 100) were used to obtain the streamlines in Fig. 3(a), while each curve in Fig. 3(b) indicates an individual particle track. These figures evidence no recirculation in the wake of the partition plate. In general, the angles of streamlines with respect to the x coordinate are significantly smaller in the ignited stream than those in the isothermal stream, indicating the buoyancy effect on hot combustion gases. The region bounded by the innermost streamline and the outer surface of the partition plate in both cases is a very low-velocity (nearly stagnant) region.

Figure 4 shows the horizontal distributions of the velocity components in both axial and lateral directions (U_x and U_y , respectively) at different heights in the ignited stream. In the region well below the flame base ($x \leq -0.8$ mm), the axial velocity is essentially uniform over the range of $1 < y < 3$ mm, while downstream ($-0.4 \leq x \leq 1.2$ mm) the acceleration is seen in the region near the flame zone, which is overridden by the acceleration near the dividing streamline ($y = 0$) as the fuel jet spreads farther downstream ($x \geq 2$ mm). As a result, the axial velocity exhibits peculiar distribution, having a peak near the flame zone and a trough in the wake of the partition plate. The lateral velocity profiles also show accelerations near the flame zone, having peaks just inside the flame zone. These results reveal that the flame base resides in the periphery or outside of the shear layer of the primary jet field, and thus the thermal expansion and buoyancy, which cause the streamwise acceleration, predominate the flow field around the base. This feature, which has never been clearly shown previously, is of particular importance when applying a numerical model to the structure around the flame base (Lee and Dai, 1984; Takahashi, 1986; Ueda et al., 1986).

Temperature Distributions and the Heat Flux Vector Field.

Figure 5 shows measured temperature distributions at different horizontal sections. The temperature starts to rise in the region as low as 2 mm below the flame base. The flame temperature at the base was about 1520°C (including the radiation correction: 70°C), which is considerably lower than the adiabatic flame temperature of the stoichiometric methane-air mixture (1949°C). This measured temperature is close to the previous results by Robson and Wilson (1969) (1490°C including the radiation correction: 50°C and the conduction correction: 150°C) and Kawamura and Asato (1975) (1450°C with no correction) who both used circular tube burners but which are significantly higher than that of Kawamura et al. (1980) (1200°C with no correction) obtained in a planar flame. The temperature profile crossing the flame zone shows a dent in the fuel side of the flame zone, as is seen in counterflow diffusion flames (Tsuji and Yamaoka, 1971), which is generally considered to be due to endothermic pyrolysis-type reactions (Pandya and Weinberg, 1964; Tsuji and Yamaoka, 1971). Figure 6 shows isotherms near the flame base, exhibiting extreme similarities to the interferogram (Fig. 2c). A comparison between the interferogram and isotherms reveals that each line in the interferogram indicates approximately a 140°C interval.

Figure 7 shows the local heat flux vectors near the flame base. In the fuel side of the flame zone, a significant amount of heat flows downstream as a result of bulk flow convection as well as conduction. By contrast, in the air side (upstream) of the flame zone, heat conduction is opposed to the bulk flow and thus the net heat transfer is insignificant. It is also noticeable that a significant amount of heat flows from the flame base toward the burner wall.

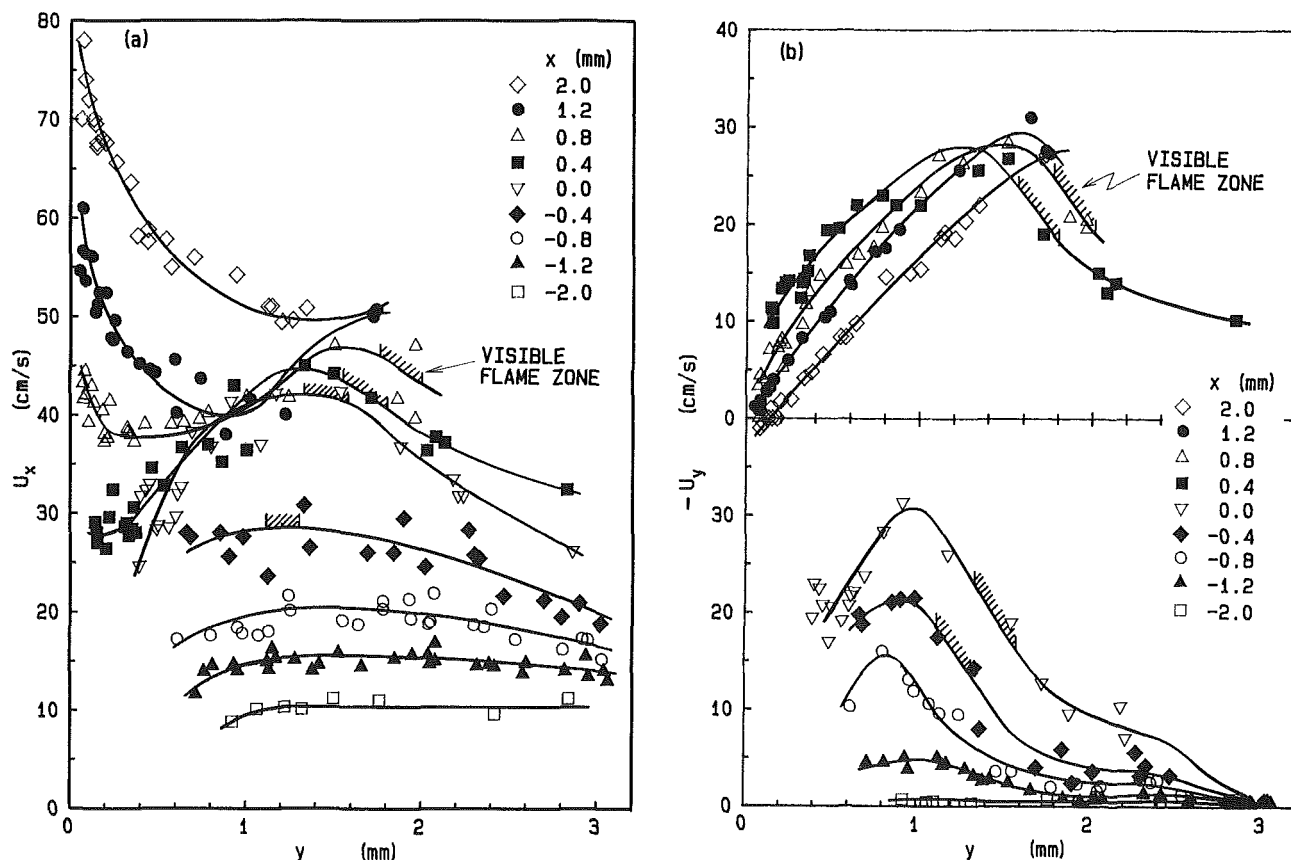


Fig. 4 Velocity distributions: (a) axial component; (b) lateral component

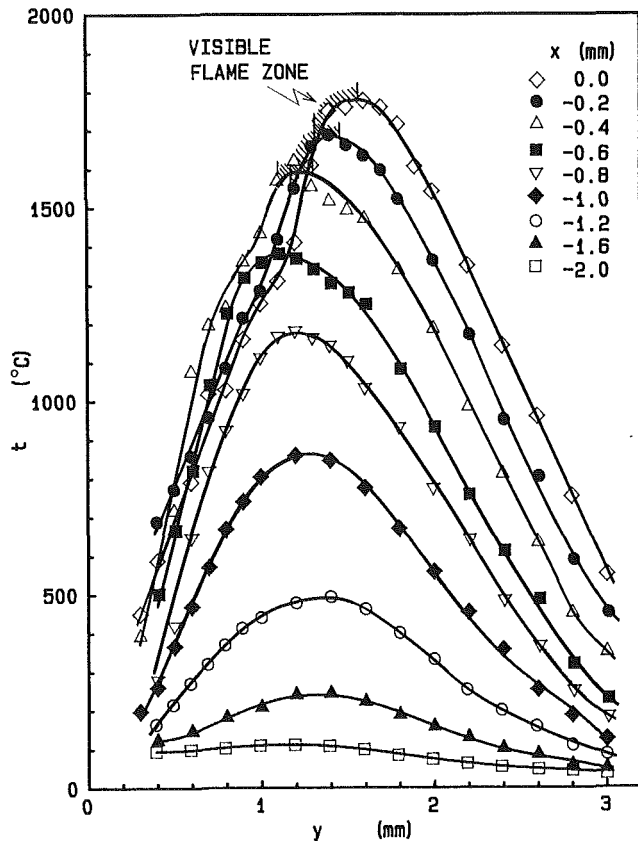


Fig. 5 Temperature distributions

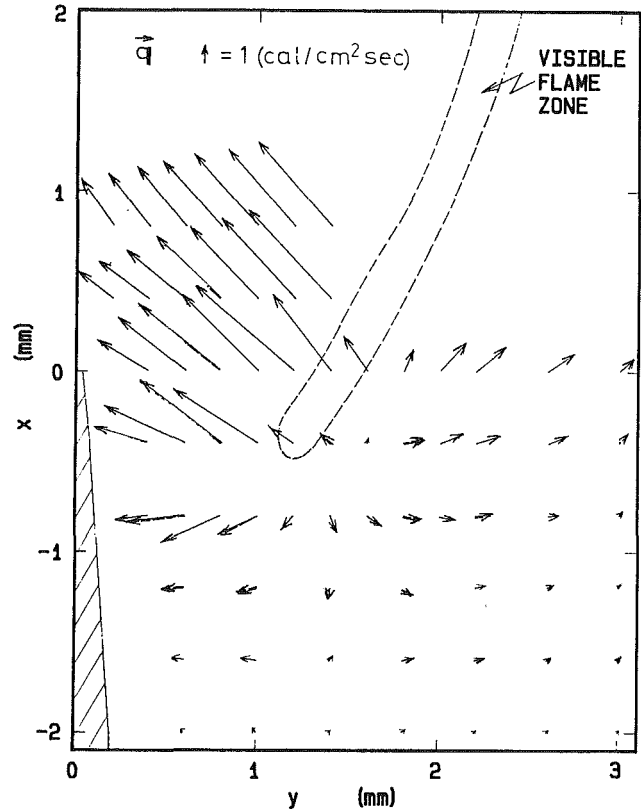


Fig. 7 Local heat flux vectors

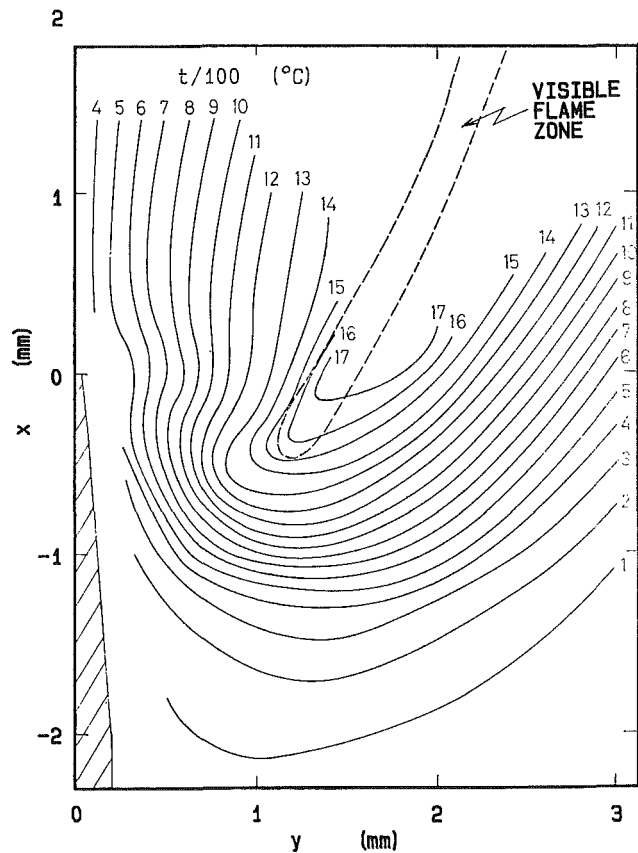


Fig. 6 Isotherms

Species Concentration Distributions and the Molar Flux Vector Field. Figure 8 shows a typical result of the gas analysis, showing distributions of mole fractions of major species at the horizontal section ($x = -0.4$ mm) crossing near the flame base. The species concentration profiles are similar to those of the counterflow diffusion flame (Tsuji and Yamaoka, 1971) except for oxygen, which convectively penetrates into the fuel side of the flame zone through the dark space between the flame base and the burner wall where mixing with methane is taking place. Figure 9 shows isopleths of the methane and oxygen concentration in the vicinity of the flame base. The general trends in the isopleths are similar to those obtained by Robson and Wilson (1969) in an axisymmetric flame under a high-velocity jetting condition, although the base of their flame resides 0.5 mm above the burner exit. The lines of constant equivalence ratio, calculated from the methane and oxygen mole fractions in the premixed zone, are also included in Fig. 9, although actual local equivalence ratio should be calculated based on the molar flux fractions. It is noticed that the direction of the premixed zone is almost perpendicular to the streamline passing the flame base (compare Figs. 3a and 9).

Figure 10 shows the local molar flux vectors of methane and oxygen near the base. As compared to the direction of bulk flow (see Fig. 3a), the oxygen flux near the flame base is almost in the same direction, while the methane flux is opposite, which is exactly the same as the counterflow diffusion flame (Tsuji and Yamaoka, 1971). Along the streamline passing the flame base, the amounts of both the oxygen and methane fluxes in the opposite direction decrease toward the flame zone, indicating the consumptions of these species in the flame zone. The amounts of methane and oxygen fluxes at $x = -0.4$, $y = 1.1$ mm, in immediate proximity to the flame base, are 0.43×10^{-5} and 1.5×10^{-5} mol/cm²s, respectively,

corresponding to the equivalence ratio of 0.6. The flame base is thus in a fuel-lean condition, as was found and discussed by Robson and Wilson (1969).

Flame-Base Properties. In a system such as the base region of jet diffusion flames, whether attached to a burner rim or lifted, where partial mixing of the fuel and oxidizer takes place prior to combustion, the broad definition of a diffusion flame (Williams, 1985), based on whether the fuel and oxidizer initially are separated, may no longer be sufficient to characterize the flame zone locally. To define the flame zone more precisely including pure diffusion and premixed flames, one can use the mass, or molar, fluxes of the fuel and oxidizer, which is the net rate of convective and diffusive transport, to see how the fuel and oxygen molecules enter into the flame zone. In a pure diffusion flame, the components of these flux vectors normal to the flame zone are in opposite directions (Tsuji and Yamaoka, 1971), characterizing diffusion processes of the fuel and oxidant from separate regions, while in a pure premixed flame they are in the same direction (Fristrom and Westenberg, 1965), characterizing propagation of the flame zone with respect to the reactant gas mixture, resulting in a burning velocity. Thus any initially nonpremixed flame with partial mixing of the fuel and oxidant may be categorized into a diffusion or premixed flame by looking at the directions of these fluxes normal to the flame zone.

However, at the leading edge of a diffusion flame, i.e., the base, which can be regarded just as a line ignition source in a premixed gas, the components parallel to the flame zone should also be considered. If there are no common components of the fuel and oxidant fluxes in this direction at the base, the flame is a pure diffusion flame, while if there are such common components, the base bears properties of a

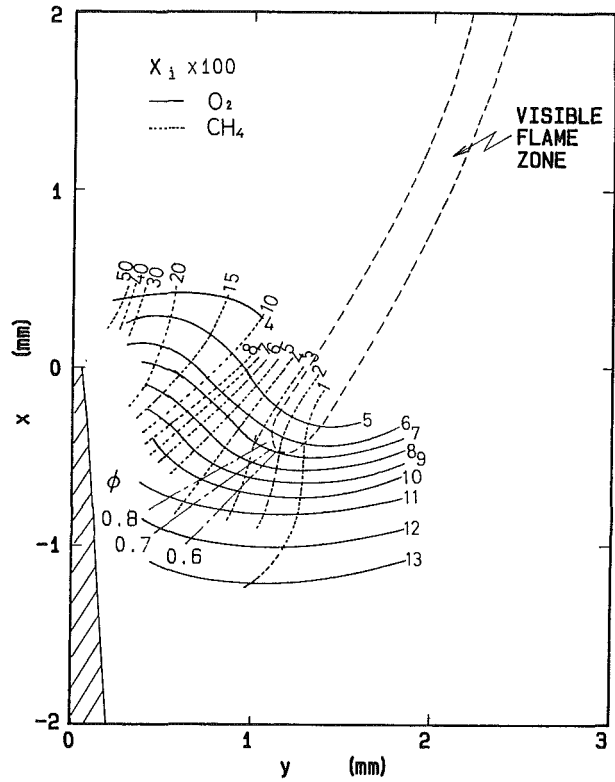


Fig. 9 Isoleths of methane and oxygen concentrations

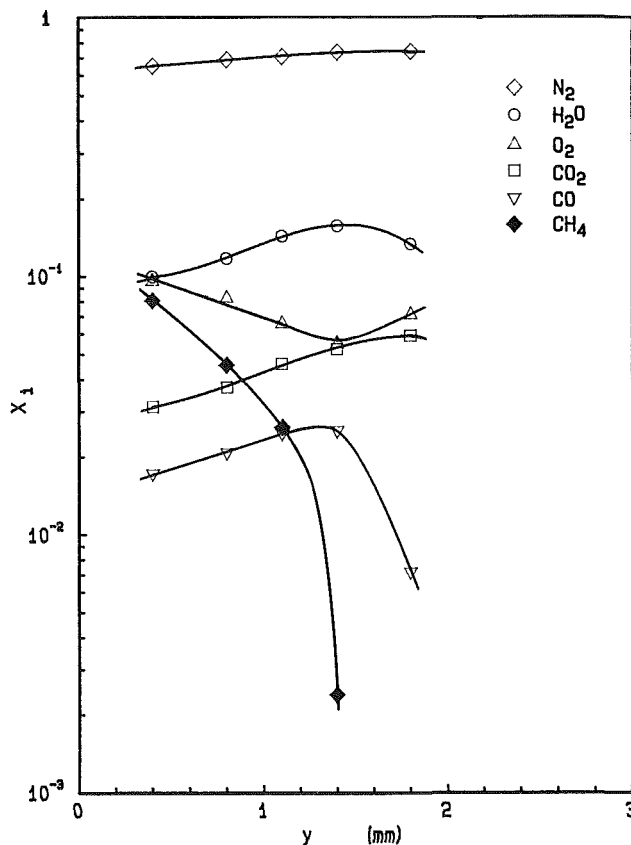


Fig. 8 Species concentration distributions ($x = -0.4$ mm)

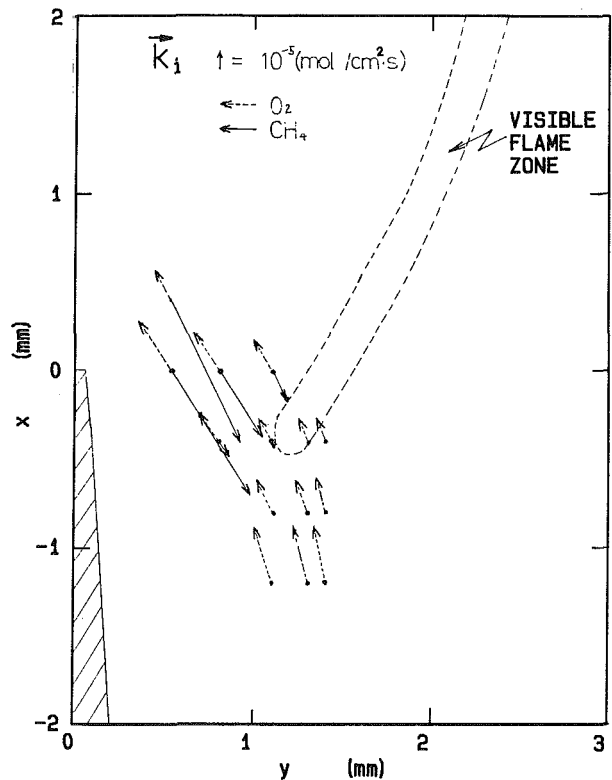


Fig. 10 Local molar flux vectors of methane and oxygen

premixed flame, i.e., the propagating velocity against the incoming fluxes, as well as a diffusion flame. Thereby using these flux vectors and the geometric configuration relative to the flame zone, it must be possible to examine mathematically the properties of the flame in this respect. It is particularly important when discussing the characteristics of the diffusion flame base, since it would be a hasty conclusion to regard the base as a premixed flame that anchors the diffusion flame, solely based on the presence of a premixed gas mixture adjacent to the flame base.

Flame Structure and Stability. Some characteristic structural data at the base of methane flames, relevant to the flame stability, are summarized in Table 1 using notations shown in Fig. 11. Robson and Wilson (1969) and Kawamura and Asato (1975) used circular tube burners and Kawamura et al. (1980) and this study used rectangular burners. The external air velocity U_e was very low ("still" air conditions) in Robson and Wilson (1969) and this study in which the effect of mean jet velocity \bar{U}_j was examined, while it was relatively high in Kawamura and Asato (1975) and Kawamura et al. (1980) in which the air-velocity effect was examined. The mean jet velocity along with its fraction to the critical value at lifting \bar{U}_{jc} are shown in the table. The height of the flame base from the burner exit x^* was positive for tube burners (Robson and Wilson, 1969; Kawamura and Asato, 1975) and negative for rectangular burners (Kawamura et al., 1980; and this study), and it increased as either the jet or air velocity was increased. The horizontal location of the flame base y^* was almost the same (about half a minimum quenching distance: 2 mm (Anon., 1957)) for all cases except for the high jet velocity case closest to lifting (Robson and Wilson, 1969) where shrinkage of the flame base circle occurred. The inclination of the streamline passing the flame base with respect to the x axis (θ) was similar for all cases except for the high jet velocity case (Robson and Wilson, 1969). The inclination of the flame zone γ was smaller for circular tube burners in which the flame base resided above the burner exit than that for rectangular burners in which the base was below the exit. The absolute velocity coming into the flame base U^* was a weak function of the mean jet velocity. The velocity component in the direction of the flame zone U_f^* was almost independent of either the jet velocity (see two cases in Robson and Wilson, 1969) or the air velocity (see cases in Kawamura et al., 1980). This velocity component was relatively high in Kawamura and Asato (1975) in which the flame base position is relatively high above the burner, as a result of relatively high \bar{U}_j and U_e , and low in this study in which the base was lowest below the jet exit with low \bar{U}_j and U_e . The inclination ω of the premixed zone in the dark space was determined from lines of constant equivalence ratio based on the measured mole fraction of methane and oxygen. The resulting ω values for the equivalence ratio ϕ of 0.7 are shown in the table for Robson and Wilson (1969) and this study in which gas analyses were made. The inclination of the premixed zone in this study was twice that in Robson and

Wilson (1969), mainly resulting from the low flame-base location. This premixed zone inclination was close to the flame inclination under high-velocity conditions (Robson and Wilson, 1969), closest to the lifting limit, where the base resided above the burner. It is notable that the velocity component at the flame base in the opposite direction of the premixed zone U_p^* vanishes (even becoming negative at $\phi > 0.75$) in this study since the angle $(\theta + \omega)$ is close to a right angle, while there is still some velocity component in the case of the high jet velocity (Robson and Wilson, 1969). This result thus suggests that at low jet velocity there is no burning velocity at the flame base to propagate toward the premixed zone, and that as the lifting limit is approached, the burning velocity arises as the flame base shifts above the burner exit to form the premixed zone more vertically.

Concluding Remarks

A flame structure study in the vicinity of the base of a planar, laminar jet diffusion flame, in which the jet velocity was significantly lower than the critical value at lifting, revealed that the fuel-oxygen premixed zone was formed in the dark space between the flame base and the burner rim in the direction nearly perpendicular to the bulk-flow streamline crossing the base. The species molar flux vectors of the fuel and oxygen at the flame base were in opposite directions with no common component. By defining the categories of diffusion and premixed flames, in a more precise manner than the conventional one, based on the fuel and oxidant flux vectors, it can be concluded from these results that the flame base has a typical diffusion flame structure and there is no evidence of the nature of a propagating premixed flame. Under these con-

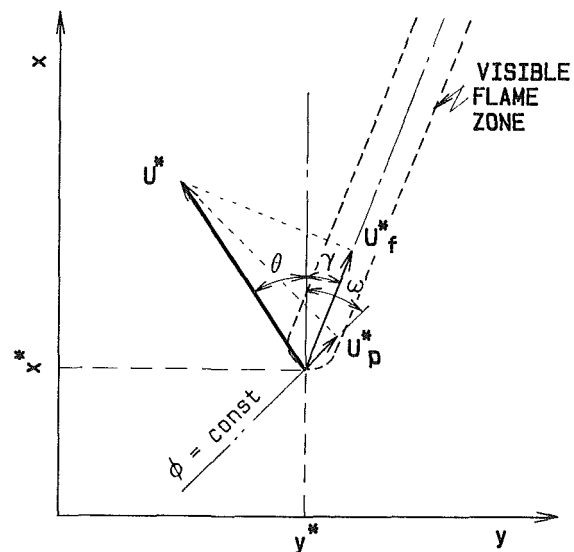


Fig. 11 Schematic of the flame base defining notations

Table 1 Comparisons of structural data at the base of methane diffusion flames

Investigators	Burner system	U_e , m/s	\bar{U}_j , m/s	\bar{U}_j/\bar{U}_{jc}	x^* , mm	y^* , mm	θ , deg	γ , deg	ω , deg	U^* , m/s	U_f^* , m/s	U_p^* , m/s
Robson and Wilson (1969)	Tube (0.7 mm)	0.02	13.80	0.66	0.5	0.7	50	18	27	0.59	0.23	0.13
		0.02	2.08	0.10	0.15	1.05	30	16	—	0.40	0.28	—
Kawamura and Asato (1975)	Tube (4.0 mm)	0.50	2.63	0.40	0.42	1.07	29	13	—	0.47	0.35	—
Kawamura et al. (1980)	Two-dimensional (2 × 14 mm)	0.60	1.16	—	-0.15	1.24	28	26	—	0.36	0.21	—
		0.40	1.16	—	-0.31	1.24	25	25	—	0.37	0.24	—
This study	Two-dimensional (2.2 × 31 mm)	0.02	1.22	<0.12	-0.46	1.15	33	30	54	0.31	0.14	0.02
		0.02	0.61	<0.06	-0.73	1.10	29	29	—	—	—	—
		0.02	0.31	<0.03	-0.74	1.04	26	28	—	—	—	—

ditions, the flame base is the very end of diffusion flames and the dark space is formed simply by extinguishing due to heat (and radical) losses to the burner wall. Comparisons with previous results suggest that if the jet velocity approaches the lifting limit, however, the flame base shifts downstream and the flux vectors of both fuel and oxygen may have common components parallel to the flame zone, thus resulting in the propagation of the flame base toward the combustible zone in the dark space against the incoming bulk-flow velocity component. The physical ideas that have been proposed here should be used to develop numerical models for the structure of the stabilizing region of jet diffusion flames. If a successful numerical model is obtained for calculating the flame structural data in the present experiments, then predictions of the flame stability trends can be made.

Acknowledgments

The assistance of Mr. M. Takami in conducting experiments is gratefully acknowledged. One of the authors (F. T.) would like to thank Dr. R. Yetter and Prof. F. A. Williams for stimulating discussions on the flame-base properties. Most of the material in this paper was extracted from the M. Eng. Thesis of F. Takahashi.

References

- Anon., 1957, "Basic Consideration in the Combustion of Hydrocarbon Fuels With Air," NACA Report 1300.
- Datta, P., Hayward, B. M., and Reed, S. B., 1971, "A Flame Structure Study of the Stabilizing Region of a Near-Stoichiometric Laminar Burner Flame," *Combustion and Flame*, Vol. 17, pp. 399-408.
- Datta, P., and Reed, S. B., 1972, "A Flame Structure Study of the Stabilizing Region of a Fuel-Rich Flame and the Effects of Vitiating," *Combustion and Flame*, Vol. 19, pp. 89-99.
- Friedman, R., 1953, "Measurement of the Temperature Profile in a Laminar Flame," *Fourth Symposium (International) on Combustion*, Williams and Wilkins, Baltimore, pp. 259-263.
- Fristrom, R. M., and Westenberg, A. A., 1965, *Flame Structure*, McGraw-Hill, New York, Chaps. 7-9, 13.
- Gaydon, A. G., and Wolfhard, H. G., 1979, *Flames—Their Structure, Radiation, and Temperature*, 4th ed., Chapman and Hall, London, p. 39.
- Grant, A. J., and Jones, J. M., 1975, "Low-Frequency Diffusion Flame Oscillations," *Combustion and Flame*, Vol. 25, pp. 153-160.
- Hirschfelder, J. O., Curtiss, C. F., and Bird, R. B., 1954, *Molecular Theory of Gases and Liquids*, Wiley, New York, p. 539.
- Ikai, S., Mizomoto, M., and Takahashi, F., 1975, "A Study of the Flame Structure of a Laminar Diffusion Flame," *Proceedings, 52nd Ordinary General Meeting*, Japan Society of Mechanical Engineers, Tokyo, Japan, No. 750-5, pp. 157-160.
- Kaskan, W. E., 1957, "The Dependence of Flame Temperature on Mass Burning Velocity," *Sixth Symposium (International) on Combustion*, Reinhold, New York, pp. 134-143.
- Kawamura, T., and Asato, K., 1975, "The Structure of the Stabilizing Region of a Laminar Fuel Jet Flame," *2nd European Combustion Symposium*, The Combustion Institute, pp. 611-616.
- Kawamura, T., Asato, K., and Mazaki, T., 1980, "Structure Analysis of the Stabilizing Region of Plane, Laminar Fuel-Jet Flames," *Combustion Science and Technology*, Vol. 22, pp. 211-216.
- Lee, S. T., and Dai, C. S., 1984, "A Study of the Stabilizing Zone of a Two-Dimensional, Laminar Diffusion Flame," *Journal of the Chinese Society of Mechanical Engineers*, Vol. 15, pp. 67-74.
- Pandya, T. P., and Weinberg, F. J., 1964, "The Structure of Flat, Counterflow Diffusion Flames," *Proceedings of the Royal Society, Ser. A*, Vol. 279, pp. 544-561.
- Robson, K., and Wilson, M. J. G., 1969, "Stability of Laminar Diffusion Flames of Methane," *Combustion and Flame*, Vol. 13, pp. 626-634.
- Takahashi, F., 1975, "A Study of the Flame Structure of a Laminar Diffusion Flame," M. Eng. Thesis, Keio University, Yokohama, Japan.
- Takahashi, F., 1982, "Studies of the Transition to Turbulence and the Flame Stability of Jet Diffusion Flames," D. Eng. Thesis, Keio University, Yokohama, Japan.
- Takahashi, F., 1986, "JET—a Computer Program for Solving the Navier-Stokes Elliptic Conservation Equation Set, Including One-Step Finite-Rate Kinetics, With Particular Applications to Transient Phenomena in Laminar Jet Diffusion Flames," Department of Mechanical and Aerospace Engineering Report, No. 1772, Princeton University, Princeton, NJ.
- Takahashi, F., Mizomoto, M., and Ikai, S., 1980, "Stability of Hydrogen Jet Diffusion Flames," *Hydrogen Energy Progress*, T. N. Veziroglu, ed., Pergamon Press, New York, pp. 1165-1176.
- Takahashi, F., Mizomoto, M., and Ikai, S., 1982, "Transition From Laminar to Turbulent Free Jet Diffusion Flames," *Combustion and Flame*, Vol. 48, pp. 85-95.
- Takahashi, F., Mizomoto, M., Ikai, S., and Futaki, N., 1985, "Lifting Mechanism of Free Jet Diffusion Flames," *Twentieth Symposium (International) on Combustion*, The Combustion Institute, Pittsburgh, pp. 295-302.
- Tsuji, H., and Yamaoka, I., 1971, "Structure Analysis of Counterflow Diffusion Flames in the Forward Stagnation Region of a Porous Cylinder," *Thirteenth Symposium (International) on Combustion*, The Combustion Institute, Pittsburgh, pp. 723-731.
- Ueda, T., Mizomoto, M., Takahashi, F., and Ikai, S., 1986, "Structure of the Flame-Base Region of a Two-Dimensional Laminar Jet Diffusion Flame," *Twenty-Fourth Symposium (Japanese) on Combustion*, Paper No. 50, pp. 148-150.
- Williams, F. A., 1985, *Combustion Theory*, 2nd ed., Benjamin/Cummings, Menlo Park, CA, p. 38.

Group Combustion of a Cylindrical Cloud of Char/Carbon Particles

K. Annamalai

Associate Professor.
Mem. ASME

S. Ramalingam

Graduate Research Assistant.

T. Dahdah

Graduate Research Assistant.

D. Chi

Graduate Research Assistant.

Department of Mechanical Engineering,
Texas A&M University,
College Station, TX 77843

Extensive experiments were carried out in the past in order to obtain kinetics data on the pyrolysis of coal particles and the char reactions. The literature survey distinctively reveals two kinds of studies: (i) Individual Particle Combustion (IPC) and (ii) Combustion of Particle Streams or Clouds. The experimental data obtained with particle streams are normally interpreted using IPC models with the a priori assumption that the cloud is dilute. But the term "dilute" is rarely quantified and justified considering the collective behavior of a cloud of particles. The group combustion model accounts for the reduction in burning rate due to the collective behavior of a large number of particles. While the spherical group combustion model may be employed for coal/char spray combustion modeling, the cylindrical group combustion model is more useful in interpreting the experimental data obtained with a monosized stream of particles. Hence a cylindrical group combustion model is presented here. As in the case of spherical group combustion models, there exist three modes of combustion: (i) Individual Particle Combustion (IPC), (ii) Group Combustion (GC), and (iii) Sheath Combustion (SC). Within the range of parameters studied, it appears that the cylindrical and spherical cloud combustion models yield similar results on nondimensional cloud burning rates and on the combustion modes of a cloud of particles. The results from group theory are then used to identify the mode of combustion (IPC, GC, or SC) and to interpret the experimental data.

1 Introduction

Most of the coal-fired utility boilers adopt suspension firing because of the high intensity of combustion and good flame stability behavior at widely varying loads. The flame stability is commonly related to the ratio of residence time of the particle in the vicinity of the burner to the characteristic combustion time. The estimation of combustion time is usually carried out using the individual particle combustion (IPC) model. The IPC model needs data on the kinetics of pyrolysis and heterogeneous reactions, and the transport processes between the particle and ambience. Extensive experiments have been carried out in the past in order to obtain kinetics data on pyrolysis of coal and char reactions. The literature review distinctively reveals two kinds of studies: (i) Individual Particle Combustion (Golovina and Khaustovich, 1962; Matalon, 1980; Choi and Kruger, 1985; Bhandyopadhyay and Bhaduri, 1972; Essenhigh, 1963), and (ii) Combustion of Monosized Particle Stream or Clouds (Hamor et al., 1973; Howard and Essenhigh, 1967a, 1967b; Kimber and Gray, 1971; Nettleton and Stirling, 1971; Anthony et al., 1975; Niksa et al., 1984; Horton et al., 1977; Ayling and Smith, 1972; Mulcahy and Smith, 1969). The kinetics data obtained from the combustion experiments on monosized particle streams are somewhat more useful than those obtained from the IPC experiments since the former experiments, to a certain extent, simulate the spray (cloud) conditions existing in a boiler. Even those data obtained with particle streams are interpreted using IPC models with the a priori assumption that the cloud is "dilute." The term "dilute" is quantified in the sense that the interparticle distance is often greater than the characteristic film thickness evaluated with the IPC model. Labowsky (1978) has shown from quasi-steady (QS) models that the distance between the droplets should exceed 7000 times the radius of the droplet, if a cloud containing 1000 droplets were to burn in a QS individual flame mode. Thus for a droplet of 50 μm

diameter, this leads to a number density of 200 drops per m^3 and possibly higher if transient effects are included (Labowsky, 1980). On the other hand, the particle number density used in small-scale experiments is of the order of about 1 particle per mm^3 (10^9 particles/ m^3) (Hamor et al., 1973; Kimber and Gray, 1971; Niksa et al., 1984; Ayling and Smith, 1972; Mulcahy and Smith, 1969, 1971) and the droplets/particles in a spray combustor typically have interparticle separations of 10 to 100 times the radius of the droplets. The particle interactions are expected to play a significant role in the reduction of burning rate. Thus it is essential that the cloud effects on the burning rate be investigated so that a criterion for "diluteness" can be developed based on the group combustion (GC) model. In simple terms group combustion implies the formation of a flame around a large number of drops/particles rather than a flame around an individual drop/particle. In broader terms such a behavior could be interpreted as the change in burning characteristics due to the collective behavior of a cloud of particles.

A literature review on group combustion has been presented in Annamalai and Ramalingam (1986a). The earliest work on group combustion was carried out by Suzuki and Chiu (1971). Labowsky and Rosner (1978) studied the group combustion of a cloud of liquid drops and used the analogy of porous char combustion and group combustion for correlating the results in terms of Thiele modulus. Chiu et al. (1977, 1983) presented a detailed model on group combustion and presented criteria for the occurrence of group combustion in terms of group combustion number G . Correa and Sichel (1982, 1983) and Sichel and Palaniswamy (1984) adopted asymptotic analyses for the group evaporation, ignition, and combustion. Bellan and Cuffel (1983) included the interactive effects in modeling the group evaporation of a cloud of drops. Annamalai et al. (1984, 1985a, 1985b, 1985c) carried out a generalized treatment on group evaporation, ignition, and combustion and presented relations between the burning rate of a drop located inside the cloud and the burning rate of a single drop located in an infinite atmosphere. For simplicity most of these models involve the analysis of a spherically symmetric cloud of liquid

Contributed by the Heat Transfer Division and presented at the Second ASME/JSME Thermal Engineering Conference, Honolulu, Hawaii, March 22-26, 1987. Manuscript received by the Heat Transfer Division November 22, 1986.

drops burning in quiescent air. Recently a study has been initiated to model the ignition and combustion of a cloud of coal particles as a group behavior (Annamalai et al., 1986a). Such a model includes the transient effects (nonsteady, NS), pyrolysis with competing reactions, heterogeneous char reactions, and gas phase oxidation of volatiles and carbon monoxide (CO). QS results have already been obtained for a spherical cloud of char particles (Annamalai and Ramalingam, 1986b). While the results from spherical cloud models may be useful in coal spray combustion models, the application of the spherical cloud model in interpreting the experimental data obtained with a stream of char particles is rather limited since a stream is better approximated by a cylindrical cloud of particles. Further a QS approach is used rather than a NS approach since the derivations can be kept in tractable form. As shown later, such a treatment leads to explicit solutions for the burning rate and provides the necessary dimensionless groups even to correlate the NS results. Thus the objectives of the present paper are twofold: (i) to model the quasi-steady combustion of a cylindrical cloud of char particles and compare the results with those from the spherical cloud model; (ii) to interpret earlier experimental data obtained with a stream of particles with the group combustion model.

Conservation equations will be presented for mass, species, and energy. Normalizations will be performed in order to identify the dimensionless groups governing the group combustion process. Explicit solutions are then presented for the group burning rate and the flame structure. Numerical results illustrating the importance and influence of model parameters are presented and their relevance discussed. Three modes of combustion are identified:

- (I) Individual particle combustion (IPC)
- (II) Group combustion (GC)
- (III) Sheath combustion (SC)

The cloud conditions of earlier experimenters are then used to identify the combustion mode and then the experimental data are interpreted with appropriate IPC, GC, and SC models.

2 Analysis

2.1 Model and Assumptions. A detailed description of the group combustion model for a spherical cloud is given by

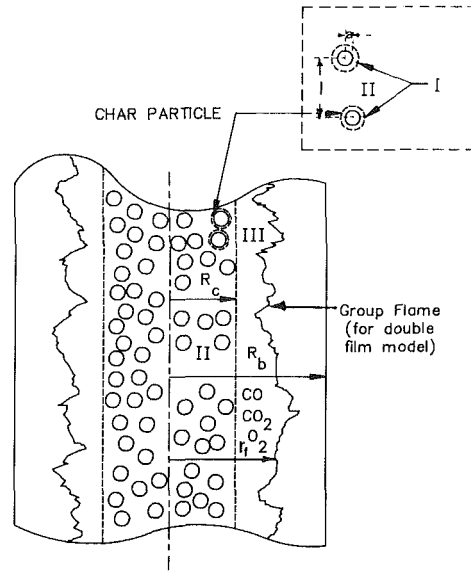


Fig. 1 Group combustion model for a cylindrical cloud of char particles

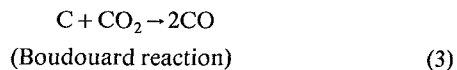
Annamalai et al. [1984b, 1985a]. The model will be briefly described below.

Consider a cylindrical cloud of radius R_c containing char/carbon particles (Fig. 1). The particle size a and the particle separation distance l may vary as a function of the radius r from the center of the cloud. The cloud is essentially a two-phase zone, consisting of solid and gas phases. The gas phase inside the cloud can be divided into the film zone around the particle, zone I, and the bulk gas zone, zone II (see the inset of Fig. 1). The particle reacts with the species O_2 and CO_2 to produce CO and CO_2 . The CO and CO_2 produced at the particle surface diffuse through the film zone, into the bulk gas zone where CO is oxidized to CO_2 . Both CO and CO_2 diffuse into the single-phase outer zone, zone III, where CO is oxidized further. The O_2 diffuses from a duct of radius R_b through zone III into zone II and then into the film region, zone I. In order to simplify the analysis of cloud combustion, the following assumptions are made:

Nomenclature

a = radius of single char particle in the cloud, m	bustion number, equation (13k)	cloud of radius R_c for cylindrical cloud
B = local transfer number, equation (5e)	g = term in equation (9c)	$M_s = \dot{m}_s/[4\pi\rho Da]$ = normalized burning rate of a single char particle
B_k = transfer number for the case where heterogeneous reactions are finite, equation (5d)	h_c = heat released due to reactions (1) and (4) and heat absorbed for Boudouard reaction (reaction (3)), kJ/kg	\dot{m} = mass flow rate at any radius r for cylindrical cloud, kg/m - s
B_w = term in equation (5f)	\bar{h}_c = heat released per kg after accounting for radiation heat loss, equations (8c) and (8d), kJ/kg	\dot{m}_c = mass burning rate of the cloud for cylindrical cloud, kg/m-2
C_p = specific heat at constant pressure, kJ/kgK	h_m = mass transfer coefficient, kg/m ² s	$\dot{m}_{s,c}$ = averaged burning rate of a single char particle of radius a inside the cloud kg/s
D = diffusion coefficient, m ² /s	h_T = thermal enthalpy, kJ/kg	n = number of particles per unit volume, m ⁻³
f = term in equation (9b)	Le = Lewis number	Q = q in figures
G = group combustion number, equations (13h) and (27)	l = interparticle spacing, m	q = see equation (13k)
G_1 = modified group combustion number, equation (13i)	M = $\dot{m}/[2\pi\rho D]$ = normalized burning rate of a	$\dot{q}_{r,p}$ = radiation heat loss from particle, kW

1 The solid particle normally undergoes the following reactions:



The primary product is mainly CO above 800 K and as such reaction (2) is insignificant.

2 A global reaction scheme is applicable for the oxidation of CO



3 The film zone is considered to be frozen. This assumption leads to simplified relations for the heat and mass transfer processes between the bulk gas and the particles. Significant oxidation takes place in the bulk gas phase (zone II) since the volume of zone II is of the order of l^3 while the volume of the film zone is of the order of a^3 and typically $(l/a) \gg 1$. Thus the approximation is justified for $l/a \gg 1$.

4 A QS state¹ and cylindrical symmetry exist; $\rho D = \text{const}$ and $Le = 1$.

5 The cloud may consist of particles of different sizes and nonuniform particle number density. The product of particle size and number density is a monotonic function of radius r so that cylindrical symmetry is maintained.

6 The cloud zone is a continuum.

7 The gas is quiescent. This assumption may be relaxed to account for relative velocity effects by using the empirical correlation for mass transfer coefficient.

8 In order to illustrate the group combustion behavior and to simplify the analysis it is assumed that the burning rate of an individual char particle inside the cloud is controlled by the mass transfer across the film. Such an assumption seems to be valid for $a > 50 \mu\text{m}$ at particle temperatures greater than 1200 K (Mulcahy, 1971). For smaller particles, the temperature has to be higher than 1200 K for the diffusion control approximation to be valid.

2.2 Conservation Equations. With assumptions (1) and (4), the conservation equations in the standard form are written as follows:

Mass:

$$\begin{aligned} d\dot{m}/dr &= 2\epsilon\pi r^{\epsilon} \dot{m}''' , & r < R_c \\ &= 0, & r > R_c \end{aligned} \quad (5a)$$

where

\dot{m} = mass flow at any radius r for a spherical cloud and mass flow per unit length for a cylindrical cloud

\dot{m}''' = mass burning rate of all particles within a unit volume

$$\dot{m}_s = \dot{m}_s n \quad (5b)$$

$\epsilon = 1$ for cylindrical and 2 for spherical clouds.

Assumptions (3), (4), and (7) lead to a simple expression for the burning rate of individual carbon particles inside the cloud.²

$$\dot{m}_s = 4\pi\rho Da \ln(1 + B_k) \quad (5c)$$

where B_k is the local transfer number for kinetically controlled heterogeneous combustion and CO oxidation in the film zone.

$$B_k = (B - B_w) / (1 + B_w) \quad (5d)$$

$$B = (Y_{CO_2})/(\nu_3) + (Y_{O_2})/(\nu_1) \quad (5e)$$

$$B_w = (Y_{CO_2,w})/(\nu_3) + (Y_{O_2,w})/(\nu_1) \quad (5f)$$

If $B_w \ll B$, then equation (5c) simplifies to

$$\dot{m}_s = 4\pi\rho Da \ln(1 + B) \quad (5g)$$

With assumption (8), $B_w = 0$. Thus the diffusion control approximation inherently leads to the relation for the burning rate independent of CO kinetics in the film zone. The single-particle combustion studies show similar results on the burning rate for both the double film model (DFM, fast CO kinetics) and the single film model (SFM, frozen CO kinetics)

¹Nonsteady results are currently being generated.

²For particles under convection one can replace 4 by 2Sh, where $Sh = 2h_m a / \rho D$.

Nomenclature (cont.)

\dot{q}_s'' = heat flux per unit area of the particle surface, kW/m ²	ϵ = defined after equation (5b)	ch = chemically reacted
R_b = radius of the oxidant boundary, m	$\kappa = a/a_{\text{ref}}$	f = flame
R_c = radius of the cloud, m	λ = thermal conductivity, kW/mK	GC = group combustion
R_o = duct radius, m	$\nu_1, \nu_2, \nu_3, \nu_4$ = stoichiometric coefficients of oxygen for reactions (1), (2), and (4) and CO ₂ for reaction (3)	I = inerts
r = radius, m	ξ = normalized inverse radius = R_c/r	IPC = individual particle combustion
Sh = Sherwood number = $h_m(2a)/\rho D$	ρ = density, kg/m ³	i = species i
T = temperature, K	σ = fuel volume fraction	ij = species i and j
\dot{w}''' = rate of production per unit volume for the chemical reaction $CO + 1/2 O_2 \rightarrow CO_2$, kg/m ³ s	ϕ = coupling function, equation (13a)	k = kinetics
Y_i = mass fraction of species i	ω = normalized reaction rate for the reaction, $CO + 1/2 O_2 \rightarrow CO_2$	p = produced by heterogeneous reactions at particles surfaces
α = normalized mass flow rate = \dot{m}/\dot{m}_c		R, p = radiation from particles
β = Shvab-Zel'dovich variable, see Table 1		SC = sheath combustion
	Subscripts	s = single particle
	b = boundary	w = wall of particle
	c = cloud	∞ = ambience
	Superscripts	
		" = per unit area
		''' = per unit volume

(Annamalai, 1984a). It should be noted that a is a function of r (assumption 5) and B represents the local transfer number around the particle evaluated with the conditions of zone II.

Species:

$$\begin{aligned} (d/dr)(\dot{m}Y_i) - [d/dr][2\epsilon\pi r^\epsilon \rho D(dY_i/dr)] \\ = (\dot{m}_{i,p}''' - \dot{m}_{i,ch}''')2\epsilon\pi r^\epsilon, \quad r < R_c \\ = \dot{m}_{i,ch}'''2\epsilon\pi r^\epsilon, \quad r > R_c \end{aligned} \quad (6)$$

where $\dot{m}_{i,p}'''$ represents species i produced per unit volume due to the heterogeneous (particle) reactions, $\dot{m}_{i,ch}'''$ is species i produced or consumed per unit volume through chemical reaction in the bulk gas phase and in the single-phase zones, and the index i represents the species CO, CO₂, and O₂.

Energy:

Applying the First Law of Thermodynamics for the control volume bounded within the cylindrical surfaces of radii (r) and ($r + dr$) and the surfaces of all particles within (r) and ($r + dr$):

$$\begin{aligned} (d/dr)(\dot{m}h_T) - [d/dr][(\lambda(dT/dr)2\epsilon\pi r^\epsilon) \\ = (\dot{q}_s''4\pi a^2)2\epsilon\pi r^\epsilon n \\ + |\dot{m}_{CO,ch}'''|h_{c,4}2\epsilon\pi r^\epsilon, \quad r < R_c \\ = |\dot{m}_{CO,ch}'''|h_{c,4}2\epsilon\pi r^\epsilon, \quad r > R_c \end{aligned} \quad (7)$$

where \dot{q}_s'' is the heat flux per unit area leaving the char particle.

With assumption (1), the energy balance analysis at the surface of char yields the expression for \dot{q}_s''

$$4\pi a^2 \dot{q}_s'' = \dot{m}_{s,1}h_{c,1} - \dot{m}_{s,3}h_{c,3} - \dot{q}_{R,p} \quad (8a)$$

We rewrite equation (8a) as

$$4\pi a^2 \dot{q}_s'' = \dot{m}_{s,1}[\bar{h}_{c,1}] - \dot{m}_{s,3}[\bar{h}_{c,3}] \quad (8b)$$

where

$$\bar{h}_{c,1} = \{h_{c,1} - (\dot{q}_{R,p}/\dot{m}_s)\} \quad (8c)$$

$$\bar{h}_{c,3} = \{h_{c,3} + (\dot{q}_{R,p}/\dot{m}_s)\} \quad (8d)$$

$$\dot{m}_s = \dot{m}_{s,1} + \dot{m}_{s,3} \quad (8e)$$

The term $h_{c,1}$ is the heat released due to direct oxidation and $h_{c,3}$ is the heat absorbed due to the Boudouard reaction. With $Le = 1$ and using equation (8b) in equation (7), the energy conservation equation is written as

$$\begin{aligned} (d/dr)(\dot{m}h_T) - [d/dr][\rho D2\epsilon\pi r^\epsilon (dh_T/dr)] \\ = \dot{m}'''2\epsilon\pi r^\epsilon [fh_{c,1} - gh_{c,3}] \\ + 2\epsilon\pi r^\epsilon h_{c,4} |\dot{m}_{CO,ch}'''|, \quad r < R_c \\ = 2\epsilon\pi r^\epsilon h_{c,4} |\dot{m}_{CO,ch}'''|, \quad r > R_c \end{aligned} \quad (9a)$$

where

$$f = \dot{m}_{s,1}/\dot{m}_s \quad (9b)$$

$$g = \dot{m}_{s,3}/\dot{m}_s \quad (9c)$$

$$f + g = 1 \quad (9d)$$

The term f represents the fraction of carbon removed due to oxidation reaction while g represents the fraction due to the Boudouard reaction. The thermal enthalpy h_T is evaluated with the reference condition at the particle surface

$$h_T = \int_{T_w}^T C_p dT \quad (10)$$

With assumption (1),

$$(\dot{m}_{CO,p}'''/\dot{m}''') = f(1-\nu_1) + g(1+\nu_3) \quad (11)$$

Using the definition of Shvab-Zel'dovich variables (column 2 of Table 1) and assumptions (1) and (2), a simplified form of conservation equations is obtained. The details of the derivations are similar to those given by Annamalai et al. (1986a, 1986b).

For species and thermal enthalpy

$$\begin{aligned} d/dr(\dot{m}\beta_{i-j}) - d/dr[2\epsilon\pi r^\epsilon \rho D(d\beta_{i-j}/dr)] \\ = -\dot{m}'''2\epsilon\pi r^\epsilon, \quad r < R_c \\ = 0, \quad r > R_c \end{aligned} \quad (12a, b, c)$$

where $\beta_{i-j} = \beta_{CO-O_2}$, $\beta_{CO_2-O_2}$, $\beta_{h_T-O_2}$, respectively. For oxygen

$$\begin{aligned} d/dr(\dot{m}\beta_{O_2}) - d/dr[2\epsilon\pi r^\epsilon \rho D(d\beta_{O_2}/dr)] \\ = -[\dot{m}'''f + \dot{w}'''(\nu_4/\nu_1)]2\epsilon\pi r^\epsilon, \quad r < R_c \\ = -\dot{w}'''(\nu_4/\nu_1)2\epsilon\pi r^\epsilon, \quad r > R_c \end{aligned} \quad (12d)$$

Equations (5a) and (12) constitute the conservation equations for the present problem.

2.3 Nondimensional Form of Conservation Equations. The following nondimensional variables are introduced in order to obtain the dimensionless form of the conservation equations:

Coupling function:

$$\phi_{i-j} = (1 + \beta_{i-j}) / (1 + \beta_{i-j,\infty}) \quad (13a)$$

$$\beta_{O_2} = (1 + \beta_{O_2}) / (1 + \beta_{O_2,\infty}) \quad (13b)$$

Nondimensional inverse radius:

$$\xi = R_c / r \quad (13c)$$

Normalized mass flow rate at any radius r :

$$\alpha = \dot{m} / \dot{m}_c \quad (13d)$$

where the overall mass burning rate of cloud \dot{m}_c is given as

$$\dot{m}_c = \int_0^{R_c} \dot{m}'''2\epsilon\pi r^\epsilon dr \quad (13e)$$

Fuel volume fraction:

$$\sigma = (4\pi/3)na_{ref}^3 \quad (13f)$$

Normalized particle size:

$$\kappa = a/a_{ref} \quad (13g)$$

Group combustion numbers:

$$G = 3\sigma R_c^2 / a_{ref}^2 \quad (13h)$$

Normalized cloud burning rate:

$$M = \dot{m}_c / [2\epsilon\pi \rho D R_c^{\epsilon-1}] \quad (13i)$$

(It should be noted that for cylindrical clouds $\epsilon = 1$ and hence $M = \dot{m}_c / [2\pi \rho D]$.) With equations (5b), (5c), and (13c)-(13h) in (13i), the normalized cloud burning rate M can be written as

$$M = \int_{1.0}^{\infty} [G\kappa/\xi^{(2+\epsilon)}] \ln(1+B)d\xi \quad (13j)$$

With assumption (5) and equations (13f)-(13h), the term $G\kappa$ in equation (13j) can be expressed as

$$G\kappa = G_1 \xi^q, \quad q \leq 1 \quad (13k)$$

Table 1 Definitions of modified Shvab-Zel'dovich variables: $\phi_{i-j} = (1 + \beta_{i-j}) / (1 + \beta_{i-j,\infty})$

$i-j$	β_{i-j}	Remarks
CO-O ₂	$(1/2)[(Y_{O_2}/\nu_1) - (Y_{CO}\nu_4/\nu_1)]$	$B = \beta_{CO_2-O_2}$
CO ₂ -O ₂	$(Y_{CO_2}/\nu_3) + (Y_{O_2}/\nu_1)$	Note that B is a function of radius r
h_T -O ₂	$[(h_T/\bar{h}_{c,3}) + (Y_{O_2}h_{c,4})/(\nu_4\bar{h}_{c,3})]$	
O ₂	Y_{O_2}/ν_1	In this case the "j" notation does not apply

where G_1 is a proportionality constant and may be called the modified group combustion number. For monosized and uniform clouds, $G_1 = G$. The upper bound on q is due to the condition that mass $\rightarrow 0$ within a sphere of radius r as $r \rightarrow 0$.

Normalized CO reaction rate:

$$\omega = \dot{w}''' \nu_4 R_c^2 / [\rho D \nu_1 \{1 + (Y_{O_2,\infty}/\nu_1)\}] \quad (13)$$

Using equation (5g) and equations (13c)-(13j), the mass conservation equation (5a) is written as

$$(M\xi^{\epsilon+2}/G\kappa)d\alpha/d\xi = -\ln(1+B) \quad (14)$$

Adding equation (5a) to equations (12a)-(12c) and using the nondimensional variables, the following equations are obtained:

$$M(d/d\xi)(\alpha\phi_{i-j}) + (d/d\xi)[\xi^{(2-\epsilon)}d\phi_{i-j}/d\xi] = 0 \quad (15a, b, c)$$

where $\phi_{i-j} = \phi_{CO-O_2}$, $\phi_{CO_2-O_2}$, $\phi_{h_T-O_2}$, respectively. Similarly,

$$M(d/d\xi)(\phi_{O_2}) + (d/d\xi)(\xi^{(2-\epsilon)}d\phi_{O_2}/d\xi) = \left[\omega - \frac{[G\kappa \ln(1+B)](1-f)}{(1+Y_{O_2,\infty}/\nu_1)} \right] / \xi^{(2+\epsilon)}, \quad \xi \geq 1$$

$$= \omega, \quad \xi \leq 1 \quad (15d)$$

(It is apparent from equation (15d) that if $f = 1$ (no CO₂ reduction) the second term on the right hand side of equation (15d) disappears). The boundary conditions for a cylindrical cloud ($\epsilon = 1$) burning in a larger duct are as follows:

as $\xi \rightarrow \xi_b$,

$$\phi_{CO-O_2} \rightarrow 1 \quad (16a)$$

$$\phi_{CO_2-O_2} \rightarrow 1 \quad (16b)$$

$$\phi_{h_T-O_2} \rightarrow 1 \quad (16c)$$

$$\phi_{O_2} \rightarrow 1; \quad (16d)$$

as $\xi \rightarrow \infty$,

$$d\phi_{CO-O_2}/d\xi \rightarrow 0 \quad (17a)$$

$$d\phi_{CO_2-O_2}/d\xi \rightarrow 0 \quad (17b)$$

$$d\phi_{h_T-O_2}/d\xi \rightarrow 0 \quad (17c)$$

$$d\phi_{O_2}/d\xi \rightarrow 0 \quad (17d)$$

$$\alpha \rightarrow 0 \quad (17e)$$

Since the boundary conditions for all ϕ_{i-j} are the same (equations (16a, b, c), and (17a, b, c)) and the differential equations (15a, b, c) are the same, then the solutions are identical:

$$\phi_{CO-O_2} = \phi_{CO_2-O_2} = \phi_{h_T-O_2} = \phi$$

As in the case of the combustion of a spherical cloud of particles (Annamalai and Ramalingam, 1986b) the solution of equation (15d) is unnecessary in obtaining the results for the burning rate and the particle temperature for both the following cases:

- (i) kinetically limited CO oxidation
- (ii) infinitely fast CO oxidation

For case (i), the flame structure and the mass fractions of CO and CO₂ will depend upon the extent of CO oxidation. Further the derivation of the equation (15c) from equation (12c) implicitly assumes that the temperature of the char particle inside the cloud is not a strong function of the radius r . It has been shown in earlier works that the char particle temperature remains the same throughout the cloud independent of the extent of the CO oxidation rate as long as the diffusion controlled combustion approximation is valid for each particle inside the cloud (Annamalai and Ramalingam, 1985b).

3 Solutions

3.1 Finite CO Kinetics. The procedure for obtaining the solutions for α , ϕ , $(1+B)$, and the cloud burning rate M , is the same as used for a spherical cloud of liquid drops and char particles (Annamalai, 1984b, 1985a, 1985b, 1986a). For clarity, the solution procedure is briefly outlined in Appendix A. The results are presented below.

(A) Dimensionless mass flow rate

$$\alpha(\xi) = \xi^{(q-2)/2} I_1 [Z\xi^{(q-2)/2}] / I_1 [Z], \quad \xi > 1$$

$$= 1, \quad \xi_b < \xi < 1 \quad (18)$$

where $Z = G_1^{1/2}(2/(2-q))$.

I_1 is a modified Bessel function of order 1.

(B) Coupling function and transfer number

$$\phi = \xi_b^M \exp[-(2M/\{Z(q-2)I_1(z)\}) (I_0(Z\xi^{(q-2)/2}) - I_0(Z))], \quad \xi > 1$$

$$= [\xi/\xi_b]^{-M}, \quad \xi_b < \xi < 1 \quad (19a)$$

$$(1+B) = \phi(1+B_\infty) \quad (19b)$$

(C) Cloud burning rate

The results for cloud burning rate can be expressed in two forms. Expressing cloud burning rate as a fraction of sheath combustion rate

$$(M/M_{SC}) = 1/\{1 + [I_0(Z)/(I_1(Z)\sqrt{G_1 \ln(1/\xi_b)})]\} \quad (20a)$$

where M_{SC} is the (sheath) burning rate of a char cylinder of radius equal to the cloud radius but with the density equal to the cloud density. Thus

$$M_{SC} = \ln(1+B_\infty)/\ln(1/\xi_b) \quad (20b)$$

The relation given in equation (20a) indicates that the mass burning rate of the cloud is independent of CO kinetics.

Expressing the cloud burning rate as a fraction of burning rate that would have been obtained in the event each particle in the cloud burns individually

$$(M/M_{IPC}) = (M/M_{SC})\{(2-q)/[G_1 \ln(1/\xi_b)]\} \quad (20c)$$

(D) Particle temperature. The particle temperature relation is the same as the relation for a spherical cloud (Annamalai, 1986b)

$$-(h_{T,\infty}/\bar{h}_{c,1}) = (Y_{O_2,\infty}/\nu_1) - [(Y_{CO_2,\infty}/\nu_3)(\bar{h}_{c,3}/\bar{h}_{c,1})] \quad (21)$$

This relation is the same as the relation obtained for a single char particle placed in an infinite atmosphere. If the cloud is dilute, the thermal radiation loss is significant and hence $\bar{h}_{c,1} < h_{c,1}$ and $\bar{h}_{c,3} > h_{c,3}$. Equation (21) then yields the lower bound on particle temperature. If the cloud is dense, the radiation loss may be insignificant and hence $\bar{h}_{c,1} \sim h_{c,1}$ and $\bar{h}_{c,3} \sim h_{c,3}$. Then equation (21) provides the upper bound on particle temperature. The upper bound temperature is estimated to be 2300 K for an ambient temperature of 1000 K with $Y_{O_2,\infty} = 0.23$, $\nu_1 = 1.333$, and $Y_{CO_2,\infty} = 0$. Thus diffusion-controlled approximation seems to be justified as long as radiation loss is negligible.

The results given in equations (18)–(21) for dimensionless mass flow rate, mass burning rate, and particle temperature are valid irrespective of whether CO oxidation is kinetically limited or infinitely fast. Further it should be noted that the particle temperature is independent of ξ in the absence of radiation loss. But the quantitative evaluation of temperature T and species mass fraction Y_i profiles needs the solution of ϕ_{O_2} (for Y_{O_2}) for the kinetically limited CO oxidation rates.

3.2 Infinite CO Oxidation. Since CO kinetics are infinitely fast there exists a group flame, and oxygen will not reach the particle surface (Fig. 1). Therefore the significant reaction at the particle surface is the Boudouard reaction. Further

$$Y_{O_2} = 0, \quad \xi > \xi_f \quad (22a)$$

and

$$Y_{CO} = 0, \quad \xi < \xi_f \quad (22b)$$

where ξ_f is the flame location. From equation (5e)

$$B = Y_{CO_2}/\nu_3, \quad \xi > \xi_f \quad (22c)$$

$$B = (Y_{CO_2}/\nu_3) + (Y_{O_2}/\nu_1), \quad \xi < \xi_f \quad (22d)$$

(A) *Flame Location.* Group flame is possible only if $\xi_f < 1$ ($r_f > R_c$, see Fig. 1) and as such the coupling function at the flame is given by equation (19a)

$$\phi_f = (\xi_f/\xi_b)^{-M}, \quad \xi_b < \xi_f < 1 \quad (23)$$

Solving for ξ_f ,

$$(\xi_f/\xi_b) = \phi_f^M \quad (24)$$

Using the definition of coupling function at the flame location and equations (20a) and (20b) in (24), the flame location is given as:

$$\ln(R_c/R_f)/\ln(\xi_b) = 1 - \{ \ln[1 + (1/2)(Y_{O_2,\infty}/\nu_1)] \times \ln(1/\xi_b) / [(M/M_{SC}) \ln(1 + B_\infty)] \} \quad (25)$$

(B) *Flame Temperature.* The flame temperature relation is the same as the one derived for a spherical cloud

$$(h_{T,f} - h_{T,\infty})/\bar{h}_{c,1} = (Y_{O_2,\infty}/\nu_1) \{ 1 + [(\bar{h}_{c,3}/\bar{h}_{c,1}) \times (1 - Y_{CO_2,\infty}/\nu_3)] / (2 + Y_{O_2,\infty}/\nu_1) \} \quad (26)$$

4 Results and Discussion

The solutions for the QS burning rate of a cylindrical cloud are generally a function of G_1 , q , and ξ_b ($= R_c/R_b$) (Section 3). Thus the specifications of ambient conditions are unnecessary in obtaining the results for M/M_{SC} and M/M_{IPC} versus G_1 . For monosized clouds, $a = a_{ref}$, $q = 0$, and hence³

³The G number can also be expressed in terms of the mass of the particles in the cloud as: $G = 9 \times (\text{mass of particles in cloud}) / [4\pi a^2 R_c \times (\text{density of particle})]$.

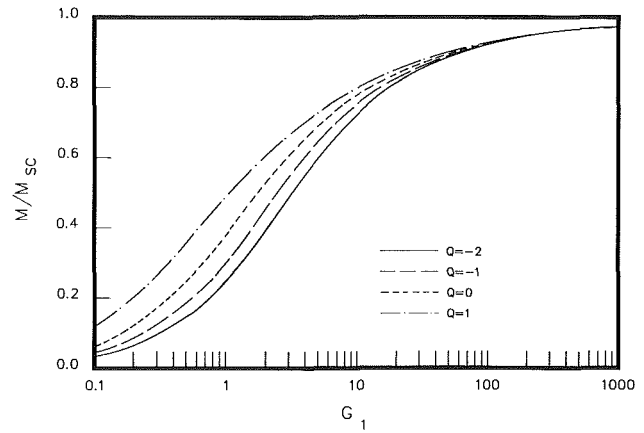


Fig. 2 Ratio of cloud burning rate M to sheath combustion rate M_{SC} versus modified group combustion number; $R_b/R_c = 2$

$$G_1 = G = 3\sigma(R_c^2/a^2) \quad (27)$$

The number G could be interpreted as the ratio of mass transfer between the particles in the cloud and the bulk gas (MTBP) to the mass transfer between the cloud surface and the ambience (MTAC). [Various forms of G -number definitions are given by Annamalai et al. (1986a)]. It will be seen later that this interpretation is useful in discussing the generalized results for the burning rate and in identifying the regimes of combustion while equation (27) is useful for interpreting the experimental data.

4.1 Cloud Burning Rate. Figure 2 shows a plot of M/M_{SC} versus G_1 for various values of q . A negative value of q implies an increasing particle size with increasing radius r from the center of the cloud. A positive value of q represents the opposite case. It should be noted that the ratio M/M_{SC} is a function of G_1 , q , and ξ_b . At a fixed ξ_b of 0.5, the effect of q on (M/M_{SC}) is not significant at small and large G numbers.

The behavior shown in Fig. 2 can be explained by considering a monosized cloud ($q = 0$ and hence $G_1 = G$). As the number of particles in the cloud increases, G increases. The increase in number of particles results in the increase of mass transfer rate between the particles in the cloud and the bulk gas (MTBP) and hence the burning rate increases. However the increase in MTBP results in the decrease of the mass fractions of O_2 and CO_2 at the cloud surface ($Y_{O_2,c}$, $Y_{CO_2,c}$). As G number is further increased (or as the mass of the cloud is increased), a limit is reached at which $Y_{O_2,c} \rightarrow 0$ and $Y_{CO_2,c} \rightarrow 0$. Beyond this limit, irrespective of the number of particles, the burning rate of the cloud is controlled by MTAC. Thus a high G number implies burning limited by MTAC. Under this condition the whole cloud behaves like a single char cylinder of radius R_c but with the density equal to the cloud density and hence $M/M_{SC} \rightarrow 1.0$ as $G \rightarrow \infty$.

The G number can also be increased with decreasing particle size for the same mass of cloud (i.e., increased pulverization) and cloud radius (refer to footnote 3). Decrease in a results in increased burning rate since the total reaction surface area is increased.

In order to determine the effects of group combustion on the burning rate, one should compare the burning rate of the cloud M to the total burning rate M_{IPC} , which could be obtained if each particle inside the cloud burned as though it were located in an infinite atmosphere. The results are presented in Fig. 3. Again the effect of size distributions q on the result is not significant at large and small G numbers. It is seen from Fig. 3 that IPC modeling may be adopted at low G numbers.

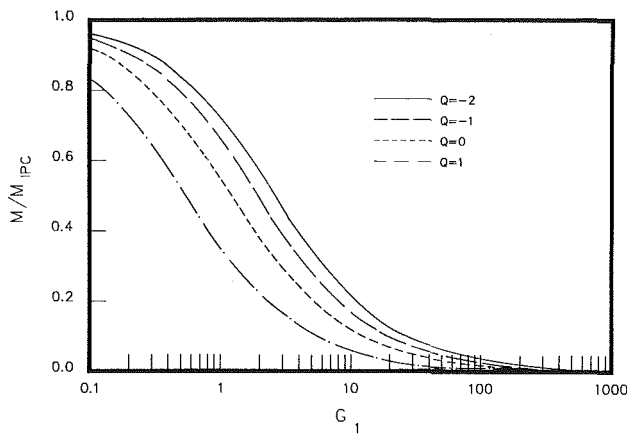


Fig. 3 Ratio of cloud burning rate M to burning rate based on individual particle combustion model M_{IPC} for a cylindrical cloud of char particles; $R_b/R_c = 2$

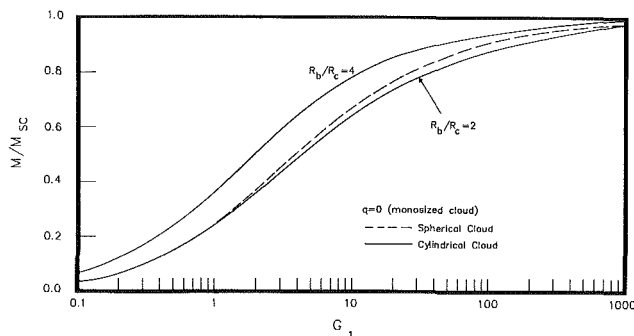


Fig. 4 Comparison of results for M/M_{SC} obtained with cylindrical and spherical cloud models

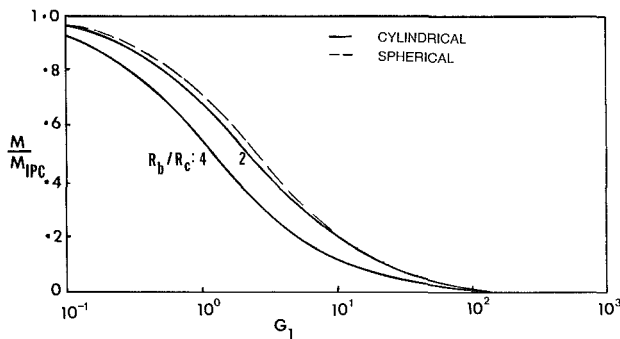


Fig. 5 Comparison of results for M/M_{IPC} obtained with cylindrical and spherical cloud models

Figures 4 and 5 compare the results of M/M_{SC} and M/M_{IPC} for the monosized uniform spherical and cylindrical clouds.⁴ The G -number definition remains the same for both clouds. There is almost no difference between the results for spherical clouds and cylindrical clouds of $\xi_b = 0.5$ ($R_b/R_c = 2$). Qualitatively the curves appear to be similar. However as ξ_b is reduced to 0.25 ($R_b/R_c = 4$), M/M_{SC} increases. While the sheath combustion rate decreases significantly as R_b/R_c is increased from 2 to 4, the decrease in cloud burning rate is not significant due to the group effect which causes increased values for M/M_{SC} with reduction in ξ_b . This result is clearly

⁴Figures 2-5 are valid irrespective of the extent of CO kinetics as long as $Y_{O_2,w}, Y_{CO_2,w} \ll Y_{O_2}, Y_{CO_2}$.

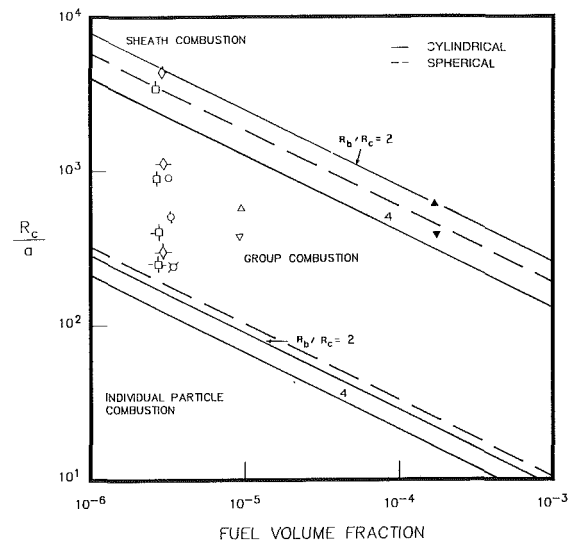


Fig. 6 Combustion modes of a cloud of particles on cloud radius—fuel volume fraction plane (experimental data points for a cloud of radius 1 cm):

- Δ Kimber and Gray, $a = 17 \mu\text{m}$
- ∇ Kimber and Gray, $a = 27 \mu\text{m}$
- \circ Hamor et al., $a = 11, 25, 40 \mu\text{m}$
- \square Ayling and Smith, $a = 3, 11, 25, 40 \mu\text{m}$
- \diamond Mulcahy and Smith, $a = 2, 9, 34 \mu\text{m}$
- \blacktriangle Kimber and Gray (fuel volume fraction based on carrier flow)

seen in Fig. 5. At a given G , M_{IPC} will remain the same. As R_b/R_c is increased from 2 to 4, the cloud burning rate M decreases.

It should be noted that the ratios M/M_{SC} and M/M_{IPC} are independent of ambient conditions and transport properties since any change in ambient conditions or transport properties affects M , M_{SC} , and M_{IPC} proportionately.

4.2 Combustion Modes of Cloud. In order to identify the regimes of combustion of a cloud of particles we will use the following criteria.

The cloud combustion could be treated as sheath combustion (SC) if $M/M_{SC} \geq 0.90$ within 10 percent accuracy. Such a condition occurs at $G \geq G_{SC} = 100$ for a spherical cloud. The cylindrical cloud combustion cloud be treated as SC for $G > G_{SC} = 200$ with $R_b/R_c = 2$ and $G > G_{SC} = 50$ with $R_b/R_c = 4$ (see Fig. 4).

The particles in the cloud could be modeled as individual particle combustion (IPC) if $M/M_{IPC} \geq 0.90$. Such a condition occurs at $G < G_{IPC} = 0.3$ for a spherical cloud. For cylindrical clouds, the IPC model can be adopted for $G < G_{IPC} = 0.24$ with $R_b/R_c = 2$ and $G < G_{IPC} = 0.13$ with $R_b/R_c = 4$.

Using the above criteria and equation (27), one can identify the mode of combustion. Figure 6 shows the results. At a given fuel volume fraction, the increased cloud radius or decreased particle radius results in GC and SC modes. It is also seen that the identification of the combustion regime is not very sensitive with respect to the geometry of the model (i.e., spherical or cylindrical model). Further it should be noted that no assumption regarding the kinetics of CO oxidation has been made in obtaining Fig. 6.

4.3 Experimental Data. In most of the earlier small-scale experiments, the coal/char particles were injected at the center while the hot oxidant gas flows around the fuel nozzle (Hamor and Smith, 1973; Howard and Essenhig, 1967a, 1967b; Kimber and Gray, 1971; Niksa et al., 1984; Ayling and Smith,

Table 2 Experimental conditions of several investigators and interpretation with group theory

No.	Authors	Study on	Experimental conditions	Radius of particle μm	Fuel volume fraction ²	l/a estimated	R_c/a	G	M/M_{SC}	M/M_{IPC}	$[(\dot{m}_{s,c}^{small})/(\dot{m}_{s,c}^{large})]^{-1}$	Remarks
1	2	3	4	5	6	7	8	9	10	11	12	13
1	Kimber and Gray	Reaction rate of char coal/ carbon, 800-2800K	Entrained reactor \dot{m}_F : 20 to 200 mg/min \dot{m}_g up to 2 L/min \dot{m}_{car} : 0.1 L/min	17 27	9.2×10^{-6} (1.83×10^{-4})	77 (28)	588 (37360) 370 (9314)	9.5 (191) 3.8 (75.4)	0.64 (0.90) 0.48 (0.85)	0.19 (0.014) 0.37 (0.033)	0.81 (0.67) 1.00 (1.00)	Flow rates are not available for each data point. Assumed $\dot{m}_F = 110$ mg/min, $\dot{m}_g = 2$ L/min. Particle size: medium size. A peak in burning rate was observed. Assumed that particles are well mixed with gas, $T_{gas} \sim 1800$ K. Quantities in parentheses are based on carrier flow.
2	Hamor, Smith, and Taylor	Kinetics of combustion of Brown coal char, 630-2200 K	$\dot{m}_F \sim 40$ mg/s O_2-N_2 Mix ~ 2.5 L/s 5 cm dia entrained reactor centerline injection	11 25 45	3.4×10^{-6} (5.1×10^{-5})	107 (43)	909 (3.8×10^4) 400 (3292) 222 (559)	8.5 (126) 1.7 (24.69) 0.5 (7.6)	0.62 (0.88) 0.32 (0.75) 0.14 (0.60)	0.21 (0.020) 0.57 (0.087) 0.81 (0.23)	1.06 (0.36) 1.27 (0.69) 1.00 (1.00)	Assumed that particles are well mixed with gas, $T_{gas} \sim 1415$ K carrier flow rates are not available.
3	Ayling and Smith	Measurement of particle temperature and measurement of primary re-action product 1400-2200 K	Entrainment reactor same as Hamor et al. $\dot{m}_F \sim 42$ mg/s $\dot{m}_g \sim 150$ L/min 5 cm dia	3 11 25 40	2.8×10^{-6} (4.3×10^{-5}) ³	114 (46)	3333 (1.6×10^6) 909 (3.1×10^4) 400 (2691) 250 (657)	93.5 (1402) 6.6 (104) 1.3 (20) 0.5 (7.9)	0.86 (0.96) 0.58 (0.87) 0.28 (0.73) 0.15 (0.61)	0.027 (0.002) 0.25 (0.024) 0.63 (0.10) 0.80 (0.22)	0.45 (0.12) 1.14 (0.40) 1.26 (0.73) 1.00 (1.00)	$T_{gas} \sim 1800$ K no data are available for carrier flow.

¹ $[(\dot{m}_s^{small})/(\dot{m}_s^{large})] = [(M/M_{SC})^{small} \times a^{small}] / [(M/M_{SC})^{large} \times a^{large}]$

² Quantities in parentheses are based on carrier flow.

³ Assumed carrier flow: 1/15 of main gas flow.

Table 3 Comparison of the results for spherical and cylindrical clouds: $R_c = 1$ cm, $R_b/R_c = 2.0$

No.	Authors	$a, \mu\text{m}$	$[M/M_{SC}]$		$[M/M_{IPC}]$		$[(\dot{m}_{s,c}^{\text{small}})/(\dot{m}_{s,c}^{\text{large}})]$	
			Sphere	Cylinder	Sphere	Cylinder	Sphere	Cylinder
1	Kimber and Gray	17	0.68 (0.93)	0.64 (0.90)	0.21 (0.025)	0.19 (0.014)	0.84 (0.70)	0.81 (0.67)
		27	0.51 (0.88)	0.48 (0.85)	0.40 (0.035)	0.37 (0.033)	1.00 (1.00)	1.00 (1.00)
2	Hamor, Smith, and Taylor	11	0.66 (0.91)	0.62 (0.88)	0.23 (0.022)	0.21 (0.020)	1.15 (0.35)	1.06 (0.36)
		25	0.33 (0.80)	0.32 (0.75)	0.61 (0.097)	0.57 (0.087)	1.31 (0.69)	1.27 (0.69)
		45	0.14 (0.64)	0.14 (0.60)	0.83 (0.26)	0.81 (0.23)	1.00 (1.00)	1.00 (1.00)
3	Ayling and Smith	3	0.90 (0.97)	0.86 (0.96)	0.029 (0.0021)	0.027 (0.0020)	0.45 (0.11)	0.45 (0.12)
		11	0.62 (0.90)	0.58 (0.87)	0.27 (0.026)	0.25 (0.024)	1.14 (0.38)	1.14 (0.40)
		25	0.30 (0.78)	0.28 (0.73)	0.64 (0.12)	0.63 (0.10)	1.25 (0.75)	1.26 (0.73)
		40	0.15 (0.65)	0.15 (0.61)	0.83 (0.25)	0.80 (0.22)	1.00 (1.08)	1.00 (1.00)

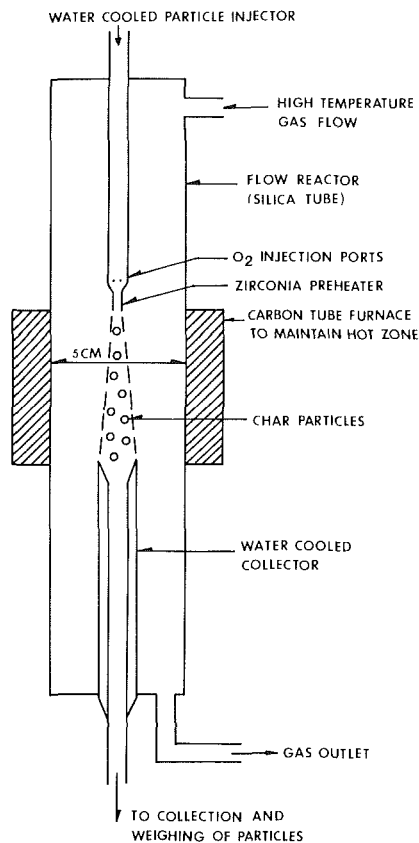


Fig. 7 Schematic of a typical experimental setup

1972; Mulcahy and Smith, 1971). Figure 7 illustrates a typical experimental apparatus used in dust combustion studies. Howard's experiments (1967a, 1967b) allow premixing of oxidant and coal particles prior to ignition and combustion while the other experimenters have used coaxial laminar jets (with the center jet typically having higher velocities), which invariably involve mixing delay. Since the mixing time is proportional to the square of the fuel injector radius R_F , the mixing delay can be reduced significantly by reducing the injector radius. Many of the fuel injectors used in the experiments involve small diameters. Thus it can be assumed that the thermal

mixing time is small. Furthermore, the radii of char particles utilized in combustion studies range from $2 \mu\text{m}$ to $45 \mu\text{m}$ (Table 2, column 5). The characteristic heating time is of the order of 0.0004 to 10 ms. Hence the assumption of quasi-steady-state combustion of the cloud appears to be reasonable. Figure 6 can then be used to identify the mode of combustion. The fuel volume fraction is estimated using fuel flow and air flow data (Table 2, columns 4 and 6). The quantities in parentheses are upper bounds and are based on carrier flow while the lower bounds are evaluated assuming that char particles are dispersed uniformly throughout the cross section of the duct. For example the experimental conditions of Howard and Essenhigh (1967a) may correspond to the lower bound on fuel volume fraction. The experiments of Leslie et al. (1982) with CO_2 injection through a multiholed fuel nozzle show that the diffusion of CO_2 takes place rather gradually. Hence fuel volume fraction is expected to be bracketed between the upper and lower bounds for the experimental conditions of Kimber and Gray (1971) and Ayling and Smith (1972).

Two other data needed are R_c and R_b . The development of a free boundary layer (Kuo, 1986) outside the potential core (due to air entrainment) results in the gradual radial movement of the particles. While the G number is estimated to remain the same during the development of free boundary layer, the cloud radius keeps increasing. Thus the cloud radius is higher than the fuel jet radius but less than the duct radius. For qualitative evaluation of the group effects on the combustion rate the cloud radius is assumed to be half of the duct radius. Considering the experiments cited in Table 2 the radius of the cloud is assumed to be 1 cm. The radius R_b can be at the most equal to the duct radius, which is about 2.5 cm. Hence $R_b/R_c \sim 2$. (It should be mentioned that within the intervals of $2 < R_b/R_c < 4$, the combustion modes are not sensitive with respect to R_b/R_c .) Table 2, column 8 tabulates (R_c/a) values. With the estimation of σ and (R_c/a) , the combustion mode can then be identified.

It is seen that the combustion modes of many of the earlier experimenters range from GC to SC. Hence the group combustion model is more appropriate than the IPC model. With the estimation of G numbers from equation (27), Figs. 3 to 5 could be used to obtain an estimation of the cloud burning rate as well as to interpret the experimental data. We will demonstrate the use of the present results with the Kimber and Gray data.

The fuel, carrier and oxidant flows, particle size, and temperature ranges are indicated in Table 2 and schematic of

the experimental apparatus is illustrated in Fig. 7. They investigated the effect of particle size and gas temperature on the burning rate of char particles and found that the burning rate of 27 μm particles falls midway between the diffusion limited burning rates of reactions $\text{C} + 1/2 \text{O}_2 \rightarrow \text{CO}$ and $\text{C} + \text{O}_2 \rightarrow \text{CO}_2$. The reduction of the particle size to 17 μm resulted only in a slight increase of burning rate per unit area of particle (20 percent on the average) while the application of diffusion-controlled combustion theory shows that the burning rate per unit area should have increased by about 60 percent. It was speculated that the burning rate of smaller particles probably corresponded to the diffusion-controlled burning rate of the reaction $\text{C} + \text{O}_2 \rightarrow \text{CO}_2$. An alternate explanation using group theory is as follows:

From Table 2 it is seen that as particle size is reduced, (R_c/a) increases moving the burning mode closer to the sheath combustion mode (Fig. 6). Further the G number is increased leading to lower values for M/M_{IPC} (Fig. 5). The ratio M/M_{IPC} can also be interpreted as the ratio of average burning rate of each particle in the cloud to the burning rate of a particle burning in IPC mode. Hence column 11 provides an estimate of error associated with the GC and IPC models. It is seen from Table 2 that $M/M_{\text{IPC}} (= \dot{m}_{s,c}''/\dot{m}_s'') \sim 0.37$ for $a = 27 \mu\text{m}$ while for $a = 17 \mu\text{m}$, $M/M_{\text{IPC}} \sim 0.19$. However \dot{m}_s'' for the 17 μm particle is 1.6 times \dot{m}_s'' for the 27 μm particle. Thus the net effect of reduced particle size is that the burning rate per unit area of 17 μm is only 81 percent (column 12, Table 2) of the burning rate per unit area of 27 μm particles. It should not be construed that the cloud burning rate decreases with reduction in particle size. At the same mass loading, the reduction in particle size increases the total surface area of all the particles in the cloud thereby increasing the cloud burning rate. However the increase is less than the increase in total surface area and hence particle burning rate per unit area of each smaller particle in the cloud can be less than the rate for each larger sized particle in a cloud with the same mass loading. If carrier gas flow is used for the estimation of fuel volume fraction, then the burning rate per unit area of the 17 μm particle is only 67 percent of the rate per unit area of the larger sized particles! Thus the reductions can be attributed to group effects rather than to the change in heterogeneous reaction mechanisms.

Hamor et al. (1973) and Ayling and Smith (1972) also found that the burning rates per unit area of smaller sized particles are sometimes less than those for larger sized particles at the same temperature, 900–1300 K. The temperature range seems to indicate a kinetically limited combustion regime. Even though the present group combustion model qualitatively explains such behavior, it awaits confirmation from the results obtained with finite kinetics for char reactions.

The group effect can also cause an increase in burning rate with increase in gas temperature. The gas temperature normally increases ρD ($\rho D \propto T$), which results in the higher burning rate for diffusion controlled combustion. However even with constant ρD as assumed in the text, the burning rate can increase with temperature due to dilution effect. Consider the injection of a cold monosized stream of particles into a confined duct. As the duct is heated, the gas expands increasing the velocity of gas. If the relaxation time is small, the particles will travel with gas velocity. The leading particles far ahead of the injector (hotter end) have higher velocity while the trailing particles near the injector (colder end) have a lower velocity. Thus the interparticle separation distance increases which leads to dilution (or lower G number, Fig. 3) resulting in the increase of burning rate. The same result can be shown mathematically as follows:

$$(\text{No. of particles/volume}) \times (\text{mass of particle}) \times \text{area} \times \text{velocity} = \text{mass flow of particles}$$

For the same mass flow of particles, an increase of temperature results in an increase in velocity, and hence the number of particles per unit volume should decrease resulting in dilution. Thus the increase of burning rate with temperature is due to the change in G number rather than due to chemical or property effects.

Table 3 shows a comparison of the quantitative results for a spherical cloud of radius $R_c = 1 \text{ cm}$ (Annamalai, 1986b) and a cylindrical cloud of radius $R_c = 1 \text{ cm}$ and $R_b/R_c \sim 2$. It is apparent that one could still use the results of a spherical cloud for interpreting the experimental data obtained with a stream of particles.

5 Summary

1 A QS group combustion model has been carried out for a cylindrical cloud of char particles.

2 The results reveal the following:

(i) The G number definition remains the same for both the spherical and cylindrical cloud models.

(ii) For $R_b/R_c \sim 2.0$, the nondimensional results for the cloud burning rate, as a fraction of either sheath combustion rate or individual particle combustions rate of the cloud, do not differ significantly from the results for a spherical cloud.

(iii) The combustion modes could be identified from the data on fuel volume fraction in the cloud and particle radius.

3 The experimental conditions of earlier investigators reveal that the combustion mode varies from GC to SC modes. Thus all the experimental data that were previously interpreted with the IPC model must now be reinterpreted with the GC model.

4 The G number is proportional to the mass of the cloud and inversely proportional to square of particle size cloud radius. Thus for fixed total mass of the cloud, the decrease in particle size (increased pulverization) results in the increase of the G number and in the increase of total cloud burning rate. But the increase is less compared to the increase of total surface area of all particles.

5 Since the group combustion number is a strong function of cloud radius, the group effects can be minimized by reducing the cloud radius.

6 QS calculations predict long-range interaction effects since they involve steady-state profiles that involve a certain time to establish. Thus the QS results should be used with caution.

Acknowledgments

This work was supported with a grant from DOE/PETC, Grant No. DE-FG 22-85 PC 805283. However any opinions, findings, conclusions, or recommendations expressed herein are those of the authors and do not necessarily reflect the view of DOE.

References

- Annamalai, K., 1984a, "Peculiar Results for Burning on Char/Carbon Particles," Central States Section of the Combustion Institute, Minnesota, CSS/CI 84-12; *The Canadian Journal of Chemical Engineering*, 1987, in press.
- Annamalai, K., Madan, A., and Mortada, Y. I., 1984b, "Ignition of a Cloud of Droplets," presented at ASME Winter Annual Meeting, New Orleans, LA, Paper No. 84-WA/HT-18.
- Annamalai, K., 1985a, "The Evaporation and Combustion of a Cloud of Droplets," *Heat Transfer in Fire and Combustion Systems*, ASME, New York, HTD Vol. 45, pp. 27-35.
- Annamalai, K., and Ramalingam, S., 1985b, "Group Combustion of Char Particles," Report No. CF-85-03, Combustion and Fire Research Laboratory, Mechanical Engineering, Texas A&M University, College Station, TX.
- Annamalai, K., 1985c, "The Evaporation, Ignition, and Combustion of Cloud Droplets," Central States Section of the Combustion Institute, Spring Meeting, San Antonio, TX, WSS/CSS 3-6B-85.
- Annamalai, K., Ramalingam, S., and Marsh, K., 1986a, "Group Combustion of Coal Particles," Annual Report No. 1, DE-FG22-85 PC 80528, Pittsburgh Energy Technology Center—Department of Energy, Pittsburgh, PA.

Annamali, K., and Ramalingam, S., 1986b, "Group Combustion of Char/Carbon Particles," Central States Section of the Combustion Institute, Spring Meeting, NASA Lewis, Cleveland, OH, CSS/CI 86-5-B2; *Combustion and Flame*, 1987, in press.

Anthony, D. B., Howard, J. B., Hottel, H. C., and Meissner, H. P., 1975, "Rapid Devolatilization of Pulverized Coal," *Proc. 15th Symposium (International) on Combustion*, Pittsburgh, PA, pp. 1303-1317.

Arpaci, V. S., 1966, *Conduction Heat Transfer*, Addison-Wesley, Reading, MA, pp. 136-143.

Ayling, A. B., and Smith, I. W., 1972, "Measured Temperatures of Burning Pulverized Fuel Particles, and the Nature of Primary Reaction Products," *Combustion and Flame*, Vol. 18, pp. 173-184.

Bandyopadhyay, S., and Bhaduri, D., 1972, "Prediction of Ignition Temperature of a Single Coal Particles," *Combustion and Flame*, Vol. 21, pp. 411-415.

Bellan, J., and Cuffel, R., 1983, "A Theory of Nondilute Spray Evaporation Based Upon Multiple Drop Interactions," *Combustion and Flame*, Vol. 51, pp. 55-67.

Chiu, H. H., and Liu, T. M., 1977, "Group Combustion of Liquid Droplets," *Combustion Science Technology*, Vol. 17, pp. 127-142.

Chiu, H. H., Kim, H. Y., and Croke, E. J., 1982, "Internal Group Combustion of Liquid Droplets," *Proc. 19th Symposium (International) on Combustion*, Combustion Institute, Pittsburgh, PA, pp. 971-980.

Choi, S., and Kruger, C. H., 1985, "Modeling Coal Particle Behavior Under Simultaneous Devolatilization and Combustion," *Combustion and Flame*, Vol. 61, pp. 131-144.

Correa, S. M., and Sichel, M., 1982, "The Boundary Layer Structure of a Vaporizing Fuel Cloud," *Combustion Science and Technology*, Vol. 28, pp. 121-130.

Correa, S. M., and Sichel, M., 1982, "The Group Combustion of a Spherical Cloud of Monodisperse Fuel Droplets," *Proc. 19th Symposium (International) on Combustion*, Combustion Institute, Pittsburgh, PA, pp. 981-991.

Essenhigh, R. H., 1963, "The Influence of Coal Rank on the Burning Times of Single Captive Particles," *ASME Journal Engineering for Power*, Vol. 85, pp. 183-190.

Golovina, E. S., and Khaustovich, G. P., 1962, "The Interaction of Carbon With Carbon Dioxide and Oxygen at Temperatures up to 3000°K," *Proc. 8th Symposium (International) on Combustion*, Combustion Institute, Pittsburgh, PA, pp. 784-792.

Hamor, R. J., Smith, I. W., and Taylor, R. J., 1973, "Kinetics of Combustion of Pulverized Brown Coal Char Between 630 and 2200 K," *Combustion and Flame*, Vol. 21, pp. 153-162.

Horton, M. D., Goodson, F. P., and Smooth, L. D., 1977, "Characteristics of Flat, Laminar and Dust Flames," *Combustion and Flame*, Vol. 28, pp. 187-195.

Howard, J. B., and Essenhigh, R. H., 1967a, "Pyrolysis of Coal Particles in Pulverized Fuel Flames," *Industriall Engineering Chemical Process Design and Development*, Vol. 6, pp. 74-84.

Howard, J. B., and Essenhigh, R. H., 1967b, "Mechanisms of Solid Particles Combustion With Simultaneous Gas Phase Volatiles Combustion," *Proc. 11th Symposium (International) on Combustion*, Combustion Institute, Pittsburgh, PA, pp. 399-408.

Kimber, G. M., and Gray, M. D., 1971, "Reaction Rates of Char Coal and Coal Char Particles (<100 μm) With Oxidizing Gases in the Range 1800-2800°K," *Third Conference on Industrial Carbon and Graphite*, Imperial College, London, pp. 278-281.

Kuo, K., 1986, *Principles of Combustion*, Wiley, New York, p. 364.

Labowsky, M., and Rosner, D. E., 1978, "'Group' Combustion of Droplets in Fuel Clouds. I. Quasi-Steady Predictions," in: *Evaporation—Combustion of Fuels*, Advances in Chemistry Series, J. T. Chang, ed., American Chemical Society, Washington, DC, No. 166, pp. 63-79.

Labowsky, M., 1980, "Calculation of the Burning Rates of Interacting Fuel Droplets," *Combustion Science and Technology*, Vol. 22, pp. 217-226.

Leslie, J., Jost, M., and Kruger, 1982, "Oxidation Reactivity of Pulverized Montana Rosebed Coal During Combustion" *Western States Section of the Combustion Institute*, WSS/CI 82.2.

Matalon, M., 1980, "Complete Burning and Extinctions of a Carbon Particle in an Oxidizing Atmosphere," *Combustion Science and Technology*, Vol. 24, pp. 115-127.

Mulcahy, M. F. R., and Smith, I. V., 1969, "The Kinetics of Combustion of Pulverized Coke, Anthracite, and Coal Chars," *Rev. Pure and Applied Chemistry*, Vol. 19, pp. 81-108.

Mulcahy, M. F. R., and Smith, I. W., "The Kinetics of Combustion of Pulverized Coke, Anthracite, and Coal Chars," *GSIRO, CHEMICA '70*, Session 2, pp. 101-118.

Nettleton, M. A., and Stirling, R., 1971, "The Combustion of Clouds of Coal Particles in Shock Heated Oxygen," *Proc. of Roy. Soc., London, A*, Vol. 322, pp. 207-221.

Niksa, S., Mitchell, R. E., Hencken, K. R., and Tichenor, D. A., 1984, "Optically Determined Temperatures, Sizes, and Velocities of Individual Carbon Particles Under Typical Combustion Conditions," *Combustion and Flame*, Vol. 60, pp. 183-193.

Sichel, M., and Palaniswamy, S., 1984, "Sheath Combustion of Sprays," *Proc. 20th Symposium (International) on Combustion*, Combustion Institute, Pittsburgh, PA, pp. 1789-1798.

Suzuki, T., and Chiu, H. H., 1971, "Multi-droplet Combustion of Liquid Propellants," *Proceedings of the 9th International Symposium on Space Technology and Science*, AGNE Publishing Co., Tokyo, Japan, pp. 145-154.

APPENDIX

Outline of Method for Solving Governing Equations

Using equation (13a) with $i = \text{CO}_2$ and $j = \text{O}_2$, and the definition of B (equation (5e))

$$\phi = (1 + B)/(1 + B_\infty), \quad \xi > 1 \quad (\text{A1})$$

With $i = \text{CO}_2$ and $j = \text{O}_2$ in equations (15a, b, c), integrating, and then using equation (A1) to eliminate ϕ

$$M\alpha = -d[\ln(1 + B)]/d[\ln \xi], \quad \xi \geq 1 \quad (\text{A2})$$

Differentiating equation (14) with respect to ξ

$$d[(M\xi^3/G\kappa)d\alpha/d\xi]/d\xi = -d[\ln(1 + B)]/d\xi, \quad \xi \geq 1 \quad (\text{A3})$$

Using the result (A2) in (A3) in order to eliminate B and substituting the size distribution function given by equation (13k) in the result, one can obtain

$$d[\xi^{3-q}d\alpha/d\xi]/d\xi - (\alpha G_1/\xi) = 0, \quad \xi \geq 1 \quad (\text{A4})$$

The solution for α can be obtained in terms of modified Bessel functions (Arpaci, 1966).

Using the solution for α in equations (A2) and integrating, the B -number profile is obtained. Finally using equation (A1), the solution for ϕ is obtained (equation (19a)). Substituting the B profiles and the size distribution function given by equation (13k), in equation (13j), the nondimensional cloud burning rate is obtained. The results are given in equations (20a) and (20c).

A. Mirzamoqhadam

Fluid Mechanics and Thermophysics,
TRW,
Redondo Beach, CA 90278
Assoc. Mem. ASME

I. Catton

Professor,
Mechanical, Aerospace and
Nuclear Engineering Department,
University of California,
Los Angeles, CA 90024
Mem. ASME

A Physical Model of the Evaporating Meniscus

Transport phenomena associated with the heating of a stationary fluid near saturation by an inclined, partially submerged copper plate were studied analytically. Under steady-state evaporation, the meniscus profile was derived using an appropriate liquid film velocity and temperature distribution in an integral approach similar to boundary layer analysis. Derivation of the meniscus profile led to predicting heat transfer and performance as a function of angle of inclination of the plate.

Introduction

The various factors contributing to augmentation of heat and mass transfer to or from an enhanced tube are not yet well understood. Here, "enhanced tube" refers to a straight tube whose surface has been grooved circumferentially with a particular depth and pitch. In engineering processes, it is desirable to find ways of improving performance by increasing the effectiveness of the underlying phenomena. For example, the proper utilization of surface wettability yields a flow field that will augment heat transfer. The optimal design of a heat exchanger is the one that provides the highest heat transfer rate at the lowest overall cost. For horizontal evaporator tubes, over which the liquid to be evaporated is run, enhancement may be achieved by threading the outer surface of the tube like a screw. Menisci form on the upper portion of the grooves, and in these thin films the evaporation rate becomes much higher than for a tube with no grooves. The design problem then becomes that of choosing the optimal groove geometry.

Derjaguin et al. (1957), having realized the advantage of a meniscus in heat and mass transfer, introduced the concept of the "disjoining pressure" and its role in preventing liquid film dryout. At a particular film thickness, there would exist a film where the flow of evaporated liquid is hindered by an absorption layer or so-called "boundary phase," i.e., interfacial resistance to mass transfer. Beyond this film thickness, however, they suggested that thin film transport is capable of increasing the evaporation rate from capillaries severalfold. This explanation became the first of its kind to allow some insight into the physics of the evaporating thin film.

Following their experimental observations, Potash and Wayner (1972) combined Derjaguin's disjoining pressure concept to their findings on a vertical flat plate and described two distinct regions of the evaporating extended meniscus. Firstly, the intrinsic meniscus, where fluid flows as a result of the conventional equation of capillarity, i.e., surface curvature; secondly, the thin film portion above the intrinsic meniscus, which consists of evaporating and equilibrium portions depending upon the magnitude of the disjoining pressure. If the height of the plate above the pool surface, i.e., the unsubmerged portion, is sufficiently greater than the height of the intrinsic meniscus, a stable nonevaporating film of thickness δ_0 at its lower end is absorbed onto the unsubmerged portion of the plate above the evaporating thin film. The interfacial temperature of the equilibrium film is assumed equal to the local plate temperature. However, the film does not evaporate due to the reduced vapor pressure of the film caused by the disjoining pressure. A short distance below this region

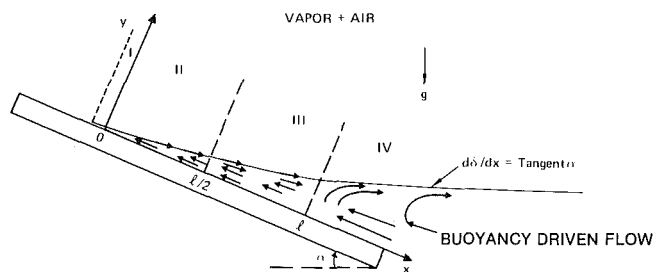


Fig. 1 Location of various regions of interest: (I) nonevaporating region (monolayer); (II) evaporating thin film (microlayer); (III) transition layer; (IV) natural convection region. Note: varying film thickness δ for II, III, and IV: $0 \leq x \leq l$.

where film thickness increases, the disjoining pressure sufficiently decreases to raise the vapor pressure and evaporation occurs. Potash and Wayner (1972) described the fluid mechanics of the evaporating meniscus, assuming that at any location, it is equal to that in fully developed flow in the wedge formed by the intersection of the coordinate along the wall with the tangent to the curve at that location. In addition, the heat transfer was described by balancing conduction in a direction normal to the plate surface with the interfacial resistance to evaporation from the film. Their analysis showed that the velocity, pressure gradient, and heat flux reach a maximum in the evaporating thin film portion of the extended meniscus.

Later, Miller (1973) studied the stability of liquid-vapor interfaces moving as a result of phase transformation or mass transfer. He arrived at a relation (for small wavenumber) showing the stabilizing effect of gradients in the interfacial surface tension that arise as a result of temperature or concentration gradients along the free surface. His analysis showed that instability during vaporization of a liquid film is likely to occur only when pure liquids of relatively low volatility are vaporized under vacuum, or that the liquid has a very low surface tension.

In 1979, Renk analyzed an evaporating ethanol meniscus (Renk and Wayner, 1979). Surface tension was assumed constant and a flow model was proposed that forced the flow rate to be zero at the interline (junction of evaporating and nonevaporating portions). Renk noted that a more extensive model is needed that would include both capillarity and the disjoining forces such that a smooth transition to regions of dominance would occur. He did verify that fluid velocity, heat flux, and local temperature differences between liquid-vapor interface and substrate surface reached a maximum very near the interline but dropped precipitously to zero at the interline.

The proposed physical model of the evaporating meniscus is a result of experimental investigations of the transport

Contributed by the Heat Transfer Division and presented at the ASME Winter Annual Meeting, Miami Beach, Florida, November 1985. Manuscript received by the Heat Transfer Division May 8, 1986.

phenomena associated with the heating of a stationary saturated liquid approximately one degree above saturation. The inclined partially submerged copper plate was uniformly heated from behind, and the temperature field in the liquid was measured using laser holographic interferometry (Mirzamoghadam and Catton, 1988).

With the aid of experimental data relevant to the variation of wall temperature (Mirzamoghadam and Catton, 1988), a functional dependence for T_w in the x direction is chosen such that the interline temperature and the temperature a distance l away are specified. This distance refers to the meniscus length. Use of a first-order approximation to the integrated Clausius-Clapeyron equation defines a region where the interfacial temperature is superheated, and this superheat is related to the disjoining pressure (i.e., solid-liquid attraction forces) of the meniscus. In this region, called the monolayer, the disjoining pressure gradient is balanced against gravity, and the specified interline wall superheat fixes its thickness. Outside the monolayer, i.e., $\delta > \delta_0$, the momentum and energy integral equations are coupled by the interfacial temperature gradient. Outside the microlayer (i.e., $\delta \approx 1$ mm), the interfacial temperature is equal to saturation temperature, and there exists a transition layer to the natural convection controlled region (Fig. 1). The meniscus profile and theoretical convective heat transfer coefficient obtained as results are then discussed as functions of plate angle of inclination.

Analysis

In support of the experimental observation, an analysis of the evaporating meniscus of a slightly superheated liquid is performed with the following assumptions:

- (a) pure liquid; smooth surface;
- (b) steady-state, two-dimensional laminar flow;
- (c) incompressible constant density throughout the meniscus region ($\delta < 1$ mm); outside the meniscus, the conventional Boussinesq approximation for buoyancy driven flow is assumed;
- (d) no slip at the wall;
- (e) the interfacial shear stress at liquid free surface is balanced by surface tension within the meniscus;
- (f) fluid flows as a result of gradients in disjoining pressure,

surface curvature, surface thickness, and surface tension, as well as gravitational effects;

- (g) viscous dissipation is neglected;
- (h) no blowing at the wall;
- (i) the advective and convective terms are neglected when solving the integral equations;
- (j) the liquid saturation temperature is equal to the ambient temperature;
- (k) the upper surface of the meniscus is open to the environment and heat loss is occurring in the form of surface evaporation into a medium at lower temperature ($T_\infty = T_{\text{sat}}$). The environment serves only as a heat sink and exerts no mechanical forces on the liquid other than a tangential shear stress; and
- (l) due to the small film thickness and temperature difference, bulk values for the physical properties (i.e., density) are used except for the variation of surface tension with temperature.

In order to establish the interline thickness, the concept of a disjoining pressure, introduced by Derjaguin et al. (1957), is used. By definition, the location at which a reduction in liquid saturation pressure, caused by intermolecular solid-liquid forces, chokes evaporation, the liquid-vapor interfacial temperature becomes equal to the wall temperature. Expanding the Clausius-Clapeyron equation

$$\left(\frac{dP}{dT}\right)_{\text{sat}} = \frac{h_{fg}}{T_{\text{sat}} \left(\frac{1}{\rho_v} - \frac{1}{\rho_l}\right)} \quad (1)$$

gives

$$\frac{T_{\text{sat}}(dP_v)}{\rho_v} = \frac{T_{\text{sat}}(dP_l)}{\rho_l} + h_{fg}dT_{\text{sat}} \quad (2)$$

where dP_v is the change in the saturated pressure in the vapor phase and dP_l is the change in the liquid saturation pressure. It is assumed that the pressure in the vapor phase P_v is constant (first-order approximation). Integrating equation (2) from temperature T_{sat} to T_i , with $\int_1^2 dP_l = -P_d$, one obtains the desired relation for the interfacial temperature in the non-evaporating meniscus region

Nomenclature

A = Hamaker constant in disjoining pressure term	t = plate thickness, m	
b = upflow velocity, m/s	T = temperature, °C	
c_p = specific heat, J/kg-°C	u = velocity in X direction, m/s	d = disjoining
g = gravitational acceleration, m/s ²	U_δ = axial interfacial velocity, m/s	f = liquid
h = heat transfer coefficient, W/m ² -°C	v = velocity in Y direction, m/s	f_g = vapor-liquid
k = heat conductivity, W/m-°C	X = axial coordinate along plate, m	i = interfacial
K = ratio of upflow velocity to axial interfacial velocity	Y = normal to plate coordinate, m	l = liquid
l = prescribed meniscus length, m	$Z = [1 + (d\delta/dx)^2]^{3/2}$	m = meniscus
m = molecular weight, kg/kg-mole	α = plate angle of inclination, deg;	0 = prescribed
Nu = Nusselt number = $h\delta/k_l$	diffusivity, m ² /s	s = solid
P = pressure, N/m ²	Γ = evaporation rate, m/s	sat = saturation state
Pr = Prandtl number = ν/α_τ	δ = film thickness, m	T = thermal
P_{vl} = pressure difference between vapor and liquid phases	Δ = change of	v = vapor
q = heat flux, W/m ²	θ = meniscus contact angle, deg = $\tan^{-1}(d\delta/dx)$	w = wall
R = radius of curvature, m	μ = dynamic viscosity, kg/m-s	x = function of X
	ν = kinematic viscosity, m ² /s	y = function of Y
	ρ = density, kg/m ³	δ = with respect to delta
	σ = surface tension, N/m	∞ = ambient condition

Subscripts

c = contact angle; critical property

Superscripts

* = nondimensional
- = steady-state value

$$T_i = T_{\text{sat}} \left[1 + \frac{-P_d}{\rho_l h_{fg}} \right] \quad (3)$$

The negative sign associated with the disjoining pressure P_d comes from how Derjaguin (1957) has defined it: for nonpolar liquids, $P_d = -A/\delta^3$; for polar liquids, there is a logarithmic dependence, $P_d = -A/\delta^3 \ln(\delta/\delta_0)$, where δ_0 is a suitable reference length adjusted by the experimental data and A is the Hamaker constant which depends on solid-liquid properties. Gregory (1969) has developed an expression for calculating the value of A that depends mainly upon the square of the limiting refractive index of the liquid. Here an average value of $A = 1.0 \times 10^{-20}$ J is used. At the interline, $\delta = \delta_0$,

$$T_i = T_{w,0} \quad (4)$$

Substituting equation (4) and the expression for P_d (nonpolar) into equation (3) and solving for δ_0 yields

$$\delta_0 = \left(\frac{A}{\rho_l h_{fg} \left(\frac{T_{w,0} - T_{\text{sat}}}{T_{\text{sat}}} \right)} \right)^{1/3} \quad (5)$$

Further, the contact angle at the interline can be found by balancing the disjoining pressure gradient with the body force (gravity) assuming zero mass flow at the interline

$$-\frac{dP_d}{dx} + \rho_l g \sin \alpha = 0 \quad (6)$$

expanding

$$\frac{d\delta}{dx} \Big|_{\delta_0} \left(\frac{3A}{\delta_0^4} \right) = \rho_l g \sin \alpha \quad (7)$$

and solving for $d\delta/dx$ yields

$$\frac{d\delta}{dx} \Big|_{\delta_0} = \frac{\delta_0^4 \rho_l g \sin \alpha}{3A} \quad (8)$$

The velocity and temperature profiles in the meniscus layer are assumed one dimensional in the y direction. The x -direction momentum equation for this region is written

$$\rho_l \left(u \frac{\partial u}{\partial x} + v \frac{\partial u}{\partial y} \right) = \left(-\frac{\partial P_l}{\partial x} \right)_m + \mu \frac{d^2 u}{dy^2} + \rho_l g \sin \alpha \quad (9)$$

In conjunction with continuity

$$\frac{\partial u}{\partial x} + \frac{\partial v}{\partial y} = 0 \quad (10)$$

the integral momentum equation is derived

$$\frac{d}{dx} \int_0^\delta (u^2 - uU_\delta) dy + \frac{dU_\delta}{dx} \int_0^\delta u dy = \frac{1}{\rho_l} \left[\mu \frac{du}{dy} \Big|_0 - \mu \frac{du}{dy} \Big|_\delta \right] + g\delta \sin \alpha + \frac{1}{\rho_l} \int_0^\delta \left(-\frac{\partial p_l}{\partial x} \right)_m dy \quad (11)$$

where the meniscus pressure gradient is a sum of the curvature/surface tension gradient, the contribution due to hydrostatic head, and the disjoining pressure effect

$$\frac{\partial P}{\partial x} \Big|_m = \frac{d}{dx} \left(\frac{\sigma_i}{R_i} \right) - \rho_l g \frac{d\delta}{dx} \cos \alpha - \frac{dP_d}{dx}$$

where $R_i = (1 + (d\delta/dx)^2)^{3/2} / d^2\delta/dx^2$ and U_δ is the liquid velocity at the interface. In order to solve the integral momentum equation, the velocity profile is chosen, using a Pohlhausen-type approach. First, the velocity boundary conditions are

$$\begin{aligned} y = 0, & \quad u = 0 \\ y = \delta, & \quad u = U_\delta \end{aligned} \quad (13)$$

and the shear stress at the interface is

$$\mu \frac{du}{dy} \Big|_\delta = \frac{d\sigma_i}{dx} \quad (14)$$

The imposed condition on the interface represents fluid motion induced by temperature gradients on the superheated liquid surface. The sign of $d\sigma_i/dx$ as well as the thickness of the meniscus will determine the direction U_δ . A final boundary condition is the compatibility relation at the wall

$$\frac{d^2 u}{dy^2} \Big|_0 = \frac{-\rho_l g \sin \alpha + (\partial P_l / \partial x)_m}{\mu_l} \quad (15)$$

The velocity profile is represented by a cubic to allow for flow reversal within the meniscus region (see Fig. 1). The profile with equation (13) satisfied is

$$u = by^*(1-y^*) + U_\delta y^{*3} \quad (16)$$

where $y^* = y/\delta$, and b and U_δ are to be determined. The first term represents flow into the meniscus (positive flow) whereas the second is flow away from the interline. Boundary conditions (14) and (15) are used to find b and U_δ

$$\begin{aligned} b = \frac{\delta^2}{2\mu_l} \left[\frac{1}{Z} \left[\sigma_i \frac{d^3 \delta}{dx^3} + \frac{d^2 \delta}{dx^2} \cdot \frac{d\sigma_i}{dx} \right] \right. \\ \left. - \rho_l g \cos \alpha \left[\frac{d\delta}{dx} - \tan \alpha \right] - \frac{3A}{\delta^4} \frac{d\delta}{dx} \right] \end{aligned} \quad (17)$$

and

$$U_\delta = \frac{b}{3} + \frac{\delta}{3\mu_l} \frac{d\sigma_i}{dx} \quad (18)$$

From equation (16), the average velocity is calculated and nondimensionalized

$$\bar{u}^* = \frac{\bar{u}}{b} = \frac{1}{6} - \frac{1}{4K} \quad (19)$$

where

$$K = \frac{b}{\left(\frac{b}{3} + \frac{\sigma}{3\mu_l} \frac{d\sigma_i}{dx} \right)} \quad (20)$$

In the limit, as $d\sigma/dx \rightarrow 0$, $K \rightarrow +3$. Since evaporation is occurring along the surface of the meniscus, the evaporation velocity normal to the liquid surface is

$$\Gamma_{l,\delta} = V_\delta \cos \theta + U_\delta \sin \theta \quad (21)$$

where

$$V_\delta = -\frac{d}{dx} (\bar{u}\delta) \quad (22)$$

and

$$\theta = \tan^{-1}(d\delta/dx) \quad (23)$$

Temperature is subject to the following boundary conditions:

$$\begin{aligned} y = 0, & \quad T = T_w(x) \\ y = \delta, & \quad T = T_i(x) \end{aligned} \quad (24)$$

Experimental observations, in addition to an order-of-magnitude analysis, show that the contribution to axial heat transfer by the interfacial temperature gradient is negligible when compared to conduction across the meniscus film. Therefore, the convective terms in the integral energy equation are neglected yielding

$$\frac{d}{dx} \int_0^\delta \rho_l C_p \mu (T - T_i) dy + \rho_l C_p \frac{dT_i}{dx} \int_0^\delta u dy = k \frac{dT}{dy} \Big|_0 \quad (25)$$

A linear temperature profile satisfies equation (24)

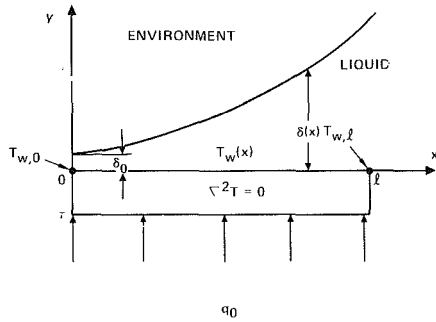


Fig. 2 Solid conduction model

$$\frac{T - T_i}{T_w - T_i} = 1 - \frac{y}{\delta} \quad (26)$$

and heat transfer to the surface is balanced by evaporation normal to the liquid surface

$$-k_l \frac{dT}{dy} \Big|_{\delta} = \rho \Gamma_{\ell, \delta} (h_{fg}) \quad (27)$$

Using equations (25)-(27), a relation for the interfacial temperature is obtained

$$T_i = T_w - \left(\frac{\rho_l h_{fg}}{h_x} \right) \Gamma_{\ell, \delta} \quad (28)$$

where

$$h_x = \frac{k}{\delta(x)}$$

Equation (28) relates the solid conductance to the hydrodynamics of the liquid and evaporation on the surface. The location where evaporation is a maximum will, at the same time, maximize the temperature difference between wall the liquid-vapor interface. Transition to the nonevaporating region occurs when the evaporation rate is zero. Here, although the resistance to heat transfer is low, the driving force goes to zero, i.e., $T_i = T_{w,0}$, with equation (3) defining $T_i(x)$. In the macroregion, $\delta > 1 \mu\text{m}$, the evaporation rate is low enough to allow T_i to approach T_{∞} and, $dT_i/dx \rightarrow 0$.

The model for solid conduction is shown in Fig. (2). By choosing the interline wall temperature and the temperature a distance ℓ away to be the same, and imposing a constant heat flux on the back side of the cooper plate of thickness τ , the wall surface temperature variation, whose minimum is located at $\ell/2$, is obtained

$$T_w(x) = P \left(\frac{x^2}{2} - \frac{\ell x}{2} \right) + T_{w,0} \quad (29)$$

where

$$P = \frac{q_0}{k_{\text{solid}} \tau}$$

With the aid of equations (19), (22), (28), and (29), an approximate expression for dT_i/dx in terms of conditions at the wall and the meniscus profile is derived

$$\begin{aligned} \frac{dT_i}{dx} = & \left(\frac{dT_w}{dx} - \left(\frac{1}{6} - \frac{1}{4K} \right) \frac{\rho h_{fg} \delta^2}{6\mu k} \left[3\rho g \sin \alpha \left(\delta \frac{d^2 \delta}{dx^2} \right. \right. \right. \\ & \left. \left. \left. + 3 \left(\frac{d\delta}{dx} \right)^2 \right) - \rho g \cos \alpha \cdot \frac{d\delta}{dx} \left(9 \left(\frac{d\delta}{dx} \right)^2 + 10\delta \frac{d^2 \delta}{dx^2} \right) \right] \right) \\ & + \left(1 + \left(\frac{1}{6} - \frac{1}{4K} \right) \frac{\rho h_{fg} \delta}{6\mu k} \right) \frac{d\sigma_i}{dT_i} \left[8 \left(\frac{d\delta}{dx} \right)^2 + 4\delta \frac{d^2 \delta}{dx^2} \right] \end{aligned} \quad (30)$$

In dimensionless form, the integral momentum equation

(neglecting the advective term) and equation (30) reduce to the following nonlinear ordinary differential equations:

$$\frac{d^3 \delta^*}{dx^{*3}} + \frac{d^2 \delta^*}{dx^{*2}} \left[\frac{2}{\delta^*} \frac{d\delta^*}{dx^*} + A_2 \frac{\left(\frac{dT_i^*}{dx^*} \right)}{\sigma^*} \right]$$

curvature surface gradient surface tension gradient

$$- \frac{z}{\sigma^*} \left[\frac{2A_2}{\delta^*} \left(\frac{dT_i^*}{dx^*} \right) + \right.$$

interfacial shear stress

$$\left. A_3 \left(\frac{d\delta^*}{dx^*} - \tan \alpha \right) + \frac{B}{\delta^{*4}} \left(1 + \frac{4}{3} \frac{d\delta^*}{dx^*} \right) \right] = 0 \quad (31)$$

gravitational effects disjoining pressure

$$\frac{dT_i^*}{dx^*} = \left\{ A_1 (2x^* - \ell/\delta_0) \right.$$

interfacial temperature gradient

$$\left. + \left(\frac{1}{6} - \frac{1}{4K} \right) \frac{A_4 A_3}{A_2} \left[9 \left(\frac{d\delta^*}{dx^*} \right)^2 \left(\frac{d\delta^*}{dx^*} \right. \right. \right.$$

wall temperature gradient evaporation

$$\left. - \tan \alpha \right) + \delta^* \frac{d^2 \delta^*}{dx^{*2}} \left(10 \frac{d\delta^*}{dx^*} - 3 \tan \alpha \right) \right] \left\{ 1 \right.$$

$$\left. + \left(\frac{1}{6} - \frac{1}{4K} \right) A_4 \delta^* \left[8 \left(\frac{d\delta^*}{dx^*} \right)^2 + 4\delta^* \frac{d^2 \delta^*}{dx^{*2}} \right] \right\} \quad (32)$$

hydrodynamics

where

$$A_1 = \frac{q_0 \delta_0^2}{2k_{\text{solid}} \tau T_{\text{sat}}}, \quad A_2 = \frac{T_{\text{sat}}}{\sigma_0} \left(\frac{d\sigma_i}{dT_i} \right)$$

$$A_3 = \rho g \delta_0^2 \cos \alpha / \sigma_0, \quad A_4 = \left(\frac{\rho h_{fg} \delta_0}{6\mu k} \right) \cdot \frac{d\sigma_i}{dT_i},$$

$$B = \frac{A}{\sigma_0 \delta_0^2}$$

and δ and x are scaled with respect to the interline thickness δ_0 .

The variation of surface tension with temperature is obtained by linearizing the relation given by Katayama-Guggenheim (1960) to obtain

$$\sigma_i^* = \frac{\sigma_i}{\sigma_{\text{sat}}} - \left[1 - \frac{1.22}{T_c} (T_i - T_{\text{sat}}) \right] \quad (33)$$

Three prescribed boundary conditions for the third-order nonlinear differential equation are

$$x=0, \quad \delta = \delta_0$$

$$\frac{d\delta}{dx} = \frac{d\delta}{dx} \Big|_{\delta_0} \quad (34)$$

$$\frac{d^2 \delta}{dx^2} \Big|_{\delta_0} = 0 \quad (\text{no curvature at the interline})$$

Equations (31) and (32) were solved simultaneously using a fourth-order Runge-Kutta method. The starting point was the interline where the value of dT_i^*/dx^* was computed and used in equation (31) to compute the next δ and its derivatives using a variable step size. Marching continued for a prescribed

Table 1 Interline conditions for a stable meniscus profile solution

$(T_{w,0} - T_s) \text{ } ^\circ\text{C}$	(nm)	α $^\circ$
.0095	4.5	30
.11	2.0	45
1.0	1.0	63

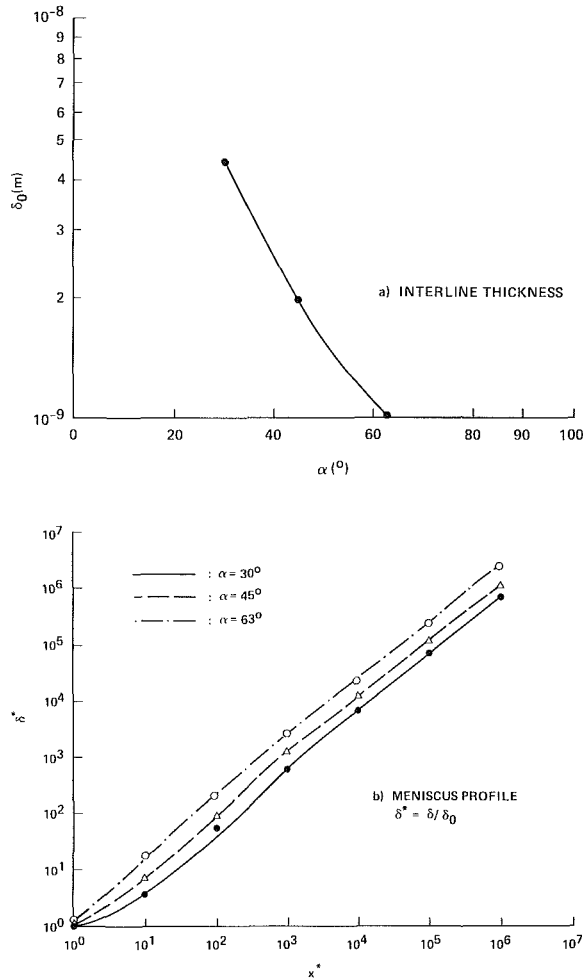


Fig. 3 The effect of inclination angle of plate on (a) interline thickness, and (b) meniscus profile

distance ℓ so that as $d\delta/dx \rightarrow \tan \alpha$, the meniscus connects to the pool surface and $T_{w,x} = T_{w,\ell}$.

Results and Discussion

The model has produced a meniscus profile whose shape is dependent upon the specified interline superheat and independent of dT_w/dx . For certain values of the input heat flux (interline superheat conditions), however, an unstable solution results when solving for the meniscus profile. To resolve this problem, two approaches were considered. The first was to allow a one degree wall superheat at the interline of a plate inclined at 30 deg from the horizontal. The second approach was to search for the interline superheat whose plate tilt gave a stable solution, i.e., $\tan \alpha = d\delta/dx|_{x=1}$. The results indicated that for a given fluid, the lower plate tilt is associated with a decrease in interline superheat, i.e., interline thickness in-

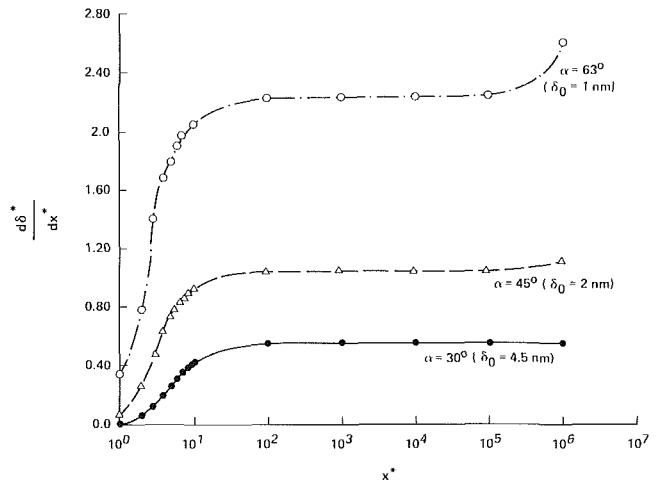


Fig. 4 Convergence of local gradient of film thickness for different plate angles

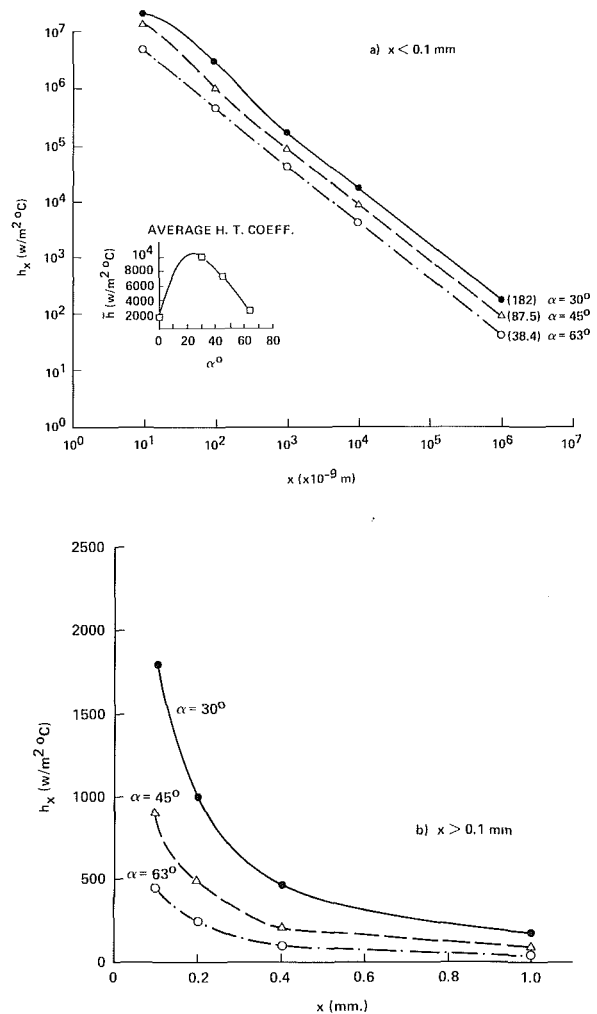


Fig. 5 Local heat transfer coefficient at different plate angles of inclination (fluid: freon)

creases, and that an optimum angle for a stable meniscus profile solution exists given the interline superheat. Table 1 shows the corresponding interline conditions for these plate angles of inclination.

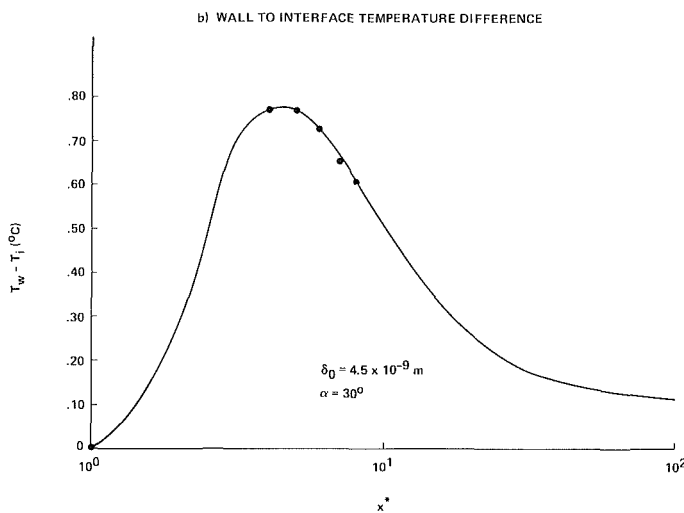
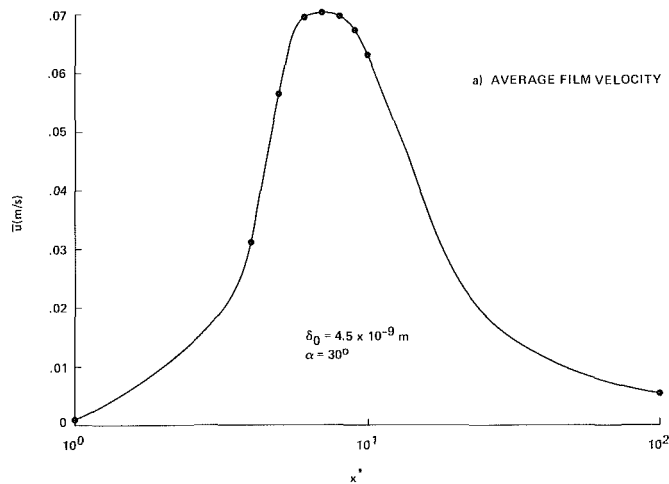


Fig. 6 Average film velocity and wall-to-interface temperature difference along the film

Figure 3(a) shows the behavior of the interline film thickness as a function of plate angle of inclination. With the aid of Fig. 4 it can be seen that for $\alpha = 30$ deg, the interline superheat satisfying the “infinity” boundary condition is 0.01°C . If the superheat were 1°C , the solution convergence would require a plate tilt angle of 63 deg. The corresponding meniscus profiles are shown in Fig. 3(b). The effect of plate tilt on meniscus performance, then, becomes evident. With the meniscus shape known, the variation of local heat transfer coefficient with plate tilt is calculated assuming a Nusselt number of unity. The results are shown in Fig. 5(a). This graph reveals the logarithmic decrease of heat transfer up to a distance 1 mm from the interline. The location of the maximum local heat transfer (i.e., evaporation rate), however, lies within $0.1 \mu\text{m}$ of the interline. Referring to Fig. 6, one can see that this corresponds to the location where the average velocity across the film as well as the local temperature difference between wall and free surface reach their maximum values. In addition, it is observed that as the plate angle decreases, curvature of the local heat transfer coefficient begins to increase for $x < 1 \mu\text{m}$ and shows asymptotic behavior close to the interline. This directs one to note that there is a critical plate angle of inclination below which the overall average heat transfer coefficient exhibits a decreasing trend.

The graph included as a part of Fig. 5(a) was plotted using an experimental value of 1500 W/m^2 at a temperature dif-

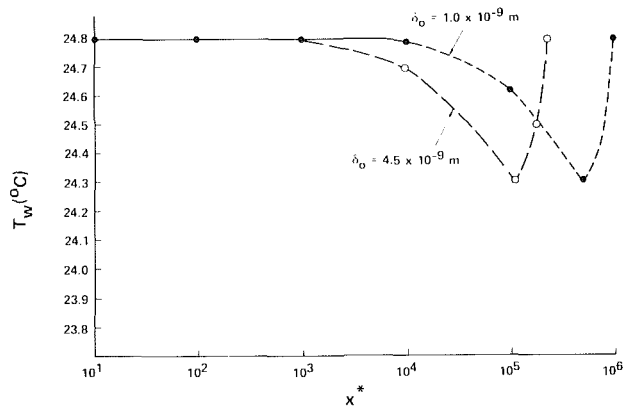


Fig. 7 Wall temperature distribution for a plate angle of 30 deg and different interline film thicknesses

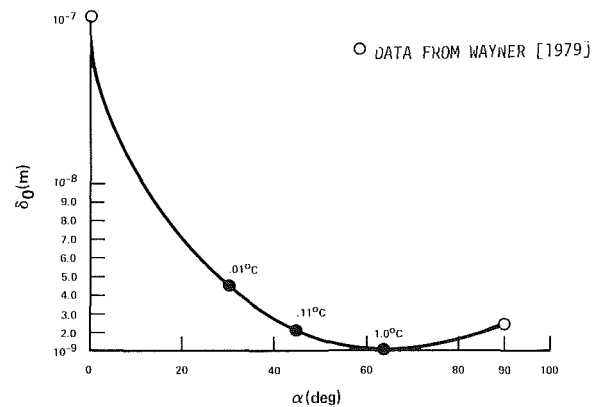


Fig. 8 Effect of plate angle on interline thickness; different interline film thicknesses

ference of 1°C for $\alpha = 0$. The optimum plate tilt lies between 20 and 30 deg and is approximately seven times more efficient in overall heat transfer. At a distance of 1 mm downstream, for plate tilts of 30 , 45 , and 63 deg, the heat transfer coefficient is, respectively, 182 , 87.5 , and $38.4 \text{ W/m}^2\text{C}$. As shown in Fig. 5(b), an increase in curvature and magnitude of the local heat transfer coefficient with decreasing plate tilt verifies enhancement in heat transfer. At $x = 0.1$ mm, the values of the local heat transfer coefficient are 1800 , 900 , and $450 \text{ W/m}^2\text{C}$ for plate angles of 30 , 45 , and 63 deg, respectively. These predictions are in reasonable agreement with the experimental measurements of local heat transfer coefficient reported by the authors (Mirzamoghadam and Catton, 1988).

The interline wall superheat needed to obtain a converged solution from the steady-state integral model was found to be in agreement with experimental observations of the effect wall superheat has on meniscus shape. The experimental data show that a heated meniscus extends itself in order to approach complete wetness, i.e., $d\delta/dx \rightarrow 0$. This phenomenon stems from the evaporation criterion established at the interline along with the nonevaporating region of the meniscus being controlled by solid/liquid cohesive forces, which keep the surface wet. Recently, Mirzamoghadam and Catton (1986) predicted the frequency of oscillation measured experimentally by performing a linear stability analysis. Efficient heat transfer from solid to liquid (i.e., a superheated meniscus and a high thermal conductivity solid) allows the wall temperature to remain nearly constant in the x direction. However, a transition layer connecting the natural convection region to the conduction controlled region disrupts the constant wall temperature in a manner depicted in Fig. 7. The wall

temperature reaches a minimum at an approximate distance of 0.5 mm from the interline.

The reported calculations of $\delta(x)$ agree with values of the interline thickness of 23.9A for a 90 deg tilted plate and approximately 100 nm for a horizontal plate reported by Potash and Wayner (1972). Figure 8 shows these limiting values as well as those from Table 1. Also, the behavior of the average velocity and the temperature difference between the wall and the interface near the interline are in agreement with past studies.

Concluding Remarks

An integral model was developed and used to calculate the heated meniscus profile. The model was similar to models used for boundary layer analysis. The resulting film thickness as a function of location and plate angle was used to predict heat transfer. The model was also used to identify a change in the physical shape of the meniscus when superheated. It was found that there is an optimum angle for enhancing heat transfer from the plate to the film vapor interface. The enhancement in heat transfer coefficient was found to be ap-

proximately a factor of seven relative to a horizontal plate when the plate angle was between 20 and 30 deg.

References

- Darjaguin, B. V., and Zorin, Z. M., 1957, "Optical Study of the Absorption and Surface Condensation of Vapors in the Vicinity of Saturation on a Smooth Surface," *Proc. 2nd. International Congress on Surface Activity* (London), Vol. 2, pp. 145-152.
- Gregory, J., 1969, "The Calculation of Hamaker Constants," *Advances in Colloid and Interface Science*, Vol. 2, pp. 396-417.
- Miller, C. A., 1973, "Stability of Moving Surfaces in Fluid Systems With Heat and Mass Transport," *AIChE Journal*, Vol. 19, pp. 909-915.
- Mirzamoghdam, A. V., and Catton, I., 1986, "Analysis on the Evaporating Meniscus Oscillation," *Proceedings of the Eighth International Heat Transfer Conference*, Hemisphere Publishing Company.
- Mirzamoghdam, A. V., and Catton, I., 1988, "Holographic Interferometry Investigation of Enhanced Tube Meniscus Behavior," *ASME JOURNAL OF HEAT TRANSFER*, Vol. 110, this issue.
- Ono, S., and Kondo, S., 1960, *Handbook of Physics*, Vol. 10, S. Flugge, ed., Springer-Verlag, Berlin, pp. 174-175.
- Potash, M., Jr., and Wayner, P. C., Jr., 1972, "Evaporation From a Two-Dimensional Extended Meniscus," *International Journal of Heat and Mass Transfer*, Vol. 15, pp. 1851-1863.
- Renk, F. J., and Wayner, P. C., Jr., 1979, "An Evaporating Ethanol Meniscus, Part II: Analytical Studies," *ASME JOURNAL OF HEAT TRANSFER*, Vol. 101, pp. 59-62.

Holographic Interferometry Investigation of Enhanced Tube Meniscus Behavior

A. V. Mirzamoghadam

I. Catton

Mechanical, Aerospace and Nuclear
Engineering Department,
University of California, Los Angeles,
Los Angeles, CA 90024

Transport phenomena associated with the heating of stationary saturated fluid approximately one degree above saturation by an inclined partially submerged copper plate were studied using laser holographic interferometry. Interpretation of the hologram yielded the general characteristics of the meniscus region where the combined influence of natural convection, conduction, and surface tension gradients are important. Water and tri-chloro-fluoro-methane (Freon-11) were used as the working fluids.

Introduction

The various factors contributing to the augmentation of heat and mass transfer to or from an enhanced tube are not well understood. Here, "enhanced tube" refers to a straight tube whose surface has been grooved circumferentially with a particular depth and pitch to improve condensation or evaporation. In engineering processes, it is desirable to find ways of improving performance by increasing the effectiveness of the underlying phenomena. One such phenomenon is the proper utilization of surface wettability such that the resulting flow field would augment heat transfer. The optimal design of a heat exchanger is one that provides the highest heat transfer rate at the lowest capital cost. For horizontal evaporator tubes, over which the liquid to be evaporated is run, enhancement may be achieved by threading the outer surface of the tube like a screw. Menisci form on the upper portion of the grooves, and in these thin films the evaporation rate becomes much higher than that for an ordinary Nusselt-type tube. The design problem then becomes one of choosing the optimal groove geometry.

Miller (1981) studied the effects of groove geometry by comparing heat flux and wall superheat for several groove shapes. He found that groove geometry does affect the heat transfer. All geometries considered (i.e., V-groove, circular, trapezoidal) maintained a parabolic curve of heat transfer coefficient versus wall superheat in close proximity to one another. Miller notes that at low superheat conduction through the thin film is dominant and high values are obtained. As the superheat is increased conduction becomes less efficient due to the onset of nucleate boiling. Once transition occurs (minimum heat transfer coefficient) the curve begins to rise due to bubble-cavity excitation. Interest is, however, in the small temperature difference regime because of thermodynamic efficiency considerations. Since most of the heat transfer and evaporation occur in the thin film known as the meniscus, it is important that the physical processes causing the augmentation of heat transfer be understood to design enhanced tubes better. This work is a study of a half-groove in which the temperature profile and meniscus behavior shall be investigated.

There have been a number of studies of the evaporating meniscus. However limited experimental data are available for this region because of the associated very small dimensions and the resulting very large gradients. Wayner (1979) divided the extended meniscus into three zones: (1) the immediate vicinity of the interline (the thin film region) where the

thickness of the liquid can vary from a monolayer to approximately $0.05 \mu\text{m}$ and fluid flow results from the pressure gradient produced in the liquid by the varying force of attraction between the liquid and solid (disjoining pressure); (2) the inner intrinsic region where the thickness range is approximately $(0.05\text{-}10) \mu\text{m}$ and fluid flow resulting from very large pressure gradients due to curvature is possible; (3) the outer intrinsic meniscus region where the thickness is greater than $10 \mu\text{m}$ and fluid flow resulting from small pressure gradients due to curvature is possible. Renk (1977) formed a meniscus between a horizontal glass substrate and teflon insert, then heated the glass from above. The limitations of his results are their applicability to an enhanced tube where a high thermal conductivity material inclined at an angle is heated from below. Nevertheless, he developed a model to match his experimental observations which forced the evaporative heat flux distribution to be zero at the interline, go through a maximum, and become zero again at a large value of meniscus thickness. The local temperature difference between the liquid/vapor interface and substrate surface also followed the aforementioned trend. The grouping $(\nu_l k_l / \sigma_l h_{fg})$ was identified as the parameter that measures the distortion of the meniscus profile due to evaporation for a given wall superheat. Tung (1982) improved the understanding of meniscus evaporation by slightly inclining the solid substrate and including the effect of surface tension variation with temperature and concentration. Although the hydrodynamics of the evaporating meniscus was better defined, the heat flux and temperature distribution in the region remained unclear. Some of the important observations noted by Tung were that wavy isotherms, nonuniform liquid/vapor temperatures, and oscillation of the contact line need be considered. He also compared meniscus curvature of a pure fluid with an impure fluid and found that the latter meniscus had stretched (curvature increase). With the aid of the experimental apparatus described below, meniscus evaporation more appropriate for application to the enhanced tube will be studied.

Experimental Apparatus

A test section was designed to study meniscus evaporation important to the evaporating enhanced tube. It consists of a frame, 16 cm long \times 10 cm high \times 4 cm wide, constructed of 2.5-cm thick aluminum; two glass plate windows (0.95 cm thick) each separated from the frame by a 0.31-cm-dia rubber O-ring; and a copper plate (11.2 \times 3.6 \times 0.5 cm) oriented at an angle from the horizontal. The plate has a sandwich construction. On top is the copper plate and the meniscus forms against it. A piece of nichrome conductor cut roughly in the

Contributed by the Heat Transfer Division and presented at the 23rd National Heat Transfer Conference, Denver, Colorado, August 1985. Manuscript received by the Heat Transfer Division May 8, 1986.

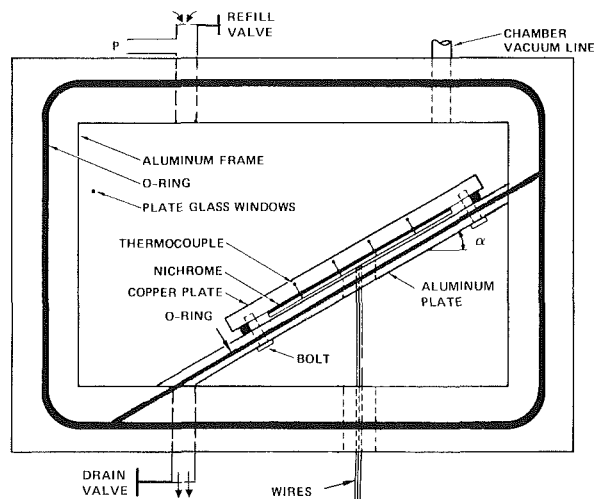


Fig. 1 Test section

shape of the plate is attached to the back of the plate and becomes the source of electric heating. A 0.31-cm gap separates the nichrome from the back plate, also aluminum, which is welded to the original frame. This gap is filled with fiberglass insulation. The copper and aluminum plates are themselves separated by a 0.31-cm-dia rubber O-ring and held together by four steel bolts. Six K-type thermocouples are embedded from the back side into the copper plate. All wiring leaves the plate and test section through a hole machined on the aluminum side plate and frame. The welded aluminum side plate divides the test section by a similar rubber O-ring between it and the glass plates such that liquid remains only on one side of the copper plate (see Fig. 1). The test section sits on a pivot axle allowing the copper plate angle to vary with respect to horizontal liquid surface.

The holographic interferometer used in this study is essentially the same as that described by Aung and Oregan (1971), and is shown schematically in Fig. 2. Coherent light ($0.633 \mu\text{m}$) from a 15-mW Spectra-Physics model 124-A He-Ne laser is split into an object beam and a reference beam by a variable-silvered mirror and each beam is expanded to a 90-mm planar wave via a $40\times$ microscope objective and collimating lens. Pinholes of $5 \mu\text{m}$ diameter are located at the focal points of the microscope objectives in order to eliminate intensity variations in the wave fronts. The two wave fronts intersect at a photographic plate (here at an angle of 26°) and produce a hologram when the photographic emulsion is exposed simultaneously to the two beams and then developed in situ. The hologram, which is essentially a diffraction grating in the emulsion produced by a constructive and destructive interference of the object and reference wavefronts, has the property that when it is illuminated with only the reference

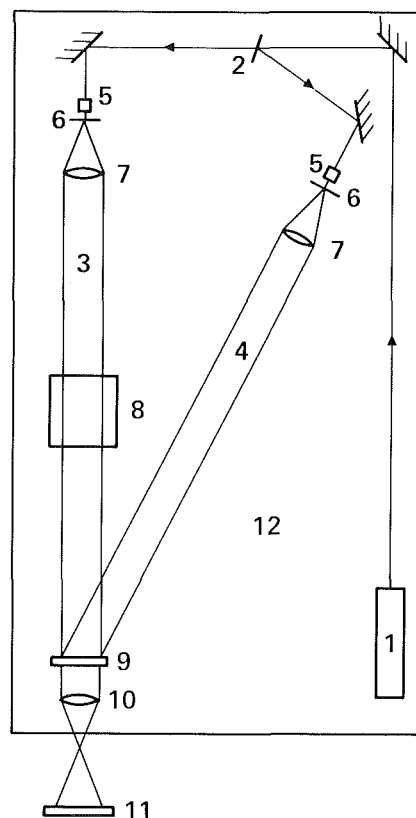


Fig. 2 Schematic of holographic interferometer: (1) helium-neon laser; (2) variable beam splitter; (3) objective beam; (4) reference beam; (5) microscope objective; (6) pinhole; (7) collimating lens; (8) test cell; (9) holographic plate; (10) lens; (11) opal glass window or filmholder; (12) air-suspension table

beam, the object beam is reconstructed and vice versa. In particular the phase and amplitude of a wavefront that has passed through a transparent medium placed in the test section can be stored permanently in the hologram. In real-time holographic interferometry, the reconstructed wavefronts are focused by an achromatic lens and interfere to produce an interferogram. The interferogram consists of lines or fringes of equal optical path length through the nonhomogeneous medium, which are equivalent to isotherms (average in direction parallel to the object beam). The interferometer components and test section are mounted securely to a $1.2 \times 3.0 \text{ m}$ vibration-isolated optical table.

Experimental Procedure

The procedure followed to produce interferograms of the

Nomenclature

b = fringe thickness, mm
 g = acceleration due to gravity, m/s^2
 h = heat transfer coefficient, $\text{W/m}^2\text{-}^\circ\text{C}$; enthalpy of vaporization, J/kg
 k = heat conductivity, $\text{W/m-}^\circ\text{C}$
 l = model length in ray direction, m
 Nu = Nusselt number
 q = heat flux, W/m^2
 Ra = Rayleigh number
 S = loci of constant phase difference

T = temperature, $^\circ\text{C}$
 u = velocity in x direction, m/s
 x = axial coordinate (along plate), m
 y = normal coordinate, m
 α = plate angle of inclination, deg
 β = thermal coefficient of expansion, K^{-1}
 Δ = change of
 δ = film thickness, mm
 θ = angle, deg
 κ_T = thermal diffusivity, m^2/s

λ = laser beam wavelength = $0.633 \times 10^{-6} \text{ m}$
 ν = kinematic viscosity, m^2/s
 σ = surface tension, N/m

Subscripts

c = contact
 i = fringe order; interfacial (temperature)
 l = liquid
 $W(x)$ = wall at x location
 0 = prescribed
 δ = with respect to δ

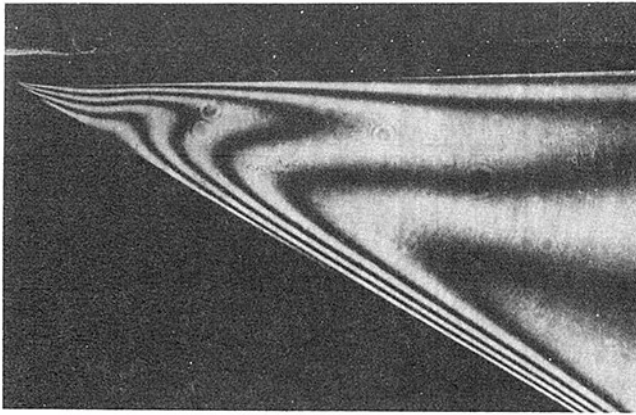


Fig. 3 Interferogram of water meniscus region for a plate angle of 30 deg, and fluid temperature of 23.3°C (saturation); approximate 1°C wall superheat; $\times 4$

temperature field of a stationary fluid heated by an inclined partially submerged copper plate was as follows:

1 The room temperature is controlled by a thermostat. Before every run, a "clean" environment is insured by the consistency of the room temperature, purity of the working fluid (distilled water, 99.9 percent pure Freon-11), and a polished copper surface.

2 A hologram (with a Kodak 120-02 plate) is made with the fluid in the test section essentially in thermal equilibrium with the room.

3 Wall heating is initiated and controlled such that the average reading of the thermocouples does not exceed one degree centigrade above fluid saturation temperature (i.e., room temperature).

4 Once steady state is achieved, the input heat flux along with the thermocouple readings are recorded.

5 The laser is then turned on and when the reference beam reconstructs the homogeneous medium, the object beams reflects nonuniformities in the heated fluid on the hologram via a set of fringes.

6 The images produced are then viewed through ground glass or recorded permanently on photographic film for data reduction.

Data Reduction

A typical interferogram for distilled water is shown in Fig. 3. The dark lines represent isotherms. Assuming that the liquid index of refraction is a function of liquid density, and the object beam does not change directions along the longitudinal axis of the test section, the interferometer equation is as follows (Hauf and Grigull, 1970):

$$\frac{dS}{dT} = (l/\lambda) \cdot \frac{dn}{dT} \quad (1)$$

where $dn/dT = \text{const}$ and

$$s(i) - s(i-1) = \frac{l}{\lambda} \cdot \frac{dn}{dT} (T_{s_i} - T_{s_{i-1}}) \quad (2)$$

where $S(i)$ is the fringe order and $S(0)$ corresponds to the wall. Equation (2) is the basic relation used to find the temperature differences associated with each fringe, which is found by setting $S(i) - S(i-1) = 1$. Knowledge of at least one temperature and the temperature difference in the region of interest will produce the approximate heat transfer behavior from solid to liquid to vapor.

Qualitative information about the velocity profile can be obtained from the recorded interferogram. Provided there is no change in the direction of fluid motion, the width of a

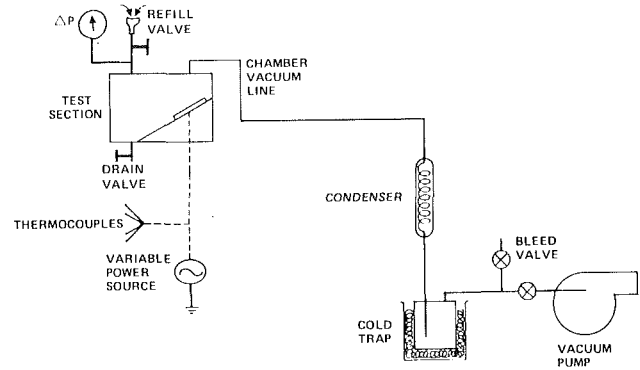


Fig. 4 Vacuum circuit to decrease water saturation temperature

Table 1 Heat transfer data reduction from the interferogram

mm \	WATER							FREON - 11								
	0°	2.5	8.8	22.5	41.3	48.8	0°	1.3	3.5	6	11	25	2.5	5	8.8	12.5
mm δ	.025	1.5	5	13	24	28.3	.025	1.3	3.5	6	11	25	1	2	3.5	5
mm b	.025	.2	.4	.25	.23	.2	.025	.13	.15	.15	.15	.15	.05	.21	.15	.15
$T_w(x) - T_f(x)$ °C	.165	4 x .165	6 x .165	5 x .165	4 x .165	4 x .165	.035	4 x .038	8 x .038	12 x .038	18 x .038	24 x .038	9 x .038	6 x .038	13 x .038	14 x .038
NU_δ	1.0	1.875	2.08	10.4	26.7	35.3	1.0	2.5	2.9	3.3	4.1	6.94	2.2	1.6	1.8	2.4
$\frac{h}{m^2 \cdot ^\circ C}$	234	731.6	243.8	468.2	650.3	731.6	3500	175	72.5	48.5	31.9	24.3	194	70	45	41.7
$\frac{q_w}{m^2}$	3861	482.8	243.8	386.3	429.2	482.8	140	28	23.3	23.3	22.9	22.2	66.4	16	22.2	22.18

$$k_{\text{WATER}} = .587 \frac{W}{m \cdot ^\circ C}$$

$$k_{\text{FREON}} = .0875 \frac{W}{m \cdot ^\circ C}$$

fringe will remain constant along its path. However, when direction changes, very low exposure time is needed so that the photograph will not thicken the fringe due to two-dimensional motion. On the other hand, when fringes become thinner and get closer to each other, this implies a region of high heat transfer. Although the holographic technique offers valuable information concerning the transport phenomenon, quantitative results require precise photography. Referring to Fig. 3, which has been magnified by a factor of roughly four, the x-axis has been directed down the inclined plate and the y-axis is normal to it in the direction of the free surface. This orientation of axis allows the width of the fringe b and the depth of the fluid (δ) to be measured in the y direction. Heat transfer in the liquid is defined in terms of a Nusselt number

$$Nu_\delta = \frac{k_l (dT/dy)_{\text{WALL}}}{k_l / \delta (T_w - T_i)} \quad (3)$$

and the temperature gradient is found from measurement

$$\left(\frac{dT}{dy} \right)_w \cong \left(\frac{\Delta T}{\Delta Y} \right)_w = \frac{(T_{s_i} - T_{s_{i-1}})_w}{b} \quad (4)$$

allowing the following relationship to be used:

$$Nu_\delta = \left(\frac{T_{s_i} - T_{s_{i-1}}}{T_w - T_i} \right) \cdot \left(\frac{\delta}{b} \right) \quad (5)$$

From equation (3), the heat transfer coefficient is given by

$$h_\delta = Nu_\delta \cdot \left(\frac{k_l}{\delta} \right) \quad (6)$$

and the local heat flux is

$$q_x = h_\delta (T_w - T_i) \quad (7)$$

It must be emphasized that the intention of this study is qualitatively to describe enhanced tube meniscus heat transfer by examining the interferogram covering the macrolayer meniscus formed by an inclined flat plate. Here, the meniscus region is fed by natural convection driven by gravity. The

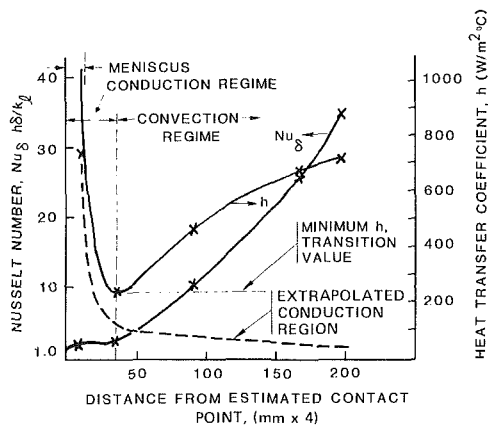


Fig. 5 Water meniscus heat transfer

Table 2 Validity of data assuming laminar natural convection thermal boundary layer growth

δ	x'	h MEASURED	h_{x_i}/h_{x_i-1} (EXPERIMENT)	h_{x_i}/h_{x_i-1} (THEORY)	% DIFFERENCE
20	135	117.4	—	—	—
19	100	123.5	1.05	1.07	1.80
15	60	156.5	1.27	1.13	-12.4
10	30	234.8	1.50	1.19	-26.0
9	15	260.9	1.11	1.19	6.70

$l = 135 \text{ mm (} \times 4 \text{ M)}$

grooved tube, however, would have natural convection driven only by surface tension and curvature gradient.

Results

Tests run with distilled water at saturation temperature equal to the ambient temperature via pressure control (as depicted in the circuit diagram of Fig. 4) were performed. The interferogram shown in Fig. 3 illustrates the thermal behavior of a stationary steady-state pool of distilled water heated approximately one degree above saturation temperature. The meniscus region is defined as the region where x is less than 10 mm. Table 1 summarizes results for several locations measured along the inclined plate. Fringe temperatures in water were calculated using the empirical relation for refraction index given by Tilton and Taylor (1938). The calculation led to 0.165°C per fringe with a plate tilt of 30 deg. For Freon, an approximate 1.0°C wall superheat was achieved. Tabulated values are for plate tilts of 45 and 22 deg with a 0.038°C temperature change per fringe.

Discussion

From the interferogram for water, two distinct regions, one of conduction and one of natural convection, are observed (see Fig. 5). For the latter region, the wall temperature is nearly constant and boundary layer like as expected and the driving mechanism is buoyancy.

In order to examine the obtained data in this region, laminar free convection thermal boundary layer growth along an inclined plate with constant surface temperature is assumed. From the lower edge of the plate, the local heat transfer coefficient decreases as follows:

$$h_\delta \sim (x')^{-1/4} \quad (8)$$

where x' is the distance from the bottom edge of the plate. Table 2 lists the percent deviation of measured values from

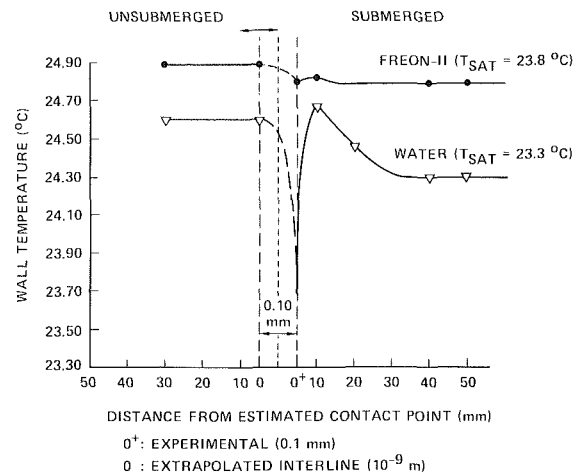


Fig. 6 Fluid-recorded wall temperature distribution

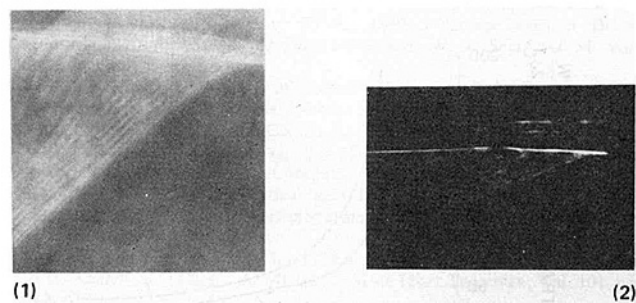


Fig. 7 Interferograms of Freon-11 meniscus region; fluid at saturation temperature (23.8°C); approximate 1°C wall superheat; $\times 4$: (1) $\alpha = 45^\circ$; (2) $\alpha = 22^\circ$

those predicted by theory assuming $x' = l$ (the natural convection boundary layer length) to be marked by the location where wall surface temperature begins to increase. The table reflects relative error in reducing data from holographic interferometry. The noticeable result is that this error varies with location from a minimum of 1.8 percent to a maximum of 26 percent.

The transition point to the conduction region marks the minimum heat transfer coefficient where part of the fluid flows toward the contact line to evaporate and the net flow circulates as if the free surface was a boundary. In the conduction region, there is no heat flow along the free surface and one-dimensional heat conduction in the y direction is well justified. It is expected that deep in the meniscus, the wall temperature is nearly constant in the x direction.

Figure 6 shows recorded wall temperatures along the plate for both fluids. The wall temperature is essentially constant in the natural convection region. The high heat sink near the interline disrupts the parallel isotherms at a critical point causing a slight increase (in the order of a fringe) in wall temperature. Between this point and the interline, results have shown that the behavior of the wall temperature will depend upon the degree to which the environment above the evaporating meniscus is saturated. The interferogram for water was obtained using a vacuum system to reduce the pressure above the liquid surface. From Fig. 3, it can be seen that in the absence of air above the liquid surface, the parallelness of the interfacial temperature isotherm indicates that evaporation occurs with little or no resistance from the environment. In this case, transition to the micro layer meniscus ($x \leq 10^{-4}\text{m}$) occurs when the wall temperature is at its lowest value. The temperature measurements of the unsubmerged portion of the plate have been used to extrapolate the behavior of the wall temperature in the microlayer meniscus.

Table 3 Rayleigh number comparison

$$Ra_{\delta} = \frac{(g \sin \alpha) \beta (T_w(x) - T_i(x)) \delta^3}{\nu k_T}$$

WATER		FREON - 11			
		($\alpha = 45^\circ$)		($\alpha = 22^\circ$)	
δ mm	Ra_{δ}	δ	Ra_{δ}	δ	Ra_{δ}
.025	1.88×10^{-5}	.025	2.19×10^{-4}	1	178
1.5	16.3	1.3	1.09×10^2	2	954
5	903	3.5	4.820×10^3	3.5	11077
13	13200	6	36000	5	13000
24	6.66×10^4	11	3.36×10^5		
28.3	1.086×10^5	25	5.27×10^6		

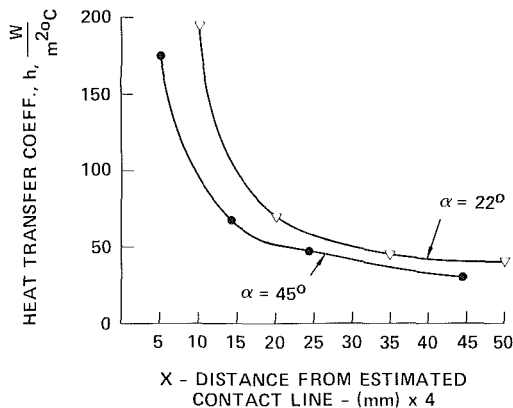


Fig. 8 Heat transfer coefficient from Freon at respective plate angles

The interferogram for Freon-11 (Fig. 7), on the other hand, was obtained in open-atmospheric conditions. In this case, the interfacial temperature isotherms intersect the liquid free surface such that there is an increase in T_i toward the micro layer meniscus. For this reason, the wall temperature is more uniform along the evaporating meniscus. Using thermocouple readings of the unsubmerged portion of the plate has again allowed extrapolating the wall temperature to the interline.

Due to the very low temperature difference per fringe, the interferogram for Freon shows more fringes close to the wall. The fringe closest to the wall in the natural convection region remains unchanged in direction but decreases in thickness as it approaches the interline. The higher order fringes possess high curvature due to flow reversal. There is, however, an instability present which can be noticed by the thicker arc-shaped isotherms. The variation in saturation pressure at the liquid/vapor interface due to the pressure gradient driving the flow into the meniscus has led to a variation of T_i in the microlayer meniscus.

The temperature at the liquid-vapor interface increases measurably with decrease in film thickness. The deviation from a constant value gives rise to variations in surface tension, producing flow (Marangoni effect) and disrupting the isotherms. This flow pattern enhances the heat transfer process. To see whether or not the disruption could be caused by $B' \gamma \psi \kappa \delta \mu$ -type convection, some Rayleigh numbers were calculated (see Table 3). The values in the vicinity of the contact line are too small for natural convection to be a con-

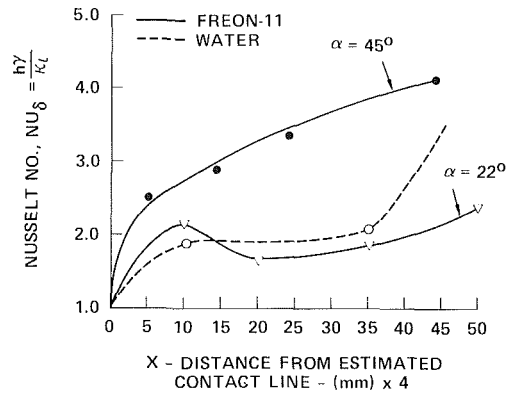


Fig. 9 Nusselt number comparison

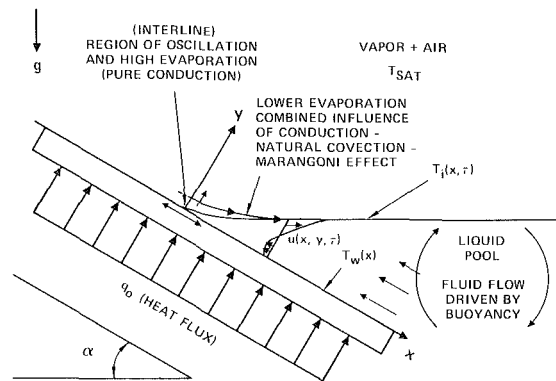


Fig. 10 Meniscus profile under oscillation

tributor. Farther away, their magnitudes are large enough to be a consideration. Recently, Mirzamoghadam and Catton (1986) have analyzed meniscus oscillation due to marangoni convection. The mechanism contributing to meniscus oscillation at film thickness of less than 1 mm was found to be an interaction between thermocapillarity, evaporation, and liquid inertia feeding the meniscus.

The results for Freon with tilt angle of 22 deg showed fewer fringes parallel to the wall entering the extended meniscus. This extends the conduction region (i.e., h increases), and weakens the natural convection influence. Figure 8, verifying this phenomenon, indicates that the large differences in local heat transfer occur at distances of less than 1 mm from the interline. In addition, the heat sink is concentrated near the interline.

The effect of the type of liquid used has manifested itself in meniscus oscillation. An indication of this phenomenon was first found in the analysis of isothermal behavior. The observed isothermal curvature difference associated with each fluid was investigated further. For water, this curvature was concave, thereby increasing the number of fringes between wall and the free surface at that location; whereas, for Freon, the fringe curvature is convex and the number of fringes has decreased. The apparent oscillation creates an inflection point in the Nusselt number, where for Freon the Nusselt number decreased due to the inhibition of heat transfer at the particular time during oscillation that the photo was taken (Fig. 10).

It is evident that if the contact line is superheated, circulation currents will arise on the interphase boundary and drive flow in the adjacent areas of both phases such that the surface does not remain undisturbed. Levitch and Krylov (1969) mention the possibility of normal and tangential pulsations of the interface, which tends to intensify heat and mass transfer. It

has been suggested that the reason for this behavior is the presence of local gradients of surface tension, which arise in different areas of the interface due to fluctuations of temperature and concentration. The initial motion no matter how small and localized in a small region, may under certain conditions develop into large-scale motion that is usually observed in experiments. This phenomenon has been observed when the fluid is Freon-11. When the contact line was superheated, surface tension was reduced and the contact angle decreased, enhancing evaporation. At the same time, cooling due to high evaporation rates increase the surface tension thereby increasing contact angle. The pulsation of the contact line amplifies with increasing heat flux (see Fig. 9).

Conclusion

The behavior of a fluid near saturation evaporating due to heating of an inclined partially submerged copper plate was examined using holographic interferometry. Results of this evaluation showed two distinct regions of fluid flow and heat transfer. Focusing on the region where augmentation of heat and mass transfer occurs, the meniscus layer was identified and qualitatively described. The meniscus length where Nusselt number is one and buoyancy is negligible was found to be under 1 mm. The difference in isothermal behavior between distilled water and Freon-11 was credited to the existence of a strong interfacial temperature gradient in the case of Freon-11, which in turn caused meniscus oscillation due to change in surface tension with temperature. In addition, the meniscus of the fluid with lower heat of vaporization (in this case Freon-11) was seen to oscillate with the unaided eye. The same fluid with a higher tilt angle exhibited a stronger natural convection influence on the Nusselt number. However, due to the extended meniscus of the lower tilted plate, meniscus thickness decreases, and local heat transfer coefficient increased. The inflection point for Nusselt number in the case of

Freon at 22 deg and water (30 deg tilt) is believed to be due to the extended meniscus and oscillation.

It was observed that surface roughness and fluid contamination were mechanisms contributing to the enhancement of bubble nucleation and wetting characteristics of the meniscus. Due to the sensitivity of the evaporating meniscus to a "clean" environment, it is recommended that these properties be actually measured before and after every run to establish a performance standard. The presence of a noncondensable in the environment, i.e., air, created a resistance to mass transfer resulting in an enhancement in the variation of the microlayer interfacial temperatures. The mechanism of liquid inertia, thermocapillarity, and rate of evaporation were seen to affect shear stability.

References

- Aung, W., and O'Regan, R., 1971, "Precise Measurement of Heat Transfer Using Holographic Interferometry," *Review of Scientific Instruments*, Vol. 42, pp. 1755-1758.
- Hauf, W., and Grigull, U., 1970, "Optical Methods in Heat Transfer," *Advances in Heat Transfer*, J. P. Hartnett, ed., Academic Press, New York.
- Levitch, V. G., and Krylov, V. S., 1969, "Surface Tension Driven Phenomena," *Annual Review of Fluid Mechanics*, W. R. Sears and M. Van Dyke, eds., Vol. 1.
- Miller, D. L., 1980, "A Study of Geometric Effects on Enhanced Horizontal Tube Evaporation," M.S. Thesis, UCLA, Los Angeles, CA.
- Mirzamoghadam, A. V., and Catton, I., 1986, "Analysis on the Evaporating Meniscus Oscillation," *Proceedings of the 8th International Heat Transfer Conference*, Hemisphere Publishing Company, Washington, DC.
- Renk, F. J., 1977, "Analytical and Experimental Investigation of an Evaporating Meniscus," Ph.D. Dissertation, Rensselaer Polytechnic Institute, Troy, NY.
- Renk, F., and Wayner, P. C., Jr., 1979, "An Evaporating Ethanol Meniscus: Part II, Analytical Studies," *ASME JOURNAL OF HEAT TRANSFER*, Vol. 101, pp. 59-62.
- Tilton, L. W., and Taylor, J. K., 1938, "Refractive Index and Dispersion of Distilled Water for Visible Radiation at Temperatures 0 to 60 Degrees Centigrade," *J. Res. Natl. Bur. Std.*, Vol. 20.
- Tung, C. Y., 1982, "Evaporative Heat Transfer in the Contact Line of a Mixture," Ph.D. Thesis, Rensselaer Polytechnic Institute, Troy, NY.

Dynamics of Droplets Impacting on Thin Heated Strips

S. C. Yao

Professor,
Department of Mechanical Engineering,
Carnegie-Mellon University,
Pittsburgh, PA 15213

L. E. Hochreiter

Westinghouse Electric Corporation,
Pittsburgh, PA 15230

K. Y. Cai

Southwestern Reactor Research
and Design Institute,
Chendu, People's Republic of China

Experiments were conducted with water droplets impacting on the edge of thin steel strips that were heated to beyond the Leidenfrost temperature. High-speed movies were taken and analyzed and showed that the shattered droplets were generally bimodal in size distribution. The volume ratio of these two size groups of generated droplets, the mean diameter of droplets, and the ejection angles and velocities of shattered droplets are shown as a function of incoming droplet Weber number, the ratio of incoming droplet diameter to strip thickness, and the offset of the droplet relative to the strip. The data are presented in nondimensional form and correlations are provided for the mean diameter of the shattered droplets. The theoretical limiting conditions of a droplet impacting normally to a large plate and cutting by a strip of zero thickness are analyzed. The present results are compared with those of the limiting conditions. The application to a nuclear reactor spacer grid behavior during two-phase dispersed flow is discussed.

Introduction

It has been observed that the interfacial heat and mass transfer in a vapor continuous two-phase flow is greatly enhanced when the liquid phase is in the form of small droplets. This is due to the large surface-to-volume ratio of droplets, which increases the interfacial area. Therefore, if there is a change of droplet size spectrum in such a system the heat transport capability of the dispersed two-phase flow will be affected significantly. In practice, one possible mechanism that may alter the droplet size spectrum is the impact of droplets on solid surfaces positioned in the flow passage.

Information on droplet dynamics has been reported when the droplet impacts normally on a large plate. When the plate is heated beyond the Leidenfrost temperature, the droplet will not be able to wet or stick to the surface because of the formation of a vapor curtain. At a low Weber number, a droplet may rebound as a single or double droplets [1, 2] from such a heated plate. At high Weber numbers, a droplet may deform into a liquid sheet on the surface and then disintegrate into many smaller droplets [2, 3]. The details of droplet interactions with heated flat plates have been reported in [3]. When the plate is not heated, a liquid film usually exists on the surface. The impacting of a droplet splashes the liquid film. Sometimes, more liquid will be ejected than the amount of incoming liquid, but at lower velocities.

In contrast, very little information has been reported on the dynamics of droplets impacting on the edge of heated strip with finite thickness. As shown in Fig. 1, when the droplet diameter and the strip thickness are comparable, the impact mechanism will become a combination of splashing and cutting. This phenomenon is important to understand the thermal performance of nuclear reactor spacer grids during the reflooding phase of a postulated loss-of-coolant accident. During the reflooding of a reactor core, high-temperature and high-velocity steam flows entrain dispersed droplets in the superheated steam. Heat is removed from the hot fuel rods by convection to the steam and, in turn, the steam is cooled by the evaporating droplets in the flow channel. The presence of droplets may be regarded as a distributed heat sink in the hot steam [4]. As a result, the cooling of the fuel rod is significantly influenced by the heat transfer between the vapor and the droplets.

In reactor fuel bundles there are spacer grids that hold the rods in position at various locations. The typical thickness of

the spacers (0.3 mm) is comparable to the typical diameter of the droplets in the flow (1.2 mm). The impact of flowing droplets onto the spacers can shatter the original droplets into much smaller ones, and subsequently, will enhance the heat sink effects of droplets in hot steam, thereby increasing the cooling of the fuel rod downstream of the grid spacers. There have been other research studies in this area related to finding the shattering effects of grids and grid straps on the entrained droplet sizes and distributions. The mean diameters of droplets in vapor flows at the upstream and downstream of a grid spacer in a heated rod bundle have been measured with a laser-Doppler anemometer [5]. The size spectra of droplets at upstream and downstream of the grid are related; however, no details of interaction mechanisms have been observed. Another study involves falling drops impacting on hot strips at its center plane [6]. Offset of droplet center to the center plane

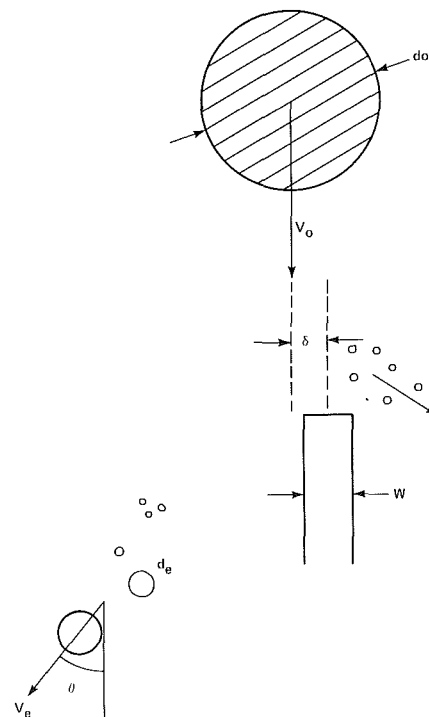


Fig. 1 Schematic of droplet and heated strip interaction

Contributed by the Heat Transfer Division for publication in the JOURNAL OF HEAT TRANSFER. Manuscript received by the Heat Transfer Division February 11, 1985.

of strip was not varied. The results of generated droplets are reported as the total number count instead of size spectrum of mean sizes.

In this paper, various offsets of incoming droplets with respect to a heated strip are investigated. The resulting droplet spectrum and dynamics are reported together with the explanation of the droplet breakup mechanism. The objective of this paper is to report the available data base in nondimensional form, provide correlation of mean diameter of shattered droplets, and discuss the results and their application to reactor safety research.

Experimental Setup and Procedure

Water droplets are atomized from a hypodermic needle of 1.5 mm i.d., injected downward. Depending upon the applied water pressure the droplet velocity can be varied in a range of 3-10 m/s. At a fixed velocity the atomized droplets have diameters over the range 0.7-2 mm. Therefore, the droplet Weber numbers (defined in equation (1)) at the point of generation will also cover a wide range of variation. Thin stainless steel strips with square edges, which simulate the grid spacer straps, were used to study the droplet-grid impactions. The length of the strip is 8 cm, which is about twice the width of the spray at the observation point. The height of the strip is 2.5 cm. The typical thickness of the strips was 0.33 mm and it was situated in the middle of the spray. The strips of 0.175 mm thickness were also studied for comparison.

At the beginning of each test, the stainless strip was heated by propane torch to a red hot temperature. The spray was then initiated and a high-speed movie was taken. The experiments were conducted so that after the movie was taken the strip was still warmer than the Leidenfrost temperature. A Hycam camera with a closeup microlens was operated at 8000 frames per second. Back lighting was employed with a semi-transparent diffuser. In the experiments, usually 10 to 12 s are required before the spray starts to wet the leading edge of the strip. (When the wetting occurs it is observed that fine mists are generated by the bursting of the falling liquid film due to the grid strap stored energy release.) The data were taken from the first 2 s of the high-speed movies, which cover about 4 s right after the spray is applied. In order to avoid local disturbance, no thermocouples are installed on the strip; however, the movies showed clearly that the surface is beyond the Leidenfrost temperature and drop-surface interaction is insensitive to the exact temperature of the strip. The developed movies were then analyzed manually frame by frame on a projected screen. Experiments corresponding to various ranges of incoming droplet Weber numbers were performed. Only a few selected size groups of incoming drops are analyzed. A case of a cold and wet strip was also studied for comparison.

Results and Discussion

Phenomena. A typical relationship for a droplet impacting on a thin metal strip is described in Fig. 1. The controlling parameters are the incoming droplet diameter d_o , droplet velocity V_o , strip thickness W , and the relative offset of the droplet to the strip δ . A more generalized representation in nondimensional form is the incoming droplet Weber number We_o , the offset parameter Δ , and the ratio of droplet diameter to the strip, do/W . They are:

$$We_o = \frac{\rho_l V_o^2}{(\sigma/d)_o} \quad (1)$$

$$\Delta = \frac{\delta}{(d_o + W)/2} \quad (2)$$

The offset value δ can be positive, as shown in Fig. 1, or negative when the droplet is biased at the other side. As a result, the range of Δ will be between 1.0 and -1.0 .

The resulting information from the impact can be described by the diameter of ejected droplet d_e , the ejection angle θ , and ejection velocity v_e . Since the number of ejected droplets could be large, an overall description is necessary.

Usually, the shattered droplets travel in groups. There is one group at each side of the strip. Due to the equal probability of the offsets, only the group at one side of the strip needs to be analyzed when all the possible offsets are considered. The diameters of shattered droplets usually appear as a spectrum with bimodal distribution. For simple representation, the mean diameter will be evaluated. The general results of the impact behavior will be presented in nondimensional form as V_e/V_o , θ , and d_e/d_o .

A typical impaction process has been observed through examination of high-speed movies. In the present study, the droplets are usually larger than the strip thickness. During the interaction, a combination of cutting and splashing of droplets by the strip was observed. The portion of the droplet outside the projected area of the strip has large momentum and moves forward with little deviation after intercepted by the strip. The portion of the droplet intercepted by the strip tends to splash sideways as very fine fragments. Some of them even move along the longer top edge of the strip. Due to the surface tension, these two portions are interlinked at the beginning of impact but separate later on. The trajectory of the whole group is determined by the compromise of the intercepted and nonintercepted liquid movements. During the impaction, the liquid also deforms into a flattened sheet. Depending on the incoming droplet Weber number and offsets, the liquid sheet may further disintegrate into small droplets or become restored back to one or several large droplets. As the incoming Weber number is increased the

Nomenclature

d_e = diameter of ejected droplets
 d_n = number mean diameter of droplets, defined in equation (3)
 d_o = diameter of incoming droplets
 d_{32} = Sauter mean diameter of droplets, defined in equation (4)
 n = number of droplets in a particular size range
 V_e = velocity of ejected droplets
 V_o = velocity of incoming droplets
 W = width of the strip

We_o = Weber number of the incoming droplets, defined in equation (1)
 α = fraction of droplet kinetic energy converted to surface energy
 δ = offset of the incoming droplet with respect to the center plane of the strip
 Δ = nondimensional offset, defined in equation (2)
 θ = angle of ejected droplet, see Fig. 1

η = volume ratio of a group of droplets to the overall liquid
 ρ_l = density of the liquid
 σ = surface tension of liquid to gas

Subscripts

crit = critical value
 j = index of a particular size range of droplets
 s = group of small droplets, defined in Table 1

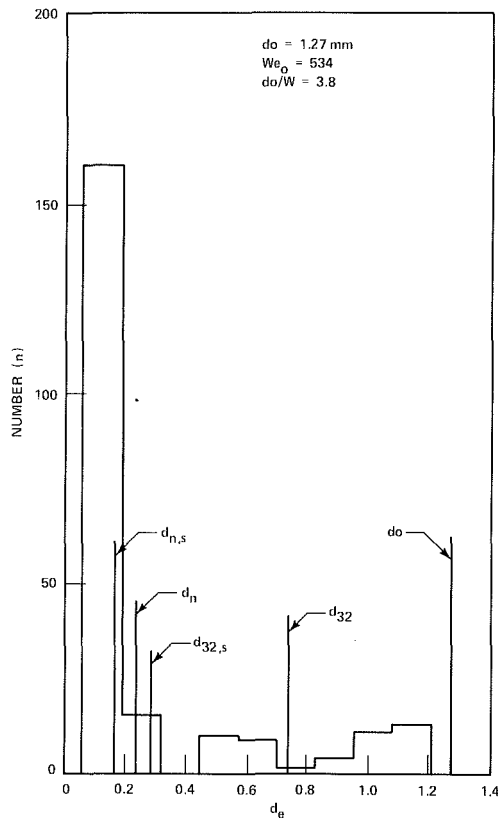


Fig. 2 Shattered droplet spectrum for $We_0 = 534$

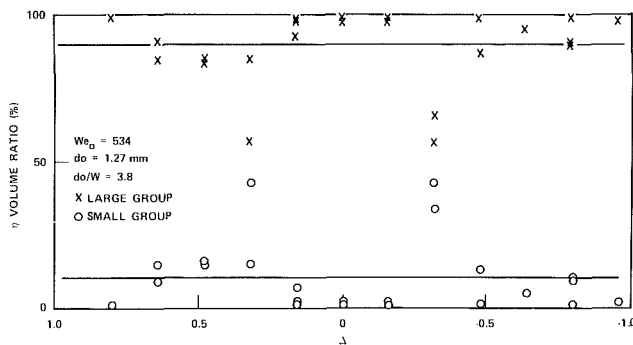


Fig. 3 Volume ratio of generated droplet groups at various offsets with $We_0 = 534$

liquid sheet will disintegrate into finer droplets. As a result, the droplet size distribution shifts to smaller droplets downstream of a grid, which increases the vapor-to-droplet heat transfer.

Data. A large amount of data has been compiled for various conditions of experiments. For the case with incoming Weber number equal to 534 and droplet diameter-to-strip thickness ratio of 3.8, the ejected droplet size spectrum is shown in Fig. 2. The incoming droplets have a 1.27-mm diameter. The ejected droplets are of two size groups: One is fine with a large number of samples (popular) and the other one is larger in size but has fewer samples (less popular). They are generated by the splashing and cutting mechanisms, respectively. In all the data analysis, the size of 0.76 mm is used arbitrarily to separate the data in terms of "large" or "small" droplet groups. The use of this single value to distinguish the droplet groups has an advantage of simplifying the calculation in practical problems where droplets of various sizes and

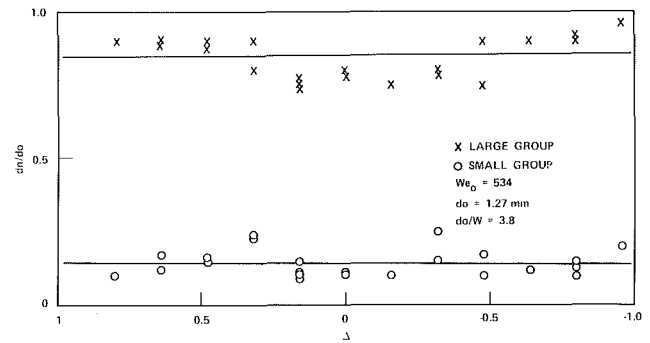


Fig. 4 Number mean diameter of shattered droplets at various offsets with $We_0 = 534$

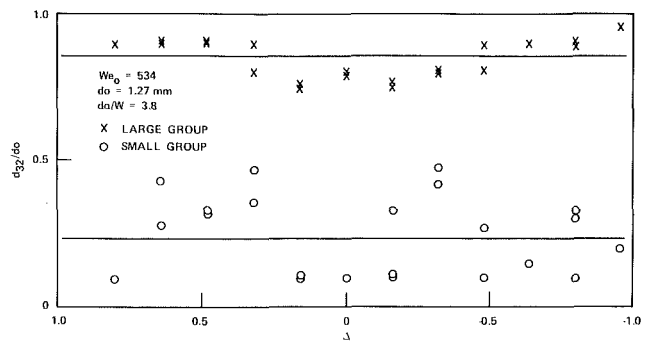


Fig. 5 Sauter mean diameter of shattered droplets at various offsets with $We_0 = 534$

velocities impact on strips. The droplets with diameter less than 0.08 mm appear to be too small to be measured accurately from the movie records. Therefore they are not counted in the data reduction.

The volume ratio of these two groups of ejected droplets is shown in Fig. 3 as a function of the nondimensional offset Δ . The large droplets dominate the volume of ejected droplets because the volume of a droplet is proportional to the cube of its diameter. Although the data are scattered, they are relatively independent of the offset. When the offset Δ is at about ± 0.3 , the data are away from the trend. This is because the two groups are separated with the diameter of 0.76 mm, but all the droplets generated at this offset are about this size. About half of ejected droplets are categorized into a large droplet group and the other half are considered as a small droplet group. This figure and some latter figures (Figs. 4–7) are symmetric with respect to the zero offset because the ejected droplets at both sides of the strip are analyzed.

Figures 4 and 5 show the number mean and Sauter mean diameters of ejected droplets for each size group. The definitions of the mean diameters are

$$d_n = \frac{\sum_j n_j d_j}{\sum_j n_j} \quad (\text{number mean}) \quad (3)$$

$$d_{32} = \frac{\sum_j n_j d_j^3}{\sum_j n_j d_j^2} \quad (\text{Sauter mean}) \quad (4)$$

where the index j is for a particular size range of consideration. The mean diameters are also found to be independent of the offset, as shown in the figures. The mean diameters of the small droplet group and the mean diameters of all the ejected droplets are shown in Fig. 2 for comparison. The overall number mean diameter is much less than the overall Sauter mean due to the large population of the smaller droplets and the large weight fraction of the large droplets. However, it is

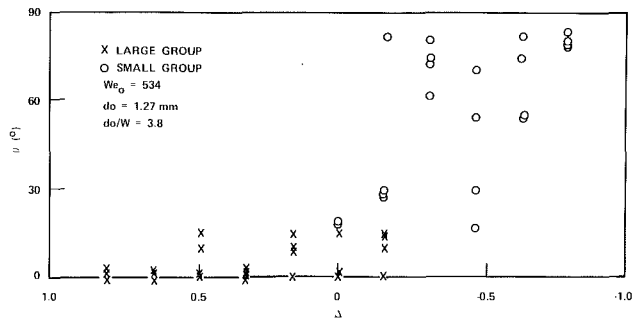


Fig. 6 Angle of deflection of shattered droplets at various offsets with $We_0 = 534$

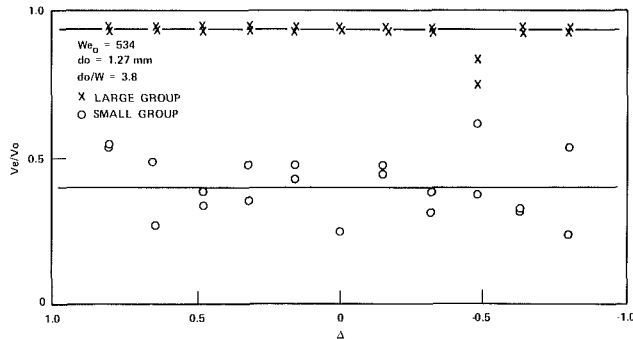


Fig. 7 Velocities of shattered droplets at various offsets with $We_0 = 534$

interesting to observe that the number mean of the overall droplets is usually close to the Sauter mean of the small droplet group. As will be discussed later, this feature has significance in practical applications.

It is interesting to point out that the volume ratio of the two droplet groups and the mean diameter of the shattered droplets are insensitive to the variation of the offset between the incoming droplet and the strip. As stated before, a droplet impacting on a thin strip breaks up in both the cutting and the splashing mechanisms. The small droplets come mainly from the splashing. The portion of the incoming droplet intercepted by the strip tends to splash by being converted into thin liquid sheets attaching to the unintercepted portion of the incoming droplet, which are ejected at an angle θ . The tail portion of this thin liquid sheet then disintegrates into small droplets. Since the diameter of the incoming droplet is always several times bigger than the width of the strip in the present experiments, the liquid sheets always appear during the interaction and the small droplets are usually generated in a similar manner irrespective of the variation of the offset. Furthermore, the small droplets are produced from a small portion of liquid at the top of the intercepted part of the incoming droplet; therefore, the amount is also relatively insensitive to the magnitude of offset.

The angle of ejected droplets at left side of the strip is reported in Fig. 6 at various offsets. When the droplets are offset at the left side of the strip, the ejected droplets at this side are large and they move at a small angle with respect to the incoming direction. When incoming droplets are offset to the right side of the strip, the ejected droplets at the left side are small and are at a large angle due to the effect of splashing. In all, the smaller droplets are ejected at large angles while the large droplets are ejected at small angles. The ejecting velocities at both sides of the strip are shown in Fig. 7. The large droplets have a velocity close to the incoming droplet velocity. The small droplets have a speed slightly less than half of the incoming droplet velocity.

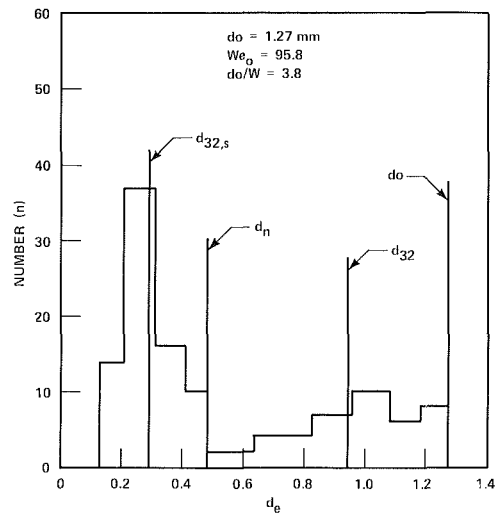


Fig. 8 Shattered droplet spectrum for $We_0 = 95.8$

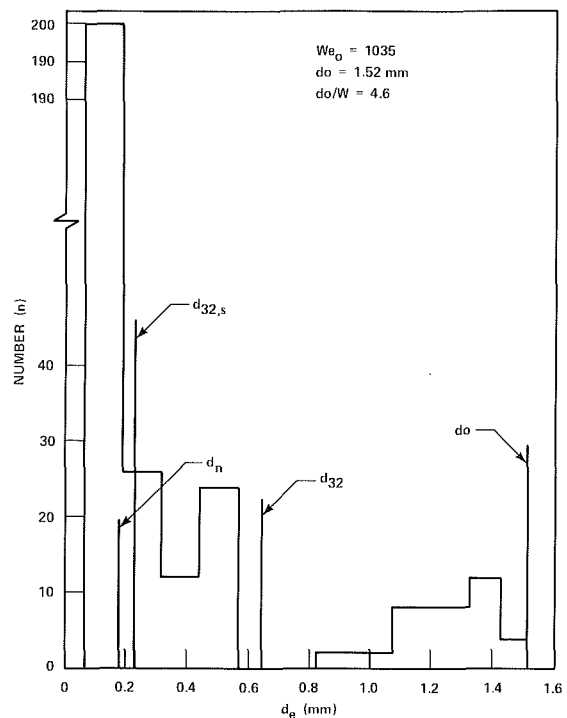


Fig. 9 Shattered droplet spectrum for $We_0 = 1035$

The impact of droplets at other incoming Weber numbers gives results similar in nature to this set of data for $We_0 = 534$. The size spectrum of the ejected droplets at the extremes of $We_0 = 96$ and 1035 are shown in Figs. 8 and 9 for comparison. It is obvious that the higher the incoming Weber number, the greater the number of small droplets generated and the more the two size groups are separated. The number mean diameters of all the ejected droplets become closer to the Sauter mean diameter of the smaller size group when the incoming Weber number is increased. The average results of the overall spectrum and of each size group at four different incoming Weber numbers are listed in Table 1. The incoming droplets in case 4 are slightly larger than those in cases 1-3; however, all these four cases can be considered in the same group for the data analysis.

Experiments using a thin strip 0.175 mm thick were also performed at two different incoming droplet Weber numbers of

Table 1 Averaged data of shattered droplets at various conditions

	Small group $d_e < 0.76$ mm	Large group $0.76 \text{ mm} \leq d_e < 1.27$ mm	Overall
<i>Case 1 (17 events): $We_o = 95.8$; $d_o = 1.27$ mm; $d_o/W = 3.8$</i>			
Vol. ratio	4.20%	95.8%	100%
d_n/d_o	0.21	0.83	0.38
d_{32}/d_o	0.22	0.84	0.74
V_e/V_o	0.31	0.87	0.46
θ (deg)	90	27	72.7
<i>Case 2 (23 events): $We_e = 534$; $d_o = 1.27$ mm; $d_o/W = 3.8$</i>			
Vol. ratio	10%	90%	100%
d_n/d_o	0.14	0.85	0.17
d_{32}/d_o	0.23	0.85	0.57
V_e/V_o	0.40	0.94	0.42
θ (deg)	65	6	62.7
<i>Case 3 (25 events): $We_o = 862$; $d_o = 1.27$ mm; $d_o/W = 3.8$</i>			
Vol. ratio	11%	89%	
d_n/d_o	0.13	0.86	0.15
d_{32}/d_o	0.17	0.86	0.52
V_e/V_o	0.50	1.0	0.74
θ (deg)	76	4	74.2
<i>Case 4 (26 events): $We_o = 1035$; $d_o = 1.52$ mm; $d_o/W = 4.6$</i>			
Vol. ratio	10%	90%	
d_n/d_o	0.11	0.86	0.12
d_{32}/d_o	0.15	0.88	0.42
V_e/V_o	0.43	1.0	0.61
θ (deg)	76	8	74.8
<i>Case 5 (15 events): $We_o = 317$; $d_o = 1.0$ mm; $d_o/W = 5.7$</i>			
Vol. ratio	4%	96%	
d_n/d_o	0.25	0.90	0.31
d_{32}/d_o	0.27	0.90	0.80
<i>Case 6 (5 events): $We_o = 1322$; $d_o = 1.0$ mm; $d_o/W = 5.7$</i>			
Vol. ratio	9%	91%	
d_n/d_o	0.20	0.88	0.26
d_{32}/d_o	0.23	0.89	0.68

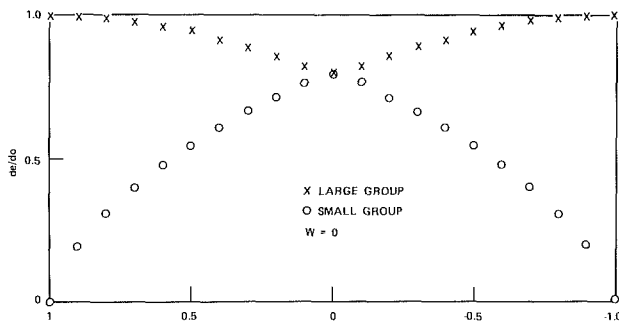


Fig. 10 Droplet sizes generated by cutting with a strip of zero thickness at various offsets

317 and 1322. The data are listed in Table 1. Impaction dynamics features similar to previous experiments were observed, but the behavior of cutting by the strip was more obvious.

Experiments have also been performed when the strip was cold. A liquid film may attach to the strip to form a wetted surface. When impaction occurs, the generated droplets are slightly bigger than when the strip is hot, and the ejected drops are moving with slower velocities. The large droplets ejected at very small angles may attach to the liquid film and eventually merge into the liquid film while sliding along the strip. Large droplets drip from the bottom edge of the strip.

It is also interesting to observe the quenching behavior when the red hot strip was cooled down by impacting droplets. The quench usually starts at the top edge where impaction occurs predominantly. The quench front propagates downward along the stream. Once the top edge is quenched, the impaction mechanism becomes similar to that of a cold strip. At the quench front, sputtering occurs such that nucleate boiling

destroys the flowing liquid film into many fine droplets. This is similar to the observations reported on the top quenching of hot rod by liquid film [7].

Comparisons. In the present experiment, the ratio of the droplet diameter to the thickness of the strip is between 3 and 6. The impaction mechanism appears to be a combination of splashing and cutting, which are the typical phenomena when the ratio of droplet diameter to strip thickness approaches zero or infinity, respectively. Therefore, it is relevant to compare the present results with respect to the results of these limiting conditions.

One limiting condition occurs when the thickness of the strip approaches zero such that the incoming droplets are cut into halves at impaction. At various offsets, the two droplet parts will be different in volume and will have different diameters after the liquid surface tension restores the spherical shape. The size of ejected droplets can be evaluated. A typical result is shown in Fig. 10 with the number mean diameter and Sauter mean diameter equal to $0.74 d_o$ and $0.86 d_o$, respectively.

When the incoming Weber number is very low, the surface tension will resist the cutting action. The limiting condition occurs when the droplet is cut into two drops at the center of the original drop and the kinetic energy of the incoming droplet just equals the increased surface energy at the maximum depth of cutting. It could be assumed that at this moment the drop is in the form of two hemispheres where the new surface equals the two disk areas adjacent to the surface of the strip. A balance of incoming kinetic energy and the newly generated droplet surface energy gives

$$\frac{1}{2} \left(\frac{1}{6} \pi d_o^3 \rho_l \right) V_o^2 = 2 \left(\pi \left(\frac{d_o}{2} \right)^2 \right) \sigma \quad (5)$$

where d_o is the diameter of the newly generated disk area and

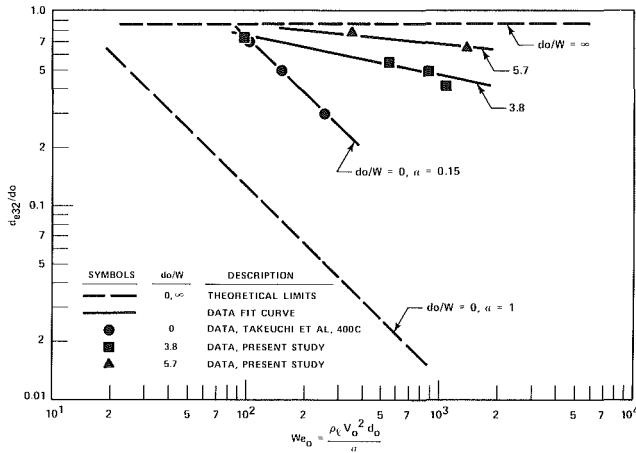


Fig. 11 Sauter mean diameter of shattered droplets at various conditions

the surface tension σ is between the liquid and air because the solid is not wetted by the liquid during the impaction. This gives

$$\left(\frac{\rho_l V_o^2}{\sigma/d_o}\right) = We_{crit} = 6 \quad \text{for } \frac{d_o}{W} \sim \infty \quad (6)$$

The critical Weber number is 6. Beyond this Weber number, the droplets can always be cut by a strip of zero thickness.

The other limiting condition occurs when the strip is of infinite thickness such that the droplet, in fact, impacts normally onto a plate. A theoretical limiting criterion for the size of generated droplets can be estimated from the assumption that a fraction α of the kinetic energy of the incoming droplet converts to the new surface energy of the generated small droplets. That gives

$$\alpha \frac{1}{2} \left(\frac{\pi}{6} d_o^3 \rho_l\right) V_o^2 = n \sigma \pi d_e^2 - \sigma \pi d_o^2 \quad (7)$$

where d_e is the diameter of the splashed drops.

Conservation of liquid volume gives

$$\frac{\pi}{6} d_o^3 = n \frac{\pi}{6} d_e^3 \quad (8)$$

Neglecting the surface energy of the original droplet as compared with the surface energy of the generated smaller drops, the second term in the right-hand side of equation (7) can be deleted. Then the diameter of the generated droplets can be derived as

$$\frac{d_e}{d_o} = \frac{12}{\alpha} \frac{1}{We_o} \quad \text{for } \frac{d_o}{W} \sim 0 \quad (9)$$

The diameter of generated droplets is inversely proportional to the incoming Weber number. The ultimate limit occurs when the α equals unity. Generally, the factor α is always less than unity due to the existence of viscous dissipation during the impact and the nonzero kinetic energy of the splashed droplets.

Extensive experiments have been conducted by Takeuchi et al. [3] on droplets impacting normally onto a hot plate. Liquid deforms as a circular sheet then disintegrates into fine droplets. The Sauter mean diameters of the splashed droplets were reported as a function of droplet incoming Weber number and the temperature of the plate. The present authors observed that the results of [3] can be approximated by equation (9) with the factor α set to 0.15. In other words, approximately 15 percent of the original droplet kinetic energy was converted into the surface energy of the generated small droplets.

From the present experiments the diameter ratios of the generated droplets and the incoming droplet are shown in

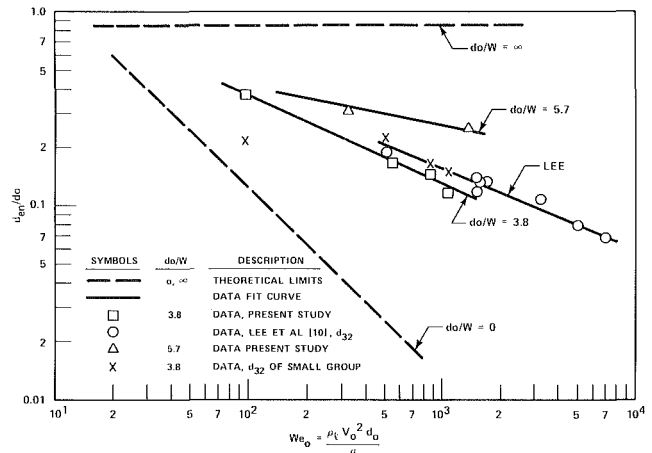


Fig. 12 Number mean diameter of shattered droplets at various conditions

Figs. 11 and 12 as a function of incoming droplet Weber number. The Sauter mean diameter and the number mean diameter of the present experiment, as shown in Figs. 11 and 12, respectively, appear as straight lines on the log-log plot. They can be correlated, as shown in the figures, in the form of

$$\frac{d_{32}}{d_o} = 1.84 We_o^{-0.2} \quad \text{for } \frac{d_o}{W} = 3.8 \quad (10)$$

$$\frac{d_{32}}{d_o} = 1.21 We_o^{-0.08} \quad \text{for } \frac{d_o}{W} = 5.7 \quad (11)$$

$$\frac{d_n}{d_o} = 3.05 We_o^{-0.46} \quad \text{for } \frac{d_o}{W} = 3.8 \quad (12)$$

$$\frac{d_n}{d_o} = We_o^{-0.2} \quad \text{for } \frac{d_o}{W} = 5.7 \quad (13)$$

The Sauter mean diameters of Takeuchi's experiment [3] and of the limiting theoretical conditions are also presented in the figures. The mean diameters of the present experiments for a strip of finite width (equations (10)–(13)) fall in between the two limiting results of zero thickness strips and infinite plates. This is because the droplets, in the present experiment, disintegrate in terms of both the cutting and splashing mechanisms when impacting on the edge of a strip with finite width.

Figure 12 also presents an interesting comparison of the small drop sizes measured downstream of a heated strip (this study) and a heated grid in a rod bundle [10] using two entirely different techniques. Lee et al. [10] used a laser-Doppler anemometer method with a small drop and large drop field measurement technique, whereas the present study used high-speed photography. The comparison of the resulting small drop sizes (splashed drops) is very good considering the vastly different measurement methods.

Application to Reactor Spacer Grid Behavior in Dispersed Flow

Light water reactor fuel assemblies have spacer grids located along the length of the fuel rods at approximately 0.5-m intervals. During a postulated LOCA, the fuel rods are calculated to heat up to temperatures of 800–900°C when reflow begins. Licensing calculations result in low reflow rates in the core and hence long periods of dispersed nonequilibrium two-phase flow over most of the length of the rod bundle. The spacer grid can enhance the fuel rod heat transfer by four mechanisms: direct radiation from the fuel rods, single-phase convective enhancement due to thermal boundary layer

separation and reattachment [8], spacer grid early rewetting [9], and breakup of the entrained droplets into smaller fragments [9]. The present study is most relevant to the last heat transfer mechanism. Generation of a population of smaller droplets downstream of a grid results in an increased liquid-vapor interfacial area for heat transfer. As a result, it augments the desuperheat of the vapor phase and provides a larger wall-to-vapor temperature difference and a higher wall heat flux [9].

In order to make proper predictions, a simple model of the spacer grid-droplet interaction is needed to characterize the observed bimodal droplet spectrum downstream of the grid. Examination of the data indicates that the group of the larger droplets has an average diameter not much smaller than the original sizes. An effective approach is to characterize the shattered new drops by the Sauter mean diameter of the smaller drops. The Sauter mean diameters of the smaller group of droplets of the present experiment are shown in Fig. 12. In the same figure, the recent data of Lee et al. [10] from laser-Doppler measurements for strips similar to those used in our experiment of $d_o/W = 3.8$ are also presented. Their correlation is $d_{32}/d_o = 2.4 We_o^{-0.4}$.

In the experiment of [10] the sizes of incoming droplets form a spectrum; however, these two sets of data agree well with each other. It is also interesting to observe that coincidentally when the Weber number is higher than 400 the Sauter mean diameter of the smaller group of droplets can be fairly approximated by the number mean diameter of all the ejected droplets. This is also indicated in the droplet size distribution plots in Figs. 2 and 9. Spacer grids have been modeled in advanced two-phase computer codes such as COBRA-TF [11] using the droplet break-up model presented in this paper. The addition of this heat transfer effect as well as the other grid heat transfer effects mentioned above results in more accurate predictions of rod bundle heat transfer for postulated accident conditions.

Conclusions

Data for droplets impacting on hot thin strips at beyond Leidenfrost temperature have been correlated and compared

to two limiting conditions. The mechanism of droplet disintegration during impaction with $d_o/W \sim 3$ to 6 is both a shattering and cutting by the edge of the strip. Generally, two groups of small and large droplets are generated by the two mechanisms, respectively. The smaller droplets contribute much to the increased liquid-to-vapor interfacial area for heat and mass transfer. As shown in equations (10)–(13), the average size of the generated droplets may be correlated in terms of the incoming Weber number for a specific value of d_o/W . Basic knowledge of this phenomenon is essential in improving the understanding of many industrial processes and the emergency cooling of reactor cores.

References

- 1 Pederson, C. O., "The Dynamics and Heat Transfer Characteristics of Water Droplets Impinging Upon a Heated Surface," Ph.D. Thesis, Carnegie-Mellon University, Pittsburgh, PA, 1967.
- 2 Wachters, L. H. J., and Westerling, N. A. J., "The Heat Transfer from a Hot Wall to Impinging Water Drops in the Spheroidal State," *Chemical Engineering Science*, Vol. 21, 1966, pp. 1047–1056.
- 3 Takeuchi, K., Senda, J., and Sato, Y., "Experimental Studies on the Behavior of a Small Droplet Impinging Upon a Hot Surface," *Proceedings of the Second International Conference on Liquid Atomization and Spray Systems*, 1982, pp. 397–404.
- 4 Rane, A., and Yao, S. C., "Turbulent Mist Flow Heat Transfer in Straight Ducts," *ASME JOURNAL OF HEAT TRANSFER*, Vol. 103, 1981, pp. 679–684.
- 5 Lee, S. L., Sheen, H. J., Cho, S. K., Issapour, I., and S. G. Hua, "Measurement of Grid Spacer's Enhanced Droplet Cooling Under Reflood Conditions in a PWR by LDA," presented at 11th Water Reactor Safety Meeting, Garthursburg, MD, Oct. 24–28, 1983.
- 6 Adams, J. E., and Clare, A. J., "A Preliminary Study of Droplet Breakup at PWR Spacer Grids," Central Electric Generating Board Report, PWR/HTW/P(83)-130 Draft, 1983.
- 7 Sun, K. H., Dix, G. E., and Tien, C. L., "Cooling of a Very Hot Vertical Surface by a Falling Liquid Film," *ASME Paper No. 73-WA/HT-22*, 1973.
- 8 Yao, S. C., Hochreiter, L. E., and Leech, W. J., "Heat Transfer Augmentation in Rod Bundles Near Grids," *ASME JOURNAL OF HEAT TRANSFER*, Vol. 104, 1982, pp. 76–81.
- 9 Chiou, J., Hochreiter, L. E., Utton, D. B., and Young, M. Y., "Spacer Grid Heat Transfer Effects During Reflood," *Proceedings Joint ANS/NRC Meeting on Basic Thermal Hydraulic Mechanisms in LWR Analysis*, Bethesda, MD, Sept. 1982.
- 10 Lee, S. L., Private Communication, Department of Mechanical Engineering, State University of New York at Stony Brook, Stony Brook, NY, 1984.
- 11 Paik, C. Y., Hochreiter, L. E., Kelly, J. M., and Kohrt, R. J., "Analysis of FLECHT-SEASET 163-Rod Bundle Data Using COBRA-TF," *NUREG-CR-4166*, Oct. 1985.

Nucleate Boiling in Thermally Developing and Fully Developed Laminar Falling Water Films

M. Cerza

National Research Council/Naval Research
Laboratory,
Laboratory for Computational Physics and
Fluid Dynamics,
Washington, DC 20375-5000
Assoc. Mem. ASME

V. Sernas

Department of Mechanical and Aerospace
Engineering,
Rutgers University,
Piscataway, NJ 08854

This paper reports an experimental investigation of nucleate boiling in thin water films falling down the outside of a cylindrical heated tube. A mathematical model for the convective (nonboiling) heat transfer coefficient in the laminar thermal entry length was developed and used as a comparison to the experimental boiling heat transfer coefficients. A heat transfer correlation based on mechanistic arguments is presented and is shown to represent the experimental data fairly well. The experimental data were also compared with existing heat transfer data in the literature. The flow rates utilized in this study corresponded to a Reynolds number range from 670 and 4300 and the heat flux range was 6 to 70 kW/m².

Introduction

Thin liquid films have long been utilized in industry because of such inherent characteristics as large heat transfer rates, low feedwater rates, and high heat transfer coefficients. Major industrial applications utilizing thin liquid film condensation and evaporation processes can be found in the dairy, chemical, pulp and paper, desalination, and refrigeration industries.

Past investigations on the boiling of falling liquid films have been undertaken by Chun and Seban (1971), Shah and Darby (1973), Fujita and Ueda (1978), Parken (1975), and Cerza (1983). Chun and Seban's work centered mainly on the evaporation of falling liquid films down vertical tubes, while Shah and Darby investigated primarily the effect of surfactants on the heat transfer in plane falling films. Fujita and Ueda reported extensive experiments on boiling in thin liquid films falling down vertical tubes. Considerable insight into the boiling phenomenon in thin films was reported by Parken (1975), Mesler (1979), and Cerza (1983).

Boiling in thin liquid films differs markedly from its pool boiling counterpart. In nucleate pool boiling, bubble growth is generally confined to the thickness of the superheated thermal layer next to the heated wall. A pool bubble grows both due to transient conduction from the thermal layer that a newly formed bubble tends to pick up, and due to evaporation from the superheated microlayer at the bubble's base. Once the pool boiling bubble departs from the thermal layer, it is surrounded by saturated liquid. Consequently, very little growth by means of thermal energy transfer can then occur. Other contributions to the overall heat transfer coefficient in nucleate pool boiling are associated with the turbulent convection caused by bubble agitation.

Bubbles in moving liquid films, on the other hands, have been observed by high-speed photography (Parken, 1975; Cerza, 1983) to continue to grow as they are being swept downstream by the falling film. These bubbles were seen to detach from their nucleating site at a diameter larger than the thickness of the liquid film itself and to grow to a diameter that was an order of magnitude larger than the film thickness. Parken (1975) estimated that the local heat flux at the bubble base might be several times larger than the average evaporative flux from the film's ambient surface. He concluded that the liquid film under the base of the bubble might be thinner than the surrounding ambient film thickness, thus exposing the bubble base to a larger thermal gradient caused by the smaller depth of the superheated liquid that exists below the free sur-

face. The fact that the bubble base in a moving thin liquid film is imbedded in the liquid was later demonstrated by Sernas and Stanzone (1981). In their experiments, soap bubbles were floated on a thin, dyed, water film down an inclined glass plate. Colored photographs of the bubbles showed that the tint under the bubble base was lighter than the shade of the ambient water film. This proved that the film under the bubble base was thinner than the ambient film. They also showed that the bubble's falling velocity was slower than the surface velocity of the film. It was then deduced by Cerza (1983) and later reported by Cerza and Sernas (1985) that the growth of a vapor bubble in a falling, laminar, superheated water film is caused by transient heat conduction through the bubble base. It was also shown that the bubble's leading semicircular base edge is continuously exposed to new superheated liquid because the bubble moves faster than the fluid beneath its base.

The present paper reports an experimental investigation of heat transfer in falling thin water films in the thermally developing entrance region. A simple mathematical model is developed for the film in the development region in order to assess the convective contribution to heat transfer in this region. Nucleate boiling data are then presented and compared with the convective heat transfer model in order to assess the influence of nucleate boiling and waviness in the film. The experimental data are also compared with existing data in the literature, and with a newly developed expression for the Nusselt number.

Experimental Facility

The experimental test section built for this study is shown in Fig. 1. It consisted of a 6.03 cm o.d. brass tube, 93 cm long, electrically heated on the inside for the first 25 cm of length. To the top of this tube was soldered a 6.03 cm o.d. hemispherical brass cap, which acted as a flow distributor. The brass tube and cap were enclosed inside a 15.2 cm o.d. Pyrex tube with blind aluminum flanges at the top and bottom. The water flow was introduced through a 1.27 cm o.d. copper tube protruding through the center of the top blind flange and sitting approximately 1 cm above the center of the hemispherical cap. The water was always close to the saturation temperature and it spread itself fairly uniformly over the cap and then flowed down the side of the brass tube. Flow uniformity was checked via peripheral wall temperature measurements. The water formed a pool at the bottom of the Pyrex tube where two 1 kW immersion heaters kept the pool and test chamber environment at saturated conditions. An outlet through the bottom blind flange led the water first to a recirculating pump

Contributed by the Heat Transfer Division and presented at the ASME-JSME Joint Thermal Engineering Conference, Honolulu, Hawaii, March 1983. Manuscript received by the Heat Transfer Division July 10, 1984.

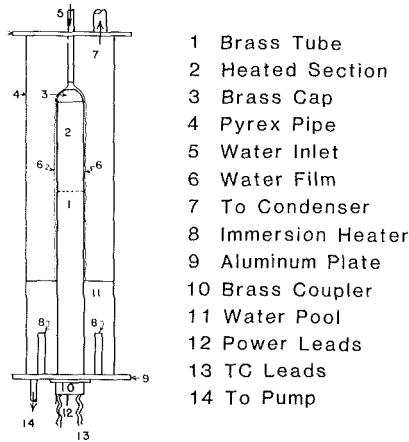


Fig. 1 Schematic of test chamber

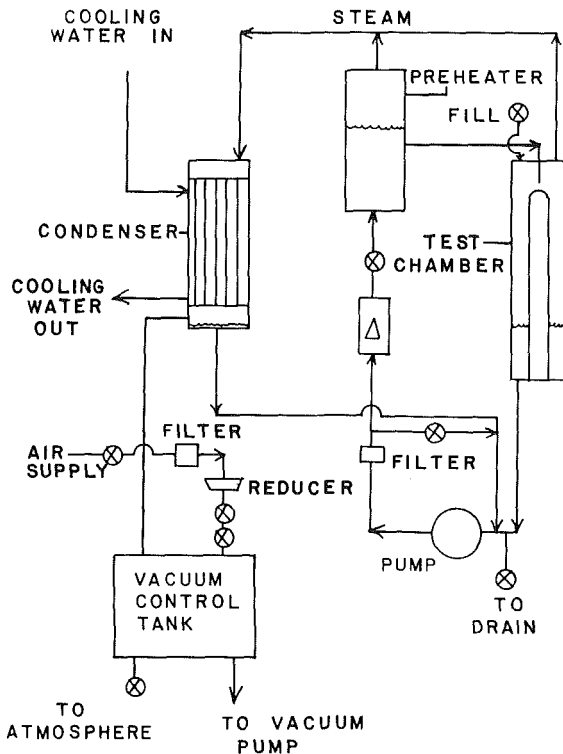


Fig. 2 Schematic of circulating system and system accessories

(see Fig. 2), then through a flowmeter to a preheater where sufficient heat was added to make the water saturated. A free surface existed within the preheater so that the vapor formed by the electric immersion heater separated from the liquid.

The vapor from the preheater and the test chamber was fed to a condenser (see Fig. 2) where it was condensed and introduced back into the recirculating loop upstream of the pump. The flow in the pipe supplying saturated water from the preheater to the test chamber was produced by a hydrostatic head difference between the free surface in the preheater and the hemispherical cap in the test chamber.

On the inner side of the heated brass tube (fabricated from two shells 0.5 cm thick) were thermocouples peened and imbedded with lead in drill holes in the brass walls. The thermocouple beads were located 1 mm beneath the outside tube surface. Conduction corrections were applied to the thermocouple readings in order to obtain the temperature at the outside surface of the tube. There were four levels of thermocouples and four thermocouples per level around the tube periphery in order to measure overall heat transfer conductance values. The levels of the thermocouples were 1.59, 6.67, 11.75, and 23.18 cm from the soldered seam separating the hemispherical cap from the tube. Heat flux to the heater on the inside of the tube was obtained via a calibrated 7 kW powerstat. The pressure in the test section was maintained by coupling the test section and condenser to a drum that could be maintained at a preset absolute pressure by an independent pressure control system. The ranges of operating conditions were as follows: Reynolds number from 670 to 4300, heat flux from 6 to 70 kW/m². The saturation temperature was kept constant at 100°C. The film itself was estimated to be approximately 0.2 to 0.6 mm thick depending on flow rate.

The experimental apparatus required approximately one hour to reach saturation conditions. An additional hour of vigorous boiling in the test chamber was required to completely purge the noncondensibles from the test chamber. The noncondensibles were driven out of the test chamber (and into the condenser) by the steam generated in the test chamber. Heat transfer test data were then collected by selecting a film flow rate and recording all wall temperatures at various wall heat fluxes.

Flow Field Observations for No Heat Flux

Visual observations of the liquid jet impinging on the hemispherical cap showed a very smooth flow distribution over the cap for the flow rates tested. As the film left the cap and flowed down the cylindrical side of the brass tube, there was a small distance over which the flow remained fairly laminar. The length of this laminar zone depended on the liquid film flow rate. The lower the flow rate the longer was the laminar region for the tested flow rates. It could not be determined whether very small flow rates would maintain a smooth region for very long lengths due to wetting problems of the film. It is doubtful whether very long laminar regions can be maintained due to inherent fluid instabilities that create waves in the film. For very small film flow rates, $Re < 20$, the film may appear to be smooth throughout flow lengths of practical

Nomenclature

g = acceleration due to gravity
 h = overall conductance
 $\equiv q_w'' / (T_w - T_s)$
 k = fluid thermal conductivity
 G_o = odd parabolic cylinder function
 Nu = Nusselt number = $h\delta/k$
 Pe = film Peclet modulus = $RePe = (4\Gamma/\mu)Pr$
 Pr = Prandtl number = $\mu C_p/k$
 \dot{q}_w = wall heat flux
 Re = Reynolds number = $4\Gamma/\mu$

T = temperature
 v = velocity component in y direction
 x = distance from wall into film (defined on Fig. 3)
 y = distance downstream
 α = thermal diffusivity
 Γ = mass flow rate per unit of circumferential length of tube, (kg/s)/m
 δ = film thickness = $[(3/4)(Re\mu^2/\rho^2g)]^{1/2}$

θ = dimensionless temperature = $(T - T_s)k / (\dot{q}_w \delta)$
 λ = eigenvalue
 μ = dynamic viscosity
 ρ = density

Subscripts

s = saturation condition
 w = wall
 δ = free surface

Table 1

Reynolds No.	Flow rate kgm ⁻¹ s ⁻¹	Length of laminar zone, cm
4400	0.309	3.8
3400	0.243	4.5
2800	0.199	5.7
2200	0.156	7.0
1600	0.113	7.6

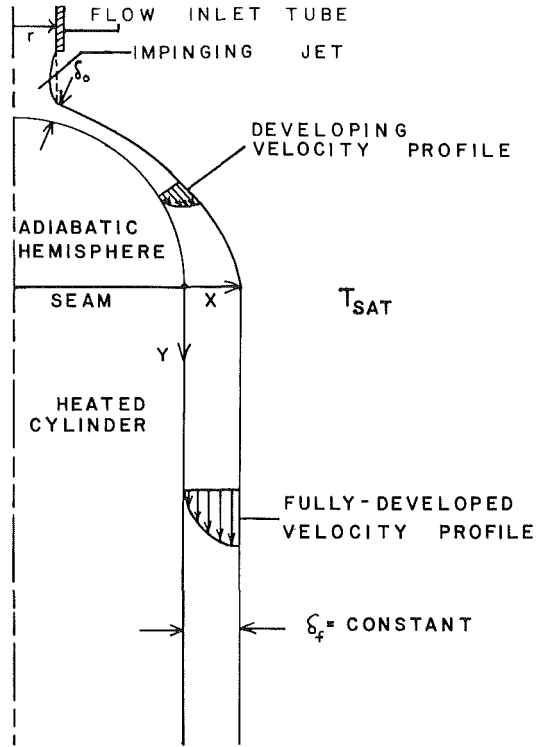


Fig. 3 Thin falling film model; film thickness not drawn to scale

importance (Benjamin, 1957; Hirshburg and Florschuetz, 1981a). Table 1 summarizes the approximate laminar entry region length observed in our apparatus at various flow rates. It should also be noted that for all rates tested there was always some laminar flow region present. This indicates that if a liquid falling film can be started very evenly and smoothly a laminar regime may be maintained for a short distance even though its Reynolds number is indicative of turbulent or transitional flow.

As the falling water film progresses down the brass tube the free surface starts to get wavy. Salazar and Marschall (1978) have concluded that for their range of flow rates tested, the wavy motion is of a two-dimensional nature for $200 < Re < 1500$. This conclusion was reached from detailed optical studies involving laser techniques. The region of wave formation from the laminar regime is now called the wavy-laminar regime since the waves do appear to be laminar. Ueda and Tanaka (1975) have shown from experimental studies that a parabolic profile for the velocity distribution beneath the wave is quite accurate. Farther down the tube the waves are seen to group closer together, i.e., wavelengths are shortened, and three-dimensional effects become apparent.

Analytical Solution of Thermal Entry Length (TEL)

Since the flow was observed to be laminar for some distance from the beginning of the heated section, it was reasonable to analyze the flow over the hemispherical cap and the heated

cylinder tube as a laminar film flow. The analysis for the film flow over the unheated hemispherical cap showed that the film was fully hydrodynamically developed by the time it reached the edge (seam) of the hemisphere at all $Re < 3000$. (This analysis is not presented in this paper. For more complete details, see Cerza (1983).) Thus the laminar film entered the cylindrical section with a fully developed velocity profile (as shown schematically in Fig. 3), and it began to be heated by a constant heat flux at the wall. The assumptions that went into the nonboiling, convective model of the film over the heated cylindrical section were:

- 1 the film thickness was constant at δ ;
- 2 surface evaporation over the length of the heated section was negligible (this assumption was verified using the evaporation criteria developed by Fujita and Ueda, 1978);
- 3 the velocity profile stayed fully developed (i.e., no radial component of velocity);
- 4 the cylindrical radius was much larger than the film thickness (i.e., Cartesian coordinates were adopted);
- 5 the liquid was homogeneous, isotropic, and incompressible;
- 6 axial conduction in the film was negligible; and
- 7 the density of vapor was small compared to the liquid density.

The energy equation for the film was simplified to the following for the coordinates shown in Fig. 3:

$$v \frac{\partial T}{\partial y} = \alpha \frac{\partial^2 T}{\partial x^2} \quad (1)$$

The boundary conditions were

$$\text{at } x=0, -k \frac{\partial T}{\partial x} = \dot{q}_w \text{ for } y > 0$$

$$\text{at } x=\delta, T = T_s \text{ for } y > 0$$

and

$$\text{at } y=0, T = T_s \text{ for all } x$$

It should be noted that the chosen boundary condition at the free surface produces a thermal gradient in the film at the free surface. This gradient, in turn, causes evaporation at the film surface. However, it is assumed that the amount evaporated does not substantially change the film thickness.

The variables were nondimensionalized in the following way:

$$\theta(x, y) = (T - T_s)k / (\dot{q}_w \delta)$$

$$\bar{x} = x / \delta$$

and

$$\bar{y} = y / \delta$$

When equation (1) was nondimensionalized and a parabolic (fully developed) velocity profile

$$v = \frac{g\rho}{\mu} \left(\delta x - \frac{x^2}{2} \right)$$

was used for v , the result became

$$\frac{\partial^2 \theta}{\partial \bar{x}^2} = \frac{3}{8} Pe (2\bar{x} - \bar{x}^2) \frac{\partial \theta}{\partial \bar{y}} \quad (2)$$

subject to

$$\text{at } \bar{x}=0, \frac{-\partial \theta}{\partial \bar{x}} = 1 \text{ for } \bar{y} > 0,$$

$$\text{at } \bar{x}=1, \theta = 0 \text{ for } \bar{y} > 0 \text{ and}$$

$$\text{at } \bar{y}=0, \theta = 0 \text{ for all } \bar{x}$$

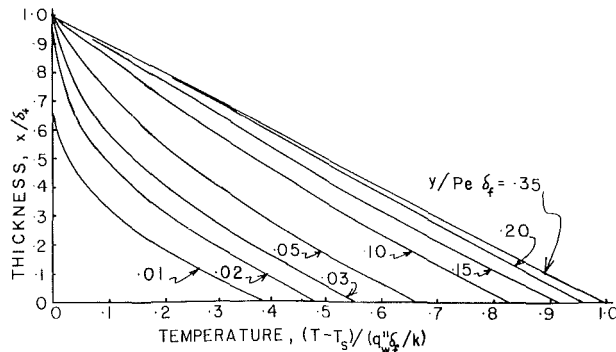


Fig. 4 Nondimensional temperature distribution in the laminar thermal entry length

The problem formulated in this way is an extension of the Graetz problem. In the present case, the free shear interface boundary condition has a constant temperature boundary associated with it, while the parallel flat plate counterpart has its zero shear surface (i.e., centerline) associated with an adiabatic boundary condition. This leads to odd functions instead of even functions in a power series solution similar to that made by Siegel et al. (1958) and Cess and Shaffer (1959). Details of the solution to equation (2) can be found in Cerza (1983). The solution is

$$\theta(\bar{x}, \bar{y}) = (1 - \bar{x}) + \sum_{n=0}^{\infty} B_n e^{-\left(\frac{8\lambda_n^2}{3Pe}\right)\bar{y}} G_o(\lambda_n, 1 - \bar{x}) \quad (3)$$

where

$$B_n = \frac{-(2/\lambda_n)}{\left[\frac{\partial}{\partial \lambda} \left(\frac{\partial G_o}{\partial \bar{x}}\right)\right]_{\bar{x}=0, \lambda=\lambda_n}}$$

$$G_o(\lambda_n, 1 - \bar{x}) = (1 - \bar{x}) + \sum_{m=2}^{\infty} b_{2m-1} (1 - \bar{x})^{2m-1}$$

and

$$b_{2m-1} = \frac{\lambda_n^2}{(2m-1)(2m-2)} (b_{2m-5} - b_{2m-3})$$

If $2m-5 < 0$ then $b_{2m-5} = 0$, and $b_1 = 1.0$. The first four terms of the series function are

$$G_o(\lambda_n, 1 - \bar{x}) = (1 - \bar{x}) - \frac{1}{6} \lambda_n^2 (1 - \bar{x})^3 + \frac{\lambda_n^2}{20} \left(1 + \frac{\lambda_n^2}{6}\right) (1 - \bar{x})^5 - \frac{\lambda_n^4}{42} \left(\frac{13}{60} + \frac{\lambda_n^2}{120}\right) (1 - \bar{x})^7 + \dots$$

The eigenvalues for the case of constant wall heat flux are:

$$\begin{array}{lll} \lambda_0 = 2.263, & \lambda_1 = 6.297, & \lambda_2 = 10.308, \\ \lambda_3 = 14.313, & \lambda_4 = 18.316, & \lambda_5 = 22.318 \end{array}$$

For $n > 5$, $\lambda_{n+1} = \lambda_n + 4.0$.

Figure 4 shows the dimensionless temperature profiles in the film as predicted by equation (3). The abscissa represents dimensionless superheat, $(T - T_s) / (\dot{q}_w \delta / k)$, while the or-

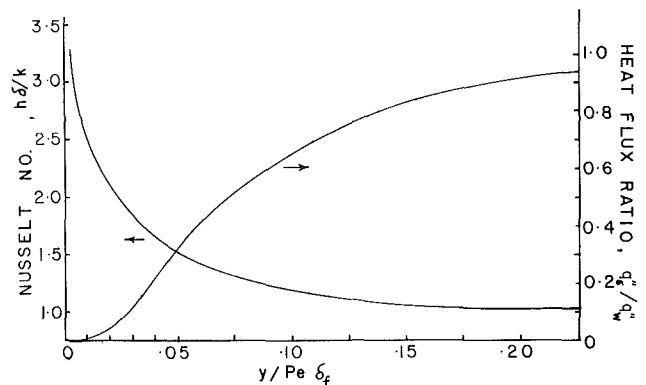


Fig. 5 Variation of the local Nusselt number with dimensionless distance downstream from the seam; also shown is the ratio of the surface heat flux to the wall heat flux at the same location on the heated tube

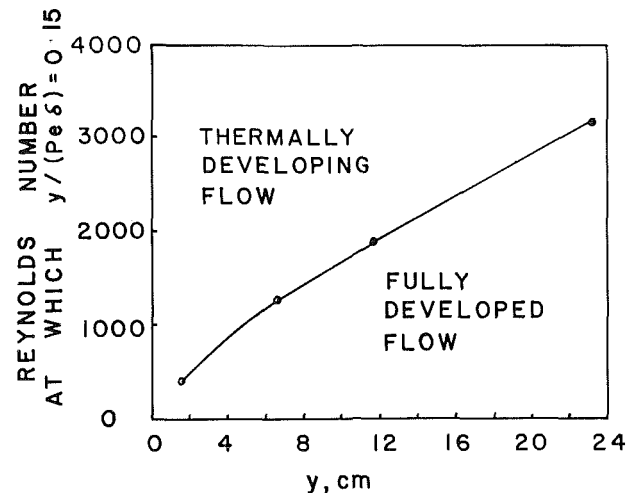


Fig. 6 Approximate distance downstream where the film temperature profile is fully established, i.e., linear; the values taken are for $y/(Pe\delta) = 0.15$

dinate is the dimensionless thickness, x/δ . The varying parametric curves represent the family of $y/(Pe\delta)$, which is the dimensionless location downstream of the origin based on flow conditions and fluid characteristics, i.e., film Peclet number Pe . As can be seen from Fig. 4, when $y/(Pe\delta) \geq 0.35$, a fully developed linear temperature profile is established providing, of course, there is no boiling or other disturbances. Actually, $y/(Pe\delta) \geq 0.15$ may be a good approximation to the developed state. Thus by knowing the heat flux, flow rate, and fluid properties, the film temperature profile in the laminar thermal entry length can be constructed.

Figure 5 shows the local Nusselt number versus the flow parameter $y/(Pe\delta)$. The local Nusselt number is defined as $Nu = h\delta/k$ where $h = \dot{q}_w / (T_w - T_s)$. Thus, $Nu = \dot{q}_w \delta / [k(T_w - T_s)]$, which can be evaluated from equation (3) by setting $\bar{x} = 0$, i.e.,

$$Nu = \left[1 + \sum_{n=0}^{\infty} B_n \exp\left(-\frac{8\lambda_n^2 \bar{y}}{3Pe}\right) G_o(\lambda_n, 1) \right]^{-1} \quad (4)$$

For fully developed laminar film flow heated by a constant heat flux (or whose hot surface is maintained at a constant temperature for that matter) the fully developed Nusselt number is $Nu_{\infty} = 1.0$.

Figure 5 also shows how the ratio of the heat flux at the free surface to that of the wall varies with $y/(Pe\delta)$. The heat flux at the free surface was calculated from the temperature gradient at $\bar{x} = 1$. This curve shows that thermal penetration of the wall

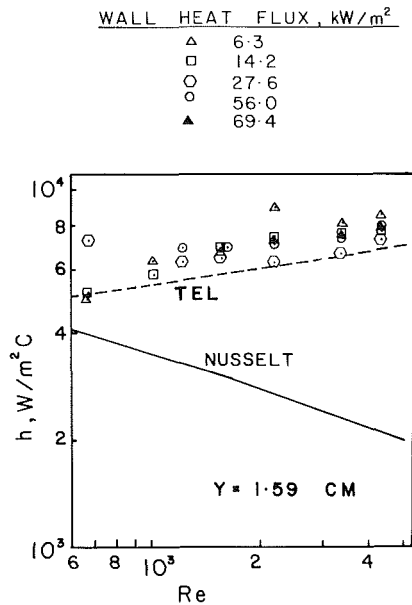


Fig. 7(a) Effect of Reynolds number on the overall heat transfer coefficient of the thin film 1.59 cm downstream from the seam

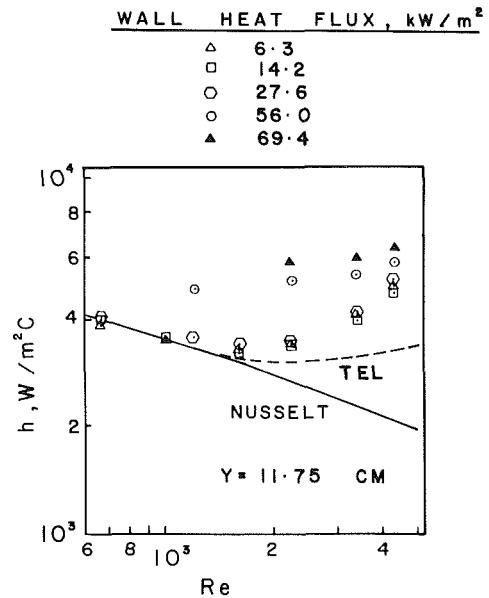


Fig. 7(c) Effect of Reynolds number on the overall heat transfer coefficient of the thin film 11.75 cm downstream from the seam

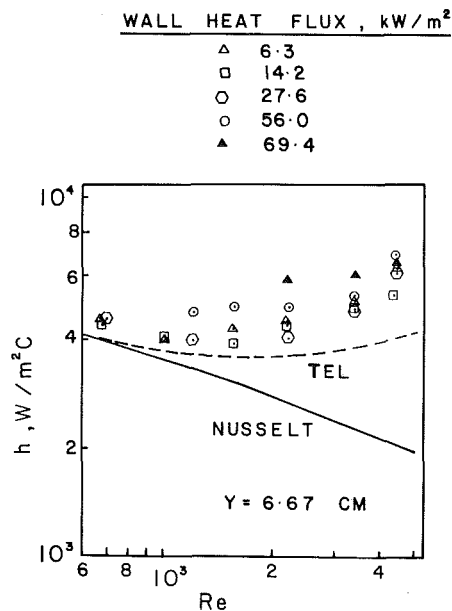


Fig. 7(b) Effect of Reynolds number on the overall heat transfer coefficient of the thin film 6.67 cm downstream from the seam

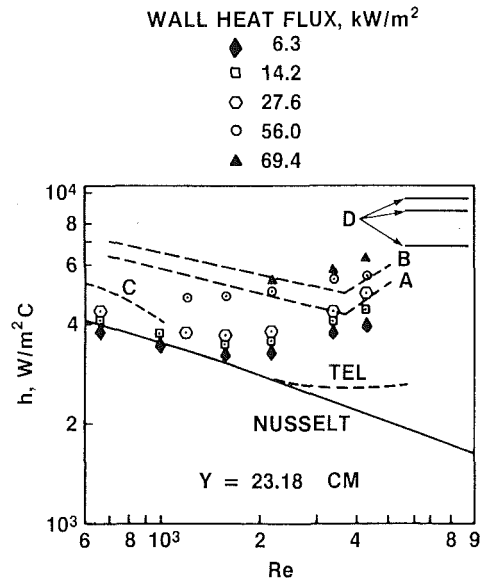


Fig. 7(d) Effect of Reynolds number on the overall heat transfer coefficient of the thin film 23.18 cm downstream from the seam. Also shown are results of other studies in the literature: (A) Chun and Seban (1971) (B) Fujita and Ueda (1978) (C) Hirshburg and Florschuetz (1981a) (D) Shah and Darby (1973)

heat flux through the film begins at $y/(Pe\delta) = 0.008$ and that the surface heat flux rises slowly to 94 percent of the wall heat flux at approximately $y/(Pe\delta) = 0.225$.

Figure 6 has been constructed to predict the existence of fully developed flow at any downstream location y , and Reynolds number. The four circles on the figure correspond to the four thermocouple locations in the test section. This figure graphically shows what the Re has to be at a chosen distance y , in order for $y/(Pe\delta)$ to be larger than 0.15.

Heat Transfer Results and Observations

For all the flow rates tested it was observed that heat fluxes below 14.2 kW/m^2 produced no nucleate boiling in the film. At 14.2 kW/m^2 only one feeble nucleation site was observed. As the heat flux increased, more sites became active, and at a heat flux of 56 kW/m^2 so many bubbles were growing in the

film that a significant portion of the film was covered with bubbles. Once nucleation had been achieved, the distance from the cap-tube seam to the location where the nucleation started shortened as the heat flux increased. Heat fluxes of 56 kW/m^2 and above were not used at low flow rates in order to prevent dry patches from forming on the heated tube.

The experimental heat transfer results for 100°C saturation conditions are shown in Figs. 7(a-d). Seven different flow rates and five different heat fluxes were investigated. The experimental data are shown as points, while the theoretical values of h derived from the thermal entry length (TEL) model of equation (3) are drawn in as dashed lines. The thermally fully developed laminar film solution due to Nusselt is shown as a solid line and is labeled "Nusselt."

Figure 7(a) shows the experimental data at the first ther-

mocouple location 1.59 cm downstream from the seam. The experimental data show no influence of the heat flux on the heat transfer coefficient because no boiling occurred on the tube this close to the leading edge. Otherwise, the data points seem to follow the trend of the TEL solution. Most data points fall above the TEL solution probably because the thermocouples this close to the seam read low due to some conduction heat transfer into the hemispherical cap at the seam.

Figure 7(b) shows the overall heat transfer coefficient at the second thermocouple location 6.67 cm downstream from the seam. The TEL solution merges with the Nusselt solution at low Re. At low heat fluxes (less than 27.6 kW/m^2) and low Re (less than 1800) the experimental data are close to the TEL solution. This agreement occurs because there is still little boiling on the tube at this axial location for low heat fluxes, and because the film was still laminar (see Table 1). For Re larger than 1800 and heat fluxes less than 27.6 kW/m^2 the heat transfer coefficient starts to increase above the TEL solution. This increase is caused primarily by the onset of film waviness, which is brought about by flow instabilities inherent in the liquid film, or by instabilities caused by bubble agitation. As the heat flux was increased to values greater than 27.6 kW/m^2 , a substantial increase in h above that of the TEL solution occurred at all Re tested. Agitation of the thin film by bubble nucleation is certainly one enhancement mechanism. However, a more significant mechanism is due to the growth of the many vapor bubbles via transient conduction through their bases, as was shown by Cerza and Sernas (1985).

At very large heat fluxes (69.4 kW/m^2), when the bubble population on the film is high, there appears to be only a slight increase in the heat transfer coefficient with Re. It seems that at these high heat fluxes the heat transfer mechanism is dominated by boiling, during which transient conduction at the bubble bases is much more important than the convective heat transfer mechanism that is dependent on the Reynolds number.

The data at the third thermocouple location shown in Fig. 7(c) exhibits the same general trends as the data at the second thermocouple location of Fig. 7(b). Again, at heat fluxes less than 27.6 kW/m^2 where little boiling occurred, reasonable agreement exists with the experimental data and the TEL solution for Re less than about 1800. For these same small heat fluxes, at Re greater than 1800, the heat transfer coefficient increases above the TEL solution. This increase in h is slightly larger in Fig. 7(c) than it is in Fig. 7(b) because the flow is wavier further down the tube. As the heat flux is increased beyond 27.6 kW/m^2 the increased bubble populations again enhance the heat transfer for all the flow rates tested.

The last thermocouple location and consequently the one that can be compared with fully developed data in the literature is shown in Fig. 7(d). The theoretical thermal entry length solution merges with the Nusselt solution for $Re < 2000$. For low heat fluxes and $Re < 1200$, the data compare well with the TEL (and Nusselt) model, i.e., the waviness in the film must still be small at these conditions. Curves A and B on Fig. 7(d) represent the nucleate boiling data correlations for thin falling films as presented by Chun and Seban (1971) and Fujita and Ueda (1978), respectively. The Chun and Seban data were taken at a distance of approximately 61 cm down a 2.86 cm o.d. vertical stainless steel tube that was heated by passing an electric current through it. Wall heat fluxes ranged from 22.4 to 30.0 kW/m^2 . Fujita and Ueda used a stainless steel tube 1.6 cm o.d., 0.093 cm thick, and obtained data 77 cm downstream. The heat fluxes for their curve ranged from 30 to 70 kW/m^2 . Below $Re = 3000$, the curves do not correspond well with the present data at low heat fluxes. The reason for this is that in our low heat flux tests, few active sites were present and consequently very little boiling occurred. Our flow field may not have been as disturbed as that of the

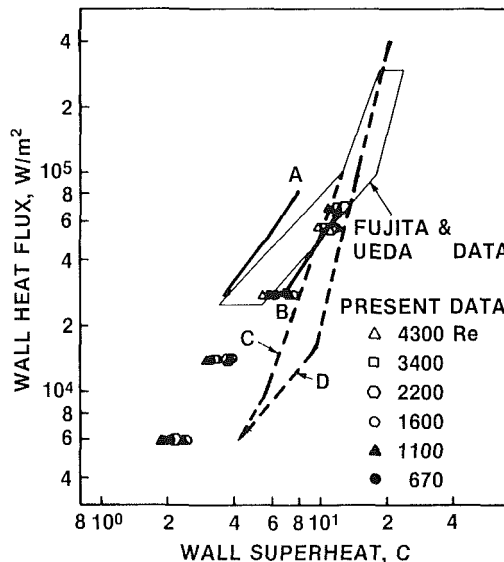


Fig. 8 A comparison of present data (taken 23.18 cm downstream from the seam) with data from the literature:

- (A) Shah and Darby (1973)
- (B) Marto et al. (1977)—1 mm thick horizontal film
- (C) Nishikawa et al. (1984)—pool boiling on vertical surface
- (D) Nishikawa et al. (1984)—pool boiling on horizontal surface

abovementioned authors, who collected their data much farther downstream where very wavy flow most likely had developed for the lower Reynolds numbers. The data of Struve (1967), who measured heat transfer coefficients approximately 5 cm past unheated entry lengths of 15, 30, 45, 60, 80, 100, and 120 cm, seem to indicate that the overall heat transfer coefficient increases continually with entry length at a fixed Reynolds number. Perhaps if the present experiment had a longer heated section the film coefficients would increase (due to increased flow waviness) and approach those of curves A and B. Above $Re = 3500$ the curves A and B correlate better with the present data. This higher Reynolds number regime may be getting just as “choppy” at 23.18 cm downstream as at 77 cm downstream. At higher heat fluxes ($56\text{--}69.4 \text{ kW/m}^2$) our data show the same magnitude of overall heat transfer coefficient as A and B but a different trend: a slight, almost linear increase past $Re = 1500$ for the range of flow rates tested. This trend is very similar to that obtained by Fujita and Ueda for heat fluxes of 160 kW/m^2 where vigorous boiling was observed.

Curve C in Fig. 7(d) shows the h predicted by Hirshburg and Florschuetz (1981a) for wavy films at $Re < 1000$. The frequency of the wave imposed on the fully developed flow field corresponded to the frequency occurring most often in their experiments at that Reynolds number. Even though their results are applicable to a limited Re range, their results do show the enhancement one can expect from the waviness of the film.

Also shown on Fig. 7(d) as lines marked D are the experimental results of Shah and Darby (1973), who studied the effects of surfactants on evaporative heat transfer falling water films on a rectangular plate. Their data for a zero concentration of surfactants were taken from their Fig. 5 using the English unit scales on that figure. The heat flux for the three lines shown in Fig. 7(d) were approximately 30, 55, and 80 kW/m^2 . These Shah and Darby heat transfer coefficients show no variation with Reynolds number, and appear to be slightly higher than our data extrapolated to higher Reynolds numbers.

In Fig. 8, our experimental data at the last thermocouple location are replotted on log-log coordinates of wall heat flux versus wall superheat. These coordinates are often used to pre-

sent boiling heat transfer results and are used in this figure to compare the present data with the data of others. It should first be noted that the film was boiling only at wall heat fluxes of 27.6 kW/m² and above, so that the data points shown for a heat flux of 6.3 and 14.2 kW/m² are data points for a strictly convective heat transfer mechanism. These convective points fall on a line of slope equal to approximately one. The boiling data points at heat fluxes of 27.6 to 69.4 kW/m² are the ones to be compared with other boiling studies, some of which were not of boiling falling films.

Figure 8 shows that our boiling data points fall around the lower limits of the experimental data of Fujita and Ueda (1978), who performed experiments on a boiling water film on vertical stainless steel tubes. This study is perhaps the closest reported study to ours in terms of geometry, Reynolds number, and emphasis on boiling. Their data, which fell within the outlined box in Fig. 8, were taken 77 cm below the start of the film. Since the lower limits of their data were taken at a Reynolds number of about 2200 (which is about the middle of our Re range) it is evident that our data match their data very well.

The solid line marked A on Fig. 8 represents the Shah and Darby (1973) data for no surfactants in a high Re falling film. Their data seem to be high just as they were high in Fig. 7(d).

The solid line marked B in Fig. 8 represents the data of Marto et al. (1977) for boiling in a thin (1 mm thick) stationary horizontal film of water. Since this solid line seems to be a good fit to our data, it shows that the magnitude of the heat transfer coefficient in the two distinctly different thin film experiments was about the same.

Pool boiling data from a vertical and horizontal surface are shown as dotted lines marked C and D, respectively, in Fig. 8. These data come from the recent pool boiling study of Nishikawa et al. (1984). It can be seen that at moderate heat fluxes the falling film produces higher heat transfer coefficients than pool boiling. It should also be noted that the slope of the pool boiling curves is much steeper than the line that would connect our falling film data points.

Heat Transfer Correlation

Since nucleate boiling in the thermal development region of a falling liquid film presents a new study to be added to the literature, an effort will now be made to determine a heat transfer correlation for that region. In the "Heat Transfer Results and Observations" section, it was disclosed that the heat transfer coefficient was dependent on the following:

- 1 the thermal entrance effect (TEL solution);
- 2 the film Reynolds number (film waviness);
- 3 the wall heat flux (nucleation/agitation); and
- 4 length downstream beyond the development region that might produce a different flow regime.

The correlation that will be developed for the Nusselt number, $h\delta/k$, will incorporate the first three effects. Comment will be reserved however, for the last-mentioned effect.

The heat transfer and fluid mechanics of the falling film ebullition problem certainly represents a very complex problem in which all of the above-mentioned effects interact with each other in very complex ways. The authors wish to point this out because their method of correlating the present data may only represent one style of data correlation. Since the objective of data correlation is to present a useful expression, the following form of the Nusselt number in thermally developing falling film ebullition is greatly simplified.

The expression we choose to correlate to is

$$Nu = [Nu]_{TEL} [1 + aRe^b] \left[1 + c \left(\frac{q_w - q_{incip}}{q_{incip}} \right)^d \right] \quad (5)$$

where Nu_{TEL} = a simplified single expression for the infinite

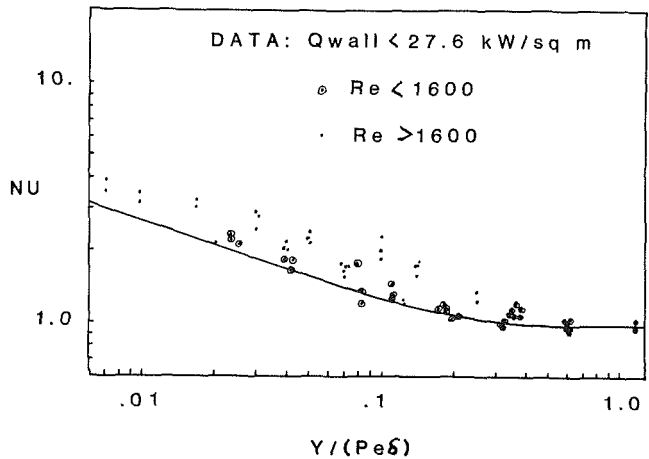


Fig. 9 Nusselt number versus $y/(Pe\delta)$ grouping for present data at low wall heat flux; solid line represents equation (6)

series of equation 4; q_w = wall heat flux, kW/m²; q_{incip} = boiling incipient heat flux, kW/m², which for the present experiment is fixed at 14.2 kW/m² (by choice); a, b, c, d are constants determined from the experimental data. The terms on the right signify the effects of the thermal entry length, film Reynolds number, and wall heat flux over that of boiling incipient heat flux, respectively.

For $y/(Pe\delta)$ greater than 0.008, the expression for the TEL solution, equation (4), can be approximated by

$$Nu_{TEL} \approx \left[1 - 0.72 \exp\left(-13.7 \frac{y}{Pe\delta}\right) \right]^{-1} \quad (6)$$

Here only the first eigenvalue is retained, and the constant before the exponent was slightly adjusted to fit the TEL solution. For $y/(Pe\delta)$ less than 0.008, more eigenvalue terms are required and the expression no longer is simple.

For heat fluxes less than 14.2 kW/m², no nucleate boiling was present, so the last expression in equation (5) is set to unity, and equation (5) can be rewritten as

$$Nu_{nonboiling} \approx \left[1 - 0.72 \exp\left(-13.7 \frac{y}{Pe\delta}\right) \right]^{-1} [1 + aRe^b] \quad (7)$$

Figure 9 shows a log-log plot of Nu_{ACTUAL} versus $y/(Pe\delta)$. The approximated Nu_{TEL} solution is also shown. Heat fluxes of up to 27.6 kW/m² are displayed. It can be seen that equation (6) matches the data for Re less than 1600 very well.

The next step was to rearrange equation (7) to

$$\left[\frac{Nu}{[Nu]_{TEL, EQ. 6}} - 1 \right] = aRe^b \quad (8)$$

and to determine a and b from a curve fit of those data points that have $Re > 1600$ and $q_w < 27.6$ kW/m². It was found that a was approximately equal to 1.9×10^{-7} and b approximately 1.7. Thus the correlation that fit the nonboiling data became

$$Nu_{nonboiling} \approx \left[1 - 0.72 \exp\left(-13.7 \frac{y}{Pe\delta}\right) \right]^{-1} \left[1 + (1.9 \times 10^{-7}) Re^{1.7} \right] \quad (9)$$

A similar procedure was used to evaluate the constants c and d in the third bracketed expression of equation (5) by curve fitting the data points in which boiling was present. The authors felt it desirable to correlate the boiling data with non-dimensional excess heat flux, that is, the wall heat flux in excess of the boiling incipient heat flux. The incipient heat flux q_{incip} is actually dependent on various parameters such as film

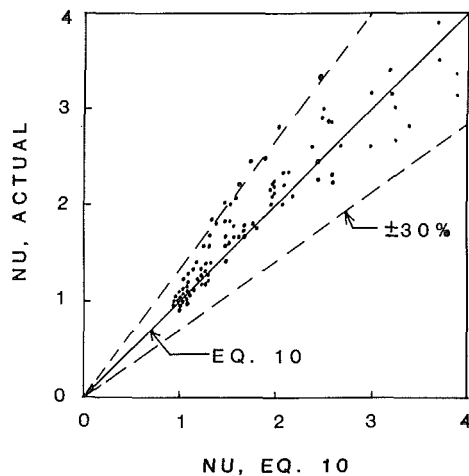


Fig. 10 Thermal development falling film Nusselt correlation with present data; data lying outside the 30 percent error interval were all at $y = 23.18$ cm downstream

Reynolds number (this establishes the nominal film thickness) and tube surface characteristics. A value of 14.2 kW/m^2 was chosen for the incipient heat flux because it was quite representative of the present data. The resulting curve fit for c and d yielded 0.05 and 1.36, respectively. Hence, equation (10) represents the expression for the correlation on the Nusselt number for nucleate boiling in thermally developing falling water films

$$\text{Nu} \approx \left[1 - 0.72 \exp\left(-13.7 \frac{y}{\text{Pe}\delta}\right) \right]^{-1} \left[1 + (1.9 \times 10^{-7}) \text{Re}^{1.7} \right] \left[1 + (0.05) \left(\frac{q_w - q_{\text{incip}}}{q_{\text{incip}}} \right)^{1.36} \right] \quad (10)$$

Figure 10 depicts the actual Nusselt number obtained from the present data versus the Nusselt number predicted by equation (10). The comparison is quite good. In addition, a statistical analysis revealed that the mean deviation of the actual data from equation (10) was ± 10 percent and the standard deviation was ± 16 percent. The number of data points analyzed was 104 with only eight lying outside ± 2 standard deviations; all at $y = 23.18$ cm downstream.

One last comment will now be made concerning the length downstream beyond the thermal entry length. It became apparent upon analyzing the data that a secondary influence from $y = 11.75$ to $y = 23.18$ cm downstream was present. The authors, therefore, believe that length enhances heat transfer by possibly causing a change in film flow characteristics such as a trip from wavy laminar to actual transitional flow. This might explain the slightly higher results by Fujita and Ueda, and the report of length enhancement by Struve. However, due to the lack of present data beyond $y = 23.18$ cm, this comment is only speculative.

Concluding Remarks

Boiling heat transfer in thin falling superheated water films was investigated. A theoretical model (TEL) for thermally

developing laminar film flows (assuming a fully developed parabolic velocity profile) was developed and used to solve for the overall heat transfer coefficient in a nonboiling thin film. This mathematical model was used as a baseline to compare with boiling thin film experimental data. At low heat fluxes, where only feeble boiling existed, and at $\text{Re} < 1800$ the model compared well with the experimental data. For the same low heat fluxes, but higher Reynolds numbers, the heat transfer coefficient increased above the TEL solution. This increase was attributed to increased film waviness brought about by increased film Reynolds number. As the heat flux was increased to levels where vigorous boiling was present in the thin film, further enhancement of the heat transfer coefficient occurred. This enhancement was attributed both to increased agitation of the film by the bubbles, and to transient conduction from the thin superheated bubble bases. Finally, a heat transfer correlation for the Nusselt number in the thermally developing region was presented.

References

- Benjamin, T. B., 1957, "Wave Formation in Laminar Flow Down an Inclined Plane," *J. Fluid Mech.*, Vol. 2, pp. 554-574.
- Cerza, M., 1983, "An Investigation Into the Mechanism for Nucleate Boiling in Thin, Falling Water Films," Ph.D. Dissertation, Rutgers University, New Brunswick, NJ.
- Cerza, M., and Sernas, V., 1985, "A Bubble Growth Model for Nucleate Boiling in Thin, Falling, Superheated, Laminar Water Films," *Int. J. Heat Mass Transfer*, Vol. 28, No. 7, pp. 1307-1316.
- Cess, R. D., and Shaffer, E. C., 1959, "Heat Transfer to Laminar Flow Between Parallel Plates With a Prescribed Wall Heat Flux," *Appl. Sci. Res.*, Sec. A., Vol. 8, p. 339.
- Chun, K. R., and Seban, R. A., 1971, "Heat Transfer to Evaporating Liquid Films," *ASME JOURNAL OF HEAT TRANSFER*, Vol. 93, No. 4, pp. 391-396.
- Fujita, T., and Ueda, T., 1978, "Heat Transfer to Falling Liquids Films and Film Breakdown—Part II. Saturated Liquid Films With Nucleate Boiling," *Int. J. Heat Mass Transfer*, Vol. 21, No. 2, pp. 109-118.
- Hirshburg, R. I., and Florschuetz, L. W., 1981a, "Laminar Wavy-Film Flow—Part I. Hydrodynamic Analysis," ASME Paper No. 81-HT-13.
- Hirshburg, R. I., and Florschuetz, L. W., 1981b, "Laminar Wavy-Film Flow—Part II. Condensation and Evaporation," ASME Paper No. 81-HT-14.
- Marto, P. J., MacKenzie, D. K., and Rivers, A. D., 1977, "Nucleate Boiling in Thin Liquid Films," *Solar and Nuclear Heat Transfer*, AICHE Symp. Ser., No. 164, Vol. 73, pp. 228-235.
- Mesler, R., 1979, "Nucleate Boiling in Thin Liquid Films," in: *Boiling Phenomena*, Vol. 2, S. van Stralen and R. Cole, eds., Hemisphere, Washington, DC, pp. 813-819.
- Nishikawa, K., Fujita, Y., Uchida, S., and Ohta, H., 1984, "Effect of Surface Configuration on Nucleate Boiling Heat Transfer," *Int. J. Heat Mass Transfer*, Vol. 27, No. 9, pp. 1559-1571.
- Parken, W., 1975, "Heat Transfer to Thin Water Films on Horizontal Tubes," Ph.D. Dissertation, Rutgers University, New Brunswick, NJ.
- Salazar, R. P., and Marschall, E., 1978, "Three-Dimensional Surface Characteristics of a Falling Liquid Film," *Int. J. Multiphase Flow*, Vol. 4, pp. 487-496.
- Sernas, V., and Stanzione, K., 1981, "Some Aspects of the Heat Transfer Mechanism During Boiling of Falling Water Films," AIAA 16th Thermophysics Conference, Palo Alto, CA, Paper No. AIAA-81-1064.
- Shah, B. H., and Darby, R., 1973, "The Effect of Surface on Evaporative Heat Transfer in Vertical Film Flow," *Int. J. Heat Mass Transfer*, Vol. 16, pp. 1889-1903.
- Siegel, R., et al., 1958, "Steady Laminar Heat Transfer in a Circular Tube With Prescribed Wall Heat Flux," *Appl. Sci. Res.*, Sec. A, Vol. 7, p. 386.
- Struve, H., 1967, "Heat Transfer to an Evaporating Falling Refrigerant Film," presented at the 12th Congress of the International Institute of Refrigeration, Madrid, Spain.
- Ueda, T., and Tanaka, H., 1975, "Measurements of Velocity, Temperature and Velocity Fluctuation Distributions in Falling Liquid Films," *Int. J. Multiphase Flow*, Vol. 2, pp. 261-272.

An Experimental Study of Convective Boiling in a Partially Heated Horizontal Channel With Offset Strip Fins

G. D. Mandrusiak

Research Assistant.

V. P. Carey

Associate Professor.

X. Xu

Research Assistant.

Department of Mechanical Engineering,
University of California,
Berkeley, CA 94720.

Measured local heat transfer data and visually observed two-phase flow behavior are reported for convective boiling of methanol and water in a partially heated horizontal channel with offset strip fins. In this study, a special test section was used that permitted direct visual observation of the two-phase flow while simultaneously measuring the convective boiling heat transfer coefficient at several locations along the channel. One wall of the channel was heated while the opposite and lateral walls were adiabatic. Measured local heat transfer coefficients on the heated portion of the channel wall were obtained for top heating and bottom heating of the horizontal channel. For the conditions examined here, the two-phase flow was in the stratified, wavy, or annular flow regime over almost the entire length of the channel. It was visually observed that virtually no nucleate boiling is present when the flow is in these regimes. A flow regime map is presented, which summarizes the observed two-phase flow characteristics. At the same quality and mass flux levels, the measured heat transfer coefficients for top heating and bottom heating were found to be virtually the same for the conditions examined here. In addition for the same quality and mass flux, the convective boiling heat transfer coefficients for top heating and bottom heating agree well with the results for comparable experiments with the channel oriented vertically. Hence, prior to dryout of the liquid film, the boiling heat transfer performance appears to be insensitive to channel orientation. Observed differences in the dryout conditions for top heating and bottom heating are also discussed.

Introduction

Offset strip fin geometries have been widely used for many years in compact heat exchangers for single-phase applications. Recently, however, it has become increasingly apparent that geometries of this type may also provide weight savings or improved performance in applications involving convective boiling. This has resulted in the increasing use of offset fin surfaces for evaporators in refrigeration, air-conditioning, and cryogenic systems. Convective boiling of a coolant in a channel with offset strip fins may also prove to be an effective means of cooling electronic components or fusion reactor walls under high heat flux conditions. It may also be possible to develop improved high-efficiency evaporators for desalination systems using offset fin geometries.

The need to understand the performance characteristics of these configurations better in the applications noted above has prompted several recent studies of convective boiling in offset strip fin geometries. In an early study, Panitsidis et al. (1975) measured the total heat transfer for a compact heat exchanger with offset strip fins operating as a thermosyphon boiler. Data were obtained using R-113 and isopropanol as the test fluids. They also developed a multiple-node analysis for boiling over one fin as a model of the transport. In this analysis, the local heat transfer coefficient was assumed to depend only on the local wall superheat. In a later study, Chen et al. (1981) refined this model to include the effect of flow velocity on heat transfer. Values of the total heat duty predicted by this model for compact heat exchangers were found to be in good agreement with measured results at moderate to high wall superheat.

Measurements of heat transfer coefficients for thermosyphon boiling of R-12 and R-22 in several offset strip fin geometries were also obtained by Galezha et al. (1976). They also proposed correlations relating heat flux and wall superheat, based on thermodynamic similitude.

The studies mentioned above all considered convective boiling at moderate to high wall superheat levels where nucleate boiling is expected to have an important effect on heat transfer. Flow boiling processes in a channel with offset strip fins at very low wall superheat levels have been investigated in a series of recent studies by Robertson (1979, 1982, 1984) and Robertson and Lovegrove (1983). For the conditions considered in these studies, nucleate boiling effects were negligible, and forced convective boiling was the dominant heat transfer mechanism. Measured local heat transfer coefficients were presented for nitrogen (Robertson, 1979) and R-11 (Robertson and Lovegrove, 1983). Film flow models were also proposed to predict boiling heat transfer coefficients for annular film-flow boiling in offset strip fin geometries (Robertson, 1982, 1984).

A film-flow model for forced convective boiling and film condensation in offset fin geometries was also proposed by Yung et al. (1980). The predictions of this model were found to agree well with available data for forced convective boiling in offset fin geometries.

In a very recent study, Carey and Mandrusiak (1986) experimentally investigated the two-phase flow and heat transfer during convective boiling in a partially heated vertical channel with offset strip fins. Visual observations of the flow through a transparent wall of the test section indicated the flow was in the annular film-flow regime over most of the length of the channel. Measured values of the local heat transfer coefficient were presented for convective boiling of water, methanol, and

Contributed by the Heat Transfer Division for publication in the JOURNAL OF HEAT TRANSFER. Manuscript received by the Heat Transfer Division December 13, 1985.

n-butanol at atmospheric pressure. A correlation for the local heat transfer coefficient for annular film-flow boiling was also derived from an approximate model of transport in the liquid film. The measured data were found to be in good agreement with the proposed correlation.

The studies described above have provided valuable insight into the nature of convective boiling processes in offset strip fin geometries. However, there are several aspects of the transport for these circumstances that have not been explored. In particular, all the investigations mentioned above have considered convective boiling only in vertical channels. None of these studies has examined the boiling heat transfer performance of offset fin geometries in horizontal channels.

In some applications, the orientation of the boiling channel may be dictated by considerations other than heat transfer. This is true in compact evaporators used in automotive air-conditioning systems, for example. Knowledge of the dependence of heat transfer performance on the channel orientation is important in applications of this type. Furthermore, geometries and flow conditions that are not strongly affected by the direction of the gravity vector are also expected to be least affected by the zero-gravity conditions encountered in spacecraft applications. For convective boiling in offset strip fin geometries, the studies described above provide no information about how the transport in horizontal channels differs from that in vertical flows.

The study described here was undertaken to determine the two-phase flow and boiling heat transfer characteristics for a horizontal channel with offset strip fins, and to compare them with corresponding results for vertical flows. In the configuration considered here, only one side of the channel was heated. Heating of a coolant channel on one side only may arise in electronics cooling and other thermal control applications. In addition, the results for one-sided heating also provide insight into the boiling mechanisms that occur when both sides are heated.

Experiments were conducted using a special test section that permitted us to observe visually the two-phase flow during convective boiling in the channel with offset strip fins. This

test section also permitted simultaneous measurement of local values of the convective boiling heat transfer coefficient in the channel. The flow was visually observed and heat transfer coefficients were measured over wide ranges of mass flux and quality. This study specifically focused on the behavior of flows at moderate to high quality levels where the two-phase flow is usually in a wavy or annular flow configuration. Measured values of the local heat transfer coefficient are presented for saturated flow boiling of water and methanol at atmospheric pressure. In this study, data were obtained for the channel positioned horizontally with the heated wall on the top and also with it on the bottom. The results of these horizontal tests are compared with a correlation which fits the data reported in a previous paper (Carey and Mandrusiak, 1986) for upward flow with the channel oriented vertically.

Experimental Apparatus

Experimental studies of the convective boiling process in an offset strip fin geometry were conducted using the test section shown in Fig. 1. One end of the rectangular copper slab shown in Fig. 1 was machined to form a surface with offset strip fins. This end of the copper slab fits into the assembly shown in Fig. 1 to form a channel with offset strip fins. The side walls of the channel are Teflon to minimize lateral heat loss, and the inner glass plate forms the top wall of the channel to permit visual observation of the boiling process all along the channel.

A thin coating of RTV silicone sealant was applied to the top edges of the fins to eliminate heat leakage to the glass cover plate. A second glass plate covers the inner one as shown in Fig. 1 to reduce heat losses from the top of the assembly. The channel formed by the Teflon side walls, inner glass plate, and copper slab is 1.91 cm wide, 3.8 mm high, and 45.7 cm long. The fins machined in the copper slab are 1.59 mm thick, 12.7 mm long in the flow direction, and extend to the top (glass) wall of the channel (3.8 mm high). The distance between adjacent fins is 7.94 mm. The hydraulic diameter based on the heated perimeter for this surface, d_{hp} , is 7.78

Nomenclature

A = constant in equation (6)
 A_f = surface area of fins in channel section of length L_c
 A_p = prime surface area of channel section of length L_c
 A_o = cross-sectional open area of channel
 c_p = specific heat at constant pressure
 d_h = hydraulic diameter based on wetted perimeter = $4A_o/P_w$
 d_{hp} = hydraulic diameter based on heated perimeter = $4A_o/P_H$
 f = friction factor
 F = flow regime parameter = $[\rho_g j_g^2 / (\rho_f - \rho_g) d_h g]^{1/2}$
 G = mass flux
 h = heat transfer coefficient
 H = dimension of fins from root to tip
 j_f = volume flux of liquid = $G(1-x)/\rho_f$
 j_g = volume flux of vapor = Gx/ρ_g
 k = fluid thermal conductivity
 k_c = conductivity of copper

K = flow regime parameter = $[\rho_g j_g^2 / (\rho_f - \rho_g) g \nu_f]^{1/2}$
 L = length of fin in the downstream direction
 L_c = length of channel section
 n = exponent in equation (6)
 p = pressure
 P_H = heated perimeter
 P_w = wetted perimeter
 Pr_f = liquid Prandtl number
 q'' = surface heat flux based on total heated surface area
 Re_f = liquid Reynolds number = $G(1-x)d_h/\mu_f$
 Re_g = vapor Reynolds number = Gxd_h/μ_g
 Re_{fp} = liquid Reynolds number based on heated perimeter = $G(1-x)d_{hp}/\mu_f$
 St = Stanton number = h/Gc_p
 t = fin thickness
 T_c = temperature in copper slab
 T_w = wall temperature of prime surface of channel
 T_M = bulk mean temperature of the coolant

T_{sat} = saturation temperature of coolant
 W_c = width of copper slab
 x = mass quality
 X_{tt} = Martinelli parameter for turbulent-turbulent flow = $[(dp/dz)_{FF} / (dp/dz)_{FG}]^{1/2}$
 μ = absolute viscosity
 ν = kinematic viscosity
 ρ = fluid density
 Ψ = parameter defined in equation (9)

Subscripts

f = liquid properties or corresponding to liquid flow alone in the channel
 g = vapor properties or corresponding to vapor flow alone in the channel
 fp = corresponding to liquid flow alone in the channel heated on one side only
 F = friction component of pressure gradient
 tp = corresponding to two-phase flow conditions

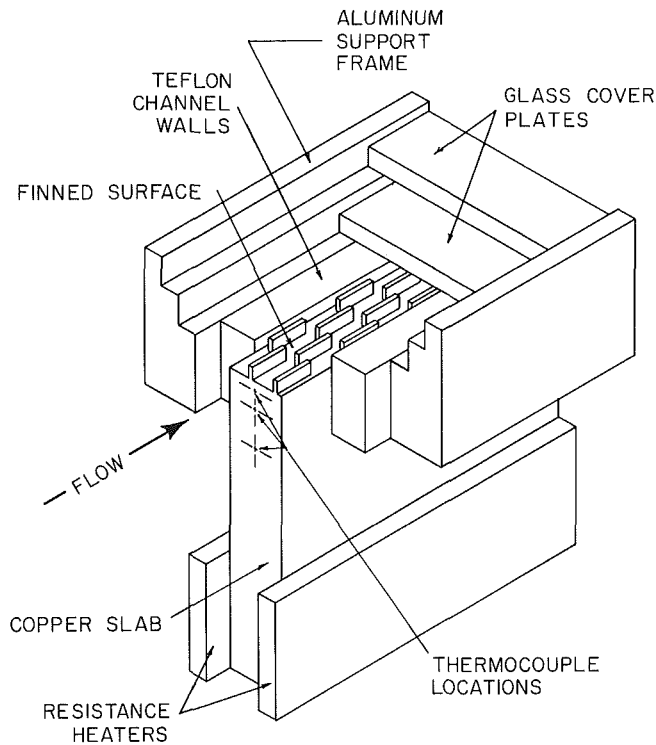


Fig. 1 Cutaway view of test section

mm, and the hydraulic diameter based on wetted perimeter, d_h , is 5.15 mm. The fin dimensions and spacing were chosen to be slightly larger than those typically used in most applications, to allow better visual observation of the flow, and to make it easier to machine the fins precisely.

The copper slab was heated at the bottom end by two electrical resistance heaters, which provided a virtually uniform heat input along the length of the channel. Heat is conducted from the heaters along the copper slab to the finned surface where it is transferred to the fluid in the channel. The back of the copper slab and heat assembly was completely enclosed in insulation so that heat leakage to the surroundings was negligible.

Thermocouples were embedded in the copper slab, as indicated in Fig. 1, to determine the temperature gradient and surface temperature at three locations along the length of the channel. Small diameter thermocouples (0.9 mm beads) were used to measure the temperature distribution in the copper. These thermocouples were installed in precisely located 1-mm-dia holes drilled to the centerline of the copper slab. The spacing between the first and third thermocouples was sufficiently large (19 mm) that uncertainty in the bead locations was small compared to the separation distance. For the boiling data, the temperature difference between the first and third thermocouples was typically greater than 4°C . A least-squares fit of a straight line to the three thermocouple readings was used to determine the temperature gradient and surface temperature. Generally, all three points fit the line very closely. The measured temperature gradient was used to calculate the heat flux to the surface.

Thermocouples were also installed through the channel wall at these locations to measure the local fluid temperature. This result was combined with the calculated heat flux and surface temperature to compute the local heat transfer coefficient. The thermocouple wires and bead inserted into the flow were small compared with the channel dimensions and visual observations indicated that the flow was not significantly affected by them. Thermocouples in the test section were read using an

Omega two-pole selector switch and a precision Fluke digital readout with a resolution of $\pm 0.06^\circ\text{C}$. With this configuration, the uncertainty in the heat flux is estimated to be ± 6 percent and the uncertainty in the heat transfer coefficients is estimated to be ± 11 percent.

A small pump was used to deliver a steady flow of liquid from a reservoir to the test section. The flow leaving the test section went to a water-cooled condenser. Liquid coolant leaving the condenser was returned to the reservoir. The power to heaters in the reservoir, and the condenser water flow rate could be varied to control the temperature of the liquid at the inlet to the test section. The flow rate to the test section was set using a flow control valve.

The liquid flow rate to the test section was measured using a Cole Parmer rotameter. This flow meter was calibrated at several liquid temperatures so that the effect of property variation with temperature was taken into account. Separate rotameter calibration curves were determined for water and methanol. The pressure at the exit of the test section was measured with a calibrated gauge. Local pressures along the channel were not directly measured, but they could be inferred from measurements of the local saturation temperature downstream of the onset of saturated boiling.

Prior to running the heat transfer experiments, the finned surface of the copper slab was cleaned with a mild acid solution and then thoroughly rinsed before filling the system with the test liquid. This procedure kept the finned copper surface clean and free of tarnish throughout the test program. It also helped maintain consistency in the nucleation characteristics of the surface.

In the experiments reported here, the channel was positioned horizontally, with the heated wall either on the top or bottom. Power to the heaters in the test section was controlled by two rheostats which could be adjusted to vary the heat input to the channel. For some of the tests, photographs of the two-phase flow at various locations along the channel were taken using a Pentax 35 mm camera with a 50 mm macro lens and a high-speed strobe flash unit.

Experimental Procedure

Prior to running the convective boiling experiments, the single-phase heat transfer characteristics were determined for the channel with offset strip fins in the test section. Local heat transfer coefficients were measured at low heat flux and high inlet subcooling where no vaporization occurs. After setting the flow rate and power to the heaters at the desired levels, the system was allowed to stabilize for 10 to 15 min before thermocouple and flow readings were taken. The resulting single-phase heat transfer data for water are plotted in nondimensional form in Fig. 2. The measured heat transfer coefficients represented in Fig. 2 are average values over the heated perimeter of the channel at each downstream location where thermocouple measurements were made. These values of h were iteratively calculated from the energy balance relation

$$W_c L_c k_c \nabla T_c = h (A_p + \eta_F A_F) (T_w - T_M) \quad (1)$$

where ∇T_c is the measured local temperature gradient in the copper and η_F is the fin efficiency given by

$$\eta_F = \frac{\tanh(MH)}{MH}, \quad M = \sqrt{2h(t+L)/k_c tL} \quad (2)$$

In Fig. 2, the transition from laminar to turbulent flow appears to occur at a Reynolds number of about 750. The correlations shown in Fig. 2 for the laminar and turbulent ranges are least-squares fits to the data below $Re_{fp} = 750$ and above $Re_{fp} = 750$, respectively.

In the flow boiling experiments, the system was allowed to stabilize at the selected power and flow settings before flow visualization photographs or data were taken. The thermocou-

ple readings and the liquid flow rates were recorded in the same manner as for the single-phase data. The test fluid entered the channel as subcooled liquid. The downstream location where saturated nucleate boiling first began was determined by visually inspecting the flow in the channel. This zero quality point was typically 20 to 30 hydraulic diameters downstream of the inlet. Boiling heat transfer data were obtained at the two thermocouple locations nearest the exit end, which were 44 and 66 hydraulic diameters downstream of the inlet. For comparable conditions, heat transfer data for these two locations were only slightly different, suggesting that inlet effects were not significant beyond 40 hydraulic diameters (15 fin lengths) downstream.

As for single-phase flow, the local heat transfer coefficient was obtained by iteratively solving equations (1) and (2) using the measured data at the location of interest. However, in the saturated boiling experiments, T_M in equation (1) was equal to T_{sat} , the saturation temperature of the coolant. The local boiling heat transfer coefficients calculated in this manner are average values over the heated perimeter of channel. Fin efficiencies for the boiling data points were typically near 90 percent for the conditions tested here.

The mass flux G was determined from the flow meter reading and the geometry of the channel. The quality at the two uppermost thermocouple locations was determined from any energy balance over the portion of the channel where saturated boiling occurred. In this energy balance, the heat input to the flow along the channel was determined from the heat flux computed at the thermocouple locations. These calculations using the measured data thus indicated the value of h_{ip} which corresponded to specific values of x and G .

Values of h_{ip} were determined for convective boiling of water and methanol for values of quality and mass flux in the ranges of $0.03 < x < 0.7$ and $4 < G < 60 \text{ kg/m}^2\text{s}$. The values of mass flux considered in these experiments are relatively low. However, mass flux levels between 20 and $60 \text{ kg/m}^2\text{s}$ are commonly encountered in evaporators for small refrigeration and air-conditioning systems and other thermal control applications in which a low evaporator pressure drop is desirable. Specific examples include automotive air-conditioning evaporators, and evaporator cold plates for electronics cooling (see Carey et al., 1987). Hence, the results of these experiments relate most directly to applications of this type. Values of heat flux up to 150 kW/m^2 were used in these experiments. The estimated uncertainty in the measurements is ± 5 percent for G , ± 9 percent for x , and ± 11 percent for

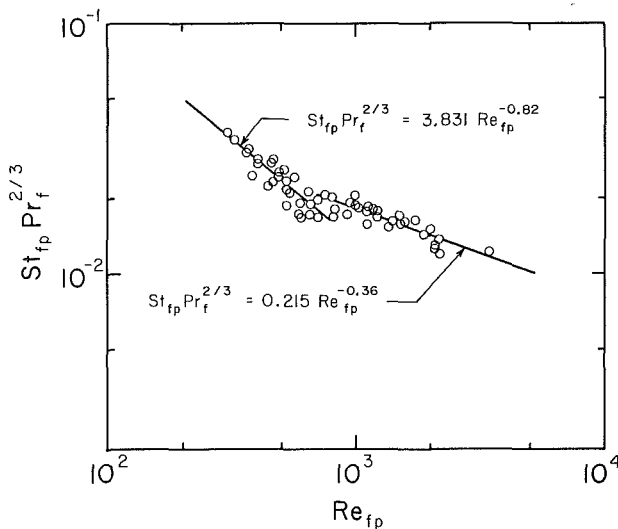


Fig. 2 Single-phase heat transfer data for test section channel

h_{ip} . The reproducibility of the heat transfer data was checked and found, in all cases, to be better than the uncertainty in the measurements.

Results and Discussion

By observing the flow at various angles through the glass wall of the channel, it was possible to distinguish between different two-phase flow regimes in the offset fin matrix. The observed flow regimes for points at which heat transfer measurements were made are indicated on a flow regime map of the type proposed by Taitel and Dukler (1976) for horizontal co-current flow in Fig. 3. Heat transfer data were taken for conditions corresponding to stratified, wavy, or annular flow. Note that data for both top and bottom heating are shown.

The transition from stratified to wavy flow is observed in the lower part of Fig. 3 where the data for stratified and wavy flow are plotted in terms of X_{tt} and K . Here, X_{tt} is the Martinelli parameter for turbulent-turbulent flow

$$X_{tt} = [(dp/dz)_{Ff} / (dp/dz)_{Fg}]^{1/2} \quad (3)$$

and K is defined as

$$K = \left[\frac{\rho_g j_g^2 j_f}{g(\rho_f - \rho_g) \nu_f} \right]^{1/2} \quad (4)$$

The single-phase pressure gradients in equation (3) are evaluated as

$$(dp/dz)_{Ff} = - \frac{2f_f G^2 (1-x)^2}{\rho_f d_h} \quad (5a)$$

$$(dp/dz)_{Fg} = - \frac{2f_g G^2 x^2}{\rho_g d_h} \quad (5b)$$

Although some of our data correspond to liquid film Reynolds numbers less than 500, it is expected that interfacial waves, interaction with bubbles or entrainment, and impingement on the fins will cause the liquid film to have at least a weakly turbulent character, even at lower Reynolds numbers. Virtually all of our heat transfer data correspond to vapor Reynolds numbers, above 2000. Hence, all our data are treated as if they are in the turbulent-turbulent regime. This is also consistent with most previous treatments of flow-boiling data for round tubes (see, for example, Bennett and Chen, 1980).

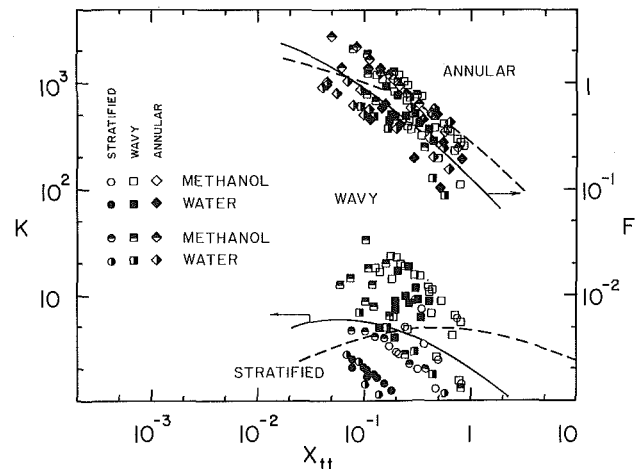


Fig. 3 Two-phase flow regimes during convective boiling in a horizontal channel with offset strip fins. The open and solid symbols correspond to top heating whereas the half-filled symbols designate bottom heating. The solid curves denote the approximate transitions based on visual observations. The broken curves indicate the transitions proposed by Taitel and Dukler (1976) for round tubes.

In equations (5a) and (5b), the single-phase friction factors are determined using the modified Reynolds analogy with the heat transfer correlation determined experimentally for turbulent flow in this geometry

$$f_f/2 = St_f Pr_f^{2/3} = A Re_f^{-n} \quad (6a)$$

$$f_g/2 = St_g Pr_g^{2/3} = A Re_g^{-n} \quad (6b)$$

The single-phase friction factor determined in this way is not the same as that for the entire fin matrix, which includes the effect of form drag on the fins. The modified Reynolds analogy relation accounts only for the wall shear in the channel formed by two adjacent fins. Also, since the wall shear acts around the entire channel perimeter, the hydraulic diameter based on heated perimeter in the heat transfer correlation is replaced by the hydraulic diameter based on wetted perimeter.

Combining equations (3), (5), and (6), it can be shown that

$$X_{tt} = \left(\frac{\rho_g}{\rho_f}\right)^{1/2} \left(\frac{\mu_f}{\mu_g}\right)^{n/2} \left(\frac{1-x}{x}\right)^{1-n/2} \quad (7)$$

Equation (7) with $n = 0.36$ was used to calculate X_{tt} for the experimental data shown in Fig. 3.

The solid curves in Fig. 3 indicate the approximate location of flow regime transitions, based on visual observations. The transition from stratified to wavy flow is approximately the same as that proposed by Taitel and Dukler (1976) for horizontal flow in a continuous channel. However, for the offset fin geometry, the exact position of the transition is slightly different.

The transition from wavy to annular flow is observed in the upper part of Fig. 3, where the data for wavy and annular flow are plotted in terms of X_{tt} and F . Here, F is defined as

$$F = \left[\frac{\rho_g j_g^2}{(\rho_f - \rho_g) d_{hg}} \right]^{1/2} \quad (8)$$

For the offset fin geometry studied here, the observed transition from wavy to annular flow is approximately the same as that indicated on the Taitel and Dukler (1976) flow regime map for horizontal channel flow. The transition curve for the offset fin geometry is in a slightly different position and has a slightly steeper slope, but the differences are not large.

It can be also seen in Fig. 3 that the transitions from stratified to wavy flow and from wavy to annular flow are not very distinct. Symbols for adjacent regimes are mixed together in the transition regions, with no clear dividing line. The solid curves should therefore be interpreted as estimates of the approximate transition conditions in this figure.

During the convective boiling process, the flow appeared to be in the bubbly regime very near the location of the onset of saturated boiling, with bubble nucleation visible both on the channel floor and on the fins. A very short distance downstream, the flow had undergone a transition to slug flow, and a short distance thereafter, the transition from slug flow to stratified, wavy, or annular flow was observed. At high flow rates and high heat flux levels, the flow went directly from slug to annular flow, while at low values of these parameters, stratified or wavy flow was observed before a transition to an annular film flow. Because of the rapid transition to one of these three regimes, virtually all of our measured heat transfer data are in the stratified, wavy, or annular flow regime.

A photograph of the annular two-phase flow observed during the convective boiling of methanol is shown in Fig. 4. For this experiment, $G = 22.5 \text{ kg/m}^2\text{s}$, and at the thermocouple location indicated by the arrow, $x = 0.13$ and $h_{tp} = 6.00 \text{ kW/m}^2\text{K}$. Much of the time the flow looked like the relatively undisturbed annular film flow shown in Fig. 4. However, intermittently, wave disturbances would travel downstream, making the flow appear more chaotic for brief intervals. In

general, the annular flow observed in our experiments was virtually the same in appearance as the vertical annular flow observed by Carey and Mandrusiak (1986) in similar experiments.

It can be seen in Fig. 4 that there is virtually no nucleate boiling present, even though the superheat of the prime surface is over 4°C . In a few locations, bubbles can be observed in the corner where the fin meets the glass or copper surface. The convective component of heat transport is expected to be weaker, and the liquid film is thicker in these corner regions. Consequently, there will be less tendency to suppress nucleation there. Hence, it is not surprising that nucleation persists at a few points in these locations, even though it has been thoroughly suppressed along the flat surfaces of the channel.

The experimentally determined variations of h_{tp} with x for various G values are shown in Figs. 5–8. Water data for bottom heating and top heating of the channel are shown in Figs. 5 and 6, respectively. Methanol data for the same two heating conditions are shown in Figs. 7 and 8. The variation of h_{tp} with x is shown for low to moderate values of G in these plots. Additional data were obtained for higher values of G , but the systematic variation of h_{tp} with x was not determined.

For both top and bottom heating, the measured value of h_{tp} is seen to increase with increasing G and x for both water and methanol. For each fluid and heating circumstance, the data obtained at higher values of mass flux were consistent with the

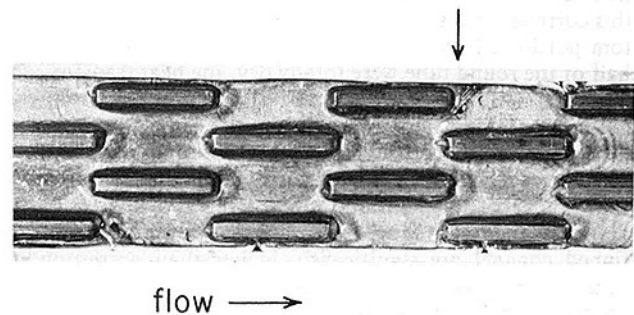


Fig. 4 Photograph of annular film flow boiling of methanol in a bottom-heated horizontal channel with offset strip fins at $G = 22.5 \text{ kg/m}^2\text{s}$ and $q'' = 27.8 \text{ kW/m}^2$. At the thermocouple location indicated by the arrow, $x = 0.13$ and $h_{tp} = 6.00 \text{ kW/m}^2\text{K}$.

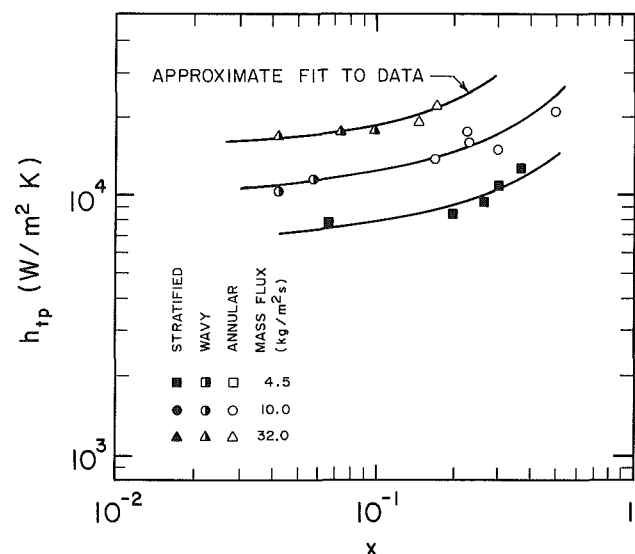


Fig. 5 Measured local heat transfer coefficients for convective boiling of water in a horizontal bottom-heated channel

trends observed in Figs. 5–8. The shading of each symbol in Figs. 5–8 indicates the flow regime visually observed for each data point. It can be seen that stratified flow was observed only at very low values of mass flux. At higher mass flux levels, a transition from wavy to annular flow is generally observed as the quality increases.

When Figs. 5 and 6 are compared, the results for water indicate that, at the same G and x values, the values of h_{tp} for bottom heating and top heating are essentially the same. The h_{tp} values for bottom heating are slightly higher for given values of G , but the difference between the curves is comparable to the uncertainty in the measurements (± 11 percent in h_{tp}).

Likewise, the results in Figs. 7 and 8 indicate that, for methanol, the measured h_{tp} obtained at specified x and G values for top heating and bottom heating are very close. The results differ slightly at lower quality, but, as for the water data, the deviation is less than the uncertainty in our measurements.

In addition to experimental data, Fig. 7 also shows the variation of the convective boiling heat transfer coefficient predicted by the Shah (1976) correlation for a horizontal round tube with the same hydraulic diameter as the channel used in our experiments. The variation of h_{tp} was calculated using the Shah correlations for the heat flux and mass flux values measured in our experiments.

For horizontal flow, and Shah correlation accounts for the fact that the upper portion of the tube wall may be at least partially dry. Consequently, the average value of h_{tp} predicted by this correlation may be somewhat lower than that for the bottom portion of the channel alone. However, even if the top half of the round tube were totally dry, the heat transfer coefficient over the lower wetted half of the wall would only be twice the average value predicted by the Shah correlation. It can be seen in Fig. 7 that, for comparable conditions, the heat transfer coefficient for the offset fin geometry is as much as four times that for the round tubes. Even allowing for partial dryout of the round tube, the h_{tp} values for the bottom of the finned channel are significantly higher than corresponding values for the bottom of a round tube. The data in Fig. 8 for the top of the channel are similarly higher than the corresponding round tube results.

In addition, for both fluids tested, the curves for both top heating and bottom heating agree well with the trends in the

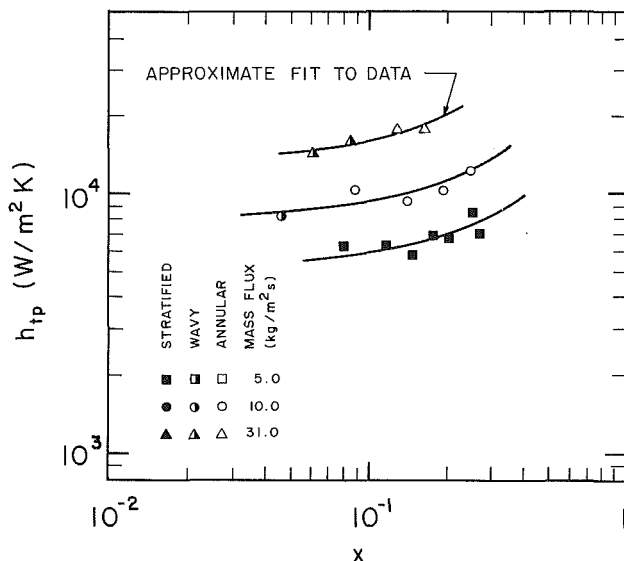


Fig. 6 Measured local heat transfer coefficients for convective boiling of water in a horizontal top-heated channel

heat transfer data obtained in comparable earlier experiments with the channel oriented vertically (see Carey and Mandrusiak, 1986). Apparently, for the conditions studied here, the heat transfer coefficient is not very sensitive to the direction of the gravity vector.

Based on an approximate model of the transport on the liquid film, Carey and Mandrusiak (1986) derived the following correlations for the heat transfer coefficients for annular film-boiling in a partially heated vertical channel:

$$\Psi = \left(\frac{h_{tp}}{h_{fp}} \right) \frac{4.74 \sqrt{A} \tan^{-1} [0.149 \sqrt{\text{Re}_{fp}} \text{Pr}_f \sqrt{d_h/d_{hp}}]}{\text{Re}_{fp}^{n/2} \text{Pr}_f^{1/6} (d_{hp}/d_h)^{n/2}} \quad (9a)$$

$$= \left[1 + \frac{20}{X_{ii}} + \frac{1}{X_{ii}^2} \right]^{1/2} \quad (9b)$$

where n and A are constants from equation (6) and X_{ii} is given by equation (7). For the fin geometry studied here, $n = 0.36$ and $A = 0.215$. For a vertical partially heated channel with the same strip-fin geometry used in the present study, Carey and Mandrusiak (1986) found that the measured values of h_{tp} in the churn-flow and annular flow regimes agree well with the correlation given in equation (9).

The measured water and methanol heat transfer data obtained here for horizontal flows in the wavy and annular film-flow regimes are plotted in terms of Ψ and $1/X_{ii}$ in Figs. 9 and 10. For all the data in Figs. 5–8 and the data indicated by square and circular symbols in Figs. 9 and 10, the heated surface of the channel appeared to be thoroughly wetted with liquid. Even for top-heated wavy flow, the fins were fully wetted and periodic waves would wet the top of the channel when they hit the upstream end of the fins. Some additional data for water were also obtained at higher quality conditions where the heated surface was not completely wetted with liquid. These data are represented by triangular symbols in Fig. 9. In Figs. 9 and 10, the solid symbols represent top heating and the open symbols represent bottom heating. It can be seen that when the surface is thoroughly wetted, the data for both flow regimes and the two different heating conditions agree very well with correlation (9).

The good agreement is somewhat expected for the data in the annular film-flow regime since horizontal annular flow can only be achieved when the vapor shear is much stronger than gravitational forces. The orientation of the channel relative to the gravity vector will then be of little importance, and, consequently, the heat transfer coefficient for the channel in the vertical and horizontal positions will be the same.

Since gravity usually plays a more important role in the

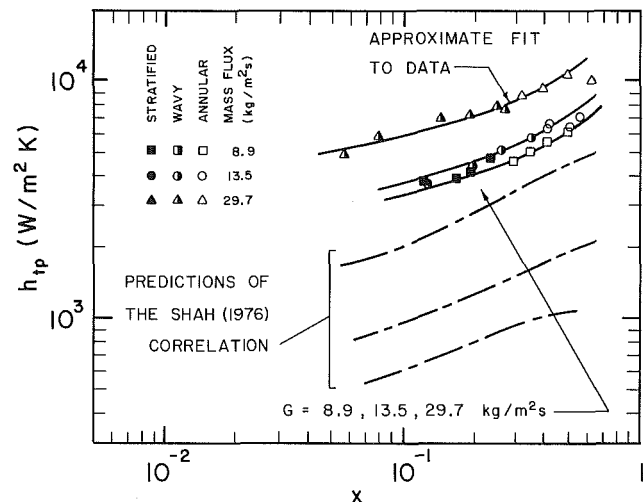


Fig. 7 Measured local heat transfer coefficients for convective boiling of methanol in a horizontal bottom-heated channel

wavy-flow regime, good agreement with correlation (9) for conditions in this regime is not generally expected. However, as seen in the flow regime map in Fig. 3, the wavy flows observed in our experiments are very close to the transition between wavy and annular flow. Hence, gravity effects, although present, may not be very strong, and the vapor shear may dominate the flow behavior. If the effects of gravity are not large for these conditions, the transport again may not be sensitive to the orientation of the channel. Changing the channel position from vertical to horizontal may simply convert a vertical churn flow to a horizontal wavy flow, which is only slightly different in behavior.

It can also be seen in Fig. 9 that when the surface is partially dry, the heat transfer performance may be significantly reduced below that for a fully wetted surface. In general it was observed that when partial dryout occurred, as the quality increased, the fraction of the surface that was dry increased and the local heat transfer coefficient decreased. This trend is reflected in the partial dryout data shown in Fig. 9 as decrease in the measured Ψ as $1/X_{tt}$ increases. As indicated in Fig. 9, for top heating, the initial appearance of dry patches on the heated surface was generally found at values of x (and $1/X_{tt}$) that were lower than those for bottom heating. This was somewhat expected since gravity thins the liquid film on the top of channel and thickens it on the bottom making the top surface more prone to dryout.

Our limited data for stratified flow were not plotted in Figs. 9 and 10 because they were not well correlated by equation (9b). This was somewhat expected since the stronger effects of gravity for these conditions alter the morphology of the two-phase flow such that an annular flow analysis is not applicable.

Conclusions

Measurements of local heat transfer coefficients have been obtained for convective boiling in a horizontal channel with offset strip fins that was heated on one side only. Heat transfer data have been reported for convective boiling of water and methanol for top heating and bottom heating of the channel. In addition, the two-phase flow in the channel was visually observed and photographed during the convective boiling process to determine the flow regime at the locations where heat transfer data were obtained.

Visual observations indicated that for the relatively low

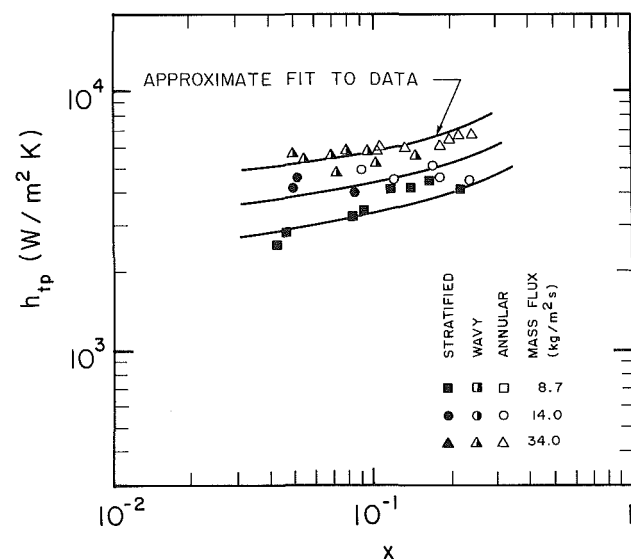


Fig. 8 Measured local heat transfer coefficients for convective boiling of methanol in a horizontal top-heated channel

pressure conditions considered here, the two-phase flow entered the stratified, wavy, or annular flow regime a short distance downstream of the beginning of saturated boiling. For the flows in the stratified, wavy, or annular flow regimes, nucleate boiling was suppressed over virtually all of the heated surface. The dominant boiling heat transfer mechanism in these regimes was convective evaporation of the liquid film. Visual observations indicated that the transitions from stratified to wavy and wavy to annular flow occur at approximately the same conditions as those indicated on the map of Taitel and Dukler (1976) for horizontal flow in continuous channels.

At the same values of G and x , the measured values of convective boiling heat transfer coefficient, for top heating and bottom heating were essentially the same. This was observed to be true for both the water and methanol data. For methanol, the measured heat transfer coefficients for these configurations at low to moderate quality were found to be as much as four times the values predicted by the Shah (1976) correlation for convective boiling in a horizontal round tube at the same heat flux, quality, mass flux, and hydraulic diameter.

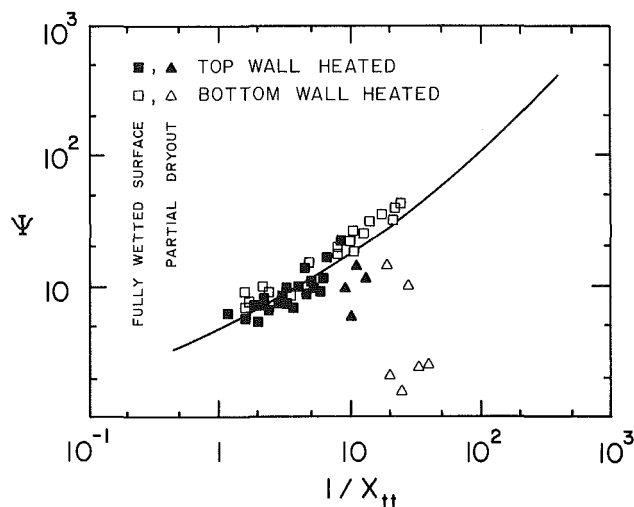


Fig. 9 Comparison of the measured heat transfer data for water with correlation (9) of Carey and Mandrusiak (1986). The data shown are for flows in the wavy or annular flow regimes.

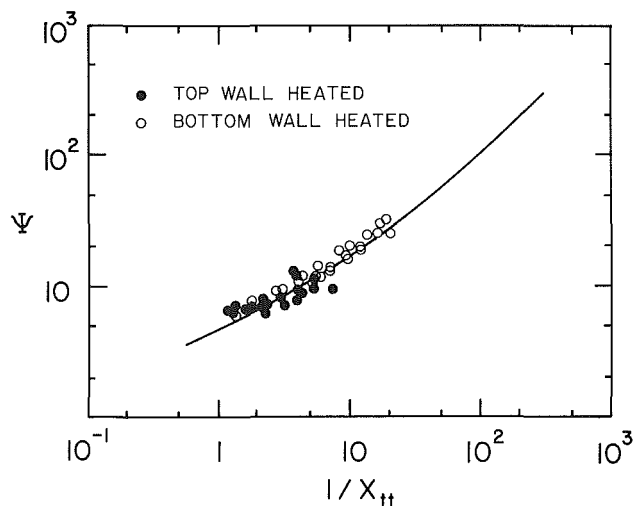


Fig. 10 Comparison of the measured heat transfer data for methanol with correlation (9) of Carey and Mandrusiak (1986). The data shown are for flows in the wavy or annular flow regimes.

These results suggest that, when the heated portion of the tube is fully wetted, use of geometries of this type may provide a significant enhancement of the convective boiling heat transfer coefficient over a round tube under comparable conditions. In addition, for both fluids tested, the variations of h_{tp} with G and x for top heating and bottom heating all agree well with trends in the data reported by Carey and Mandrusiak (1986) for similar earlier experiments with the channel oriented vertically.

The heat transfer data obtained here for horizontal flow in the wavy and annular film-flow regimes were also found to agree very well with the correlation proposed by Carey and Mandrusiak (1986) for annular flow convective boiling in a partially heated vertical channel with offset strip fins. The very good agreement between the horizontal data and the corresponding heat transfer results for vertical flow implies that for these circumstances, the boiling heat transfer performance is not sensitive to channel orientation with respect to gravity.

The trends described above were observed for data obtained at conditions where the heated surface was thoroughly wetted with liquid. In addition to the fully wetted results, some data were also obtained for higher quality conditions where portions of the heated surface were dry. For the same flow and heat flux conditions, partial dryout was generally found to occur at lower quality in top-heating experiments than in bottom heating ones because of the tendency of the liquid to form a thicker film on the bottom of the channel. When partial dryout occurred, as the quality increased, a larger portion of the surface was dry, and the measured heat transfer coefficients dropped further and further below the values indicated by the correlation of Carey and Mandrusiak (1986). Hence, the predictions of this correlation are not expected to hold at very high values of quality where appreciable portions of the heated surface are likely to be dry. At low to moderate qualities in the wavy and annular flow regimes, where the surface is fully wetted, this correlation is expected to predict the heat transfer coefficient with good accuracy. These observations indicate that, while the heat transfer performance for these flow conditions is virtually independent of channel orientation at low to moderate quantities, at high qualities, the heat transfer may vary with channel orientation because of its effect on dryout.

Acknowledgments

The authors wish to acknowledge support for this research by the National Science Foundation under research grant No. CBT84-51781. The assistance of Sue Bavonese in preparation of the manuscript is also appreciated.

References

- Bennett, D. L., and Chen, J. C., 1980, "Forced Convective Boiling in Vertical Tubes for Saturated Pure Components and Binary Mixtures," *AIChE Journal*, Vol. 26, pp. 454-461.
- Carey, V. P., and Mandrusiak, G. D., 1986, "Annular Film-Flow Boiling of Liquids in a Partially-Heated Vertical Channel With Offset Strip Fins," *International Journal of Heat and Mass Transfer*, Vol. 29, pp. 927-939.
- Carey, V. P., Mandrusiak, G. D., and Roddy, T., 1987, "Analysis of the Heat Transfer Performance of Offset Strip Fin Geometries in a Cold Plate Operating as Part of a Two-Phase Thermosyphon," *Proceedings of the 1987 International Symposium on Cooling Technology for Electronic Equipment*, Honolulu, Hawaii, pp. 565-582.
- Chen, C. C., Loh, J. V., and Westwater, J. W., 1981, "Prediction of Boiling Heat Transfer Duty in a Compact Plate-Fin Heat Exchanger Using the Improved Local Assumption," *International Journal of Heat and Mass Transfer*, Vol. 24, pp. 1907-1912.
- Galezha, V. B., Usyukin, I. P., and Kan, K. D., 1976, "Boiling Heat Transfer With Freons in Finned-Plate Heat Exchangers," *Heat Transfer—Soviet Research*, Vol. 8, pp. 103-110.
- Panitsidis, H., Gresham, R. D., and Westwater, J. W., 1975, "Boiling of Liquids in a Compact Plate-Fin Heat Exchanger," *International Journal of Heat and Mass Transfer*, Vol. 18, pp. 37-42.
- Robertson, J. M., 1979, "Boiling Heat Transfer with Liquid Nitrogen in Brazed-Aluminum Plate-Fin Heat Exchangers," *AIChE Symposium Series*, Vol. 75, pp. 151-164.
- Robertson, J. M., 1982, "The Correlation of Boiling Coefficients in Plate-Fin Heat Exchanger Passages With a Film-Flow Model," *Proceedings, 7th International Heat Transfer Conference*, Vol. 6, pp. 341-345.
- Robertson, J. M., 1984, "The Prediction of Convective Boiling Coefficients in Serrated Plate-Fin Passages Using an Interrupted Liquid-Film Flow Model," *ASME HTD-Vol. 34*, pp. 163-171.
- Robertson, J. M., and Lovegrove, P. C., 1983, "Boiling Heat Transfer With Freon 11 (R11) in Brazed Aluminum Plate-Fin Heat Exchangers," *ASME JOURNAL OF HEAT TRANSFER*, Vol. 105, pp. 605-610.
- Shah, M. M., 1976, "A New Correlation for Heat Transfer During Boiling Flow Through Pipes," *ASHRAE Transactions*, Vol. 82, pp. 66-86.
- Taitel, Y., and Dukler, A. E., 1976, "Model for Predicting Flow Regime Transitions, in Horizontal and Near-Horizontal Gas-Liquid Flow," *AIChE Journal*, Vol. 22, pp. 47-55.
- Yung, D., Lorenz, J. J., and Panchal, C., 1980, "Convective Vaporization and Condensation in Serrated-Fin Channels," *ASME HTD-Vol. 12*, pp. 29-37.

Experimental Measurement of Water Evaporation Rates Into Air and Superheated Steam

M. Haji

Dept. of Mechanical Engineering,
Washington State University,
Pullman, WA 99164

L. C. Chow

Dept. of Mechanical Engineering,
University of Kentucky,
Lexington, KY 40506

The rates of evaporation of water from a horizontal water surface into a turbulent stream of hot air or superheated steam at different free-stream mass fluxes and modulated temperatures were experimentally measured. The pressure of the free stream was atmospheric. For steam, the experimental results are mostly within 10 percent of the available analytical results. Two previous experimental results are about 50 percent and 300 percent higher than the analytical results. For air, the measured evaporation rates are consistently higher than the analytical results. An estimate of the conduction heat transfer from the walls of the test section to water was made for several air tests. If the conduction heat transfer were subtracted from the total heat transfer, the measured evaporation rates are actually quite close to the analytical results. The present experiment also confirms the existence of a temperature, called the inversion temperature, below which the water evaporation rate is higher in air than in steam, but above which the opposite is true. The inversion temperature is in good agreement with the analytical prediction. The results for both air and superheated steam show that a certain scaled expression for the evaporation rate is independent of the free-stream mass flux, also in agreement with the analytical prediction.

Introduction

Since the beginning of the twentieth century, the evaporation of water in air has received considerable attention due to its widespread use in drying, air conditioning, and film cooling. Many experiments concerning water evaporation into air were performed using flat pans (Lurie and Michaloff, 1936, Shepherd et al., 1938), wetted-wall columns (Barnet and Kobe, 1941; Gilliland and Sherwood, 1934), and water droplets (Ranz and Marshall, 1952). However, there have been much fewer experiments performed with superheated steam as the drying medium. Experimental studies of steam drying in various situations have shown higher drying rates in superheated steam than in air at the same temperature and mass flow rate of the free stream. For the case of drying with superheated steam, the water removed during the drying process becomes a part of the drying medium whereas, in air drying, the moist air must ultimately be removed.

Wenzel and White (1951) experimentally provided a quantitative basis for comparing steam and air as drying media for granular materials that are not temperature sensitive. Their results indicated that higher drying rates and thermal efficiencies are possible when drying with superheated steam rather than with air. Chu et al. (1959) studied the evaporation of water into superheated steam-air mixtures. They reported that the drying rate increases as the percentage of superheated steam in the mixture increases. Yoshida and Hyodo (1966) demonstrated that superheated steam can provide an excellent medium for drying food products. Steam drying allows a higher retention of nutrients and a higher evaporation rate as compared to air at the same temperature and mass flow rate.

Chu et al. (1953) conducted an experimental investigation of the evaporation of three liquids, water, one-butanol and benzene, by direct contact with their superheated vapors. For all three liquids, they reported significantly higher rates of evaporation with superheated vapor than with air except when the superheated vapor temperature is relatively close to the saturation temperature.

Yoshida and Hyodo (1970) carried out an investigation of the water evaporation rate into air, humid air, and superheated steam and concluded that, for a constant mass flow rate, there is a temperature, called the inversion temperature, at which the evaporation rates at different degrees of humidity are the same. Below this inversion temperature, the evaporation rate decreases as the humidity increases, and above it there is a reversed situation. Using a wetted-wall column with countercurrent flow of water and air, humid air, or superheated steam, they confirmed this relation and had determined the inversion temperature to be 175°C.

Chow and Chung (1983a) explained the physical reason for the existence of the inversion temperature for laminar flow of air, steam, or a mixture of both over a horizontal water surface. The inversion temperature is due to the combined effects of higher heat transfer coefficients for steam drying and the interfacial temperature depression by the presence of air for air drying. Based on this, they demonstrated that for the same mass flux of the free steam, and at lower free-stream temperatures, water evaporates faster in air than in humid air and superheated steam. However, the trend is reversed at higher free-stream temperatures. The inversion temperature, as defined, is around 250°C.

Trommelen and Crosby (1970) also reported an inversion temperature of 250°C from their experimental investigation of evaporation of water from drops. Their drops were small in size and the free-stream Reynolds number was about 100. Hence, the flow was laminar over most of the drop surface.

Chow and Chung (1983b) conducted an investigation of the rate of evaporation of water for turbulent flow. In their method of prediction, they utilized the Couette flow approximation and the 1/3 rule for variable property effects. They considered the steady-state evaporation of water into a turbulent stream of air, humid air, or superheated steam at atmospheric pressure. Assumptions were made that the water-fluid interface is flat and stationary and no energy is supplied from beneath the interface. Thus the energy required for the evaporation of water must come from the free stream itself. They also explained the existence of an inversion

Contributed by the Heat Transfer Division for publication in the JOURNAL OF HEAT TRANSFER. Manuscript received by the Heat Transfer Division December 23, 1985.

temperature, which was again due to the same reason as for laminar flow. However, for turbulent flow, the inversion temperature was determined to be around 190°C.

There have been serious disagreements among the previous experimental data on the rate of evaporation of water into a stream of superheated steam. A comparison of the experimental results of Chu et al. (1953) and Yoshida and Hyodo (1970) with the analytical results of Chow and Chung (1983b) illustrates the disagreements. Yoshida and Hyodo (1970) have measured evaporation rates of water that are about 50 percent higher than the analytical prediction of Chow and Chung (1983b). The experimental results of Chu et al. (1953) are about 300 percent higher. These discrepancies indicate that more careful experiments should be done to determine the validity of the previous experimental and analytical studies.

The objective of the present experimental work is to study the rate of evaporation of water from a horizontal surface into a turbulent stream of air or superheated steam at different free-stream mass flow rates and temperatures at atmospheric pressure.

Analysis

In the analytical prediction of water evaporation from a horizontal water surface into a turbulent stream of hot air, humid air, and superheated steam by Chow and Chung (1983b), it was assumed that the water interface is flat and stationary and no heat is supplied from beneath the interface. Also, convection heat transfer is the only mode of heat transfer. Chow and Chung derived two equations for a water surface of length L , one for the average evaporation rate of water into air and humid air

$$\frac{\dot{m}_{wo}L^{0.2}}{\dot{m}_{\infty}^{0.8}} = 0.0359Sc^{-0.4}\ln(1+B_m)(\rho/\rho_{\infty})^{0.8}\mu^{0.2} \quad (1)$$

and the other for the average evaporation rate of water into pure superheated steam

$$\frac{\dot{m}_{wo}L^{0.2}}{\dot{m}_{\infty}^{0.8}} = 0.0359Pr^{-0.4}\ln(1+B_h)(\rho/\rho_{\infty})^{0.8}\mu^{0.2} \quad (2)$$

In equations (1) and (2), B_m and B_h are the mass transfer driving potential and heat transfer driving potential, respectively, and are given by

$$B_m = \frac{m_o - m_{\infty}}{1 - m_o}, \quad B_h = \frac{i_{\infty} - i_o}{i_{fg}} \quad (3)$$

The plots shown in Fig. 1 are for the rates of evaporation of water into three different compositions of the free stream having the same mass flux. The three compositions are air, superheated steam, and equal percentages by mass of air and superheated steam. The evaporation rate curves for the three compositions of the free stream do not intercept at the same point. This is contrary to a statement made by Yoshida and Hyodo (1970) who stated that, at the inversion temperature,

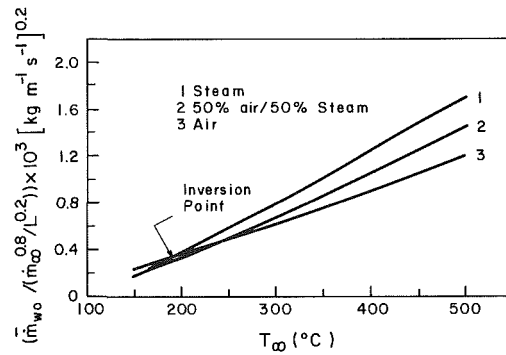


Fig. 1 Evaporation rates for different free-stream fluids

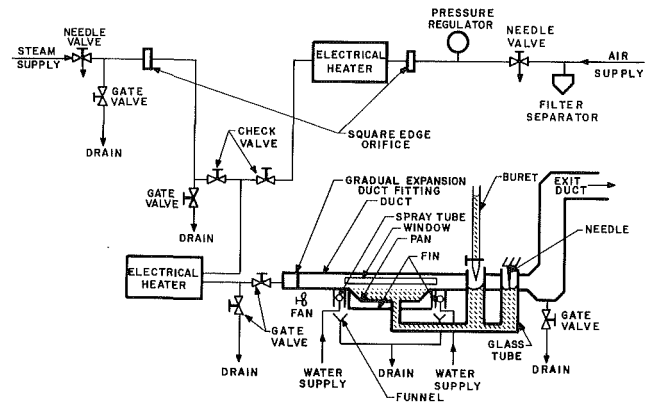


Fig. 2 Experimental apparatus schematic

the rates of evaporation of water into a free stream having the same mass flux are the same for all compositions of the free stream.

Apparatus

The experimental apparatus, shown in Fig. 2, consisted of the following: the air and steam supply system, the heating system, the test section, and the water evaporation rate measurement system.

Air and Steam Supply System. Compressed air at 722 kPa (90 psig) and steam line at 515 kPa (60 psig) were available next to the experimental apparatus. To measure the air or steam flow, two square-edged orifices were used. The air was first sent through a filter/separator unit before being throttled to the pressure regulator, and the steam was throttled to the system by a needle valve to prevent or reduce possible fluctuations in the steam line.

Four gate valves were installed at the proper locations for drainage. Another gate valve was put in front of the test sec-

Nomenclature

B = driving potential
 c_p = specific heat of fluid, $J kg^{-1} ^\circ C^{-1}$
 D = binary mass diffusion coefficient, $m^2 s^{-1}$
 i = enthalpy, $J kg^{-1}$
 i_{fg} = latent heat of vaporization, $J kg^{-1}$
 k = thermal conductivity, $W m^{-1} ^\circ C^{-1}$

L = length of water surface, m
 m = mass fraction of steam
 \dot{m} = mass flux, $kg m^{-2} s^{-1}$
 Pr = Prandtl number = $\mu c_p / k$
 Re = Reynolds number = $\rho u_{\infty} L / \mu$
 Sc = Schmidt number = $\mu / \rho D$
 u = fluid velocity, $m s^{-1}$
 T = temperature, $^\circ C$
 μ = dynamic viscosity of fluid, $N s m^{-2}$

ρ = density of fluid, $kg m^{-3}$

Subscripts

h = heat transfer
 m = mass transfer
 o = water interface
 w = water
 ∞ = free stream

Superscript

$\bar{}$ = average over L

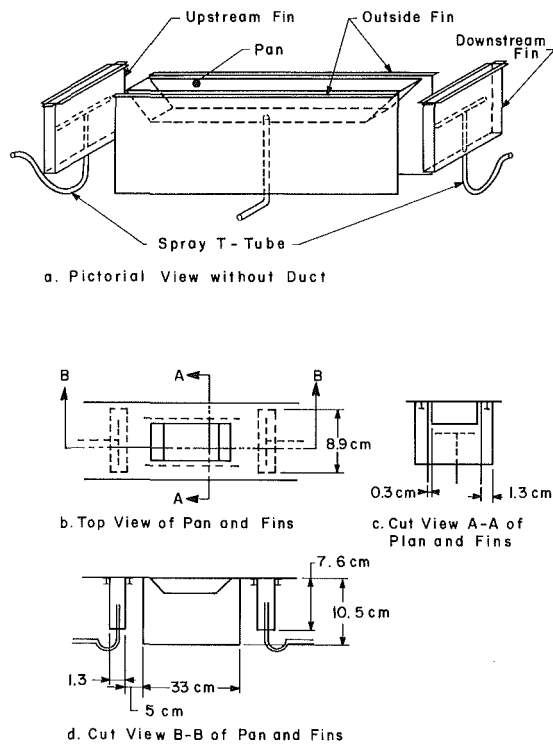


Fig. 3 Locations of fins and spray tee tubes around the pan

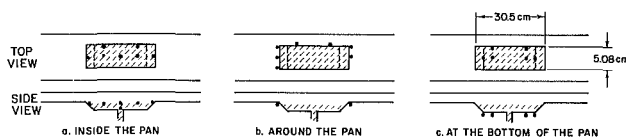


Fig. 4 Locations of thermocouples inside and around the pan

tion for turnon or shutoff of the incoming flow. All the pipings (2.5 cm diameter) were insulated with 2.5-cm-thick fiberglass pipe insulation. The steam orifice was covered with an extra 2.5-cm-thick insulation.

Heating System. Air at room temperature and steam at about 118°C could be heated up to about 260°C by utilizing two electrical heaters. The heaters could be adjusted at 10°C increments. The heat exchanger tubes in the heaters are 1.91 cm in diameter and are made of stainless steel.

In order to allow possible future use of this setup for heating mixtures of air and steam, the air line was first sent through one of the electrical heaters before it was connected to the steam line by a 2.54-cm tee pipe fitting, allowing the air to be heated to above the steam saturation temperature and thus preventing the condensation of steam during the mixing of air and steam. On both sides of the tee, check valves were installed to prevent the flow of air into the steam line or the flow of steam into the air line. The other heater could further heat the air or steam or a mixture of both to about 260°C .

Test Section. The test section, shown in Fig. 2, consisted of a duct and a pan made of stainless steel. The duct, with a cross section of 2.54 cm by 10.62 cm and an overall length of 92 cm, was connected upstream to a 2.54-cm-dia pipe by a gradual expansion duct fitting. In order to have a uniform turbulent flow inside the duct, a sheet of stainless steel mesh was used at the junction of the gradual expansion duct fitting and the duct. The pan, which has a 5.08-cm by 30.48-cm surface area and a depth of 2.54 cm, was welded to the bottom center of the duct.

Water could be fed into the pan through a 0.64-cm-dia opening at the bottom center of the pan. The duct was connected downstream to a 15.24-cm diameter duct leading to the exhaust outlet. The inside of the pan was covered with a layer of 0.16-cm-thick gasket. A piece of styrofoam, 1.35 cm thick, was glued to the bottom of the pan over the gasket, so the actual depth of the water in the pan was approximately 1.03 cm. A window was installed on each side of the test section, allowing one to observe the level of the water in the pan or to check the existence of any waves on the water surface.

To reduce the heat conduction from the walls of the test section to the water in the pan, four copper sheet fins, shown in Fig. 3, were held in place by screws around the pan and at the bottom of the duct. Two fins were about 5 cm away from the upstream and downstream ends of the pan. The other two fins were each about 0.3 cm from the sides of the pan. The upstream and downstream ends of the pan could be cooled by spraying water from tee-shaped copper tubes on to the fins. Many small holes were drilled at the top of the copper tubes for uniform spraying. Also, a small fan was used to enhance the removal of heat from beneath the duct.

To determine the free-stream temperature, copper-constantan thermocouples were placed at two locations, upstream and downstream of the pan; the average reading of the two thermocouples was chosen as the free-stream temperature. The vertical positions of the thermocouple beads were adjusted for maximum flow temperature in the duct. The temperature readings were adjusted by accounting for the conduction and radiation heat losses at the thermocouple beads. To minimize the conduction losses, all the thermocouples were insulated for a sufficient length, about 150 cm. In all test cases, the error for unshielded thermocouples is less than 2°C . To measure the water temperature and the wall temperature in the vicinity of the pan, 20 thermocouples were used. The locations of these thermocouples are shown in Fig. 4.

Water Evaporation Rate Measurement System. The most crucial part of this experiment was to obtain an accurate measurement of the rate of evaporation of water. For any liquid level reading in a glass tube, a small error might result in a significant error in the volume of the water in the pan as compared to the measured volume of the evaporated water. This was resolved by employing a buret tube, a stopwatch, a needle, and two 1.27-cm-dia glass tubes which were connected to the pan by a 1.27-cm-dia plastic tube with fittings. Both glass tubes were connected to a fine adjustment carrier that could move vertically.

At the beginning of a test, the time at which the needle in one glass tube barely detached from the meniscus was noted. During the test, exactly 24 cc of water was added slowly through the other glass tube. The addition of water caused the reattachment of the needle point to the meniscus. The water flow rate could be adjusted by the buret valve to avoid overflowing in the pan. The time at which the needle again detached from the water surface was recorded. The difference in the two recorded times was the time required to evaporate 24 cc of water because the amounts of water in the pan were the same at the beginning and end of the test.

Data Acquisition System

The data were collected, processed, and stored both manually and by the use of a computer-controlled system. The air flow data, the volume of the evaporated water, and the time for the evaporation were recorded manually. To measure the air flow rate, two manometers were used: one to measure the differential pressure of the air across the orifice plate, and the other to measure the upstream pressure relative to the local atmospheric pressure. A mercury barometer was available close to the experiment to measure the local atmospheric

Table 1 Water temperature T_w

Air	T_∞ (°C)	T_w (°C)
	150	40
	175	43
	200	47
	230	50
	260	52
Steam	150	97
	175	96
	200	97

pressure in inches of mercury. A buret having a capacity of 24 cc was utilized to measure the amount of water evaporated. A stopwatch was used to measure the time needed for the evaporation of a prescribed amount of water.

The use of the computer-controlled system was essential due to the large amount of data for temperature readings. The system was comprised of two pressure transducers, two demodulators, a data logger, a microcomputer with a video display, a printer, a disk drive, and a plotter.

The pressure transducers were calibrated to measure the pressure at the steam orifice. The pressure transducers were connected to two demodulators to provide analog voltage signals to be sent to the data logger and to be converted to digital signals. Thirty-three thermocouples were used to measure the temperatures. The thermocouples were welded beads and were made of copper-constantan. They were calibrated, ice bathed, and directly connected to the data logger to provide digital signals.

To process the digital signals in the desired fashion, the data logger was connected to a microcomputer. A software program enabled the microcomputer to process the data in the following manner: The pressure transducers, the air or steam temperature at the orifices, and the upstream and downstream free-stream temperatures at the test section were read once per second and were averaged every 60 s and displayed and printed. The other temperatures were read, displayed and printed every minute. All of these data were also averaged over time for each experimental run.

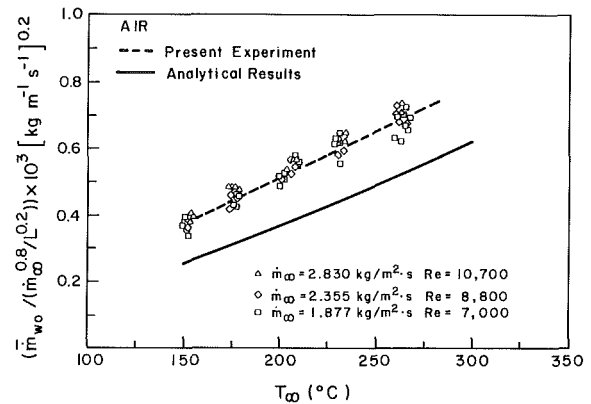
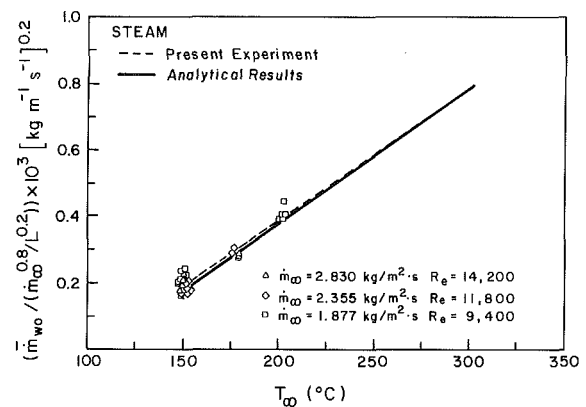
The processed data were displayed and printed during each run and were stored on a disk at the end of each run. The time trace temperatures could be plotted at any time after the end of each run.

Results and Discussion

The air data for three different mass fluxes were collected at various modulated free-stream temperatures, starting from 150°C with 10°C increments up to 260°C. The steam data for a mass flow of 1.877 kg/m²·s were collected at 150°C and 200°C, and for the other two flow rates at 150°C and 177°C. The true free-stream temperatures, at the higher temperature tests, were approximately 2°C higher than the readings given by the thermocouples. This was determined by using heat balance equations at the thermocouples beads. As mentioned earlier, the mean value of the temperatures, measured just upstream and downstream of the water pan, was selected as the free-stream temperature.

The average water temperatures for all tests are listed in Table 1. For the air tests, the water temperature is approximately the same as the wet bulb temperature and is independent of the free-stream mass flow rate. The water temperature for the steam tests is very close to the saturation temperature at the ambient pressure of 0.92 bar.

In Figs. 5 and 6, the scaled evaporation rates of water into air and steam are plotted versus the free-stream temperatures at the three average mass fluxes. It can be seen from Fig. 5 that the data points for air flows are above the predicted evapora-

**Fig. 5 Water evaporation rates into air****Fig. 6 Water evaporation rates into steam**

tion line given by Chow and Chung (1983b). This is due to (explained later in this paper) the high conduction heat transfer from the walls of the test section to the water in the pan when air was used.

In the present experimental work, convective heat transfer is the dominant mode of heat and mass transfer. However, the other two modes of heat transfer, namely conduction and radiation, are also present. The portion of the total heat transfer due to radiation from the free stream and the wall of the test section to the water surface is higher for the higher free-stream temperatures and lower free-stream Reynolds numbers. In the present work, the highest free-stream temperature is 260°C. At 260°C, the lowest Reynolds numbers at the test section for air and steam are 7000 and 9400, respectively. The magnitude of the radiation heat transfer in these extreme situations were estimated using the actual temperature measurements. For an air run with a free-stream temperature of 260°C and a mass flux of 1.877 kg/m²·s, the wall temperature varied from about 65°C near the water surface to about 120°C far away from the surface. The water temperature was 52°C. An average wall temperature was calculated based on the fourth root of the average of the wall temperatures to the fourth power. The emissivity of the stainless-steel wall was assumed to be 0.3. Based on a simple enclosure radiative exchange between the wall and the water, the radiative heat transfer from the wall to the water surface was about 5 percent of the total heat transfer. For the steam runs, the wall temperatures were only slightly higher than the water temperature. The radiative heat transfer from the wall to the water surface was therefore negligible. At the highest free-stream temperature for steam (200°C), the gaseous radiation contribution was estimated, based on Hottel's charts, to be about 7 percent of the total heat transfer.

For the experiments with air, the temperature of the water

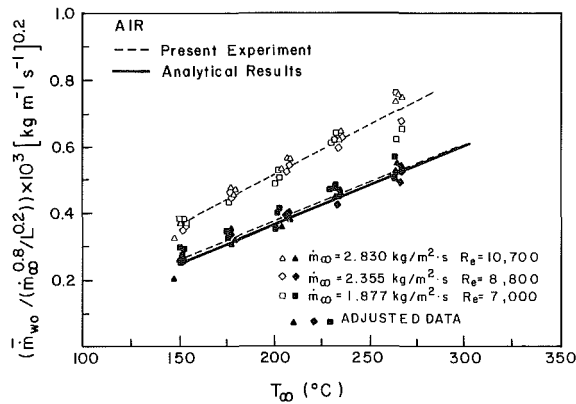


Fig. 7 Comparison of actual water evaporation rates into air and their corresponding adjusted values with the analytical results

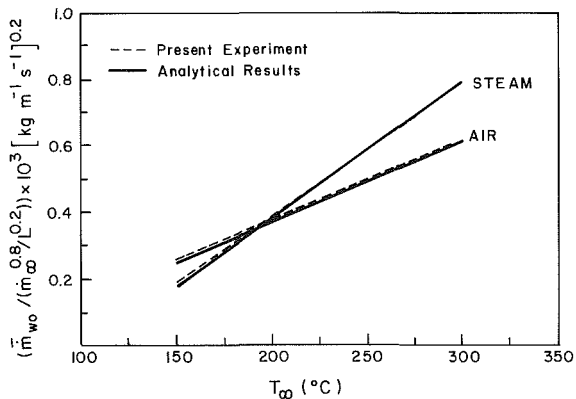


Fig. 8 Comparison of adjusted evaporation rates into air and the actual evaporation rates into steam with the analytical results

in the pan ranged from 40°C to 52°C, whereas the temperatures at the sides of the pan were significantly higher. For example, at the air mass flux and free-stream temperature of 1.877 kg/m² and 200°C, respectively, the average temperature at the edges of the pan was approximately equal to 60°C, while the water temperature was 47.3°C. The conduction heat transfer to the pan was estimated by considering the differences between the water temperatures and the wall temperatures at the sides of the pan. Because of the high thermal resistance due to the presence of the styrofoam and gasket placed at the bottom of the pan and the small temperature difference between the water and the bottom of the pan, the conduction heat transfer from the bottom of the pan was very small and was therefore neglected. The conduction heat transfer to the pan was estimated for the three air mass fluxes, involving 40 randomly selected data points. If the measured rates of evaporation of water into air are modified by accounting for these heat conduction estimates, the experimental data would be in good agreement with the analytical results (Chow and Chung, 1983b). This is shown in Fig. 7.

It can be seen from Fig. 6 that the data points are very close to the predicted theoretical line for superheated steam. These evaporation rates are due to convection and a certain amount of radiation heat transfer. Again, the contribution of radiation heat transfer is less than 7 percent for the worst case. During the data collection for steam, a fan was used occasionally to remove heat from beneath the duct. The surrounding temperature of the pan was kept close to the temperature of the water in the pan by reading the values of the test section temperatures on the video display and by turning the fan on and off. The temperature gradient across the edge of the pan

was so small that conduction heat transfer could be neglected. For example, at the steam mass flux and free-stream temperature of 1.877 kg/m² and 200°C, respectively, the average temperature at the edge of the pan was approximately 98.0°C while the water temperature was 97.2°C.

One important explanation needed to be made about the degree of scatter exhibited by the data shown in Fig. 5 and 6. The scatter was due to the difficulty in measuring the amount of water evaporated over a period of 15 to 30 mins. When the needle point barely detached and broke off from the meniscus of the water in the glass tube, the experiment was stopped. Due to the large area ratio of the water pan and glass tube, a small change in the water level in the pan could result in a significant change in the volume of water in the pan. During the experiment, surface waves of very small amplitude on the water surface were observed. These waves (barely observable) could not affect the heat and mass transfer process in any significant way. However, they could affect the measurement of the evaporation rate by affecting the time at which the needle point detached from the meniscus. These waves introduced a certain degree of randomness in the data. Therefore, it was decided to repeat every test at least five times for a given set of conditions. Except at the lowest temperature runs, the scatter in the data was less than 20 percent. The curves (dashed lines) shown in Figs. 5 and 6 were obtained by least-squares fit of all the data. Even though the uncertainty in the experimental data could be 20 percent, it is clear that the slopes of the curves are reliable. It should be emphasized that the present experiment was a fairly difficult one and extreme care was exercised to come up with reliable, repeatable, and statistically meaningful data. There are significant discrepancies among similar experiments done previously. The available data published by different investigators differed by as much as 300 percent. In summary, the degree of uncertainty in the experimental data was about 20 percent. However, the confidence in the data was increased by repeating each test a minimum of five times.

From Figs. 6 and 7, it can be seen that the scaled expression for the water evaporation rate into both air and steam is independent of the free-stream mass flux. This is in agreement with the analytical prediction (Chow and Chung, 1983b).

Figure 8 illustrates the existence of the inversion temperature, both experimentally and analytically. The dashed lines represent and modified data points for air and all three flow rates of steam. The solid lines present the analytical results of Chow and Chung (1983b). Below the inversion temperature, water evaporates faster in air than in steam, whereas above the inversion temperature, water evaporates faster in steam. Despite the uncertainty of the experimental data (20 percent), with a large number of data points, it is clear that the slopes of the curves in Fig. 8 for air and steam are different. This difference in slope establishes the existence of the inversion temperature. The exact intersection of the two curves depends on the accuracy of the experimental data. With a 20 percent scatter in the data, it can only be stated with confidence that the inversion temperature is between 170°C and 220°C.

For steam, the present experimental results are about 10 to 20 percent higher than the analytical results of Chow and Chung (1983b), whereas the experimental results of Chu et al. (1953) are about 300 percent higher than the analytical results. Table 2 shows the comparisons. The comparison was made for the same steam mass flux of 1.877 kg/m². The surface area of water in the experiments of Chu et al. was 10.2 cm by 10.2 cm compared to 5.08 cm by 30.48 cm in the present experiment. They had a higher Reynolds number since the cross-sectional area of their duct was 5.1 cm by 10.2 cm compared to 2.54 cm by 10.62 cm in the present experiment.

Another comparison was made between the experimental results of Yoshida and Hyodo (1970) and analytical results of

Table 2 Comparison of present experimental results and results of Chu et al. (1953) with analytical results of Chow and Chung (1983b) at $\dot{m}_\infty = 1.877 \text{ kg/m}^2 \cdot \text{s}$

$T, ^\circ\text{C}$	Present experiment*			Chu et al. experiment†		
	Analytical $\times 1000,$ $\text{kg/m}^2 \cdot \text{s}$	Experimental $\times 1000,$ $\text{kg/m}^2 \cdot \text{s}$	Ratio	Analytical $\times 1000,$ $\text{kg/m}^2 \cdot \text{s}$	Experimental $\times 1000,$ $\text{kg/m}^2 \cdot \text{s}$	Ratio
150	0.371	0.443	1.19	0.463	1.735	3.75
177	0.600	—	—	0.748	2.697	3.61
200	0.796	0.858	1.08	0.991	4.392	4.43

*Length of water surface is 30.48 cm.

†Length of water surface is 10.16 cm.

Table 3 Comparison of experimental results of Yoshida and Hyodo (1970) with analytical results by Chow and Chung (1983b) at $\dot{m}_\infty = 2.53 \text{ kg/m}^2 \cdot \text{s}$

$T, ^\circ\text{C}$	Analytical $\times 1000,$ $\text{kg/m}^2 \cdot \text{s}$	Experimental* $\times 1000,$ $\text{kg/m}^2 \cdot \text{s}$	Ratio
150	0.37	0.61	1.65
177	0.60	0.91	1.52
200	0.80	1.17	1.46

*Length of water surface is 1 m.

Chow and Chung (1983b). Yoshida and Hyodo measured the rate of evaporation of water into stream of air, humid air, and superheated steam on a cylindrical wetted wall-tube column. Their results are about 50 percent higher than the analytical results. Table 3 shows the comparison.

Conclusions

The rates of evaporation of water into a free steam of air and superheated steam were experimentally measured. From the results the following conclusions are made:

(i) The measured evaporation rates of water into steam are in good agreement with the analytical results.

(ii) The measured evaporation rates for air are higher than the analytical results for air. However, if the measured water evaporation rates are adjusted by accounting for the contribution of heat conduction to the pan, the modified rates of evaporation would be in good agreement with the analytical results.

(iii) The existence of the predicted inversion temperature by Chow and Chung (1983b) is confirmed. However, due to a 20 percent scatter in the experimental data, a reliable inversion temperature cannot be obtained.

(iv) For the steam case, the present experimental results are about 10 to 20 percent higher than the analytical results of Chow and Chung (1983b), but the experimental results of Chu et al. (1953) are about 300 percent higher than the analytical results.

References

- Barnet, W. I., and Kobe, K. A., 1941, "Heat and Vapor Transfer in a Wetted-Wall Tower," *Ind. Engng. Chem.*, Vol. 33, pp. 436-442.
- Chow, L. C., and Chung, J. N., 1983a, "Evaporation of Water Into a Laminar Stream of Air and Superheated Steam," *Int. Journal of Heat and Mass Transfer*, Vol. 26, pp. 373-380.
- Chow, L. C., and Chung, J. N., 1983b, "Water Evaporation Into a Turbulent Stream of Air, Humid Air or Superheated Steam," 21st ASME/AIChE National Heat Transfer Conference, Seattle, WA, ASME Paper No. 83-HT-2.
- Chu, J. C., Lane, A. M., and Conklin, D., 1953, "Evaporation of Liquids Into Their Superheated Vapors," *Ind. Engng. Chem.*, Vol. 45, pp. 1586-1591.
- Chu, J. C., Finelt, S., Hoerrner, W., and Lin, M. S., 1959, "Drying With Superheated Steam-Air Mixture," *Ind. Engng. Chem.*, Vol. 51, pp. 275-280.
- Gilliland, E. R., and Sherwood, T. K., 1934, "Diffusion of Vapors Into Air Streams," *Ind. Engng. Chem.*, Vol. 26, pp. 516-523.
- Lurie, M., and Michaloff, N., 1936, "Evaporation From Free Water Surface," *Ind. Engng. Chem.*, Vol. 28, pp. 345-349.
- Ranz, W. E., and Marshall, W. R., 1952, "Evaporation From Drops: I and II," *Chem. Engng. Progr.*, Vol. 48, pp. 141-146, 173-180.
- Shepherd, C. B., Handlock, C., and Brewer, R. C., 1938, "Drying Materials in Trays, Evaporation of Surface Moisture," *Ind. Engng. Chem.*, Vol. 30, pp. 388-397.
- Trommelen, A. M., and Crosby, E. J., 1970, "Evaporation and Drying of Drops in Superheated Vapors," *AIChE Journal*, Vol. 16, pp. 857-867.
- Wenzel, L., and White, R. R., 1951, "Drying Granular Solids in Superheated Steam," *Ind. Engng. Chem.*, Vol. 43, pp. 1829-1837.
- Yoshida, T., and Hyodo, T., 1966, "Superheated Vapor Speeds Drying of Foods," *Food Engng.*, Vol. 38, pp. 86-87.
- Yoshida, T., and Hyodo, T., 1970, "Evaporation of Water in Air, Humid Air and Superheated Steam," *Ind. Engng. Chem. Process Des. Dev.*, Vol. 9, pp. 207-214.

Heat Transfer-Based Reconstruction of the Concepts and Laws of Classical Thermodynamics

A. Bejan

Professor,
Department of Mechanical Engineering
and Materials Science,
Duke University,
Durham, NC 27706
Mem. ASME

As an alternative to the mechanistic point of view expressed in Carathéodory's axioms, it is shown that the laws and concepts of thermodynamics are covered also by two statements made from a purely heat transfer perspective: Axiom I'—The heat transfer is the same in all zero-work processes that take a system from a given initial state to a given final state. Axiom II'—In the immediate neighborhood of every state of a system there are other states that cannot be reached from the first via a zero-work process. The primary concepts of this formulation are heat transfer, temperature, entropy, and zero-work boundary. Axiom I' is used to define the property "energy," and to deduce the secondary (derived) concept of "work transfer." Axiom II' is used to define the thermodynamic properties of "volume" and "pressure." In this new heat transfer-based scheme, the analog of the Kelvin-Planck statement of the second law is: " $\oint \delta W < 0$ is impossible" for an integral number of cycles executed by a closed system while in communication with no more than one pressure reservoir.

Introduction

Not long ago Professor Lienhard drew our attention to the common origins of what today we practice as two distinct fields, heat transfer engineering and engineering thermodynamics (Lienhard, 1983). I found his essay particularly meaningful because of my own interest in reuniting these two fields through the thermodynamic design methodology of entropy generation minimization. Professor Lienhard's essay and another captivating historical account that appeared at about the same time (Truesdell, 1984) invited me to take a closer look at the original writings of the pioneers of these two fields.

One conclusion that emerges from a study of the literature produced between the late 1700s and early 1900s is that heat transfer-type ideas played a central role in the Rankine-Clausius-Thomson development of classical thermodynamics. What these three men produced forms the core of what we mechanical engineers today speak of as engineering thermodynamics. The early crystallization of the subject was followed by a long process of "generalization" that continues today, a process whose original mission was to reconcile the early thermodynamics of heat engine and refrigeration "cycles" with the powerful mathematical apparatus that accounted for so much success in continuum mechanics, hydrodynamics, and pure conduction heat transfer. An integral part of this modern phase of generalization is the current interest in distilling classical thermodynamics to the smallest number of axioms or postulates.

If one is to begin to appreciate what an axiomatic formulation represents on the colorful phenomenological background painted by the pioneers, sooner or later one has to become acquainted with Carathéodory's two axioms. One difficulty that a heat transfer-minded engineer is likely to face in this effort is that Carathéodory's axioms are stated from the point of view of the mechanist, by employing a language that avoids all the "heat" sounding words that even the common man expects to find in "thermo" dynamics. I experienced these difficulties

first-hand, and it is out of this struggle that the present study was born.

In this paper I outline a heat transfer-based alternative to Carathéodory's two axioms of classical thermodynamics, with the final objective of illustrating the essence of any axiomatization effort in general. That essence is the idea of reducing the vocabulary and laws of classical thermodynamics to the smallest number of primary concepts (words) and axioms, from which the remainder of subject can be "derived."

An additional objective is to show that heat transfer thinking can be used in the process of learning and understanding thermodynamics. This objective is pursued in order to balance the strong case made for the reverse application of the thermodynamics-heat transfer connection in the field of second-law analysis, where thermodynamics is used to strengthen the foundation of heat transfer engineering.

A final objective is to propose a new axiomatic formulation of classical thermodynamics, not because a new one is needed, but in order to complete a very interesting line of thought that was conceived and abandoned at the first-law level by Keenan and Shapiro (1947).

Review: Carathéodory's Two Axioms

Shortly after the turn of the century Carathéodory's (1909) proposed a two-axiom condensation of the two laws of thermodynamics. There were important reasons for such a step, for example, some mathematicians' lack of familiarity with the heat engine cycle arguments of the Carnot-Clausius line, and the need for an "analytical" thermodynamics that would make the subject applicable to systems more general than the power and refrigeration examples contemplated by the pioneers. Carathéodory's original presentation has become the subject of a sustained process of simplification, whose chief objective is to improve the accessibility of his two axioms (see, for example, Sears, 1963, 1966; Kestin, 1970; Buchdahl, 1960; Turner, 1960, 1962; Landsberg, 1961, 1964; Pippard, 1964). An important step toward establishing the equivalence between Carathéodory's axiom II and classical statements of the second law was made by Landsberg (1964), who showed

Contributed by the Heat Transfer Division for publication in the JOURNAL OF HEAT TRANSFER. Manuscript received by the Heat Transfer Division December 4, 1986.

that axiom II follows from the Kelvin-Planck statement of the second law.

Reworded by Sears (1966), Carathéodory's closed-system axioms read as follows:

- *Axiom I.* The work is the same in all adiabatic processes that take a system from a given initial state to a given final state.

- *Axiom II.* In the immediate neighborhood of every state of a system there are other states that cannot be reached from the first by an adiabatic process.

The basic function of axiom I is to introduce the thermodynamic property called "energy" (E). The change in energy is taken as equal to the negative of the adiabatic work transfer, which is a unique quantity when the end states (1) and (2) are specified,¹

$$-W_{1-2, \text{adiabatic}} = U_2 - U_1 \quad (1)$$

Carathéodory's formulation relies on the concepts of "work transfer" and "adiabatic boundary" as primary concepts. The work transfer concept is taken directly from mechanics. While avoiding any reference to thermal concepts that would certainly sound more appealing and natural, the adiabatic wall is defined by the special feature that the "equilibrium of a body enclosed by (this wall) is not disturbed by any external process as long as no part of the wall is moved (distance forces being excluded in the whole consideration)" (Born, 1949).

Under the Carathéodory's scheme "heat transfer interaction" becomes a derived concept as δQ is defined simply as the sum $dU + \delta W$. The empirical "temperature" becomes also a derived concept: Two bodies are said to have the same temperature when the heat transfer interaction δQ (or $dU + \delta W$) is zero in the absence of an adiabatic wall.

Finally, the second axiom (or the Kelvin-Planck statement) is used to prove sequentially the existence of three additional concepts:

- 1 reversible and adiabatic surfaces, or the property "empirical entropy"
- 2 the property "entropy" (S)
- 3 the property "thermodynamic temperature" (T)

The systematic recovery of these concepts from the second axiom is presented in detail in a number of modern treatises on classical thermodynamics (Kestin, 1979; Baehr, 1973; Zemansky, 1968).

Two Axioms From a Heat Transfer Perspective

Carathéodory's axiomatic encapsulation of the essence of the first and second laws represents a mechanistic's point of view, because the first primary concept chosen for this formulation (work transfer) is a concept borrowed from the field of mechanics. Taken together, the two axioms and the primary concepts deliver the remaining pieces of engineering thermodynamics as we learn it, namely the concepts of heat transfer, entropy, and thermodynamic temperature. One develops a better feel for what this axiomatic formulation accomplishes, by rethinking the idea of combining a few primary

¹For simplicity, throughout this paper kinetic and potential energy changes are neglected, i.e., the energy change dE is the same as the change in internal energy dU .

concepts with two axioms, this time using the very language that Carathéodory tried so hard to avoid.

Imagine a world in which man was considerably more at ease with thermal effects and their quantitative analysis than with mechanics, in other words a world in which "temperature," "heat transfer," and "zero-work boundary" were the obvious choices as primary concepts. The same choice was made by Keenan and Shapiro (1947) in their second scheme, in which they defined the temperature and heat transfer in the same way as Poincaré (1891). The size of the heat transfer interaction was measured by counting the number of auxiliary standard systems that must be placed in thermal communication with the system of interest. The function of the standard systems is to undergo a temperature excursion between two standard temperature levels under the influence of the heat transfer interaction that is to be measured. Finally, the concept of zero-work boundary is an instrument needed to get to the first law while avoiding any reference to work transfer (note here the relationship between this idea and Carathéodory's). In Keenan and Shapiro's definition, "a zero-work wall is a wall which is motionless (except in the absence of force at the wall) and through which pass no moving force fields and no electrical currents."

The members of this make-believe society had already established the convention that "temperature" always means the ideal gas thermometer temperature (the "absolute temperature") and labeled it T . Note that the adoption of the ideal gas temperature as the true thermodynamic temperature scale is practiced sometimes even here as a pedagogically effective move in introductory engineering thermodynamics courses (e.g., Cravalho and Smith, 1981).

The fact that these heat transfer-minded people were not comfortable with mechanical things does not mean in any way that they were backward. On the contrary, their mathematics was the same as ours despite trivial differences in language, notation, and ways of measuring things. For example, it was considered proper to measure the size of a closed system in terms of its "entropy" (labeled S): this method had been perfected two thousand years earlier by their own "old Greeks," so that even children could tell that the entropy of the closed system of Fig. 1 is forever equal to the sum of the entropies of its two subsystems

$$S = S_A + S_B \quad (2)$$

In short, these people were about as conversant in entropy measurement and accounting as you and I are today when it comes to measuring, say, "volume."

Incidentally, the people I am describing heard about the concept of volume also (in college); however, they also learned to fear this concept along with everything else geometrical or mechanical. Contributing to this fear was the fact that the name "volume" sounded alien: It had been invented by a classics-loving professor who had made it up by piecing together two interesting and otherwise very dead words. Feared as it was, the word volume was quite popular among the practitioners of name dropping, especially at conferences on pure heat and congressional hearings on all sorts of nongeometric topics. There were even passionate references to the "volume death" of the universe, when, in fact, no one

Nomenclature

E = energy	U = internal energy	
F = function of empirical volume	V = volume	
P = pressure	W = work transfer interaction	ω = empirical volume
Q = heat transfer interaction	Λ = partial differential, equation (13)	Subscripts
S = entropy	π = empirical pressure	A = subsystem (A), Fig. 1
T = thermodynamic temperature	Φ, Φ_1 = functions of empirical pressure	B = subsystem (B), Fig. 1
		rev = reversible

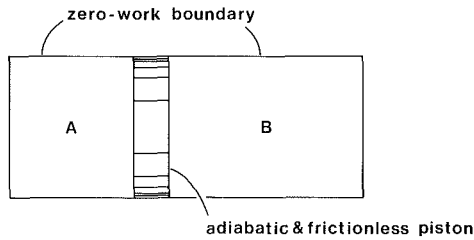


Fig. 1 Two-part system in a state of uniform pressure

remembered anymore the professor's original theory with the same name.

Relatively late in its scientific development, this make-believe society learned to attach great importance to the quantity TdS , which was called "reversible heat transfer interaction" and labeled δQ_{rev}

$$\delta Q_{rev} = TdS \quad (3)$$

The word "reversible" was used as a reminder of the special state of tranquility and temperature uniformity (T) that reigned during the entropy change dS . At ease with measuring both T and S , these people had no trouble calculating δQ_{rev} using equation (3).

Consider now the implications of the following two axioms, which—it is easy to see—are my entropy-seeing society's alternative to Carathéodory's axioms:

- *Axiom I'*.—The heat transfer is the same in all zero-work processes that take a system from a given initial state to a given final state.

- *Axiom II'*.—In the immediate neighborhood of every state of a system there are other states that cannot be reached from the first via a zero-work process.

The first of these new axioms amounts to saying that the zero-work heat transfer interaction is a thermodynamic property. Energy, then, is the name given to this property

$$Q_{1-2, zero-work} = U_2 - U_1 \quad (4)$$

As a derived concept, the work transfer interaction is defined as the difference

$$\delta W = \delta Q - \delta Q_{zero-work} = \delta Q - dU \quad (5)$$

Finally, the "adiabatic boundary" is the one for which we can write $\delta Q = 0$.

Axiom I' is my summary of Keenan and Shapiro's (1947) second scheme for the introduction of the first law of thermodynamics. Axiom II' is entirely new: In three steps that parallel the steps (1)–(3) listed at the end of the preceding section, this second axiom delivers the remaining missing concepts of classical thermodynamics, specifically, the thermodynamic properties "volume" and "pressure."

Reversible and Zero-Work Surfaces

Consider the two-compartment system sketched in Fig. 1. Subsystems (A) and (B) are separated by an adiabatic wall (piston) that can slide without encountering any resistance from the cylinder wall. The "empirical pressure" π is measured with a locally available pressure gage, which is not a standardized instrument. The gage shows that the measured value of π is the same on both sides of the sliding partition.

In the initial state (1), the system's "entropic configuration" is (S_{A_1}, S_{B_1}) , as shown in the horizontal plane of Fig. 2. If the system is to evolve to a second configuration (S_{A_2}, S_{B_2}) , then, according to axiom II', not all the states that have this new configuration are accessible from state (1) via zero-work processes. Through reasoning that is geometrically analogous to the one leading to the existence of reversible and adiabatic surfaces in Carathéodory's scheme (e.g., Zemansky, 1968), one can argue that the states of configuration (S_{A_2}, S_{B_2}) that

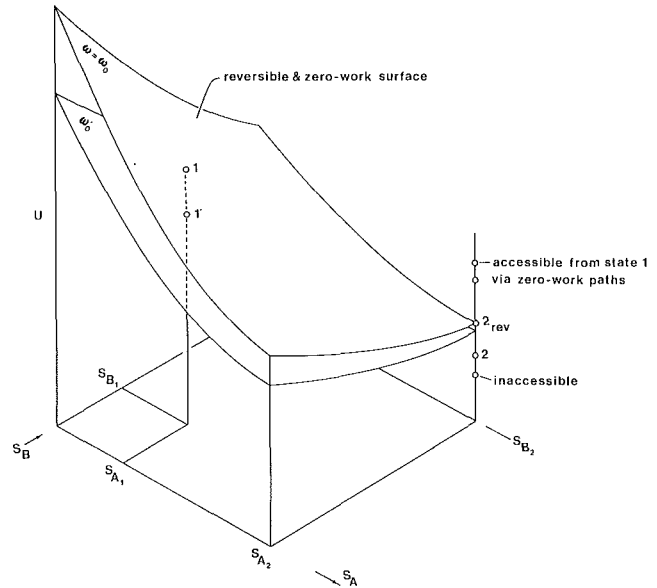


Fig. 2 Family of reversible and zero-work surfaces for the "(A) + (B)" system of Fig. 1

are accessible from (1) via zero-work processes are separated from inaccessible states of the same configuration by a unique state (2_{rev}). The special state (2_{rev}) is defined by two features: First, state (2_{rev}) can be reached from state (1) via a zero-work process, and, second, state (1) can be reached from state (2_{rev}) via a zero-work process. For each new configuration (S_{A_n}, S_{B_n}) , a unique state (n_{rev}) can be identified in the same manner. The collection of all the states of type (n_{rev}) forms a "reversible and zero-work" surface that passes through state (1). Two points on this surface are mutually accessible via zero-work processes.

The existence of reversible and zero-work surfaces can be expressed analytically as

$$\omega(U, S_A, S_B) = \omega_0, \text{ (constant)} \quad (6)$$

where the numerical value ω_0 distinguishes the particular surface that passes through state (1) (Fig. 2). The numerical values $(\omega_0, \omega'_0, \dots)$ are chosen so that they vary monotonically with the empirical pressures (π, π', \dots) measured at states $(1, 1', \dots)$. Therefore, states that have the same entropy configuration (S_A, S_B) also have a one-to-one relationship between their respective π and ω_0 values.

For reasons that will soon become clear, the value ω_0 can be called the "empirical volume" of system at state (1). Going back to the uniqueness of states of type (2_{rev}), we recognize also that equation (6) represents a family of nonintersecting surfaces. This feature is illustrated by the two surfaces sketched in Fig. 2, where $\omega_0 \neq \omega'_0$. Stationed at (1) on the surface $\omega = \omega_0$, reading axiom II' we conclude that all the states of configuration (S_{A_1}, S_{B_1}) that cannot be reached via zero-work processes from (1) must be situated either above or below (1), that is, on one side of the reversible and zero-work surface that passes through (1). The question "which side?" forms the subject of the closing segment of this paper.

Volume

For an infinitesimally small reversible change of state we can now write

$$\delta W_{rev} = -dU + \delta Q_{rev} \quad (7)$$

and, with special reference to the two-fluid system sketched in Fig. 1,

$$\delta W_{\text{rev}} = -dU + T_A dS_A + T_B dS_B \quad (8)$$

According to equation (8), δW_{rev} is a linear differential form, or Pfaffian form. The question that forms the subject of this and the next section is whether δW_{rev} possesses an integrating denominator.

We begin with the observation that U can be regarded as a function of ω , S_A , and S_B (equation (6)); therefore

$$dU = \left(\frac{\partial U}{\partial \omega} \right)_{S_A, S_B} d\omega + \left(\frac{\partial U}{\partial S_A} \right)_{\omega, S_B} dS_A + \left(\frac{\partial U}{\partial S_B} \right)_{\omega, S_A} dS_B \quad (9)$$

Comparing this differential with equation (8) we identify

$$T_A = \left(\frac{\partial U}{\partial S_A} \right)_{\omega, S_B} \quad (10)$$

$$T_B = \left(\frac{\partial U}{\partial S_B} \right)_{\omega, S_A} \quad (11)$$

and, in particular,

$$\delta W_{\text{rev}} = \Lambda d\omega \quad (12)$$

where the coefficient Λ is itself a function of (ω, S_A, S_B) , or (π, S_A, S_B) or (π, ω, S_A) , etc.

$$\Lambda = - \left(\frac{\partial U}{\partial \omega} \right)_{S_A, S_B} \quad (13)$$

We show next that Λ can only be a function of π and ω , and that the form of this function is

$$\Lambda(\pi, \omega) = \Phi(\pi)F(\omega) \quad (14)$$

Applied to the closed subsystem (A) alone, the analysis contained between equations (8) and (12) concludes with

$$\delta W_{\text{rev}, A} = \Lambda_A d\omega_A \quad (15)$$

where Λ_A is a function of (π, ω_A) , or of (π, S_A) , etc. For the adjacent system we write similarly

$$\delta W_{\text{rev}, B} = \Lambda_B d\omega_B \quad (16)$$

where $\Lambda_B = \Lambda_B(\pi, \omega_B)$. We ask now whether the empirical volume of the aggregate system (A) + (B) is only a function of the empirical volumes of the two subsystems

$$\omega = \omega(\omega_A, \omega_B) \quad (17)$$

Note that the question is not whether ω is equal to the sum ($\omega_A + \omega_B$), but whether ω depends only on ω_A and ω_B . The answer falls out of equations (13), (15), and (16), which, combined into the statement that the work transfer interaction experienced by (A) + (B) must be the sum of the work transfer interactions experienced by (A) and (B) individually,

$$\delta W_{\text{rev}} = \delta W_{\text{rev}, A} + \delta W_{\text{rev}, B} \quad (18)$$

yields

$$\Lambda d\omega = \Lambda_A d\omega_A + \Lambda_B d\omega_B \quad (19)$$

or

$$d\omega = \frac{\Lambda_A}{\Lambda} d\omega_A + \frac{\Lambda_B}{\Lambda} d\omega_B \quad (20)$$

Equation (20) states that ω is constant whenever ω_A and ω_B are held fixed, i.e., that ω is a function of ω_A and ω_B only. As partial derivatives of $\omega(\omega_A, \omega_B)$, the two coefficients (Λ_A/Λ) and (Λ_B/Λ) are also functions of only ω_A and ω_B

$$\frac{\Lambda_A}{\Lambda} = f_1(\omega_A, \omega_B) \quad (21)$$

$$\frac{\Lambda_B}{\Lambda} = f_2(\omega_A, \omega_B) \quad (22)$$

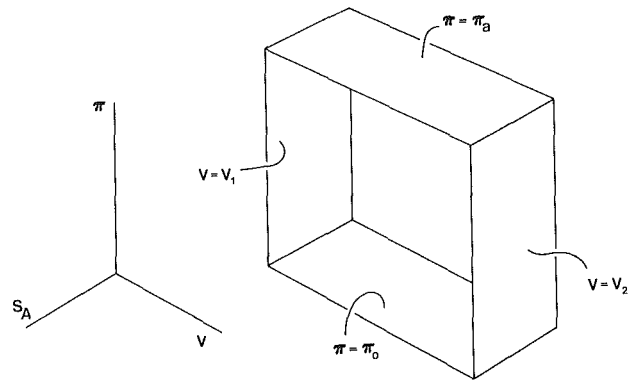


Fig. 3 Four-plane locus of the family of reversible cycles (i)-(iv)

Equation (21) implies that since Λ_A is not dependent on S_B , the denominator Λ cannot be a function of S_B either. Similarly, equation (22) states that the denominator Λ is also independent of S_A . There is only one possibility left

$$\Lambda(\pi, \omega_A, \omega_B), \quad \Lambda_A(\pi, \omega_A), \quad \Lambda_B(\pi, \omega_B) \quad (23)$$

which, by virtue of equations (21) and (22), means

$$\frac{\partial}{\partial \pi} \left(\frac{\Lambda_A}{\Lambda} \right) = 0 \quad (24)$$

$$\frac{\partial}{\partial \pi} \left(\frac{\Lambda_B}{\Lambda} \right) = 0 \quad (25)$$

This two-equation system is the same as

$$\frac{\partial}{\partial \pi} (\ln \Lambda) = \frac{\partial}{\partial \pi} (\ln \Lambda_A) = \frac{\partial}{\partial \pi} (\ln \Lambda_B) \quad (26)$$

where the three terms are, in order, functions of $(\pi, \omega_A, \omega_B)$, (π, ω_A) , and (π, ω_B) . However, since ω_A and ω_B can be varied independently of π , equations (26) imply that each term must equal the same function of π , for example,

$$\frac{\partial}{\partial \pi} (\ln \Lambda) = \Phi_1(\pi) \quad (27)$$

or

$$\Lambda = F(\omega) \exp[\Phi_1(\pi) d\pi] \quad (28)$$

or, finally,

$$\Lambda = F(\omega) \Phi(\pi) \quad (29)$$

The reversible work transfer expression (12) is therefore of the form

$$\delta W_{\text{rev}} = \Phi(\pi) F(\omega) d\omega \quad (30)$$

Recognizing $F(\omega) d\omega$ as the total differential of a new function V called "volume"

$$dV = F(\omega) d\omega \quad (31)$$

we finally conclude that

$$\delta W_{\text{rev}} = \Phi(\pi) dV \quad (32)$$

The reversible and zero-work surfaces of Fig. 2 are therefore the familiar constant-volume or isochoric surfaces. It remains to show that the empirical pressure function $\Phi(\pi)$ is what we have been calling "pressure."

Thermodynamic Pressure

The final step consists of constructing a reversible cycle that is a sequence of four processes:

- (i) reversible and isobaric expansion in the $\pi = \pi_a$ plane (to be concrete, assume $V_2 > V_1$)
- (ii) reversible and zero-work depressurization in the $V = V_2$ plane

Table 1 Parallel thermodynamics structure of the classical scheme due to Carathéodory and the heat transfer-based reconstruction outlined in the paper

Structure	Classical scheme, rooted in mechanics	Heat transfer-based reconstruction
Primary concepts	Pressure (force) Volume (displacement) Work transfer Adiabatic boundary	Temperature* Entropy Heat transfer* Zero-work boundary*
First law	$\int_1^2 \delta W_{\text{adiabatic}} = f(1, 2)$	$\int_1^2 \delta Q_{\text{zero-work}} = f(1, 2)^*$
Definition of energy change, dE	$-\delta W_{\text{adiabatic}}$	$\delta Q_{\text{zero-work}}^*$
Derived definition of heat transfer	$\delta W - \delta W_{\text{adiabatic}}$	---
Derived definition of work transfer	---	$\delta Q - \delta Q_{\text{zero-work}}^*$
Derived concepts	Heat transfer Zero-work boundary Reversible and adiabatic surface	Work transfer* Adiabatic boundary* Reversible and zero-work surface
Second law for a closed system executing an integral number of cycles while in communication with no more than one "reservoir"	Entropy Temperature "∫δQ > 0 is impossible"	Volume Pressure "∫δW < 0 is impossible"
Type of reservoir	Temperature, T_0	Pressure, P_0

*Entries found also in Keenan and Shapiro's (1947) second scheme for stating the first law.

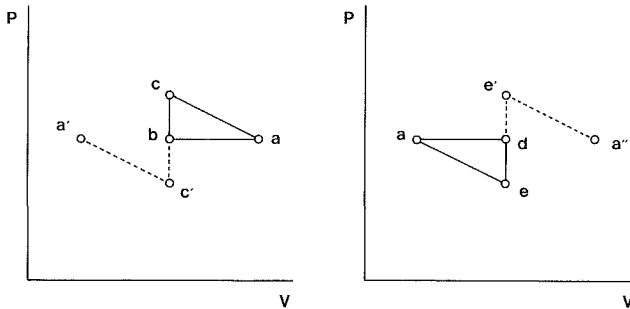


Fig. 4 Two examples of cycles executed by a closed simple system while in communication with only one pressure reservoir

(iii) reversible and isobaric contraction in the $\pi = \pi_0$ plane

(iv) reversible and zero-work pressurization in the $V = V_1$ plane

The four planes that house this cycle are sketched in Fig. 3. Note that in many cases² the reversible and zero-work depressurization process (ii) means a process of zero-work reversible cooling. Note further that the heat transfer interaction during this process [as well as during the heating process (iv)] is of type $\delta Q_{\text{rev}} = TdS$, i.e., that the system makes contact with a sequence of heat reservoirs whose temperatures match the continuous variation of the system temperature T .

Invoking equation (32) in connection with each of the isobaric processes (i) and (iii), we write

$$\delta W_{\text{rev},a} = \Phi(\pi_a)(V_2 - V_1) \quad (33)$$

$$\delta W_{\text{rev},0} = \Phi(\pi_0)(V_1 - V_2) \quad (34)$$

Dividing side-by-side

²For example, when the system contains a fluid that expands upon heating at constant pressure.

$$\Phi(\pi_a) = \Phi(\pi_0) \left(\frac{\delta W_{\text{rev},a}}{-\delta W_{\text{rev},0}} \right) \quad (35)$$

This last relation can be used to define the "thermodynamic pressure" scale $P \equiv \Phi$, in the same way that an analytical identical relation is used as definition for the thermodynamic temperature scale in Carathéodory's scheme. The pressure scale P is based on one fiducial point, so that, as a matter of convention, the factor $\Phi(\pi_0)$ is a constant. For example, that factor may be chosen as $\Phi(\pi_0) = 0.6113 \text{ kPa}$ if the fiducial point is the triple point of water. Note also that relative to the linear differential form (8) the thermodynamic pressure P serves as integrating denominator.

Equivalent of the Kelvin-Planck Statement of the Second Law

The perfect symmetry between the classical (historical) construction of thermodynamics and the present, heat transfer-based, reconstruction is outlined in Table 1. The concepts assembled in this table are only the frontispiece of the voluminous subject of thermodynamics known here (the left column) or in the heat transfer-minded world described earlier (the right column). The table can be continued downward by identifying one by one the (derived) analytical highlights of our own thermodynamics, and then working out the equivalent analytical fact or statement that must be entered in the right column.

As an example of how Table 1 might be continued, consider the so-called "two parts" of the second law according to the classical line:

(i) the uniqueness of the reversible and adiabatic surface that passes through a given state, and

(ii) the fact that the states that can be reached adiabatically from the given state are all situated on the same side of the reversible and adiabatic surface.

The same "two parts" can be identified on the right side of the table as well. They are:

(i)' the uniqueness of the reversible and zero-work surface drawn through state (1) (Fig. 2), and

(ii)' the fact that the states that are accessible via zero-work processes from state (1) are all situated on the same side of the constant- ω (or constant- V) surface drawn through (1).

The immediate question is whether the "accessible" states referred to in part (ii)' are situated above or below the reversible and zero-work surface. The equivalent question on the left side of the table is settled by invoking the Kelvin-Planck statement of the second law (see, for example, Zemansky, 1968). This means that in order to be able to differentiate between the two sides of the constant- ω surface, we must first state the equivalent of the "Kelvin-Planck second law" that would fit on the right side of Table 1. Looking again at the vast evidence on which the second law is based, the equivalent of the Kelvin-Planck statement must be:

"The net work transfer interaction of a closed system that executes a cycle while in communication with no more than one pressure reservoir cannot be negative, i.e.,

$$\oint \delta W < 0 \text{ is impossible.} \quad (36)$$

Had this statement not been true, man would have opted a long time ago for letting the atmospheric pressure reservoir do work for him.

There are other ways of arriving at equation (36). Consider for example a simple system defined as in Callen (1960), and assume further that it is closed. The system possesses only one mode of reversible heat transfer (TdS) and only one mode of reversible work transfer (PdV). The lone pressure reservoir with which this system may experience work transfer during one cycle is (P_0). Let the initial state of the system be one of equilibrium with the (P_0) reservoir. This state is denoted by (a) in the first frame of Fig. 4. An example of a complete cycle executed while in contact with only one pressure reservoir is the cycle (a)-(b)-(c)-(a), where the individual processes are

- (a)-(b): reversible and isobaric contraction while in contact with (P_0)
- (b)-(c): reversible and zero-work pressurization (by heating)
- (c)-(a): adiabatic extension while in contact with the (P_0) reservoir, whose pressure is lower than the system pressure.

The important feature of this cycle is its clockwise direction, which means

$$\oint \delta W > 0 \quad (37)$$

or that during one full cycle our system manages to "reject" work to the lone pressure reservoir. We can also try the alternative (a)-(b)-(c)-(a') shown in the first frame of Fig. 4, where the new processes are

- (b)-(c'): reversible and zero-work depressurization (cooling)
- (c')-(a'): adiabatic contraction while in contact with the (P_0) reservoir, where P_0 is greater than the system pressure.

That the alternative (a)-(b)-(c)-(a') is not a full cycle stems from the empirical observation that if the system is exposed to a higher pressure in the absence of heat transfer, it contracts [hence the end state (a')]. The reverse of this observed behavior is responsible for the orientation of process (c)-(a) in the first example.

The second frame of Fig. 4 shows another cycle that can be executed while in contact with (P_0) only:

- (a)-(d): reversible and isobaric dilation, while in contact with (P_0)
- (d)-(e): reversible and zero-work depressurization (cooling)
- (e)-(a): adiabatic contraction while in contact with the

(P_0) reservoir, whose pressure is higher than the system pressure.

This cycle is also clockwise (equation (37)). If we try to complete the cycle in the counterclockwise direction, then, for the same reasons as at the end of the preceding paragraph, we cannot arrive back at (a) [see the path (a)-(d)-(e')-(a')].

In conclusion, accepting equation (36) we return to Fig. 2 to decide which side of the constant- ω surface faces the "accessible" states. We assume first that state (2) is accessible via a zero-work process from state (1), and that it is situated below state (2_{rev}). Since (1) is accessible from (2_{rev}) via a zero-work process, we imagine the three-part cycle:

- (2_{rev})-(1): zero-work process
- (1)-(2): zero-work process (assumed)
- (2)-(2_{rev}): adiabatic process, in the presence of (P_1)

The net work transfer for this cycle is

$$\oint \delta W = W_{2-2_{\text{rev}}} \quad (38)$$

However, the first-law statement

$$W_{2-2_{\text{rev}}} = U_2 - U_{2_{\text{rev}}} \quad (39)$$

and the original assumption that (2) might be situated below (2_{rev}), i.e., that $U_2 < U_{2_{\text{rev}}}$ (Fig. 2), mean that the quantities of equation (38) are negative. This conclusion violates the equivalent of the Kelvin-Planck statement (36); therefore, the states that are accessible from state (1) via zero-work processes are situated on or above the constant- ω surface that passes through state (1).

Conclusion

Reviewing the progress made after the enunciation of axioms I' and II' we retain the three-step definition of the concepts of reversible and zero-work surface, volume, and, finally, thermodynamic pressure. The expression for the infinitesimal reversible work transfer interaction is PdV , which means that the glossary of words possessed now by the heat transfer-biased individual is as complete as the glossary of the mechanist who just finished digesting Carathéodory's two axioms.

One of the reviewers of this paper wrote: "Carathéodory's approach is useful because his basic properties V and P are relatively easy to measure. It is not clear how T and S —the basic properties in the new approach—would be measured when P and V are not known. Specifically, the ideal gas thermometer cannot be used if the pressure is unknown." These comments are valuable because they help clarify the purpose of this article. Regarding the first comment, of course, history proved already that Carathéodory's approach was more useful to us, because from our standpoint, V and P were defined and understood before T and S . In this article I am asking the reader to imagine the reverse sequence of events, precisely in order to appreciate why Carathéodory's approach (and not mine) was embraced by the mathematicians at the turn of the century. Regarding the use of the ideal gas thermometer in my heat transfer-biased, entropy-seeing world, I think it is perfectly all right to imagine the experimentalist who is famous for noting the monotonic relationship between the seen entropy of the air column and the temperature of the body with which the air column is in equilibrium (this, even when the constant pressure of the surrounding atmosphere was still an unknown concept).

The merit of the mental exercise stimulated by this paper is not that it teaches us the elements of an imagined and, surely, more abstract thermodynamics; rather it is that it forces us to identify the structure of our own thermodynamics. We learn to appreciate more a certain subject, by *tolerating more than one point of view* on that subject. This approach is pursued in a new graduate textbook (Bejan, 1988).

Acknowledgments

Professor Bejan's research during 1986 and 1987 was supported by Duke University, the Electric Power Research Institute (Contract No. RP 8006-4), the Lord Foundation of North Carolina, and the National Science Foundation (Grant No. CBT-8711369).

References

- Baehr, H. D., 1973, *Thermodynamik*, 3rd ed., Springer-Verlag, Berlin, pp. 91-108.
- Bejan, A., 1988, *Advanced Engineering Thermodynamics*, Wiley, New York.
- Born, M., 1949, *Natural Philosophy of Cause and Chance*, Oxford University Press, Oxford, pp. 34-35.
- Buchdahl, H. A., 1960, "The Concepts of Classical Thermodynamics," *American Journal of Physics*, Vol. 28, pp. 196-201.
- Callen, H. B., 1960, *Thermodynamics*, Wiley, New York, p. 8.
- Carathéodory, C., 1909, "Untersuchungen über die Grundlagen der Thermodynamik," *Math. Ann.* (Berlin), Vol. 67, pp. 355-386.
- Cravalho, E. G., and Smith, J. L., Jr., 1981, *Engineering Thermodynamics*, Pitman, Boston, MA.
- Keenan, J. H., and Shapiro, A. H., 1947, "History and Exposition of the Laws of Thermodynamics," *Mechanical Engineering*, Vol. 69, pp. 915-921.
- Kestin, J., 1970, "A Simple, Unified Approach to the First and Second Laws of Thermodynamics," *Pure Appl. Chem.*, Vol. 22, pp. 511-518.
- Kestin, J., 1979, *A Course in Thermodynamics*, revised printing, Vol. I, Hemisphere, Washington, DC, Chapt. 10.
- Landsberg, P. T., 1961, "On Suggested Simplifications of Carathéodory's Thermodynamics," *Physica Status Solidi*, Vol. 1, pp. 120-126.
- Landsberg, P. T., 1964, "A Deduction of Carathéodory's Principle from Kelvin's Principle," *Nature*, Vol. 201, pp. 485-486.
- Lienhard, J. H., 1983, "Notes on the Origins and Evolution of the Subject of Heat Transfer," *Mechanical Engineering*, Vol. 105, No. 6, pp. 20-27.
- Pippard, A. B., 1964, *Elements of Classical Thermodynamics*, Cambridge University Press, Cambridge, United Kingdom, pp. 39-40.
- Poincaré, H., 1982, *Thermodynamique*, Georges Carré, Paris, pp. 66-68.
- Sears, F. W., 1963, "A Simplified Simplification of Carathéodory's Treatment of Thermodynamics," *American Journal of Physics*, Vol. 31, pp. 747-752.
- Sears, F. W., 1966, "Modified Form of Carathéodory's Second Axiom," *American Journal of Physics*, Vol. 34, pp. 665-666.
- Truesdell, C., 1984, *Rational Thermodynamics*, 2nd ed., Springer-Verlag, New York, "Historical Introit," pp. 1-57.
- Turner, L. A., 1960, "Simplification of Carathéodory's Treatment of Thermodynamics," *American Journal of Physics*, Vol. 28, pp. 781-786.
- Turner, L. A., 1962, "Simplification of Carathéodory's Treatment of Thermodynamics. II," *American Journal of Physics*, Vol. 30, pp. 506-508.
- Zemansky, M. W., 1968, *Heat and Thermodynamics*, 5th ed., McGraw-Hill, New York, pp. 197-211.

This section contains shorter technical papers. These shorter papers will be subjected to the same review process as that for full papers.

Transient Temperature Resulting From Periodic On-Off Heat Flux for a Semi-infinite Medium

D. E. Glass¹ and M. N. Özisik¹

Introduction

Transient heat conduction in solids subjected to a periodic on-off surface heat flux has numerous practical applications, including, among others, the frictional heating of solids and high-energy laser pulses directed at surfaces.

In this work, we determine the transient temperature variation of a semi-infinite medium resulting from a periodic on-off heat flux at the surface by including in the analysis the effects of nonlinear surface radiation. The effects of periodically applied heat flux on temperatures may be compared to those of a constant heat flux in one of two ways: (1) the total energy supplied over a given period remains the same, but the magnitude of the heat flux is allowed to increase during the intermittent heating, or (2) the magnitude of the heat flux remains the same, but the total energy supplied over a given period is reduced as a result of the intermittent heating. In the present analysis, the former comparison is chosen.

Analysis

Consider a semi-infinite region, initially at zero temperature, and for times $t > 0$ a periodic on-off heat flux is applied at the boundary surface $x=0$, while the surface dissipates heat by radiation into an ambient at zero temperature. Assuming constant properties, the mathematical formulation of this heat conduction problem in the dimensionless form is given by

$$\frac{\partial \theta(\eta, \xi)}{\partial \xi} = \frac{1}{2} \frac{\partial^2 \theta(\eta, \xi)}{\partial \eta^2} \quad 0 < \eta < \infty, \quad \xi > 0 \quad (1a)$$

$$-\frac{N}{2} \frac{\partial \theta(0, \xi)}{\partial \eta} = f(\xi) - \epsilon_0 \theta^4(0, \xi) \quad \eta = 0 \quad (1b)$$

$$\theta(\eta, \xi) = 0 \quad \eta \rightarrow \infty \quad (1c)$$

$$\theta(\eta, 0) = 0 \quad \xi = 0 \quad (1d)$$

where

¹Department of Mechanical and Aerospace Engineering, North Carolina State University, Raleigh, NC 27695-7910.

Contributed by the Heat Transfer Division for publication in the JOURNAL OF HEAT TRANSFER. Manuscript received by the Heat Transfer Division April 14, 1986.

$$f(\xi) = \text{dimensionless applied heat flux} = q(t)/f_0 \quad (1e)$$

$$\theta = \text{dimensionless temperature} = T/T_r \quad (1f)$$

$$\eta = \text{dimensionless distance} = x/2L \quad (1g)$$

$$\xi = \text{dimensionless time} = \alpha t/2L^2 \quad (1h)$$

$$T_r = \text{reference temperature} = (f_0/\sigma)^{1/4} \quad (1i)$$

$$N = \text{conduction-to-radiation parameter} = KT_r/L/\sigma T_r^4 \quad (1j)$$

$$f_0 = \text{reference heat flux}$$

$$L = \text{reference length}$$

$$q(t) = \text{applied surface heat flux}$$

The problem is nonlinear because the radiation effects are included at the boundary surface. Here, we assume the dimensionless applied periodic surface heat flux $f(\xi)$ is defined as

$$f(\xi) = \begin{cases} 1/\beta, & (j-1)P < \xi \leq [(j-1) + \beta]P \\ 0, & [(j-1) + \beta]P < \xi \leq jP \end{cases} \quad (2)$$

with j representing the number of periods, P , and β the fraction of the period P during which the surface heat flux is nonzero.

The above periodic nonlinear problem is solved numerically by using an implicit, central differenced, finite difference scheme with iterations applied due to the nonlinear boundary condition. The finite difference equations, obtained from a control volume analysis, are given for the internal nodes as

$$\begin{aligned} & -\frac{\Delta \xi}{2(\Delta \eta)^2} (\theta_{i+1})^{n+1, k+1} \\ & + \left[1 + \frac{2\Delta \xi}{2(\Delta \eta)^2} \right] (\theta_i)^{n+1, k+1} \\ & - \frac{\Delta \xi}{2(\Delta \eta)^2} (\theta_{i-1})^{n+1, k+1} = (\theta_i)^n \quad 0 < \eta \end{aligned} \quad (3a)$$

and for the boundary surface at $\eta = 0$ as

$$\begin{aligned} & \left(1 + \frac{\Delta \xi}{(\Delta \eta)^2} + \frac{2\Delta \xi}{N\Delta \eta} \epsilon_0 \theta_0^3 \right)^{n+1, k} (\theta_0)^{n+1, k+1} \\ & - \frac{\Delta \xi}{(\Delta \eta)^2} (\theta_1)^{n+1, k+1} = (\theta_0)^n + \frac{2\Delta \xi}{N\Delta \eta} f(\xi) \quad \eta = 0 \end{aligned} \quad (3b)$$

where we define

$$\theta_0 = \theta(0, \xi) \quad (4a)$$

$$\theta_1 = \theta(\Delta \eta, \xi) \quad (4b)$$

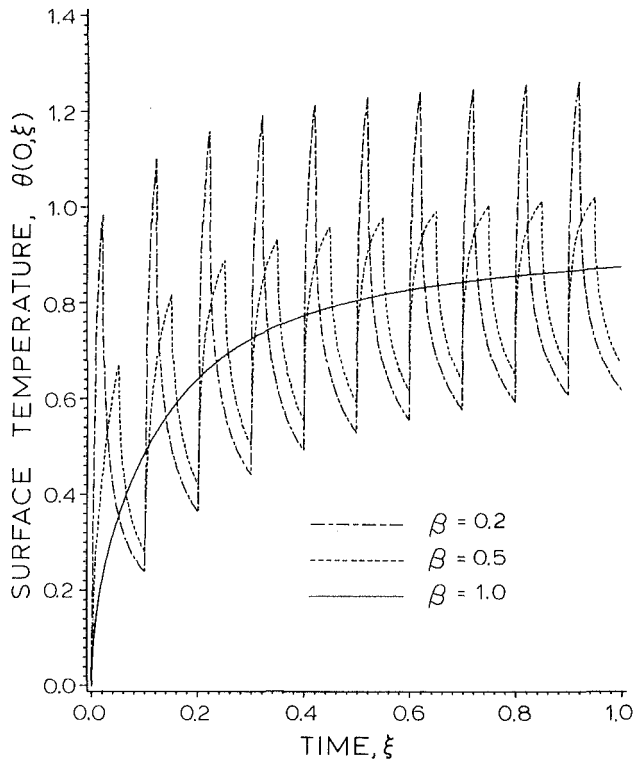


Fig. 1 Effects of β on surface temperature for applied periodic surface heat flux of period $P=0.1$ with $\epsilon_0 = 1$.

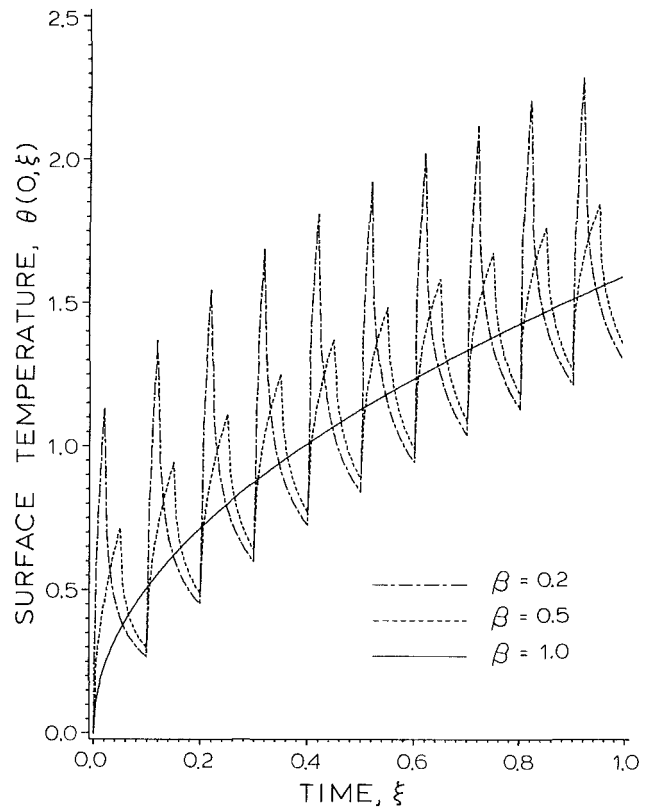


Fig. 2 Effects of β on surface temperature for applied periodic surface heat flux of period $P=0.1$ with no surface radiation (i. e., $\epsilon_0 = 0$).

The subscript i represents the nodal location in the space domain, while the superscripts n and k represent, respectively, the time and iteration levels.

The accuracy of the numerical scheme was verified first by testing the independence of the solution relative to the number of nodes in the spacial domain, and then by comparing the numerical solution for the case $\epsilon_0 = 0$ with the analytical solution of the linear problem with no radiation. Both of these tests verified the accuracy of the numerical solution.

The analytical solution of the linear problem with no surface radiation was determined by the superposition of Carslaw and Jaeger's (1959) solution for a semi-infinite solid, initially at zero temperature, with heat supplied at a constant rate at $x=0$ for a period T , by utilizing Duhamel's theorem. The resulting solution is given in the form

$$\theta(\eta, \xi) = 2\sqrt{2} \sum_{i=0}^{\infty} (\Delta F_i / N) \sqrt{\xi - \lambda_i} \times \text{ierfc} \left(\frac{\eta}{\sqrt{2(\xi - \lambda_i)}} \right) U(\xi - \lambda_i) \quad (5)$$

where $U(z)$ is the unit step function

$$U(z) = \begin{cases} 1, & z > 0 \\ 0, & z \leq 0 \end{cases} \quad (6)$$

and $\text{ierfc}(z)$ is the integral of the complementary error function

$$\text{ierfc}(z) = \frac{1}{\sqrt{\pi}} e^{-z^2} - (z) \text{erf}(z) \quad (7)$$

For the periodic problem with period P where the duration of heating is equal to βP , the parameter λ_i is defined as

$$\lambda_i = \begin{cases} [i/2]P, & \text{for } i=0, 2, 4, 6, \dots \\ [(i-1)/2 + \beta]P, & \text{for } i=1, 3, 5, 7, \dots \end{cases} \quad (8)$$

and the magnitude of the step change in the surface heat flux ΔF_i is related to β by

$$\Delta F_i = \frac{(-1)^i}{\beta} \quad (9)$$

Equation (9) implies that the total amount of energy supplied to the surface during each period is equal to that which would have been supplied by a constant heat flux of unity applied over the entire period, P . The term $(-1)^i$ represents the on-off aspect of the heating.

Discussion of Results

The effects of a periodic on-off heat flux on the surface temperatures of a semi-infinite medium for the cases involving surface radiation are studied by solving the problem with the implicit numerical scheme given by equations (3) and (4). The solution for the linear problem is obtained from equation (5). The temperature transients are examined for several different values of β . For all the test cases considered here, the length of the period is taken as $P=0.1$, while the conduction-to-radiation parameter N is taken equal to unity. For each case, heat flux of strength equal to $1/\beta$ stayed on for a time of βP from the beginning of each period P . Thus, the total heat supplied to the medium for each period P remained the same regardless of the value of β . The special case $\beta=1.0$ corresponds to a constant heat flux of unity applied at the boundary continuously over the entire period.

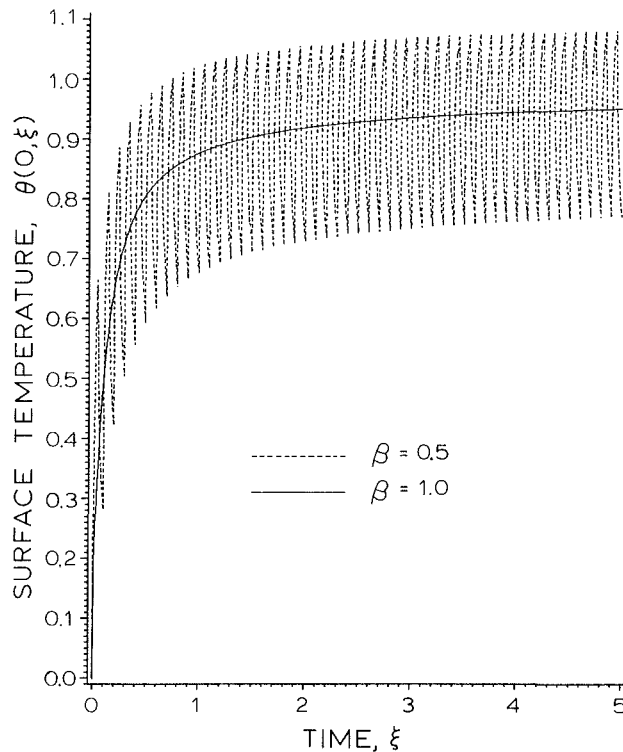


Fig. 3 Effects of β on surface temperature at long times for applied periodic surface heat flux of period $P=0.1$ with $\epsilon_0=1$

Figure 1 shows the surface temperatures resulting from a periodically applied on-off heat flux for the nonlinear case when radiation losses occur from the black surface (i.e., $\epsilon_0=1$) into an ambient at zero temperature. The surface temperature is shown for the first ten periods. Three different values of β used in this figure include $\beta=0.2, 0.5$, and 1.0 . The surface temperature corresponding to $\beta=1.0$ (i.e., uniform heat flux) remains between the maximum and minimum surface temperatures for the cases $\beta<1.0$. We notice that as β decreases from 0.5 to 0.2 , the jump in surface temperature increases significantly. However, at the end of each period, after the cooldown time, the temperature differences between the cases for $\beta=0.2$ and $\beta=0.5$ are relatively small. For comparison purposes, Fig. 2 shows similar results obtained from equation (5) for the linear case with no surface radiation. An examination of these two figures reveals that the effect of radiation is to lower the surface temperature for all values of β considered, as well as to decrease the amplitudes of the temperature oscillations. Furthermore, with radiation, the surface temperature for the case $\beta=1.0$ tends to reach an equilibrium, which occurs when the sum of the radiation loss and the conduction into the medium equals to the heat supplied to the surface. Figure 3 is prepared to illustrate how the amplitude of the oscillating surface temperature behaves at larger times for the nonlinear case for $\beta=0.5$ with the same conditions as specified in Fig. 1.

Acknowledgments

This work was supported through the National Science Foundation Grant #MEA. 83 13301.

References

Carslaw, H. S., and Jaeger, J. C., 1959, *Conduction of Heat in Solids*, Oxford Press, London, pp. 75-76.

Heat Transfer in Laminar Flow Along Circular Rods in Infinite Square Arrays

J. H. Kim¹ and W.-H. Li²

Nomenclature

- c_p = specific heat at constant pressure
- d = cylinder diameter
- d_e = equivalent thermal diameter = $4 \times$ flow area/heated perimeter
- f = friction factor = $\bar{\tau}/\frac{1}{2}\rho\bar{u}^2$
- h = heat transfer coefficient
- k = thermal conductivity
- M = dimensionless group representing mass flow, equation (5a)
- N = normal direction to boundary of typical 45 deg element, Fig. 1
- Nu_d = hd/k = Nusselt number based on the cylinder diameter
- Nu_{d_e} = hd_e/k = Nusselt number based on the thermal diameter
- p = pressure
- Pr = Prandtl number = $C_p\mu/k$
- Q = heat transfer rate per unit length from one cylinder
- q = local surface heat flux
- \bar{q} = circumferential average of $q = Q/2\pi r_0$
- r = radial coordinate
- r_0 = cylinder radius
- r^* = outer radius of equivalent annulus
- Re_d = Reynold number = $\rho\bar{u}d/\mu$
- Re_{d_e} = Reynolds number = $\rho\bar{u}d_e/\mu$
- s = half space between centers of two adjacent cylinders
- T = temperature
- T_w = wall temperature
- T_b = bulk fluid temperature
- T_0 = inlet bulk temperature
- u = axial velocity
- \bar{u} = mean axial velocity
- w = mass flow rate associated with one cylinder
- z = axial coordinate
- θ = angular coordinate
- λ = normalized radial coordinate = r/r_0
- μ = absolute viscosity
- ρ = density
- $\bar{\tau}$ = average wall shear stress

Introduction

The need to understand heat transfer characteristics over rods or tube bundles often arises in the design of compact heat exchangers and safety analysis of nuclear reactors. In particular, the fuel bundles of typical light water nuclear reactors are composed of a large number of circular rods arranged in square array pattern. The purpose of the present study is to analyze heat transfer characteristics of flow in such a multirod

¹Electric Power Research Institute, Palo Alto, CA 94303; Mem. ASME.

²Department of Chemical Engineering, Stanford University, CA 94305; presently at Department of Chemical Engineering, UCLA, Los Angeles, CA 90024.

Contributed by the Heat Transfer Division for publication in the JOURNAL OF HEAT TRANSFER. Manuscript received by the Heat Transfer Division August 13, 1985.

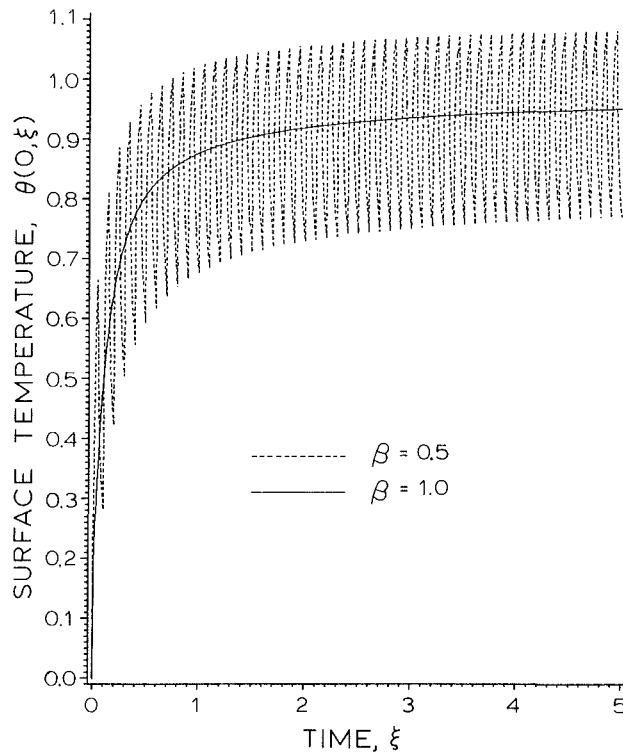


Fig. 3 Effects of β on surface temperature at long times for applied periodic surface heat flux of period $P=0.1$ with $\epsilon_0=1$

Figure 1 shows the surface temperatures resulting from a periodically applied on-off heat flux for the nonlinear case when radiation losses occur from the black surface (i.e., $\epsilon_0=1$) into an ambient at zero temperature. The surface temperature is shown for the first ten periods. Three different values of β used in this figure include $\beta=0.2, 0.5$, and 1.0 . The surface temperature corresponding to $\beta=1.0$ (i.e., uniform heat flux) remains between the maximum and minimum surface temperatures for the cases $\beta<1.0$. We notice that as β decreases from 0.5 to 0.2 , the jump in surface temperature increases significantly. However, at the end of each period, after the cooldown time, the temperature differences between the cases for $\beta=0.2$ and $\beta=0.5$ are relatively small. For comparison purposes, Fig. 2 shows similar results obtained from equation (5) for the linear case with no surface radiation. An examination of these two figures reveals that the effect of radiation is to lower the surface temperature for all values of β considered, as well as to decrease the amplitudes of the temperature oscillations. Furthermore, with radiation, the surface temperature for the case $\beta=1.0$ tends to reach an equilibrium, which occurs when the sum of the radiation loss and the conduction into the medium equals to the heat supplied to the surface. Figure 3 is prepared to illustrate how the amplitude of the oscillating surface temperature behaves at larger times for the nonlinear case for $\beta=0.5$ with the same conditions as specified in Fig. 1.

Acknowledgments

This work was supported through the National Science Foundation Grant #MEA. 83 13301.

References

- Carslaw, H. S., and Jaeger, J. C., 1959, *Conduction of Heat in Solids*, Oxford Press, London, pp. 75-76.

Heat Transfer in Laminar Flow Along Circular Rods in Infinite Square Arrays

J. H. Kim¹ and W.-H. Li²

Nomenclature

- c_p = specific heat at constant pressure
 d = cylinder diameter
 d_e = equivalent thermal diameter = $4 \times$ flow area/heated perimeter
 f = friction factor = $\bar{\tau}/\frac{1}{2}\rho\bar{u}^2$
 h = heat transfer coefficient
 k = thermal conductivity
 M = dimensionless group representing mass flow, equation (5a)
 N = normal direction to boundary of typical 45 deg element, Fig. 1
 Nu_d = hd/k = Nusselt number based on the cylinder diameter
 Nu_{d_e} = hd_e/k = Nusselt number based on the thermal diameter
 p = pressure
 Pr = Prandtl number = $C_p\mu/k$
 Q = heat transfer rate per unit length from one cylinder
 q = local surface heat flux
 \bar{q} = circumferential average of $q = Q/2\pi r_0$
 r = radial coordinate
 r_0 = cylinder radius
 r^* = outer radius of equivalent annulus
 Re_d = Reynold number = $\rho\bar{u}d/\mu$
 Re_{d_e} = Reynolds number = $\rho\bar{u}d_e/\mu$
 s = half space between centers of two adjacent cylinders
 T = temperature
 T_w = wall temperature
 T_b = bulk fluid temperature
 T_0 = inlet bulk temperature
 u = axial velocity
 \bar{u} = mean axial velocity
 w = mass flow rate associated with one cylinder
 z = axial coordinate
 θ = angular coordinate
 λ = normalized radial coordinate = r/r_0
 μ = absolute viscosity
 ρ = density
 $\bar{\tau}$ = average wall shear stress

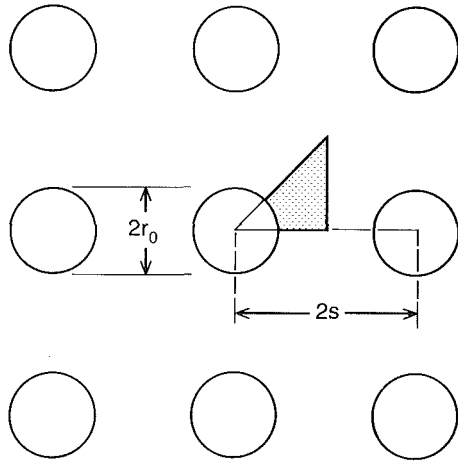
Introduction

The need to understand heat transfer characteristics over rods or tube bundles often arises in the design of compact heat exchangers and safety analysis of nuclear reactors. In particular, the fuel bundles of typical light water nuclear reactors are composed of a large number of circular rods arranged in square array pattern. The purpose of the present study is to analyze heat transfer characteristics of flow in such a multirod

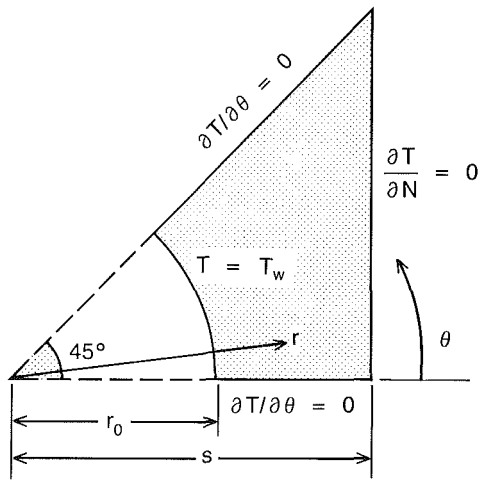
¹Electric Power Research Institute, Palo Alto, CA 94303; Mem. ASME.

²Department of Chemical Engineering, Stanford University, CA 94305; presently at Department of Chemical Engineering, UCLA, Los Angeles, CA 90024.

Contributed by the Heat Transfer Division for publication in the JOURNAL OF HEAT TRANSFER. Manuscript received by the Heat Transfer Division August 13, 1985.



(a) Cross-sectional view



(b) Typical 45° element

Fig. 1 Cross-sectional view and typical 45 deg element

geometric configuration. The analysis given here will follow as closely as possible the method of Sparrow et al. [1] who analyzed a similar problem for circular cylinders arranged in an equilateral triangular array.

The following major assumptions are made in the present analysis:

- 1 Flow is fully developed laminar flow parallel to the axis of rods.
- 2 The axial profile of the surface heat flux to the fluid is uniform.
- 3 Thermodynamic properties are assumed constant.

Formulation of the Problem

Figure 1 shows a cross-sectional view of the circular rods arranged in square array pattern. Due to the symmetry of the configuration, consideration need be given only to the typical 45 deg element as shown in Fig. 1(b). The energy equation in a cylindrical coordinate system is

$$\rho c_p u \frac{\partial T}{\partial z} = k \left(\frac{\partial^2 T}{\partial r^2} + \frac{1}{r} \frac{\partial T}{\partial r} + \frac{1}{r^2} \frac{\partial^2 T}{\partial \theta^2} + \frac{\partial^2 T}{\partial z^2} \right) \quad (1)$$

The conditions to be applied along the boundary of a typical area element shown in Fig. 1(b) are: On the rod surface $r = r_0$, the wall temperature T_w is assumed to be a function of z only, i. e., no circumferential variation of T_w . Along the remainder

Table 1 Numerical values of δ_n

s/r_0	$\delta_1 \times 10^2$	$\delta_2 \times 10^3$	$\delta_3 \times 10^4$	$\delta_4 \times 10^5$	$\delta_5 \times 10^6$
1.00	-8.0362	10.5299	21.0963	-47.981	-107.99
1.02	-8.4542	9.3678	26.0958	-16.466	-64.50
1.04	-8.8486	8.0313	29.4573	10.757	-24.91
1.06	-9.2172	6.5884	30.8559	30.077	4.74
1.08	-9.5585	5.1058	30.539	41.481	23.820
1.10	-9.8718	3.6405	28.995	46.66	34.36
1.12	-10.1572	2.2353	26.7065	47.594	38.93
1.14	-10.4154	0.9177	24.0536	45.922	39.72
1.16	-10.6477	-0.2974	21.2957	42.818	38.29
1.18	-10.8559	-1.4043	18.595	39.048	35.70
1.20	-11.0416	-2.4036	16.0442	35.081	32.58
1.30	-11.7019	-6.0048	6.3642	18.360	18.04
1.50	-12.2597	-9.0623	-2.0158	3.340	4.55
1.80	-12.4725	-10.2238	-5.1664	-2.218	-0.38
2.00	-12.5099	-10.4278	-5.7161	-3.178	-1.23
3.00	-12.5372	-10.5765	-6.1164	-3.875	-1.84
4.00	-12.5382	-10.5820	-6.1310	-3.900	-1.86

of the boundary, the normal derivative of the temperature should vanish as a condition of symmetry.

The uniform surface heat flux condition can be expressed as

$$\frac{\partial T}{\partial z} = \frac{Q}{wc_p} = \frac{Q/8}{c_p w/8} = \text{const} \quad (2)$$

The velocity to be used in equation (1) can be adopted from the solution of Sparrow and Loeffler [2] who analyzed the laminar flow problem for the present geometric configuration. It is given by

$$\frac{u}{s^2 \left(-\frac{1}{\mu} \frac{dP}{dz} \right)} = \frac{2}{\pi} \ln \frac{r}{r_0} - \frac{1}{4} \left[\left(\frac{r}{s} \right)^2 - \left(\frac{r_0}{s} \right)^2 \right] + \sum_{n=1}^{\infty} \frac{\delta_n}{4n} \left(\frac{r}{s} \right)^{4n} \left[1 - \left(\frac{r_0}{r} \right)^{8n} \right] \cos 4n\theta \quad (3)$$

The first few values of the coefficient δ_n were recalculated for the present study and are presented in Table 1. The recalculated values accurately duplicated the previous results [2].

From the velocity solution given by equation (3), it can be shown that

$$f \text{Re}_d = \left[4 - \pi \left(\frac{r_0}{s} \right)^2 \right]^2 / (4\pi M) \quad (4)$$

where

$$M \equiv \frac{w/(8\rho)}{s^4 \left(-\frac{1}{\mu} \frac{dP}{dz} \right)} = \frac{1}{2\pi} \left(2 \ln \frac{s}{r_0} + \ln 2 - 3 \right) + \frac{1}{6} + \frac{1}{4} \left(\frac{r_0}{s} \right)^2 - \frac{\pi}{64} \left(\frac{r_0}{s} \right)^4 + \sum_{j=1}^{\infty} \frac{\delta_j}{4j} \left[\frac{\lambda_j}{4j+2} + \left(\frac{r_0}{s} \right)^{8j} \frac{\beta}{4j-2} \right] \quad (5)$$

with

$$\lambda_j = \int_0^{\pi/4} \frac{\cos 4j\theta}{(\cos \theta)^{2+4j}} d\theta$$

and

$$\beta_j = \int_0^{\pi/4} \frac{\cos 4j\theta}{(\cos \theta)^{2-4j}} d\theta$$

Reference [2] gives a plot of $f \text{Re}_d$ versus porosity $\epsilon = \text{flow area}/(\text{flow area} + \text{cylinder area})$. Table 3 presents numerical

values of M , f , Re_d , and $f Re_{d_e}$ versus s/r_0 as calculated from equations (4) and (5), respectively. Reference [7] also shows a plot of $f Re_{d_e}$ versus s/r_0 . However, from the relation $f Re_{d_e} = f Re_d (d_e/d)$, it can be shown that the plot given in [7] overpredicts the correct values.

Making use of equations (2), (3), and (5), the governing differential equation (1) becomes

$$\frac{\partial^2 T}{\partial r^2} + \frac{1}{r} \frac{\partial T}{\partial r} + \frac{1}{r^2} \frac{\partial^2 T}{\partial \theta^2} = \frac{Q/(8k)}{Ms^2} \left\{ \frac{2}{\pi} \ln \frac{r}{r_0} - \frac{1}{4} \left[\left(\frac{r}{s} \right)^2 - \left(\frac{r_0}{s} \right)^2 \right] + \sum_{n=1}^{\infty} \frac{\delta_n}{4n} \left(\frac{r}{s} \right)^{4n} \left[1 - \left(\frac{r_0}{r} \right)^{8n} \right] \cos 4n\theta \right\} \quad (6)$$

The boundary conditions are

$$(a) \quad T = T_w(z) \text{ at the cylinder wall} \quad (7a)$$

$$(b) \quad \frac{\partial T}{\partial \theta} = 0 \text{ on } \theta = 0, \frac{\pi}{4} \quad (7b)$$

$$(c) \quad \frac{\partial T}{\partial N} = \frac{\partial T}{\partial r} \cos \theta - \frac{\partial T}{\partial \theta} \frac{\sin \theta}{r} = 0$$

on the right-hand boundary of the typical element, i.e., on $r = s/\cos \theta$ (7c)

Solution of the Governing Equation

The general solution for equation (6) can be obtained by following the same procedure as in Sparrow et al. [1], and will not be described here.

The final solution that satisfies all the boundary conditions is given by

$$T - T_w = \frac{Q/(8k)}{Ms^2} \left\{ \left[\frac{1}{2\pi} (r^2 + r_0^2) - \frac{1}{16} \frac{r_0^4}{s^2} - \frac{4Ms^2}{\pi} \right] \ln \frac{r}{r_0} - \frac{1}{64} \frac{r^4 - r_0^4}{s^2} + \left[-\frac{1}{2\pi} + \frac{1}{16} \left(\frac{r_0}{s} \right)^2 \right] (r^2 - r_0^2) \right\} + \frac{Q/(8k)}{M} \sum_{n=1}^{\infty} \frac{\omega_n}{4n} \left(\frac{r}{s} \right)^{4n} \left[1 - \left(\frac{r_0}{r} \right)^{8n} \right] \cos 4n\theta + \frac{Q/(8k)}{M} \left(\frac{r}{s} \right)^2 \sum_{n=1}^{\infty} \delta_n \cos 4n\theta \left\{ \frac{(r/s)^{4n}}{16n} \left[\frac{1}{4n+1} + \frac{(r_0/r)^{8n}}{4n-1} \right] - \frac{(r_0/r)^2}{2(16n^2-1)} \frac{r_0^{8n}}{r^{4n}s^{4n}} \right\} \quad (8)$$

In the above, ω_n can be determined from

$$\sum_{n=1}^{\infty} \omega_n (\cos \theta)^{1-4n} \left[\cos (4n-1)\theta + \left(\frac{r_0 \cos \theta}{s} \right)^{8n} \cos (4n+1)\theta \right] = - \sum_{n=1}^{\infty} \delta_n \left\{ \frac{2n}{16n^2-1} \left(\frac{r_0}{s} \right)^{8n+2} (\cos \theta)^{4n+1} \cos (4n+1)\theta + \frac{2n \cos (4n-1)\theta + \cos \theta \cos 4n\theta}{8n(1+4n)(\cos \theta)^{4n+1}} + \frac{(r_0/s)^{8n} (\cos \theta)^{4n-1}}{8n(1-4n)} [2n \cos (4n+1)\theta - \cos \theta \cos 4n\theta] \right\}$$

Table 2 Numerical values of ω_n

s/r_0	$\omega_1 \times 10^2$	$\omega_2 \times 10^3$	$\omega_3 \times 10^4$	$\omega_4 \times 10^5$	$\omega_5 \times 10^6$
1.00	0.8993	-1.2138	-0.1873	6.088	8.45
1.02	0.9654	-1.2695	-0.7138	5.195	8.10
1.04	1.0362	-1.2981	-1.2907	3.593	6.56
1.06	1.1108	-1.2971	-1.8292	1.761	4.53
1.08	1.1890	-1.2684	-2.2668	0.058	2.49
1.10	1.2699	-1.2146	-2.5820	-1.337	0.76
1.12	1.3531	-1.1399	-2.7782	-2.382	-0.60
1.14	1.4378	-1.0485	-2.8728	-3.105	-1.57
1.16	1.5236	-0.9447	-2.8863	-3.563	-2.24
1.18	1.6100	-0.8321	-2.8386	-3.815	-2.66
1.20	1.6967	-0.7137	-2.7465	-3.915	-2.91
1.30	2.1256	-0.1040	-2.0004	-3.323	-2.77
1.50	2.9322	0.9406	-0.6079	-1.498	-1.37
1.80	4.0279	2.0875	0.5699	-0.074	-0.27
2.00	4.7000	2.7087	1.0578	0.407	-0.06
3.00	7.5146	5.1360	2.5878	1.547	0.70
4.00	9.6593	6.9491	3.6456	2.230	1.04

$$+ \left[\frac{4M}{\pi} - \frac{1}{2\pi} \left(\frac{r_0}{s} \right)^2 + \frac{1}{16} \left(\frac{r_0}{s} \right)^4 \right] \cos^2 \theta - \frac{1}{8} \left(\frac{r_0}{s} \right)^2 - \frac{1}{\pi} \ln \frac{s}{r_0 \cos \theta} + \frac{1}{2\pi} + \frac{1}{16 \cos^2 \theta} \quad (9)$$

The first five numerical values of ω_n are tabulated in Table 2 as a function of s/r_0 .

Heat Transfer Characteristics

(a) **Determination of Nusselt Number.** It is now possible to obtain the wall-to-bulk temperature difference from which the Nusselt numbers can be calculated.

By definition, the bulk temperature is given by

$$T_b = \frac{\iint_{\text{Area}} T_p \rho u r dr d\theta}{\iint_{\text{Area}} \rho u r dr d\theta} = \frac{\rho \int_0^{\pi/4} \int_{r_0}^{s/\cos \theta} T u r dr d\theta}{w/8} \text{ so that} \quad (10)$$

$$\frac{T_w - T_b}{Q/(8k)} = -\frac{1}{M^2} \left(\frac{r_0}{s} \right)^2 \int_0^{\pi/4} \int_1^{s/r_0 \cos \theta} F(\lambda, \theta) \lambda d\lambda d\theta$$

where $\lambda = r/r_0$ was introduced. Here, $F(\lambda, \theta)$ is given by

$$F(\lambda, \theta) = \left[\frac{2}{\pi} \ln \lambda - \frac{1}{4} \left(\frac{r_0}{s} \right)^2 (\lambda^2 - 1) + \sum_{n=1}^{\infty} \frac{\delta_n}{4n} \left(\frac{r_0}{s} \right)^{4n} (\lambda^{4n} - \lambda^{-4n}) \cos 4n\theta \right] \left\{ \left[\frac{1}{2\pi} \left(\frac{r_0}{s} \right)^2 (\lambda^2 + 1) - \frac{1}{16} \left(\frac{r_0}{s} \right)^4 - \frac{4M}{\pi} \right] \ln \lambda - \frac{1}{64} \left(\frac{r_0}{s} \right)^4 (\lambda^4 - 1) + \left(\frac{r_0}{s} \right)^2 \left[-\frac{1}{2\pi} + \frac{1}{16} \left(\frac{r_0}{s} \right)^2 \right] (\lambda^2 - 1) + \sum_{n=1}^{\infty} \frac{\omega_n}{4n} \left(\frac{r_0}{s} \right)^{4n} (\lambda^{4n} - \lambda^{-4n}) \cos 4n\theta + \left(\frac{r_0}{s} \right)^2 \sum_{m=1}^{\infty} \delta_m \left(\frac{r_0}{s} \right)^{4m} \cos 4m\theta \left[\frac{\lambda^2}{16m} \left(\frac{\lambda^{4m}}{4m+1} + \frac{\lambda^{-4m}}{4m-1} \right) - \frac{\lambda^{-4m}}{2(16m^2-1)} \right] \right\} \quad (11)$$

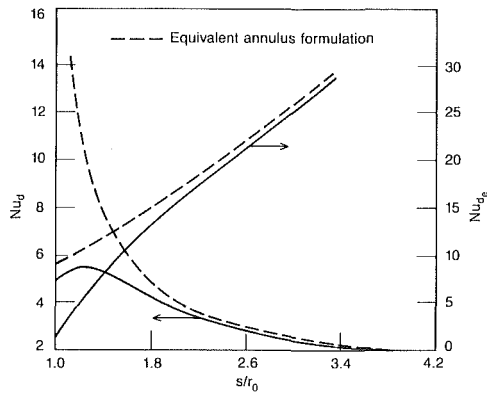


Fig. 2 Nusselt number results

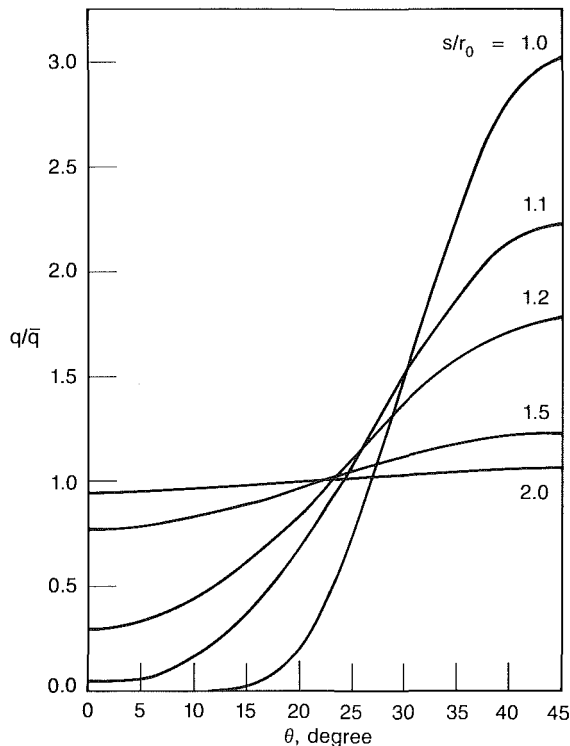


Fig. 3 Peripheral variation of surface heat flux

Now, if the heat transfer coefficient is defined $h = Q/\pi d(T_w - T_b)$, the Nusselt number based on the cylinder diameter d becomes

$$\text{Nu}_d = \frac{hd}{k} = \frac{8}{\pi} \frac{Q/(8k)}{T_w - T_b} \quad (12)$$

Equations (10)–(12) show that the Nusselt number depends only on the spacing-to-diameter ratios. Of course, this is fully expected from the results obtained for equilateral triangular array case investigated in [1]. Figure 2 presents a plot of Nu_d as a function of s/r_0 . The Nusselt number Nu_{d_e} based on the equivalent thermal diameter d_e is shown on the same plot. Nu_d increases with s/r_0 for small values of s/r_0 , achieving a maximum value at approximately $s/r_0 = 1.3$, and then monotonically decreases as s/r_0 increases. This is a surprising finding, but it is consistent with the behavior of $f \text{Re}_d$ versus porosity (equivalently, s/r_0) reported in [2]. Table 3 shows that $f \text{Re}_d$ also increases with s/r_0 , reaches a maximum value at approximately $s/r_0 = 1.08$, and thereafter decreases as s/r_0 increases. Note that the maximum values of Nu_d and $f \text{Re}_d$ do

Table 3 Numerical values of M , $f \text{Re}_d$, $f \text{Re}_{d_e}$, Nu_d , and Nu_{d_e}

s/r_0	M	$f \text{Re}_d$	$f \text{Re}_{d_e}$	Nu_d	Nu_{d_e}
1.00	0.002431	24.122	6.591	4.934	1.348
1.02	0.002961	25.829	8.386	4.985	1.618
1.04	0.003559	26.833	10.120	5.047	1.903
1.06	0.004225	27.302	11.757	5.118	2.204
1.08	0.004962	27.379	13.282	5.191	2.518
1.10	0.005769	27.176	14.692	5.262	2.845
1.12	0.006646	26.781	15.992	5.329	3.182
1.14	0.007591	26.257	17.190	5.389	3.528
1.16	0.008603	25.651	18.296	5.442	3.881
1.18	0.009680	24.996	19.318	5.485	4.239
1.20	0.010820	24.317	20.267	5.519	4.600
1.30	0.017382	20.988	24.173	5.537	6.377
1.50	0.033841	15.942	29.729	5.066	9.448
1.80	0.063035	11.593	36.232	4.157	12.992
2.00	0.083536	9.844	40.291	3.678	15.055
3.00	0.180351	5.881	61.514	2.412	25.227
4.00	0.260185	4.425	85.720	1.891	36.638

not occur at the same value of s/r_0 , as the functional dependences of Nu_d and $f \text{Re}_d$ on s/r_0 given by equations (4) and (12) are quite different. The ratio $\text{Nu}_d/f \text{Re}_d$ reaches a minimum value at approximately $s/r_0 = 1.06$ and keeps increasing with s/r_0 .

Table 3 shows numerical values of Nu_d and Nu_{d_e} versus s/r_0 . Comparing the present results with those for an equilateral triangular array shows that the present results for the Nusselt number Nu_d lie below those for the equilateral triangular array case at any given s/r_0 . This is expected physically, because the wall-to-bulk temperature difference will increase as the number of rods immediately adjacent to a cylinder decreases.

The wall temperature can be easily derived

$$\frac{T_w - T_0}{Q/k} = \frac{z}{(w/\mu)\text{Pr}} + \frac{1}{\pi \text{Nu}_d} \quad (13)$$

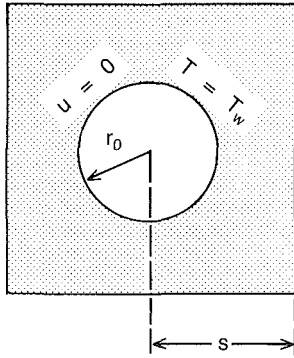
(b) **Peripheral Variation of Local Heat Transfer.** Since we have the temperature distribution solution given by equation (8), the circumferential variation of local heat flux can also be determined. The local surface heat flux is given by the Fourier law, $q = -k(\partial T/\partial r)_{r_0}$. Using the temperature solution given by equation (8), the normalized local heat flux is found to be

$$\frac{q}{\bar{q}} = 1 - \frac{\pi}{4M} \sum_{n=1}^{\infty} \left[2\omega_n \left(\frac{r_0}{s}\right)^{4n} + \frac{\delta_n}{2(4n-1)} \left(\frac{r_0}{s}\right)^{4n+2} \right] \cos 4n\theta \quad (14)$$

The numerical results for the normalized local heat flux are plotted in Fig. 3 as a function of the angle θ and the spacing-to-diameter ratio s/r_0 . The plot shows that the peripheral variation of the local heat flux is practically negligible for values of s/r_0 greater than 2, that is, for large values of s/r_0 , the circumferentially uniform wall temperature may be treated as the circumferentially uniform heat flux and vice versa.

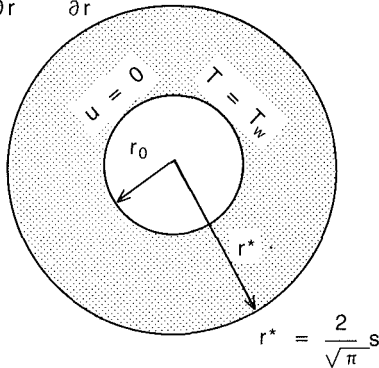
(c) **Simplified Annulus Formulation.** It is interesting to investigate a simplified situation where all the circumferential variations are suppressed. This situation will be achieved by reformulating the problem in an equivalent annulus. Figure 4 describes a simplified equivalent annulus situation. Here, we let the flow area associated with a single rod be equal to that

$$\frac{\partial u}{\partial N} = \frac{\partial T}{\partial N} = 0$$



(a) Actual configuration

$$\frac{\partial u}{\partial r} = \frac{\partial T}{\partial r} = 0$$



(b) Equivalent annulus

Fig. 4 Description of equivalent annulus formulation

for the actual configuration. Thus, the fictitious outer cylinder radius r^* should be given by $r^* = 2/\sqrt{\pi}s$.

The velocity distribution inside the annulus is now characterized by

$$\frac{\partial^2 u}{\partial r^2} + \frac{1}{r} \frac{u}{r} = \frac{1}{\mu} \frac{dP}{dz} \quad (15a)$$

$$u(r_0) = 0, \quad \frac{\partial u}{\partial r}(r^*) = 0 \quad (15b)$$

The solution to the above problem is found to be

$$\frac{u}{s^2 \left(-\frac{1}{\mu} \frac{dP}{dz} \right)} = \frac{2}{\pi} \ln \frac{r}{r_0} - \frac{1}{4} \left[\left(\frac{r}{s} \right)^2 - \left(\frac{r_0}{s} \right)^2 \right] \quad (16)$$

The dimensionless group M defined by equation (5) is now given by

$$M = \frac{1}{\pi} \ln \left(\frac{2}{\sqrt{\pi}} \frac{s}{r_0} \right) - \frac{3}{4\pi} + \frac{1}{4} \left(\frac{r_0}{s} \right)^2 - \frac{\pi}{64} \left(\frac{r_0}{s} \right)^4 \quad (17)$$

Using the velocity distribution given by equation (16), the temperature distribution problem for the annulus can be formulated as

$$\frac{\partial^2 T}{\partial r^2} + \frac{1}{r} \frac{\partial T}{\partial r} = \frac{Q/(8k)}{Ms^2} \left\{ \frac{2}{\pi} \ln \frac{r}{r_0} - \frac{1}{4} \left[\left(\frac{r}{s} \right)^2 - \left(\frac{r_0}{s} \right)^2 \right] \right\} \quad (18a)$$

$$T(r_0) = T_w, \quad \frac{\partial T}{\partial r}(r^*) = 0 \quad (18b)$$

The solution for the above problem is now found to be

$$T - T_w = \frac{Q/(8k)}{Ms^2} \left\{ \left[\frac{1}{2\pi} (r^2 + r_0^2) - \frac{1}{16} \frac{r_0^4}{s^2} - \frac{4Ms^2}{\pi} \right] \ln \frac{r}{r_0} - \frac{1}{64} \frac{r^4 - r_0^4}{s^2} + \left[-\frac{1}{2\pi} + \frac{1}{16} \left(\frac{r_0}{s} \right)^2 \right] (r^2 - r_0^2) \right\} \quad (19)$$

Equations (16) and (19) represent the nonseries terms of the more complete solutions given by equations (3) and (8), demonstrating that the series parts appearing in equations (3) and (8) represent correction terms to account for the peripheral variation due to the nonannulus geometry.

Now, it can be shown that the Nusselt number based on the inner cylinder diameter d is given by

$$Nu_d = \frac{hd}{k} = \frac{8}{\pi} \left[-\frac{\pi}{4M^2} \left(\frac{r_0}{s} \right)^2 \int_1^{\frac{2}{\sqrt{\pi}} \frac{s}{r_0}} F(\lambda) \lambda d\lambda \right]^{-1} \quad (20)$$

where $F(\lambda)$ is identical to the nonseries part of $F(\lambda, \theta)$ defined by equation (11). The numerical results for the equivalent annulus formulation are plotted as a dotted curve in Fig. 2. They show that the effect of circumferential variation becomes increasingly significant at smaller spacing-to-diameter ratios. The Nusselt numbers predicted for the equivalent annulus formulation lie above the more complete solution, and this implies that the heat transfer is more effective when the temperature distribution is peripherally uniform.

One of the assumptions made in the present analysis was constant thermodynamic properties. If the temperature varies significantly within the fluid, the temperature-dependent properties (such as viscosity and density) can also vary significantly. To understand the heat transfer characteristics in a multirod geometry under such a condition will require a much more rigorous analysis. At the present, the effects of variable properties on the heat transfer in multirod geometries are not fully understood. These effects are relatively well understood only for simple geometries such as flows in a tube. For example, for laminar gas flow in a tube, experimental verification of Kays and Nicoll [3] and numerical solution by Worsøe-Schmidt and Leppert [4] indicate that the Nusselt numbers are relatively insensitive to the property variation due to the temperature change. For laminar liquid flow in a tube, Deissler [5] and Yang [6] give simple correction rules to account for the variable viscosities. However, it is not clear whether the same conclusion can be extended to a more complex multirod geometry.

Reference [1] presented some remarks regarding thermal entry problems, boundary conditions, and other assumptions in relation to the equilateral triangular array case. All of those remarks are qualitatively valid for the present situation also.

Acknowledgments

The authors had useful discussions with Dr. M. Merilo. The computational assistance provided by Mr. D. A. Hamon is appreciated.

References

- 1 Sparrow, E. M., Loeffler, A. L., Jr., and Hubbard, H. A., "Heat Transfer to Laminar Flow Between Cylinders," *ASME JOURNAL OF HEAT TRANSFER*, Vol. 83, 1961, pp. 415-422.

2 Sparrow, E. M., and Loeffler, A. L., Jr., "Longitudinal Laminar Flow Between Cylinders Arranged in Regular Array," *AIChE Journal*, Vol. 5, No. 3, 1959, pp. 325-330.

3 Kays, W. M., and Nicoll, W. B., "Laminar Flow Heat Transfer to a Gas With Large Temperature Differences," *ASME JOURNAL OF HEAT TRANSFER*, Vol. 85, 1963, pp. 329-338.

4 Worsøe-Schmidt, P. M., and Leppert, G., "Heat Transfer and Friction for Laminar Flow of Gas in a Circular Tube at High Heating Rate," *Int. Journal of Heat and Mass Transfer*, Vol. 8, 1965, pp. 1281-1301.

5 Deissler, R. G., "Analytical Investigation of Fully Developed Laminar Flow in Tubes, With Heat Transfer With Fluid Properties Variable Along the Radius," NACA TN 2410, Washington, DC, July 1951.

6 Yang, K. T., "Laminar Forced Convection of Liquids in Tubes With Variable Viscosity," *ASME JOURNAL OF HEAT TRANSFER*, Vol. 84, 1962, pp. 353-362.

7 Kays, W. M., and Perkins, H. C., "Forced Convection, Internal Flow in Ducts," *Handbook of Heat Transfer*, W. M. Rohsenow and J. P. Hartnett, eds., McGraw-Hill, New York, 1973.

Free Convection Flow of Non-Newtonian Fluids Along a Vertical Plate Embedded in a Porous Medium

Han-Taw Chen¹ and Cha'o-Kuang Chen¹

Nomenclature

- D = packing diameter
 e = porosity of bed
 f = dimensionless stream function, equation (14)
 g = gravitational acceleration
 h = local heat transfer coefficient
 \bar{h} = average heat transfer coefficient, equation (30)
 k = new bed permeability, equation (1e)
 k_1 = bed permeability
 k_m = thermal conductivity of the fluid-saturated porous medium
 K = new power law constant, equation (1c)
 K_1 = power law constant
 l = length of the plate
 L = length of bed or capillary
 n = new power law index, equation (1f)
 n_1 = power law index
 p = pressure
 Ra = modified Rayleigh number for the flow of a non-Newtonian power law fluid in the porous medium = $\rho_\infty g \beta k(n) (T_w - T_\infty)^{1/n} / K \alpha^n$
 Ra^* = dimensionless parameter = $Ra^{1/n}$
 T = temperature
 u = superficial velocity in x direction
 u^* = dimensionless velocity = $u / [\rho_\infty g \beta k(n) (T_w - T_\infty) / K]^{1/n}$
 v = superficial velocity in y direction
 v^* = dimensionless velocity = $v / [\rho_\infty g \beta k(n) (T_w - T_\infty) / K]^{1/n}$
 V_0 = superficial velocity
 x = transverse coordinate
 x^* = dimensionless coordinate = x/l
 y = longitudinal coordinate
 y^* = dimensionless coordinate = y/l
 α = equivalent thermal diffusivity

¹Department of Mechanical Engineering, National Cheng-Kung University, Tainan, Taiwan, Republic of China.

Contributed by the Heat Transfer Division for publication in the *JOURNAL OF HEAT TRANSFER*. Manuscript received by the Heat Transfer Division September 18, 1985.

- β = coefficient of thermal expansion
 η = dimensionless similarity variable, equation (13)
 θ = dimensionless temperature = $(T - T_\infty) / (T_w - T_\infty)$
 ρ = density of the non-Newtonian fluid
 ψ = stream function

Subscripts

- m = edge of momentum boundary layer
 T = edge of thermal boundary layer
 w = wall
 ∞ = infinity

Introduction

Previous studies for free convection flow along a vertical flat plate embedded in a porous medium were restricted, in general, to Newtonian fluid only (Na and Pop, 1983; Cheng and Minkowycz, 1977; Masuoka, 1983). Few pay attention to the problem of natural convection of non-Newtonian fluids in a porous medium. However, the prediction of heat transfer characteristics is of importance in a number of geophysical and other engineering applications, such as petroleum drillings, especially in the studies of natural convection of non-Newtonian fluids in a porous medium adjacent to the heated surface.

The problem of free convection flow of a non-Newtonian power law fluid along an isothermal vertical flat plate embedded in the porous medium is considered in the present study. The physical coordinate system is shown schematically in Fig. 1. In the present study, it is assumed that the modified Darcy law and the boundary layer approximation are applicable. This implies that the present solutions are valid at a high Rayleigh number. With these simplifications, the governing partial nonlinear differential equations can be transformed into a set of coupled ordinary differential equations which can be solved by the fourth-order Runge-Kutta method. Algebraic equations for heat transfer rate and boundary layer thickness as a function of the prescribed wall temperature and physical properties of liquid-porous medium are obtained. The similarity solutions can be applied to problems in geophysics and engineering.

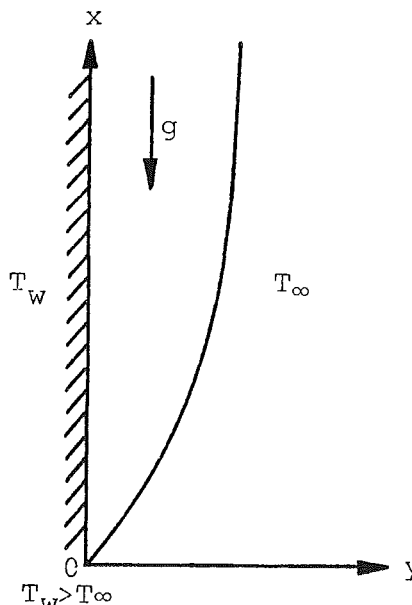


Fig. 1 Physical coordinate system

2 Sparrow, E. M., and Loeffler, A. L., Jr., "Longitudinal Laminar Flow Between Cylinders Arranged in Regular Array," *AIChE Journal*, Vol. 5, No. 3, 1959, pp. 325-330.

3 Kays, W. M., and Nicoll, W. B., "Laminar Flow Heat Transfer to a Gas With Large Temperature Differences," *ASME JOURNAL OF HEAT TRANSFER*, Vol. 85, 1963, pp. 329-338.

4 Worsøe-Schmidt, P. M., and Leppert, G., "Heat Transfer and Friction for Laminar Flow of Gas in a Circular Tube at High Heating Rate," *Int. Journal of Heat and Mass Transfer*, Vol. 8, 1965, pp. 1281-1301.

5 Deissler, R. G., "Analytical Investigation of Fully Developed Laminar Flow in Tubes, With Heat Transfer With Fluid Properties Variable Along the Radius," NACA TN 2410, Washington, DC, July 1951.

6 Yang, K. T., "Laminar Forced Convection of Liquids in Tubes With Variable Viscosity," *ASME JOURNAL OF HEAT TRANSFER*, Vol. 84, 1962, pp. 353-362.

7 Kays, W. M., and Perkins, H. C., "Forced Convection, Internal Flow in Ducts," *Handbook of Heat Transfer*, W. M. Rohsenow and J. P. Hartnett, eds., McGraw-Hill, New York, 1973.

Free Convection Flow of Non-Newtonian Fluids Along a Vertical Plate Embedded in a Porous Medium

Han-Taw Chen¹ and Cha'o-Kuang Chen¹

Nomenclature

- D = packing diameter
 e = porosity of bed
 f = dimensionless stream function, equation (14)
 g = gravitational acceleration
 h = local heat transfer coefficient
 \bar{h} = average heat transfer coefficient, equation (30)
 k = new bed permeability, equation (1e)
 k_1 = bed permeability
 k_m = thermal conductivity of the fluid-saturated porous medium
 K = new power law constant, equation (1c)
 K_1 = power law constant
 l = length of the plate
 L = length of bed or capillary
 n = new power law index, equation (1f)
 n_1 = power law index
 p = pressure
 Ra = modified Rayleigh number for the flow of a non-Newtonian power law fluid in the porous medium = $\rho_\infty g \beta k(n) (T_w - T_\infty)^{1/n} / K \alpha^n$
 Ra^* = dimensionless parameter = $Ra^{1/n}$
 T = temperature
 u = superficial velocity in x direction
 u^* = dimensionless velocity = $u / [\rho_\infty g \beta k(n) (T_w - T_\infty) / K]^{1/n}$
 v = superficial velocity in y direction
 v^* = dimensionless velocity = $v / [\rho_\infty g \beta k(n) (T_w - T_\infty) / K]^{1/n}$
 V_0 = superficial velocity
 x = transverse coordinate
 x^* = dimensionless coordinate = x/l
 y = longitudinal coordinate
 y^* = dimensionless coordinate = y/l
 α = equivalent thermal diffusivity

- β = coefficient of thermal expansion
 η = dimensionless similarity variable, equation (13)
 θ = dimensionless temperature = $(T - T_\infty) / (T_w - T_\infty)$
 ρ = density of the non-Newtonian fluid
 ψ = stream function

Subscripts

- m = edge of momentum boundary layer
 T = edge of thermal boundary layer
 w = wall
 ∞ = infinity

Introduction

Previous studies for free convection flow along a vertical flat plate embedded in a porous medium were restricted, in general, to Newtonian fluid only (Na and Pop, 1983; Cheng and Minkowycz, 1977; Masuoka, 1983). Few pay attention to the problem of natural convection of non-Newtonian fluids in a porous medium. However, the prediction of heat transfer characteristics is of importance in a number of geophysical and other engineering applications, such as petroleum drillings, especially in the studies of natural convection of non-Newtonian fluids in a porous medium adjacent to the heated surface.

The problem of free convection flow of a non-Newtonian power law fluid along an isothermal vertical flat plate embedded in the porous medium is considered in the present study. The physical coordinate system is shown schematically in Fig. 1. In the present study, it is assumed that the modified Darcy law and the boundary layer approximation are applicable. This implies that the present solutions are valid at a high Rayleigh number. With these simplifications, the governing partial nonlinear differential equations can be transformed into a set of coupled ordinary differential equations which can be solved by the fourth-order Runge-Kutta method. Algebraic equations for heat transfer rate and boundary layer thickness as a function of the prescribed wall temperature and physical properties of liquid-porous medium are obtained. The similarity solutions can be applied to problems in geophysics and engineering.

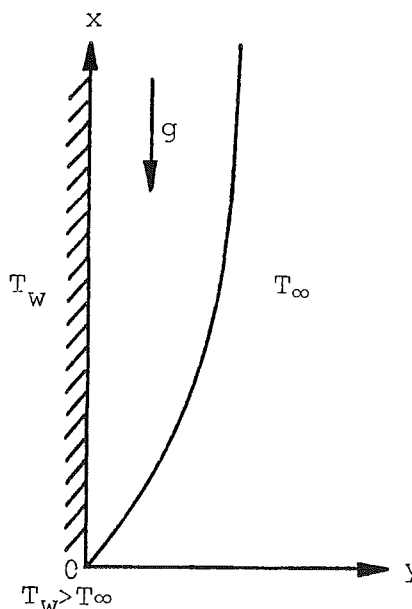


Fig. 1 Physical coordinate system

¹Department of Mechanical Engineering, National Cheng-Kung University, Tainan, Taiwan, Republic of China.

Contributed by the Heat Transfer Division for publication in the *JOURNAL OF HEAT TRANSFER*. Manuscript received by the Heat Transfer Division September 18, 1985.

The primary purpose of the present study is to predict the characteristics of steady natural convection heat transfer using the model of the flow of a non-Newtonian power law fluid in a porous medium given by Dharmadhikari and Kale (1985). Secondly, the effects of the new power law index n on heat transfer are investigated.

Analysis

In accordance with previous reports given by Christopher and Middleman (1965), the model of laminar flow of a non-Newtonian power law fluid through a porous medium is written as follows:

$$V_0^{n_1} = \frac{k_1(n_1)}{K_1} \frac{\Delta p}{L} \quad (1a)$$

where

$$k_1(n_1) = \frac{6}{25} \left(\frac{n_1 e}{3n_1 + 1} \right)^{n_1} \left(\frac{De}{3(1-e)} \right)^{n_1 + 1} \quad (1b)$$

The model given by Christopher and Middleman (1965) may be used to analyze the present study. However, it has been shown that this model is greatly inadequate for the flow of a non-Newtonian fluid through a porous medium, especially with low values of n_1 (Dharmadhikari and Kale, 1985). In addition, it is also assumed that the power law constant K_1 is not temperature dependent. Therefore, the model given by Pascal (1983) is not applied in the present study. For these reasons, this paper supposes that the flow of a non-Newtonian fluid through the porous medium is governed by the modified Darcy law given by Dharmadhikari and Kale (1985). Under this circumstance, the new power law constant K , power law index n , and permeability of the porous medium $k(n)$ are introduced as

$$K = \frac{5n_1}{2 + 3n_1} \left(\frac{150}{32} \right)^{n_2} K_1 \quad (1c)$$

$$n = n_1 + 0.3(1 - n_1) \quad (1d)$$

and

$$k(n) = \frac{2}{e} \left[\frac{De^2}{8(1-e)} \right]^{n+1} \quad (1e)$$

where

$$n_2 = \frac{3n_1}{2 + n_1} \quad (1f)$$

If we assume that (i) the convective fluid and the porous medium are everywhere in local thermodynamic equilibrium, (ii) the temperature of the fluid is everywhere below boiling point, (iii) the properties of the fluid and the porous medium are constant, and (iv) the Boussinesq approximation is employed, the governing equations for the present study are given by

$$\frac{\partial u}{\partial x} + \frac{\partial v}{\partial y} = 0 \quad (2)$$

$$u^n = -\frac{k(n)}{K} \left[\frac{\partial p}{\partial x} + \rho g \right] \quad (3)$$

$$v^n = -\frac{k(n)}{K} \frac{\partial p}{\partial y} \quad (4)$$

$$u \frac{\partial T}{\partial x} + v \frac{\partial T}{\partial y} = \alpha \left[\frac{\partial^2 T}{\partial x^2} + \frac{\partial^2 T}{\partial y^2} \right] \quad (5)$$

$$\rho = \rho_\infty [1 - \beta(T - T_\infty)] \quad (6)$$

with appropriate boundary conditions

$$v = 0, \quad T = T_w \quad \text{at } y = 0 \quad (7)$$

$$u = 0, \quad T = T_\infty \quad \text{at } y \rightarrow \infty \quad (8)$$

In the region outside the boundary layer, the flow of the power law fluid remains stagnant. Using the Bernoulli equation gives

$$-(dp/dx) = \rho_\infty g \quad (9)$$

Thus, equations (2), (3), and (5) can be written as

$$\frac{\partial u^*}{\partial x^*} + \frac{\partial v^*}{\partial y^*} = 0 \quad (10)$$

$$\theta = (u^*)^n \quad (11)$$

$$u^* \frac{\partial \theta}{\partial x^*} + v^* \frac{\partial \theta}{\partial y^*} = \frac{1}{Ra^*} \frac{\partial^2 \theta}{\partial y^{*2}} \quad (12)$$

where $x^* = x/l$, $y^* = y/l$, $u^* = u/[\rho_\infty g \beta k(n)(T_w - T_\infty)/K]^{1/n}$, $v^* = v/[\rho_\infty g \beta k(n)(T_w - T_\infty)/K]^{1/n}$, $Ra = \rho_\infty g \beta k(n)(T_w - T_\infty)l^n/K\alpha^n$, $Ra^* = (\rho_\infty g \beta k(n)(T_w - T_\infty)l^n/K\alpha^n)^{1/n} = Ra^{1/n}$, $\theta = (T - T_\infty)/(T_w - T_\infty)$. Note that Ra is defined as the modified Rayleigh number for the flow of a non-Newtonian power law fluid through the porous medium.

To transform equations (10)-(12) into a set of ordinary differential equations, the following dimensionless variables are introduced:

$$\eta = y^*(Ra^*/x^*)^{1/2} \quad (13)$$

$$\psi = (x^*/Ra^*)^{1/2} f(\eta) \quad (14)$$

In terms of the new variables, it can be shown that the velocity components are

$$u^* = \frac{\partial \psi}{\partial y^*} = f'(\eta) \quad (15)$$

$$v^* = -\frac{\partial \psi}{\partial x^*} = \frac{1}{2} (f'\eta - f)/(Ra^*x^*)^{1/2} \quad (16)$$

whereas equations (11) and (12) with appropriate boundary conditions are

$$\theta = (f')^n \quad (17)$$

$$\theta'' + 1/2 \theta' f = 0 \quad (18)$$

$$\theta = 1, \quad f = 0 \quad \text{at } \eta = 0 \quad (19)$$

$$\theta = 0, \quad f' = 0 \quad \text{at } \eta \rightarrow \infty \quad (20)$$

where the primes indicate differentiation with respect to η . Using the Newton method given by Na (1979), equation (18) can be written as

$$\frac{d\theta}{d\eta} = u, \quad \frac{du}{d\eta} = v = -1/2 u f \quad (21)$$

The following missing slope is used to solve the present problem:

$$\frac{d\theta(0)}{d\eta} = s \quad \text{or} \quad u(0) = s \quad (22)$$

Differentiating equations (19)-(21) with respect to s gives

$$\frac{d\bar{f}}{d\eta} = \frac{1}{n} \theta^{1/n-1} \bar{\theta} \quad (23)$$

$$\frac{d\bar{\theta}}{d\eta} = \bar{u}, \quad \frac{d\bar{u}}{d\eta} = -1/2(\bar{u}f + u\bar{f}) \quad (24)$$

with

$$\bar{\theta} = 0, \quad d\bar{\theta}/d\eta = 1, \quad \bar{f} = 0 \quad \text{at } \eta = 0 \quad (25)$$

where $\bar{\theta} = \partial\theta/\partial s$, $\bar{u} = \partial u/\partial s$, and $\bar{f} = \partial f/\partial s$.

The iteration formula for s is given by

$$s^{(n+1)} = s^{(n)} - \frac{\theta(\infty)}{\bar{\theta}(\infty)} \quad (26)$$

This process is continued until the change in the value of s is within a certain prescribed accuracy.

Table 1 Values of η_T , η_m , $[-\theta'(0)]$, and $f(\infty)$ for selected values of n

n	η_T	η_m	$-\theta'(0)$	$f(\infty)$
0.5	8.635	4.658	0.3768	1.089
0.8	6.958	5.693	0.4238	1.421
1.0	6.493	6.493	0.4437	1.618
1.5	5.468	7.797	0.4752	2.053
2.0	5.010	8.913	0.4938	2.403
2.5	4.729	9.902	0.5059	2.728

$-\theta'(0) = 0.4440$, when $n = 1$, given by Cheng and Minkowycz (1977).
 $-\theta'(0) = 0.4437$, when $n = 1$, given by Masuoka (1968).

Table 2 Dimensionless temperature distribution and dimensionless velocity distribution when $n = 1$

η	Successive approximation		Present analysis	
	f	$f' = \theta = u^*$	f	$f' = \theta = u^*$
0.00	0.00000	1.00000	0.00000	1.00000
1.0	0.78620	0.58715	0.78624	0.58722
4.0	1.53307	0.06624	1.53353	0.06643
7.0	1.60867	0.00600	1.60977	0.00624

The local heat flux at the wall $q_w(x)$ is

$$q_w = -k_m \left(\frac{\partial T}{\partial y} \right)_{y=0} = -k_m (T_w - T_\infty) \theta'(0) \frac{1}{l} (Ra^*/x^*)^{1/2} \quad (27)$$

The local Nusselt number Nu_x can be expressed as

$$Nu_x = hx/k_m = q_w x/k_m (T_w - T_\infty) \quad (28)$$

where h denotes the local heat transfer coefficient and k_m is the thermal conductivity of the fluid-saturated porous medium. Substituting equation (27) into equation (28) yields

$$Nu_x / (Ra^* x^*)^{1/2} = -\theta'(0) \quad (29)$$

The average heat transfer coefficient \bar{h} is

$$\bar{h} = \frac{1}{l} \int_0^l h dx = 2k_m Ra^{*1/2} \theta'(0) / l \quad (30)$$

The average Nusselt number \bar{Nu} can be defined as

$$\bar{Nu} = \bar{h}l/k_m = 2Ra^{*1/2} \theta'(0) \quad (31)$$

Results and Discussion

The values of η_T , η_m , and $[-\theta'(0)]$ for selected values of n are shown in Table 1. It is found from Table 1 that the value $[-\theta'(0)]$ for $n = 1$ agrees with values given by Cheng and Minkowycz (1977) and Masuoka (1968). Table 2 shows a comparison of the present calculations of the dimensionless velocity distribution and the dimensionless temperature distribution with those of the successive approximation given by Masuoka (1968). It can be seen from Table 2 that the values of the dimensionless temperature and the dimensionless velocity compare well with those of the successive approximation. Therefore, the present results should have a relatively fair degree of accuracy, although no available results can be compared with the present results when $n \neq 1$. In the present study, the equivalent step size $\Delta\eta = 0.1$ and $\eta_\infty = 12$ are used.

The expressions for momentum and thermal boundary-layer thickness can be obtained from equation (13) if the edges of the boundary layers are defined as the points where θ or u/u_w have a value of 0.01, where u_w is denoted as the slip velocity along the wall. The edges of the boundary layers are defined as η_T and η_m , respectively. The values of η_T and η_m for selected values of n are tabulated in Table 1. It is shown in Table 1 that the values of η_T are larger than those of η_m when $n < 1$ and the values of η_T are less than those of η_m when $n > 1$. In other words, the thermal boundary layer thickness is

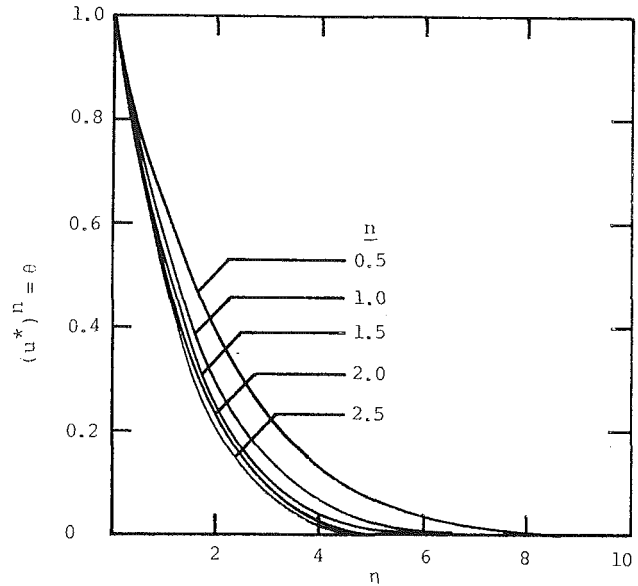


Fig. 2 Dimensionless temperature distribution along η corresponding to n

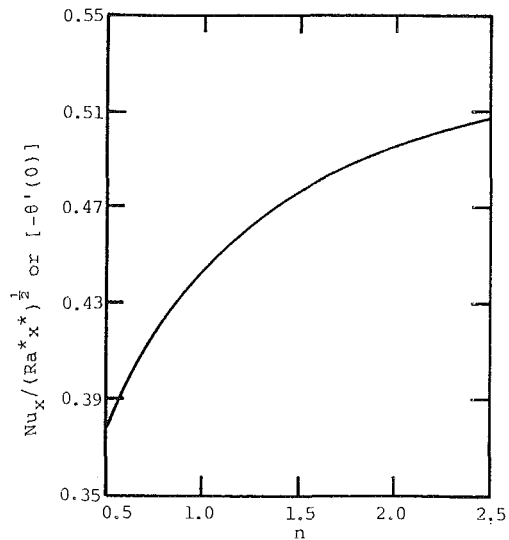


Fig. 3 Values of $Nu_x / (Ra^* x^*)^{1/2}$ or $[-\theta'(0)]$ versus n

greater than the momentum boundary layer thickness when $n < 1$ and the thermal boundary layer thickness is less than the momentum boundary layer thickness when $n > 1$. In addition, it can also be found from Table 1 that η_m is increasing with n . This implies that the larger the value of n is, the larger the viscosity of the fluid will be. The phenomenon agrees with the observations of Dharmadhikari and Kale (1985). Thus, it is obvious that the present analysis is reasonable. However, η_T is decreasing with n . This implies that the larger of n is, the lower the equivalent thermal diffusivity will be.

Figure 2 shows the dimensionless temperature distribution for selected values of n . It is found from Fig. 2 that the variation of the dimensionless temperature distribution is decreasing with n . It further shows that the larger the value of n is, the lower the equivalent thermal diffusivity will be.

The relationship between $[-\theta'(0)]$ or $Nu_x / (Ra^* x^*)^{1/2}$ and the new power law index n is tabulated in Table 1 and plotted in Fig. 3. It is found that the dimensionless temperature gradient at the wall $[-\theta'(0)]$ increases as n increases. It should be noted that the variation of the value of $[-\theta'(0)]$ is larger for low values of n . Therefore, the heat transfer characteristics for

natural convection of a non-Newtonian fluid with low values of the new power law index n in the porous medium are worth investigating.

Concluding Remarks

The present study provides a simple mathematical model for solving the problem of free convection flow of a non-Newtonian power law fluid along an isothermal vertical flat plate embedded in the porous medium. Comparison between the present results and previous results for a Newtonian fluid, i.e., $n = 1$, is satisfactory. However, the best way is to appeal to experimental methods to prove the accuracy of the mathematical model.

References

- Bird, R. B., Stewart, W. E., and Lightfoot, E. N., 1960, *Transport Phenomena*, Wiley, New York.
- Cheng, P., and Minkowycz, W. J., 1977, "Free Convection About a Vertical Flat Plate Embedded in a Porous Medium With Application to Heat Transfer From a Dike," *J. of Geophys. Res.*, Vol. 82, No. 14, pp. 2040-2044.
- Christopher, R. H., and Middleman, S., 1965, "Power-Law Flow Through a Packed Tube," *Ind. Engng. Chem. Fundts.*, Vol. 4, No. 4, pp. 422-426.
- Dharmadhikari, R. V., and Kale, D. D., 1985, "Flow of Non-Newtonian Fluids Through Porous Media," *Chem. Engng. Sci.*, Vol. 40, No. 3, pp. 527-529.
- Kozicki, W., Hsu, C. J., and Tiu, C., 1967, "Non-Newtonian Flow Through Packed Beds and Porous Media," *Chem. Engng. Sci.*, Vol. 22, pp. 487-502.
- Masuoka, T., 1968, "A Study of the Free Convection Heat Transfer About a Vertical Flat Plate Embedded in a Porous Medium," *Trans. JSME*, Vol. 34, No. 321, pp. 491-500.
- McKinley, R. M., Jahns, H. O., Harris, W. W., and Greenkorn, R. A., 1966, "Non-Newtonian Flow in Porous Media," *AIChE J.*, Vol. 12, No. 1, pp. 17-20.
- Na, T. Y., 1979, "Computational Methods in Engineering Boundary Value Problems," *Math. in Sci. and Engng.*, Academic Press, New York, Vol. 145.
- Na, T. Y., and Pop, I., 1983, "Free Convection Flow Past a Vertical Flat Plate Embedded in a Saturated Porous Medium," *Int. J. Engng. Sci.*, Vol. 21, No. 5, pp. 517-526.
- Pascal, H., 1983, "Nonsteady Flow of Non-Newtonian Fluids Through a Porous Medium," *Int. J. Engng. Sci.*, Vol. 21, No. 3, pp. 199-210.
- Pascal, H., and Pascal, F., 1985, "Flow of Non-Newtonian Fluid Through Porous Media," *Int. J. Engng. Sci.*, Vol. 23, No. 5, pp. 571-585.
- White, D. A., 1967, "Non-Newtonian Flows in Porous Media," *Chem. Engng. Sci.*, Vol. 2, pp. 669-672.

The Mushy Zone in a Phase Change Model of a Semitransparent Material With Internal Radiative Transfer

S. H. Chan¹ and K. Y. Hsu²

Introduction

The generalized phase change model proposed by Chan et al. (1980, 1981, 1983) and Rivard and Scott (1976) postulates a mushy zone between the purely liquid and purely solid zones, as illustrated in Fig. 1 for the melting of a semitransparent medium as a result of volumetric thermal radiation. In the mushy zone, solid and liquid coexist and their volume fractions may vary. The mushy zone is expected to occur, for example, in a semitransparent material when the material is subjected to intense laser beam radiation to induce melting. The extent and the thickness of the mushy zone are governed mainly by intrinsic radiation properties of the semitransparent medium. This new model has been applied by several authors

¹Professor and Chairman, Department of Mechanical Engineering, University of Wisconsin—Milwaukee, Milwaukee, WI 53211.

²Graduate Student, Department of Mechanical Engineering, University of Wisconsin—Milwaukee, Milwaukee, WI 53211.

Contributed by the Heat Transfer Division for publication in the JOURNAL OF HEAT TRANSFER. Manuscript received by the Heat Transfer Division August 11, 1986.

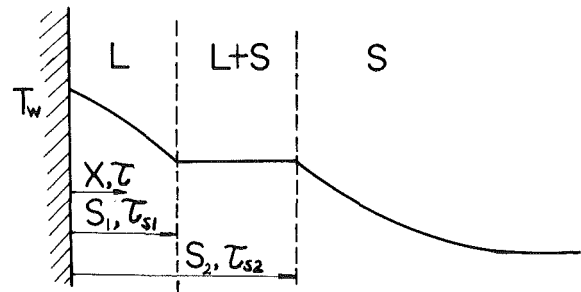


Fig. 1 Generalized three-zone phase change model

in order to study the problem of transient solidification of semitransparent material (Chan and Hsu, 1984), the problem with an internal heat generation in an opaque medium (Oruma et al., 1985), the phase change problem with anisotropic scattering (Oruma et al., 1985), and high-intensity laser-induced vaporization without internal superheating (Beckett, 1985).

Internal melting in the mushy zone has been observed (Dorsey, 1968; Knight, 1967) when ice was exposed to light. Small cavities partly filled with water were seen to form throughout the body of ice. This mushy zone should not be confused with, say, the conventional dendritic growth in ice at the freezing/melting interface. The latter can occur in opaque and semitransparent media because of subcooling effects (not thermal radiation effects) and is not the subject of interest here. It should also be mentioned in passing that the mushy zone may occur in metal/alloy processing due to the effect of composition on the melting/solidification temperature and mass transfer. The present studies are only concerned with the mushy zone in a semitransparent medium due to the internal radiative transfer effect.

The essence of this tech note is to convey the idea that in an idealized way the mushy zone evolves naturally in the phase change heat transfer analysis, without the necessity of postulating the existence of such a mushy zone and then analyzing the impact of the mushy zone on the phase change as was done in all previous studies (Chan et al., 1980, 1981, 1983, 1984; Rivard and Scott, 1976; Oruma et al., 1985; Beckett, 1985). This is accomplished by employing the well-known enthalpy method, which, by the way, possesses some mathematical advantages, such as simplifying the mathematical complexity of moving interfaces in three zones and eliminating the mathematical singularity difficulty encountered in another method (Chan and Beiruty, 1981). To ensure the accuracy of the numerical results, solutions are first obtained for the identical problem (namely, solidification of a semi-infinite liquid) solved previously (Chan et al., 1981, 1983), except longer time solutions in dimensionless form are now presented. An extension is made to solve for a finite slab geometry where no prior solutions are available.

Analytical Formulation

To show the essence of the three-zone model without unnecessary complications, the idealized assumptions made by Chan et al. (1980, 1981, 1983) and Rivard and Scott (1976) are also made here for the investigation of a semitransparent medium undergoing a phase change process as illustrated in Fig. 1. The assumptions about the medium include homogeneity, constant gray radiation and thermophysical properties, no density change, no superheating or subcooling, and a unique phase change temperature.

In accordance with the enthalpy method, the dimensionless energy equation, which is valid everywhere in the medium, is

$$\frac{d\theta}{d\tau} = N_{cc} \frac{\partial^2 \phi}{\partial \tau^2} - \frac{1}{4 N_{cr}} \frac{\partial q_r^*}{\partial \tau} \quad (1)$$

natural convection of a non-Newtonian fluid with low values of the new power law index n in the porous medium are worth investigating.

Concluding Remarks

The present study provides a simple mathematical model for solving the problem of free convection flow of a non-Newtonian power law fluid along an isothermal vertical flat plate embedded in the porous medium. Comparison between the present results and previous results for a Newtonian fluid, i.e., $n = 1$, is satisfactory. However, the best way is to appeal to experimental methods to prove the accuracy of the mathematical model.

References

- Bird, R. B., Stewart, W. E., and Lightfoot, E. N., 1960, *Transport Phenomena*, Wiley, New York.
- Cheng, P., and Minkowycz, W. J., 1977, "Free Convection About a Vertical Flat Plate Embedded in a Porous Medium With Application to Heat Transfer From a Dike," *J. of Geophys. Res.*, Vol. 82, No. 14, pp. 2040-2044.
- Christopher, R. H., and Middleman, S., 1965, "Power-Law Flow Through a Packed Tube," *Ind. Engng. Chem. Fundts.*, Vol. 4, No. 4, pp. 422-426.
- Dharmadhikari, R. V., and Kale, D. D., 1985, "Flow of Non-Newtonian Fluids Through Porous Media," *Chem. Engng. Sci.*, Vol. 40, No. 3, pp. 527-529.
- Kozicki, W., Hsu, C. J., and Tiu, C., 1967, "Non-Newtonian Flow Through Packed Beds and Porous Media," *Chem. Engng. Sci.*, Vol. 22, pp. 487-502.
- Masuoka, T., 1968, "A Study of the Free Convection Heat Transfer About a Vertical Flat Plate Embedded in a Porous Medium," *Trans. JSME*, Vol. 34, No. 321, pp. 491-500.
- McKinley, R. M., Jahns, H. O., Harris, W. W., and Greenkorn, R. A., 1966, "Non-Newtonian Flow in Porous Media," *AIChE J.*, Vol. 12, No. 1, pp. 17-20.
- Na, T. Y., 1979, "Computational Methods in Engineering Boundary Value Problems," *Math. in Sci. and Engng.*, Academic Press, New York, Vol. 145.
- Na, T. Y., and Pop, I., 1983, "Free Convection Flow Past a Vertical Flat Plate Embedded in a Saturated Porous Medium," *Int. J. Engng. Sci.*, Vol. 21, No. 5, pp. 517-526.
- Pascal, H., 1983, "Nonsteady Flow of Non-Newtonian Fluids Through a Porous Medium," *Int. J. Engng. Sci.*, Vol. 21, No. 3, pp. 199-210.
- Pascal, H., and Pascal, F., 1985, "Flow of Non-Newtonian Fluid Through Porous Media," *Int. J. Engng. Sci.*, Vol. 23, No. 5, pp. 571-585.
- White, D. A., 1967, "Non-Newtonian Flows in Porous Media," *Chem. Engng. Sci.*, Vol. 2, pp. 669-672.

The Mushy Zone in a Phase Change Model of a Semitransparent Material With Internal Radiative Transfer

S. H. Chan¹ and K. Y. Hsu²

Introduction

The generalized phase change model proposed by Chan et al. (1980, 1981, 1983) and Rivard and Scott (1976) postulates a mushy zone between the purely liquid and purely solid zones, as illustrated in Fig. 1 for the melting of a semitransparent medium as a result of volumetric thermal radiation. In the mushy zone, solid and liquid coexist and their volume fractions may vary. The mushy zone is expected to occur, for example, in a semitransparent material when the material is subjected to intense laser beam radiation to induce melting. The extent and the thickness of the mushy zone are governed mainly by intrinsic radiation properties of the semitransparent medium. This new model has been applied by several authors

¹Professor and Chairman, Department of Mechanical Engineering, University of Wisconsin—Milwaukee, Milwaukee, WI 53211.

²Graduate Student, Department of Mechanical Engineering, University of Wisconsin—Milwaukee, Milwaukee, WI 53211.

Contributed by the Heat Transfer Division for publication in the JOURNAL OF HEAT TRANSFER. Manuscript received by the Heat Transfer Division August 11, 1986.

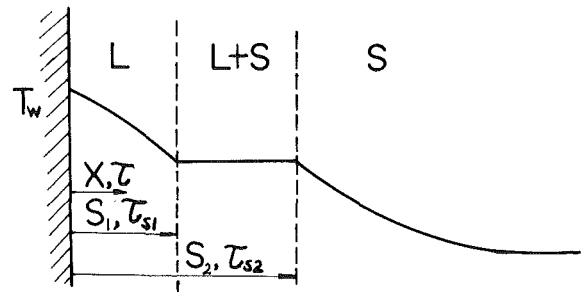


Fig. 1 Generalized three-zone phase change model

in order to study the problem of transient solidification of semitransparent material (Chan and Hsu, 1984), the problem with an internal heat generation in an opaque medium (Oruma et al., 1985), the phase change problem with anisotropic scattering (Oruma et al., 1985), and high-intensity laser-induced vaporization without internal superheating (Beckett, 1985).

Internal melting in the mushy zone has been observed (Dorsey, 1968; Knight, 1967) when ice was exposed to light. Small cavities partly filled with water were seen to form throughout the body of ice. This mushy zone should not be confused with, say, the conventional dendritic growth in ice at the freezing/melting interface. The latter can occur in opaque and semitransparent media because of subcooling effects (not thermal radiation effects) and is not the subject of interest here. It should also be mentioned in passing that the mushy zone may occur in metal/alloy processing due to the effect of composition on the melting/solidification temperature and mass transfer. The present studies are only concerned with the mushy zone in a semitransparent medium due to the internal radiative transfer effect.

The essence of this tech note is to convey the idea that in an idealized way the mushy zone evolves naturally in the phase change heat transfer analysis, without the necessity of postulating the existence of such a mushy zone and then analyzing the impact of the mushy zone on the phase change as was done in all previous studies (Chan et al., 1980, 1981, 1983, 1984; Rivard and Scott, 1976; Oruma et al., 1985; Beckett, 1985). This is accomplished by employing the well-known enthalpy method, which, by the way, possesses some mathematical advantages, such as simplifying the mathematical complexity of moving interfaces in three zones and eliminating the mathematical singularity difficulty encountered in another method (Chan and Beiruty, 1981). To ensure the accuracy of the numerical results, solutions are first obtained for the identical problem (namely, solidification of a semi-infinite liquid) solved previously (Chan et al., 1981, 1983), except longer time solutions in dimensionless form are now presented. An extension is made to solve for a finite slab geometry where no prior solutions are available.

Analytical Formulation

To show the essence of the three-zone model without unnecessary complications, the idealized assumptions made by Chan et al. (1980, 1981, 1983) and Rivard and Scott (1976) are also made here for the investigation of a semitransparent medium undergoing a phase change process as illustrated in Fig. 1. The assumptions about the medium include homogeneity, constant gray radiation and thermophysical properties, no density change, no superheating or subcooling, and a unique phase change temperature.

In accordance with the enthalpy method, the dimensionless energy equation, which is valid everywhere in the medium, is

$$\frac{d\theta}{d\tau} = N_{cc} \frac{\partial^2 \phi}{\partial \tau^2} - \frac{1}{4 N_{cr}} \frac{\partial q_r^*}{\partial \tau} \quad (1)$$

where

$$\theta = \frac{1}{\rho \Delta x} \int_x^{x+\Delta x} \rho \frac{i-i_1}{\lambda} dx; \quad \phi = C(T-T_m)/\lambda \quad (2)$$

and $\bar{i} = i/t_r$, and $\bar{q}_r = q_r/\sigma n_1^4 T_r^4$; $t_r = \rho \lambda / \beta_1^2 k T_r$, and the optical distance $\tau = \beta_1 x$. C , ρ , λ , k , β_1 , and i_1 denote specific heat, density, latent heat of fusion, conductivity, the absorption coefficient of phase one, and saturated liquid enthalpy, respectively. The reference temperature is taken as $T_r = 1000$ K, the inverse Stefan number is $N_{cc} = \lambda/T_r C$, and the conduction-radiation parameter $N_{cr} = k\beta_1/4n_1^2\sigma T_r^3$. The dimensionless enthalpy θ is treated as the dependent variable and the dimensionless temperature ϕ has to be expressed in terms of θ . From the definitions of θ and ϕ , they are related by

$$\begin{aligned} \phi &= \theta & \text{when } \theta > 0 & \quad (\text{liquid region}) \\ \phi &= 0 & \text{when } 0 \geq \theta \geq -1 & \quad (\text{mushy zone}) \\ \phi &= \theta + 1 & \text{when } -1 > \theta & \quad (\text{solid region}) \end{aligned} \quad (3)$$

From θ , both interfaces τ_{s1} ($= \beta_1 s_1$) and τ_{s2} ($= \beta_1 s_2$) can be determined. In the case of melting, for example, τ_{s1} and τ_{s2} are located at $\theta = 0$ and -1 , respectively.

In this study, two types of interface are considered. The first is termed the diffuse interface to allow for different phases with different indices of refraction, n_i , and for a rough interface such as the one formed at a grain boundary. Radiation incident on the diffuse interface is subject to diffuse reflection and transmission (or refraction). The other type is termed an idealized interface when the indices of refraction are the same in all phases. Then radiation passes through the interface as if no interface exists. In the latter case, the introduction of the idealized interface is still necessary to mark the boundary between phases.

1 Diffuse Interface. By reference to Fig. 2, the dimensionless radiative terms in different regions are given below:

Phase 1 Region:

$$-\frac{\partial \bar{q}_{r,1}}{\partial \tau} = 2\{J_1^+ E_2(\tau) + J_1^- E_2(\tau_{s1} - \tau) + I_1 - 2\bar{T}(\tau)\} \quad (4)$$

where the radiosities, J_1^+ and J_1^- , and the emission terms I_1 are given by

$$I_1 = \int_0^{\tau_{s1}} \bar{T}^4(\xi) E_1(|\tau - \xi|) d\xi$$

$$J_1^+ = \epsilon_w \bar{T}_w^4 + 2\rho_w \{J_1^- E_3(\tau_{s1}) + \bar{H}_{1w}^-\}$$

$$J_1^- = 2\rho_{1s} \{J_1^+ E_3(\tau_{s1}) + \bar{H}_{1s}^+\} + 2r_{21} \{ \bar{H}_{2s}^- + J_2^- E_3(\beta_{21}(\tau_{s2} - \tau_{s1})) \}$$

and other emission terms are

$$\bar{H}_{1w}^- = \int_0^{\tau_{s1}} \bar{T}^4(\xi) E_2(\xi) d\xi$$

$$\bar{H}_{1s}^+ = \int_0^{\tau_{s1}} \bar{T}^4(\xi) E_2(\tau_{s1} - \xi) d\xi$$

$$\begin{aligned} \bar{H}_{2s}^- &= \int_{\tau_{s1}}^{\tau_{s2}} \bar{n}_{21}^2 \beta_{21} \bar{T}_m^4 E_2(\beta_{21}(\xi - \tau_{s1})) d\xi \\ &= \bar{n}_{21}^2 \bar{T}_m^4 [1/2 - E_3(\beta_{21}(\tau_{s2} - \tau_{s1}))] \end{aligned}$$

Mushy Region: Similarly,

$$-\frac{\partial \bar{q}_{r,2}}{\partial \tau} = 2\beta_{21} \left\{ J_2^+ E_2(\beta_{21}(\tau - \tau_{s1})) + J_2^- E_2(\beta_{21}(\tau_{s2} - \tau)) + I_2 - 2\bar{n}_{21}^2 \bar{T}_m^4 \right\} \quad (5)$$

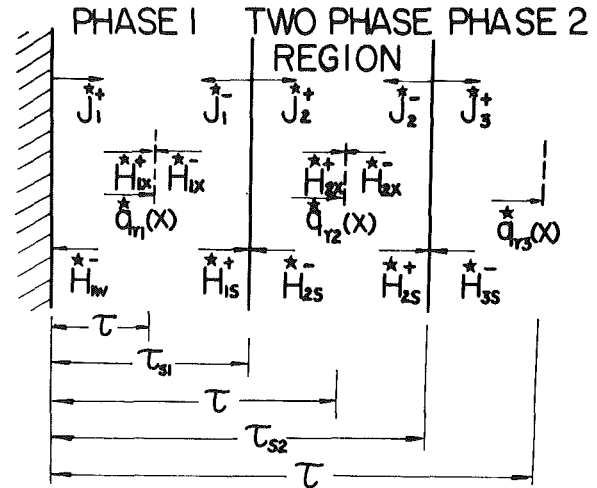


Fig. 2 Radiative heat flux during solidification

where

$$J_2^+ = 2\gamma_{12} \{ J_1^+ E_3(\tau_{s1}) + \bar{H}_{1s}^+ \} + 2\rho_{1s} \bar{H}_{1s}^-$$

$$J_2^- = 2\gamma_{32} \bar{H}_{3s}^- + 2\rho_{2s} \bar{H}_{2s}^+$$

$$\begin{aligned} I_2 &= \int_{\tau_{s1}}^{\tau_{s2}} \bar{n}_{21} \beta_{21} \bar{T}_m^4 E_1(\beta_{21}|\tau - \xi|) d\xi \\ &= \bar{n}_{21}^2 \bar{T}_m^4 \{ 2 - E_2(\beta_{21}(\tau - \tau_{s1})) - E_2(\beta_{21}(\tau_{s2} - \tau)) \} \end{aligned}$$

$$\begin{aligned} \bar{H}_{2s}^+ &= \int_{\tau_{s1}}^{\tau_{s2}} \beta_{21} \bar{n}_{21}^2 \bar{T}_m^4 E_2(\beta_{21}(\tau_{s2} - \xi)) d\xi \\ &= \beta_{21} \bar{T}_m^4 \bar{n}_{21}^2 [1/2 - E_3(\beta_{21}(\tau_{s2} - \tau_{s1}))] \end{aligned}$$

$$\bar{H}_{3s}^- = \int_{\tau_{s2}}^{\infty} \beta_{31} \bar{n}_{31}^2 \bar{T}^4 E_2(\beta_{31}(\xi - \tau_{s2})) d\xi$$

Phase 2 Region:

$$-\frac{\partial \bar{q}_{r,3}}{\partial \tau} = 2\beta_{31} \{ J_3^+ E_2[\beta_{31}(\tau - \tau_{s2})] + I_3 - 2\bar{n}_{31}^2 \bar{T}^4(\beta_{31}\tau) \} \quad (6)$$

where

$$I_3 = \int_{\tau_{s2}}^{\infty} \beta_{31} \bar{n}_{31}^2 \bar{T}^4(\xi) E_1(\beta_{31}|\tau - \xi|) d\xi$$

$$J_3^+ = 2\rho_{2s} \bar{H}_{3s}^- + 2\gamma_{23} \{ \bar{H}_{2s}^+ + J_2^+ E_3(\beta_{21}(\tau_{s2} - \tau_{s1})) \}$$

In the above equations, ϵ_w and ρ_w are, respectively, the wall emissivity and reflectivity, $\bar{T} = T/T_r$, $\bar{n}_{ij} = n_i/n_j$, and $\beta_{ij} = \beta_i/\beta_j$, the absorption coefficient ratio of the i and j regions. The superscript $*$ represents the normalization with respect to $\sigma n_1^4 T_r^4$, γ_{ij} is the interface reflectivity between the i and j regions, and ρ_{is} is the gray reflectance back to region i by the interface. The subscripts m , s , and w designate melting point, interfacial surface, and wall condition, respectively.

2 Idealized Interface. The idealized interface does not interfere with radiative transfer and, therefore, the following single expression is valid for all regions:

$$-\frac{\partial \bar{q}_r}{\partial \tau} = 2(J_1^+ E_2(\tau) + I_1 - 2\bar{T}^4(\tau)) \quad (7)$$

where

$$J_1^+ = \epsilon_w \bar{T}_w^4 + 2\rho_w \bar{H}_{1w}^-$$

$$\bar{H}_{1w}^- = \int_0^{\tau_{s1}} \bar{T}^4(\xi) E_2(\xi) d\xi$$

$$I_1 = \int_0^{\tau_{s1}} \bar{T}^4(\xi) E_1(\tau - \xi) d\xi$$

Numerical Computations and Results

The above system of equations is applicable to the melting or solidification of a semitransparent material. The equations were cast in finite difference forms, which were solved by an implicit iterative method, until a desirable convergence criterion was satisfied. Before dimensionless numerical results are presented, a large number of dimensionless parameters that are involved should be summarized and consolidated first. From equations (1) and (2), it is clear that

$$\theta, \phi = f(N_{cc}, N_{cr}, \frac{\partial q_{r,i}^*}{\partial \tau})$$

For the diffuse interface, $\partial q_{r,i}^*/\partial \tau$ is in terms of $\beta_{ij}, \tilde{n}_{ij}, \gamma_{ij}, \rho_w, \rho_{1s}, \rho_{2s}, \tilde{T}_m, \phi_w, \epsilon_w,$ and N_{cc} . However, ρ_w is related to ϵ_w through the gray wall assumption, β_{ij} is related to β_i , and \tilde{n}_{ij} and γ_{ij} are related to n_i . In view of the assumptions made previously, $\beta_1 = \beta_2 = \beta_3$ and $n_1 = n_2 = n_3$. Consequently, $\beta_{ij} = \tilde{n}_{ij} = \gamma_{ij} = 1$ and $\rho_{1s} = \rho_{2s} = 0$. Similarly, the dimensionless parameters for the idealized interface have been examined and the independent parameters for θ, ϕ are $N_{cc}, N_{cr}, \tilde{T}_m, \tilde{T}_w,$ and ϵ_w . In the present calculations their values, unless indicated otherwise in the figures, are varied or chosen as follows:

N_{cr} is varied from 0.01 to 0.1; $N_{cc} = 0.55$; $\tilde{T}_m = 1.1$; ϵ_w is varied from 1.0 to 0.1; \tilde{T}_w or θ_w values shall depend on boundary conditions. It is noted that \tilde{T}_w is related to θ_w through the use of the identity $\tilde{T}_w = \phi_w N_{cc} + \tilde{T}_m$, and ϕ - θ relations given in equation (3).

The dimensionless solutions to the solidification of a semi-infinite, semitransparent medium initially at its melting temperature, $\theta(0, \tau) = 0$, with its surface suddenly dropped to a fixed temperature of $\theta(\tilde{t}, 0) = -1.2$, are presented respectively in Figs. 3 and 4 for the growth of the solidified layer, τ_s , and for the propagation front profiles of various liquid volume fractions, ϵ . The values of medium properties are taken from Chan et al. (1981, 1983). Good agreement is shown with the short time solutions of Chan et al. (1981, 1983). However, at larger time, because the solution of Chan et al. (1983) lost its accuracy and Chan and Bierutty (1981) encountered a mathematical singularity, the short time solutions are not as accurate as the present one. For completeness, the opaque solution is given in Fig. 3 representing the pure conduction solution. Also shown are the equivalent solidified thickness profiles, τ_{eq} , that would result if all the solidified media, including that solidified in the two-phase region, are packed together (Chan et al., 1983). It is also seen in Fig. 3 that the present solutions yield the same results whether the interface between the solid and mushy zones is assumed as diffuse or is idealized as if no interface exists. This is because of the use of the same value of the refractive indices in all phases in the present illustration.

Once the accuracy of the numerical method is established, detailed mushy zone characteristics and others, not available in previous works, are calculated and presented next. In Fig. 5, the dimensionless enthalpy profiles θ and the liquid volume fraction profiles ϵ at various dimensionless times are given for two cases, one with black wall ($\epsilon_w = 1$) and the other gray wall ($\epsilon_w = 0.1$).

The values of the results show how solidification may occur if internal radiation absorption or emission is considered. Due to internal radiation to the cooler boundary, various states of the liquid/solid follow directly from the local amount of the nonuniform internal radiative cooling, resulting in a solid layer close to the boundary, a mushy zone, and a pure liquid layer away from the boundary. It is essential to note that the enthalpy method (see equations (1) and (7), for example) makes no presumption about the existence of the mushy zone. Yet Fig. 5 illustrates how the mushy zone (L & S region) can

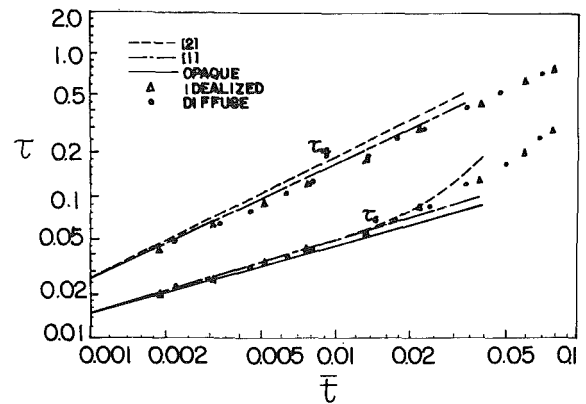


Fig. 3 Comparison between present work and other results for the interfacial and equivalent thickness [$\theta(0, \tau) = 0, \theta(\tilde{t}, 0) = -1.2, N_{cc} = 0.55, \tilde{T}_m = 1.1, \epsilon_w = 1,$ and $N_{cr} = 0.01$]

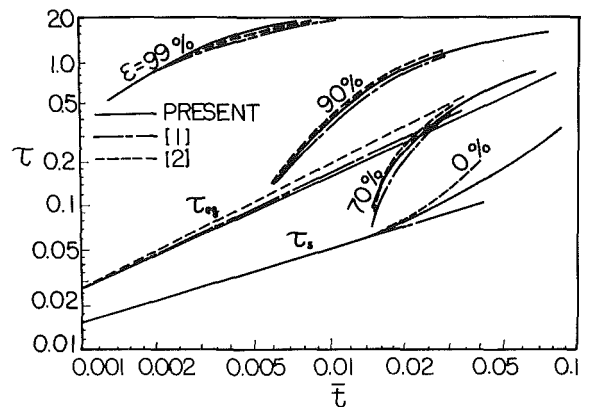


Fig. 4 Propagation front of various liquid volume fractions (same conditions as Fig. 3)

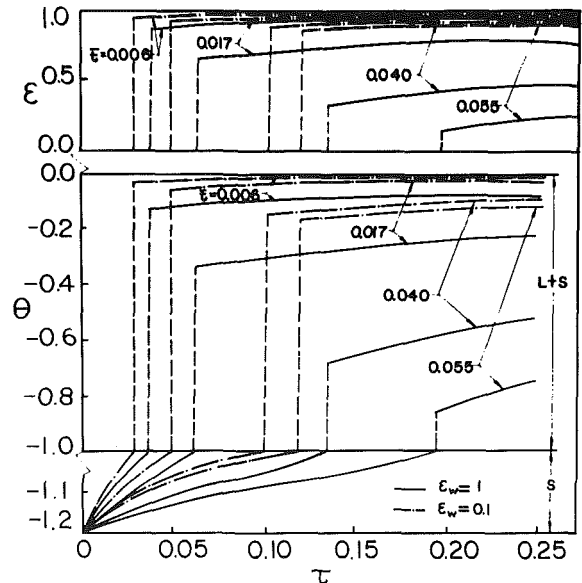


Fig. 5 Enthalpy and liquid volume fraction profiles (same conditions as Fig. 3)

evolve naturally from the solution obtained by the enthalpy method under the local equilibrium condition. The discontinuity at the propagation front of the interface where the liquid volume fraction drops to nil should also be noted. Finally, the effect of the conduction-radiation parameter, N_{cr} , and wall emissivity, ϵ_w , on the dimensionless enthalpy

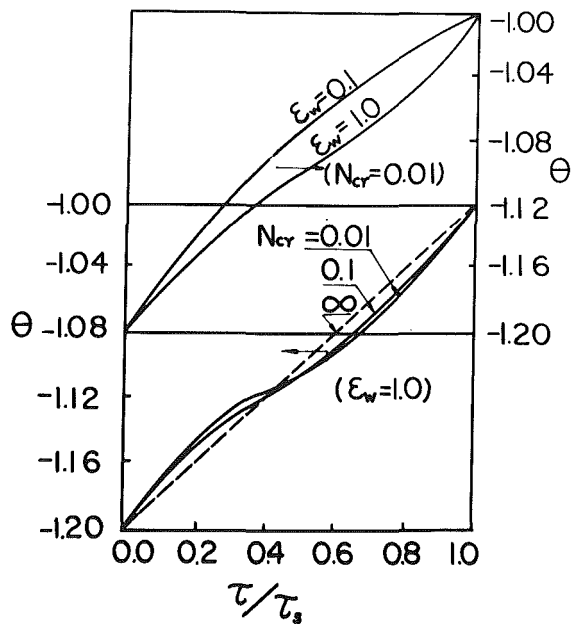


Fig. 6 θ distribution in the solidified region with ϵ_w , N_{cr} as variable parameters [$\theta(0, \tau) = 0$, $\theta(\bar{t}, 0) = -1.2$, $N_{cc} = 0.55$, $T_m = 1.1$, and $\tau_s = 0.2424$]

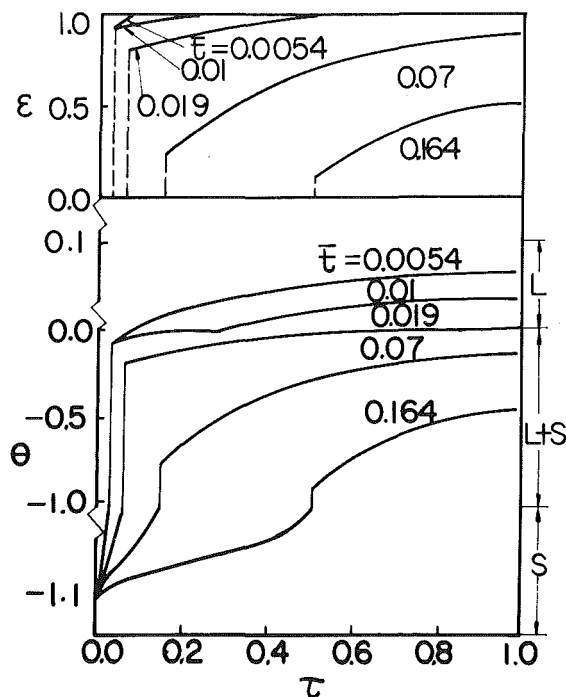


Fig. 7 Enthalpy and liquid volume fraction profiles in a slab [$\theta(0, \tau) = 0.1$, $\theta(\bar{t}, 0) = \theta(\bar{t}, 2) = -1.1$, $N_{cc} = 0.55$, $N_{cr} = 0.01$, $T_m = 1.1$, and $\epsilon_w = 1$]

distribution within the newly solidified layer at a given time (or given solidified layer thickness τ_s) are presented in Fig. 6. As N_{cr} decreases or ϵ_w increases, the radiation effect becomes more significant, resulting in an inverted S type of profile, which is expected and need not be elaborated.

The above has illustrated the essence of the paper and confirmed the validity of the numerical technique used. It is relatively easy to extend this technique to a finite slab geometry in which no prior solutions exist. Consideration is now given to the solidification of a liquid slab with the conditions: $\theta(0, \tau) = 0.1$, $\theta(\bar{t}, 0) = \theta(\bar{t}, 2) = -1.1$. Other conditions and values of parameters are the same as before. Due to

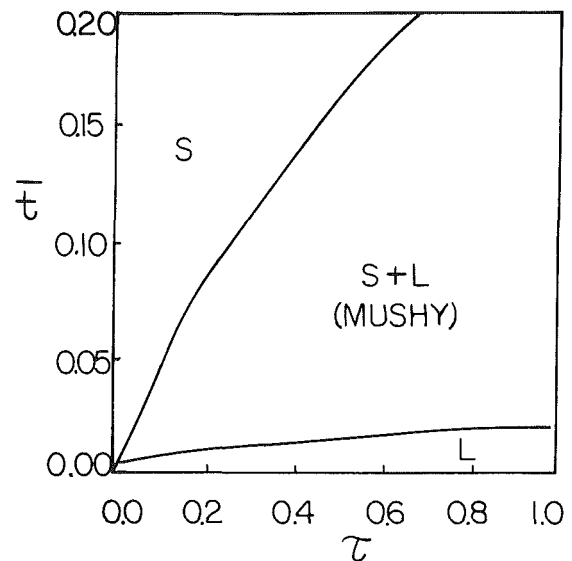


Fig. 8 Mapping of liquid, solid, and mushy zones in a slab (same conditions as Fig. 7)

symmetry, only the transient enthalpy profiles and liquid volume fraction profiles of the half region are presented in Fig. 7. Many features discussed before also prevail and will not be reiterated here, except to point out the appearance of all three zones versus two zones (solid and mushy zones) as in the previous case. The appearance of the liquid zone is expected, since the medium is initially at a temperature higher than the melting temperature. A mapping of the three possible zones at any time is summarized in Fig. 8. As time proceeds, it is seen how a pure liquid layer is turned into a composite layer of three zones (liquid, mushy, and solid), two zones (liquid and mushy), and ultimately into a single solid layer. If one insists on using the traditional phase change model, which allows only the liquid and solid zones, the significance of the mushy zone shown in Fig. 8 can not be predicted and the observations made in Dorsey (1968) and Knight (1967) can not be explained.

In short, a few idealized dimensionless solutions have been presented for phase change problems with internal radiation to illustrate the essence of the mushy zone that evolves naturally from the present analysis.

References

- Becket, P. M., 1985, "High Intensity Laser Induced Vaporization Without Internal Superheating," *J. Appl. Phys.*, Vol. 58, No. 8, pp. 2943-2948.
- Chan, S. H., Cho, D. H., and Kocamustafaogullari, G., 1980, "Radiative Transfer With Phase Change. A New Formulation and Solution," ASME Paper No. 80-HT-30.
- Chan, S. H., and Beiruty, M., 1981, "Use of B-Splines Collocation in Solidification by Combined Conduction and Internal Radiation," *Proceedings of the Second International Conference on Numerical Methods in Thermal Problems*, Vol. II, Venice, Italy; Pineridge Press, Swansea, United Kingdom, pp. 180-192.
- Chan, S. H., Cho, D. H., and Kocamustafaogullari, G., 1983, "Melting and Solidification With Internal Radiative Transfer—A Generalized Phase Change Model," *Int. J. Heat Mass Transfer*, Vol. 26, No. 4, pp. 621-633.
- Chan, S. H., and Hsu, K. Y., 1984, "Applications of a Generalized Phase Change Model for Melting and Solidification of Materials With Internal Heat Generation," 19th Thermophysics Conference, Snowmass, CO, Paper No. AIAA-84-1736.
- Dorsey, N. E., 1968, *Properties of Ordinary Water Substance*, Hafner, New York, p. 404.
- Knight, C. A., 1967, *The Freezing of Supercooled Liquids*, Van Nostrand, Princeton, p. 125.
- Oruma, F. O., Ozisik, M. N., and Boles, M. A., 1985, "Effects of Anisotropic Scattering on Melting and Solidification of a Semi-infinite, Semitransparent Medium," *Int. J. Heat Mass Transfer*, Vol. 28, No. 2, pp. 441-450.
- Rivard, J. B., and Scott, M. R., 1976, "The Two-Phase, Three-Zone Melting Problem—Response to Pulse Heating," *Appl. Math. Computation*, Vol. 2, pp. 173-187.

Radiation Shape Factors for Channels With Varying Cross Sections

T. L. Eddy¹ and G. E. Nielsson²

Introduction

Radiative heat transfer in chambers with flow is important in rocket nozzles [1]; MHD nozzles and diffusers; furnaces and boilers; burning rooms, halls, and stairwells; solid fueled rocket combustors; and underground coal gasification (UCG). UCG research [2, 3] prompted this work. The irregular shape of the cavity precluded the use of Robin's [1] method directly. The present paper extends Robin's method of blocking "by an intermediate segment" to include blocking "by the horizon" and "by the orientation of the area radiated to," presents good approximations for converting irregular cross section to effective circular cross sections, and finally provides techniques for using these view factors to model radiation within irregularly shaped enclosures with nonisothermal cross sections.

Shape Factors for Circular Concentric Cross Sections

The shape factor F between a particular differential element dA_k and a general finite area A_j is given by [4]

$$F_{dA_k-A_j} = \frac{1}{\pi} \int_{A_j} \frac{\cos \beta_j \cos \beta_k}{R^2} dA_j$$

where β is the angle between the normal to the surface area element and the line connecting two surface area elements. Robin [1] finds that for a surface of revolution

$$F_{dA_k-A_j} = \frac{1}{\pi} \int_x \frac{d\bar{x}}{\cos \eta_j} \int_\theta \frac{\bar{a} + \bar{b} \cos \theta + \bar{c} \cos^2 \theta}{(\bar{d} + \bar{e} \cos \theta)^2} d\theta \quad (1)$$

where η_k and η_j are the respective angles between the normal of the area to the vertical, θ is the azimuthal angle (as shown in Fig. 1), r is the radius from the axis, x is a convenient axial coordinate and the other variables have been normalized as follows [1]:

$$\begin{aligned} \bar{r} &= r/r_k, & \bar{x} &= (x-x_k)/r_k, \\ \bar{a} &= \bar{r}^2 \cos \eta_j \cos \eta_k - \bar{r}^2 \bar{x} \cos \eta_j \sin \eta_k \\ &\quad + \bar{r} \bar{x} \sin \eta_j \cos \eta_k - \bar{r} \bar{x}^2 \sin \eta_j \sin \eta_k, \\ \bar{b} &= -\bar{r}^3 \cos \eta_j \cos \eta_k - \bar{r} \cos \eta_j \cos \eta_k \\ &\quad + \bar{r} \bar{x} \cos \eta_j \sin \eta_k - \bar{r}^2 \bar{x} \sin \eta_j \cos \eta_k, \\ \bar{c} &= \bar{r}^2 \cos \eta_j \cos \eta_k, \\ \bar{d} &= \bar{r}^2 + \bar{x}^2 + 1, \quad \text{and} \quad \bar{e} = -2\bar{r} \end{aligned}$$

If the θ part of the integral in equation (1) is integrated, the result is

$$F_{dA_k-A_j} = \frac{1}{\pi} \int_x \left\{ I_1 + \left(\bar{a} - \frac{\bar{c}\bar{d}^2}{\bar{e}^2} \right) I_2 + \left(\bar{b} - \frac{2\bar{c}\bar{d}}{\bar{e}} \right) I_3 \right\} \frac{d\bar{x}}{\cos \eta_j} \quad (2)$$

where

$$I_1 = \bar{c}\theta/\bar{e}^2, \\ I_2 = \frac{\bar{d} \sin \theta}{(\bar{e}^2 - \bar{d}^2)(\bar{d} + \bar{e} \cos \theta)}$$

¹School of Mechanical Engineering, Georgia Institute of Technology, Atlanta, GA 30332; Mem. ASME.

²VERMIR Consulting Engineers, Reykhjavik, Iceland.

Contributed by the Heat Transfer Division for publication in the JOURNAL OF HEAT TRANSFER. Manuscript received by the Heat Transfer Division January 17, 1986.

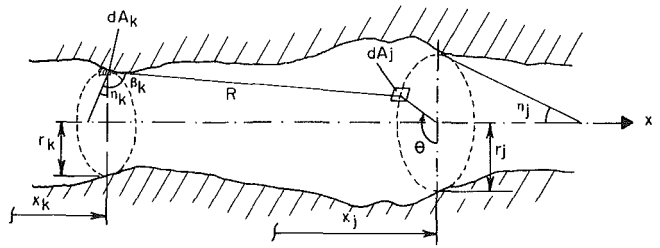


Fig. 1 Coordinate system for a surface of revolution

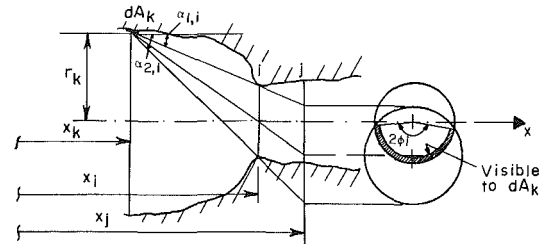


Fig. 2 Blocking by an intermediate segment

$$\begin{aligned} &+ \frac{2\bar{d}}{(\bar{d}^2 - \bar{e}^2)^{3/2}} \tan^{-1} \frac{(\bar{d} - \bar{e}) \tan \theta/2}{(\bar{d}^2 - \bar{e}^2)^{1/2}}, \\ I_3 &= \frac{\bar{d} \sin \theta}{(\bar{d}^2 - \bar{e}^2)(\bar{d} + \bar{e} \cos \theta)} \\ &- \frac{2\bar{e}}{(\bar{d}^2 - \bar{e}^2)^{3/2}} \tan^{-1} \frac{(\bar{d} - \bar{e}) \tan \theta/2}{(\bar{d}^2 - \bar{e}^2)^{1/2}} \end{aligned}$$

The expression in equation (1) must be integrated only over those parts of A_j which are visible to dA_k . When A_j is completely visible to dA_k , the integration limits in the θ integral are from 0 to 2π and equation (1) reduces to

$$F_{dA_k-A_j} = \int_x \frac{d\bar{x}}{\cos \eta_j} \left(\frac{\bar{c}}{\bar{e}^2} + \frac{\bar{d} \left(\bar{a} - \frac{\bar{c}^2 \bar{d}}{\bar{e}^2} \right) - \bar{e} \left(\bar{b} - \frac{2\bar{c}\bar{d}}{\bar{e}} \right)}{(\bar{d}^2 - \bar{e}^2)^{3/2}} \right) \quad (3)$$

If A_j is assumed of small width, Δx , no visibility restrictions appear over Δx . The problem then becomes the determination of the integration limits for θ in equation (2), which is determined by the minimum θ for various types of blocking.

The visibility of the narrow ring element A_j to dA_k can be restricted because of three factors, which are: (a) blocking by an intermediate segment, (b) blocking by the horizon (β_k becomes $> \pi/2$), and (c) blocking due to the orientation of A_j (β_j becomes $> \pi/2$). The first is discussed in [1] but the second and third types of blocking are presented for the first time herein.

Blocking by an Intermediate Segment. Blocking occurs when rays from parts of ring element A_j to dA_k are blocked because of the cavity geometry between dA_k and A_j as shown in Fig. 2 [1]. All rays from dA_i that pass through the "throat" at position i are within a cone with its vertex at dA_k . The line of intersection between the cone and a surface perpendicular to the x axis is a circle. In Fig. 2 the part of A_j which lies within the circle is visible to dA_k . It can be shown that the angle ϕ_i is given by

$$\phi_i = \cos^{-1} \frac{r_k^2 (x_j - x_k)^2 - r_i^2 (x_j - x_k)^2 + r_j^2 (x_i - x_k)^2}{2(x_j - x_i)(x_i - x_k)r_j r_k}$$

The two boundary conditions, where ϕ_i is either 0 or π (α is defined in Fig. 2), are

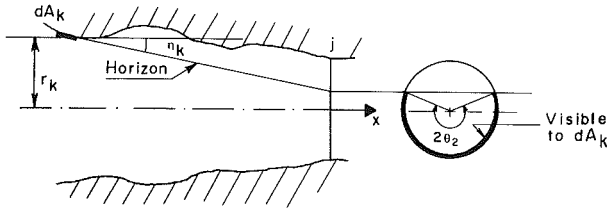


Fig. 3 Blocking by the horizon

$$\phi_i = 0, \text{ if } \alpha_{2i} \leq \tan^{-1} \frac{r_k + r_j}{x_j - x_k},$$

$$\phi_i = \pi, \text{ if } \alpha_{1i} \leq \tan^{-1} \frac{r_k - r_j}{x_j - x_k}$$

Most blocking occurs when ϕ_i is a minimum as a function of the i th cross section. If θ_1 is the integration limit due to blocking by an intermediate segment then θ_1 is given by

$$\theta_1 = \text{Min}(\phi_i), \quad k+1 \leq i \leq j-1$$

Blocking by the Horizon. This type of blocking occurs because the element dA_k sees only the part of A_j which lies beneath an extended plane (the horizon) which is tangent to dA_k . The integration limit for blocking by the horizon θ_2 is given by (see Fig. 3)

$$\theta_2 = \cos^{-1} \frac{(x_j - x_k) \tan \eta_k - r_k}{r_j}$$

For two special cases, θ_2 is given by

$$\theta_2 = 0, \text{ if } (x_j - x_k) \tan \eta_k \geq r_k + r_j,$$

$$\theta_2 = \pi, \text{ if } (x_j - x_k) \tan \eta_k \leq r_k - r_j$$

Blocking Due to the Orientation of A_j . Figure 4 illustrates this case. When β_j , the angle between the ray from dA_k to A_j and the normal to A_j , becomes $\geq \pi/2$, the ray no longer reaches the inner surface of A_j . This restriction will in most cases be accounted for by case (a) above. Due to the integration by finite increments, there are cases when this has to be checked for separately. In Fig. 4 there is no blocking of rays from dA_k to A_j by intermediate segments, but it is clear that the whole area A_j is not visible to dA_k .

The expression for $\cos \beta_j$ is found to be

$$\cos \beta_j = \frac{(x_j - x_k)r_k \tan \eta_k - r_k r_j \sin \phi + r_j^2}{\frac{r_j}{\cos \eta_k} [r_k^2 + r_j^2 - 2r_k r_j \sin \phi + (x_j^2 - x_k^2)]^{1/2}}$$

When $\beta_j = \pi/2$, an expression for ϕ results. The integration limit for blocking due to orientation, $\theta_3 = \phi = \pi/2 + \lambda$ (see Figs. 1 and 4), is

$$\phi_3 = \frac{\pi}{2} + \sin^{-1} \left[\frac{(x_j - x_k) \tan \eta_j + r_j}{r_k} \right]$$

The two extreme cases, where θ_3 is equal to 0 or π , are

$$\theta_3 = 0 \text{ if } -n_j \geq \tan^{-1} \frac{r_k - r_j}{x_j - x_k},$$

$$\theta_3 = \pi \text{ if } \left| \frac{x_j - x_k}{r_k} \tan \eta_j + \frac{r_j}{r_k} \right| \geq 1$$

and

$$-n_j < \tan^{-1} \frac{r_k + r_j}{x_j - x_k}$$

In summary, the shape factor $F_{dA_k-A_i}$ is in general given by

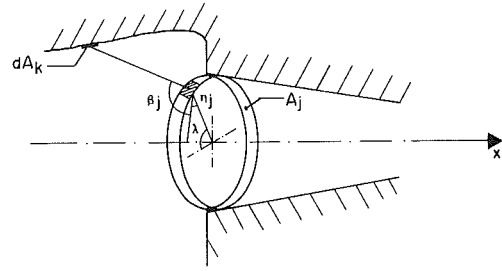


Fig. 4 Blocking due to the orientation of A_j

equation (2) where $\theta = \text{Min}(\theta_1, \theta_2, \theta_3)$. The area-to-area shape factors are given by

$$F_{A_j-A_k} = (1/A_j) \int_{A_k} F_{dA_k-A_j} dA_k \quad (4)$$

If the width of A_k is small, then $F_{dA_k-A_j}$ can be averaged and hence constant over that width for any given θ . From symmetry, $F_{dA_k-A_j}$ is independent of θ ; therefore

$$F_{A_j-A_k} \approx (A_k/A_j) F_{dA_k-A_j} \quad (5)$$

From reciprocity, $F_{A_k-A_j}$ is given by

$$F_{A_k-A_j} = (A_j/A_k) F_{A_j-A_k} = F_{dA_k-A_j} \quad (6)$$

Note that these relations are obtained for areas in which Δx is small, e.g., for finite difference calculations.

Radiation Between Circular and Rectangular Cross Sections

The above results permit a simplified analysis of noncircular cross sections. As an example, we consider rectangular cross sections, with the additional complication of different temperatures on horizontal and vertical walls. The bottom and top or burden walls (b) will be at a lower temperature than the side or reacting warmer walls (w) in this example.

Three cases of interest occur when either the k th or j th or both cross sections are rectangular: (1) circular to rectangular, (2) rectangular to circular, and (3) rectangular to rectangular. The derivations of the radiation energy terms Q_{rad,k_w-j} and Q_{rad,k_b-j} for the three cases are presented below. Radiation energy leaving a surface is considered to be positive. Shape factors from, or to, a rectangular element are calculated using three assumptions:

(I) The rectangular cross section can be treated as circular using the concept of the hydraulic diameter with $d_h = 2(d_z + d_y)/\pi$ where d_z is the width and d_y is the height.

(II) The shape factor from one element to a part of another element, $F_{k-\Delta j}$, is assumed to be equal to the shape factor between the two elements, F_{k-j} , multiplied by the fraction of the receiving area

$$F_{k-\Delta j} = (A_{\Delta j}/A_j) F_{k-j}$$

(III) The shape factor from a part of one element to another element, $F_{\Delta k-j}$ is assumed to be equal to the shape factor from k (whole) to j as obtained per equation (6)

$$F_{\Delta k-j} = F_{k-j}$$

The resulting equations are then of the form

$$Q_{\text{rad},k_w-j} = \sigma F_{k-j} \Omega_k - \sigma F_{j-k} \Omega_j, \quad (7)$$

$$Q_{\text{rad},k_b-j} = \sigma F_{k-j} \Omega_{k_b} - \sigma F_{j-k} \Omega_{j_b} \quad (8)$$

where Ω_k , Ω_j , Ω_{k_b} , and Ω_{j_b} are given by the appropriate expressions derived below.

Radiation From a Circular to a Rectangular Element. The net radiative energy rate exchanged between the two elements is

$$Q_{\text{rad},k-j} = \sigma F_{k-j} A_k T_k^4 - \sigma F_{j_b-k} A_{j_b} T_{j_b}^4 - \sigma F_{j_w-k} A_{j_w} T_{j_w}^4$$

From assumption (III) above, F_{j_b-k} and F_{j_w-k} are equal to F_{j-k} ; hence,

$$\Omega_k = A_k T_k^4 \text{ and } \Omega_j = A_{j_b} T_{j_b}^4 + A_{j_w} T_{j_w}^4$$

Radiation From a Rectangular to a Circular Element. In this case, both Q_{rad,k_w-j} and Q_{rad,k_b-j} have to be accounted for. The net radiation exchange between the vertical wall of the k th section and the j th element is

$$Q_{\text{rad},k_w-j} = \sigma F_{k_w-j} A_{k_w} T_{k_w}^4 - \sigma F_{j-k_w} A_j T_j^4$$

By assumption (III), $F_{k_w-j} = F_{k-j}$ and by assumption (II), $F_{j-k_w} = (A_{k_w}/A_k) F_{j-k}$; hence

$$\Omega_k = A_{k_w} T_{k_w}^4 \text{ and } \Omega_j = (A_{k_w}/A_k) A_j T_j^4$$

The net radiation heat transfer from the horizontal walls to the j th section is given by

$$Q_{\text{rad},k_b-j} = \sigma F_{k_b-j} A_{k_b} T_{k_b}^4 - \sigma F_{j-k_b} A_j T_j^4$$

which, using assumptions (II) and (III), yields

$$\Omega_{k_b} = A_{k_b} T_{k_b}^4 \text{ and } \Omega_{j_b} = (A_{k_b}/A_k) A_j T_j^4$$

Radiation Between Two Rectangular Elements. The net radiative heat transfer between the k th wall and the j th element is

$$Q_{\text{rad},k_w-j} = \sigma F_{k_w-j} A_{k_w} T_{k_w}^4 - \sigma F_{j_b-k_w} A_{j_b} T_{j_b}^4 - \sigma F_{j_w-k_w} A_{j_w} T_{j_w}^4$$

Applying assumptions (II) and (III)

$$\Omega_k = A_{k_w} T_{k_w}^4 \text{ and } \Omega_j = (A_{k_w}/A_k) (A_{j_b} T_{j_b}^4 + A_{j_w} T_{j_w}^4)$$

The net radiant energy rate between the k th burden and the j th element is:

$$Q_{\text{rad},k_b-j} = \sigma F_{k_b-j} A_{k_b} T_{k_b}^4 - \sigma F_{j_b-k_b} A_{j_b} T_{j_b}^4 - \sigma F_{j_w-k_b} A_{j_w} T_{j_w}^4$$

Using assumptions (I)-(II) above

$$\Omega_{k_b} = A_{k_b} T_{k_b}^4 \text{ and } \Omega_{j_b} = (A_{k_b}/A_k) (A_{j_b} T_{j_b}^4 + A_{j_w} T_{j_w}^4)$$

Note in each case that the "driving force" variable for the radiation heat transfer is an AT^4 term. A FORTRAN subroutine for these calculations is available from the authors.

Acknowledgments

This work was performed at West Virginia University and sponsored in part under DOE contract EY-77-C-21-8087 through the Morgantown Energy Technology Center, J. W. Martin, Technical Project Monitor. The authors appreciate the assistance of Barbara Gregory in the preparation of the manuscript.

References

- 1 Robin, W. H., "An Analysis of Thermal Radiation Heat Transfer in a Nuclear-Rocket Nozzle," NASA-TN D-586, 1961.
- 2 Schwartz, S. H., Eddy, T. L., and Nielsson, G. E., "A Simple UCG Cavity Model With Complex Energy Balance," *Proceedings of the 6th Underground Coal Conversion Symposium*, Afton, OK, July 14-17, 1980, pp. III-69-III-83.
- 3 Eddy, T. L., and Schwartz, S. H., "A Side Wall Burn Model for Cavity Growth in Underground Coal Gasification," *ASME Journal of Energy Resources Technology*, Vol. 105, 1983, pp. 145-155.
- 4 Siegel, R., and Howell, J. R., *Thermal Radiation Heat Transfer*, McGraw-Hill, New York, 1972.

Pool Boiling Enhancement of a Modified GEWA-T Surface in Water

Z. H. Ayub¹ and A. E. Bergles²

Introduction

It is becoming increasingly important to improve the performance of heat exchangers involving shellside boiling; hence, boiling at low superheat is highly desirable. This is possible if plain tubes are replaced by tubes with enhanced boiling surfaces. Structured surfaces are a particularly important part of this new technology, and numerous surfaces have been commercialized (Webb, 1981).

Some investigators have developed composite structures, e.g., by wrapping a metal or nylon wire within the grooves of a conventional low fin tube (Webb, 1970; Schmittle and Starner, 1978) or by applying a porous metallic matrix coating over such a tube (Shum, 1980). These modifications resulted in further enhancement of boiling heat transfer. Marto et al. (1985) performed pool boiling tests on a GEWA-T surface (T-shaped fins) in R-113 by wrapping the channels with 0.1-mm-dia copper wires. Three wires resulted in enhancement at all heat fluxes, with particularly significant enhancement at low heat fluxes. At 20,000 W/m² the enhancement factor (defined as a ratio of wall superheats at a fixed heat flux) was 1.7 and 3.7 relative to an unwrapped GEWA-T tube and a plain tube, respectively.

An experimental study was undertaken to examine the boiling behavior of a GEWA-T surface in water using a different type of added material. It was decided to insert into portions of the channels of a GEWA-T test section polystyrene di-vinyl benzene polymer (ordinary kitchen sponge). This potentially combines the enhancement features of porous boiling surfaces with an inexpensive material that can be removed should fouling occur.

Test Facility and Test Section

The test facility and experimental procedure were the same as described by Ayub and Bergles (1985). The test sections were constructed from thick-walled copper tubes of 25.4 mm o.d., 12.7 mm i.d., and 150 mm length. An electrical resistance heater was soldered in the central hole, and thermocouples were located in three 1.4 mm holes equally spaced around the circumference and drilled to a depth of 40 mm from either end of the tube. The reference plain tube was finished with 600 grit abrasive paper; the GEWA-T tube had 740 fins/m with a fin gap of 0.35 mm. Silicone rubber was applied to either end of the tubes to minimize heat loss. The test section was mounted horizontally in a tank of distilled water.

After completing the plain tube and unfilled GEWA-T reference tests, the filler sponge, initially of about 99 percent porosity, was pushed into the channels as shown in Fig. 1 so that it covered the lower 120 deg (180 ± 60 deg) of the test section. Filling the channels partially in this fashion was an arbitrary choice for this exploratory study.

Test section and auxiliary pool heater powers were controlled via powerstats to maintain saturated conditions. A nearly constant liquid level of 10 cm above the test section midplane was maintained. The pressure at the test section was very close to 738 mm of mercury. Prior to each test the pool and test section were degassed for about 2 hr.

¹E. L. Nickell Co., Inc., Constantine, MI 49042.

²Rensselaer Polytechnic Institute, Troy, NY 12180-3590.

Contributed by the Heat Transfer Division for publication in the JOURNAL OF HEAT TRANSFER. Manuscript received by the Heat Transfer Division May 15, 1986.

$$Q_{\text{rad},k-j} = \sigma F_{k-j} A_k T_k^4 - \sigma F_{j_b-k} A_{j_b} T_{j_b}^4 - \sigma F_{j_w-k} A_{j_w} T_{j_w}^4$$

From assumption (III) above, F_{j_b-k} and F_{j_w-k} are equal to F_{j-k} ; hence,

$$\Omega_k = A_k T_k^4 \text{ and } \Omega_j = A_{j_b} T_{j_b}^4 + A_{j_w} T_{j_w}^4$$

Radiation From a Rectangular to a Circular Element. In this case, both Q_{rad,k_w-j} and Q_{rad,k_b-j} have to be accounted for. The net radiation exchange between the vertical wall of the k th section and the j th element is

$$Q_{\text{rad},k_w-j} = \sigma F_{k_w-j} A_{k_w} T_{k_w}^4 - \sigma F_{j-k_w} A_j T_j^4$$

By assumption (III), $F_{k_w-j} = F_{k-j}$ and by assumption (II), $F_{j-k_w} = (A_{k_w}/A_k) F_{j-k}$; hence

$$\Omega_k = A_{k_w} T_{k_w}^4 \text{ and } \Omega_j = (A_{k_w}/A_k) A_j T_j^4$$

The net radiation heat transfer from the horizontal walls to the j th section is given by

$$Q_{\text{rad},k_b-j} = \sigma F_{k_b-j} A_{k_b} T_{k_b}^4 - \sigma F_{j-k_b} A_j T_j^4$$

which, using assumptions (II) and (III), yields

$$\Omega_{k_b} = A_{k_b} T_{k_b}^4 \text{ and } \Omega_{j_b} = (A_{k_b}/A_k) A_j T_j^4$$

Radiation Between Two Rectangular Elements. The net radiative heat transfer between the k th wall and the j th element is

$$Q_{\text{rad},k_w-j} = \sigma F_{k_w-j} A_{k_w} T_{k_w}^4 - \sigma F_{j_b-k_w} A_{j_b} T_{j_b}^4 - \sigma F_{j_w-k_w} A_{j_w} T_{j_w}^4$$

Applying assumptions (II) and (III)

$$\Omega_k = A_{k_w} T_{k_w}^4 \text{ and } \Omega_j = (A_{k_w}/A_k) (A_{j_b} T_{j_b}^4 + A_{j_w} T_{j_w}^4)$$

The net radiant energy rate between the k th burden and the j th element is:

$$Q_{\text{rad},k_b-j} = \sigma F_{k_b-j} A_{k_b} T_{k_b}^4 - \sigma F_{j_b-k_b} A_{j_b} T_{j_b}^4 - \sigma F_{j_w-k_b} A_{j_w} T_{j_w}^4$$

Using assumptions (I)-(II) above

$$\Omega_{k_b} = A_{k_b} T_{k_b}^4 \text{ and } \Omega_{j_b} = (A_{k_b}/A_k) (A_{j_b} T_{j_b}^4 + A_{j_w} T_{j_w}^4)$$

Note in each case that the "driving force" variable for the radiation heat transfer is an AT^4 term. A FORTRAN subroutine for these calculations is available from the authors.

Acknowledgments

This work was performed at West Virginia University and sponsored in part under DOE contract EY-77-C-21-8087 through the Morgantown Energy Technology Center, J. W. Martin, Technical Project Monitor. The authors appreciate the assistance of Barbara Gregory in the preparation of the manuscript.

References

- 1 Robin, W. H., "An Analysis of Thermal Radiation Heat Transfer in a Nuclear-Rocket Nozzle," NASA-TN D-586, 1961.
- 2 Schwartz, S. H., Eddy, T. L., and Nielsson, G. E., "A Simple UCG Cavity Model With Complex Energy Balance," *Proceedings of the 6th Underground Coal Conversion Symposium*, Afton, OK, July 14-17, 1980, pp. III-69-III-83.
- 3 Eddy, T. L., and Schwartz, S. H., "A Side Wall Burn Model for Cavity Growth in Underground Coal Gasification," *ASME Journal of Energy Resources Technology*, Vol. 105, 1983, pp. 145-155.
- 4 Siegel, R., and Howell, J. R., *Thermal Radiation Heat Transfer*, McGraw-Hill, New York, 1972.

Pool Boiling Enhancement of a Modified GEWA-T Surface in Water

Z. H. Ayub¹ and A. E. Bergles²

Introduction

It is becoming increasingly important to improve the performance of heat exchangers involving shellside boiling; hence, boiling at low superheat is highly desirable. This is possible if plain tubes are replaced by tubes with enhanced boiling surfaces. Structured surfaces are a particularly important part of this new technology, and numerous surfaces have been commercialized (Webb, 1981).

Some investigators have developed composite structures, e.g., by wrapping a metal or nylon wire within the grooves of a conventional low fin tube (Webb, 1970; Schmittle and Starner, 1978) or by applying a porous metallic matrix coating over such a tube (Shum, 1980). These modifications resulted in further enhancement of boiling heat transfer. Marto et al. (1985) performed pool boiling tests on a GEWA-T surface (T-shaped fins) in R-113 by wrapping the channels with 0.1-mm-dia copper wires. Three wires resulted in enhancement at all heat fluxes, with particularly significant enhancement at low heat fluxes. At 20,000 W/m² the enhancement factor (defined as a ratio of wall superheats at a fixed heat flux) was 1.7 and 3.7 relative to an unwrapped GEWA-T tube and a plain tube, respectively.

An experimental study was undertaken to examine the boiling behavior of a GEWA-T surface in water using a different type of added material. It was decided to insert into portions of the channels of a GEWA-T test section polystyrene di-vinyl benzene polymer (ordinary kitchen sponge). This potentially combines the enhancement features of porous boiling surfaces with an inexpensive material that can be removed should fouling occur.

Test Facility and Test Section

The test facility and experimental procedure were the same as described by Ayub and Bergles (1985). The test sections were constructed from thick-walled copper tubes of 25.4 mm o.d., 12.7 mm i.d., and 150 mm length. An electrical resistance heater was soldered in the central hole, and thermocouples were located in three 1.4 mm holes equally spaced around the circumference and drilled to a depth of 40 mm from either end of the tube. The reference plain tube was finished with 600 grit abrasive paper; the GEWA-T tube had 740 fins/m with a fin gap of 0.35 mm. Silicone rubber was applied to either end of the tubes to minimize heat loss. The test section was mounted horizontally in a tank of distilled water.

After completing the plain tube and unfilled GEWA-T reference tests, the filler sponge, initially of about 99 percent porosity, was pushed into the channels as shown in Fig. 1 so that it covered the lower 120 deg (180 ± 60 deg) of the test section. Filling the channels partially in this fashion was an arbitrary choice for this exploratory study.

Test section and auxiliary pool heater powers were controlled via powerstats to maintain saturated conditions. A nearly constant liquid level of 10 cm above the test section midplane was maintained. The pressure at the test section was very close to 738 mm of mercury. Prior to each test the pool and test section were degassed for about 2 hr.

¹E. L. Nickell Co., Inc., Constantine, MI 49042.

²Rensselaer Polytechnic Institute, Troy, NY 12180-3590.

Contributed by the Heat Transfer Division for publication in the JOURNAL OF HEAT TRANSFER. Manuscript received by the Heat Transfer Division May 15, 1986.

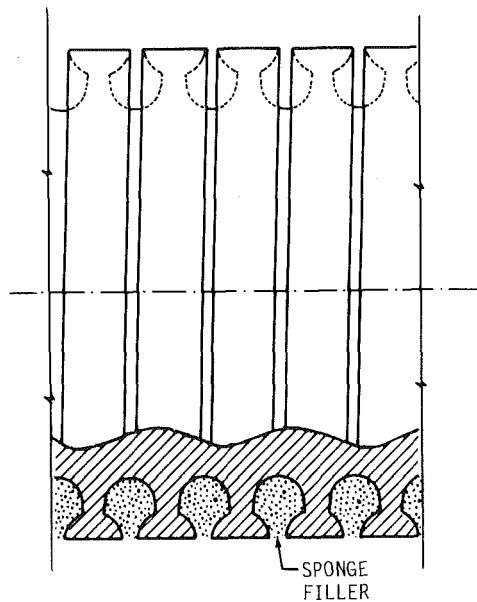


Fig. 1 Sectional view of GEWA-T tube with filler

Test section power was measured by a wattmeter with an accuracy of $\pm 89 \text{ W/m}^2$ at a heat flux of $80,000 \text{ W/m}^2$. The area used for the heat flux is based on the length and the outside diameter. The pool temperature was monitored by three thermocouples immersed in the tank at different locations around the test section. The wall thermocouple readings were adjusted for the small temperature gradients from the thermocouple beads to the smooth tube surface or to the fin base. The uncertainty in average wall superheat is estimated to be $\pm 0.1 \text{ K}$.

Results and Discussion

After reaching saturation, at the initial startup power, many bubbles were observed covering the filled area of the test section. As the heat flux was increased, the overall activity of the bubbles increased. At a heat flux of $65,000 \text{ W/m}^2$, very vigorous boiling was observed. Qualitatively, the overall bubble activity was significantly higher than boiling with the non-filled test section. Large bubbles were observed at the bottom of the test section; the site density there was high compared to the nonfilled area of the tube.

As shown in Fig. 2 the enhancement factor at a heat flux of $80,000 \text{ W/m}^2$ is 1.5 and 2.3 relative to the unfilled GEWA-T tube and the smooth tube, respectively. The enhancement is even greater during the decreasing heat flux mode; for example, at a heat flux of $10,000 \text{ W/m}^2$ the respective enhancement factors are 4.5 and 13.6. A hysteresis phenomenon between increasing and decreasing power is observed that is similar to observations with other porous surfaces (Bergles and Chyu, 1982). This is likely due to activation of large, initially inactive nucleation sites with increasing heat flux; these larger sites remain active with decreasing heat flux.

The normal boiling process with the GEWA-T surface involves vaporization of a thin film of liquid within the channel (Ayub and Bergles, 1987). Bubbles are formed at random circumferential locations; liquid inflow to the film occurs at adjacent regions during a low-pressure portion of the cycle. In the present case the heat transfer in the filled region is enhanced due to increased latent heat transport. The trapped liquid is vaporized at the high-conductivity metallic extended surface and bubbles out through selected pores. Liquid feed takes place through other pores. The increased bubble activity from the filled region also increases the heat transfer at the fin tips.

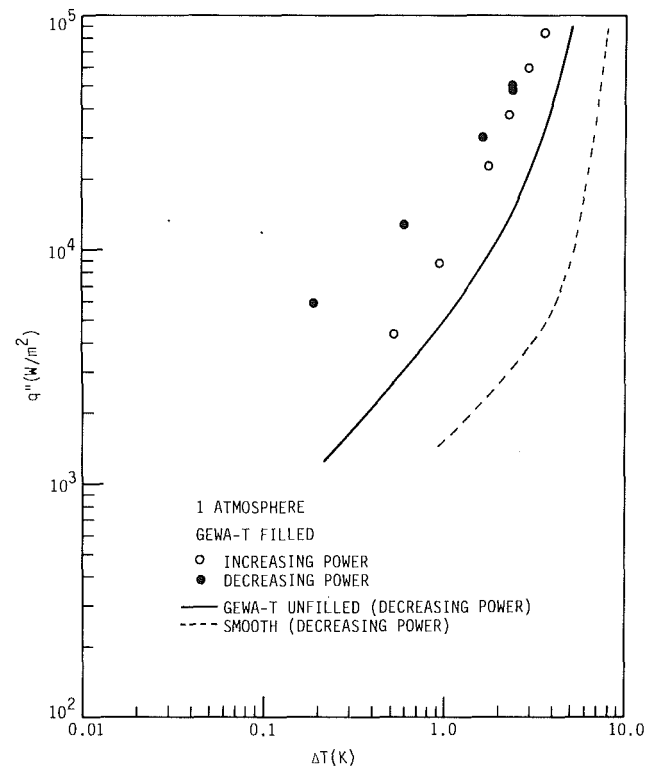


Fig. 2 Nucleate pool boiling data for filled GEWA-T tube compared with data for unfilled tube and plain tube

Bubbles formed at the edge of the filler within the channels enhance the normal boiling heat transfer process in the open portions of the channels.

Conclusions

A GEWA-T surface was tested in a pool of saturated distilled water at atmospheric pressure. The lower portions of all channels of the test section were filled with a sponge. This technique provided a substantial nucleate boiling enhancement relative to an unfilled GEWA-T tube; for example, the enhancement factor was 1.5 at a heat flux of $80,000 \text{ W/m}^2$ and 4.5 at $10,000 \text{ W/m}^2$ (decreasing power). This simple surface modification could be important for some commercial applications.

Acknowledgments

This study was carried out in the Heat Transfer Laboratory of Iowa State University. The authors extend their thanks to the U.S. Department of Energy, for providing funds under Contract DE-FG07-81ID12222, and Mr. Klaus Menze of Wieland-Werke AG, Federal Republic of Germany, for providing the GEWA-T test tube.

References

- Ayub, Z. H., and Bergles, A. E., 1985, "Pool Boiling From GEWA Surfaces in Water and R-113," *Augmentation of Heat Transfer in Energy Systems*, HTD-Vol. 52, ASME, New York, pp. 57-66.
- Ayub, Z. H., and Bergles, A. E., 1987, "Pool Boiling From GEWA Surfaces in Water and R-113," *Wärme- und Stoffübertragung*, Vol. 21, pp. 209-219.
- Bergles, A. E., and Chyu, M.-C., 1982, "Characteristics of Nucleate Pool Boiling From Porous Metallic Coatings," *ASME JOURNAL OF HEAT TRANSFER*, Vol. 104, pp. 279-285.
- Marto, P. J., Wanniarachchi, A. S., and Pulido, R. J., 1985, "Augmenting the Nucleate Pool-Boiling Characteristics of GEWA-T Finned Tubes in R-113," *Augmentation of Heat Transfer in Energy Systems*, HTD-Vol. 52, ASME, New York, pp. 67-73.
- Schmittle, K. V., and Starner, K. E., 1978, "Heat Transfer in Pool Boiling," US Patent No. 4,074,753.

Shum, M. S., 1980, "Finned Heat Transfer Tube With Porous Boiling Surface and Method for Producing Same," US Patent No. 4,182,412.

Webb, R. L., 1970, "Heat Transfer Surface Which Promotes Nucleate Ebullition," US Patent No. 3,521,708.

Webb, R. L., 1981, "The Evolution of Enhanced Surface Geometries for Nucleate Boiling," *Heat Transfer Engineering*, Vol. 2, Nos. 2-3, pp. 46-69.

Effect of Surface Curvature on Laminar Film Condensation

K. Taghavi¹

Nomenclature

- C = constant of integration, equation (7)
- c_p = specific heat of condensate
- $g(x)$ = gravitational acceleration tangent to film surface
- g_{eff} = effective gravity, equation (16)
- h'_{fg} = heat of vaporization corrected for condensate subcooling = $h_{fg} + 0.68 c_p \Delta T$
- k = thermal conductivity of condensate
- Nu = Nusselt number = $q''_w x / k \Delta T$
- Nu_∞ = Nusselt number for a surface with very large radius
- ΔNu = change in Nusselt number due to surface curvature = $Nu - Nu_\infty$
- q''_w = heat flux at wall
- R = dimensionless radius = r/r_0
- R_δ = dimensionless radius at film surface = $(r_0 + \delta)/r_0$
- r = radial coordinate
- r_0 = radial position of wall
- T = temperature
- T_w = wall temperature
- ΔT = difference between saturation temperature and wall temperature
- U = dimensionless velocity = $3\nu u / [g(x)\delta^2]$
- U_b = dimensionless bulk velocity
- u = velocity in the x direction
- u_b = bulk velocity, equation (9)
- x = coordinate along wall
- δ = film thickness
- ϵ = perturbation parameter = δ/r_0
- θ = angle from top stagnation point
- ν = kinematic viscosity of condensate
- ρ = mass density of condensate

Introduction

Nusselt (1916) was the first to study laminar film condensation. He considered condensation on an isothermal vertical wall, assuming negligible inertia and convective effects, a linear temperature profile in the film, and that no shear stress was present at the condensate-vapor interface. Subsequently, Rohsenow (1956) relaxed Nusselt's assumption of a linear temperature profile and accounted for convective terms. The result was an improvement over the Nusselt relation. Thereafter, many studies were conducted in which more of Nusselt's original assumptions were relaxed. Of special importance among these studies were the works by Sparrow and

Gregg (1959) and later by Dhir and Lienhard (1971, 1973). Sparrow and Gregg were able to consider the full boundary-layer type momentum and energy equations by employing a similarity transformation. They presented the results for laminar film condensation for a wide range of Prandtl and Jacob numbers. Dhir and Lienhard (1971, 1973) extended the studies performed by Nusselt (1916) and Sparrow and Gregg (1959) to cases of variable gravity and body shape.

Traditionally, the momentum equation written in Cartesian coordinates has been used as long as the film thickness is much less than the radius of the surface (e.g., Dhir and Lienhard, 1971, 1973). However, no criterion or relation is available for estimating the error involved in such an approximation.

Recently, Churchill (1986) investigated the effect of curvature on laminar film condensation outside and inside of vertical tubes. He found that the effect was significant for Nusselt numbers less than 26.

In this work, laminar film condensation on curved surfaces is considered. It should be noted that the surface curvature considered here is in the direction of the flow. The analysis starts with solving the momentum equation in cylindrical coordinates. The results are then written in terms of the solution for the case of negligible curvature effect, i.e., solution to momentum equation written in Cartesian coordinates, and a correction due to the effect of the curvature of the surface.

Analysis

Figure 1 shows the physical model for film condensation on a curved surface. Although the analysis is, in principle, valid for most curved surfaces, here, for the purpose of illustration, a cylinder is considered. It is assumed that the inertia and convective terms are negligible, the shear at the condensate surface is zero, and the surface tension effects are small. The momentum equation in the r direction may be written as

$$g(x) + \nu \left[\frac{1}{r} \frac{d}{dr} \left(r \frac{du}{dr} \right) - \frac{u}{r^2} \right] = 0 \quad (1)$$

with the following boundary conditions:

$$u = 0 \text{ at } r = r_0 \quad (2)$$

and

$$du/dr = 0 \text{ at } r = r_0 + \delta \quad (3)$$

Equation (2) is the no-slip condition at the wall, while equation (3) implies no shear stress at the free surface. The

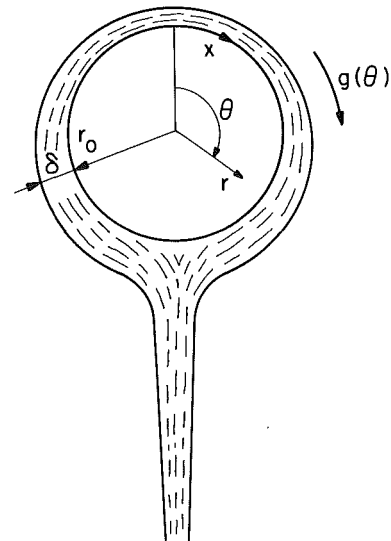


Fig. 1 Physical model for laminar film condensation on a horizontal cylinder

¹Department of Mechanical Engineering, University of Kentucky, Lexington, KY 40506-0046.

Contributed by the Heat Transfer Division for publication in the JOURNAL OF HEAT TRANSFER. Manuscript received by the Heat Transfer Division August 28, 1986.

Shum, M. S., 1980, "Finned Heat Transfer Tube With Porous Boiling Surface and Method for Producing Same," US Patent No. 4,182,412.

Webb, R. L., 1970, "Heat Transfer Surface Which Promotes Nucleate Ebullition," US Patent No. 3,521,708.

Webb, R. L., 1981, "The Evolution of Enhanced Surface Geometries for Nucleate Boiling," *Heat Transfer Engineering*, Vol. 2, Nos. 2-3, pp. 46-69.

Effect of Surface Curvature on Laminar Film Condensation

K. Taghavi¹

Nomenclature

- C = constant of integration, equation (7)
- c_p = specific heat of condensate
- $g(x)$ = gravitational acceleration tangent to film surface
- g_{eff} = effective gravity, equation (16)
- h'_{fg} = heat of vaporization corrected for condensate subcooling = $h_{fg} + 0.68 c_p \Delta T$
- k = thermal conductivity of condensate
- Nu = Nusselt number = $q''_w x / k \Delta T$
- Nu_∞ = Nusselt number for a surface with very large radius
- ΔNu = change in Nusselt number due to surface curvature = $Nu - Nu_\infty$
- q''_w = heat flux at wall
- R = dimensionless radius = r/r_0
- R_δ = dimensionless radius at film surface = $(r_0 + \delta)/r_0$
- r = radial coordinate
- r_0 = radial position of wall
- T = temperature
- T_w = wall temperature
- ΔT = difference between saturation temperature and wall temperature
- U = dimensionless velocity = $3\nu u / [g(x)\delta^2]$
- U_b = dimensionless bulk velocity
- u = velocity in the x direction
- u_b = bulk velocity, equation (9)
- x = coordinate along wall
- δ = film thickness
- ϵ = perturbation parameter = δ/r_0
- θ = angle from top stagnation point
- ν = kinematic viscosity of condensate
- ρ = mass density of condensate

Introduction

Nusselt (1916) was the first to study laminar film condensation. He considered condensation on an isothermal vertical wall, assuming negligible inertia and convective effects, a linear temperature profile in the film, and that no shear stress was present at the condensate-vapor interface. Subsequently, Rohsenow (1956) relaxed Nusselt's assumption of a linear temperature profile and accounted for convective terms. The result was an improvement over the Nusselt relation. Thereafter, many studies were conducted in which more of Nusselt's original assumptions were relaxed. Of special importance among these studies were the works by Sparrow and

Gregg (1959) and later by Dhir and Lienhard (1971, 1973). Sparrow and Gregg were able to consider the full boundary-layer type momentum and energy equations by employing a similarity transformation. They presented the results for laminar film condensation for a wide range of Prandtl and Jacob numbers. Dhir and Lienhard (1971, 1973) extended the studies performed by Nusselt (1916) and Sparrow and Gregg (1959) to cases of variable gravity and body shape.

Traditionally, the momentum equation written in Cartesian coordinates has been used as long as the film thickness is much less than the radius of the surface (e.g., Dhir and Lienhard, 1971, 1973). However, no criterion or relation is available for estimating the error involved in such an approximation.

Recently, Churchill (1986) investigated the effect of curvature on laminar film condensation outside and inside of vertical tubes. He found that the effect was significant for Nusselt numbers less than 26.

In this work, laminar film condensation on curved surfaces is considered. It should be noted that the surface curvature considered here is in the direction of the flow. The analysis starts with solving the momentum equation in cylindrical coordinates. The results are then written in terms of the solution for the case of negligible curvature effect, i.e., solution to momentum equation written in Cartesian coordinates, and a correction due to the effect of the curvature of the surface.

Analysis

Figure 1 shows the physical model for film condensation on a curved surface. Although the analysis is, in principle, valid for most curved surfaces, here, for the purpose of illustration, a cylinder is considered. It is assumed that the inertia and convective terms are negligible, the shear at the condensate surface is zero, and the surface tension effects are small. The momentum equation in the r direction may be written as

$$g(x) + \nu \left[\frac{1}{r} \frac{d}{dr} \left(r \frac{du}{dr} \right) - \frac{u}{r^2} \right] = 0 \quad (1)$$

with the following boundary conditions:

$$u = 0 \text{ at } r = r_0 \quad (2)$$

and

$$du/dr = 0 \text{ at } r = r_0 + \delta \quad (3)$$

Equation (2) is the no-slip condition at the wall, while equation (3) implies no shear stress at the free surface. The

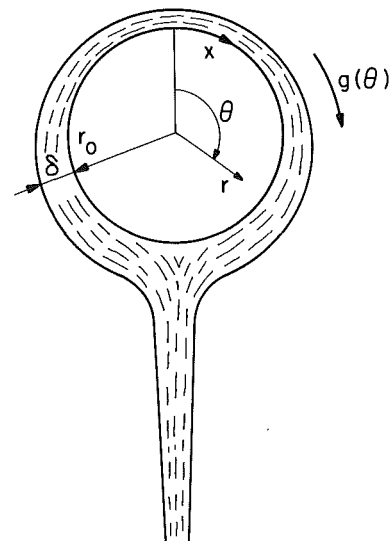


Fig. 1 Physical model for laminar film condensation on a horizontal cylinder

¹Department of Mechanical Engineering, University of Kentucky, Lexington, KY 40506-0046.

Contributed by the Heat Transfer Division for publication in the JOURNAL OF HEAT TRANSFER. Manuscript received by the Heat Transfer Division August 28, 1986.

variables involved in equations (1)–(3) are nondimensionalized as

$$U = 3\nu u / [g(x)\delta^2] \quad (4)$$

and

$$R = r/r_0 \quad (5)$$

It should be noted that in equation (4), the velocity u is normalized by the bulk velocity for the case of no curvature effect (e.g., Lienhard, 1981).

Equation (1) along with the boundary conditions (2) and (3) may be solved analytically for the velocity profile. The result in terms of the nondimensionalized variables is written as

$$U = [CR + (1 - C)/R - R^2]/(R_\delta - 1)^2 \quad (6)$$

where

$$C = (2R_\delta^3 + 1)/(R_\delta^2 + 1) \quad (7)$$

In equations (6) and (7), R_δ is defined as:

$$R_\delta = (r_0 + \delta)/r_0 \quad (8)$$

A bulk velocity can be defined as

$$u_b = \left[\int_{r_0}^{r_0+\delta} u dr \right] / \left[\int_{r_0}^{r_0+\delta} dr \right] \quad (9)$$

In dimensionless form, the bulk velocity becomes

$$U_b = [C(R_\delta^2 - 1)/2 + (1 - C)\ln R_\delta - (R_\delta^3 - 1)/3]/(R_\delta - 1)^3 \quad (10)$$

The temperature profile, neglecting convection, is

$$T - T_w = (\ln R / \ln R_\delta) \Delta T \quad (11)$$

where ΔT is the temperature difference across the condensate film. An energy balance written on an element with the dimensions of dx and δ yields

$$d/dx [\rho u_b \delta h'_g] = kdT/dr|_{r=r_0} \quad (12)$$

Equation (12) may be rewritten by substituting for u_b from equation (4) and for T from equation (11) to get

$$\delta \frac{d}{dx} \left[U_b \delta^3 g(x) \right] = \frac{3\nu k \Delta T}{\rho h'_g} \frac{R_\delta - 1}{\ln R_\delta} \quad (13)$$

The boundary condensate condition for the condensate film is

$$\delta g(x) = 0 \quad \text{at} \quad x = 0 \quad (14)$$

This boundary condition may be thought of as implying a stagnation surface where $\delta(0) = \text{finite}$ and $g(0) = 0$ or a nonstagnation surface where $\delta(0) = 0$ and $g(0) = \text{finite}$.

In order to continue with the analysis, an approximation about the dependence of U_b on x must be made. It is assumed here that U_b is a weaker function of x than is δ or $g(x)$. This approximation, realizing that U_b is the bulk velocity normalized with the bulk velocity for the case of no curvature effect, is reasonable, especially if only the first term in the perturbation is to be retained. The last term on the right-hand side of equation (13) is also, in principle, a function of x . That this term is also a weak function of x may be seen by examining its limit as $R_\delta \rightarrow 1$. Therefore, for the purpose of integration only, it is assumed that U_b and the right-hand side of equation (13) are independent of x . Equation (13) may be integrated with the boundary condition (14). The result is the following expression for δ :

$$\delta = \left[\frac{4\nu k \Delta T x}{\rho h'_g g_{\text{eff}}} \right]^{1/4} \left[\frac{R_\delta - 1}{U_b \ln R_\delta} \right]^{1/4} \quad (15)$$

where, following Dhir and Lienhard (1971), an effective gravity is defined as

$$g_{\text{eff}} = \left[g^{4/3} x \right] / \left[\int_0^x g^{1/3} dx \right] \quad (16)$$

A Nusselt number based on the heat transfer at the wall may be defined and calculated as

$$\text{Nu} = \left[\frac{\rho h'_g g_{\text{eff}} x^3}{4\nu k \Delta T} \right]^{1/4} \left[\frac{U_b^{1/4} (R_\delta - 1)}{\ln R_\delta} \right]^{3/4} \quad (17)$$

In equations (15) and (17), the first term in brackets on the right-hand side is identical to the result that would have been obtained under the assumption of negligible curvature effect, and the second term is the correction due to the effect of curvature. Next, a perturbation parameter ϵ is introduced as

$$R_\delta = 1 + \epsilon \quad (18)$$

which implies that

$$\epsilon = \delta/r_0 \quad (19)$$

The preceding results will be expanded in terms of the perturbation parameter ϵ . Of specific interest are the expansion terms in the velocity and the Nusselt number.

$$U_b = 1 + 3\epsilon/8 - 19\epsilon^2/40 \dots \quad (20)$$

The correction due to the effect of curvature in the Nusselt number relation, equation (17), may now be evaluated using equations (18) and (20)

$$\text{Nu} = \text{Nu}_\infty (1 + 15\epsilon/32 \dots) \quad (21)$$

In equation (21), Nu_∞ is used to denote the Nusselt number when the effect of curvature is neglected. That is

$$\text{Nu}_\infty = \left[\frac{\rho h'_g g_{\text{eff}} x^3}{4\nu k \Delta T} \right]^{1/4} \quad (22)$$

The correction term in equation (21) may also be written as

$$\text{Nu} = \text{Nu}_\infty + \Delta \text{Nu} \quad (23)$$

The term ΔNu may be further calculated by noting that ϵ is δ/r_0 and that $\delta \text{Nu}_\infty = \delta \text{Nu}$. Upon substitution for Nu and δ from equations (17) and (15), ΔNu becomes

$$\Delta \text{Nu} \approx (15/32)x/r_0 \quad (24)$$

For a cylinder, where x may be as large as πr_0 , equation (24) yields the maximum change in the Nusselt number as

$$\Delta \text{Nu} = 1.47 \quad (25)$$

Numerical Verification

In light of the assumptions made in the course of the analysis, it is helpful to compare the present perturbation result with the exact solution. The exact problem, i.e., equation (13), cannot be solved analytically. Therefore, this equation is solved numerically to obtain the corresponding Nusselt

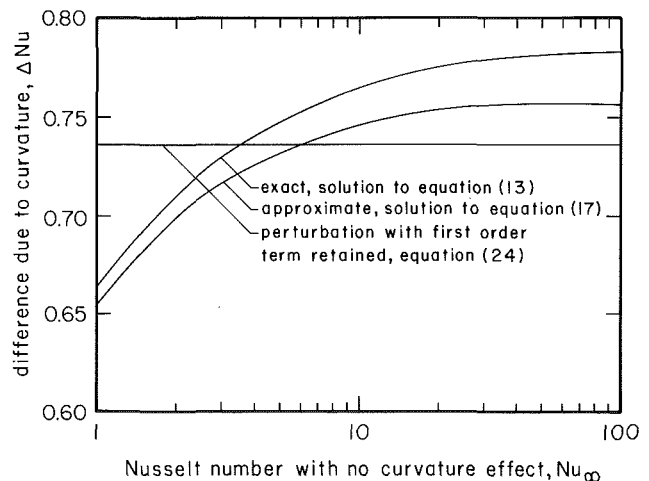


Fig. 2 Comparison of local Nusselt numbers for a cylinder at $\theta = 90$ deg ($x = \pi r_0/2$)

number. The result is then compared both with the approximate relation for the Nusselt number, equation (17), and with the first-order term in the perturbation result, equation (24).

Figure 2 shows the result of the comparison for a cylinder. This figure presents the correction to the local Nusselt number due to the effect of curvature for a cylinder at $\theta = 90$ deg as a function of the Nusselt number. It is seen that, in general, the correction is small for most common situations (e.g., a refrigerant condensing on an 80 K subcooled, 1 cm o.d. horizontal tube) where Nu is usually greater than 100. In some special applications, however, such as condensation under reduced gravity, smaller Nusselt numbers are expected, and consequently, the effect of surface curvature becomes important. Figure 2 also shows that the approximations involved in obtaining equation (15) are valid in the range of Nusselt numbers considered. This figure also indicates that the first term in the perturbation result compares favorably with the exact result.

Summary and Conclusions

The correction to the Nusselt number due to the effect of surface curvature may be written as

$$\text{Nu} = \text{Nu}_\infty + \Delta\text{Nu} \quad (26)$$

A perturbation analysis has revealed that the first-order correction term is not proportional to Nu_∞ , but rather is independent of it. The correction to Nusselt number, ΔNu , obtained from the present work, when compared with Nu_∞ , is a helpful indicator of whether the effect of surface curvature is negligible or not.

For the range of ordinary Nusselt numbers, the assumption of negligible surface curvature is justifiable and accurate. In this range, the error in making such an approximation is less than 1 percent.

References

- Churchill, S. W., 1986, "Laminar Film Condensation," *International Journal of Heat and Mass Transfer*, Vol. 29, No. 8, pp. 1219-1226.
- Dhir, V. K., and Lienhard, J. H., 1971, "Laminar Film Condensation on Plane and Axisymmetric Bodies in Nonuniform Gravity," *ASME JOURNAL OF HEAT TRANSFER*, Vol. 93, pp. 97-100.
- Dhir, V. K., and Lienhard, J. H., 1973, "Similar Solutions for Film Condensation With Variable Gravity or Body Shape," *ASME JOURNAL OF HEAT TRANSFER*, Vol. 95, pp. 483-486.
- Lienhard, J. H., 1981, *A Heat Transfer Textbook*, Prentice Hall, New Jersey, p. 369.
- Nusselt, W., 1916, "Die Oberflächenkondensation des Wasserdampfes," *Zeitschrift des Vereins deutscher Ingenieure*, Vol. 60, pp. 541-546.
- Rohsenow, W. M., 1956, "Heat Transfer and Temperature Distribution in Laminar Film Condensation," *ASME JOURNAL OF HEAT TRANSFER*, Vol. 78, pp. 1645-1648.
- Sparrow, E. M., and Gregg, J. L., 1959, "A Boundary-Layer Treatment of Laminar-Film Condensation," *ASME JOURNAL OF HEAT TRANSFER*, Vol. 81, pp. 13-18.

Transient Experimental Technique for the Determination of the Thermal Diffusivity of Fibrous Insulation

S. P. Rooke¹ and R. E. Taylor²

Introduction

The iron and steel industry has considerable interest in developing improvements in the thermal performance of fur-

nace insulation lining systems, particularly fiberboards and fiberblankets. Currently, conductivity values are often determined using steady-state techniques, which are time consuming for poorly conducting materials. For instance, determining the effective thermal conductivity of a fibrous insulating material over a 1200°C temperature range can take more than 20 h. The current investigation is an attempt to develop a transient technique that will circumvent these long experiment times. The present technique is fundamentally different from the hot-wire and hot-strip techniques, currently the only practical (but limited) transient techniques available for determining the thermal conductivity of insulators.

In 1983, a step heat technique involving planar geometry was presented (Bittle, 1983; Bittle and Taylor, 1984; Bittle and Taylor, 1985) that allowed for the measurement of large-grained and nonfibrous insulators up to 400-500°C. The technique is an extension of the flash technique in that it allows for larger sample sizes and longer heating times. It was found that the step heat technique is inappropriate for fibrous insulators because of boundary condition violations. At the front face of the sample, the assumption of constant heat flux into the surface of a semi-infinite medium being heated with irradiation is invalid for radiant fluxes and time durations typical in measuring poorly conducting materials. In addition, at the rear of the sample where the temperature rise is monitored, the assumption of no heat loss is violated; this is especially true for insulators at elevated temperatures. While the apparatus for the present technique and the step heat technique are similar, the present technique involves the substitution of measured values for mathematical approximations and thus is a marked departure from previous practices.

Diffusivity Determination

A wide variety of refractory insulations can be modeled as radiating and conducting. The model used in this technique assumes that the insulation is isotropic and homogeneous with temperature-independent properties. A diffusion approximation is assumed for the radiant contribution of heat transfer. Under these assumptions the heat equation becomes

$$\frac{\partial^2 T}{\partial x^2} = \frac{1}{\alpha} \frac{\partial T}{\partial t} \quad (1)$$

where α is the effective diffusivity $k_{\text{eff}}/(\rho C_p)_{\text{eff}}$, with k_{eff} and $(\rho C_p)_{\text{eff}}$ being effective or "bulk" values for thermal conductivity and density-specific heat product, respectively.

In the step-heat technique, a constant heat flux condition was imposed at the front face of the specimen with temperatures measured at the back face. The thermal diffusivity was then calculated from an exact solution of the heat equation with constant heat flux applied at the front face. In *modifying the step-heat technique for fibrous insulators*, the constant heat flux condition at the front face is replaced with a temperature condition, which is allowed to be a function of time. Temperatures are measured at the front face of the specimen and at two or more known axial positions within the sample. With temperature measurement locations and temperatures known, the thermal diffusivity can then be inferred by the method of parameter estimation.

The inverse problem of solving for the thermal diffusivity in the heat equation from temperature measurements has been addressed by Beck, who has discussed the problem in detail (Beck, 1964; Beck and Dhanak, 1965) and developed one-dimensional numerical analysis, which was used in obtaining the present results.

In the method, the sum of squares function S

$$S = \sum_{j=1}^m \sum_{i=1}^n [Y_{ij}(\alpha, x, h) - T_{ij}(\alpha, x, t)]^2 \quad (2)$$

¹Thermophysical Properties Research Laboratory, School of Mechanical Engineering, Purdue University, West Lafayette, IN 47906; Assoc. Mem. ASME.

²Senior Researcher, Thermophysical Properties Research Laboratory, School of Mechanical Engineering, Purdue University, West Lafayette, IN 47906.

Contributed by the Heat Transfer Division for publication in the *JOURNAL OF HEAT TRANSFER*. Manuscript received by the Heat Transfer Division October 29, 1986.

number. The result is then compared both with the approximate relation for the Nusselt number, equation (17), and with the first-order term in the perturbation result, equation (24).

Figure 2 shows the result of the comparison for a cylinder. This figure presents the correction to the local Nusselt number due to the effect of curvature for a cylinder at $\theta = 90$ deg as a function of the Nusselt number. It is seen that, in general, the correction is small for most common situations (e.g., a refrigerant condensing on an 80 K subcooled, 1 cm o.d. horizontal tube) where Nu is usually greater than 100. In some special applications, however, such as condensation under reduced gravity, smaller Nusselt numbers are expected, and consequently, the effect of surface curvature becomes important. Figure 2 also shows that the approximations involved in obtaining equation (15) are valid in the range of Nusselt numbers considered. This figure also indicates that the first term in the perturbation result compares favorably with the exact result.

Summary and Conclusions

The correction to the Nusselt number due to the effect of surface curvature may be written as

$$\text{Nu} = \text{Nu}_\infty + \Delta\text{Nu} \quad (26)$$

A perturbation analysis has revealed that the first-order correction term is not proportional to Nu_∞ , but rather is independent of it. The correction to Nusselt number, ΔNu , obtained from the present work, when compared with Nu_∞ , is a helpful indicator of whether the effect of surface curvature is negligible or not.

For the range of ordinary Nusselt numbers, the assumption of negligible surface curvature is justifiable and accurate. In this range, the error in making such an approximation is less than 1 percent.

References

- Churchill, S. W., 1986, "Laminar Film Condensation," *International Journal of Heat and Mass Transfer*, Vol. 29, No. 8, pp. 1219-1226.
- Dhir, V. K., and Lienhard, J. H., 1971, "Laminar Film Condensation on Plane and Axisymmetric Bodies in Nonuniform Gravity," *ASME JOURNAL OF HEAT TRANSFER*, Vol. 93, pp. 97-100.
- Dhir, V. K., and Lienhard, J. H., 1973, "Similar Solutions for Film Condensation With Variable Gravity or Body Shape," *ASME JOURNAL OF HEAT TRANSFER*, Vol. 95, pp. 483-486.
- Lienhard, J. H., 1981, *A Heat Transfer Textbook*, Prentice Hall, New Jersey, p. 369.
- Nusselt, W., 1916, "Die Oberflächenkondensation des Wasserdampfes," *Zeitschrift des Vereins deutscher Ingenieure*, Vol. 60, pp. 541-546.
- Rohsenow, W. M., 1956, "Heat Transfer and Temperature Distribution in Laminar Film Condensation," *ASME JOURNAL OF HEAT TRANSFER*, Vol. 78, pp. 1645-1648.
- Sparrow, E. M., and Gregg, J. L., 1959, "A Boundary-Layer Treatment of Laminar-Film Condensation," *ASME JOURNAL OF HEAT TRANSFER*, Vol. 81, pp. 13-18.

Transient Experimental Technique for the Determination of the Thermal Diffusivity of Fibrous Insulation

S. P. Rooke¹ and R. E. Taylor²

Introduction

The iron and steel industry has considerable interest in developing improvements in the thermal performance of fur-

nace insulation lining systems, particularly fiberboards and fiberblankets. Currently, conductivity values are often determined using steady-state techniques, which are time consuming for poorly conducting materials. For instance, determining the effective thermal conductivity of a fibrous insulating material over a 1200°C temperature range can take more than 20 h. The current investigation is an attempt to develop a transient technique that will circumvent these long experiment times. The present technique is fundamentally different from the hot-wire and hot-strip techniques, currently the only practical (but limited) transient techniques available for determining the thermal conductivity of insulators.

In 1983, a step heat technique involving planar geometry was presented (Bittle, 1983; Bittle and Taylor, 1984; Bittle and Taylor, 1985) that allowed for the measurement of large-grained and nonfibrous insulators up to 400-500°C. The technique is an extension of the flash technique in that it allows for larger sample sizes and longer heating times. It was found that the step heat technique is inappropriate for fibrous insulators because of boundary condition violations. At the front face of the sample, the assumption of constant heat flux into the surface of a semi-infinite medium being heated with irradiation is invalid for radiant fluxes and time durations typical in measuring poorly conducting materials. In addition, at the rear of the sample where the temperature rise is monitored, the assumption of no heat loss is violated; this is especially true for insulators at elevated temperatures. While the apparatus for the present technique and the step heat technique are similar, the present technique involves the substitution of measured values for mathematical approximations and thus is a marked departure from previous practices.

Diffusivity Determination

A wide variety of refractory insulations can be modeled as radiating and conducting. The model used in this technique assumes that the insulation is isotropic and homogeneous with temperature-independent properties. A diffusion approximation is assumed for the radiant contribution of heat transfer. Under these assumptions the heat equation becomes

$$\frac{\partial^2 T}{\partial x^2} = \frac{1}{\alpha} \frac{\partial T}{\partial t} \quad (1)$$

where α is the effective diffusivity $k_{\text{eff}}/(\rho C_p)_{\text{eff}}$, with k_{eff} and $(\rho C_p)_{\text{eff}}$ being effective or "bulk" values for thermal conductivity and density-specific heat product, respectively.

In the step-heat technique, a constant heat flux condition was imposed at the front face of the specimen with temperatures measured at the back face. The thermal diffusivity was then calculated from an exact solution of the heat equation with constant heat flux applied at the front face. In modifying the step-heat technique for fibrous insulators, the constant heat flux condition at the front face is replaced with a temperature condition, which is allowed to be a function of time. Temperatures are measured at the front face of the specimen and at two or more known axial positions within the sample. With temperature measurement locations and temperatures known, the thermal diffusivity can then be inferred by the method of parameter estimation.

The inverse problem of solving for the thermal diffusivity in the heat equation from temperature measurements has been addressed by Beck, who has discussed the problem in detail (Beck, 1964; Beck and Dhanak, 1965) and developed one-dimensional numerical analysis, which was used in obtaining the present results.

In the method, the sum of squares function S

$$S = \sum_{j=1}^m \sum_{i=1}^n [Y_{ij}(\alpha, x, h) - T_{ij}(\alpha, x, t)]^2 \quad (2)$$

¹Thermophysical Properties Research Laboratory, School of Mechanical Engineering, Purdue University, West Lafayette, IN 47906; Assoc. Mem. ASME.

²Senior Researcher, Thermophysical Properties Research Laboratory, School of Mechanical Engineering, Purdue University, West Lafayette, IN 47906.

Contributed by the Heat Transfer Division for publication in the *JOURNAL OF HEAT TRANSFER*. Manuscript received by the Heat Transfer Division October 29, 1986.

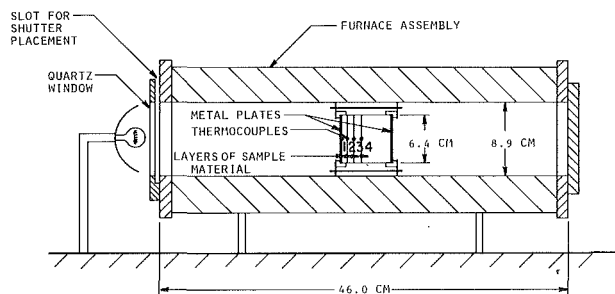


Fig. 1 Cross-sectional view of apparatus and sample

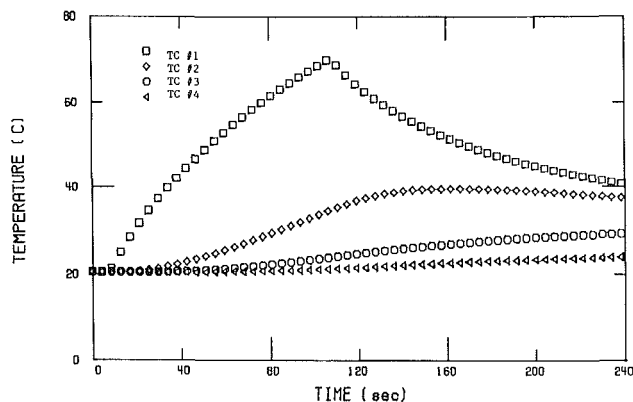


Fig. 2 Time-temperature history for sample with thermocouples arranged as in Fig. 1

is minimized with respect to the thermal diffusivity, so that the diffusivity is estimated to produce the best possible agreement between the experimentally measured temperatures Y_{ij} and the temperatures T_{ij} produced by a finite difference solution of the heat equation subjected to the measured specimen front face temperatures and interior initial conditions. In equation (2), i represents time and j refers to the number of thermocouples not on the boundary. In the analysis, a Crank-Nicolson finite difference solution of the heat equation was implemented.

In addition to accounting for interior temperature measurements and allowing front face temperatures to be a function of time, the parameter estimation technique also allows sequential calculation of the sensitivity of the experiment. Sensitivity analysis produces criteria for best locations for interior thermocouples and experiment times that produce theoretical optimum estimates of the diffusivity (Beck and Dhanak, 1965; Beck and Arnold, 1977).

Experiment Design and Apparatus

In the technique, relatively small sample sizes were necessary to allow transient temperature measurements for experiment durations of 1–4 min. Thermocouple junctions were centered between relatively thin disk-shaped layers of the sample material (layers on the order of 1.0 cm thick), see Fig. 1, and the resulting stack of layers, 6.35 cm in diameter by 4–6 cm thick, was treated as a continuous medium. Thin metal plates of diameter equal to the sample diameter and thickness of 0.050 cm (0.020 in.) were placed against the front and rear of the sample, providing surfaces for the sample holder to contact; the front face plate absorbs the irradiation, and the rear surface of the front plate defines the front boundary of the sample. Typically, three or four thermocouples were used in the specimens. The area thermocouple location generally corresponded to a point within 2–4 cm of the front surface, several cm from the rear surface.

A differential scanning calorimeter was used to obtain

specific heats of the materials, and bulk density of each specimen was calculated from mass and volume measurements.

The thermocouple hot junctions were formed at the center of 0.005 cm (0.002 in.) metallic strips 2 mm × 2 mm in surface area. Type K thermocouple wire with diameter of 0.010 cm (0.004 in.) was used. A clamshell type cylindrical furnace with 8.9 cm (3.5 in.) i.d. with nichrome resistive elements was used (Fig. 1). The rear opening of the furnace was covered with a removable plate made of transite. A quartz window and shutter assembly (manually operated) was used at the front end of the furnace to control the radiant heating of the sample. High temperature Haynes alloy was used for the furnace inner sleeve. The sample holder, constructed from stainless steel threaded rods and end rings, allowed for sample compression and easy sample replacement. The sample was thermally isolated from the sample holder using Macor mounts fastened to the end rings. The radiant source was a 600 W tungsten halogen lamp, focused with a polished aluminum parabolic reflector.

Time-temperature data collection commences with the sample at steady state, a short while after which the lamp is turned on. A typical temperature history for a sample undergoing a transient event is shown in Fig. 2, where the thermocouple positions indicated correspond to Fig. 1. With the lamp on, the shutter is removed a short time after data collection begins, allowing the front face plate of the sample to be irradiated. During the irradiation, the front face temperature rises rapidly ahead of temperature rises experienced within the sample. At a time approximately midway through the data collection, the shutter is often replaced, and the temperatures in the sample respond accordingly. Experiment times were on the order of 2 to 3 min. Typically, 100 to 300 data points per thermocouple were acquired and used in the analysis.

Results and Analysis

Fibrous insulation standards that are certified at elevated temperatures are not available to the scientific community. A fiberboard certified to 90°C by the National Bureau of Standards (SRM 1450b) was used for measurements, as well as a fiberboard calibrated internally to 1000°C by the Manville Corporation (Ceraboard 141). Two less-dense and less-rigid types of insulation were also used: Fiberfrax 3000, a fiber blanket with some binder in it, manufactured by Carborundum Corporation, and Cerwool 2300, a fiber blanket manufactured by C.E Refractories. The bulk densities of the Standard Reference Material and the Ceraboard were approximately 135 and 235 kg/m³, respectively, and the bulk densities of the Fiberfrax and Cerwool were approximately 110 and 65 kg/m³, respectively. Average fiber diameters for all of the materials were in the 2–10 μm range.

Experimental results obtained on the certified NBS-1450b material were generally in good agreement (1–5 percent) with the expected values over the 25–90°C temperature range with the exception of a few tests which were within 10–15 percent. Tests generally were repeatable to within 1–2 percent, but variations from specimen to specimen were typical.

While the specific heat of the materials was measured in the dry state, the moisture content of the samples during diffusivity determination was hard to control over the room temperature to 100°C range, and the results from the NBS and other materials in this range may reflect some effect due to moisture.

The experimental results for the Ceraboard displayed in Fig. 3 indicate, with only few exceptions, that good agreement with the expected diffusivity was obtained over a 1000°C temperature range. As with the NBS material, individual diffusivity points were repeatable, but variations in results be-

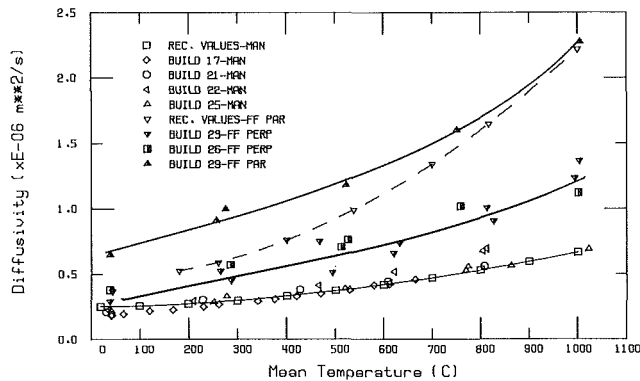


Fig 3 Thermal diffusivity of Carborundum Fiberfrax 3000 (FF) versus temperature, heat flow parallel and perpendicular to fibers and Manville Ceraboard 141 (MAN)

tween different samples for identical test conditions were often substantial.

The experimental results for the Fiberfrax are displayed in Fig. 3. The Fiberfrax is noticeably anisotropic material, with fibers arranged generally in planes parallel to the longitudinal surfaces of the insulation. The diffusivity was measured with heat flow both perpendicular (Builds 23 and 26) and parallel (Build 29) to the fiber planes. The curve of manufacturer's values is for heat flow parallel to the fiber planes (values for heat flow perpendicular to the fiber planes were not available). The results of Build 29 are in good agreement with the manufacturer's values at elevated temperatures, but are noticeably larger below 800°C. Diffusivity values measured with heat flow perpendicular to the fiber planes fell well below the manufacturer's values for heat flow parallel to the fiber planes, as expected.

The Cerwool blanket material is very compressible and manufacturer's values were given for these densities of 67, 96, and 128 kg/m³. The test results for two different sample builds of the material's as-received density of 67 kg/m³ are shown (Fig. 4) to be somewhat above the manufacturer's values, although the trends of the experimental and manufacturer's curves are in good agreement. One of these samples was compressed to 96 kg/m³ and the resulting diffusivities fell somewhat below the as-received density curves. The other sample was compressed from the as-received density to 128 kg/m³, and the results of the tests performed on this compressed build were in good agreement with the manufacturer's diffusivity values for this density range.

Sample homogeneity and the thermocouple location measurements were primary variables in the technique. The Manville material offered good control over both of these, while these variables were less controllable in the Fiberfrax and Cerwool materials. The Cerwool was particularly nonhomogeneous and layer surfaces could not be well defined; thus thermocouple position uncertainty was sizable. It is likely that this consideration explains the difference in experimental and manufacturer's diffusivity curves for the least compressed Cerwool builds.

The encouraging result was the agreement in the trends of the experimental and manufacturer's curves for the as-received density of 67 kg/m³. This indicated that the model used in the technique most probably accounts properly for the radiative contribution to heat transfer within the samples, particularly at elevated temperatures.

From considerations of the errors in the method, the thermocouple position measurement was found to be one of the largest contributors to error. (As the diffusivity has units of m²/s, an error of 5 percent in the thermocouple location measurement causes a 10 percent error in the diffusivity.) For the Cerwool, 10 percent error in thermocouple position

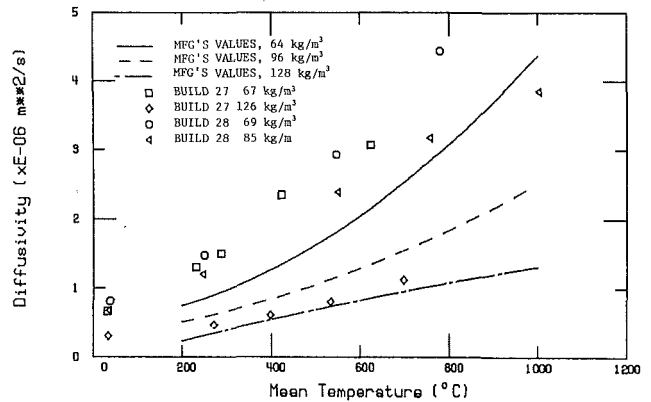


Fig. 4 Diffusivity of C.E. Refractories Cerwool 2300 versus temperature and as a function of density

estimation is quite conceivable, as thermocouple position is dependent from a practical standpoint on the assumptions that the layer thicknesses are accurately known and that the layer faces are parallel. Thus, for materials such as the Cerwool fiberblankets where the layer surfaces cannot be easily defined, the thermocouple positions cannot be as easily determined as in rigid materials, and substantial errors can be introduced in the results.

Beam uniformity incident on the front face of the sample was reasonable, but due to the finite geometry of the sample and the limitations of the furnace temperature conditions at elevated temperatures, two-dimensional heat flow was inherent in the sample. Particularly at elevated furnace temperatures, when temperatures at the furnace i.d. are hotter than the centerline temperatures and the center of the furnace is hotter than the ends of the furnace, radial temperature gradients become as large as 3–5°C/cm. The effects of the two-dimensional heat flow were studied with the aid of a finite element program.

In this program, the material was modeled as having nonuniform steady-state initial temperatures that reflected conditions in the sample with the furnace at 1000°C. In brief, the 3–5°C/cm radial gradients typically present in the sample for furnace temperatures of 1000°C indicated that errors incurred in the measured diffusivity due to two or three-dimensional heat flow were of far less importance than the thermocouple position uncertainty.

Conclusions

The adaptation of the step-heat technique described here for the measurement of the thermal diffusivity, hence thermal conductivity, of industrial fibrous insulations is a feasible alternative to time-consuming steady-state techniques. The time needed to acquire five thermal diffusivity values over a 1000°C temperature range can be as short as 4 h. The technique is suitable for measurements up to 1100–1200°C, and uses a simple tungsten-halogen projection lamp as the heat flux source.

Good agreement between measured and expected diffusivity values was obtained for a dense (240 kg/m³) calibrated fiberboard over a 1000°C temperature range. Poorer agreement was obtained for two compressible fibrous insulations with densities down to 67 kg/m³. The trend in temperature dependence of the diffusivity between experimental and manufacturer's values was similar for a density of 67 kg/m³. This trend suggests that the technique successfully accounts for the strong contribution of radiative heat transfer at elevated temperature. The dominant error introduced in the technique is thermocouple locations measurement error, which explains the disparities between measured and expected diffusivity values of the less dense materials tested. While

small sample sizes compared to steady-state techniques are utilized, the ability to use several layers per sample and to distribute thermocouples throughout the sample allows one to examine the effects of nonhomogeneities in the material. The application of parameter estimation techniques to the measurement of thermal diffusivity of fibrous insulators is novel and offers several advantages over steady-state techniques. Improvements in the accuracy of thermocouple locations, possibly using X-ray or electromagnetic techniques, would be a good extension of this work.

Acknowledgments

This work was performed under a grant by the American Iron and Steel Institute and their support was greatly appreciated. The authors would also like to acknowledge Dr. James V. Beck of Michigan State University for invaluable assistance with the analytical and computational aspects of the project. Similar assistance from Dr. Robert L. Shoemaker of

the Thermophysical Properties Research Laboratory was also greatly appreciated.

References

- Bittle, R. R., 1983, "A Step Heating Method for Measuring Thermal Diffusivity," M.S. Thesis, Mechanical Engineering Dept., Purdue University, Lafayette, IN.
- Bittle, R. R., and Taylor, R.E., 1984, "A Step Heating Technique for Thermal Diffusivity Measurements of Large-Grained Heterogeneous Materials," *Journal of the American Ceramic Society*, Vol. 67, No. 3.
- Bittle, R. R., and Taylor R. E., 1985, "Thermal Diffusivity of Heterogeneous Materials and Non-fibrous Insulators," *Proceedings of the Eighteenth International Conference on Thermal Conductivity*, T. Ashworth and C. Smith, eds., p. 379.
- Beck, J. V., 1964, "The Optimum Analytical Design of Transient Experiments for Simultaneous Determinations of Thermal Conductivity and Specific Heat," Ph.D. Dissertation, Mechanical Engineering Dept., Michigan State University, East Lansing, MI.
- Beck, J. V., and Dhanak, A. M., "Simultaneous Determination of Thermal Conductivity and Specific Heat," ASME Paper No. 65-HT-14.
- Beck, J. V., and Arnold, K. J., 1977, *Parameter Estimation in Engineering*, Wiley, New York.

